Motors on track:

Insights in kinesin function and regulation

ISBN: 978-94-6416-243-1

The studies described in this thesis were performed at the division of Cell Biology at the Faculty of Science of Utrecht University in Utrecht, The Netherlands.

The printing of this thesis was financially supported by Alzheimer Nederland.

Main cover and chapter introductions: Microscopy is the main technique used in this thesis. With a nod to the microscope, I used mirrors to make a kaleidoscope and used this optical instrument to make close up images of plant leafs. Although you can only see a small part of the plant, we get an idea how the plant as a whole looks like. We try to do something similar behind the microscope; we look at cells and try to understand the bigger picture of life.

Print: Ridderprint | www.ridderprint.nl

Copyright © Peter Jan Hooikaas, 2020
All rights reserved

Motors on track:
Insights in kinesin function and regulation

Motoreiwitten op de rit:
Inzichten in de functie en regulatie van kinesines

(met een samenvatting in het Nederlands)

Proefschrift

ter verkrijging van de graad van doctor aan de
Universiteit Utrecht
op gezag van de
rector magnificus, prof.dr. H.R.B.M. Kummeling,
ingevolge het besluit van het college voor promoties
in het openbaar te verdedigen op

maandag 14 december 2020 des middags te 2.30 uur

door

Peter Jan Hooikaas

geboren op 16 juni 1991
te Hardinxveld-Giessendam

Promotor:

Prof. dr. A.S. Akhmanova

Table of contents

Chapter 1	General Introduction	7
Chapter 2	MAP7 family proteins regulate kinesin-1 recruitment	41
Chapter 3	Concerted action of kinesin-1 KIF5B and kinesin-3 KIF13B promotes efficient transport of exocytotic vesicles to microtubule plus ends	75
Chapter 4	MAP7D2 contains a conserved motif that can tether clathrin to microtubules	113
Chapter 5	Direct observation of dynamic protein interactions involving human microtubules using solid-state NMR spectroscopy	131
Chapter 6	MKLP2 is a motile kinesin that transports the Chromosomal Passenger Complex during anaphase	151
Chapter 7	Kinesin-4 KIF21B limits microtubule growth to allow rapid centrosome polarization in T cells	179
Chapter 8	General discussion and future perspectives	221
Addendum	Summary	242
	Nederlandse samenvatting	244
	Korte samenvatting voor niet-wetenschappelijk publiek	246
	Curriculum Vitae	247
	List of publications	248
	Dankwoord	249

1

General introduction

Peter Jan Hooikaas[1]

---

[1] Cell Biology, Department of Biology, Faculty of Science, Utrecht University, Padualaan 8, 3584 CH Utrecht, the Netherlands

We humans are multicellular organisms made up of trillions of cells. These cells are organized in different types of organs and tissues where they fulfill a specialized and dedicated function. A network of blood vessels, veins and lymphatic vessels makes sure that cells within tissue have access to nutrients and have an exit to secrete compounds. Within cells, a miniature world exists, where organelles fulfill various tasks that are essential for cell maintenance and cellular function. Like organs, cellular organelles depend on the physical in- and output of molecules, which often requires transport. For that purpose, many types of human cells rely on a microtubule cytoskeleton, a network of dynamic polymers that connects organelles and also provides a connection to the cortex of the cell where secretion to the extracellular space may occur. The microtubule network is like a highway system where specialized motor proteins perform a dedicated task of transporting cargo to specific cellular sites. Cargo transport is a regulated process, as it is important that motor proteins deliver the right cargo to the right location at the right time. However, microtubules also require maintenance. Therefore, some motor proteins have the specialized task to steer the assembly and disassembly of microtubule polymers. Here, we will discuss how motor transport can be regulated in our cells and how various different motor types can regulate the (dis)assembly of microtubule networks in cells.

1. Microtubules

Microtubules are long and hollow polymers that extend throughout the cytoplasm. A single microtubule has a fixed width of 25 nm (Burton et al., 1975; Tilney et al., 1973), but its length varies and can reach up to tens of micrometres. The main building block of these polymers is tubulin: a heterodimer that consists of two very conserved globular proteins: α- and β-tubulin, which differ slightly in protein structure. Tubulin heterodimers polymerize by binding in a head to tail fashion to form protofilaments. By itself, a protofilament is a very unstable structure that does not exist in a stable form in cells. Lateral contacts between protofilaments stabilize the polymer and give rise to sheet-like structure which can be closed into a tube to form a microtubule (Brouhard and Rice, 2018). Most mammalian microtubules consists of 13 protofilaments, although tubules containing one or two filaments less or more can also be formed (Aher and Akhmanova, 2018). Polymerization of microtubule protofilaments takes place in parallel at the microtubule ends, where, during stable growth, only minor differences in protofilament length occur. The minus-ends expose the α-tubulin part of the heterodimer and this side of the tubule undergoes slow growth or, most often, is capped and stabilized in cells. In contrast, the microtubule plus ends that expose β-tubulin into the exterior are highly dynamic and generally grow much faster (Aher and Akhmanova, 2018; Brouhard and Rice, 2018). Thus, microtubules are intrinsically polarized structures, a feature that is crucial for their function as part of the intracellular cytoskeletal network.

Dynamic instability

Microtubules are intrinsically dynamic meaning that they can by themselves switch from a state of growth to shrinkage. Such a switch is called a catastrophe, and these occur stochastically in the lifetime of a microtubule. This phenomenon is known as “dynamic instability” and explains why a cell can contain both growing and shrinking microtubules at the same time (Desai and Mitchison, 1997). The structural basis to explain how microtubules can switch states so rapidly involves GTPase activity of the tubulin heterodimer. Both α- and β-tubulin contain a GTP when they are present in the cytosol as free tubulin. While the GTP of α-tubulin is not exchanged or hydrolysed, the GTP of β-tubulin is quickly converted to GDP after incorporation into a protofilament. It has been shown that head to tail docking of α-tubulin to β-tubulin is required for GTP hydrolysis; consequently, hydrolysis and polymerization are coupled as a process. Hydrolysis of GTP induces a conformational change where the normally straight tubulin dimer gets a slight outward bend. This bend puts stress on the microtubule lattice, but these outward forces are contained by lateral interactions between protofilaments and the freshly incorporated tubulin dimers at the plus end which are still in the straight GTP-state conformation during polymerization. The part of the microtubule, rich in GTP-bound tubulin subunits, at the growing microtubule end is referred to as “the GTP cap”. Microtubules that lose this cap are more prone to undergo catastrophe as the outward bending forces of GDP-tubulin dimers become exposed at the tip. Because of this outward bending force, depolymerizing microtubules that were observed by electron microscopy have been described to have the shape of a banana peel or trumpet horn (Brouhard and Rice, 2018; Desai and Mitchison, 1997; Mandelkow et al., 1991).

2. Microtubule associated proteins

The formation and maintenance of complex microtubule arrays in cells requires a special and diverse class of proteins: Microtubule Associated Proteins (MAPs). In broad terms, this group of proteins can be subdivided into motor MAPs and non-motor MAPs. The first group of MAPs consists of dynein and kinesin proteins, which will be discussed in section 3. The group of non-motor MAPs is a very heterogenous and can be subdivided based on function: 1) microtubule nucleators; 2) minus-end binding proteins 3) lattice binding MAPs (which are also referred to as structural MAPs); 4) severing enzymes that break microtubules and 5) plus-end tracking proteins (+TIPs). We will discuss these non-motor MAPs, categorized in order from the minus towards the plus end of the microtubule.

2.1 At the minus ends

Microtubule polymerization is initiated by a nucleation event where a tubulin oligomer is formed. In cells, such events are not believed to occur spontaneously in the absence of co-factors as nucleation has to overcome a large energy barrier and thus requires a very high tubulin concentration (Roostalu and Surrey, 2017). Instead, microtubule nucleation is mostly mediated by the γ-tubulin ring complex (γ-TURC), a large protein complex where several co-factors organize γ-tubulin subunits in a ring to form a template for incoming tubulin dimers. The current view is that several MAPs such as Ch-TOG, TPX2 and CLASPs contribute to γ-TURC-mediated microtubule nucleation by promoting polymerization or suppressing catastrophes, as γ-TURC alone is not an efficient nucleation factor *in vitro*. Alternatively, a combination of polymerization-promoting MAPs may induce template-independent nucleation in cells as these MAPs can locally lower the critical tubulin concentration for spontaneous nucleation. This idea is supported by experimental data where microtubule nucleation in cells was still observed in the absence of active γ-tubulin (Roostalu and Surrey, 2017).

After nucleation, many microtubules remain associated to the γ-TURC, but a subpopulation of microtubules detach from the nucleation site and subsequently become stabilized by members of the minus-end targeting family of Calmodulin Regulated Spectrin Associated Protein (CAMSAP) proteins (Akhmanova and Hoogenraad, 2015). CAMSAP proteins specifically recognize the minus-end structure of the microtubule through their CKK domain and decorate a few micron of the lattice from to the minus end (Atherton et al., 2017a; Atherton et al., 2019; Jiang et al., 2014). Next to the physical stabilization of the microtubule, CAMSAP proteins also bind other cellular factors that localize and anchor microtubule minus ends to specific sites, to organize the pool of acentrosomal microtubules in cells. For instance, CAMSAP-stabilized microtubules can be anchored at the Golgi Apparatus through a protein complex of A-kinase anchoring protein of 450 kDa (AKAP450) and Myomegalin (Wu et al., 2016). Additional interactions between this complex and the microtubule-lattice through End-binding protein 1 and 3 (EB1/EB3) and Cytoplasmic linker associated proteins (CLASPs) contribute to microtubule anchorage at Golgi sites (Yang et al., 2017). In specialized cell systems, such as epithelial cells, CAMSAP-stabilized microtubules are specifically anchored at the apical membrane through an interaction with the spectraplakin ACF7 (Khanal et al., 2016; Noordstra et al., 2016). CAMSAPs are not the only proteins that can autonomously recognize and bind microtubule minus ends. The abnormal spindle-like microcephaly-associated protein (ASPM) localizes to spindle poles where it binds to the minus ends and regulates microtubule disassembly in a complex with the microtubule severing enzyme katanin (Akhmanova and Steinmetz, 2019; Jiang et al., 2017). Another minus-end binding protein complex during mitosis is the KAT8-associated non-specific lethal (KANSL) complex, of which the KANSL3 subunit can specifically recognize the minus end of kinetochore fibres to promote their stability (Akhmanova and Steinmetz, 2019; Meunier et al., 2015). These recently discovered examples show that many more minus-end binding proteins may exist.

MAPs can also assist in the nucleation and anchorage of microtubules along the lattice of an existing microtubule. This branching nucleation is mediated via the γ-TURC together with the multi-subunit complex HAUS/augmin, which binds the microtubule lattice and recruits a γ-TURC to nucleate a new microtubule in a branch-like orientation. This type of nucleation by the HAUS/augmin complex is important for building the mitotic spindle (Sanchez-Huertas and Luders, 2015); in addition, recent work indicates that microtubule branching by HAUS/augmin is also important for the microtubule network in neurons (Cunha-Ferreira et al., 2018).

2.2 Along the lattice

Early biochemical work on tubulin relied on the polymeric character of microtubules, as they were purified from cell extracts using cycles of temperature-dependent assembly and disassembly. With this purification method, proteins that strongly bind microtubules would often be co-purified and these proteins were subsequently identified as MAPs. The first MAPs that were identified with this approach came from brain extracts, such as MAP1, MAP2 and tau, or from HeLa cell lysates, such as MAP4 and MAP7. It was shown that these nowadays well-known MAPs are very potent at promoting microtubule polymerization and that they can form very stable microtubules, that were often prone to bundling *in vitro* (Bodakuntla et al., 2019). The main experimental challenge with studying these proteins is that overexpression of MAPs, or the addition of a MAP to microtubules *in vitro*, often causes artefacts such as microtubule bundling and over-stabilization of the lattice. This likely occurs because such an approach does not take into account physiological protein levels, competing factors or regulation through post-translational modifications (Bodakuntla et al., 2019). In more detail, positively charged MAPs are capable of shielding off the highly negatively charged tubulin C-terminal tails resulting in a decreased electrostatic repulsion between microtubules and therefore causing them to bundle. This principle is strengthened by the observation that subtilisin-treated microtubules, which lack C-terminal tails, are more prone to form bundles even in the absence of MAPs (Sackett et al., 1985). Therefore, even today, it is not trivial to determine the function of a lattice-binding MAP. Nevertheless, several functions of lattice-binding MAPs have been identified over the years and these include: 1) forming crosslinks between cytoskeletal components; 2) regulating microtubule orientation and spacing; 3) microtubule severing; 4) protecting microtubules from severing; 5) regulating intracellular transport. The latter function will be reviewed in section 4 of this chapter.

Many MAPs are not highly structured proteins and often rely on intrinsically disordered regions to associate with the microtubule lattice (Bodakuntla et al., 2019; Drechsler et al., 2019). Structurally, this has been demonstrated for the protein tau which binds longitudinally without the involvement of secondary protein folds (Kellogg et al., 2018). These types of interactions are mainly governed by electrostatic interactions of the positively charged MAP with the negatively charged microtubule lattice. This has been demonstrated by a study where a multivalent synthetic peptide was able to show MAP-like behaviour through electrostatic binding of microtubules *in vitro* (Drechsler et al., 2019). Next to the established structural MAPs, many non-cytoskeletal proteins may thus exhibit weak microtubule binding through charged intrinsically disordered regions, which can contribute to various cellular processes.

As indicated above, several MAPs have been described to be able to link microtubules to actin, such as ACF7 (Leung et al., 1999) and Dystrophin (Prins et al., 2009). Members of the MAP2/Tau family can also bind actin filaments, but also have been reported to bind some intermediate filaments such as vimentin (Bodakuntla et al., 2019). While actin-microtubule crosstalk has been well studied, little is known about the physical links between microtubules and intermediate filaments. *In vitro* studies indicate that vimentin can directly interact with microtubule polymers and that these filaments can affect microtubule growth dynamics (Schaedel et al., 2020). In addition, cellular experiments show that kinesin-1 can interact with and transport neurofilaments (Uchida et al., 2009), vimentin and keratin filaments (Robert et al., 2019). Connections between microtubules and other cytoskeletal structures can thus be established by both motor and non-motor MAPs.

Many MAPs can efficiently bundle and organise microtubules. For example, the highly conserved Protein Regulator Of Cytokinesis 1 (PRC1) can potently generate anaphase microtubule bundles with an antiparallel orientation (Bieling et al., 2010; Subramanian et al., 2010). In contrast, the axon initial segment protein tripartite motif containing 46 (TRIM46) generates microtubule bundles in a parallel orientation and also determines the spacing between individual microtubules (Harterink et al., 2019; van Beuningen et al., 2015). The observation that MAPs can determine the spacing in organized microtubule bundles has been identified early on using electron microscopy on microtubule bundles caused by MAP overexpression. In these studies, it was found that the dendritic MAP2 induced bundles with larger distances between microtubules compared to bundles that where formed by axonal tau proteins and that this correlates to the spacing found between microtubules in both dendrites and axons (Chen et al., 1992). During mitosis, a microtubule-binding complex of clathrin, TACC3 and Ch-TOG form inter-microtubule bridges that stabilize kinetochore fibres. In the absence of clathrin, kinetochore fibres contain fewer microtubule and microtubule cross-bridges (revealed by electron microscopy), indicating that additional MAPs may be involved in the formation or stabilization of kinetochore fibres (Booth et al., 2011; Royle, 2012).

A special type of MAPs with an enzymatic activity are microtubule severing enzymes, which in mammals are represented by three structurally related proteins, katanin, spastin, and fidgetin. These enzymes rely on an AAA catalytic core that can extract tubulin dimers from the lattice in an ATP-driven process. Additional domains of these enzymes have microtubule binding properties (McNally and Roll-Mecak, 2018). For example, katanin consists of two subunits: the AAA-containing p60 subunit that severs microtubules and a WD40-containing p80 subunit which has microtubule affinity and is required for targeting p60 to specific sites (Faltova et al., 2019; McNally and Roll-Mecak, 2018). In particular, the minus-end binding proteins CAMSAP and ASPM can recruit the p80 subunit to induce regulated microtubule severing (Jiang et al., 2018; Jiang et al., 2017). Other lattice-binding MAPs, such as MAP2 and tau, can protect microtubules from severing enzymes (Qiang et al., 2006).

2.3 At the tips

MAPs that specifically localize at growing microtubule ends are categorized as +TIPs. In general, these end-tracking proteins only target growing, but not depolymerizing ends. A great number of +TIP have been identified thus far, and new tip-tracking proteins are identified on a regular basis. The key players in microtubule plus-end recognition and tracking are the family of EB proteins and these proteins serve as a binding hub for most other +TIPs. EBs recognize microtubules through an N-terminal Calponin homology domain and form dimers through a coiled coil domain, which is part of the so-called EB homology (EBH) domain. The EBs terminate with an acidic tail that contains a C-terminally EEY/F motif, similar to the C-terminus of α-tubulin (Akhmanova and Steinmetz, 2010). Since EBs are such a central player at growing microtubule ends, these proteins are frequently used to visualize microtubule growth, both in cells as *in vitro*. When a microtubule loses the GTP cap, it switches from growth to shrinkage; this event coincides with the loss of EB signal at the tip, indicating that EB localization may be indicative of the GTP cap. In recent work, tubulin mutants with slow and blocked GTP hydrolysis were shown to create long GTP cap structures which stabilized microtubule plus ends. EB proteins were able to bind along these elongated GTP cap structures, showing that EBs have an increased affinity for GTP microtubule lattices and may thus indeed be regarded as markers of the GTP cap (Roostalu et al., 2020).

A large number of +TIPs contain one or several SXIP amino acid motifs (X = any amino acid) which recognize and bind the EBH domain of EB proteins. Consequently, plus-end binding of SXIP-containing +TIPs is dependent on the presence of EBs (Honnappa et al., 2009). Many proteins containing an SXIP motif have been identified, of which many are cytosolic proteins; in addition, some +TIPs can form links with organelles, actin and the cell cortex (Akhmanova and Steinmetz, 2010). Another class of +TIPs contains a cytoskeleton-associated protein glycine-rich (CAP-Gly) domain. This small globular domain contains a hydrophobic cavity that can bind the C-terminal EEY/F motif of both α-tubulin and EBs (Akhmanova and Steinmetz, 2010). TOG domains are tubulin-binding domains that are also involved in plus-end association; proteins containing domains of this type are often involved in microtubule polymerization and stabilization of the GTP cap. Although TOG-domain containing proteins bind plus-end structures independently of EBs, some TOG domain-containing proteins such as CLASPs also contain an SXIP motif to support plus-end binding (Akhmanova and Steinmetz, 2010).

3. Motor proteins: dynein and kinesin

3.1 Dynein

Dynein is the main motor that drives intracellular transport directed to the minus-end of microtubules. There are more than 15 genes that encode a dynein heavy chain (DHC), although most of these heavy chains are cilia- and flagella-specific where they are important for bending of the axoneme (Kardon and Vale, 2009). Cytoplasmic dynein 1 and 2 are transporting motors; cytoplasmic dynein 1 (in short: dynein) is the main motor involved in retrograde transport, while cytoplasmic dynein 2 is dedicated to retrograde transport in cilia (Reck-Peterson et al., 2018).

In humans, DHC forms the core of a large dimeric multiprotein complex (> 1 mDa) that contains several other subunits required for dynein function. DHC contains a characteristic ring-shaped structure composed of six AAA+ domains that form the catalytic motor domain of the complex. ATP hydrolysis that drives stepping of the complex is only exerted by one of the AAA+ domains; the remaining domains regulate ATP hydrolysis of the catalytic active domain. The AAA+ ring does not bind microtubules itself; this function is performed by a small globular domain that binds the microtubule lattice and is directly involved in stepping. This microtubule binding domain is attached to a stalk region that loops out of the DHC between the fourth and fifth AAA+ domain (Bhabha et al., 2016). The length and orientation of the stalk is important for the minus-end specific motility of dynein (Can et al., 2019). For motility, dynein requires another large protein complex (> 1 mDa), called dynactin. One of the subunits of this complex is p150glued, which contains a CAP-Gly domain that forms an additional tether to microtubules to promote processivity of the dynein complex. However, dynein and dynactin only weakly bind each other *in vitro*. The N-terminus of Bicaudal D homologue 2 (BICD2) was shown to promote the interaction between dynein and dynactin to increase processivity (Reck-Peterson et al., 2018; Splinter et al., 2012). Next to BICD2, several other dynein activating adaptors have been identified that can specify dynein transport and cargo binding (Reck-Peterson et al., 2018). Interestingly, recent work has demonstrated that some adaptors such as BICDR1 and Hook3 can recruit a second dynein to a single dynactin complex, which makes the complex move faster, whereas BICD2 is biased to recruiting a single dynein (Urnavicius et al., 2018). How the wide variety of dynein adaptor proteins specify cargo and how these adaptors affect dynein motility parameters remains a very active field of research.

3.2 Kinesin

Kinesins are generally known as the cargo transporters of the cell. This superfamily contains more than 40 different genes that are subdivided into 15 kinesin families based on phylogeny (Figure 1) (Lawrence et al., 2004). Unlike dynein, which functions in a multi-component protein complex, kinesins are mostly homodimers with a similar building plan: A linker region connects the motor domains to the rest of the kinesin which contains coiled coil domains and a tail region. The coils and tails of the kinesin are typically involved in dimerization of the motor and binding to adaptor proteins and cargo (Hirokawa et al., 2009). The most conserved part of the kinesins is the motor domain, which uses ATP to drive conformational changes resulting in an hand-over-hand locomotion by which a kinesin moves along the microtubule lattice (Verhey et al., 2011b). Most kinesin families are N-KIFs, where the motor domain is located at the N-terminus of the kinesin and is responsible for plus-end directed motility. Members of the kinesin-14 family are C-KIFs; their motor domain is located at the C-terminus and consequently, these motors are exclusively minus-end directed. Kinesin-13 members are M-KIFs; these motors have the motor domain in the middle of the protein and only move in a diffusive manner (Helenius et al., 2006; Hirokawa et al., 2009). However, the M-KIF definition may be arbitrary as several N-KIFs, such as the kinesin-3 KIF14 (Zhernov et al., 2020), the kinesin-6 KIF20A (Atherton et al., 2017b) and the kinesin-11 KIF26A (Zhou et al., 2009) contain an intrinsically disordered region located at the N-terminus of the motor domain which, in principle, would make them M-KIFs as well. The kinesin nomenclature is not straightforward, as the numbered KIF genes do not match the numerical categorization of kinesin family names. On top of that, many kinesins are better known under a different name, such as KIF11 “Eg5” or KIF20A “MKLP2”. Alternative to a complex nomenclature, kinesins can also be organized according to their motility parameters, stoichiometry, functionality or specific tissue or cellular localization (Figure 1).

4. Kinesin function

4.1 Kinesins involved in intracellular transport during interphase

Kinesin-1, -2 and -3 motors are the major cargo-transporting kinesins in cells. Kinesin-1 was

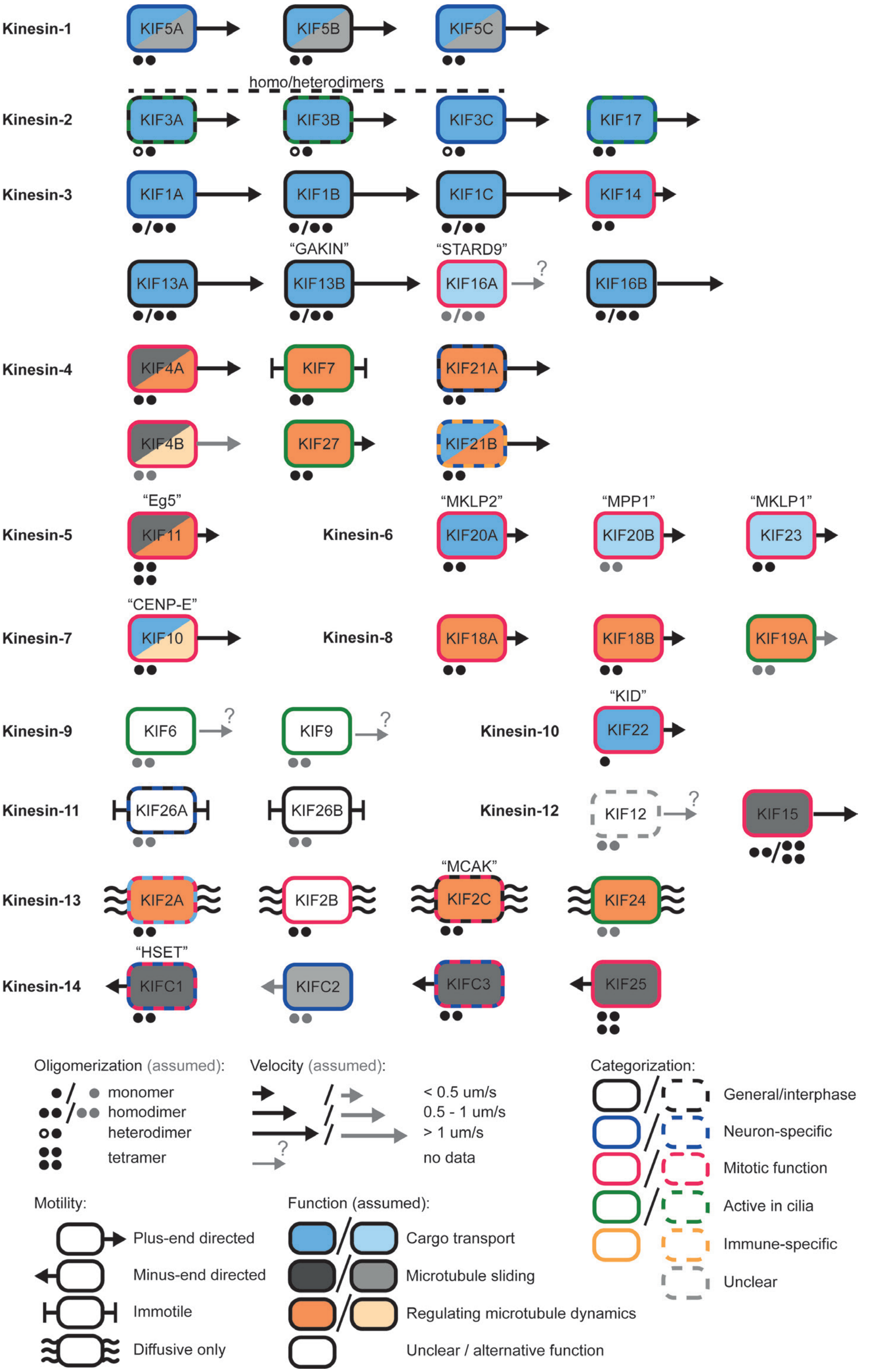
Kinesin-1
KIF5A
KIF5B
KIF5C
homo/heterodimers
Kinesin-2
KIF3A
KIF3B
KIF3C
KIF17
Kinesin-3
KIF1A
KIF1B
KIF1C
KIF14
"GAKIN"
"STARD9"
KIF13A
KIF13B
KIF16A
?
KIF16B
Kinesin-4
KIF4A
KIF7
KIF21A
KIF4B
KIF27
KIF21B
"Eg5"
"MKLP2"
"MPP1"
"MKLP1"
Kinesin-5
KIF11
Kinesin-6
KIF20A
KIF20B
KIF23
"CENP-E"
Kinesin-7
KIF10
Kinesin-8
KIF18A
KIF18B
KIF19A
"KID"
Kinesin-9
KIF6
?
KIF9
?
Kinesin-10
KIF22
Kinesin-11
KIF26A
KIF26B
Kinesin-12
KIF12
?
KIF15
"MCAK"
Kinesin-13
KIF2A
KIF2B
KIF2C
KIF24
"HSET"
Kinesin-14
KIFC1
KIFC2
KIFC3
KIF25
Oligomerization (assumed):
monomer
homodimer
heterodimer
tetramer
Velocity (assumed):
< 0.5 um/s
0.5 - 1 um/s
> 1 um/s
?
no data
Categorization:
General/interphase
Neuron-specific
Mitotic function
Active in cilia
Immune-specific
Unclear
Motility:
Plus-end directed
Minus-end directed
Immotile
Diffusive only
Function (assumed):
Cargo transport
Microtubule sliding
Regulating microtubule dynamics
Unclear / alternative function

Figure 1 – Infographic on mammalian kinesins function, localization and motor characteristics

Figure 1 (continued)
Kinesins are categorized into kinesin families based on their phylogeny. Each kinesin can be subcategorized based on many characteristics and parameters. Oligomerization state, motility and velocity parameters are intrinsic properties of a kinesin. The localization and functionality of the motor is more dependent on external factors. Some kinesins are tissue or cell-cycle specific, while others are ubiquitously (generally) expressed. Some kinesins are dedicated to a single task, while others have a varied set of functions that depend on the cellular context. The properties and functions of some kinesins is not well understood or studied.

the first kinesin motor discovered (Vale et al., 1985), and it has been extensively studied ever since. The core of kinesins-1 is composed of two heavy chains which contain the motor domain, a stalk and a tail region. The heavy chain C-terminus can associate with kinesin light chains to form a kinesin-1 heterotetramer. The light chains can directly bind to cargo or cargo-binding adaptor proteins, but in some occasions kinesin-1 functions without light chains (Sweeney and Holzbaur, 2018). Many factors have been described to regulate kinesin-1 activity and these will be described in section 5 of this chapter.

Kinesin-2 motors are involved in both cytoplasmic and ciliary transport. There are two types of kinesin-2 motor configurations. The KIF3A, -B and -C polypeptides can form heterodimers. KIF3A can bind to both KIF3B and KIF3C, while KIF3B does not form a heterodimer with KIF3C. In addition, there is some evidence that KIF3C can form homodimers in cells. Some of the KIF3 heterodimer combinations can bind to Kinesin Accessory Protein (KAP) which can mediate cargo binding. In contrast to KIF3 motors, KIF17 motors form homodimers exclusively and do not complex with any of the KIF3 proteins or KAP (Gilbert et al., 2018).

Similarly, kinesin-3 motors also have a typical dimeric configuration when they are active, although they can be monomeric in their inactive form (see below), and are well-known cargo transporters of interphase cell. They are very processive kinesins and exhibit high velocities up to 2 µm/s (Soppina et al., 2014) by which they outperform kinesins from other families in terms of speed. The kinesin-3 family also contains two mitotic motors. KIF16A (STARD9) is a centrosomal protein involved in spindle pole assembly (Torres et al., 2011). KIF14 plays a role during cytokinesis (Carleton et al., 2006; Gruneberg et al., 2006), and was shown to be a relatively slow motor compared to other kinesin-3 members (Zhernov et al., 2020).

Some members of these transporting kinesin families are more highly, and sometimes exclusively, expressed in neurons such as KIF5A and C (kinesin-1), KIF3C (kinesin-2) and KIF1A (kinesin-3), where they can transport neuron-specific cargoes. Kinesins can have many different types of cargoes and many modes of binding them, either directly or through various types of cargo adaptors. Cargo binding and transport by kinesin-1, -2 and -3 motors is an extensively studied subject and will not be discussed in detail in this chapter. Several detailed review articles discuss the transporting roles and cargo binding of kinesin-1 (Morfini et al., 2016), kinesin-2 (Scholey, 2013) and kinesin-3 (Siddiqui and Straube, 2017).

4.2 Mitotic kinesins involved in positioning of chromosomes and signaling complexes

Some mitotic motors can also be categorized as transporting kinesins and are either involved in positioning of chromosomes, or in spatiotemporal localization of critical signaling complexes. The kinesin-7 KIF10, better known as Centromere-Associated Protein E (CENP-E) is responsible for the transport of chromosomes to microtubule plus ends at the mitotic spindle (Maiato et al., 2017). After the kinetochores have established a stable association between the chromosome and microtubule plus ends, CENP-E remains associates with the microtubule plus end where it contributes to the stability of the kinetochore-microtubule attachment (Gudimchuk et al., 2013).

The kinesin-10 KIF22, also known as "Kid", also contributes to chromosome positioning. Kid contains a DNA-binding domain and generates polar ejection force on chromosome arms, thereby contributing to chromosome alignment at the spindle equator during prometaphase (Levesque and Compton, 2001; Zhong et al., 2016). Interestingly, Kid is a monomeric motor (Shiroguchi et al., 2003; Yajima et al., 2003). Although this may appear counterintuitive for a transporting function, a recent study has shown that truncated, monomeric kinesin-1, -2 and -3 motors are still capable of moving cargo in teams. This transport was depended on a short motor-to-cargo distance and limited by high force outputs (Schimert et al., 2019). Nevertheless, these results demonstrated that cargo transport by monomeric kinesins is possible.

The Kinesin-6 family consists of three family members: KIF20A, KIF20B and KIF23, which all have a mitotic function. KIF23, better known as Mitotic Kinesin-like Protein 1 (MKLP1 in mammals and ZEN-4 in *C. elegans*) forms a tetrameric Centralspindlin complex together with RACGAP1 (also known as MgcRacGAP in mammals or CYK-4 in *C. elegans*). During anaphase, Centralspindlin is concentrated to the midzone where it is an essential regulator of cytokinesis, important for bundling of antiparallel microtubules and the initiation of a signaling cascade required for the formation of the contractile ring that separates the dividing cells (White and Glotzer, 2012). In *C. elegans*, the KIF23 homologue ZEN-4 exhibits plus-end directed motility, which together with Centralspindlin clustering contributes to microtubule bundling and midzone accumulation of the complex (Hutterer et al., 2009). Whether MKLP1 is actively transporting RACGAP1 towards the midzone has not been studied in detail.

KIF20A, better known as Mitotic Kinesin-like Protein 2 (MKLP2) is essential for the anaphase-specific localization of the Chromosomal Passenger Complex (CPC) at the spindle midzone and equatorial cortex, where the CPC is important for the initiation of cytokinesis (Gruneberg et al., 2004; Hummer and Mayer, 2009; Kitagawa et al., 2013). Although it was hypothesized that MKLP2 transports the CPC during metaphase to anaphase transitioning (Gruneberg et al., 2004; Hummer and Mayer, 2009; Kitagawa et al., 2013), structural data has suggested that the atypical motor domain of MKLP2 may not be able to perform processive movement and instead acts as a tether on microtubules (Atherton et al., 2017b). Future studies may unveil whether MKLP2 also displays motility like the *C. elegans* motor ZEN-4 (MKLP1). The related KIF20B motor is the least studied member of the kinesin-6 family. During mitosis, KIF20B localizes to the spindle midzone and midbody and was suggested to be important for cytokinesis (Abaza et al., 2003; Janisch et al., 2018); yet, some reports point towards an additional interphase role in neuron polarization and morphogenesis (McNeely et al., 2017; Sapir et al., 2013).

4.3 Kinesins involved in microtubule sliding

Several kinesins are involved in microtubule sliding, a special form of kinesin-driven transport that has a crucial role in shaping complex microtubule arrays such as the mitotic spindle. Apart from its role in cargo transport, kinesin-1 motors are involved in microtubule sliding in some cellular processes. A well-studied example comes from *Drosophila* where microtubule sliding by kinesin-1 is important for cytoplasmic streaming in the fly oocyte (Jolly et al., 2010). Kinesin-1 performs sliding autonomously by binding a second "cargo" microtubule through a conserved microtubule binding domain in the kinesin tail (Jolly et al., 2010; Seeger and Rice, 2010).

In contrast, the kinesin-5 KIF11, better known as "Eg5", does not bind a second microtubule through an additional binding site, but the motor is organized into a tetramer to bridge two adjacent microtubules (Waitzman and Rice, 2014). Eg5 is a mitotic kinesin involved in the formation of a bipolar spindle. Because both parts of the tetramers exhibit plus-end directed motility, Eg5 performs microtubule sliding by which it pushes oppositely oriented microtubules apart (Kapitein et al., 2005; Waitzman and Rice, 2014). Eg5 shows partial redundancy with the kinesin-12 KIF15 which also plays a role in forming a bipolar spindle through microtubule sliding. Like Eg5, KIF15 is also assumed to form tetramers (Drechsler et al., 2014), although this has been debated. Next to KIF15, the kinesin-12 family is also represented by KIF12. Although KIF12 is thought to be expressed in the brain and pancreatic islets (Katoh and Katoh, 2005), no biochemical or functional characterization of this motor has been performed yet.

Members of the kinesin-14 family are minus-end directed motor dimers also primarily involved in microtubule sliding. During mitosis, kinesin-14 can robustly slide antiparallel microtubules and statically crosslink parallel microtubules. In addition, it can cluster and focus microtubule minus ends into poles and all these activities contribute to the formation and maintenance of the mitotic spindle (She and Yang, 2017). Next to their mitotic roles, kinesin-14 members KIFC1 and KIFC3 are involved in organizing the microtubule cytoskeleton in neurons (Cao et al., 2020; Muralidharan and Baas, 2019).

4.4 Kinesins in regulation microtubule dynamics

Next to the well-studied cargo transporting and mitotic kinesins, a number of kinesins families have a dedicated task in regulating microtubule dynamics during various cellular processes (Figure 1). Their biochemical activities can vary; some motors have been described to potently induce catastrophes, while others downregulate microtubule growth or stabilize plus-end structures. These microtubule growth regulators may be underexposed in literature compared to cargo transporting motors; therefore in the next section, we provide a more extensive summary of the roles and molecular activities of the main microtubule-regulating kinesins described so far.

Kinesin-4 family

There are six kinesins in the kinesin-4 family, which can be grouped into three subfamilies of paired paralogs. The KIF4 sub-family containing KIF4A and KIF4B, the KIF7 subfamily, containing KIF7 and KIF27 and the KIF21 sub-family, containing KIF21A and KIF21B. There are not many reports that show a cargo transporting function for these motors. Instead, they have been repeatedly shown to be potent regulators of microtubule dynamics at the plus end.

KIF4A and KIF4B

KIF4A (often referred to as KIF4), is the most well-studied member of the kinesin-4 family. Two functional pools of KIF4A have been described to be important during mitosis. In early mitosis, KIF4A has a role in the condensin I complex to regulate chromosome alignment and chromosome condensation under the control of Aurora A kinase (Poser et al., 2019; Takahashi et al., 2016). KIF4A and the *Xenopus* homolog Xklp1 are both regulators of microtubule growth as they suppress microtubule growth rates *in vitro* (Bieling et al., 2010; Bringmann et al., 2004). During anaphase, KIF4A binds the antiparallel microtubule-bundling protein PRC1, and together they form stable microtubule overlaps of the spindle midzone, where microtubule growth regulation by KIF4A limits the length of these overlaps (Bieling et al., 2010; Bringmann et al., 2004; Kurasawa et al., 2004; Subramanian et al., 2013; Subramanian et al., 2010; Zhu and Jiang, 2005). *In vitro* studies have shown that PRC1 and KIF4A can self-organize such microtubule bundles in the absence of other cellular factors (Hannabuss et al., 2019). There is little specific literature on the function and biochemical activity of KIF4B, although depletion experiments have suggested that KIF4B has a similar role in mitosis as KIF4A (Zhu and Jiang, 2005). This is not surprising as these motors are closely related (Rath and Kozielski, 2012).

KIF7 and KIF27

KIF7 is the most well-described protein of the KIF7 sub-family and is localized in cilia. Initially, KIF7 was identified as an important regulator of Hedgehog signaling at the primary cilium because it is directly involved in the processing of Gli transcription factors (Cheung et al., 2009; Endoh-Yamagami et al., 2009; Liem et al., 2009). This signaling pathway is important for embryonic development and tissue homeostasis, and several disease-related mutations have been described in the *KIF7* gene that are linked to ciliopathies such as Joubert syndrome (Barakeh et al., 2015; Dafinger et al., 2011).

Next to a signaling function, KIF7 has an important role in regulating the structure of the primary cilium. At the ciliary tip, KIF7 prevents microtubule over-elongation (He et al., 2014); consequently, KIF7 depletion results in longer cilia that tend to be less stable (Dafinger et al., 2011; He et al., 2014). *In vitro* reconstitution assays revealed that addition of KIF7 to dynamic microtubules leads to more catastrophes and reduced growth rates (He et al., 2014). Unlike KIF4 and KIF21 sub-family members, KIF7 is immotile and this is explained by its altered chemomechanical cycle where the ATP-binding pocket is different from that of other kinesins (Jiang et al., 2019; Yue et al., 2018). In addition, KIF7 preferentially binds GTP-tubulin and since it stabilizes microtubule plus ends it can consequently promote its own association to cilia tips (Jiang et al., 2019).

Little has been described about the cellular function of KIF27, but it presumably localizes at the base of motile cilia in tracheal epithelial cells (Wilson et al., 2009), where KIF27 together with the protein Fused aids in building the cilium (Nozawa et al., 2014; Wilson et al., 2009). The motor domain of KIF27 can, like all other kinesin-4 motors, suppress microtubule plus end growth and does this in a dose-dependent manner (Yue et al., 2018). KIF27 has a slow ATPase rate but unlike KIF7 it does display motility on microtubules although its velocity is very low compared to other kinesins (Yue et al., 2018). At this point, it is unclear if and how suppression of microtubule growth by KIF27 contributes to the formation or stability of motile cilia.

KIF21A and KIF21B

KIF21A and KIF21B were first described in 1999 (Marszalek et al., 1999). These motors have a very similar structural organization and both contain a characteristic WD40 beta-propeller at their tail. KIF21A is ubiquitously expressed, while KIF21B expression is restricted to neurons and the immune system (Marszalek et al., 1999).

In cells, KIF21A promotes the stabilization and cortical attachment of microtubules within the cortical microtubule stabilization complex (CMSC) that is physically linked to focal adhesions (Noordstra and Akhmanova, 2017). The connection between KIF21A and the CMSC is established via the ankyrin repeats of KANK1 (Guo et al., 2018; Pan et al., 2018; van der Vaart et al., 2013; Weng et al., 2018). KANK1 is the central hub of the CMSC, because it links the complex to focal adhesions via an interaction with Talin (Bouchet et al., 2016). Loss of KANK1 results in detachment of the CMSC from focal adhesions, while loss of KIF21A causes microtubules to detach from the CMSC after which they tend to overgrow along the cell cortex. *In vitro* reconstitution assays with purified KIF21A confirmed that this motor can suppress both microtubule growth and catastrophes, demonstrating that its biochemical role is to stabilize microtubule plus ends and limit their cortical growth (van der Vaart et al., 2013).

While KIF21A activity in neurons is mainly described in the axon, neuronal KIF21B activity is restricted to the soma and dendrites (Marszalek et al., 1999). In the latter, KIF21B is a regulator of microtubule dynamics and its depletion results in impaired dendritic branching and a reduced spine density (Ghiretti et al., 2016; Muhia et al., 2016). Furthermore, KIF21B was shown to be involved in the transport of several neuronal cargos. (Ghiretti et al., 2016; Gromova et al., 2018; Labonte et al., 2014). Kif21b knockout mice are viable but have cognitive deficits (Gromova et al., 2018; Morikawa et al., 2018; Muhia et al., 2016). In addition, Kif21b knockout mice were reported to display a thinner corpus callosum and microcephaly (Kannan et al., 2017), although such major brain abnormalities were not found in other mouse studies (Morikawa et al., 2018; Muhia et al., 2016).

Apart from its motor domain, KIF21B contains additional microtubule binding regions within the coiled coil stalk, and also the WD40 domain contributes to microtubule binding. *In vitro*, single KIF21B motors move processively to growing plus ends where they induce pausing of microtubule growth. The WD40 domain has a GTP-type lattice preference and contributes to plus-end recognition and pausing activity. Pausing involves a combination of growth inhibition and stabilization of the plus-end structure; when a single motor pauses, this ultimately results in microtubule depolymerization as a single KIF21B molecule is not sufficient to stabilize a microtubule plus end for a long time. In contrast, when multiple KIF21B motors accumulate at the microtubule tip, they can stabilize the growth-inhibited state (van Riel et al., 2017).

Kinesin-8 family

Overall, kinesin-8 motors have an evolutionary conserved role in regulating microtubule growth during mitosis (Lin et al., 2020). In yeast, the kinesin motor Kip3 is involved in regulating the length of spindle microtubules by acting both as a depolymerizing factor and a factor that stabilizes shrinking microtubules (Fukuda et al., 2014; Gupta et al., 2006; Varga et al., 2006). In humans, the kinesin-8 family is represented by three members: KIF18A, KIF18B and KIF19A, which all have distinct roles in cells. KIF18A is involved in chromosome positioning by regulating microtubule dynamics of kinetochore microtubules. The exact molecular activity of KIF18A has been debated; some have reported this kinesin to be a microtubule depolymerizing factor (Mayr et al., 2011), while others indicated that it dampens microtubule growth at plus ends (Du et al., 2010; Stumpff et al., 2011). KIF18B is also involved in mitosis, but specifically regulates astral microtubule length and spindle positioning (McHugh et al., 2018; Stout et al., 2011; Walczak et al., 2016). At plus ends, it can form a complex with EB1 and the kinesin-13 KIF2C (MCAK), which both contribute to the role of KIF18B in regulating microtubule length (Stout et al., 2011; Tanenbaum et al., 2011). *In vitro*, KIF18B can autonomously perform tip-tracking on microtubule ends where it controls microtubule length by inducing catastrophes (McHugh et al., 2018). Less studies have been focused on KIF19, but it is reported to be involved in regulating cilia length at the axoneme tip through microtubule depolymerizing activity (Niwa et al., 2012; Wang et al., 2016). Consequently, a Kif19 knockout mouse was reported to have increased cilia length (Niwa et al., 2012), a phenotype similar to that of kinesin-4 KIF7 depletion (He et al., 2014).

In general, kinesin-8 members are processive motors that use an additional non-motor microtubule binding site in their tail to prevent motor detachment and promote plus-end accumulation (Mayr et al., 2011; Stumpff et al., 2011). Interestingly, kinesin-8 motors target microtubules in a length-dependent manner, where long microtubules are more prone to growth restriction or depolymerization than short ones (Varga et al., 2006).

This is mechanistically explained by the “antenna model” (Varga et al., 2009) where the number of kinesin-8 motors that land on a microtubule is in proportion to microtubule length. Because these motors are so processive, most kinesin-8 landing events will result in accumulation of the motor at the plus end where they dampen growth or depolymerize the microtubule. The result is that longer microtubules are more prone to kinesin-8 growth regulation (Varga et al., 2009).

Kinesin-13 family

Members of the kinesin-13 family are intrinsically different from other kinesin families because their motor domain is located in the middle of the protein. Hence, these kinesins are known as M-KIFs. In humans, this family consists of four members: KIF2A, KIF2B, KIF2C and KIF24, which have all been shown to have a strong microtubule depolymerizing potential (Friel and Welburn, 2018). KIF2C is the most well-described family member and is better known as mitotic centromere-associated kinesin (MCAK) (Wordeman and Mitchison, 1995). Kinesin-13 family members do not walk towards to plus ends; they were proposed to reach microtubule ends by lateral diffusion (Helenius et al., 2006), but since the data supporting this model were obtained in low ionic strength conditions, it is unclear whether this mechanism contributes to their cellular function. In cells, MCAK associates with the plus ends of polymerizing microtubules (Moore et al., 2005), and this activity is dependent on MCAK’s plus-end tracking properties which are mediated through EB-binding via an SXIP-motif (Honnappa et al., 2009; Lee et al., 2008). Although counterintuitive at first sight, EB proteins counteract MCAK’s depolymerizing activity at the plus end, but also potentiate the ability of MCAK to induce catastrophes (Montenegro Gouveia et al., 2010). The combination of EBs and MCAK promotes microtubule switching between growth and shrinkage. Another member of kinesin-13 family, KIF2A, is localized at the centrosome during mitosis, and is important for spindle formation and microtubule flux (Ritter et al., 2015). KIF2A also displays an interphase role during neuronal development where it regulates microtubule dynamics at the axon growth cone (Homma et al., 2003). KIF2B is only expressed at low levels and its role is therefore debated although overexpression data suggested it may be involved in spindle assembly, chromosome segregation and cytokinesis (Ritter et al., 2015). KIF2C/MCAK has several functions during mitosis and is involved chromosome segregation, spindle assembly and the correct attachment of microtubules to kinetochores (Ritter et al., 2015). Together with the kinesin-8 KIF18B, MCAK also regulates astral microtubule length (Tanenbaum et al., 2011). Altogether, MCAK’s depolymerizing activity has been shown to be important for proper spindle formation and successful cell division (Ritter et al., 2015). The interphase function of MCAK is less well-described but it has been reported that MCAK has a role in depolymerizing trailing edge microtubules of migrating endothelial cells (Braun et al., 2014). KIF24 has no described role during mitosis, but is thought to be involved in ciliogenesis and timely disassembly of the axoneme (Kim et al., 2015; Kobayashi et al., 2011).

Much structural work has been done on MCAK to understand the mechanistic basis of its depolymerizing activity. Although the motor domain alone in monomeric form is sufficient to induce catastrophes, several factors enhance this activity such as motor dimerization via the C-terminus and an additional microtubule-binding site at the N-terminal neck-linker (Friel and Welburn, 2018). MCAK can distinguish the microtubule plus end from the lattice by sensing the curved conformation of tubulin at the ends (Patel et al., 2016). In fact, stabilization of this curved tubulin configuration by MCAK is believed to induce depolymerization (Trofimova et al., 2018; Wang et al., 2017).

Other kinesin families

Kinesin-4, -8 and -13 motors are established modulators of microtubule growth at the plus end. Yet, kinesins from other families may also affect microtubule dynamics to some extent. For example, kinesin-1, which is mainly involved in cargo transport and microtubule sliding, was suggested to affect microtubule dynamics in cells (Daire et al., 2009; Randall et al., 2017). Another cargo-transporting motor from the kinesin-2 family, KIF3C, is a microtubule destabilizing factor in axonal growth cones. KIF3C contains an EB-binding SXIP motif which is required to for tip tracking and microtubule growth regulation (Gumy et al., 2013). Indeed, KIF3C homodimers behave as catastrophe-inducing factors on microtubule plus ends *in vitro* (Guzik-Lendrum et al., 2017). Recent work has suggested that the mitotic kinesin-5 Eg5 (KIF10) is a tip-tracking microtubule polymerase that increases growth rates while suppressing catastrophes (Chen and Hancock, 2015). Eg5 was proposed to straighten tubulin dimers at the plus end and thus promote lateral tubulin-tubulin interactions, which are beneficial for microtubule polymerization (Chen et al., 2019). The mitotic kinesin-7 CENP-E can track both growing and depolymerizing plus ends, a property wherefore the kinesin requires its microtubule binding tail domain (Gudimchuk et al., 2013). Although it was reported that CENP-E can enhance microtubule elongation *in vitro* (Sardar et al., 2010), another study found that single motors showed no strong effect on plus end dynamics *in vitro* (Gudimchuk et al., 2013). Whether CENP-E plays a role in regulating the dynamics of kinetochore-attached microtubule ends thus requires further elucidation. These examples show that some kinesins may have an additional function in stimulating or inhibiting microtubule growth at the plus end, but their exact contribution to the overall regulation of microtubule dynamics requires further study.

4.5 Future perspectives on discovering kinesin functionalities

The kinesin superfamily is both structurally and functionally a diverse group of motor proteins and much is to be learned on their molecular activities. Kinesin families can be characterized by their cellular function, such as cargo transport, microtubule sliding or microtubule dynamics regulation. Yet, these task types are not mutually exclusive as many kinesins may exert a different function depending on the cellular context. Although the functions and molecular behavior of many kinesin families are characterized well, some families are poorly studied. For instance, kinesin-9 family has mostly been studied in unicellular organisms where these motors have a function in the flagellum (Demonchy et al., 2009). In mammals, the two kinesin-9 motors KIF6 and KIF9 are thought to have a function in motile cilia as well: KIF6 is associated with beating cilia of brain ependymal cells (Konjikusic et al., 2018), and KIF9 has a role in sperm cell motility (Miyata et al., 2020). Another less-understood family is that of kinesin-11 motors. This family contains two members, KIF26A and KIF26B, which can both associate with microtubules, but lack ATPase activity and thus motility (Terabayashi et al., 2012; Zhou et al., 2009). Instead, KIF26A and KIF26B are thought to be involved in several signaling pathways (Karuna et al., 2018; Susman et al., 2017; Terabayashi et al., 2012; Wang et al., 2018; Zhou et al., 2009). Overall, there is still much to be uncovered on the function and molecular activities of many kinesin motors.

5. Regulation of kinesins

Some level of regulation is required in order for kinesins to fulfill their cellular function in a spatiotemporally controlled manner. Without such regulation, kinesins would be constitutively active on microtubules; motile motors would crowd microtubule ends and motors that regulate microtubule dynamics would severely affect the overall architecture of the cell. On top of that, kinesins would consume ATP, thereby wasting the cell's energy resources.

Here, we give an overview on the layers of regulation kinesin motors or subject to and present examples of these mechanisms.

5.1 Autoinhibition

It is generally accepted that the majority of kinesin motors can adopt an inactive state through self-association. This autoinhibition requires two properties. First, a kinesin must contain one or multiple flexible regions, often referred to as hinges, that enables the protein to fold back on itself. Removal of such a flexible hinge was shown to abolish autoinhibition of kinesin-1, leading to constitutive active motors (Coy et al., 1999). Second, the kinesin must possess an intramolecular binding mode that can block activity or microtubule binding of the motor domain. Most often, this involves docking of the motor domain to a distal part of the kinesin stalk or a part of the tail region (Verhey and Hammond, 2009).

Kinesin-1 motors are heterotetramers that are composed of two heavy chain subunits, containing the motors domains, and two light chain subunits that bind the C-terminal tails of the heavy chains (Hirokawa et al., 2009). During autoinhibition, the heavy chain tail folds onto the motor domains and blocks microtubule interaction. In addition, the kinesin light chains change the position of the motor domains by pushing them apart (Cai et al., 2007). Such a dual mechanism for autoinhibition was also found for the homodimeric kinesin-2 KIF17. Here, the kinesin tail blocks microtubule binding of the motor domain, and a second interaction between the kinesin coiled coils and the motor domains inhibits kinesin motility (Hammond et al., 2010). The heterotrimeric kinesin-2 complex that consists of KIF3A, KIF3B and the non-motor KAP3 subunit also undergoes autoinhibition through binding of the tails to the motor domains (Chen et al., 2018); whether the coiled coil domains are also involved in a secondary autoinhibition mechanism is unclear. For kinesin-3 motors, two different autoinhibition models have been proposed. In the first model, inactive kinesin-3 motors have intramolecular interactions involving the kinesin tail and neck region that keep the motor in a monomeric conformation. Cargo binding induces dimerization where the intramolecular contacts are exchanged for intermolecular binding to another kinesin monomer. In the second model, the kinesin-3 stalk or tail domains block the motor domain or neck coils; cargo binding to the tail releases this interaction enabling motility. Kinesin-3 family members may possess one or both mechanisms to regulate their activity (Siddiqui and Straube, 2017). Autoinhibition of the kinesin-4 family member KIF21A has been studied extensively as mutations that impair autoinhibition have a direct association with Congenital fibrosis of the extraocular muscles type 1 (CFEOM1) (Traboulsi and Engle, 2004). In this kinesin, an anti-parallel coiled coil extension in the kinesin stalk can bind the motor domain to form an inactive complex (Bianchi et al., 2016; Cheng et al., 2014; van der Vaart et al., 2013). Structural studies suggest that the autoinhibitory mechanism of KIF21A is conserved among other kinesin-4 members like KIF21B, KIF7 and KIF27 (Bianchi et al., 2016). Indeed some KIF21B mutations have been described to cause neurodevelopment disorders through altered autoinhibition regulation (Asselin et al., 2020). Since all well-studied kinesin families have been described to adopt an inactive state through autoinhibitory self-association, this likely represents a general mechanism to regulate kinesin activity. Autoinhibition can be regulated and released in various ways and this will be discussed in some of the following paragraphs.

5.2 Regulation by tubulin code

The term “tubulin code” specifies a set of mechanisms that enable the cell to create specialized microtubules through post-translational tubulin modifications and the use of different α- and β-tubulin isotypes (Figure 2A) (Gadadhar et al., 2017). There have been several studies describing how this code can regulate the activity of various kinesin motors. Mutations in β-tubulin genes have been associated to human diseases. In some cases, it has been shown that these mutations can affect binding of the kinesin motor domain with the microtubule lattice (Sferra et al., 2018; Tischfield et al., 2010; Vulinovic et al., 2018). An elegant study has shown that β-tubulin isotypes can affect kinesin-1 motility *in vitro*. Here, kinesin-1 motility was analyzed on isotype-specific microtubules and it was found that TUBB7 severely reduced kinesin velocity, while TUBB1 and 3 influenced run length (Sirajuddin et al., 2014). These differences were partially explained by the differences in the length and charge of the C-terminal tubulin tails.

Early work on kinesin-1 has indeed shown that tubulin tails are important for kinesin motility. For example, enzymatic removal of such tails with subtilisin severely affects kinesin-1 motility (Thorn et al., 2000; Wang and Sheetz, 2000). Interestingly, these tails are also subjected to various post-translational modifications (PTMs) such as (poly-)glutamylation, (poly-)glycylation and removal of the most C-terminal tyrosine of α-tubulin (detyrosination) (Figure 2B). Apart from these tail modifications, α-tubulin can also be subjected to acetylation of the intraluminal lysine-40 residue, a modification that has been studied extensively both in cells in *in vitro* (Magiera et al., 2018). The impact of these PTMs on kinesin motility has been debated, especially in the case of kinesin-1. In cells, kinesin-1 displays preference for long-lived and stable microtubules that are often acetylated and detyrosinated (Dunn et al., 2008; Reed et al., 2006). Yet, *in vitro* studies indicate that the direct effect of these two PTMs on kinesin-1 motility is limited (Kaul et al., 2014; Sirajuddin et al., 2014; Walter et al., 2012). Contrary, kinesin-1 motility *in vitro* was especially promoted by the addition of long polyglutamate chains to tubulin tails (Sirajuddin et al., 2014). In the same study, kinesin-2 motors were found to be more motile on detyrosinated and also poly-glutamylated microtubules (Sirajuddin et al., 2014). These studies suggest that PTMs alone may not completely explain why motors like kinesin-1 have a certain preference for microtubule subsets in cells. PTMs may also play a role in the activity regulation of mitotic kinesins. Both kinesin-13 MCAK (KIF2C) and kinesin-7 CENP-E (KIF10) were shown have preference or detyrosinated microtubules, both in cells as *in vitro* (Barisic et al., 2015; Peris et al., 2009).

The structure of the microtubule lattice can also affect kinesin motility, independent of tubulin isotypes or PTMs. Early work indicated that kinesin-1 exhibits cooperative binding and it was concluded that motors may favor a certain lattice state (Muto et al., 2005). Detailed structural work has shown that kinesin-1 can drive conformational changes in the microtubule lattice, where motor binding to compacted GDP-type lattice structures drives the transition to a more elongated GTP-like conformation (Shima et al., 2018). Indeed, binding of kinesin-1 induces longitudinal extension of the microtubule lattice up to 2% (Peet et al., 2018; Shima et al., 2018), promoting its own binding (Figure 2C). Such recognition of microtubule lattice states has also been described for a number of microtubule growth regulating kinesins. Kinesin-8 makes a switch from motility to tight microtubule binding when it senses protofilament curvature at growing plus ends (Arellano-Santoyo et al., 2017). Such curvature sensing may also play a role in microtubule-end recognition by kinesin-13 motors (Friel and Welburn, 2018). The kinesin-4 KIF21B motor contains a WD40 domain that specifically recognizes GTP-type lattices to stably associate with the microtubule plus end and induce pausing of growth. A similar GTP-lattice preference was described for another kinesin-4 motor, KIF7 (Jiang et al., 2019).

The presence of microtubule bundles is an alternative mode of increasing kinesin processivity (Figure 2D). Acetylated microtubules, which are a preferred substrate of kinesin-1, may be subject to some extent of microtubule bundling (Balabanian et al., 2017). The

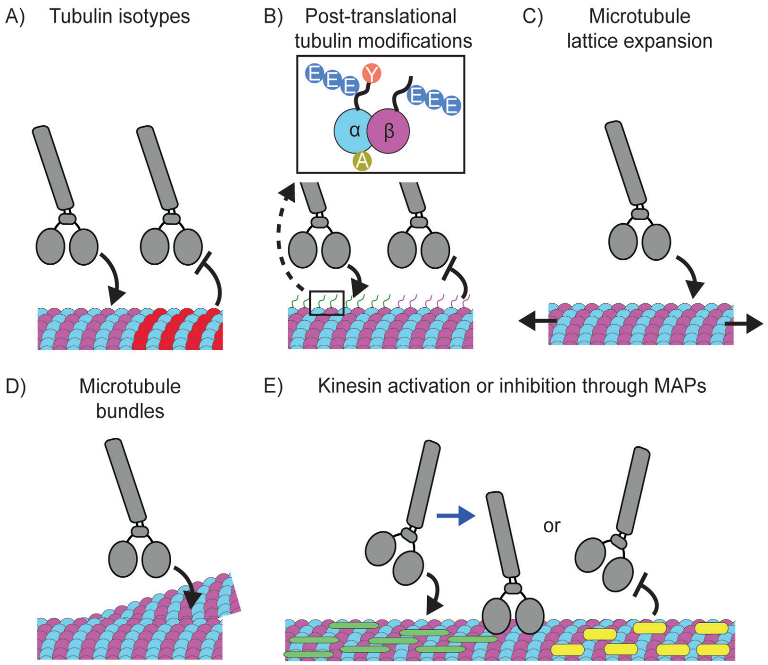
A) Tubulin isotypes
B) Post-translational tubulin modifications
E
E
E
Y
E
E
E
α
β
A
C) Microtubule lattice expansion
D) Microtubule bundles
E) Kinesin activation or inhibition through MAPs
or

Figure 2 – Kinesin regulation through the microtubule lattice
Several microtubule lattice factors can regulate kinesin motility. **(A)** β-Tubulin isotypes can promote or downregulate kinesin motility. **(B)** Post-translational modifications, such as acetylation on the luminal side or (poly)-glutamylation and detyrosination of tubulin tails have been correlated with kinesin motility parameters. **(C)** Longitudinal compaction or extension of the microtubule lattice may affect binding of the kinesin motor domain. **(D)** Microtubule bundling can promote binding of kinesin motors. (E) MAPs can stimulate, allow or inhibit kinesin movement on microtubules. The nature of this MAP-dependent regulation can differ per kinesin family.

presence of multiple microtubules in close vicinity was indeed shown to promote kinesin-1 motility (Balabanian et al., 2017; Conway et al., 2014), and was hypothesized to partially explain kinesin-1 selectivity in cells. *In vitro*, processive movement of the minus-end directed *Drosophila* Ncd motor protein (kinesin-14) was also enhanced by microtubule bundling (Furuta and Toyoshima, 2008). Therefore, microtubule bundling may be a general mechanism to promote kinesin motility as it simply provides the motor with an increased local concentration of binding substrate.

5.3 Regulation by MAP code

Cellular microtubules are not mere naked polymers that only vary in their tubulin composition and post-translational markings; they are densely populated structures where kinesins have to share the road with structural MAPs that can sterically hinder kinesin stepping. How different MAPs may affect kinesin motors has received increased attention over the recent years. Similar to the “Tubulin code”, a “MAP code” may determine directed transport where distinct combinations of MAPs can allow or impede specific types of kinesin motors (Figure 2E, Table 1) (Monroy et al., 2020).

The Alzheimer's disease related MAP tau is a potent inhibitor of kinesin-1 and kinesin-3 motility (Monroy et al., 2018). Structural studies have shown that tau inhibits kinesin through competition with its binding site at the microtubule crest (Kellogg et al., 2018; Shigematsu et al., 2018). Interestingly, MAP7 is able to efficiently compete off tau from the microtubule lattice (Monroy et al., 2018), and kinesin-1, but not kinesin-3 motors, can efficiently move over MAP7-decorated microtubules (Monroy et al., 2018; Monroy et al., 2020). Kinesin-3 inhibition by MAP7 was shown depend on the presence of a charged K-loop that is specific for kinesin-3 motor domains (Monroy et al., 2020). Other MAPs, such as MAP9 and members of the doublecortin family are positive regulators of kinesin-3 cargo transport and allow these motors to pass (Lipka et al., 2016; Liu et al., 2012; Monroy et al., 2020), while kinesin-1 motility is reduced by the presence of these MAPs (Monroy et al., 2020). These type of competitive and non-competitive footprints on the microtubule lattice determine the MAP code (Table 1). How other kinesin families and lesser abundant MAPs play a role in the MAP code is currently unclear. The MAP code is especially relevant in polarized cell types such as neurons, where both kinesin activity and MAP distribution are different between different cell compartments, such as axons and dendrites (Monroy et al., 2020). An additional layer of complexity is added through MAP phosphorylation, a PTM that can regulate microtubule affinity and thus determine the presence of MAPs on microtubule arrays (Ramkumar et al., 2018). Since many proteins are subject to phosphorylation during mitosis, it would be exciting to evaluate the MAP code of interphase versus spindle and astral microtubules and investigate the behavior of mitotic kinesins on such lattices.

Table 1 – Effects of MAPs on the motility of transporting kinesin motors

MAP	Kinesin-1	Kinesin-2	Kinesin-3
Tau	inhibits	N.D.	inhibits
MAP2	inhibits	N.D.	inhibits
MAP4	inhibits	promotes	N.D.
MAP7	promotes	N.D.	inhibits
MAP9	inhibits	N.D.	allows
DCX / DCLK1	inhibits	allows	allows

* Adapted from (Balabanian et al., 2018; Monroy et al., 2020),
N.D. = no data

5.4 Regulation by co-factors and cargo binding

Competitive binding of cargo to the kinesin tail is generally regarded as the main mechanism to relieve autoinhibition and activate motor-driven transport (Figure 3A, B) (Verhey and Hammond, 2009). Kinesin-1 cargo binding is mostly mediated through the kinesin light chains. JNK-interacting proteins JIP1 and JIP3 can link cargo to kinesin light chains and their binding has also been involved in releasing the autoinhibited state of the tetrameric kinesin-1 complex (Cockburn et al., 2018; Nguyen et al., 2018). Some cargoes, such as mitochondria, are transported by a light-chain-independent mechanism; for example, TRAK1 binds directly to the kinesin-1 heavy chain and connects the motor to mitochondria. Interestingly, binding of TRAK1 also affects kinesin-1 motility parameters *in vitro*. TRAK1 possesses weak microtubule affinity which contributes to kinesin-1 processivity on crowded microtubules

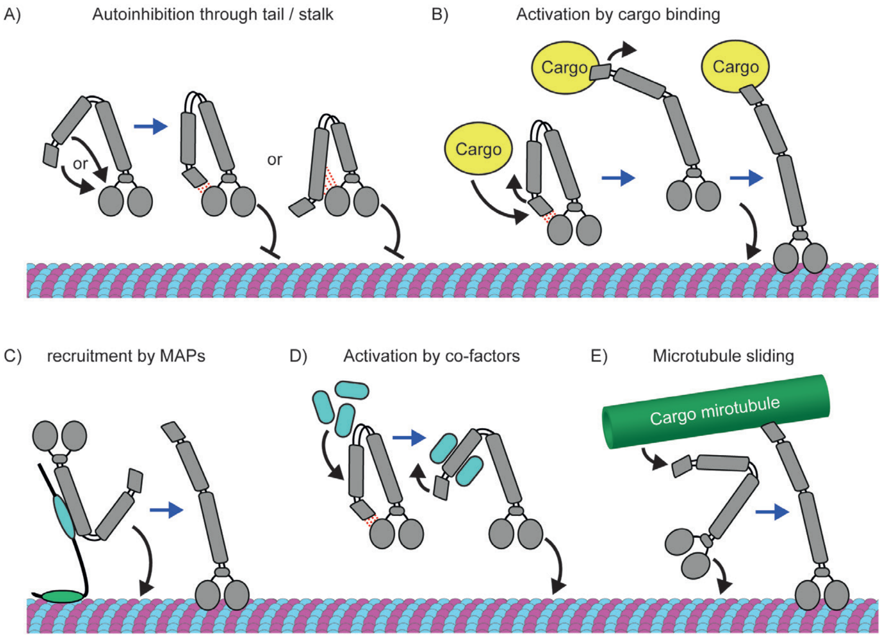

Figure 3 – Kinesin regulation through autoinhibition, co-factors and MAPs
Schematic representation of various modes of kinesin regulation. **(A)** Most kinesin motors adopt an autoinhibited state where binding of the kinesin tail or stalk to the motor domains blocks motility. **(B)** Cargo binding can relieve such autoinhibition and promote motility. **(C)** MAPs may also play a role in kinesin activation by recruitment of the motor to the microtubule lattice. **(D)** Co-factors can promote kinesin activity by relieving autoinhibition or through changing the conformation of the motor. **(E)** A microtubule may act as a kinesin cargo and promote kinesin motility along another microtubule, thereby inducing sliding.

(Henrichs et al., 2020). This weak microtubule affinity was also found for the tumor suppressor adenomatous polyposis coli (APC), which among other functions also acts as an adaptor that couples mRNA to kinesin-2 heterotrimers (KIF3A/KIF3B/KAP). Adding a weak MAP module to the motor-cargo complex was shown to promote kinesin-2 activity *in vitro*. These examples demonstrate that adaptors may provide additional microtubule-binding sites for kinesin-cargo complexes and may thus promote processive transport along microtubules. (Baumann et al., 2020).

In addition to cargo binding, kinesins may also be activated through non-cargo binding co-factors. MAP7 (or fly Ensconsin) is an interesting kinesin-1 co-factor as studies in flies suggest that activation by Ensconsin may involve a dual mechanism. MAP7/Ensconsin is a MAP containing an N-terminal microtubule-binding domain and a C-terminal kinesin-binding domain (Barlan et al., 2013; Sung et al., 2008). Microtubule-bound MAP7/Ensconsin is a recruiting factor for kinesin-1 that potently promotes its landing on microtubules (Monroy et al., 2018). However, the MAP7/Ensconsin C-terminus alone is, in many cellular processes, also sufficient to promote kinesin-1 activity independent from microtubule recruitment (Barlan et al., 2013; Metivier et al., 2019). Whether MAP7/Ensconsin actively releases autoinhibition or whether it activates kinesin-1 through an allosteric effect is not clear at this point. Apart from MAP7, several other kinesin-1 co-factors have been identified, such as RANBP2 (Cho et al., 2007; Cho et al., 2009), Casein Kinase II (Xu et al., 2012), HAP1a (Twelvetrees et al., 2019), GRIP1 (Twelvetrees et al., 2019), and also some bacterial proteins from the pathogen Salmonella enterica (Alberdi et al., 2020).

Like kinesin-1 motors, other kinesin family motors can be activated by non-cargo factors. The kinesin-3 KIF1A is a calcium-sensitive motor that displays increased cargo affinity when calcium levels are up. High calcium levels are sensed by the calcium-binding protein calmodulin which can bind the KIF1A stalk and may induce a conformational change that promotes cargo binding (Stucchi et al., 2018). Another kinesin-3 motor, KIF1C, is regulated in a completely different way: it does not form monomers when inactive, but instead adopts an autoinhibition fold where the stalk binds to the microtubule binding interface of the motor domains. Protein tyrosine phosphatase N21 (PTPN21) and the dynein adaptor Hook3 were both identified as KIF1C-binding partners that can relieve KIF1C autoinhibition by binding to the kinesin stalk. (Siddiqui et al., 2019). Less is known about the regulation of kinesin-4 family members. The ubiquitin ligase tripartite motif containing 3 (TRIM3) was reported to bind the kinesin-4 KIF21B and regulate its activity (Labonte et al., 2013); yet, it is not clear how this activation works mechanistically. Kinesin Binding Protein (KBP) is an interesting adaptor as it can bind the motor domain and regulate activity of kinesins from different families, including several kinesin-3 motors, kinesin-2 KIF3A, kinesin-8 KIF18A and kinesin-12 KIF15, but not to the major transporting motors of the kinesin-1 family (Kevenaar et al., 2016). KBP binding prevents microtubule binding of the motor domain and this was shown to modulate kinesin-3-dependent transport and microtubule dynamics by kinesin-8 KIF18A in neurons (Kevenaar et al., 2016). Furthermore, KBP regulates the kinesin-12 KIF15 during mitosis, which affects chromosome alignment and the organization of kinetochore fibers (Brouwers et al., 2017).

For some kinesins, activation through cargo binding takes place in the context of microtubule sliding where a second “cargo microtubule” promotes activity of the motor. The tetrameric state of Eg5 enables it to slide microtubules (Kapitein et al., 2005). With *in vitro* reconstitution experiments it was shown that binding to a second microtubule promotes Eg5 to switch from diffusive lattice behavior to directed movement (Kapitein et al., 2008). Other kinesins, such as kinesin-1 do not require tetramerization to slide microtubules but possess a microtubule binding region in their tail (Jolly et al., 2010), or are able to crosslink microtubules by associating with a MAP, such as MAP7 (Metzger et al., 2012). Although not formally tested, it can be assumed that direct binding of a second cargo microtubule by kinesin-1 is another mechanism to release autoinhibition as it must involve unfolding from

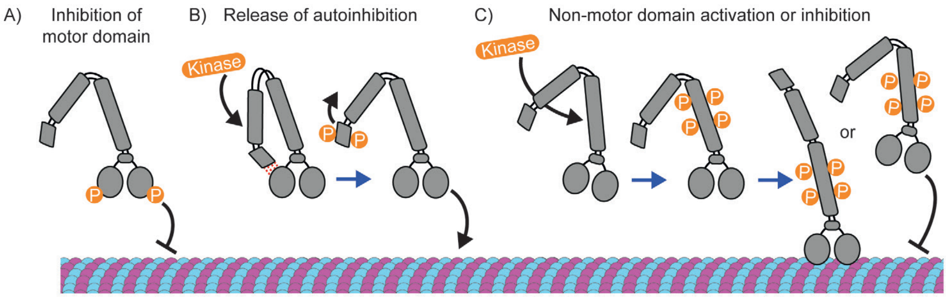
A) Inhibition of motor domain
B) Release of autoinhibition
C) Non-motor domain activation or inhibition
Kinase
P
Kinase
or

Figure 4 – Regulation of kinesins through phosphorylation
Kinesins can be regulated by phosphorylation through several mechanisms. (A) Phosphorylation of the motor domain can inhibit the engagement with the microtubule. (B) Phosphorylation can be involved in releasing kinesin autoinhibition. (C) Phosphorylation may alter the conformation of the kinesin and in this way promote or inhibit motility; in many cases, the underlying molecular mechanisms require further elucidation.

an inhibited state.

5.5 Regulation by phosphorylation

During interphase, kinesin regulation through kinase activity has been studied mostly in the context of kinesin-1. The heavy chains of kinesin-1 can be phosphorylated on the motor domain by JNK3; these modifications were reported to directly affect kinesin-1 motility parameters *in vitro* (Figure 4A)(DeBerg et al., 2013). Additionally, the light chains of kinesin-1 can also be subject to phospho-regulation; KLC2 phosphorylation by GSK3 negatively affects binding of the kinesin to cargo (Morfini et al., 2002). Also KLC1 can be specifically phosphorylated at one of its threonine residues, which negatively affects the interaction with the JIP1 adaptor protein (Chiba et al., 2017). Since association with JIP1 regulates cargo binding and stimulates kinesin-1 activity (Nguyen et al., 2018), this phosphorylation thus negatively affects cargo transport.

Kinesin regulation though phosphorylation is well-studied in the context of several mitotic motors. During anaphase, local activity of Aurora B kinase and AMP-activated protein kinase (AMPK) phosphorylate kinesin-4 KIF4A at its stalk (Li et al., 2018; Nunes Bastos et al., 2013). Here, AMPK and Aurora B compete for the same phosphorylation site (Li et al., 2018). Phosphorylated KIF4A shows increased ATPase activity and enhanced binding to its binding partner PRC1 (Nunes Bastos et al., 2013); as described before, the concerted action of KIF4A and PRC1 is important for the formation and stabilization of the spindle midzone (Bieling et al., 2010; Kurasawa et al., 2004; Zhu and Jiang, 2005). The tetrameric kinesin-5 Eg5 (KIF11) is an important mitotic motor as it slides apart anti-parallel microtubules to form and maintain a bipolar spindle (Kapitein et al., 2005). Eg5 contains a conserved threonine (T927) that is phosphorylated by Cdk1 and regulates binding of the kinesin to the mitotic spindle (Blangy et al., 1995; Cahu et al., 2008). Mitotic exit involves the dephosphorylation of this Cdk1 site by PP2A (Liu et al., 2017). Phosphorylation by the NIMA kinase Nek6 at several phospho-sites was also shown to be crucial for the mitotic function of Eg5 (Rapley et al., 2008). Furthermore, phosphorylation of the motor domain by Src family kinases has been indicated to be important for Eg5 motor activity (Bickel et al., 2017).

Phosphorylation can also directly regulate kinesin autoinhibition (Figure 4B). The kinesin-7 CENP-E (KIF10) has an inhibitory tail that associates with the motor domains to hinder microtubule binding. Phosphorylation by Cdk1 relieves this intramolecular binding and stimulates CENP-E motor activity (Espeut et al., 2008). Cdk1 was also described to regulate activity of the kinesin-10 Kid (KIF22), possibly through modulation of a microtubule binding site in the kinesin stalk (Soeda et al., 2016).

Phosphorylation can also inhibit the activity of some mitotic motors, such as in the case of kinesin-6 MKLP2 (KIF20A) where Cdk1-mediated phosphorylation of the kinesin stalk and tail prevents MKLP2 from binding chromosomes and microtubules (Hummer and Mayer, 2009; Kitagawa et al., 2014). Phosphorylated MKLP2 indeed shows reduced ATPase activity (Serena et al., 2020), but how this modification mechanistically affects MKLP2 motility is not clear. Activity regulation of the kinesin-13 MCAK (KIF2C) is under control of Aurora B kinase, which negatively affects depolymerizing activity of the motor (Andrews et al., 2004; Lan et al., 2004). MCAK inhibition through phosphorylation occurs through two distinct mechanisms: altering the conformation of the kinesin and reducing its affinity for microtubules (Ems-McClung et al., 2013; McHugh et al., 2019). In addition, several other kinases have been described to tune MCAK's activity during mitosis (Ritter et al., 2015).

5.6 Spatiotemporal regulation of kinesin activity

Whether a kinesin is active can also simply depend on its presence or absence in the cyto-

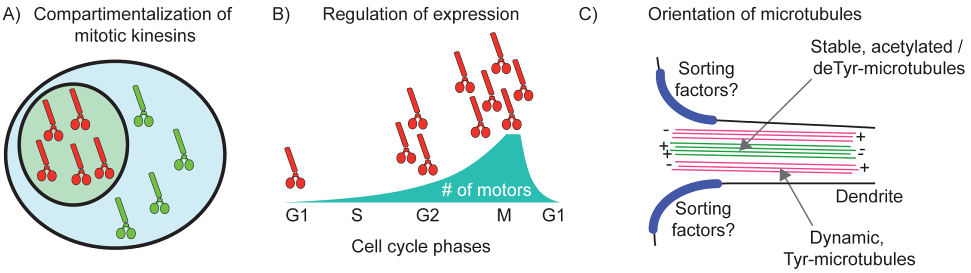
A) Compartimentalization of mitotic kinesins
B) Regulation of expression
# of motors
G1
S
G2
M
G1
Cell cycle phases
C) Orientation of microtubules
Sorting factors?
Stable, acetylated / deTyr-microtubules
+
-
+
-
+
Dendrite
Sorting factors?
Dynamic, Tyr-microtubules

Figure 5 –Spatial or temporal regulation of kinesins
Spatiotemporal regulation of kinesins can occur in different ways. **(A)** Many mitotic kinesins localize to the nucleus during interphase and only come in contact with microtubules when the nuclear envelope is broken down. **(B)** Several mitotic kinesins are expressed in a cell cycle dependent manner. **(C)** In cells with a complex microtubule organization, such as neurons, the orientation of microtubule tracks can determine compartmentalization. Some motors, like kinesin-1 prefer stable microtubules that display increased acetylation and detyrosination over dynamic microtubules that are enriched in tyrosinated tubulin. In dendrites, these stable microtubule tracks are oriented with their minus ends towards the cell body and therefore exclude the entry of kinesin-1 motors into dendrites. Additional sorting factors may contribute to this process at the initial part of the dendrite.

plasm. Some kinesins are tissue specific. For example, the kinesin-9 KIF6 and KIF9 are only expressed in some ciliated cell types (Miyata et al., 2020; Verhey et al., 2011a), while other kinesin families have one or multiple members that are enriched or exclusively expressed in neurons (Figure 1) (Hirokawa et al., 2009). It is unclear how cilia-specific motors are targeted to axonemes or cilia tips while staying mostly inactive on cytoplasmic microtubules.

In dividing cells, the activity of mitotic kinesins is tightly regulated. Many of these motors are sequestered in the nucleus during interphase and are thus kept physically separated from the microtubule cytoskeleton (Figure 5A) (Yount et al., 2015). In addition, many kinesins are synthesized and degraded in a temporally regulated fashion, and are thus present only when they are required during cell division (Figure 5B) (Yount et al., 2015).

The mechanisms responsible for the spatiotemporal control and selectivity of transport are also subject of intense study in the neuronal field. While axons only contain plus-end-out oriented microtubules, this orientation is mixed in dendrites; still, kinesin-1 transport is mostly directed to the axon and not to dendrites. One explanation is provided by a super-resolution study which revealed that dendritic microtubules of the same orientation are organized into bundles (Tas et al., 2017). In dendrites, stable kinesin-1-preferred microtubules that are marked by acetylation and detyrosination are oriented with their plus ends towards the soma, and therefore, kinesin-1 does not actively enter dendrites, though it can possibly be transported there in an inhibited state while bound to cargo or perhaps enter dendrites in an autoinhibited form by diffusion. In contrast, kinesin-3 motors that prefer dynamic and tyrosinated microtubules, which are oriented with their plus ends out, can readily enter dendrites (Figure 5C) (Tas et al., 2017). In addition, other cellular factors such as Septins also contribute to kinesin selectivity in dendrites (Karasmanis et al., 2018).
A great variety of kinesin-regulating mechanisms and factors have been identified so far, demonstrating that balanced kinesin activity in cells may involve multiple layers of complexity. Most mechanistic insights were obtained from studies on kinesin-1. Therefore, we deem it likely that many regulatory factors for other kinesin families are still to be discovered.

Scope of the thesis

Many cellular processes are dependent on the activity of kinesin motors. In this thesis, we address how kinesin transport is regulated by MAPs and cargo binding. We developed a tool to study MAP-microtubule interactions by NMR using isotope-labeled microtubules. Furthermore, we studied the kinesin-4 KIF21B and its function in regulating microtubule growth in T cells.

In **Chapter 2**, we show that MAP7 family proteins act redundantly in activating kinesin-1 in cells. MAP7 proteins recruit kinesin-1 to microtubules, but also activate motors through an allosteric effect exerted by the kinesin-binding domain of MAP7. We reveal that kinesin-1 motility is promoted through a continuous flow of weak transient interactions with MAP7 as the kinesin moves along the microtubule.

In **Chapter 3**, we zoom in at kinesin-based transport of exocytotic vesicles by the kinesin-1 KIF5B and kinesin-3 KIF13B motor. We show that both kinesins could be present on a single vesicle and that there is a clear task division: KIF5B is most active in the center of the cell where microtubules are more densely populated by MAP7 proteins. KIF13B takes the last steps towards peripheral microtubule plus ends; here, KIF5B loses its dominance since MAP7 proteins are less abundant because of their slow binding rates.

In **Chapter 4**, we explored new binding partners of all MAP7 family proteins and found that MAP7D2, but not the other MAP7 proteins, can interact with clathrin. We found that MAP7D2 contains a conserved clathrin-binding motif that can potently tether clathrin to microtubules. MAP7D2 depletion reduces clathrin localization in the proximal axon and we hypothesize that MAP7D2 might be involved in kinesin-1-dependent transport of clathrin.

In **Chapter 5**, we developed a protocol to produce isotope-labeled microtubules from HeLa cells for NMR studies. We show that MAPs such as MAP7 or the CKK domain of CAMSAP can have a different effect on the fast time-scale dynamics of the flexible tubulin tails. This approach may allow studies on intrinsically disordered MAPs and their dynamic interactions with microtubule lattices.

In **Chapter 6**, we show that the mitotic kinesin-6 MKLP2 (KIF20A) is a motile kinesin that transports the Chromosomal Passenger Complex as a cargo. We demonstrate that cargo binding promotes MKLP2 processivity *in vitro*. During anaphase, MKLP2 motor activity is essential to concentrate Chromosomal Passenger Complexes to the central spindle and sites at the cell cortex where furrow ingression is initiated.

In **Chapter 7**, we address the role of microtubule dynamics and length during rapid centrosome polarization in activated T cells. The kinesin-4 KIF21B is expressed in T cells and we demonstrate that it restricts microtubule growth by inducing catastrophes. This activity is important for centrosome polarization because it shapes the microtubule network and prevents formation of overly long microtubules that impair rapid translocation of the centrosome.

In **Chapter 8**, we discuss our results from chapters 2 to 7 and put them in a broader perspective to give an overview of the future research directions for each subject.

References

Abaza, A., J.M. Soleilhac, J. Westendorf, M. Piel, I. Crevel, A. Roux, and F. Pirollet. 2003. M phase phosphoprotein 1 is a human plus-end-directed kinesin-related protein required for cytokinesis. J Biol Chem. 278:27844-27852.

Aher, A., and A. Akhmanova. 2018. Tipping microtubule dynamics, one protofilament at a time. Curr Opin Cell Biol. 50:86-93.

Akhmanova, A., and C.C. Hoogenraad. 2015. Microtubule minus-end-targeting proteins. Curr Biol. 25:R162-171.

Akhmanova, A., and M.O. Steinmetz. 2010. Microtubule +TIPs at a glance. J Cell Sci. 123:3415-3419.

Akhmanova, A., and M.O. Steinmetz. 2019. Microtubule minus-end regulation at a glance. J Cell Sci. 132.

Alberdi, L., A. Vergnes, J.B. Manneville, D.L. Tembo, Z. Fang, Y. Zhao, N. Schroeder, A. Dumont, M. Lagier, P. Bassereau, L. Redondo-Morata, J.P. Gorvel, and S. Meresse. 2020. Regulation of kinesin-1 activity by the Salmonella enterica effectors PipB2 and SifA. J Cell Sci. 133.

Andrews, P.D., Y. Ovechkina, N. Morrice, M. Wagenbach, K. Duncan, L. Wordeman, and J.R. Swedlow. 2004. Aurora B regulates MCAK at the mitotic centromere. Dev Cell. 6:253-268.

Arellano-Santoyo, H., E.A. Geyer, E. Stokasimov, G.Y. Chen, X. Su, W. Hancock, L.M. Rice, and D. Pellman. 2017. A Tubulin Binding Switch Underlies Kip3/Kinesin-8 Depolymerase Activity. Dev Cell. 42:37-51 e38.

Asselin, L., J. Rivera Alvarez, S. Heide, C.S. Bonnet, P. Tilly, H. Vitet, C. Weber, C.A. Bacino, K. Baranano, A. Chassevent, A. Dameron, L. Faivre, N.A. Hanchard, S. Mahida, K. McWalter, C. Mignot, C. Nava, A. Rastetter, H. Streff, C. Thauvin-Robinet, M.M. Weiss, G. Zapata, P.J.G. Zwijnenburg, F. Saudou, C. Depienne, C. Golzio, D. Heron, and J.D. Godin. 2020. Mutations in the KIF21B kinesin gene cause neurodevelopmental disorders through imbalanced canonical motor activity. Nat Commun. 11:2441.

Atherton, J., K. Jiang, M.M. Stangier, Y. Luo, S. Hua, K. Houben, J.J.E. van Hooff, A.P. Joseph, G. Scarabelli, B.J. Grant, A.J. Roberts, M. Topf, M.O. Steinmetz, M. Baldus, C.A. Moores, and A. Akhmanova. 2017a. A structural model for microtubule minus-end recognition and protection by CAMSAP proteins. Nat Struct Mol Biol. 24:931-943.

Atherton, J., Y. Luo, S. Xiang, C. Yang, A. Rai, K. Jiang, M. Stangier, A. Vemu, A.D. Cook, S. Wang, A. Roll-Mecak, M.O. Steinmetz, A. Akhmanova, M. Baldus, and C.A. Moores. 2019. Structural determinants of microtubule minus end preference in CAMSAP CKK domains. Nat Commun. 10:5236.

Atherton, J., I.M. Yu, A. Cook, J.M. Muretta, A. Joseph, J. Major, Y. Sourigues, J. Clause, M. Topf, S.S. Rosenfeld, A. Houdusse, and C.A. Moores. 2017b. The divergent mitotic kinesin MKLP2 exhibits atypical structure and mechanochemistry. Elife. 6.

Balabanian, L., C.L. Berger, and A.G. Hendricks. 2017. Acetylated Microtubules Are Preferentially Bundled Leading to Enhanced Kinesin-1 Motility. Biophys J. 113:1551-1560.

Balabanian, L., A.R. Chaudhary, and A.G. Hendricks. 2018. Traffic control inside the cell: microtubule-based regulation of cargo transport. The Biochemist. 40:14-17.

Barakeh, D., E. Faqeih, S. Anazi, S.A.-D. M, A. Softah, F. Albadr, H. Hassan, A.M. Alazami, and F.S. Alkuraya. 2015. The many faces of KIF7. Hum Genome Var. 2:15006.

Barisic, M., R. Silva e Sousa, S.K. Tripathy, M.M. Magiera, A.V. Zaytsev, A.L. Pereira, C. Janke, E.L. Grishchuk, and H. Maiato. 2015. Mitosis. Microtubule detyrosination guides chromosomes during mitosis. Science. 348:799-803.

Barlan, K., W. Lu, and V.I. Gelfand. 2013. The microtubule-binding protein ensconsin is an essential cofactor of kinesin-1. Curr Biol. 23:317-322.

Baumann, S., A. Komissarov, M. Gili, V. Ruprecht, S. Wieser, and S.P. Maurer. 2020. A reconstituted mammalian APC-kinesin complex selectively transports defined packages of axonal mRNAs. Sci Adv. 6:eaaz1588.

Bhabha, G., G.T. Johnson, C.M. Schroeder, and R.D. Vale. 2016. How Dynein Moves Along Microtubules. Trends Biochem Sci. 41:94-105.

Bianchi, S., W.E. van Riel, S.H. Kraatz, N. Olieric, D. Frey, E.A. Katrukha, R. Jaussi, J. Missimer, I. Grigoriev, V. Olieric, R.M. Benoit, M.O. Steinmetz, A. Akhmanova, and R.A. Kammerer. 2016. Structural basis for misregulation of kinesin KIF21A autoinhibition by CFEOM1 disease mutations. Sci Rep. 6:30668.

Bickel, K.G., B.J. Mann, J.S. Waitzman, T.A. Poor, S.E. Rice, and P. Wadsworth. 2017. Src family kinase phosphorylation of the motor domain of the human kinesin-5, Eg5. Cytoskeleton (Hoboken). 74:317-330.

Bieling, P., I.A. Telley, and T. Surrey. 2010. A minimal midzone protein module controls formation and length of antiparallel microtubule overlaps. Cell. 142:420-432.

Blangy, A., H.A. Lane, P. d'Herin, M. Harper, M. Kress, and E.A. Nigg. 1995. Phosphorylation by p34cdc2 regulates spindle association of human Eg5, a kinesin-related motor essential for bipolar spindle formation in vivo. Cell. 83:1159-1169.

Bodakuntla, S., A.S. Jijumon, C. Villablanca, C. Gonzalez-Billault, and C. Janke. 2019. Microtubule-Associated Proteins: Structuring the Cytoskeleton. Trends Cell Biol. 29:804-819.

Booth, D.G., F.E. Hood, I.A. Prior, and S.J. Royle. 2011. A TACC3/ch-TOG/clathrin complex stabilises kinetochore fibres by inter-microtubule bridging. EMBO J. 30:906-919.

Bouchet, B.P., R.E. Gough, Y.C. Ammon, D. van de Willige, H. Post, G. Jacquemet, A.M. Altelaar, A.J. Heck, B.T. Goult, and A. Akhmanova. 2016. Talin-KANK1 interaction controls the recruitment of cortical microtubule stabilizing complexes to focal adhesions. Elife. 5.

Braun, A., K. Dang, F. Buslig, M.A. Baird, M.W. Davidson, C.M. Waterman, and K.A. Myers. 2014. Rac1 and Aurora A regulate MCAK to polarize microtubule growth in migrating endothelial cells. J Cell Biol. 206:97-112.

Bringmann, H., G. Skiniotis, A. Spilker, S. Kandels-Lewis, I. Vernos, and T. Surrey. 2004. A kinesin-like motor inhibits microtubule dynamic instability. Science. 303:1519-1522.

Brouhard, G.J., and L.M. Rice. 2018. Microtubule dynamics: an interplay of biochemistry and mechanics. Nat Rev Mol Cell Biol. 19:451-463.

Brouwers, N., N. Mallol Martinez, and I. Vernos. 2017. Role of Kif15 and its novel mitotic partner KBP in K-fiber dynamics and chromosome alignment. PLoS One. 12:e0174819.

Burton, P.R., R.E. Hinkley, and G.B. Pierson. 1975. Tannic acid-stained microtubules with 12, 13, and 15 protofilaments. J Cell Biol. 65:227-233.

Cahu, J., A. Olichon, C. Hentrich, H. Schek, J. Drinjakovic, C. Zhang, A. Doherty-Kirby, G. Lajoie, and T. Surrey. 2008. Phosphorylation by Cdk1 increases the binding of Eg5 to microtubules in vitro and in Xenopus egg extract spindles. PLoS One. 3:e3936.

Cai, D., A.D. Hoppe, J.A. Swanson, and K.J. Verhey. 2007. Kinesin-1 structural organization and conformational changes revealed by FRET stoichiometry in live cells. J Cell Biol. 176:51-63.

Can, S., S. Lacey, M. Gur, A.P. Carter, and A. Yildiz. 2019. Directionality of dynein is controlled by the angle and length of its stalk. Nature. 566:407-410.

Cao, Y., J. Lipka, R. Stucchi, M. Burute, X. Pan, S. Portegies, R. Tas, J. Willems, L. Will, H. MacGillavry, M. Altelaar, L.C. Kapitein, M. Harterink, and C.C. Hoogenraad. 2020. Microtubule Minus-End Binding Protein CAMSAP2 and Kinesin-14 Motor KIFC3 Control Dendritic Microtubule Organization. Curr Biol. 30:899-908 e896.

Carleton, M., M. Mao, M. Biery, P. Warrener, S. Kim, C. Buser, C.G. Marshall, C. Fernandes, J. Annis, and P.S. Linsley. 2006. RNA interference-mediated silencing of mitotic kinesin KIF14 disrupts cell cycle progression and induces cytokinesis failure. Mol Cell Biol. 26:3853-3863.

Chen, G.Y., J.M. Cleary, A.B. Asenjo, Y. Chen, J.A. Mascaro, D.F.J. Arginteanu, H. Sosa, and W.O. Hancock. 2019. Kinesin-5 Promotes Microtubule Nucleation and Assembly by Stabilizing a Lattice-Competent Conformation of Tubulin. Curr Biol. 29:2259-2269 e2254.

Chen, J., Y. Kanai, N.J. Cowan, and N. Hirokawa. 1992. Projection domains of MAP2 and tau determine spacings between microtubules in dendrites and axons. Nature. 360:674-677.

Chen, K., W.-G. Saw, D. Lama, C. Verma, G. Grüber, and C.-G. Koh. 2018. Phosphorylation regulates auto-inhibition of kinesin KIF3A. bioRxiv:503680.

Chen, Y., and W.O. Hancock. 2015. Kinesin-5 is a microtubule polymerase. Nat Commun. 6:8160.

Cheng, L., J. Desai, C.J. Miranda, J.S. Duncan, W. Qiu, A.A. Nugent, A.L. Kolpak, C.C. Wu, E. Drokhlyansky, M.M. Delisle, W.M. Chan, Y. Wei, F. Propst, S.L. Reck-Peterson, B. Fritzsch, and E.C. Engle. 2014. Human CFEOM1 mutations attenuate KIF21A autoinhibition and cause oculomotor axon stalling. Neuron. 82:334-349.

Cheung, H.O., X. Zhang, A. Ribeiro, R. Mo, S. Makino, V. Puviindran, K.K. Law, J. Briscoe, and C.C. Hui. 2009. The kinesin protein Kif7 is a critical regulator of Gli transcription factors in mammalian hedgehog signaling. Sci Signal. 2:ra29.

Chiba, K., K.Y. Chien, Y. Sobu, S. Hata, S. Kato, T. Nakaya, Y. Okada, A.C. Nairn, M. Kinjo, H. Taru, R. Wang, and T. Suzuki. 2017. Phosphorylation of KLC1 modifies interaction with JIP1 and abolishes the enhanced fast velocity of APP transport by kinesin-1. Mol Biol Cell. 28:3857-3869.

Cho, K.I., Y. Cai, H. Yi, A. Yeh, A. Aslanukov, and P.A. Ferreira. 2007. Association of the kinesin-binding domain of RanBP2 to KIF5B and KIF5C determines mitochondria localization and function. Traffic. 8:1722-1735.

Cho, K.I., H. Yi, R. Desai, A.R. Hand, A.L. Haas, and P.A. Ferreira. 2009. RANBP2 is an allosteric activator of the conventional kinesin-1 motor protein, KIF5B, in a minimal cell-free system. EMBO Rep. 10:480-486.

Cockburn, J.J.B., S.J. Hesketh, P. Mulhair, M. Thomsen, M.J. O'Connell, and M. Way. 2018. Insights into Kinesin-1 Activation from the Crystal Structure of KLC2 Bound to JIP3. Structure. 26:1486-1498 e1486.

Conway, L., M.W. Gramlich, S.M. Ali Tabei, and J.L. Ross. 2014. Microtubule orientation and spacing within bundles is critical for long-range kinesin-1 motility. Cytoskeleton (Hoboken). 71:595-610.

Coy, D.L., W.O. Hancock, M. Wagenbach, and J. Howard. 1999. Kinesin's tail domain is an inhibitory regulator of the motor domain. Nat Cell Biol. 1:288-292.

Cunha-Ferreira, I., A. Chazeau, R.R. Buijs, R. Stucchi, L. Will, X. Pan, Y. Adolfs, C. van der Meer, J.C. Wolthuis, O.I. Kahn, P. Schatzle, M. Altelaar, R.J. Pasterkamp, L.C. Kapitein, and C.C. Hoogenraad. 2018. The HAUS Complex Is a Key Regulator of Non-centrosomal Microtubule Organization during Neuronal Development. Cell Rep. 24:791-800.

Dafinger, C., M.C. Liebau, S.M. Elsayed, Y. Hellenbroich, E. Boltshauser, G.C. Korenke, F. Fabretti, A.R. Janecke, I. Ebermann, G. Nurnberg, P. Nurnberg, H. Zentgraf, F. Koerber, K. Addicks, E. Elsobky, T. Benzing, B. Schermer, and H.J. Bolz. 2011. Mutations in KIF7 link Joubert syndrome with Sonic Hedgehog signaling and microtubule dynamics. J Clin Invest. 121:2662-2667.

Daire, V., J. Giustiniani, I. Leroy-Gori, M. Quesnoit, S. Drevensek, A. Dimitrov, F. Perez, and C. Pous. 2009. Kinesin-1 regulates microtubule dynamics via a c-Jun N-terminal kinase-dependent mechanism. J Biol Chem. 284:31992-32001.

DeBerg, H.A., B.H. Blehm, J. Sheung, A.R. Thompson, C.S. Bookwalter, S.F. Torabi, T.A. Schroer, C.L. Berger, Y. Lu, K.M. Trybus, and P.R. Selvin. 2013. Motor domain phosphorylation modulates kinesin-1 transport. J Biol Chem. 288:32612-32621.

Demonchy, R., T. Blisnick, C. Deprez, G. Toutirais, C. Loussert, W. Marande, P. Grellier, P. Bastin, and L. Kohl. 2009. Kinesin 9 family members perform separate functions in the trypanosome flagellum. J Cell Biol. 187:615-622.

Desai, A., and T.J. Mitchison. 1997. Microtubule polymerization dynamics. Annu Rev Cell Dev Biol. 13:83-117.

Drechsler, H., T. McHugh, M.R. Singleton, N.J. Carter, and A.D. McAinsh. 2014. The Kinesin-12 Kif15 is a processive track-switching tetramer. Elife. 3:e01724.

Drechsler, H., Y. Xu, V.F. Geyer, Y. Zhang, and S. Diez. 2019. Multivalent electrostatic microtubule interactions of synthetic peptides are sufficient to mimic advanced MAP-like behavior. Mol Biol Cell. 30:2953-2968.

Du, Y., C.A. English, and R. Ohi. 2010. The kinesin-8 Kif18A dampens microtubule plus-end dynamics. Curr Biol. 20:374-380.

Dunn, S., E.E. Morrison, T.B. Liverpool, C. Molina-Paris, R.A. Cross, M.C. Alonso, and M. Peckham. 2008. Differential trafficking of Kif5c on tyrosinated and detyrosinated microtubules in live cells. J Cell Sci. 121:1085-1095.

Ems-McClung, S.C., S.G. Hainline, J. Devare, H. Zong, S. Cai, S.K. Carnes, S.L. Shaw, and C.E. Walczak. 2013. Aurora B inhibits MCAK activity through a phosphoconformational switch that reduces microtubule association. Curr Biol. 23:2491-2499.

Endoh-Yamagami, S., M. Evangelista, D. Wilson, X. Wen, J.W. Theunissen, K. Phamluong, M. Davis, S.J. Scales, M.J. Solloway, F.J. de Sauvage, and A.S. Peterson. 2009. The mammalian Cos2 homolog Kif7 plays an essential role in modulating Hh signal transduction during development. Curr Biol. 19:1320-1326.

Espeut, J., A. Gaussen, P. Bieling, V. Morin, S. Prieto, D. Fesquet, T. Surrey, and A. Abrieu. 2008. Phosphorylation relieves autoinhibition of the kinetochore motor Cenp-E. Mol Cell. 29:637-643.

Faltova, L., K. Jiang, D. Frey, Y. Wu, G. Capitani, A.E. Prota, A. Akhmanova, M.O. Steinmetz, and R.A. Kammerer. 2019. Crystal Structure of a Heterotetrameric Katanin p60:p80 Complex. Structure. 27:1375-1383 e1373.

Friel, C.T., and J.P. Welburn. 2018. Parts list for a microtubule depolymerising kinesin. Biochem Soc Trans. 46:1665-1672.

Fukuda, Y., A. Luchniak, E.R. Murphy, and M.L. Gupta, Jr. 2014. Spatial control of microtubule length and lifetime by opposing stabilizing and destabilizing functions of Kinesin-8. Curr Biol. 24:1826-1835.

Furuta, K., and Y.Y. Toyoshima. 2008. Minus-end-directed motor Ncd exhibits processive movement that is enhanced by microtubule bundling in vitro. Curr Biol. 18:152-157.

Gadadhar, S., S. Bodakuntla, K. Natarajan, and C. Janke. 2017. The tubulin code at a glance. J Cell Sci. 130:1347-1353.

Ghiretti, A.E., E. Thies, M.K. Tokito, T. Lin, E.M. Ostap, M. Kneussel, and E.L.F. Holzbaur. 2016. Activity-Dependent Regulation of Distinct Transport and Cytoskeletal Remodeling Functions of the Dendritic Kinesin KIF21B. Neuron. 92:857-872.

Gilbert, S.P., S. Guzik-Lendrum, and I. Rayment. 2018. Kinesin-2 motors: Kinetics and biophysics. J Biol Chem. 293:4510-4518.

Gromova, K.V., M. Muhia, N. Rothammer, C.E. Gee, E. Thies, I. Schaefer, S. Kress, M.W. Kilimann, O. Shevchuk, T.G. Oertner, and M. Kneussel. 2018. Neurobeachin and the Kinesin KIF21B Are Critical for Endocytic Recycling of NMDA Receptors and Regulate Social Behavior. Cell Rep. 23:2705-2717.

Gruneberg, U., R. Neef, R. Honda, E.A. Nigg, and F.A. Barr. 2004. Relocation of Aurora B from centromeres to the central spindle at the metaphase to anaphase transition requires MKlp2. J Cell Biol. 166:167-172.

Gruneberg, U., R. Neef, X. Li, E.H. Chan, R.B. Chalamalasetty, E.A. Nigg, and F.A. Barr. 2006. KIF14 and citron kinase act together to promote efficient cytokinesis. J Cell Biol. 172:363-372.

Gudimchuk, N., B. Vitre, Y. Kim, A. Kiyatkin, D.W. Cleveland, F.I. Ataullakhanov, and E.L. Grishchuk. 2013. Kinetochore kinesin CENP-E is a processive bi-directional tracker of dynamic microtubule tips. Nat Cell Biol. 15:1079-1088.

Gumy, L.F., D.J. Chew, E. Tortosa, E.A. Katrukha, L.C. Kapitein, A.M. Tolkovsky, C.C. Hoogenraad, and J.W. Fawcett. 2013. The kinesin-2 family member KIF3C regulates microtubule dynamics and is required for axon growth and regeneration. J Neurosci. 33:11329-11345.

Guo, Q., S. Liao, Z. Zhu, Y. Li, F. Li, and C. Xu. 2018. Structural basis for the recognition of kinesin family member 21A (KIF21A) by the ankyrin domains of KANK1 and KANK2 proteins. J Biol Chem. 293:557-566.

Gupta, M.L., Jr., P. Carvalho, D.M. Roof, and D. Pellman. 2006. Plus end-specific depolymerase activity of Kip3, a kinesin-8 protein, explains its role in positioning the yeast mitotic spindle. Nat Cell Biol. 8:913-923.

Guzik-Lendrum, S., I. Rayment, and S.P. Gilbert. 2017. Homodimeric Kinesin-2 KIF3CC Promotes Microtubule Dynamics. Biophys J. 113:1845-1857.

Hammond, J.W., T.L. Blasius, V. Soppina, D. Cai, and K.J. Verhey. 2010. Autoinhibition of the kinesin-2 motor KIF17 via dual intramolecular mechanisms. J Cell Biol. 189:1013-1025.

Hannabuss, J., M. Lera-Ramirez, N.I. Cade, F.J. Fourniol, F. Nedelec, and T. Surrey. 2019. Self-Organization of Minimal Anaphase Spindle Midzone Bundles. Curr Biol. 29:2120-2130 e2127.

Harterink, M., K. Vocking, X. Pan, E.M. Soriano Jerez, L. Slenders, A. Freal, R.P. Tas, W.J. van de Wetering, K. Timmer, J. Motshagen, S.F.B. van Beuningen, L.C. Kapitein, W.J.C. Geerts, J.A. Post, and C.C. Hoogenraad. 2019. TRIM46 Organizes Microtubule Fasciculation in the Axon Initial Segment. J Neurosci. 39:4864-4873.

He, M., R. Subramanian, F. Bangs, T. Omelchenko, K.F. Liem, Jr., T.M. Kapoor, and K.V. Anderson. 2014. The kinesin-4 protein Kif7 regulates mammalian Hedgehog signalling by organizing the cilium tip compartment. Nat Cell Biol. 16:663-672.

Helenius, J., G. Brouhard, Y. Kalaidzidis, S. Diez, and J. Howard. 2006. The depolymerizing kinesin MCAK uses lattice diffusion to rapidly target microtubule ends. Nature. 441:115-119.

Henrichs, V., L. Grycova, C. Barinka, Z. Nahacka, J. Neuzil, S. Diez, J. Rohlena, M. Braun, and Z. Lansky.

2020. Mitochondria-adaptor TRAK1 promotes kinesin-1 driven transport in crowded environments. Nat Commun. 11:3123.

Hirokawa, N., Y. Noda, Y. Tanaka, and S. Niwa. 2009. Kinesin superfamily motor proteins and intracellular transport. Nat Rev Mol Cell Biol. 10:682-696.

Homma, N., Y. Takei, Y. Tanaka, T. Nakata, S. Terada, M. Kikkawa, Y. Noda, and N. Hirokawa. 2003. Kinesin superfamily protein 2A (KIF2A) functions in suppression of collateral branch extension. Cell. 114:229-239.

Honnappa, S., S.M. Gouveia, A. Weisbrich, F.F. Damberger, N.S. Bhavesh, H. Jawhari, I. Grigoriev, F.J. van Rijssel, R.M. Buey, A. Lawera, I. Jelesarov, F.K. Winkler, K. Wuthrich, A. Akhmanova, and M.O. Steinmetz. 2009. An EB1-binding motif acts as a microtubule tip localization signal. Cell. 138:366-376.

Hummer, S., and T.U. Mayer. 2009. Cdk1 negatively regulates midzone localization of the mitotic kinesin Mklp2 and the chromosomal passenger complex. Curr Biol. 19:607-612.

Hutterer, A., M. Glotzer, and M. Mishima. 2009. Clustering of centralspindlin is essential for its accumulation to the central spindle and the midbody. Curr Biol. 19:2043-2049.

Janisch, K.M., K.C. McNeely, J.M. Dardick, S.H. Lim, and N.D. Dwyer. 2018. Kinesin-6 KIF20B is required for efficient cytokinetic furrowing and timely abscission in human cells. Mol Biol Cell. 29:166-179.

Jiang, K., L. Faltova, S. Hua, G. Capitani, A.E. Prota, C. Landgraf, R. Volkmer, R.A. Kammerer, M.O. Steinmetz, and A. Akhmanova. 2018. Structural Basis of Formation of the Microtubule Minus-End-Regulating CAMSAP-Katanin Complex. Structure. 26:375-382 e374.

Jiang, K., S. Hua, R. Mohan, I. Grigoriev, K.W. Yau, Q. Liu, E.A. Katrukha, A.F. Altelaar, A.J. Heck, C.C. Hoogenraad, and A. Akhmanova. 2014. Microtubule minus-end stabilization by polymerization-driven CAMSAP deposition. Dev Cell. 28:295-309.

Jiang, K., L. Rezabkova, S. Hua, Q. Liu, G. Capitani, A.F.M. Altelaar, A.J.R. Heck, R.A. Kammerer, M.O. Steinmetz, and A. Akhmanova. 2017. Microtubule minus-end regulation at spindle poles by an ASPM-katanin complex. Nat Cell Biol. 19:480-492.

Jiang, S., N. Mani, E.M. Wilson-Kubalek, P.I. Ku, R.A. Milligan, and R. Subramanian. 2019. Interplay between the Kinesin and Tubulin Mechanochemical Cycles Underlies Microtubule Tip Tracking by the Non-motile Ciliary Kinesin Kif7. Dev Cell. 49:711-730 e718.

Jolly, A.L., H. Kim, D. Srinivasan, M. Lakonishok, A.G. Larson, and V.I. Gelfand. 2010. Kinesin-1 heavy chain mediates microtubule sliding to drive changes in cell shape. Proc Natl Acad Sci U S A. 107:12151-12156.

Kannan, M., E. Bayam, C. Wagner, B. Rinaldi, P.F. Kretz, P. Tilly, M. Roos, L. McGillewie, S. Bar, S. Minocha, C. Chevalier, C. Po, P. Sanger Mouse Genetics, J. Chelly, J.L. Mandel, R. Borgatti, A. Piton, C. Kinnear, B. Loos, D.J. Adams, Y. Herault, S.C. Collins, S. Friant, J.D. Godin, and B. Yalcin. 2017. WD40-repeat 47, a microtubule-associated protein, is essential for brain development and autophagy. Proc Natl Acad Sci U S A. 114:E9308-E9317.

Kapitein, L.C., B.H. Kwok, J.S. Weinger, C.F. Schmidt, T.M. Kapoor, and E.J. Peterman. 2008. Microtubule cross-linking triggers the directional motility of kinesin-5. J Cell Biol. 182:421-428.

Kapitein, L.C., E.J. Peterman, B.H. Kwok, J.H. Kim, T.M. Kapoor, and C.F. Schmidt. 2005. The bipolar mitotic kinesin Eg5 moves on both microtubules that it crosslinks. Nature. 435:114-118.

Karasmanis, E.P., C.T. Phan, D. Angelis, I.A. Kesisova, C.C. Hoogenraad, R.J. McKenney, and E.T. Spiliotis. 2018. Polarity of Neuronal Membrane Traffic Requires Sorting of Kinesin Motor Cargo during Entry into Dendrites by a Microtubule-Associated Septin. Dev Cell. 46:204-218 e207.

Kardon, J.R., and R.D. Vale. 2009. Regulators of the cytoplasmic dynein motor. Nat Rev Mol Cell Biol. 10:854-865.

Karuna, E.P., S.S. Choi, M.K. Scales, J. Hum, M. Cohen, F.A. Fierro, and H.H. Ho. 2018. Identification of a WNT5A-Responsive Degradation Domain in the Kinesin Superfamily Protein KIF26B. Genes (Basel). 9.

Katoh, M., and M. Katoh. 2005. Characterization of KIF12 gene in silico. Oncol Rep. 13:367-370.

Kaul, N., V. Soppina, and K.J. Verhey. 2014. Effects of alpha-tubulin K40 acetylation and detyrosination on kinesin-1 motility in a purified system. Biophys J. 106:2636-2643.

Kellogg, E.H., N.M.A. Hejab, S. Poepsel, K.H. Downing, F. DiMaio, and E. Nogales. 2018. Near-atomic model of microtubule-tau interactions. Science. 360:1242-1246.

Kevenaar, J.T., S. Bianchi, M. van Spronsen, N. Olieric, J. Lipka, C.P. Frias, M. Mikhaylova, M. Harterink, N. Keijzer, P.S. Wulf, M. Hilbert, L.C. Kapitein, E. de Graaff, A. Ahkmanova, M.O. Steinmetz, and C.C. Hoogenraad. 2016. Kinesin-Binding Protein Controls Microtubule Dynamics and Cargo Trafficking by Regulating Kinesin Motor Activity. Curr Biol. 26:849-861.

Khanal, I., A. Elbediwy, C. Diaz de la Loza Mdel, G.C. Fletcher, and B.J. Thompson. 2016. Shot and Patronin polarise microtubules to direct membrane traffic and biogenesis of microvilli in epithelia. J Cell Sci. 129:2651-2659.

Kim, S., K. Lee, J.H. Choi, N. Ringstad, and B.D. Dynlacht. 2015. Nek2 activation of Kif24 ensures cilium disassembly during the cell cycle. Nat Commun. 6:8087.

Kitagawa, M., S.Y. Fung, U.F. Hameed, H. Goto, M. Inagaki, and S.H. Lee. 2014. Cdk1 coordinates timely activation of MKlp2 kinesin with relocation of the chromosome passenger complex for cytokinesis. Cell Rep. 7:166-179.

Kitagawa, M., S.Y. Fung, N. Onishi, H. Saya, and S.H. Lee. 2013. Targeting Aurora B to the equatorial cortex by MKlp2 is required for cytokinesis. PLoS One. 8:e64826.

Kobayashi, T., W.Y. Tsang, J. Li, W. Lane, and B.D. Dynlacht. 2011. Centriolar kinesin Kif24 interacts with CP110 to remodel microtubules and regulate ciliogenesis. Cell. 145:914-925.

Konjikusic, M.J., P. Yeetong, C.W. Boswell, C. Lee, E.C. Roberson, R. Ittiwut, K. Suphapeetiporn, B. Ciruna, C.A. Gurnett, J.B. Wallingford, V. Shotelersuk, and R.S. Gray. 2018. Mutations in Kinesin family member 6 reveal specific role in ependymal cell ciliogenesis and human neurological development. PLoS Genet. 14:e1007817.

Kurasawa, Y., W.C. Earnshaw, Y. Mochizuki, N. Dohmae, and K. Todokoro. 2004. Essential roles of KIF4 and its binding partner PRC1 in organized central spindle midzone formation. EMBO J. 23:3237-3248.

Labonte, D., E. Thies, and M. Kneussel. 2014. The kinesin KIF21B participates in the cell surface delivery of gamma2 subunit-containing GABAA receptors. Eur J Cell Biol. 93:338-346.

Labonte, D., E. Thies, Y. Pechmann, A.J. Groffen, M. Verhage, A.B. Smit, R.E. van Kesteren, and M. Kneussel. 2013. TRIM3 regulates the motility of the kinesin motor protein KIF21B. PLoS One. 8:e75603.

Lan, W., X. Zhang, S.L. Kline-Smith, S.E. Rosasco, G.A. Barrett-Wilt, J. Shabanowitz, D.F. Hunt, C.E. Walczak, and P.T. Stukenberg. 2004. Aurora B phosphorylates centromeric MCAK and regulates its localization and microtubule depolymerization activity. Curr Biol. 14:273-286.

Lawrence, C.J., R.K. Dawe, K.R. Christie, D.W. Cleveland, S.C. Dawson, S.A. Endow, L.S. Goldstein, H.V. Goodson, N. Hirokawa, J. Howard, R.L. Malmberg, J.R. McIntosh, H. Miki, T.J. Mitchison, Y. Okada, A.S. Reddy, W.M. Saxton, M. Schliwa, J.M. Scholey, R.D. Vale, C.E. Walczak, and L. Wordeman. 2004. A standardized kinesin nomenclature. J Cell Biol. 167:19-22.

Lee, T., K.J. Langford, J.M. Askham, A. Bruning-Richardson, and E.E. Morrison. 2008. MCAK associates with EB1. Oncogene. 27:2494-2500.

Leung, C.L., D. Sun, M. Zheng, D.R. Knowles, and R.K. Liem. 1999. Microtubule actin cross-linking factor (MACF): a hybrid of dystonin and dystrophin that can interact with the actin and microtubule cytoskeletons. J Cell Biol. 147:1275-1286.

Levesque, A.A., and D.A. Compton. 2001. The chromokinesin Kid is necessary for chromosome arm orientation and oscillation, but not congression, on mitotic spindles. J Cell Biol. 154:1135-1146.

Li, Q.R., X.M. Yan, L. Guo, J. Li, and Y. Zang. 2018. AMPK regulates anaphase central spindle length by phosphorylation of KIF4A. J Mol Cell Biol. 10:2-17.

Liem, K.F., Jr., M. He, P.J. Ocbina, and K.V. Anderson. 2009. Mouse Kif7/Costal2 is a cilia-associated protein that regulates Sonic hedgehog signaling. Proc Natl Acad Sci U S A. 106:13377-13382.

Lin, Y., Y.L. Wei, and Z.Y. She. 2020. Kinesin-8 motors: regulation of microtubule dynamics and chromosome movements. Chromosoma. 129:99-110.

Lipka, J., L.C. Kapitein, J. Jaworski, and C.C. Hoogenraad. 2016. Microtubule-binding protein doublecortin-like kinase 1 (DCLK1) guides kinesin-3-mediated cargo transport to dendrites. EMBO J. 35:302-318.

Liu, J.S., C.R. Schubert, X. Fu, F.J. Fourniol, J.K. Jaiswal, A. Houdusse, C.M. Stultz, C.A. Moores, and C.A. Walsh. 2012. Molecular basis for specific regulation of neuronal kinesin-3 motors by doublecortin family proteins. Mol Cell. 47:707-721.

Liu, Y., Z. Zhang, H. Liang, X. Zhao, L. Liang, G. Wang, J. Yang, Y. Jin, M.A. McNutt, and Y. Yin. 2017. Protein Phosphatase 2A (PP2A) Regulates EG5 to Control Mitotic Progression. Sci Rep. 7:1630.

Magiera, M.M., P. Singh, and C. Janke. 2018. SnapShot: Functions of Tubulin Posttranslational Modifications. Cell. 173:1552-1552 e1551.

Maiato, H., A.M. Gomes, F. Sousa, and M. Barisic. 2017. Mechanisms of Chromosome Congression during Mitosis. Biology (Basel). 6.

Mandelkow, E.M., E. Mandelkow, and R.A. Milligan. 1991. Microtubule dynamics and microtubule caps: a time-resolved cryo-electron microscopy study. J Cell Biol. 114:977-991.

Marszalek, J.R., J.A. Weiner, S.J. Farlow, J. Chun, and L.S. Goldstein. 1999. Novel dendritic kinesin sorting identified by different process targeting of two related kinesins: KIF21A and KIF21B. J Cell Biol. 145:469-479.

Mayr, M.I., M. Storch, J. Howard, and T.U. Mayer. 2011. A non-motor microtubule binding site is essential for the high processivity and mitotic function of kinesin-8 Kif18A. PLoS One. 6:e27471.

McHugh, T., A.A. Gluszek, and J.P.I. Welburn. 2018. Microtubule end tethering of a processive kinesin-8 motor Kif18b is required for spindle positioning. J Cell Biol. 217:2403-2416.

McHugh, T., J. Zou, V.A. Volkov, A. Bertin, S.K. Talapatra, J. Rappsilber, M. Dogterom, and J.P.I. Welburn. 2019. The depolymerase activity of MCAK shows a graded response to Aurora B kinase phosphorylation through allosteric regulation. J Cell Sci. 132.

McNally, F.J., and A. Roll-Mecak. 2018. Microtubule-severing enzymes: From cellular functions to molecular mechanism. J Cell Biol. 217:4057-4069.

McNeely, K.C., T.D. Cupp, J.N. Little, K.M. Janisch, A. Shrestha, and N.D. Dwyer. 2017. Mutation of Kinesin-6 Kif20b causes defects in cortical neuron polarization and morphogenesis. Neural Dev. 12:5.

Metivier, M., B.Y. Monroy, E. Gallaud, R. Caous, A. Pascal, L. Richard-Parpaillon, A. Guichet, K.M. Ori-McKenney, and R. Giet. 2019. Dual control of Kinesin-1 recruitment to microtubules by Ensconsin in Drosophila neuroblasts and oocytes. Development. 146.

Metzger, T., V. Gache, M. Xu, B. Cadot, E.S. Folker, B.E. Richardson, E.R. Gomes, and M.K. Baylies. 2012. MAP and kinesin-dependent nuclear positioning is required for skeletal muscle function. Nature. 484:120-124.

Meunier, S., M. Shvedunova, N. Van Nguyen, L. Avila, I. Vernos, and A. Akhtar. 2015. An epigenetic regulator emerges as microtubule minus-end binding and stabilizing factor in mitosis. Nat Commun. 6:7889.

Miyata, H., K. Shimada, A. Morohoshi, S. Oura, T. Matsumura, Z. Xu, Y. Oyama, and M. Ikawa. 2020. Testis-enriched kinesin KIF9 is important for progressive motility in mouse spermatozoa. FASEB J. 34:5389-5400.

Monroy, B.Y., D.L. Sawyer, B.E. Ackermann, M.M. Borden, T.C. Tan, and K.M. Ori-McKenney. 2018. Competition between microtubule-associated proteins directs motor transport. Nat Commun. 9:1487.

Monroy, B.Y., T.C. Tan, J.M. Oclaman, J.S. Han, S. Simo, S. Niwa, D.W. Nowakowski, R.J. McKenney, and K.M. Ori-McKenney. 2020. A Combinatorial MAP Code Dictates Polarized Microtubule Transport. Dev Cell. 53:60-72 e64.

Montenegro Gouveia, S., K. Leslie, L.C. Kapitein, R.M. Buey, I. Grigoriev, M. Wagenbach, I. Smal, E. Meijering, C.C. Hoogenraad, L. Wordeman, M.O. Steinmetz, and A. Akhmanova. 2010. In vitro reconstitution of the functional interplay between MCAK and EB3 at microtubule plus ends. Curr Biol. 20:1717-1722.

Moore, A.T., K.E. Rankin, G. von Dassow, L. Peris, M. Wagenbach, Y. Ovechkina, A. Andrieux, D. Job, and L. Wordeman. 2005. MCAK associates with the tips of polymerizing microtubules. J Cell Biol. 169:391-397.

Morfini, G., N. Schmidt, C. Weissmann, G. Pigino, and S. Kins. 2016. Conventional kinesin: Biochemical heterogeneity and functional implications in health and disease. Brain Res Bull. 126:347-353.

Morfini, G., G. Szebenyi, R. Elluru, N. Ratner, and S.T. Brady. 2002. Glycogen synthase kinase 3 phosphorylates kinesin light chains and negatively regulates kinesin-based motility. EMBO J. 21:281-293.

Morikawa, M., Y. Tanaka, H.S. Cho, M. Yoshihara, and N. Hirokawa. 2018. The Molecular Motor KIF21B Mediates Synaptic Plasticity and Fear Extinction by Terminating Rac1 Activation. Cell Rep. 23:3864-3877.

Muhia, M., E. Thies, D. Labonte, A.E. Ghiretti, K.V. Gromova, F. Xompero, C. Lappe-Siefke, I. Hermans-Borgmeyer, D. Kuhl, M. Schweizer, O. Ohana, J.R. Schwarz, E.L.F. Holzbaur, and M. Kneussel. 2016. The Kinesin KIF21B Regulates Microtubule Dynamics and Is Essential for Neuronal Morphology, Synapse Function, and Learning and Memory. Cell Rep. 15:968-977.

Muralidharan, H., and P.W. Baas. 2019. Mitotic Motor KIFC1 Is an Organizer of Microtubules in the Axon. J Neurosci. 39:3792-3811.

Muto, E., H. Sakai, and K. Kaseda. 2005. Long-range cooperative binding of kinesin to a microtubule in the presence of ATP. J Cell Biol. 168:691-696.

Nguyen, T.Q., M. Aumont-Nicaise, J. Andreani, C. Velours, M. Chenon, F. Vilela, C. Geneste, P.F. Varela, P. Llinas, and J. Menetrey. 2018. Characterization of the binding mode of JNK-interacting protein 1 (JIP1) to kinesin-light chain 1 (KLC1). J Biol Chem. 293:13946-13960.

Niwa, S., K. Nakajima, H. Miki, Y. Minato, D. Wang, and N. Hirokawa. 2012. KIF19A is a microtubule-depolymerizing kinesin for ciliary length control. Dev Cell. 23:1167-1175.

Noordstra, I., and A. Akhmanova. 2017. Linking cortical microtubule attachment and exocytosis. F1000Res. 6:469.

Noordstra, I., Q. Liu, W. Nijenhuis, S. Hua, K. Jiang, M. Baars, S. Remmelzwaal, M. Martin, L.C. Kapitein, and A. Akhmanova. 2016. Control of apico-basal epithelial polarity by the microtubule minus-end-binding protein CAMSAP3 and spectraplakin ACF7. J Cell Sci. 129:4278-4288.

Nozawa, Y.I., E. Yao, R. Gacayan, S.M. Xu, and P.T. Chuang. 2014. Mammalian Fused is essential for sperm head shaping and periaxonemal structure formation during spermatogenesis. Dev Biol. 388:170-180.

Nunes Bastos, R., S.R. Gandhi, R.D. Baron, U. Gruneberg, E.A. Nigg, and F.A. Barr. 2013. Aurora B suppresses microtubule dynamics and limits central spindle size by locally activating KIF4A. J Cell Biol. 202:605-621.

Pan, W., K. Sun, K. Tang, Q. Xiao, C. Ma, C. Yu, and Z. Wei. 2018. Structural insights into ankyrin repeat-mediated recognition of the kinesin motor protein KIF21A by KANK1, a scaffold protein in focal adhesion. J Biol Chem. 293:1944-1956.

Patel, J.T., H.R. Belsham, A.J. Rathbone, B. Wickstead, C. Gell, and C.T. Friel. 2016. The family-specific alpha4-helix of the kinesin-13, MCAK, is critical to microtubule end recognition. Open Biol. 6.

Peet, D.R., N.J. Burroughs, and R.A. Cross. 2018. Kinesin expands and stabilizes the GDP-microtubule lattice. Nat Nanotechnol. 13:386-391.

Peris, L., M. Wagenbach, L. Lafanechere, J. Brocard, A.T. Moore, F. Kozielski, D. Job, L. Wordeman, and A. Andrieux. 2009. Motor-dependent microtubule disassembly driven by tubulin tyrosination. J Cell Biol. 185:1159-1166.

Poser, E., R. Caous, U. Gruneberg, and F.A. Barr. 2019. Aurora A promotes chromosome congression by activating the condensin-dependent pool of KIF4A. J Cell Biol. 219.

Prins, K.W., J.L. Humston, A. Mehta, V. Tate, E. Ralston, and J.M. Ervasti. 2009. Dystrophin is a microtubule-associated protein. J Cell Biol. 186:363-369.

Qiang, L., W. Yu, A. Andreadis, M. Luo, and P.W. Baas. 2006. Tau protects microtubules in the axon from severing by katanin. J Neurosci. 26:3120-3129.

Ramkumar, A., B.Y. Jong, and K.M. Ori-McKenney. 2018. ReMAPping the microtubule landscape: How phosphorylation dictates the activities of microtubule-associated proteins. Dev Dyn. 247:138-155.

Randall, T.S., Y.Y. Yip, D.J. Wallock-Richards, K. Pfisterer, A. Sanger, W. Ficek, R.A. Steiner, A.J. Beavil, M. Parsons, and M.P. Dodding. 2017. A small-molecule activator of kinesin-1 drives remodeling of the microtubule network. Proc Natl Acad Sci U S A. 114:13738-13743.

Rapley, J., M. Nicolas, A. Groen, L. Regue, M.T. Bertran, C. Caelles, J. Avruch, and J. Roig. 2008. The NIMA-family kinase Nek6 phosphorylates the kinesin Eg5 at a novel site necessary for mitotic spindle formation. J Cell Sci. 121:3912-3921.

Rath, O., and F. Kozielski. 2012. Kinesins and cancer. Nat Rev Cancer. 12:527-539.

Reck-Peterson, S.L., W.B. Redwine, R.D. Vale, and A.P. Carter. 2018. The cytoplasmic dynein transport machinery and its many cargoes. Nat Rev Mol Cell Biol. 19:382-398.

Reed, N.A., D. Cai, T.L. Blasius, G.T. Jih, E. Meyhofer, J. Gaertig, and K.J. Verhey. 2006. Microtubule acetylation promotes kinesin-1 binding and transport. Curr Biol. 16:2166-2172.

Ritter, A., N.N. Kreis, F. Louwen, L. Wordeman, and J. Yuan. 2015. Molecular insight into the regulation and function of MCAK. Crit Rev Biochem Mol Biol. 51:228-245.

Robert, A., P. Tian, S.A. Adam, M. Kittisopikul, K. Jaqaman, R.D. Goldman, and V.I. Gelfand. 2019. Kinesin-dependent transport of keratin filaments: a unified mechanism for intermediate filament transport. FASEB J. 33:388-399.

Roostalu, J., and T. Surrey. 2017. Microtubule nucleation: beyond the template. Nat Rev Mol Cell Biol. 18:702-710.

Roostalu, J., C. Thomas, N.I. Cade, S. Kunzelmann, I.A. Taylor, and T. Surrey. 2020. The speed of GTP hydrolysis determines GTP cap size and controls microtubule stability. Elife. 9.

Royle, S.J. 2012. The role of clathrin in mitotic spindle organisation. J Cell Sci. 125:19-28.

Sackett, D.L., B. Bhattacharyya, and J. Wolff. 1985. Tubulin subunit carboxyl termini determine polymerization efficiency. J Biol Chem. 260:43-45.

Sanchez-Huertas, C., and J. Luders. 2015. The augmin connection in the geometry of microtubule networks. Curr Biol. 25:R294-299.

Sapir, T., T. Levy, A. Sakakibara, A. Rabinkov, T. Miyata, and O. Reiner. 2013. Shootin1 acts in concert with KIF20B to promote polarization of migrating neurons. J Neurosci. 33:11932-11948.

Sardar, H.S., V.G. Luczak, M.M. Lopez, B.C. Lister, and S.P. Gilbert. 2010. Mitotic kinesin CENP-E promotes microtubule plus-end elongation. Curr Biol. 20:1648-1653.

Schaedel, L., C. Lorenz, A.V. Schepers, S. Klumpp, and S. Köster. 2020. Vimentin Intermediate Filaments Stabilize Dynamic Microtubules by Direct Interactions. bioRxiv:2020.2005.2020.106179.

Schimert, K.I., B.G. Budaitis, D.N. Reinemann, M.J. Lang, and K.J. Verhey. 2019. Intracellular cargo transport by single-headed kinesin motors. Proc Natl Acad Sci U S A. 116:6152-6161.

Scholey, J.M. 2013. Kinesin-2: a family of heterotrimeric and homodimeric motors with diverse intracellular transport functions. Annu Rev Cell Dev Biol. 29:443-469.

Seeger, M.A., and S.E. Rice. 2010. Microtubule-associated protein-like binding of the kinesin-1 tail to microtubules. J Biol Chem. 285:8155-8162.

Serena, M., R.N. Bastos, P.R. Elliott, and F.A. Barr. 2020. Molecular basis of MKLP2-dependent Aurora B transport from chromatin to the anaphase central spindle. J Cell Biol. 219.

Sferra, A., F. Fattori, T. Rizza, E. Flex, E. Bellacchio, A. Bruselles, S. Petrini, S. Cecchetti, M. Teson, F. Restaldi, A. Ciolfi, F.M. Santorelli, G. Zanni, S. Barresi, C. Castiglioni, M. Tartaglia, and E. Bertini. 2018. Defective kinesin binding of TUBB2A causes progressive spastic ataxia syndrome resembling sacsinopathy. Hum Mol Genet. 27:1892-1904.

She, Z.Y., and W.X. Yang. 2017. Molecular mechanisms of kinesin-14 motors in spindle assembly and chromosome segregation. J Cell Sci. 130:2097-2110.

Shigematsu, H., T. Imasaki, C. Doki, T. Sumi, M. Aoki, T. Uchikubo-Kamo, A. Sakamoto, K. Tokuraku, M. Shirouzu, and R. Nitta. 2018. Structural insight into microtubule stabilization and kinesin inhibition by Tau family MAPs. J Cell Biol. 217:4155-4163.

Shima, T., M. Morikawa, J. Kaneshiro, T. Kambara, S. Kamimura, T. Yagi, H. Iwamoto, S. Uemura, H. Shigematsu, M. Shirouzu, T. Ichimura, T.M. Watanabe, R. Nitta, Y. Okada, and N. Hirokawa. 2018. Kinesin-binding-triggered conformation switching of microtubules contributes to polarized transport. J Cell Biol. 217:4164-4183.

Shiroguchi, K., M. Ohsugi, M. Edamatsu, T. Yamamoto, and Y.Y. Toyoshima. 2003. The second microtubule-binding site of monomeric kid enhances the microtubule affinity. J Biol Chem. 278:22460-22465.

Siddiqui, N., and A. Straube. 2017. Intracellular Cargo Transport by Kinesin-3 Motors. Biochemistry (Mosc). 82:803-815.

Siddiqui, N., A.J. Zwetsloot, A. Bachmann, D. Roth, H. Hussain, J. Brandt, I. Kaverina, and A. Straube. 2019. PTPN21 and Hook3 relieve KIF1C autoinhibition and activate intracellular transport. Nat Commun. 10:2693.

Sirajuddin, M., L.M. Rice, and R.D. Vale. 2014. Regulation of microtubule motors by tubulin isotypes and post-translational modifications. Nat Cell Biol. 16:335-344.

Soeda, S., K. Yamada-Nomoto, and M. Ohsugi. 2016. The microtubule-binding and coiled-coil domains of Kid are required to turn off the polar ejection force at anaphase. J Cell Sci. 129:3609-3619.

Soppina, V., S.R. Norris, A.S. Dizaji, M. Kortus, S. Veatch, M. Peckham, and K.J. Verhey. 2014. Dimerization of mammalian kinesin-3 motors results in superprocessive motion. Proc Natl Acad Sci U S A. 111:5562-5567.

Splinter, D., D.S. Razafsky, M.A. Schlager, A. Serra-Marques, I. Grigoriev, J. Demmers, N. Keijzer, K. Jiang, I. Poser, A.A. Hyman, C.C. Hoogenraad, S.J. King, and A. Akhmanova. 2012. BICD2, dynactin, and LIS1 cooperate in regulating dynein recruitment to cellular structures. Mol Biol Cell. 23:4226-4241.

Stout, J.R., A.L. Yount, J.A. Powers, C. Leblanc, S.C. Ems-McClung, and C.E. Walczak. 2011. Kif18B interacts with EB1 and controls astral microtubule length during mitosis. Mol Biol Cell. 22:3070-3080.

Stucchi, R., G. Plucinska, J.J.A. Hummel, E.E. Zahavi, I. Guerra San Juan, O. Klykov, R.A. Scheltema, A.F.M. Altelaar, and C.C. Hoogenraad. 2018. Regulation of KIF1A-Driven Dense Core Vesicle Transport: Ca(2+)/CaM Controls DCV Binding and Liprin-alpha/TANC2 Recruits DCVs to Postsynaptic Sites. Cell Rep. 24:685-700.

Stumpff, J., Y. Du, C.A. English, Z. Maliga, M. Wagenbach, C.L. Asbury, L. Wordeman, and R. Ohi. 2011. A tethering mechanism controls the processivity and kinetochore-microtubule plus-end enrichment of the kinesin-8 Kif18A. Mol Cell. 43:764-775.

Subramanian, R., S.C. Ti, L. Tan, S.A. Darst, and T.M. Kapoor. 2013. Marking and measuring single microtubules by PRC1 and kinesin-4. Cell. 154:377-390.

Subramanian, R., E.M. Wilson-Kubalek, C.P. Arthur, M.J. Bick, E.A. Campbell, S.A. Darst, R.A. Milligan, and T.M. Kapoor. 2010. Insights into antiparallel microtubule crosslinking by PRC1, a conserved nonmotor microtubule binding protein. Cell. 142:433-443.

Sung, H.H., I.A. Telley, P. Papadaki, A. Ephrussi, T. Surrey, and P. Rorth. 2008. Drosophila ensconsin promotes productive recruitment of Kinesin-1 to microtubules. Dev Cell. 15:866-876.

Susman, M.W., E.P. Karuna, R.C. Kunz, T.S. Gujral, A.V. Cantu, S.S. Choi, B.Y. Jong, K. Okada, M.K. Scales, J. Hum, L.S. Hu, M.W. Kirschner, R. Nishinakamura, S. Yamada, D.J. Laird, L.E. Jao, S.P. Gygi, M.E. Greenberg, and H.H. Ho. 2017. Kinesin superfamily protein Kif26b links Wnt5a-Ror signaling to the control of cell and tissue behaviors in vertebrates. Elife. 6.

Sweeney, H.L., and E.L.F. Holzbaur. 2018. Motor Proteins. Cold Spring Harb Perspect Biol. 10.

Takahashi, M., T. Wakai, and T. Hirota. 2016. Condensin I-mediated mitotic chromosome assembly requires association with chromokinesin KIF4A. Genes Dev. 30:1931-1936.

Tanenbaum, M.E., L. Macurek, B. van der Vaart, M. Galli, A. Akhmanova, and R.H. Medema. 2011. A complex of Kif18b and MCAK promotes microtubule depolymerization and is negatively regulated by Aurora kinases. Curr Biol. 21:1356-1365.

Tas, R.P., A. Chazeau, B.M.C. Cloin, M.L.A. Lambers, C.C. Hoogenraad, and L.C. Kapitein. 2017. Differentiation between Oppositely Oriented Microtubules Controls Polarized Neuronal Transport. Neuron. 96:1264-1271 e1265.

Terabayashi, T., M. Sakaguchi, K. Shinmyozu, T. Ohshima, A. Johjima, T. Ogura, H. Miki, and R. Nishinakamura. 2012. Phosphorylation of Kif26b promotes its polyubiquitination and subsequent proteasomal degradation during kidney development. PLoS One. 7:e39714.

Thorn, K.S., J.A. Ubersax, and R.D. Vale. 2000. Engineering the processive run length of the kinesin motor. J Cell Biol. 151:1093-1100.

Tilney, L.G., J. Bryan, D.J. Bush, K. Fujiwara, M.S. Mooseker, D.B. Murphy, and D.H. Snyder. 1973. Microtubules: evidence for 13 protofilaments. J Cell Biol. 59:267-275.

Tischfield, M.A., H.N. Baris, C. Wu, G. Rudolph, L. Van Maldergem, W. He, W.M. Chan, C. Andrews, J.L. Demer, R.L. Robertson, D.A. Mackey, J.B. Ruddle, T.D. Bird, I. Gottlob, C. Pieh, E.I. Traboulsi, S.L. Pomeroy, D.G. Hunter, J.S. Soul, A. Newlin, L.J. Sabol, E.J. Doherty, C.E. de Uzcategui, N. de Uzcategui, M.L. Collins, E.C. Sener, B. Wabbels, H. Hellebrand, T. Meitinger, T. de Berardinis, A. Magli, C. Schiavi, M. Pastore-Trossello, F. Koc, A.M. Wong, A.V. Levin, M.T. Geraghty, M. Descartes, M. Flaherty, R.V. Jamieson, H.U. Moller, I. Meuthen, D.F. Callen, J. Kerwin, S. Lindsay, A. Meindl, M.L. Gupta, Jr., D. Pellman, and E.C. Engle. 2010. Human TUBB3 mutations perturb microtubule dynamics, kinesin interactions, and axon guidance. Cell. 140:74-87.

Torres, J.Z., M.K. Summers, D. Peterson, M.J. Brauer, J. Lee, S. Senese, A.A. Gholkar, Y.C. Lo, X. Lei, K. Jung, D.C. Anderson, D.P. Davis, L. Belmont, and P.K. Jackson. 2011. The STARD9/Kif16a kinesin associates with mitotic microtubules and regulates spindle pole assembly. Cell. 147:1309-1323.

Traboulsi, E.I., and E.C. Engle. 2004. Mutations in KIF21A are responsible for CFEOM1 worldwide. Ophthalmic Genet. 25:237-239.

Trofimova, D., M. Paydar, A. Zara, L. Talje, B.H. Kwok, and J.S. Allingham. 2018. Ternary complex of Kif2A-bound tandem tubulin heterodimers represents a kinesin-13-mediated microtubule depolymerization reaction intermediate. Nat Commun. 9:2628.

Twelvetrees, A.E., F. Lesept, E.L.F. Holzbaur, and J.T. Kittler. 2019. The adaptor proteins HAP1a and GRIP1 collaborate to activate the kinesin-1 isoform KIF5C. J Cell Sci. 132.

Uchida, A., N.H. Alami, and A. Brown. 2009. Tight functional coupling of kinesin-1A and dynein motors in the bidirectional transport of neurofilaments. Mol Biol Cell. 20:4997-5006.

Urnavicius, L., C.K. Lau, M.M. Elshenawy, E. Morales-Rios, C. Motz, A. Yildiz, and A.P. Carter. 2018. Cryo-EM shows how dynactin recruits two dyneins for faster movement. Nature. 554:202-206.

Vale, R.D., T.S. Reese, and M.P. Sheetz. 1985. Identification of a novel force-generating protein, kinesin, involved in microtubule-based motility. Cell. 42:39-50.

van Beuningen, S.F.B., L. Will, M. Harterink, A. Chazeau, E.Y. van Battum, C.P. Frias, M.A.M. Franker, E.A. Katrukha, R. Stucchi, K. Vocking, A.T. Antunes, L. Slenders, S. Doulkeridou, P. Sillevis Smitt, A.F.M. Altelaar, J.A. Post, A. Akhmanova, R.J. Pasterkamp, L.C. Kapitein, E. de Graaff, and C.C. Hoogenraad. 2015. TRIM46 Controls Neuronal Polarity and Axon Specification by Driving the Formation of Parallel Microtubule Arrays. Neuron. 88:1208-1226.

van der Vaart, B., W.E. van Riel, H. Doodhi, J.T. Kevenaar, E.A. Katrukha, L. Gumy, B.P. Bouchet, I. Grigoriev, S.A. Spangler, K.L. Yu, P.S. Wulf, J. Wu, G. Lansbergen, E.Y. van Battum, R.J. Pasterkamp, Y. Mimori-Kiyosue, J. Demmers, N. Olieric, I.V. Maly, C.C. Hoogenraad, and A. Akhmanova. 2013. CFEOM1-associated kinesin KIF21A is a cortical microtubule growth inhibitor. Dev Cell. 27:145-160.

van Riel, W.E., A. Rai, S. Bianchi, E.A. Katrukha, Q. Liu, A.J. Heck, C.C. Hoogenraad, M.O. Steinmetz, L.C. Kapitein, and A. Akhmanova. 2017. Kinesin-4 KIF21B is a potent microtubule pausing factor. Elife. 6.

Varga, V., J. Helenius, K. Tanaka, A.A. Hyman, T.U. Tanaka, and J. Howard. 2006. Yeast kinesin-8 depolymerizes microtubules in a length-dependent manner. Nat Cell Biol. 8:957-962.

Varga, V., C. Leduc, V. Bormuth, S. Diez, and J. Howard. 2009. Kinesin-8 motors act cooperatively to mediate length-dependent microtubule depolymerization. Cell. 138:1174-1183.

Verhey, K.J., J. Dishinger, and H.L. Kee. 2011a. Kinesin motors and primary cilia. Biochem Soc Trans. 39:1120-1125.

Verhey, K.J., and J.W. Hammond. 2009. Traffic control: regulation of kinesin motors. Nat Rev Mol Cell Biol. 10:765-777.

Verhey, K.J., N. Kaul, and V. Soppina. 2011b. Kinesin assembly and movement in cells. Annu Rev Biophys. 40:267-288.

Vulinovic, F., V. Krajka, T.J. Hausrat, P. Seibler, D. Alvarez-Fischer, H. Madoev, J.S. Park, K.R. Kumar, C.M. Sue, K. Lohmann, M. Kneussel, C. Klein, and A. Rakovic. 2018. Motor protein binding and mitochondrial transport are altered by pathogenic TUBB4A variants. Hum Mutat. 39:1901-1915.

Waitzman, J.S., and S.E. Rice. 2014. Mechanism and regulation of kinesin-5, an essential motor for the mitotic spindle. Biol Cell. 106:1-12.

Walczak, C.E., H. Zong, S. Jain, and J.R. Stout. 2016. Spatial regulation of astral microtubule dynamics by Kif18B in PtK cells. Mol Biol Cell. 27:3021-3030.

Walter, W.J., V. Beranek, E. Fischermeier, and S. Diez. 2012. Tubulin acetylation alone does not affect kinesin-1 velocity and run length in vitro. PLoS One. 7:e42218.

Wang, D., R. Nitta, M. Morikawa, H. Yajima, S. Inoue, H. Shigematsu, M. Kikkawa, and N. Hirokawa. 2016. Motility and microtubule depolymerization mechanisms of the Kinesin-8 motor, KIF19A. Elife. 5.

Wang, L., Y. Tanaka, D. Wang, M. Morikawa, R. Zhou, N. Homma, Y. Miyamoto, and N. Hirokawa. 2018. The Atypical Kinesin KIF26A Facilitates Termination of Nociceptive Responses by Sequestering Focal Adhesion Kinase. Cell Rep. 24:2894-2907.

Wang, W., S. Cantos-Fernandes, Y. Lv, H. Kuerban, S. Ahmad, C. Wang, and B. Gigant. 2017. Insight into microtubule disassembly by kinesin-13s from the structure of Kif2C bound to tubulin. Nat Commun. 8:70.

Wang, Z., and M.P. Sheetz. 2000. The C-terminus of tubulin increases cytoplasmic dynein and kinesin processivity. Biophys J. 78:1955-1964.

Weng, Z., Y. Shang, D. Yao, J. Zhu, and R. Zhang. 2018. Structural analyses of key features in the KANK1. KIF21A complex yield mechanistic insights into the cross-talk between microtubules and the cell cortex. J Biol Chem. 293:215-225.

White, E.A., and M. Glotzer. 2012. Centralspindlin: at the heart of cytokinesis. Cytoskeleton (Hoboken). 69:882-892.

Wilson, C.W., C.T. Nguyen, M.H. Chen, J.H. Yang, R. Gacayan, J. Huang, J.N. Chen, and P.T. Chuang. 2009. Fused has evolved divergent roles in vertebrate Hedgehog signalling and motile ciliogenesis. Nature. 459:98-102.

Wordeman, L., and T.J. Mitchison. 1995. Identification and partial characterization of mitotic centromere-associated kinesin, a kinesin-related protein that associates with centromeres during mitosis. J Cell Biol. 128:95-104.

Wu, J., C. de Heus, Q. Liu, B.P. Bouchet, I. Noordstra, K. Jiang, S. Hua, M. Martin, C. Yang, I. Grigoriev, E.A. Katrukha, A.F.M. Altelaar, C.C. Hoogenraad, R.Z. Qi, J. Klumperman, and A. Akhmanova. 2016. Molecular Pathway of Microtubule Organization at the Golgi Apparatus. Dev Cell. 39:44-60.

Xu, J., B.J. Reddy, P. Anand, Z. Shu, S. Cermelli, M.K. Mattson, S.K. Tripathy, M.T. Hoss, N.S. James, S.J. King, L. Huang, L. Bardwell, and S.P. Gross. 2012. Casein kinase 2 reverses tail-independent inactivation of kinesin-1. Nat Commun. 3:754.

Yajima, J., M. Edamatsu, J. Watai-Nishii, N. Tokai-Nishizumi, T. Yamamoto, and Y.Y. Toyoshima. 2003. The human chromokinesin Kid is a plus end-directed microtubule-based motor. EMBO J. 22:1067-1074.

Yang, C., J. Wu, C. de Heus, I. Grigoriev, N. Liv, Y. Yao, I. Smal, E. Meijering, J. Klumperman, R.Z. Qi, and A. Akhmanova. 2017. EB1 and EB3 regulate microtubule minus end organization and Golgi morphology. J Cell Biol. 216:3179-3198.

Yount, A.L., H. Zong, and C.E. Walczak. 2015. Regulatory mechanisms that control mitotic kinesins. Exp Cell Res. 334:70-77.

Yue, Y., T.L. Blasius, S. Zhang, S. Jariwala, B. Walker, B.J. Grant, J.C. Cochran, and K.J. Verhey. 2018. Altered chemomechanical coupling causes impaired motility of the kinesin-4 motors KIF27 and KIF7. J Cell Biol. 217:1319-1334.

Zhernov, I., S. Diez, M. Braun, and Z. Lansky. 2020. Intrinsically disordered domain of kinesin-3 Kif14 enables unique functional diversity. bioRxiv:2020.2001.2030.926501.

Zhong, A., F.Q. Tan, and W.X. Yang. 2016. Chromokinesin: Kinesin superfamily regulating cell division through chromosome and spindle. Gene. 589:43-48.

Zhou, R., S. Niwa, N. Homma, Y. Takei, and N. Hirokawa. 2009. KIF26A is an unconventional kinesin and regulates GDNF-Ret signaling in enteric neuronal development. Cell. 139:802-813.

Zhu, C., and W. Jiang. 2005. Cell cycle-dependent translocation of PRC1 on the spindle by Kif4 is essential for midzone formation and cytokinesis. Proc Natl Acad Sci U S A. 102:343-348.

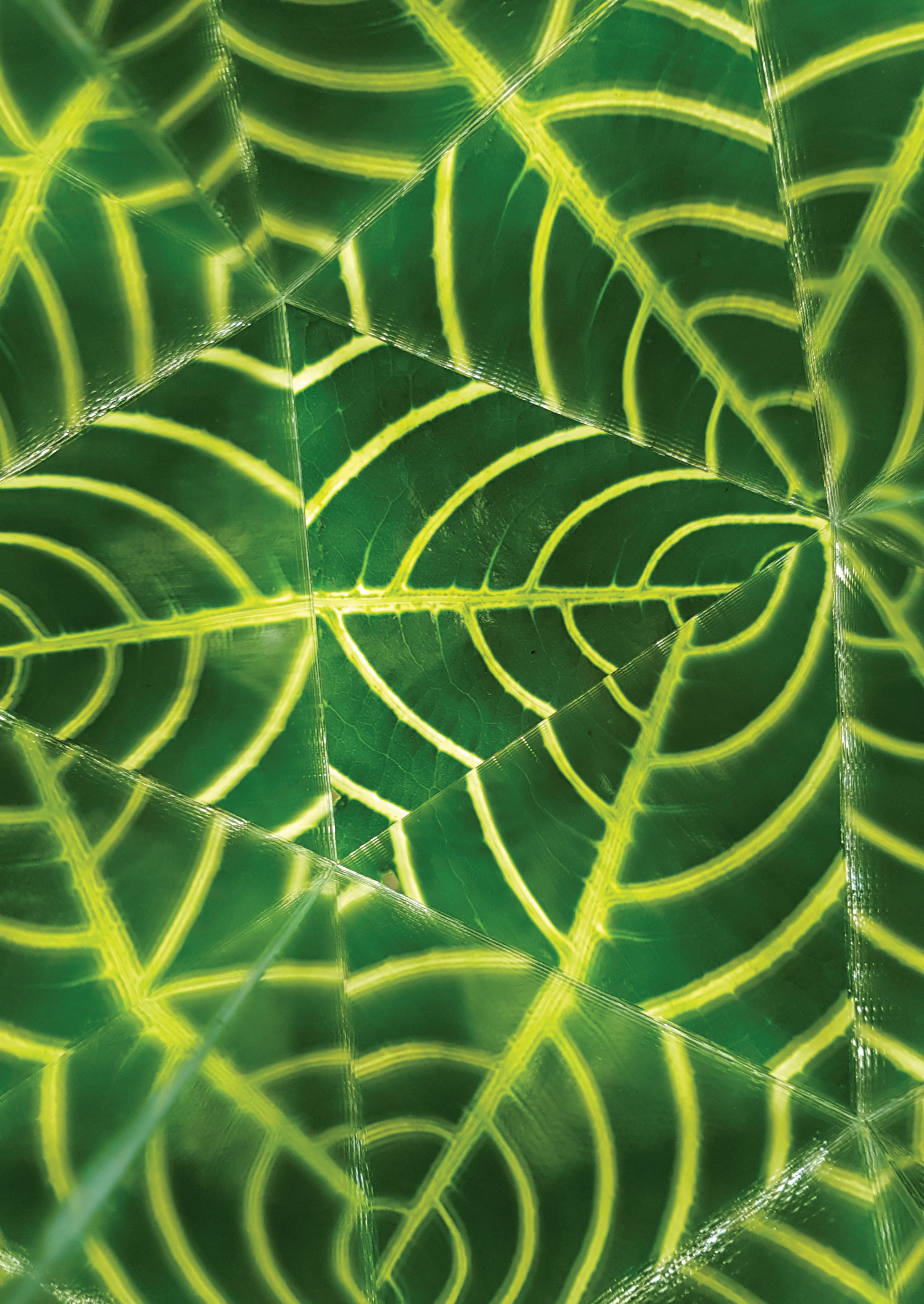

2

MAP7 family proteins regulate kinesin-1 recruitment and activation

Peter Jan Hooikaas[1*], Maud Martin[1*], Tobias Mühlethaler[2],
Gert-Jan Kuijntjes[1], Cathelijn A.E. Peeters[1], Eugene A. Katrukha[1],
Luca Ferrari[3], Riccardo Stucchi[1], Daan G. F. Verhagen[1],
Wilhelmina E. van Riel[1], Ilya Grigoriev[1], A.F. Maarten Altelaar[4],
Casper C. Hoogenraad[1], Stefan G.D. Rüdiger[3], Michel O. Steinmetz[2,5],
Lukas C. Kapitein[1] and Anna Akhmanova[1]

Journal of Cell Biology (2019); 218:1298-1318

[*] These authors contributed equally

---

[1] Cell Biology, Department of Biology, Faculty of Science, Utrecht University, Padualaan 8, 3584 CH Utrecht, the Netherlands

[2] Laboratory of Biomolecular Research, Division of Biology and Chemistry, Paul Scherrer Institut, CH-5232 Villigen PSI, Switzerland

[3] Cellular Protein Chemistry, Bijvoet Center for Biomolecular Research, Utrecht University, Padualaan 8, 3584 CH Utrecht, The Netherlands.

[4] Biomolecular Mass Spectrometry and Proteomics, Bijvoet Center for Biomolecular Research, Utrecht Institute for Pharmaceutical Sciences and The Netherlands Proteomics Centre, Utrecht University, Padualaan 8, 3584 CH Utrecht, The Netherlands.

[5] University of Basel, Biozentrum, CH-4056 Basel, Switzerland.

Abstract

Kinesin-1 is responsible for microtubule-based transport of numerous cellular cargoes. Here, we explored the regulation of kinesin-1 by MAP7 proteins. We found that all four mammalian MAP7 family members bind to kinesin-1. In HeLa cells, MAP7, MAP7D1 and MAP7D3 act redundantly to enable kinesin-1-dependent transport and microtubule recruitment of the truncated kinesin-1 KIF5B-560, which contains the stalk but not the cargo-binding and autoregulatory regions. *In vitro*, purified MAP7 and MAP7D3 increase microtubule landing rate and processivity of kinesin-1 through transient association with the motor. MAP7 proteins promote binding of kinesin-1 to microtubules both directly, through the N-terminal microtubule-binding domain and unstructured linker region, and indirectly, through an allosteric effect exerted by the kinesin-binding C-terminal domain. Compared to MAP7, MAP7D3 has a higher affinity for kinesin-1 and a lower affinity for microtubules and, unlike MAP7, can be co-transported with the motor. We propose that MAP7 proteins are microtubule-tethered kinesin-1 activators, with which the motor transiently interacts as it moves along microtubules.

Introduction

Kinesins are molecular motors responsible for the transport of different organelles and macromolecular complexes along microtubules (MTs) and for controlling MT organization and dynamics (Hirokawa and Tanaka, 2015; Verhey et al., 2011). The spatial and temporal control of kinesin localization and activity depends on numerous factors, such as cargo adaptors, post-translational modifications and the interactions with MT-associated proteins (MAPs) (Akhmanova and Hammer, 2010; Barlan and Gelfand, 2017; Fu and Holzbaur, 2014; Verhey and Hammond, 2009).

Kinesin-1 is the major MT plus-end directed motor involved in a broad variety of transport processes (Akhmanova and Hammer, 2010; Hirokawa and Tanaka, 2015; Verhey et al., 2011). This motor is well known to be regulated by different MAPs. Neuronal MAPs tau and MAP2 inhibit kinesin-1-driven motility (Dixit et al., 2008; Ebneth et al., 1998; Gumy et al., 2017; Monroy et al., 2018; Seitz et al., 2002; Trinczek et al., 1999; Vershinin et al., 2007). In contrast, MAP7 family members are firmly established to be positive regulators of kinesin-1 (Barlan et al., 2013; Metivier et al., 2018; Metzger et al., 2012; Monroy et al., 2018; Sung et al., 2008). MAP7 proteins are represented by a single homologue, ensconsin, in flies and by four isoforms encoded by different genes, MAP7, MAP7D1, MAP7D2 and MAP7D3, in mammals (Bulinski and Bossler, 1994; Metzger et al., 2012; Yadav et al., 2014). All MAP7 family members have a similar organization, with two conserved domains that are predicted to be helical, connected by an unstructured linker. The N-terminal domain of MAP7 proteins strongly interacts with MTs, while the C-terminal domain binds to the stalk region of kinesin-1 (Metzger et al., 2012; Monroy et al., 2018; Sun et al., 2011) (Fig. 1A). Additional regions with MT affinity were found in the linker of MAP7 and the C-terminal part of MAP7D3 (Tymanskyj et al., 2018; Yadav et al., 2014). In flies, ensconsin is an essential kinesin-1 cofactor required for numerous processes ranging from organelle transport to MT sliding (Barlan et al., 2013; Metivier et al., 2018; Metzger et al., 2012; Monroy et al., 2018; Sung et al., 2008). In mammalian myotubes, MAP7 is needed for proper kinesin-1-dependent nuclear distribution (Metzger et al., 2012), but whether MAP7 proteins are needed for other kinesin-1-dependent processes in mammals has not been investigated. It is also unknown whether mammalian MAP7 homologues all behave similarly and whether they have different, overlapping or redundant functions.

Interestingly, *in vitro* experiments in fly ovary extracts have shown that the full-length kinesin-1, but not its minimal dimeric kinesin-1 fragment requires ensconsin for productive interaction with MTs (Sung et al., 2008). *In vitro* reconstitutions with purified proteins demonstrated that MAP7 recruited kinesin-1 to MTs and somewhat decreased motor velocity but had only a mild effect on kinesin-1 run length (Monroy et al., 2018). Importantly, MAP7 was highly immobile in these assays and was not co-transported with the motor, suggesting that MAP7 affects only the initial recruitment of the kinesin to MTs but has little impact on kinesin-1 movement (Monroy et al., 2018). However, some observations in flies do not agree with this simple model, as it was shown that the C-terminal fragment of ensconsin, which misses the MT binding domain (Sung et al., 2008), significantly rescues kinesin-1-related transport deficiencies in cells lacking ensconsin (Barlan et al., 2013; Metivier et al., 2018). Kinesin-1 is well known to be autoinhibited by its C-terminal cargo-binding domains (Verhey and Hammond, 2009), and it was proposed that ensconsin plays a role in relieving autoinhibition of the kinesin (Barlan et al., 2013). This possibility is in line with the experiments performed in extracts (Sung et al., 2008), but was not yet tested with purified proteins.

Here, we explored the relationship between kinesin-1 activity and mammalian MAP7 proteins. We found that MAP7 family members act redundantly to promote kinesin-1-dependent distribution of mitochondria, as well as MT binding of kinesin-1 KIF5B fragment 1-560 (K560) (Case et al., 1997), which contains the motor domain and the dimerizing stalk with the MAP7-binding site, but not the cargo-binding and autoinhibitory domains. MT recruitment of K560 was rescued not only by full-length MAP7's, but also by their C-terminal domains, which lacked the major MT binding region. These results were recapitulated using *in vitro* reconstitution assays with purified proteins, which provided evidence both for MT tethering and allosteric activation of kinesin-1 by MAP7 family members. In agreement with published data, we found that MAP7 was immobile on MTs *in vitro* (Monroy et al., 2018), whereas MAP7D3 could be observed moving together with K560 motors. In spite of these differences, both MAPs increased not only the recruitment of kinesin-1 to MTs but also its processivity. Such an effect can be explained if the interaction between MAP7's and kinesin-1 is weak and transient, and this was confirmed by biochemical and imaging experiments. Taken together, our data show that MAP7 proteins redundantly regulate kinesin-1-dependent transport by acting as MT-tethered recruitment factors and activators of this kinesin.

Results

MAP7 family members act redundantly in mitochondrial distribution in HeLa cells

To test whether all four MAP7 family members can potentially act as kinesin-1 regulators, we performed a pull down assay and found that all four MAP7 proteins could bind to the kinesin-1 deletion mutant K560 (Fig. 1A, B). Gene expression analysis at the mRNA and protein level indicated that HeLa cells co-express MAP7, MAP7D1 and MAP7D3 (Kikuchi et al., 2018; Syred et al., 2013), and we confirmed these data by antibody staining (Fig. 1C). In contrast, MAP7D2, which is highly expressed in brain tissue (Niida and Yachie, 2011), was not expressed in HeLa cells. To test if all three MAP7's are required for kinesin-1 function, we initially used the distribution of mitochondria as readout, because it strongly depends

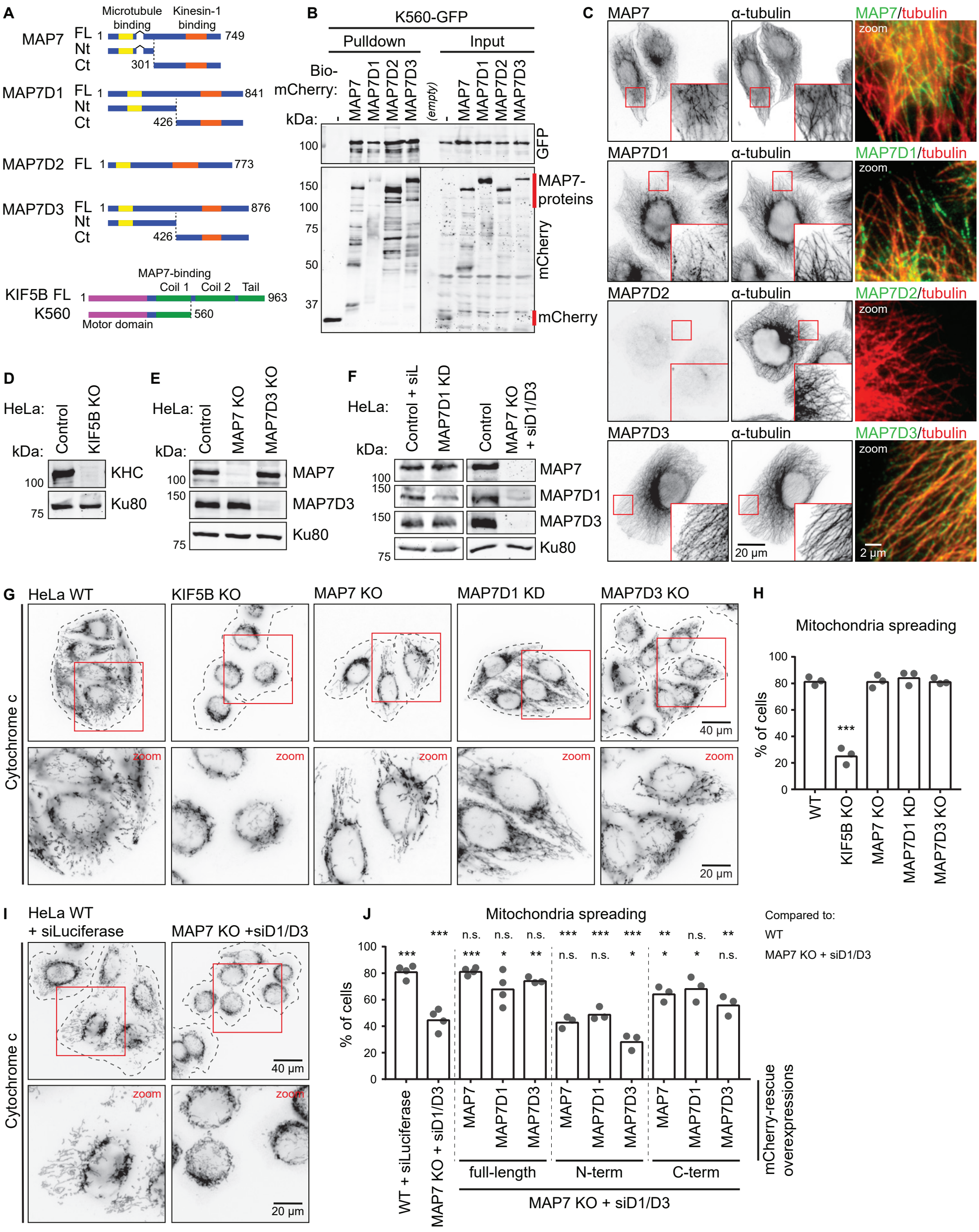

Figure 1 - Redundant function of MAP7 family proteins in kinesin-1-dependent mitochondria distribution

(A) Schemes of MAP7 family proteins and KIF5B constructs. **(B)** Streptavidin pull down assay with extracts of HEK293T cells expressing BirA, K560-GFP (prey) and the indicated Bio-mCherry-labeled proteins (bait) analyzed by Western blotting. Red lines indicate the position of mCherry (negative control) and MAP7 proteins. **(C)** Immunostaining of HeLa cells for endogenous MAP7 family members and α-tubulin imaged on a wide field microscope. **(D-F)** Western blot analysis of the indicated HeLa knockout (KO) and knockdown (KD) cells with the indicated antibodies; Ku80 was used as a loading control. **(G, I)** HeLa cells treated as indicated stained for mitochondria (cytochrome c). Cell outlines are indicated with grey dashed lines; zooms

Figure 1 (continued) (red squares) are shown below. **(H, J)** Mitochondria distribution scored per condition using cytochrome c staining, (H) n = 345, 347, 332, 338, and 373 cells from three independent experiments. Wild type (WT) vs KIF5B KO, p = 0.0002, Student's *t* test. **(J)** n = 444 (WT + siLuciferase), n = 589 (MAP7 KO + siMAP7D1/D3) and for rescue conditions on top of MAP7 KO + siMAP7D1/D3: n = 261, 277, 324, 297, 277, 296, 263, 267 and 416 cells all from three or four independent experiments, Student's *t* test: *, $p<0.05$, **, $p <0.01$ and *** $p <0.001$.

on kinesin-1 KIF5B (Tanaka et al., 1998). In the absence of KIF5B, mitochondria were no longer dispersed in the cytoplasm but were clustered around the nucleus (Fig. 1D, G, H). Next, we generated HeLa cells lacking each individual MAP7 family member. In these cells, the expression of the remaining MAP7's was not altered and no defects in the localization of mitochondria were observed (Fig. 1E-H).

We next attempted to generate a stable triple knockout of MAP7, MAP7D1 and MAP7D3, but such cells were not viable. It is unlikely that this was due to the lack of kinesin-1-mediated transport, as KIF5B knockout cells displayed no apparent growth or proliferation defects, and the two other kinesin-1 isoforms, KIF5A and KIF5C, do not seem to be expressed in HeLa cells (Nagaraj et al., 2011). Although MAP7 was shown to be phosphorylated and thus inactivated during mitosis (McHedlishvili et al., 2018), it is possible that MAP7 proteins still contribute to cell division, as ensconsin is known to participate in spindle formation in flies (Gallaud et al., 2014), and MAP7D3 was reported to modulate the recruitment of kinesin-13 to the mitotic spindle (Kwon et al., 2016). In order to remove all three MAP7 homologues simultaneously, we performed siRNA-mediated knockdown of MAP7D1 and MAP7D3 in the stable MAP7 knockout line, and this approach resulted in an efficient loss of all three MAP7 family members (Fig. 1F). Depletion of all three MAP7 homologs mimicked the effect of KIF5B knockout, leading to a strong perinuclear clustering of mitochondria (Fig. 1I, J). To exclude that this phenotype was caused by defects in MT organization, we assessed it by antibody staining and found that the overall MT arrangement and density were similar (Fig. S1A, B). Furthermore, live imaging of EB3-GFP showed no differences in MT plus-end growth, and polymerizing MT ends still reached the cell periphery (Fig. S1C-E). We conclude that MAP7 family members act redundantly in mitochondria localization and that this effect is unlikely to be due to alterations in MT network architecture.

Mitochondrial positioning in these cells was rescued by re-expressing individual full length MAP7 proteins, and it was also partially rescued by expressing the C-termini of MAP7 and MAP7D1 (Fig. 1J). Rescue with the MAP7D3 C-terminus was less efficient, because the construct was mostly accumulated in the nucleus, and, as its concentration in the cytoplasm was low, only highly expressing cells showed rescue (Fig. S1F).

Rescue of kinesin-1 function by MAP7 C-termini could be potentially explained by their residual affinity for MTs. For example, recent work has demonstrated that MAP7 contains an additional MT binding domain (termed "P-region") within the intrinsically disordered linker part of the protein (Tymanskyj et al., 2018) (Fig. 2A). To address this possibility, we systematically examined the ability of different parts of MAP7 linker to interact with MTs (Fig. 2A). Using a MT pelleting assay, we found that the C-terminal MAP7 fragment used in cellular experiments (Fig. 1A, J) did not co-sediment with MTs (Fig. 2B and S1G). We were also unable to detect the binding of the mCherry-tagged version of this fragment to MTs *in vitro* (Fig. S1H). Next, we tested MT binding of different MAP7 fragments by overexpression of their GFP-tagged fusions. Although we could re-confirm MT affinity of the P-region, its smaller fragments as well as other MAP7 deletion mutants lacking the N-terminal MT binding domain, including the MAP7-Ct and Ct(mini), showed no MT enrichment in HeLa cells

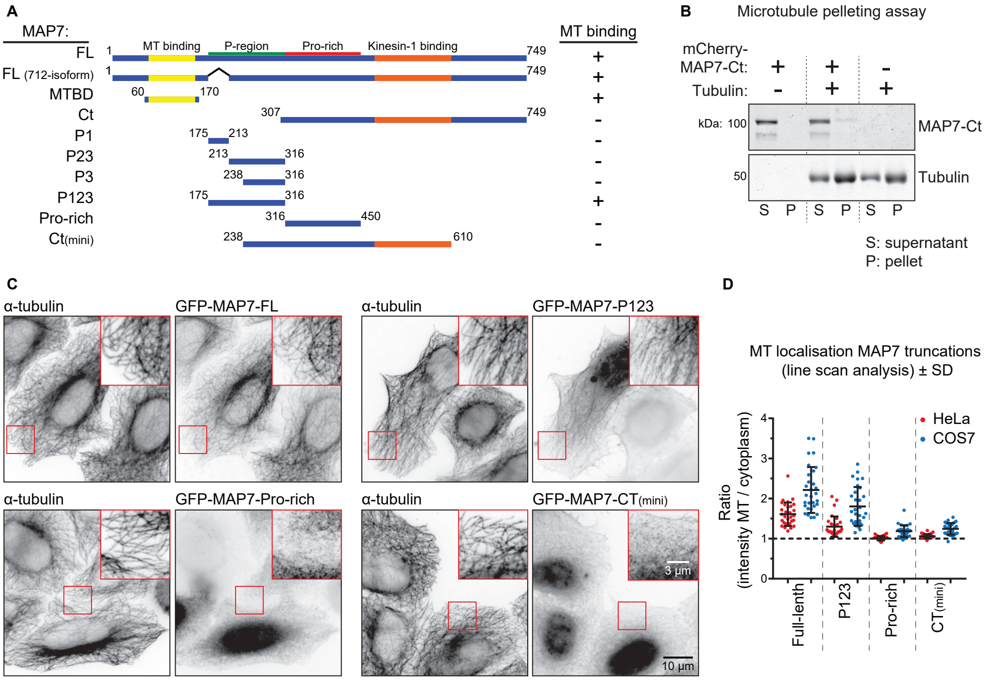

Figure 2 - Characterization of MT binding domains of MAP7
(A) Scheme of MAP7 truncations. MT binding was assayed by overexpression of GFP-tagged constructs and co-stain for α-tubulin; examples are shown in panel C. **(B)** MT pelleting assay with mCherry-MAP7-Ct analyzed by SDS-PAGE. Uncropped gel images are shown in Fig. S1G. **(C,D)** Indicated GFP-tagged MAP7 constructs were overexpressed in MAP7 KO HeLa cells co-stained for α-tubulin (C), to quantify their MT enrichment by line scan analysis (D). n = 10 cells representing 30 MTs (3 per cell) per condition.

(Fig. 2A, C and D). However, we could detect weak MT binding of the proline-rich part of the MAP7 linker as well as MAP7-Ct(mini) in COS7 cells, likely due to their flat morphology and low MT density (Fig. 2D and S2A). These data suggest that the C-terminal part of the MAP7 linker might have some weak MT affinity, which could contribute to but is unlikely to fully explain the ability of MAP7 C-terminus to rescue KIF5B-dependent mitochondria localization.

K560 binding to MTs in cells depends on MAP7 proteins

To show that the loss of MAP7 proteins has a direct effect on kinesin-1 activity, we next examined the distribution of the dimeric K560 truncation mutant that can move along MTs but does not bind to cargo. In control HeLa cells, this construct was distributed along MTs, and in most cells, it showed enhanced accumulation on MTs in cell corners, where MT plus ends are concentrated (Fig. 3A). Depletion of individual MAP7 family members did not alter this distribution except for the knockout of MAP7D3, in which less K560 accumulated on corner MTs (Fig. 3A, B). In contrast, in cells lacking all three MAP7 proteins, K560 showed a diffuse localization (Fig. 3C, E). Expression of MAP7, MAP7D1 or MAP7D2 in such cells rescued the recruitment of the kinesin to MTs, whereas expression of MAP7D3 led to strong co-accumulation of both constructs on MTs in the corners of almost all transfected

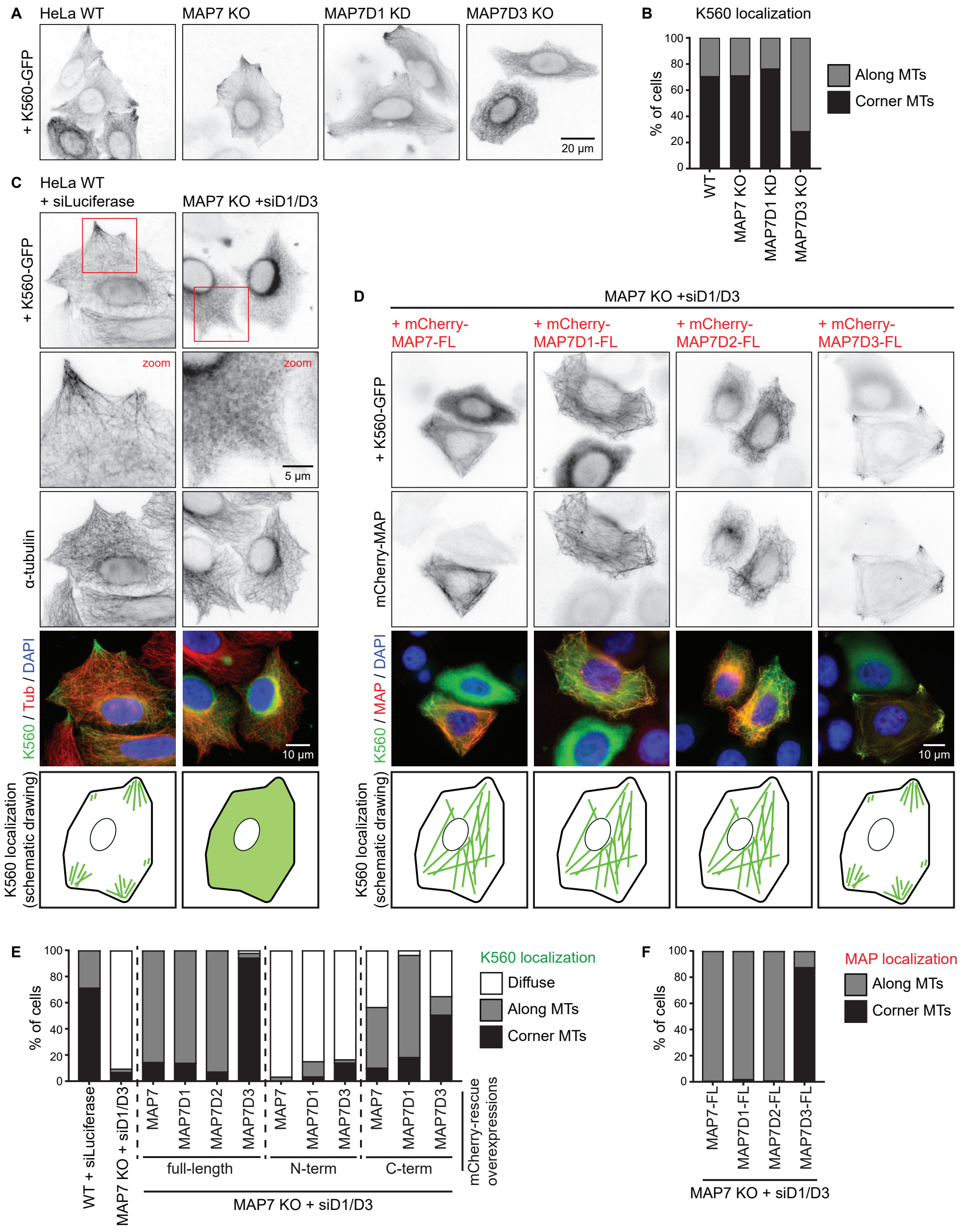
A
HeLa WT
MAP7 KO
MAP7D1 KD
MAP7D3 KO
+ K560-GFP
20 µm
B
K560 localization
% of cells
100
80
60
40
20
0
WT
MAP7 KO
MAP7D1 KD
MAP7D3 KO
Along MTs
Corner MTs
C
HeLa WT + siLuciferase
MAP7 KO +siD1/D3
+ K560-GFP
zoom
zoom
5 µm
α-tubulin
K560 / Tub / DAPI
10 µm
K560 localization (schematic drawing)
D
MAP7 KO +siD1/D3
+ mCherry-MAP7-FL
+ mCherry-MAP7D1-FL
+ mCherry-MAP7D2-FL
+ mCherry-MAP7D3-FL
+ K560-GFP
mCherry-MAP
K560 / MAP / DAPI
10 µm
K560 localization (schematic drawing)
E
% of cells
100
80
60
40
20
0
WT + siLuciferase
MAP7 KO + siD1/D3
MAP7
MAP7D1
MAP7D2
MAP7D3
MAP7
MAP7D1
MAP7D3
MAP7
MAP7D1
MAP7D3
full-length
N-term
C-term
MAP7 KO + siD1/D3
mCherry-rescue overexpressions
K560 localization
Diffuse
Along MTs
Corner MTs
F
% of cells
100
80
60
40
20
0
MAP7-FL
MAP7D1-FL
MAP7D2-FL
MAP7D3-FL
MAP7 KO + siD1/D3
MAP localization
Along MTs
Corner MTs

Figure 3. Kinesin-1 recruitment to MTs depends on MAP7 family proteins
(A,B) Wide field images of K560-GFP overexpressed in the indicated HeLa control, KO or KD conditions (A), and quantification of K560-GFP localization (B). n = 234, 252, 174, and 254 cells from three independent experiments. **(C,D)** Wide field images of K560-GFP overexpressed either alone or together with mCherry-tagged MAP7 constructs in control or MAP7 KO + siMAP7D1/D3 HeLa cells, as indicated. In (C), cells were co-stained for α-tubulin. A schematic drawing of K560-GFP localization is shown at the bottom. **(E,F)** Quantification of K560-GFP (E) and MAP7 construct (F) localization per condition, as indicated, categorized as: diffuse, along MTs or at corner MTs. n = 459 (WT + siLuciferase), n = 485 (MAP7 KO + siMAP7D1/D3) and

Figure 3 (continued) for rescue conditions: n = 113, 237, 90, 167, 210, 186, 133, 176, 197 and 193 cells from two to four independent experiments.

cells (Fig. 3D-F). Expression of the N-terminal, MT binding fragments of MAP7 and its homologs could not restore the distribution of K560, whereas significant rescue of MT binding by the kinesin was observed with the C-termini of all MAP7 proteins (Fig. 2E and S2B). We conclude that K560 displays low binding to cellular MTs in the absence of MAP7, and that this binding can be increased by kinesin-1-interacting C-terminal MAP7 fragments, which are diffusely localized in HeLa cells. The C-terminus of MAP7D3, which was mostly nuclear on its own (Fig. S1F), was retained in the cytoplasm when expressed together with K560, and shifted the localization of this kinesin fragment to MTs in cell corners, similar to the full-length MAP7D3 (Fig. 3D, E and S2B).

MAP7D3 but not MAP7 can be redistributed by kinesin-1

To understand why MAP7D3 but not the other MAP7 homologues promotes MT plus-end shifted distribution of K560, we next examined the distribution of endogenous MAP7 and MAP7D3 and found that only MAP7D3 could be efficiently relocalized by K560 to cell corners (Fig. 4A, B).

To prove that kinesin-1 can indeed rapidly relocalize MAP7D3, we have set up an optogenetics-based assay, in which K560 could be sequestered in the nucleus and then acutely released from it using a light-inducible nuclear export system (Niopek et al., 2016). A K560-mCherry, containing NLS sequences, was C-terminally tagged with an engineered domain of Avena sativa phototropin-1, AsLOV2, in which the Jα helix was modified to contain a nuclear export signal (Fig. 4C). Within 1 to 2 minutes after activation with blue light, K560 was efficiently exported from the nucleus (Fig. 4D, E, G, H). MAP7D3, but not MAP7 co-accumulated on MTs in cell corners within a 4-minute time frame (Fig. 4D-I, Video 1 and 2). We conclude that K560 can indeed acutely relocalize its own positive regulator MAP7D3, but not MAP7, when kinesin expression is sufficiently high.

To explain why the distribution of MAP7D3 but not that of MAP7 was sensitive to the presence of kinesin-1, we hypothesized that MAP7D3 might be more mobile on MTs. To test this idea, we performed Fluorescence Recovery after Photobleaching (FRAP) experiments with GFP-tagged MAP7 and MAP7D3 and found that the latter indeed exchanged much more rapidly on MTs (Fig. 4J, K). The different turnover rates of the two MAP7 family proteins on MTs, possibly combined with the different affinities to kinesin-1, seem to contribute to their differential relocalization by overexpressed kinesin-1.

MAP7 and MAP7D3 control kinesin-1 recruitment to MTs and motor processivity

To get further insight into the similarities and differences in the regulation of kinesin-1 by MAP7 proteins, we set up *in vitro* reconstitution assays. In contrast to previously published experiments, which employed taxol-stabilized MTs in the absence of free tubulin, we used dynamic MTs that were grown from GMPCPP-stabilized seeds (Bieling et al., 2007). Kinesins, MAPs and MTs were observed by Total Internal Reflection Fluorescence Microscopy (TIRFM), as described previously (van Riel et al., 2017). To study kinesin-1 motility, we purified full-length KIF5B-GFP and K560-GFP from HEK293T cells (Fig. S3A). Analyses by mass spectrometry and Western blotting showed that although some co-purification of MAP7, MAP7D1 and MAP7D3 with this kinesin was observed when the protein was washed with a low ionic strength buffer, this contamination was almost entirely removed when the

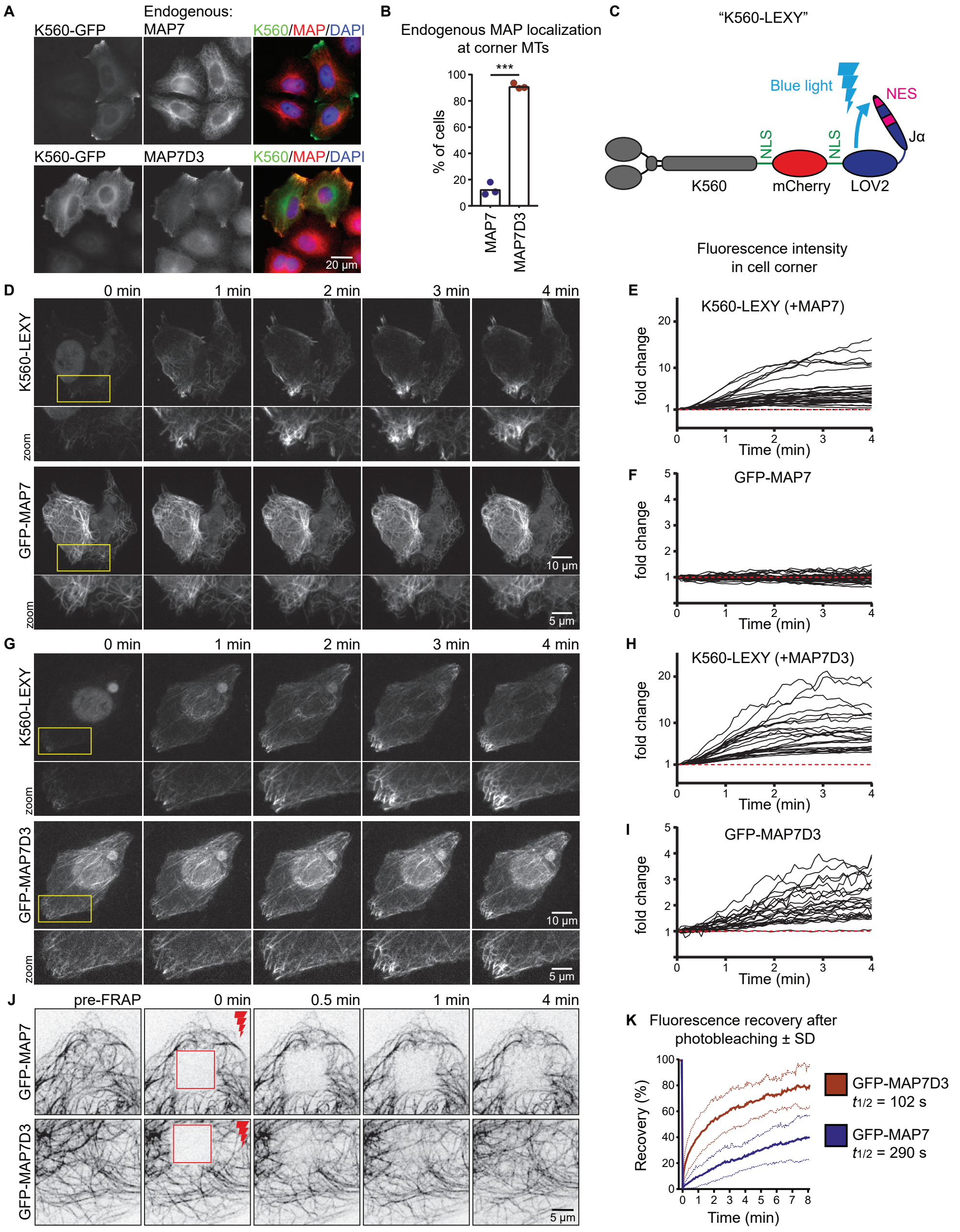
A
Endogenous:
K560-GFP
MAP7
K560/MAP/DAPI
K560-GFP
MAP7D3
K560/MAP/DAPI
20 µm
B
Endogenous MAP localization at corner MTs
***
% of cells
100
80
60
40
20
0
MAP7
MAP7D3
C
"K560-LEXY"
Blue light
NES
Jα
NLS
NLS
K560
mCherry
LOV2
D
0 min
1 min
2 min
3 min
4 min
K560-LEXY
zoom
GFP-MAP7
zoom
10 µm
5 µm
E
Fluorescence intensity in cell corner
K560-LEXY (+MAP7)
fold change
20
10
1
0
1
2
3
4
Time (min)
F
GFP-MAP7
fold change
5
4
3
2
1
0
1
2
3
4
Time (min)
G
0 min
1 min
2 min
3 min
4 min
K560-LEXY
zoom
GFP-MAP7D3
zoom
10 µm
5 µm
H
K560-LEXY (+MAP7D3)
fold change
20
10
1
0
1
2
3
4
Time (min)
I
GFP-MAP7D3
fold change
5
4
3
2
1
0
1
2
3
4
Time (min)
J
pre-FRAP
0 min
0.5 min
1 min
4 min
GFP-MAP7
GFP-MAP7D3
5 µm
K
Fluorescence recovery after photobleaching ± SD
Recovery (%)
100
80
60
40
20
0
0 1 2 3 4 5 6 7 8
Time (min)
GFP-MAP7D3
t1/2 = 102 s
GFP-MAP7
t1/2 = 290 s

Figure 4 - Kinesin-1 can redistribute MAP7D3 in cells
(A, B) Wide field images of K560-GFP overexpressed in HeLa cells stained for endogenous MAP7 or MAP7D3 (A) used to quantify endogenous MAP localization (B). n = 232 and 303 cells from three independent experiments, Student's *t* test: $p < 0.001$. **(C)** A scheme of K560-LEXY construct containing two NLS sequences and an mCherry tag. Blue light induces a conformation change, causing detachment of the Jα-peptide containing a nuclear export signal from the LOV2 domain. **(D, G)** Single frames of KIF5B KO cells co-transfected with K560-LEXY and GFP-MAP7 (D) or GFP-MAP7D3 (G) sequentially illuminated with green and blue light

Figure 4 (continued) (in that specific order). Zooms are indicated in yellow. **(E, F, H, I)** Measurements of fluorescence intensity changes over time in K560-LEXY-positive cell corners. Black lines represent single measurements of K560-LEXY (E,H), GFP-MAP7 (F) and GFP-MAP7D3 (I). n = 31 measurements from 17 cells (E, F) and n = 22 measurements from 14 cells (H, I), from two independent experiments. **(J)** Single frames of FRAP experiments on COS7 cells overexpressing GFP-MAP7 or -MAP7D3. Stills show a baseline (pre-FRAP), the first frame after photobleaching (0 min) and the indicated time points after FRAP of a 10x10 µm square region (shown in red). **(K)** Quantification of fluorescence recovery of J. The graph shows mean curves (bold lines) ±SD (light dotted lines) over time. n = 18 cells from three independent experiments for each condition.

ionic strength of the washing buffer was increased (Fig. S3B-E). We used such "high-salt washed" kinesin preparations for all our experiments. In cells, kinesin-1 can exist in a heterotetrametric form with two light and two heavy chains. Although some light chains could be detected by Western blotting (Fig. S3B), we assume that in our assays most full-length kinesins were dimers of heavy chains as no light chains were visible on a Coomassie-stained gel (Fig. S3A, red arrow).

The MAP7 binding site on kinesin-1 is well defined (Monroy et al., 2018) and pull down assays confirmed that there are no additional binding sites for MAP7 in the C-terminal coil or the tail of kinesin-1 (Fig. 5A, B). Kymograph analysis of full length kinesin-1 motors showed two populations of single molecule behavior: short binding events which did not result in processive movement (classified as events that last ≤1 second) or events of landing followed by processive movement. Addition of purified Alexa647-labeled SNAP-tag-MAP7 or -MAP7D3 (Fig. S3A) in these assays led to a dramatic increase (at least 60 fold) of both type of events (Fig. 5C, D). Furthermore, processive kinesin runs were on average ~1.6 fold longer (Fig. 5C, E), while the velocities were, especially upon addition of MAP7D3, reduced (Fig. 5C, F and S3G).

To further examine the effects of MAP7 and MAP7D3 on kinesin-1, we turned to the K560 fragment, which contains the MAP7-binding site but lacks the cargo-binding and autoinhibitory tail. When K560 was added to MAP7 or MAP7D3-decorated MTs, we observed a strong (up to 23.6 fold) increase in the motor landing frequency compared to K560 alone (Fig. 6A and B), in agreement with published data on MAP7 (Monroy et al., 2018). The landing frequency of K560 increased with higher MAP concentrations and correlated with increasing MT labeling intensity by the particular MAP (Fig. 6A-C and S4A). Furthermore, we found that MAP7D3 but not MAP7 caused a very significant decrease in kinesin velocity (Fig. 6D and S4B). Finally, we found that both MAP7 and MAP7D3 could induce a 2-fold increase in kinesin processivity (Fig. 6E-G), with some kinesin runs exceeding 10 µm in length. We note that for this quantification, we only took into account the runs, in which we observed both kinesin association and dissociation from the MT. Inclusion of all detected runs suggested that in the presence of MAP7 or MAP7D3, even longer runs could occur (not shown).

The increase of run lengths in the presence of MAP7 and MAP7D3 could be explained by kinesin multimerization or by a model where MAP7 acts as an additional MT attachment point. In these cases the distribution of run lengths is expected to be described by the sum of two or three exponential decays (Klumpp and Lipowsky, 2005). However, the corresponding best fit of distributions in Fig. 6F, G converged to a single exponential decay, suggesting that MAP7 directly affects kinesin's binding/unbinding rate constants, instead of introducing an additional intermediate binding state. Moreover, single molecule analysis of K560 moving on MTs showed that kinesin-1 intensity profiles matched that of a single dimer in assays both with and without MAP7D3 (Fig. S4C). In addition, we performed mixed kinesin assays where GFP- and SNAP(Alexa647)-tagged kinesins were used in a 1:1 ratio. If kinesin-1 would multimerize in the presence of MAP7 proteins, then one would expect to see a significant fraction of two-colored kinesin tracks per kymograph; however, such events were not observed (Fig. S4D), confirming our observation of K560 behaving as a single dimer on MAP7-decorated MTs. Taken together, these data suggest that the presence of MAP7 alters the state of single kinesin dimers.

Interestingly, MAP7 could promote kinesin processivity at high concentrations, when MTs were fully decorated, whereas MAP7D3 reduced kinesin detachment from MTs even at low concentrations (Fig. 6C, E-G). These data correlated with the observation that MAP7D3 but not MAP7 could move together with K560 *in vitro* (Fig. 6H, I). To find explanation for this difference in co-transport we examined single molecule dynamics of MAP7 and MAP7D3 on *in vitro* polymerized MTs and found that MAP7 showed very long static binding events, many of which exceeded our observation time (5 min) (Fig. 6J), in agreement with recently published data (Monroy et al., 2018). In contrast, MAP7D3 displayed a diffusive behavior, with many short binding events (Fig. 6J). These data are in agreement with the FRAP data, showing that in cells, MAP7D3 is more mobile than MAP7 (Fig. 4J, K). The density of MT labeling was higher with MAP7 than with MAP7D3 at the same protein concentration, indicating that the latter has a lower affinity for MTs (Fig. 6C, J and S4A). We

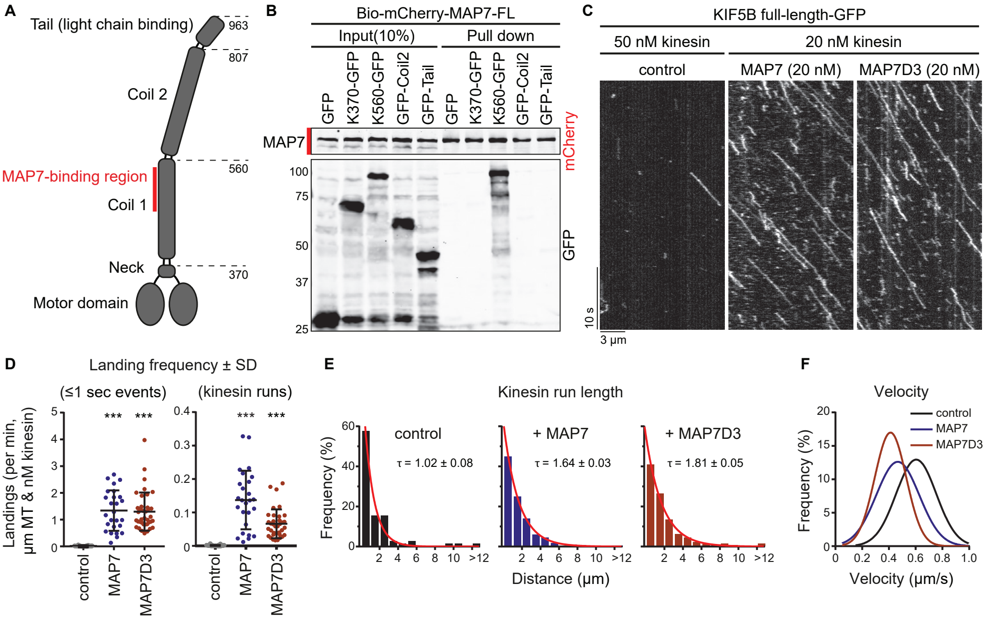

Figure 5 - Kinesin-1 is regulated by MAP7 proteins *in vitro*
(A) Overview of full-length kinesin-1 (KIF5B) domains. **(B)** Streptavidin pull down assay with extracts of HEK293T cells over-expressing BirA, the indicated KIF5B-GFP truncations (prey) and Bio-mCherry-MAP7 (bait) analyzed by Western blotting. **(C)** Kymographs of GFP-tagged full-length KIF5B (kinesin-1) on dynamic MTs in control conditions or in the presence of MAP7 or MAP7D3. **(D)** Quantification of kinesin-1 landing frequencies per MT and corrected for MT length, time of acquisition and kinesin concentration. n = 99, 26 and 38 MTs from 2 or 3 independent experiments. **(E)** Histograms of run lengths fitted to a single exponential decay (red) with indicated rate constants (tau) as a measure of mean run length. n = 71, 542 and 568 kinesin runs from 2 or 3 independent experiments. **(F)** Gaussian fits of kinesin velocities. Histograms are shown in Fig. S3G.

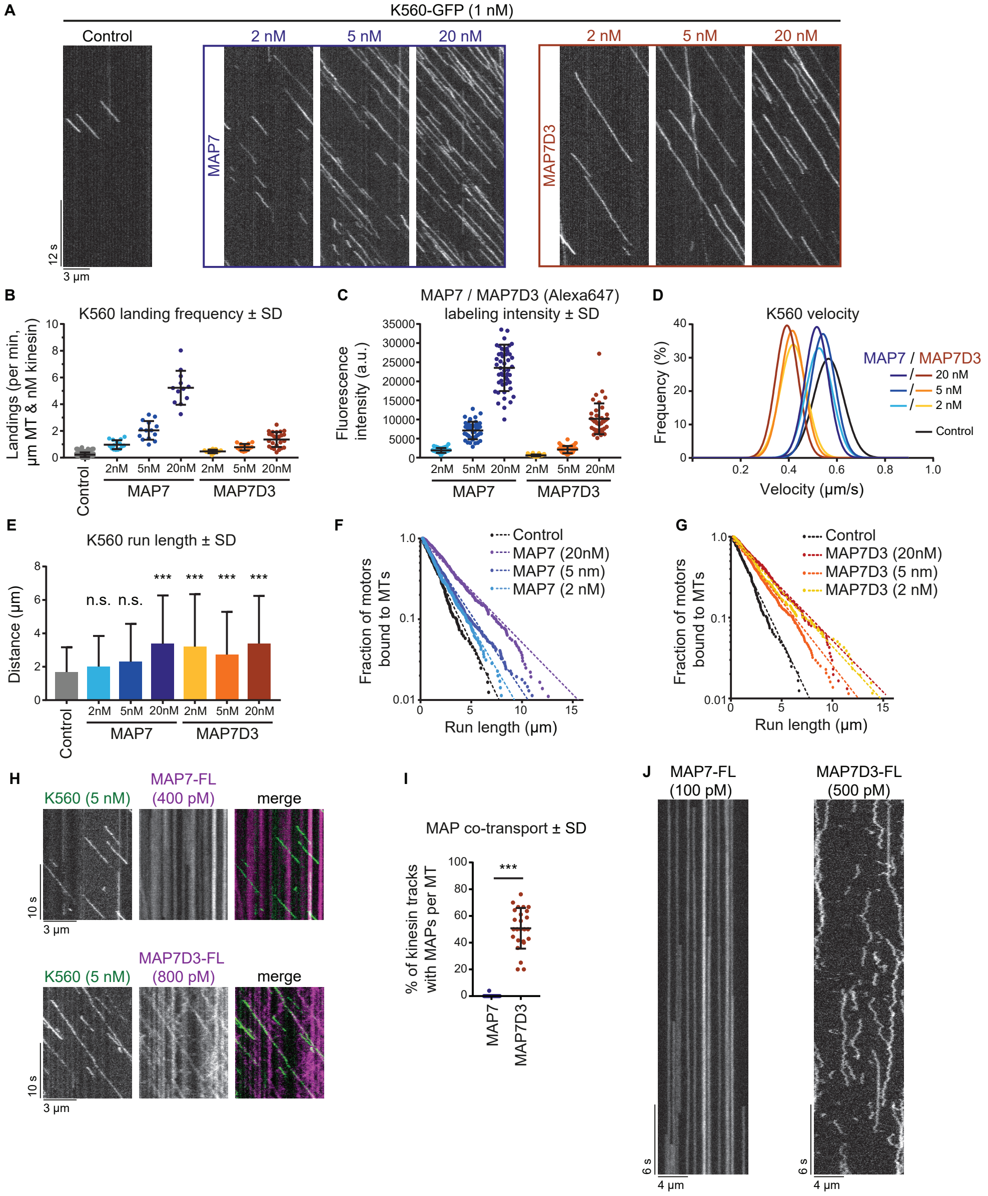

Figure 6 - Density and mobility of MAP7's determine kinesin-1 landing and processivity
(A) Kymographs of K560-GFP on dynamic MTs in control conditions or in the presence of increasing concentrations of MAP7 or MAP7D3. **(B)** Quantification of kinesin landing frequencies per MT and corrected for MT length, time of acquisition and kinesin concentration. n = 167, 15, 14, 12, 13, 15 and 25 MTs from two independent experiments. **(C)** Quantification of SNAP(Alexa647)-MAP7 and -MAP7D3 intensities on dynamic MTs using images acquired under identical conditions on a TIRF microscope. n = 39 to 49 MTs from two independent experiments. Representative images are shown in Fig. S4A. **(D)** Gaussian fits of kinesin velocities. Histograms are shown in Fig. S4B. **(E)** Quantification of K560-GFP run length. n = 241, 351, 614, 361, 257, 436 and 303 kinesin runs from two independent experiments. Mann-Whitney *U* test: ***, p <0.001. **(F, G)** Cumulative distributions of K560-GFP run lengths measured in the presence of increasing

Figure 6 (continued) concentrations of MAP7 (F) or MAP7D3 (G). Straight dashed lines correspond to single exponential fits, n numbers correspond to panel E. **(H)** Kymographs of dual-color *in vitro* reconstitution experiments with K560-GFP and SNAP(Alexa647)-tagged MAP7 or MAP7D3. **(I)** Quantification of kinesin tracks positive for MAP7 or MAP7D3 co-transport, n = 417 from 19 MTs (MAP7) and n = 344 from 25 MTs (MAP7D3) from two independent experiments, Mann-Whitney *U* test: ***, P <0.001. **(J)** Kymograph of single SNAP(Alexa647)-MAP7 or -MAP7D3 molecules on dynamic MTs *in vitro*. Movies were acquired at 25 frames/sec on a TIRF microscope.

conclude that MAP7 proteins can affect not only kinesin landing on MTs, as suggested previously (Monroy et al., 2018; Sung et al., 2008), but its processivity. Co-transport of the MAP with the kinesin could facilitate processive motion, but was not essential, as also a statically bound MAP7 could exert this effect if its density on MTs was high enough.

MAP7D3 C-terminus promotes MT recruitment and processivity of kinesin-1 in spite of having only a low MT affinity

The ability of K560 to transport MAP7D3 but not MAP7 might be caused not only by the different MT binding behavior of the two MAPs, but also by their different affinities for the kinesin. To test this possibility, we purified minimal binding constructs for MAP7, MAP7D3 and KIF5B from *E. coli* (Fig. 7A and Fig. S3F) and probed the oligomerization state of the individual proteins in solution by size exclusion chromatography followed by multi-angle light scattering (SEC-MALS). As expected, both the MAP7 and MAP7D3 fragments were monomers with the measured molecular weight (MW) values of 18.4 kDa (calculated MW of 18.8 kDa) and 22.2 kDa (calculated MW of 21.5 kDa), respectively, whereas the KIF5B fragment was a dimer (measured and calculated MW of 25.9 kDa) (Fig. 7B). Using isothermal titration calorimetry (ITC) experiments, we found an equilibrium dissociation constant KD of 3.8 ± 0.2 µM and a stoichiometry number, N, of 0.96 (monomer equivalents) for the interaction between the KIF5B and MAP7D3 fragments (Fig. 7C and S4E, F). In contrast, the MAP7 fragment had an affinity for the KIF5B fragment that was too weak to be properly determined; however, the obtained isotherm suggested a KD in the higher micromolar range (Fig. 7D and S4E, G).

Since MAP7D3 seems to be the most potent kinesin-1 interactor, we set out to compare the effect of full-length MAP7D3 and its C-terminus (Ct, also used for cellular experiments), both purified from *E. coli* (Fig. 7A and Fig. S3F), on K560 motility *in vitro* (Fig.7E). In agreement with a previous publication (Yadav et al., 2014), MAP7D3-Ct displayed weak MT binding: MT labeling intensity with 20 nM MAP7D3-Ct was 19.2 fold lower than with 20 nM full length MAP7D3 (Fig. 7F and S5A). In spite of this lower MT affinity, MAP7D3-Ct could efficiently increase K560 landing rate, promote its processivity and decrease motor velocity compared to control (Fig. 7E-I and S5A-C). The effect of MAP7D3-Ct on the landing rate was particularly obvious at 75 nM concentration, as MT labeling at this concentration was still 8.3 fold lower than with 20 nM full length MAP7D3, whereas the K560 landing frequency was 8.1 fold higher compared to control (kinesin only) (Fig. 7F,G). These data argue against the simple model that MAP7D3 acts as MT-recruiting factor for kinesin-1, but cannot exclude that the weak binding of MAP7D3 C-terminus to MTs augments K560-MT interaction. These data also show that the addition of a weak MAP module to the kinesin coil is sufficient to make kinesin-1 processive.

Simultaneous imaging of K560-GFP and mCherry-MAP7D3-Ct showed that this truncated MAP colocalized with moving kinesin (Fig. 7J). Importantly, FRAP analysis in the mCherry channel, leaving the GFP fluorescence unaffected, showed that MAP7D3-Ct

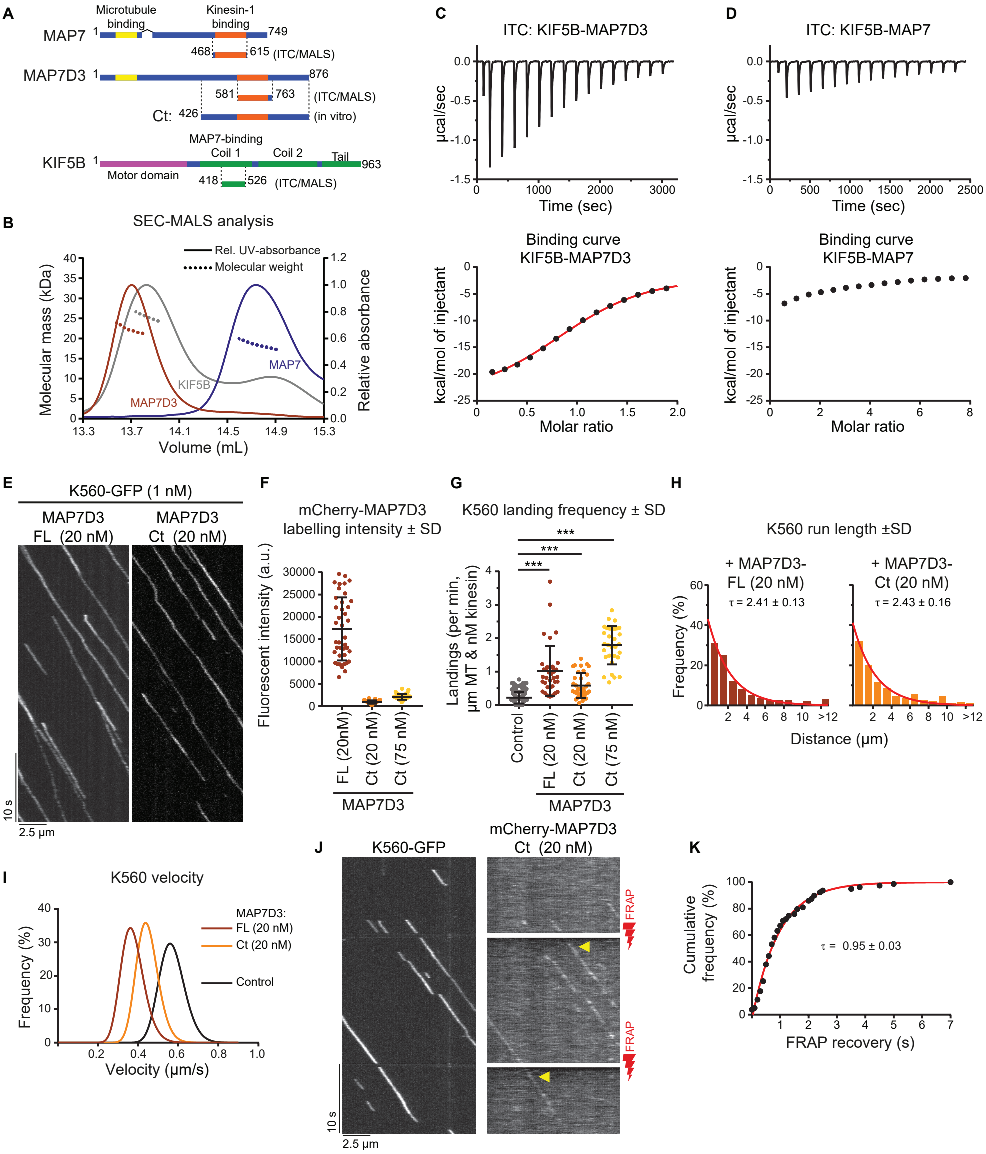

Figure 7 - MAP7D3 binds to KIF5B more tightly than MAP7 and promotes its activity *in vitro*
(A) Schemes of MAP7 family proteins and KIF5B constructs used in this figure. **(B)** SEC-MALS was used to determine the oligomerization state of indicated proteins in solution. Lines depict the relative UV-absorbance measured at 280 nm plotted against the elution volume. The molecular weight determinations by multi-angle light scattering are depicted by dashed lines. **(C, D)** ITC of MAP7D3 (C) or MAP7 (D) against KIF5B. Top panels: Enthalpograms of the respective titrations. Lower panel: integrated heat change (black dots) and the associated fitted curve (red line in C). Controls are shown in Fig. 4A-C. **(E)** Kymographs of K560-GFP on dynamic MTs in the presence of full-length (FL) MAP7D3 or MAP7D3-Ct (both purified from E.coli). **(F)** Quantifications of MAP7D3-FL or -Ct intensities on dynamic MTs using images acquired under identical conditions on a TIRF microscope. n = 40, n= 38 and n= 42 MTs from two independent experiments. Representative images are shown in Fig. S5A. **(G)** Quantification of landing frequency per MT and corrected for MT length, time of acquisition and kinesin concentration. n = 167, 36, 36 and 31 MTs from two independent experiments. **(H)** Histograms showing kinesin run lengths fitted to a single exponential decay (red) with

Figure 7 (continued) the indicated rate constants (tau) as a measure of mean run length, n = 241, 271 and 209 kinesin runs from two independent experiments; the associated bar plots are shown in Fig. S5C. **(I)** Gaussian fits of kinesin velocities. Histograms are shown in Fig. S5B. **(J)** Kymographs of single molecule FRAP experiments on K560-GFP motors and MAP7D3-Ct. Photobleaching with a 561 nm red laser was performed at time points indicated with red lightning bolts. Fluorescent recovery is indicated with a yellow arrow. **(K)** Cumulative frequency distribution plot of mCherry-MAP7D3-Ct recovery after photobleaching (black dots) fitted to an exponential decay (red line) with the indicated decay constant (tau), n = 79 from three independent experiments.

exchanged rapidly on moving K560 motors (Fig. 7J, K). Together with the micromolar-range KD of the kinesin-MAP binding (Fig. 7C, D), these data support the idea that fast binding-unbinding kinetics enables static MAP7 proteins to promote processive movement of kinesin-1.

MAP7 C-terminus promotes kinesin-1 landing on MTs independently of MT tethering

To investigate whether MAP7 family proteins can exert an effect on kinesin-1 that is independent of MT tethering, we used MAP7-Ct(mini) (Fig. 8A), which was completely diffuse in HeLa cells, showed only very weak MT binding in COS7 cells (Fig. 2A,C,D and S2A) and could be prepared from *E. coli* at high concentration in an untagged form (Fig. S3F). When added at micromolar concentrations to the assay with K560, this protein fragment caused a significant (3.4 fold) increase in the motor landing frequency (Fig. 8B, C), whereas the velocity of the kinesin was only mildly affected (Fig. S5E). Strikingly, the increase in motor processivity observed with the MAP7D3 C-terminus was not detected with MAP7-Ct(mini) (Fig. S5F, G).

To further substantiate the observation that the MAP7 C-terminus can activate kinesin-1 independently of any residual MT affinity, we developed a self-activating K560 motor, saK560, where the kinesin-binding domain of MAP7 lacking both the P-region and the Pro-rich region was fused to the C-terminus of K560. As a negative control, we generated a saK560(Δ) mutant lacking six amino acids of MAP7 essential for the kinesin binding (Fig. 8D) (Monroy et al., 2018). Comparison of these two kinesins showed that the saK560 had a higher landing frequency (Fig. 8E-G), while other parameters such as velocity and run length were not much affected (Fig. S5H-J). In further support of this observation, we examined the behavior of K560 together with the self-activating fusion proteins in HeLa cells and saw that they all behaved very similarly in wild type cells (Fig. 8H, top). However, upon depletion of all MAP7 family proteins, saK560(Δ) motor was diffuse, just like K560; yet, the saK560 kinesin showed enhanced localization on MTs in cell corners (Fig. 8H, I), demonstrating that this motor still displays activity despite of the absence of MAP7 family protein. Altogether, MT landing of kinesin-1 can be increased by MAP7 family proteins independently of their MT interaction, whereas the regulation of kinesin processivity by these MAPs depends on their association with MTs.

The stalk of K560 inhibits MT interaction

Our finding that MAP7 C-terminus improves the MT landing frequency of K560 could potentially be explained if the MAP7-interacting stalk of kinesin-1 partly interferes with MT binding. If this were true, a kinesin-1 truncation lacking this stalk should bind to MTs more efficiently. To test this idea, we generated a shorter KIF5B truncation mutant, KIF5B 1-370 (K370), which lacks the MAP7-binding coil region but still dimerizes via its neck linker

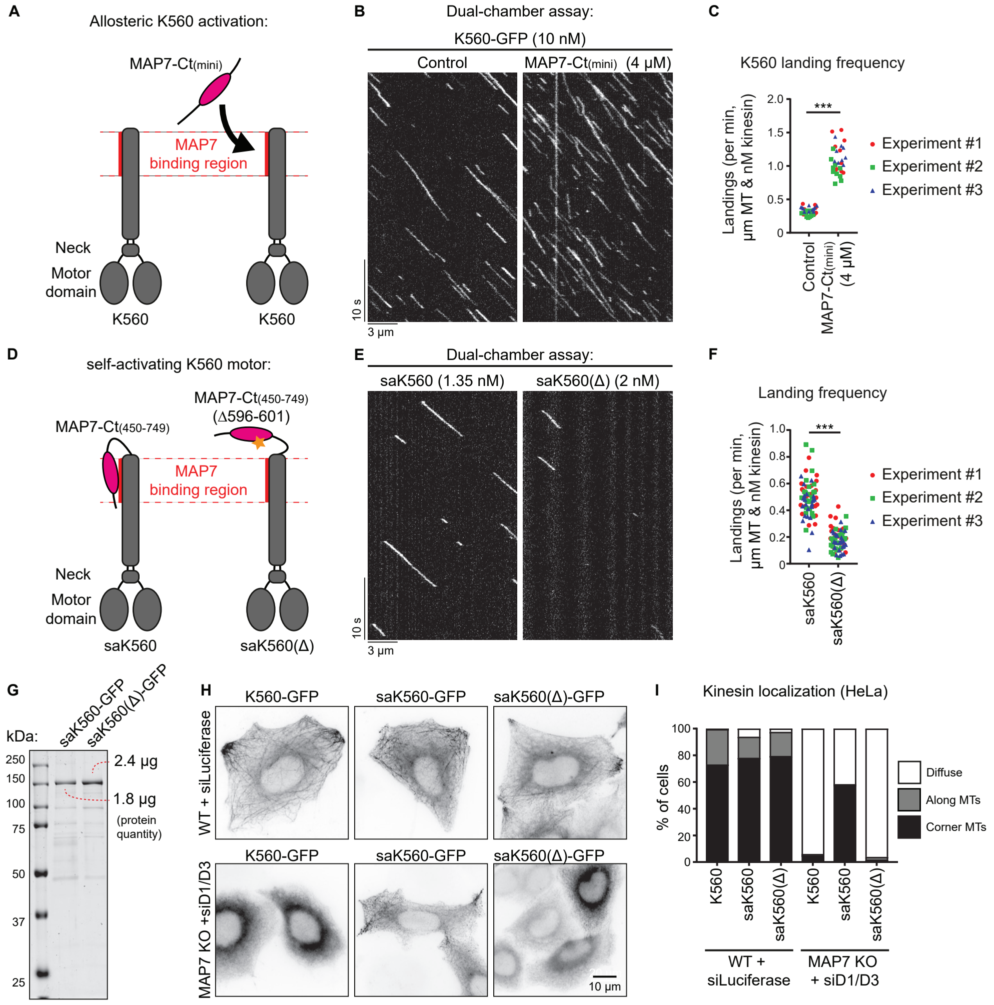

Figure 8 - MAP7 C-terminus can activate kinesin-1
(A,D) Overview of kinesin-1 and MAP7 constructs used for experiments. **(B,E)** Kymographs of a dual-chamber *in vitro* experiment, where equal concentrations of K560-GFP motors where added to chambers with or without MAP7-Ct(mini) (B), or with the indicated concentrations of saK560/ saK560(Δ) (E) on dynamic MTs. **(C,F)** Landing frequencies quantified per MT and corrected for MT length, time of acquisition and kinesin concentration. Each independent dual-chamber experiment is color-coded, n = 32 and 29 MTs (C) and n = 73 and 69 MTs (F), all from three independent experiments, Mann-Whitney *U* test: ***, p <0.001. **(G)** Analysis of purified saK560 proteins by SDS-PAGE. Protein concentrations were determined from a single gel using BSA standard. **(H)** Wide field images of overexpressed GFP-tagged kinesin constructs in control or MAP7 KO + siMAP7D1/D3 HeLa cells. **(I)** Quantification of kinesin localization categorized as: diffuse, along MTs or at corner MTs. n = 203, 172, 198, 241, 186 and 234 cells from three independent experiments.

(Kozielski et al., 1997) (Fig. 9A,B and Fig. S5D). In *in vitro* assays, K370 appeared to be a faster kinesin with slightly shorter runs compared to K560 (Fig. 9C and S5K-M). Importantly, we observed a 7.8 fold difference in motor landing frequency (Fig. 9D), indicating that the presence of the stalk region in K560 has a negative effect on its interaction with MTs.

Discussion

In this study, we have systematically analyzed the impact of mammalian MAP7 family proteins on kinesin-1 transport (Fig. 9E). We found that at least one MAP7 homolog was necessary and sufficient to enable kinesin-1-driven mitochondria distribution. These results are in agreement with the data showing that MAP7/ensconsin is an essential kinesin-1 co-factor in flies and in mammalian muscle cells (Barlan et al., 2013; Metivier et al., 2018; Metzger et al., 2012; Monroy et al., 2018; Sung et al., 2008). Dependence on MAP7 family members likely applies to many other kinesin-1-driven processes in mammals, because the core part of kinesin-1, the K560 fragment, was unable to bind to MTs efficiently in cells when all MAP7 homologues were absent.

Kinesin-1 function could be rescued to a significant extent by a MAP7 fragment that binds to kinesin, but has only low MT affinity, again in agreement with the data obtained in *Drosophila* (Barlan et al., 2013; Metivier et al., 2018). K560 recruitment to MTs was also stimulated by this MAP7 fragment both in cells and *in vitro*. This effect can likely be explained by a combination of two factors: the weak residual MT affinity present in the unstructured part of MAP7-Ct (Pro-rich region) as well as an allosteric regulation of the K560 motor by the kinesin-binding domain of MAP7. The ability of MAP7 to affect K560 allosterically is supported by the increased landing rate of the “self-activating” KIF5B-MAP7 fusion, which lacks all MAP7 linker sequences with potential MT affinity. This notion is also supported by the observation that a short kinesin-1 version (K370) lacking the MAP7-binding stalk region interacts with MTs more efficiently than K560. We propose that the stalk-containing kinesin can adopt conformations that are unfavorable for MT binding, whereas the interaction with MAP7 allosterically stabilizes a conformation that promotes landing on MTs (Fig. 9F). Diverse regulatory steps have been described for kinesin-1, mostly involving the autoinhibitory C-terminal tail region (reviewed in (Verhey and Hammond, 2009)) and also the motor domain (Xu et al., 2012). Our data add to this complexity by showing that the state of the stalk and its binding partners might directly affect kinesin interaction with MTs.

Although a MAP7 fragment lacking MT affinity can promote the engagement of kinesin-1 with MTs, the presence of MT binding regions makes this regulation much more efficient and robust. Without it, a very high concentration of the kinesin binding domain or its direct fusion to the kinesin were required to activate the kinesin. The presence of MT binding sites concentrates the kinesin binding domain of the MAP on MTs and can thus facilitate its interaction with the motor (Fig. 9F). Importantly, MT-bound MAP7 proteins have a significant effect not only on the kinesin landing rate but also on its processivity, and we excluded the possibility that this was due to kinesin multimerization. Interestingly, both a very immobile MAP (MAP7) and a more dynamic and diffusively behaving MAP (MAP7D3) could enhance kinesin-1 processivity, but the latter was able to exert this effect when present on a MT at a lower density. An obvious hypothesis is that kinesin processivity is governed by the presence of additional links to MTs. However, the distribution of run lengths of K560 was monoexponential even in the presence of MAP7 proteins, whereas a significant contribution of an additional MAP-dependent MT bound state would be expected to lead to

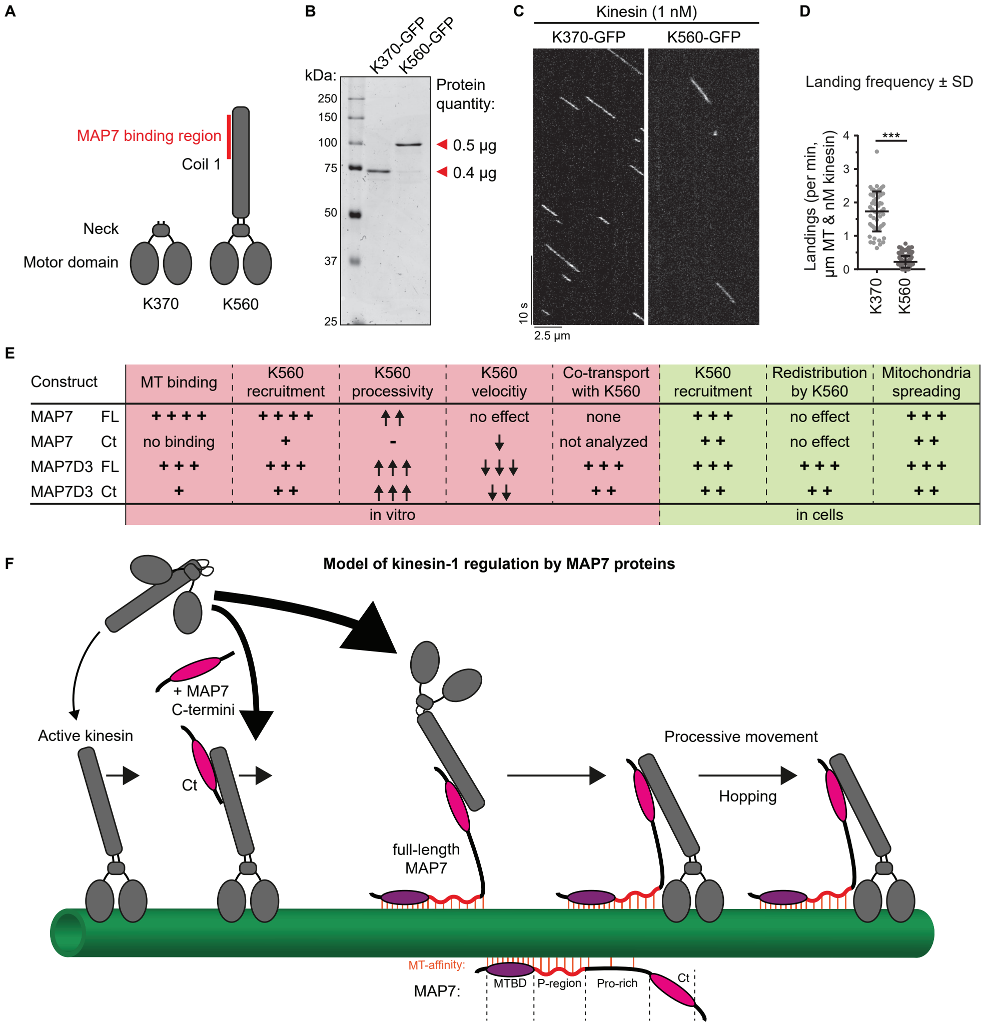
A
MAP7 binding region
Coil 1
Neck
Motor domain
K370
K560
B
K370-GFP
K560-GFP
kDa:
250
150
100
75
50
37
25
Protein quantity:
0.5 µg
0.4 µg
C
Kinesin (1 nM)
K370-GFP
K560-GFP
10 s
2.5 µm
D
Landing frequency ± SD
Landings (per min, µm MT & nM kinesin)
0
1
2
3
4
***
K370
K560
E
F
Model of kinesin-1 regulation by MAP7 proteins
Active kinesin
+ MAP7 C-termini
Ct
full-length MAP7
Processive movement
Hopping
MT-affinity:
MAP7:
MTBD
P-region
Pro-rich
Ct

Construct	MT binding	K560 recruitment	K560 processivity	K560 velocitiy	Co-transport with K560	K560 recruitment	Redistribution by K560	Mitochondria spreading
MAP7 FL	+ + + +	+ + + +	↑↑	no effect	none	+ + +	no effect	+ + +
MAP7 Ct	no binding	+	-	↓	not analyzed	+ +	no effect	+ +
MAP7D3 FL	+ + +	+ + +	↑↑↑	↓↓↓	+ + +	+ + +	+ + +	+ + +
MAP7D3 Ct	+	+ +	↑↑↑	↓↓	+ +	+ +	+ +	+ +
	in vitro					in cells		

Figure 9 - Removal of the kinesin-1 stalk domain enhances motor landing
(A) Overview of kinesin-1 constructs used. **(B)** Purified K370-GFP and K560-GFP analyzed by SDS-PAGE. Protein concentrations were determined using BSA standard. **(C)** Kymographs of K370-GFP and K560-GFP motors moving on dynamic MTs. **(D)** Quantification of kinesin landing frequencies, n = 57 (K370-GFP) from three independent experiments and n = 167 (K560-GFP) from two independent experiments, Mann-Whitney *U* test: ***, P = <0.001. **(E)** Summarizing table of the characteristics and effects of MAP7 proteins on different parameters of kinesin activity observed *in vitro* and in cells. **(F)** Working model of kinesin-1 activation by MAP7 family proteins. Red lines indicate MAP-MT interactions.

a distribution corresponding to the sum of two or three exponential decays (Klumpp and Lipowsky, 2005). These data suggest that the interaction with MT-bound MAP7's does not create an additional connection to a MT but somehow alters the conformational state of the motor to prevent its dissociation from MTs. Additional work would be needed to understand why a MT-unbound MAP7 fragment is sufficient to promote kinesin-1 landing but does not increase its processivity even when directly fused to the motor, whereas a MT-bound MAP7 version can stimulate not only the initial kinesin engagement with a MT but also its processive motility.

The relatively low affinity of the MAP-kinesin interaction and the rapid binding-unbinding kinetics suggest that the kinesin could be "hopping" from one MAP molecule to another, and this can allow even a highly immobile MAP7 to counteract kinesin dissociation without strongly affecting motor velocity. MAP7D3 is different from MAP7 because it binds less tightly to MTs and more tightly to the kinesin and can be "dragged" with the motor to some extent. This possibly explains why it slows down kinesin movement and why its low concentration is sufficient to increase motor processivity. However, because of the fast turnover within the MAP-motor complex, MAP7D3 is unlikely to be undergoing large-distance transport by the kinesin in cells. MAP7D3 can be rapidly relocalized to MT plus ends by overexpressed K560, but at the endogenous kinesin-1 expression levels, MAP7D3 is not enriched at MT plus ends, suggesting that the levels of endogenous motor are insufficient to drive MAP7D3 to the cell periphery. Still, it is possible that also the endogenous kinesin-1 could cause some redistribution of its own positive regulators, which would be in line with some previous observations (Kikuchi et al., 2018).

Recent work showed that MAP7 is a powerful MT recruiter of kinesin-1 (Monroy et al., 2018; Tymanskyj et al., 2018). Here, we confirmed these observations and provided insight into the underlying molecular mechanism. In addition, we showed that other MAP7 family members can act redundantly, but also possess unique properties that could fine-tune kinesin-1 regulation. Support for the latter idea can be found from the work in neurons, where it was shown that several individual MAP7 proteins, such as MAP7 and MAP7D1, are involved in cargo transport and neurite development (Barlan et al., 2013; Koizumi et al., 2017; Monroy et al., 2018; Sung et al., 2008; Tymanskyj et al., 2017; Tymanskyj et al., 2018). It is therefore an intriguing question whether specific combinations of MAP7 proteins could provide spatiotemporal control of kinesin transport in complex cell types and whether, as has been shown for MAP7 (Monroy et al., 2018), this involves competition with other MAPs or modulation of other transporting motors. Another unanswered question is whether the localization of MAP7 proteins contributes to the well-documented selectivity of kinesin-1 for specific MT tracks, which appear to correspond to the stable, long-lived MT populations (Cai et al., 2009; Farias et al., 2015; Guardia et al., 2016; Hammond et al., 2008; Jacobson et al., 2006; Nakata and Hirokawa, 2003; Tas et al., 2017). MAP7, which is stably associated with MTs, could potentially predispose kinesin-1 for interacting with more long-lived MTs, on which this MAP would gradually accumulate. Taken together, our data illustrate the complexity of the interplay between the motors and the tracks they use during intracellular transport processes.

Materials and Methods

Cell Culture, knockdowns and CRISPR/Cas9 knockouts

HeLa (Kyoto), COS7 and human embryonic kidney 239T (HEK293T) cell lines were cultured in medium that consisted of 45% DMEM, 45% Ham's F10, and 10% fetal calf serum supplemented with penicillin and streptomycin. The cell lines were routinely checked for mycoplasma contamination using LT07-518 Mycoalert assay (Lonza). HeLa and COS7 cells were transfected with plasmids using FuGENE 6 (Promega) for generating knockout lines, live cell imaging and immunofluorescence experiments. For streptavidin pull down assays and protein purification from HEK293T cells, plasmids were transfected with polyethylenimine (PEI; Polysciences). For generating knockdowns, HeLa cells were transfected with 100 nM siRNA for each target using HiPerfect (Qiagen). The following siRNAs were used in this study: MAP7D1 (target sequence 5'-TCATGAAGAGGACTCGGAA-3'), MAP7D3 (target sequence 5'- AACCTACATTCGTCTACTGAT-3') and luciferase (target sequence 5'- TCGAAGTATTCCGCGTACG -3'). For rescue experiments, HeLa cells were transfected 2 days after siRNA transfection.

HeLa CRISPR/Cas9 knockout lines were generated using the pSpCas9-2A-Puro (PX459) vector, purchased from Addgene (Ran et al., 2013). Guide RNAs for human KIF5B, MAP7, and MAP7D3 were designed using the CRISPR design webpage tool (http://crispr.mit.edu). The targeting sequences for gRNAs were as follows (coding strand sequence indicated): KIF5B, 5'-CCGATCAAATGCATAAGGCT-3'; MAP7, 5'-CGCCCTGCCTCTGCAATTTC-3'; MAP7D3, 5'-CCGTGCCCGCAGCTCTCTCA-3'. The CRISPR/Cas9-mediated knockout of KIF5B, MAP7, and MAP7D3-encoding genes was performed according to the protocol described in (Ran et al., 2013). In brief, HeLa cells were transfected using Fugene6 (Promega) with the vectors bearing the appropriate targeting sequences. Cells were subjected to selection with 2 µg/mL puromycin 24-48 hours post transfection for 48-72 hours. After selection, cells were allowed to recover in complete medium for approximately 7 days; meanwhile, cells were diluted in 96 wells plates for growing single cell colonies. Knockout efficiency was controlled using mixed cell populations by immunofluorescence staining, and depending on the efficiency, 5-30 individual clones were isolated and characterized by Western blotting and immunostaining.

DNA constructs

All MAP7 family protein constructs except MAP7D1-FL were cloned by a PCR-based strategy into a pBio-mCherry-C1 vector, a modified pEGFP-C1 vector, in which the open reading frame encoding EGFP was substituted for mCherry, and a linker encoding the sequence MASGLNDIFEAQKIEWHEGGG, which is the substrate of biotin ligase BirA, was inserted into the NheI and AgeI sites in front of the mCherry-encoding sequence. MAP7D1-FL has been cloned into a Bio-mCherry-C3 vector in a similar fashion. MAP7 constructs were generated using cDNA (Faire et al., 1999), was a kind gift of C. Bulinski (Columbia University Medical Center, New York, NY) or cDNA of RNA isolated from HeLa cells. MAP7D1 was derived from the IMAGE clone 6514558 (Source Bioscience), MAP7D2 was derived from the IMAGE clone 3063898 (Source Bioscience) and MAP7D3 was from the IMAGE clone 5284128 (Source Bioscience). All MAP7 linker constructs were cloned in a pEGFP-C1 vector by a PCR-based strategy. Rescue constructs for MAP7D1 and MAP7D3 were obtained by PCR-based mutagenesis of the sequence TCATGAAGAGGACTCGGAA to TCATGAAGAGAACACGCAA (MAP7D1) and AACCTACATTCGTCTACTGAT to AATCTACACTCGTCTACAGAT (MAP7D3). For protein purification from HEK293T cells, MAP7-Ct was cloned into a pmCherry-C1 vector with an N-terminal Strep-tag, and full-length MAP7 and MAP7D3 were cloned into a pTT5 vector with an N-terminal SNAP- and Strep-tag. For bacterial purifications, MAP7D3 constructs were cloned into a pET28a vector containing an N-terminal Strep-tag. MAP7-Ct(mini) construct was cloned by a PCR-based strategy into a pET24a vector containing an N-terminal SUMO-tag. All KIF5B constructs were cloned by a PCR-based strategy into pEGFP-N1 vectors. K560-GFP and full-length KIF5B-GFP used for protein purification were cloned into a pTT5 vector with a C-terminal Strep-tag. K370-GFP, saK560-GFP and saK560-GFP(Δ) used for protein purification and cellular experiments were cloned into a pEGFP-N1 vector with a C-terminal Strep-tag. KIF5B-Coil2-GFP and KIF5B-Tail-GFP were cloned in an pEGFP-C1 vector. All kinesin constructs were based on full length human KIF5B as template IMAGE clone 8991997 (van Spronsen et al., 2013). KIF5B-mCherry-LexyC was cloned by PCR-based strategy. A c-myc NLS sequence was introduced between K560 and mCherry (amino acid sequence: PAAKRVKLD) and a second SV40 Large T-antigen nuclear localization signal (NLS) was introduced between mCherry and the LEXY domain (amino acid sequence: PKKKRKV). The engineered LOV2-domain (LEXY) for blue light-inducible nuclear export was obtained from Addgene (catalog number #72655) (Niopek et al., 2016). For affinity measurements, minimal protein fragments for MAP7 and MAP7D3 where designed based on structure prediction and intron-exon analysis. For KIF5B, the designed fragment was the shortest construct still containing the cysteine at position 421 and the MAP7 binding domain (aa 508-523) (Monroy et al., 2018). All protein constructs were fused to an N-terminal thioredoxin-6xHis cleavable tag by restriction free positive selection into a pET-based bacterial expression vector by a PCR-based strategy (Olieric et al., 2010). Human EB3-GFP is described previously (Stepanova et al., 2003). Biotin ligase BirA expression construct (Driegen et al., 2005) was a kind gift from D. Meijer (University of Edinburgh, UK).

Antibodies, Western blotting and immunofluorescence cell staining

For immunofluorescence cell staining and Western blotting, we used rabbit polyclonal antibodies against MAP7D1 (HPA028075, Sigma/Atlas), MAP7D2 (HPA051508, Sigma/Atlas), MAP7D3 (HPA035598, Sigma/Atlas), Kinesin heavy chain (UKHC H-50, SC28538, Santa Cruz) and GFP (ab290; Abcam). We used a mouse polyclonal antibody against MAP7 (H00009053-B01P, Abnova) and mouse monoclonal antibodies against Ku80 (611360, BD Bioscience), mCherry (632543, Clontech), Cytochrome c (556432, BD Bioscience) and α-tubulin (T6199, Sigma), and a rat monoclonal antibody against α-tubulin (γL1/2, ab6160, Abcam). The following secondary antibodies were used: IRDye 800CW/680LT goat anti–rabbit, and anti–mouse for Western blotting and Alexa Fluor 488–, 594–, and 647–conjugated goat antibodies against rabbit, rat, and mouse IgG (Molecular Probes) for immunofluorescence. Mitotracker Red CMXRos (Molecular Probes) was alternatively used for mitochondria staining.

Total HeLa cell extracts were prepared in RIPA buffer containing 50 mM Tris-HCl pH 7.5, 150 mM NaCl, 1% Triton X-100, 0,5% SDS and cOmplete protease inhibitor cocktail (Roche).

For immunofluorescence cell staining, HeLa cells were fixed in −20°C methanol for 10 min and stained for MAP7, MAP7D1, MAP7D2, MAP7D3 and α-tubulin. In the case of cytochrome c, cells were fixed with 4% PFA in phosphate-buffered saline (PBS) for 10 min. Cells were then permeabilized with 0.15% Triton X-100 in PBS for 2 min; subsequent wash steps were performed in PBS supplemented with 0.05% Tween-20. Epitope blocking and antibody labeling steps were performed in PBS supplemented with 0.05% Tween-20 and 1% BSA. Before mounting in Vectashield mounting medium (Vector Laboratories) slides were washed with 70% and 100% ethanol and air-dried.

Pull down assays

Streptavidin pull down assays were performed from HEK293T cell lysates by coexpressing biotin ligase BirA with mCherry-tagged constructs containing a biotinylation site (pBio-mCherry) (bait), and GFP-tagged KIF5B constructs (prey). Constructs were transfected altogether into HEK293 cells using PEI with 24 hrs incubation time for protein expression. M-280 Streptavidin Dynabeads (Invitrogen) were blocked in a buffer containing 20 mM Tris pH 7.5, 20% glycerol, 150 mM NaCl, and 10 μg Chicken Egg Albumin followed by three washes with wash buffer containing 20 mM Tris pH 7.5, 150 mM NaCl and 0.1% Triton-X. HEK293T cells were scraped and collected in ice-cold PBS followed by lysis on ice in a buffer containing 20 mM Tris pH 7.5, 150 mM NaCl, 1mM $MgCl_2$, 1% Triton X-100, and cOmplete protease inhibitor cocktail (Roche). To separate cell debris, the lysates were cleared by centrifugation at 4°C for 15 min at 16000 g and 10 % of each lysate was saved as input control. Cell lysates were incubated with pre-blocked streptavidin beads for 60 min at 4°C followed by five washes with the buffer containing 20 mM Tris pH 7.5, 150 mM NaCl and 0.1% Triton-X. Streptavidin beads were pelleted and boiled in 2x Laemmli sample buffer. Protein lysates and pull down of both bait and prey proteins were analyzed by Western blotting.

Protein Purification

All KIF5B, SNAP(Alexa647)-labeled proteins and mCherry-MAP7-Ct used for *in vitro* reconstitution assays were purified from HEK293T cells using Strep(II)-streptactin affinity purification. Cells were harvested 24-40 hrs post transfection. Cells from a 15 cm cell culture dish were lysed in 800 μL of lysis buffer containing 50 mM HEPES pH 7.4, 300 mM NaCl, 1 mM $MgCl_2$, 1 mM DTT and 0.5% Triton X-100, supplemented with cOmplete protease inhibitor cocktail (Roche) on ice for 15 min. The supernatants obtained from cell lysates after centrifugation at 16000 x g for 20 min were incubated with 50 μL of StrepTactin Sepharose beads (GE Healthcare) for 1 hr. The beads were washed 5 times in a high-salt wash buffer containing 50 mM HEPES pH 7.4, 1.5 M NaCl, 1 mM $MgCl_2$, 1 mM EGTA, 1 mM DTT, and 0.05% Triton X-100 and three times with an elution wash buffer containing containing 50 mM HEPES pH 7.4, 150 mM NaCl, 1 mM $MgCl_2$, 1 mM EGTA, 1 mM DTT and 0.05% Triton X-100. The proteins were eluted with 40-150 μL of elution buffer containing 50 mM HEPES pH 7.4, 150 mM NaCl, 1 mM $MgCl_2$, 1 mM EGTA, 1 mM DTT, 2.5 mM d-Desthiobiotin and 0.05% Triton X-100. To label SNAP-tagged proteins with SNAP-Surface Alexa Fluor 647 (NEB), 20–40 μM dye was incubated with proteins on beads for 1 hr between wash and elution steps. After extensive washing, proteins were eluted in the elution buffer with 300 mM instead of 150 mM NaCl. The concentrations of purified proteins were measured by BSA standard using SDS-PAGE. All purified proteins were snap frozen in liquid nitrogen and stored in −80°C.

For protein purification of MAP7D3 constructs from bacteria, BL21 *E.coli* were transformed with the respective MAP7D3 construct. Bacteria were grown till OD600 of 0.6 at 37°C after which protein expression was induced with 1 mM IPTG for 1 hr at 37°C and 2.5 hrs at 200C. Bacteria were spun down and subjected to one freeze-thaw cycle at -80°C to stimulate proper lysis. Bacteria were resuspended and sonicated at 4°C in cold lysis buffer containing 50 mM sodium phosphate pH 8, 250 mM NaCl, 1 mM $MgCl_2$, 1 mM DTT, 0.5% Triton X-100, 1mM PMSF and cOmplete protease inhibitor cocktail (Roche). Lysates were centrifuged at 25000 x g for 45-60 min and the supernatants were incubated with Strep-Tactin Superflow high-capacity beads (IBA Lifesciences) for 60 min at 4°C, followed by 5 washes with a buffer containing 50 mM sodium phosphate pH 6.0, 250 mM NaCl, 1 mM $MgCl^2$ and 1 mM DTT. The proteins of interest were eluted with a buffer containing 50 mM sodium phosphate pH 7.0, 250 mM NaCl, 1 mM $MgCl_2$ 1 mM DTT and 5 mM d-Desthiotiotin. The eluted fractions were pooled and supplemented with 10% sucrose for preservation. Proteins were snap frozen and stored at -80°C. The concentrations of purified proteins were measured by BSA standard using SDS-PAGE.

For protein purification of the minimal MAP7, MAP7D3 and KIF5B fragments used for probing complex formation (SEC-MALS and ITC), all protein constructs were fused to an N-terminal thioredoxin-6xHis cleavable tag by restriction free positive selection into a pET-based bacterial expression vector. For expression, the, KIF5B and MAP7D3 constructs were transformed using *E. coli* expression strain BL21(DE3), whereas for MAP7 construct BL21-CodonPlus (DE3)-RIPL competent cells were chosen. All transformed cells were cultivated in LB containing

50 µg/mL Kanamycin. Subsequently, upon reaching an OD600 of 0.4 to 0.6 the cultures were induced with 1 mM isopropyl 1-thio-β-galactopyranoside (IPTG, Sigma) after cooling to 20°C for KIF5B and MAP7D3 or at 37°C for MAP7 respectively. The KIF5B and MAP7D3 constructs were expressed at 20°C overnight whereas the MAP7 construct was expressed for 4 h at 37°C. Cells were harvested by centrifugation at 4000 x g at 4°C followed by sonication for lysis in the buffer containing 50 mM HEPES, pH 7.5, 500 mM NaCl, 10 mM Imidazole, 10% Glycerol, 2 mM β-mercaptoethanol, proteases inhibitors (Roche) and DNAseI (Sigma). The lysate was cleared by centrifugation at 18000 x g for 20 min and subsequent filtration through a 0.45 µm filter. All constructs were purified by immobilized metal-affinity chromatography (IMAC) on HisTrap HP Ni2+ Sepharose columns (GE Healthcare) at 4°C according to the manufacturer's instructions. The elutions were cleaved by 3C protease during dialysis against the same buffer as above lacking protease inhibitors and DNAse I. The cleaved constructs were separated from tag and protease by a reverse IMAC run followed by a gel filtration run on a HiLoad Superdex 200 16/60 size exclusion chromatography column (GE Healthcare) in the buffer containing 10 mM Tris HCl, pH 7.5 and 150 mM NaCl. Fractions containing the constructs were pooled and concentrated by ultracentrifugation before being flash frozen and stored at -80°C.

For recombinant protein production of MAP7-Ct(mini), BL21(DE3) Rosetta2 *E. coli* cells (Novagen) containing a pET24a vector (Novagen) encoding a SUMO-MAP7-Ct(mini) construct were cultured. 2 L culture, in LB medium supplemented with the antibiotics 10 g/L kanamycin (Sigma-Aldrich) and 33 g/L chloramphenicol (Sigma-Aldrich), were grown until OD600 of ~0.8-1, after which protein production was induced with 0.1 mM IPTG (Thermo Scientific). Protein production was performed overnight at 18°C. Cells were harvested by centrifugation and subjected to one freeze-thaw cycle at -80°C to initiate cell lysis. The pellet was thawed and resuspended in 50 mM sodium phosphate buffer pH 8.0, 150 mM NaCl, cOmplete protease inhibitor cocktail (Roche) and 5 mM β-mercaptoethanol. The cells were then disrupted by an EmulsiFlex-C5 (Avestin) cell disruptor. The lysate was cleared by centrifugation (55,000 g, 45 min), filtered through a 0.22 µm polypropylene filter (VWR) and mixed for 15 min with Protino® Ni-IDA resin (Macherey-Nagel) at 4°C. After centrifugation, the protein was eluted with 50 mM sodium phosphate pH 8.0, 250 mM imidazole, 150 mM NaCl, cOmplete protease inhibitor cocktail (Roche) and 5 mM β-mercaptoethanol. To cleave off the SUMO tag, the eluate was then digested with Ulp1 overnight at 4°C while dialyzed against 50 mM phosphate buffer, pH 8.0 with a 6 kDa cut-off membrane (Spectrum Laboratories). The protein was loaded on a POROS® 20HS (Thermo Fischer Scientific) cation exchange column in the same dialysis buffer, using an ÄKTA® Purifier chromatography system (GE Healthcare). The protein was eluted by a linear gradient up to 2 M KCl over 15 CV (Carl Roth); fractions of 0.5 mL were collected. Fractions of interest were then concentrated and exchanged against 25 mM HEPES buffer pH 7.5 with 75 mM KCl, 75 mM NaCl and 10 mM DTT using a Vivaspin column (cut-off: 6 kDa). The final concentration was determined by an ND-100 spectrophotometer (Nanodrop Technologies). Purity was confirmed by SDS-PAGE and the protein was aliquoted and stored at -80°C.

Mass spectrometry

After streptavidin purification, beads were resuspended in 20 µl of Laemmli sample buffer (Biorad) and supernatants were loaded on a 4-12% gradient Criterion XT Bis-Tris precast gel (Biorad). The gel was fixed with 40% methanol/10% acetic acid and then stained for 1 hr using colloidal Coomassie dye G-250 (Gel Code Blue Stain Reagent, Thermo Scientific). After in-gel digestion, samples were resuspended in 10% formic acid (FA)/5% DMSO and analyzed using an Agilent 1290 Infinity (Agilent Technologies, CA) LC, operating in reverse-phase (C18) mode, coupled to an Orbitrap Q-Exactive mass spectrometer (Thermo Fisher Scientific, Bremen, Germany). Peptides were loaded onto a trap column (Reprosil C18, 3 µm, 2 cm × 100 µm; Dr. Maisch) with solvent A (0.1% formic acid in water) at a maximum pressure of 800 bar and chromatographically separated over the analytical column (Zorbax SB-C18, 1.8 µm, 40 cm × 50 µm; Agilent) using 90 min linear gradient from 7-30% solvent B (0.1% formic acid in acetonitrile) at a flow rate of 150 nL/min. The mass spectrometer was used in a data-dependent mode, which automatically switched between MS and MS/MS. After a survey scan from 350-1500 m/z the 10 most abundant peptides were subjected to HCD fragmentation. MS spectra were acquired in high-resolution mode (R > 30,000), whereas MS2 was in high-sensitivity mode (R > 15,000). Raw files were processed using Proteome Discoverer 1.4 (version 1.4.0.288, Thermo Scientific, Bremen, Germany). The database search was performed using Mascot (version 2.4.1, Matrix Science, UK) against a Swiss-Prot database (taxonomy human). Carbamidomethylation of cysteines was set as a fixed modification and oxidation of methionine was set as a variable modification. Trypsin was specified as enzyme and up to two miss cleavages were allowed. Data filtering was performed using percolator, resulting in 1% false discovery rate (FDR). Additional filters were; search engine rank 1 peptides and ion score >20.

Size exclusion chromatography followed by multi-angle light scattering (SEC-MALS) experiments

SEC-MALS experiments were conducted in a buffer containing 10 mM Tris HCl, pH 7.5 supplemented with 150 mM NaCl at 20°C using a Superdex 200 10/300 analytical size exclusion chromatography column (GE Healthcare) coupled to a miniDAWN TREOS light scattering and Optilab T-rEX refractive index detector (Wyatt Technology). A volume of 30 µL of protein samples at 5 mg/mL was injected and data was analyzed with the software provided by the manufacturer.

Isothermal titration calorimetry (ITC)

The proteins were dialyzed against a buffer containing 10 mM Tris HCl, pH 7.5, supplemented with 150 mM NaCl overnight at 4°C. ITC experiments were conducted on an iTC200 instrument at 25°C, using an injection volume of 2.1

μL at a reference power of 7 and stirring speed of 700 rpm. For probing the MAP7-KIF5B interaction, the MAP7 fragment was used as titrant at a concentration 576 μM against the KIF5B fragment at 15 μM in the cell. The MAP7D3-KIF5B interaction was probed with 300 μM MAP7D3 fragment as titrant and 30 μM KIF5B fragment in the cell. The resulting enthalpograms were integrated and fitted using the standard one-site-model of Origin (OriginLab).

In vitro reconstitution assays

MT seeds were prepared by incubating 20 μM porcine tubulin mix containing 70% unlabeled, 18% biotin-tubulin and 12% rhodamine-tubulin with 1 mM guanylyl-(α,β)-methylenediphosphonate (GMPCPP) at 37°C for 30 min. Polymerized MTs were separated from the mix by centrifugation in an Airfuge at 119,000 g for 5 min. MTs were subjected to one round of depolymerization and polymerization in 1 mM GMPCPP, and the final MT seeds were stored in MRB80 buffer (80 mM K-PIPES pH 6.8, 1 mM EGTA, 4 mM MgCl2) containing 10% glycerol. *In vitro* reconstitution assays were performed in flow chambers assembled from microscopy slides and plasma cleaned coverslips. The chambers were treated with 0.2 mg/mL PLL-PEG-biotin (Surface Solutions, Switzerland) in MRB80 buffer for 5 min. After washing with the assay buffer, they were incubated with 1 mg/mL NeutrAvidin for 5 min. MT seeds were attached to the biotin-NeutrAvidin links and incubated with 1 mg/mL κ-casein. The *in vitro* reaction mixture consisted of 20 μM tubulin, 50 mM KCl, 0.1% methylcellulose, 0.5 mg/mL κ-casein, 1 mM GTP, oxygen scavenging system (20 mM glucose, 200 μg/mL catalase, 400 μg/mL glucose-oxidase, 4 mM DTT), 2 mM ATP, 0.2 - 10 nM of respective kinesin (concentrations were calculated for monomeric proteins) and MAP7 or MAP7D3 at indicated concentrations. After centrifugation in an Airfuge for 5 min at 119,000 g, the reaction mixture was added to the flow chamber containing the MT seeds and sealed with vacuum grease. The experiments were conducted at 30°C and data were collected using TIRF microscopy. For some experiments without mCherry-labeled MAP7/MAP7D3, the reaction mixture was composed of 19.5 μM tubulin supplemented with 0.5 μM rhodamine-labeleld tubulin. All tubulin products were purchased from Cytoskeleton Inc.

For MT pelleting assays a reaction containing 37.5 μM porcine brain tubulin supplemented with 1 mM GTP, 1 mM DTT and 20 μM Taxol in MRB80 was prepared at 300C for 30 min. The reaction was divided and supplemented with MRB80 buffer with or without mCherry-MAP7-Ct at a final tubulin concentration of 30 μM. Also a control without tubulin was included. Subsequently, all reactions were incubated for another 15 min at 30°C. Pelleting was performed in an Airfuge at 119000 g with a pre-warmed rotor for 10 min. Supernatants were removed and pellets were resuspended in MRB80 buffer on ice by regular pipetting for 40 min. All samples were supplemented with 4x Laemmli sample buffer, boiled and analyzed by SDS-PAGE.

Image acquisition

Fixed cells were imaged with a Nikon Eclipse 80i upright fluorescence microscope equipped with Plan Apo VC N.A. 1.40 oil 100x and 60x objectives, or Nikon Eclipse Ni-E upright fluorescence microscope equipped with Plan Apo Lambda 100x N.A. 1.45 oil and 60x N.A. 1.40 oil objectives microscopes, Chroma ET-BFP2, - GFP, -mCherry, or -Cy5 filters and Photometrics CoolSNAP HQ2 CCD (Roper Scientific, Trenton, NJ) camera. The microscopes were controlled by Nikon NIS Br software.

FRAP and LEXY optogenetic experiments were done using spinning disk microscopy, which was performed on an inverted research microscope Eclipse Ti-E with the Perfect Focus System (Nikon), equipped with Plan Apo VC 100x N.A. 1.40 and Plan Apo 60x N.A. 1.40 oil objectives, a Yokogawa CSU-X1-A1 confocal head with 405-491-561 triple-band mirror and GFP, mCherry, and GFP/mCherry emission filters (Chroma), ASI motorized stage MS-2000-XYZ with Piezo Top Plate (ASI), a Photometrics Evolve 512 electron-multiplying charge-coupled device (CCD) camera (Photometrics), and controlled by MetaMorph 7.7 software (Molecular Devices). The microscope was equipped with a custom-ordered illuminator (MEY10021; Nikon) modified by Roper Scientific France/PICT-IBiSA, Institut Curie. Cobolt Calypso 491 nm (100 mW) and Cobolt Jive 561 nm (100 mW) lasers (Cobolt) were used as light sources. To keep cells at 37°C, we used a stage top incubator (model INUBG2E-ZILCS; Tokai Hit).

All *in vitro* reconstitution assays were imaged on an inverted research microscope Nikon Eclipse Ti-E (Nikon) with the perfect focus system (PFS) (Nikon), equipped with Nikon CFI Apo TIRF 100 × 1.49 N.A. oil objective (Nikon, Tokyo, Japan), Photometrics Evolve 512 EMCCD (Roper Scientific) and Photometrics CoolSNAP HQ2 CCD (Roper Scientific) and controlled with MetaMorph 7.7 software (Molecular Devices, CA). The microscope was equipped with TIRF-E motorized TIRF illuminator modified by Roper Scientific France/PICT-IBiSA, Institut Curie. For excitation lasers we used 491 nm 100 mW Stradus (Vortran), 561 nm 100 mW Jive (Cobolt) and 642 nm 110 mW Stradus (Vortran). We used an ET-GFP 49002 filter set (Chroma) for imaging of proteins tagged with GFP, an ET-mCherry 49008 filter set (Chroma) for imaging X-Rhodamine labelled tubulin or mCherry-tagged proteins and an ET-405/488/561/647 for imaging SNAP-Alexa647. For simultaneous imaging of green and red fluorescence we used an Evolve512 EMCCD camera (Photometrics), ET-GFP/mCherry filter cube (59022, Chroma) together with an Optosplit III beamsplitter (Cairn Research Ltd) equipped with double emission filter cube configured with ET525/50m, ET630/75m and T585lprx (Chroma). For simultaneous imaging of green, red and far-red fluorescence we used an Evolve512 EMCCD camera (Photometrics), quad TIRF polychroic ZT405/488/561/640rpc (Chroma) and quad laser emission filter ZET405/488/561/635m (Chroma), mounted in the metal cube (Chroma, 91032) together with an Optosplit III beamsplitter (Cairn Research Ltd) equipped with triple emission filter cube configured with ET525/50m, ET630/75m, ET700/75m emission filters and T585lprx and T660lprx dichroic (Chroma). To keep *in vitro* samples at 30°C, we used a stage top incubator (model INUBG2E-ZILCS; Tokai Hit).

Image processing and analysis

Images and movies were processed using ImageJ. All images were modified by linear adjustments of brightness and contrast. Maximum intensity projections were made using z projection. Kinesin velocities, run lengths and landing frequencies were obtained from kymograph analysis, using ImageJ plugin KymoResliceWide v.0.4. https://github.com/ekatrukha/KymoResliceWide; copy archived at https://github.com/elifesciences-publications/KymoResliceWide). Kinesin runs < 0.5 s were included for landing frequency analysis but not analyzed for run length and velocity. Kinesins running on GMPCPP MT seeds were excluded from our analysis as much as possible. Kinesin runs >2.0 sec were analyzed for MAP7/MAP7D3 co-transport events.

For quantifying mitochondria in different HeLa cell knockdown/knockout conditions, we classified mitochondria as "clustered" when ~ 80% of the cytochrome c signal was localized in a dense cluster around the nucleus, whereas all other localization patterns with more spread mitochondria were classified as "spread". K560-GFP was classified as localized on corner MTs when clear enrichment of fluorescent signal was seen at MT ends near the cell periphery over MTs that are localized in between the boundary and the cell center.

Line scan analysis of MT localization of MAP7 linker truncations was performed on widefield images of HeLa and COS7 cells overexpressing GFP-tagged constructs co-stained for α-tubulin. Average fluorescence intensities were measured from 1-3 micron line scans along MTs stained for α-tubulin and an adjacent line 5 pixels away from the same MT as a background intensity measurement. Next, the ratio was calculated by dividing fluorescent intensity of the MT line scan by the fluorescent intensity of the control line scan at the same region. No enrichment of the GFP-tagged construct on MTs would result in an intensity ratio of 1. Per condition, 30 MTs were analyzed form 10 cells (3 MTs per cell).

Imaging of MT plus ends with EB3-GFP as a marker was performed on a TIRF microscope. Imaging was performed at 2 frames per s for 50 s. Per cell, approximately 10-30 EB3 comets were traced and average growth velocity/duration was calculated and analyzed per cell using SigmaPlot.

FRAP measurements were performed by bleaching a 10 x 10 μm square region in a cytoplasmic region between the nucleus and cell cortex followed by 8.5 min imaging with a frame interval of 3 s. Mean fluorescence intensities were measured from a 4 x 4 μm square region within the original photobleached region to avoid analyzing non-bleached MTs that could slide into the analyzed region. The mean intensity of this region was double corrected for background fluorescence and photobleaching (Phair et al., 2004).

Optogenetics experiments with blue light-inducible K560-LEXY kinesin were performed using spinning disk microscopy. Prior to imaging, a round of MT disassembly was performed to promote nuclear import of K560-LEXY by treating the cells with 10 μM nocodazole (Sigma-Aldrich) for 1 h at 37°C, followed by 1 h at 4°C, followed by an extensive washout with pre-warmed medium to re-assemble MTs. Acquisitions were done with a frame interval of 5 sec after sequential exposure with green light 561 nm laser (to image kinesin) followed by blue light 491 nm laser (to image MAPs and activate K560-LEXY simultaneously). Exposure times of ~ 1 s per interval with the 491 nm laser were sufficient to induce active export of LEXY-tagged motors from the nucleus. For measuring fluorescence intensity changes at cell corners, a maximum intensity projection of the K560-LEXY channel over time was made using ImageJ, followed by Gaussian blurring and thresholding to select cell corners to analyze. Mean fluorescence values for GFP-MAP7/MAP7D3 and K560-LEXY were obtained from the same cell corners over time, background subtracted and normalized to the mean fluorescence in that region at t = 0 min. Changes in mean fluorescence intensity were plotted per cell corner.

Single molecule intensity analysis

Single molecule fluorescence histograms of monomeric GFP (control) or kinesins moving on MT lattices were built from acquisitions made on a TIRF microscope. To ensure identical imaging conditions, a single imaging slide (with a plasma cleaned coverslip) was used containing two or three flow chambers to image GFP (control) and K560-GFP (with or without MAP7 proteins) (Fig. S4C) or K370-GFP and K560-GFP (Fig. S5D). For purified GFP, the protein was diluted in MRB80 and added to an imaging flow chambers; chambers were subsequently washed with MRB80, leaving a fraction of the GFP proteins immobilized on the coverslip. Protein dilution was optimized to provide images of approximately 0.01 fluorophores per μm^2 for GFP control conditions. To estimate the number of GFP molecules per kinesin, an *in vitro* reconstitution assay with K370-GFP or K560-GFP moving on MTs in the presence or absence of MAP7 proteins was set up in the other flow chambers as described before. After sealing with vacuum grease to prevent evaporation, samples were imaged at 30ºC. For monomeric GFP, approximately 100 images were acquired at different positions on the coverslip to avoid pre-bleaching. For moving kinesins, approximately 5-10 movies were obtained where only the first 10 frames were analyzed to prevent analyzing partially photobleached motors. All acquisitions were obtained under identical laser power, exposure time and TIRF angle. ImageJ plugin Comdet v.0.3.6.1 and DoM_Utrecht v.1.1.5 https://github.com/ekatrukha/DoM_Utrecht) were used for detection and fitting of single molecule fluorescent spots as described previously (Yau et al., 2014). In short, individual spots were fitted with 2D Gaussian, and the amplitude of the fitted Gaussian function was used as a measure of the fluorescence intensity value of an individual spot. The histograms were fitted to lognormal distributions using GraphPad Prism 7.

Statistical analysis

Statistical significance was analyzed either using the Mann-Whitney *U* test or Student's *t* test, as indicated in figure legends. For the *t* test, data distribution was assumed to be normal, but this was not formally tested. Statistical significance was determined using GraphPad Prism software (version 7.04). Fitting of run lengths with the sum of two or three exponential decays was performed on the raw data using maximum likelihood estimation method implemented in mle function of MATLAB R2011b (The MathWorks, Natick, 2011).

Online supplemental material

Video 1 and 2 show HeLa cells transfected with K560-LEXY, GFP-MAP7 (Video 1) or GFP-MAP7D3 (Video 2). Exposure with blue light induces nuclear export of K560-LEXY. Total video length is 4 min. Fig. S1 shows the analysis of MT organization and dynamics in MAP7 depleted cells, the distribution of MAP7D3-Ct in HeLa cells, uncropped images of the MT pelleting assay from Figure 2B and *in vitro* assays with mCherry-MAP7-Ct. Fig. S2 illustrates the overexpression of GFP-tagged MAP7 linker constructs in COS7 cells and overexpressed Nt and Ct constructs of MAP7, MAP7D1 and MAP7D3 together with K560-GFP in HeLa cells depleted of all three MAP7 proteins. Fig. S3 provides an overview of all purified proteins used in this study, the analysis of kinesin purification contaminants and velocity parameters of full-length KIF5B. Fig. S4 and S5 include additional control conditions for the ITC experiments, illustrate binding of MAP7 proteins to MTs in *in vitro* reconstitution assays as well as quantifications of kinesin behavior from Fig. 5-9.

Acknowledgments

We thank A. Aher for the help on protein purifications and D. Meijer for the gift of materials. This work was supported by the European Research Council Synergy grant 609822 and Netherlands Organization for Scientific Research ALW Open Program grant 824.15.017 to A.A., the Marie Curie IEF fellowships to M.M. and by a grant .from the Swiss National Science Foundation (31003A_166608; to M.O.S.).
The authors declare no competing financial interests.

Author Contributions

Author contributions: P.J. H. and M. M. designed, conducted and analyzed the experiments and wrote the paper. T.M. designed, conducted and analyzed biochemical experiments. G-J.K., C.A.E.P., D.G.F.V., W,E.vR. and I.G. contributed to cellular experiments. E.A.K. contributed to data analysis. L.F. and S.G.D.R. contributed to protein purifications. A.F.M.A. and R.S. performed and analyzed mass spectrometry experiments. C.C.H., M.O.S. and L.C.K. contributed to experiment planning, data analysis and paper writing; A. A. supervised the study and wrote the paper.

References

Akhmanova, A., and J.A. Hammer, 3rd. 2010. Linking molecular motors to membrane cargo. Curr Opin Cell Biol. 22:479-487.

Barlan, K., and V.I. Gelfand. 2017. Microtubule-Based Transport and the Distribution, Tethering, and Organization of Organelles. Cold Spring Harb Perspect Biol. 9:a025817.

Barlan, K., W. Lu, and V.I. Gelfand. 2013. The microtubule-binding protein ensconsin is an essential cofactor of kinesin-1. Curr Biol. 23:317-322.

Bieling, P., L. Laan, H. Schek, E.L. Munteanu, L. Sandblad, M. Dogterom, D. Brunner, and T. Surrey. 2007. Reconstitution of a microtubule plus-end tracking system in vitro. Nature 450:1100-1105.

Bulinski, J.C., and A. Bossler. 1994. Purification and characterization of ensconsin, a novel microtubule stabilizing protein. J Cell Sci. 107:2839-2849.

Cai, D., D.P. McEwen, J.R. Martens, E. Meyhofer, and K.J. Verhey. 2009. Single molecule imaging reveals differences in microtubule track selection between Kinesin motors. PLoS Biol. 7:e1000216.

Case, R.B., D.W. Pierce, N. Hom-Booher, C.L. Hart, and R.D. Vale. 1997. The directional preference of kinesin motors is specified by an element outside of the motor catalytic domain. Cell 90:959-966.

Dixit, R., J.L. Ross, Y.E. Goldman, and E.L. Holzbaur. 2008. Differential regulation of dynein and kinesin motor proteins by tau. Science 319:1086-1089.

Driegen, S., R. Ferreira, A. van Zon, J. Strouboulis, M. Jaegle, F. Grosveld, S. Philipsen, and D. Meijer. 2005. A generic tool for biotinylation of tagged proteins in transgenic mice. Transgenic Res. 14:477-482.

Ebneth, A., R. Godemann, K. Stamer, S. Illenberger, B. Trinczek, and E. Mandelkow. 1998. Overexpression of tau protein inhibits kinesin-dependent trafficking of vesicles, mitochondria, and endoplasmic reticulum: implications for Alzheimer's disease. J Cell Biol. 143:777-794.

Faire, K., C.M. Waterman-Storer, D. Gruber, D. Masson, E.D. Salmon, and J.C. Bulinski. 1999. E-MAP-115 (ensconsin) associates dynamically with microtubules in vivo and is not a physiological modulator of microtubule dynamics. J Cell Sci. 112:4243-4255.

Farias, G.G., C.M. Guardia, D.J. Britt, X. Guo, and J.S. Bonifacino. 2015. Sorting of Dendritic and Axonal Vesicles at the Pre-axonal Exclusion Zone. Cell Rep. 13:1221-1232.

Fu, M.M., and E.L. Holzbaur. 2014. Integrated regulation of motor-driven organelle transport by scaffolding proteins. Trends Cell Biol. 24:564-574.

Gallaud, E., R. Caous, A. Pascal, F. Bazile, J.P. Gagne, S. Huet, G.G. Poirier, D. Chretien, L. Richard-Parpaillon, and R. Giet. 2014. Ensconsin/Map7 promotes microtubule growth and centrosome separation in Drosophila neural stem cells. J Cell Biol. 204:1111-1121.

Guardia, C.M., G.G. Farias, R. Jia, J. Pu, and J.S. Bonifacino. 2016. BORC Functions Upstream of Kinesins 1 and 3 to Coordinate Regional Movement of Lysosomes along Different Microtubule Tracks. Cell Rep. 17:1950-1961.

Gumy, L.F., E.A. Katrukha, I. Grigoriev, D. Jaarsma, L.C. Kapitein, A. Akhmanova, and C.C. Hoogenraad. 2017. MAP2 Defines a Pre-axonal Filtering Zone to Regulate KIF1- versus KIF5-Dependent Cargo Transport in Sensory Neurons. Neuron 94:347-362.

Hammond, J.W., D. Cai, and K.J. Verhey. 2008. Tubulin modifications and their cellular functions. Curr Opin Cell Biol. 20:71-76.

Hirokawa, N., and Y. Tanaka. 2015. Kinesin superfamily proteins (KIFs): Various functions and their relevance for important phenomena in life and diseases. Exp Cell Res. 334:16-25.

Jacobson, C., B. Schnapp, and G.A. Banker. 2006. A change in the selective translocation of the Kinesin-1 motor domain marks the initial specification of the axon. Neuron 49:797-804.

Kikuchi, K., A. Nakamura, M. Arata, D. Shi, M. Nakagawa, T. Tanaka, T. Uemura, T. Fujimori, A. Kikuchi, A. Uezu, Y. Sakamoto, and H. Nakanishi. 2018. Map7/7D1 and Dvl form a feedback loop that facilitates microtubule remodeling and Wnt5a signaling. EMBO Rep. 19: e45471.

Klumpp, S., and R. Lipowsky. 2005. Cooperative cargo transport by several molecular motors. Proc Natl Acad Sci U S A. 102:17284-17289.

Koizumi, H., H. Fujioka, K. Togashi, J. Thompson, J.R. Yates, 3rd, J.G. Gleeson, and K. Emoto. 2017. DCLK1 phosphorylates the microtubule-associated protein MAP7D1 to promote axon elongation in cortical neurons. Dev Neurobiol. 77:493-510.

Kozielski, F., S. Sack, A. Marx, M. Thormahlen, E. Schonbrunn, V. Biou, A. Thompson, E.M. Mandelkow, and E. Mandelkow. 1997. The crystal structure of dimeric kinesin and implications for microtubule-dependent motility. Cell 91:985-994.

Kwon, H.J., J.E. Park, H. Song, and C.Y. Jang. 2016. DDA3 and Mdp3 modulate Kif2a recruitment onto the mitotic spindle to control minus-end spindle dynamics. J Cell Sci. 129:2719-2725.

McHedlishvili, N., H.K. Matthews, A. Corrigan, and B. Baum. 2018. Two-step interphase microtubule disassembly aids spindle morphogenesis. BMC Biol. 16:14.

Metivier, M., B. Monroy, E. Gallaud, R. Caous, A. Pascal, L. Richard-Parpaillon, A. Guichet, K. Ori-McKenney, and R. Giet. 2018. The Kinesin-1 binding domain of Ensconsin/MAP7 promotes Kinesin-1 activation in vivo. BioRxiv:325035.

Metzger, T., V. Gache, M. Xu, B. Cadot, E.S. Folker, B.E. Richardson, E.R. Gomes, and M.K. Baylies. 2012. MAP and kinesin-dependent nuclear positioning is required for skeletal muscle function. Nature 484:120-124.

Monroy, B.Y., D.L. Sawyer, B.E. Ackermann, M.M. Borden, T.C. Tan, and K.M. Ori-McKenney. 2018. Competition between microtubule-associated proteins directs motor transport. Nat Commun. 9:1487.

Nagaraj, N., J.R. Wisniewski, T. Geiger, J. Cox, M. Kircher, J. Kelso, S. Paabo, and M. Mann. 2011. Deep proteome and transcriptome mapping of a human cancer cell line. Mol Syst Biol. 7:548.

Nakata, T., and N. Hirokawa. 2003. Microtubules provide directional cues for polarized axonal transport through interaction with kinesin motor head. J Cell Biol. 162:1045-1055.

Niida, Y., and A. Yachie. 2011. MAP7D2 is a brain expressing X-linked maternal imprinted gene in humans. Nature Precedings: http://hdl.handle.net/10101/npre.12011.16684.10101.

Niopek, D., P. Wehler, J. Roensch, R. Eils, and B. Di Ventura. 2016. Optogenetic control of nuclear protein export. Nat Commun. 7:10624.

Olieric, N., M. Kuchen, S. Wagen, M. Sauter, S. Crone, S. Edmondson, D. Frey, C. Ostermeier, M.O. Steinmetz, and R. Jaussi. 2010. Automated seamless DNA co-transformation cloning with direct expression vectors applying positive or negative insert selection. BMC Biotechnol. 10:56.

Phair, R.D., P. Scaffidi, C. Elbi, J. Vecerova, A. Dey, K. Ozato, D.T. Brown, G. Hager, M. Bustin, and T. Misteli. 2004. Global nature of dynamic protein-chromatin interactions in vivo: three-dimensional genome scanning and dynamic interaction networks of chromatin proteins. Mol Cell Biol. 24:6393-6402.

Ran, F.A., P.D. Hsu, J. Wright, V. Agarwala, D.A. Scott, and F. Zhang. 2013. Genome engineering using the CRISPR-Cas9 system. Nat Protoc. 8:2281-2308.

Seitz, A., H. Kojima, K. Oiwa, E.M. Mandelkow, Y.H. Song, and E. Mandelkow. 2002. Single-molecule investigation of the interference between kinesin, tau and MAP2c. EMBO J. 21:4896-4905.

Stepanova, T., J. Slemmer, C.C. Hoogenraad, G. Lansbergen, B. Dortland, C.I. De Zeeuw, F. Grosveld, G. van Cappellen, A. Akhmanova, and N. Galjart. 2003. Visualization of microtubule growth in cultured neurons via the use of EB3-GFP (end-binding protein 3-green fluorescent protein). J Neurosci. 23:2655-2664.

Sun, X., X. Shi, M. Liu, D. Li, L. Zhang, X. Liu, and J. Zhou. 2011. Mdp3 is a novel microtubule-binding protein that regulates microtubule assembly and stability. Cell Cycle. 10:3929-3937.

Sung, H.H., I.A. Telley, P. Papadaki, A. Ephrussi, T. Surrey, and P. Rorth. 2008. Drosophila ensconsin promotes productive recruitment of Kinesin-1 to microtubules. Dev Cell 15:866-876.

Syred, H.M., J. Welburn, J. Rappsilber, and H. Ohkura. 2013. Cell cycle regulation of microtubule interactomes: multi-layered regulation is critical for the interphase/mitosis transition. Mol Cell Proteomics 12:3135-3147.

Tanaka, Y., Y. Kanai, Y. Okada, S. Nonaka, S. Takeda, A. Harada, and N. Hirokawa. 1998. Targeted disruption of mouse conventional kinesin heavy chain, kif5B, results in abnormal perinuclear clustering of mitochondria. Cell 93:1147-1158.

Tas, R.P., A. Chazeau, B.M.C. Cloin, M.L.A. Lambers, C.C. Hoogenraad, and L.C. Kapitein. 2017. Differentiation between Oppositely Oriented Microtubules Controls Polarized Neuronal Transport. Neuron 96:1264-1271.

Trinczek, B., A. Ebneth, E.M. Mandelkow, and E. Mandelkow. 1999. Tau regulates the attachment/detachment but not the speed of motors in microtubule-dependent transport of single vesicles and organelles. J Cell Sci. 112:2355-2367.

Tymanskyj, S.R., B. Yang, A. Falnikar, A.C. Lepore, and L. Ma. 2017. MAP7 Regulates Axon Collateral Branch Development in Dorsal Root Ganglion Neurons. J Neurosci. 37:1648-1661.

Tymanskyj, S.R., B.H. Yang, K.J. Verhey, and L. Ma. 2018. MAP7 regulates axon morphogenesis by recruiting kinesin-1 to microtubules and modulating organelle transport. Elife 7: e36374.

van Riel, W.E., A. Rai, S. Bianchi, E.A. Katrukha, Q. Liu, A.J. Heck, C.C. Hoogenraad, M.O. Steinmetz, L.C. Kapitein, and A. Akhmanova. 2017. Kinesin-4 KIF21B is a potent microtubule pausing factor. Elife 6:e24746.

van Spronsen, M., M. Mikhaylova, J. Lipka, M.A. Schlager, D.J. van den Heuvel, M. Kuijpers, P.S. Wulf, N. Keijzer, J. Demmers, L.C. Kapitein, D. Jaarsma, H.C. Gerritsen, A. Akhmanova, and C.C. Hoogenraad. 2013. TRAK/Milton motor-adaptor proteins steer mitochondrial trafficking to axons and dendrites. Neuron 77:485-502.

Verhey, K.J., and J.W. Hammond. 2009. Traffic control: regulation of kinesin motors. Nat Rev Mol Cell Biol. 10:765-777.

Verhey, K.J., N. Kaul, and V. Soppina. 2011. Kinesin assembly and movement in cells. Annu Rev Biophys. 40:267-288.

Vershinin, M., B.C. Carter, D.S. Razafsky, S.J. King, and S.P. Gross. 2007. Multiple-motor based transport and its regulation by Tau. Proc Natl Acad Sci U S A 104:87-92.

Xu, J., B.J. Reddy, P. Anand, Z. Shu, S. Cermelli, M.K. Mattson, S.K. Tripathy, M.T. Hoss, N.S. James, S.J. King, L. Huang, L. Bardwell, and S.P. Gross. 2012. Casein kinase 2 reverses tail-independent inactivation of kinesin-1. Nat Commun. 3:754.

Yadav, S., P.J. Verma, and D. Panda. 2014. C-terminal region of MAP7 domain containing protein 3 (MAP7D3) promotes microtubule polymerization by binding at the C-terminal tail of tubulin. PLoS One 9:e99539.

Supplemental Figures

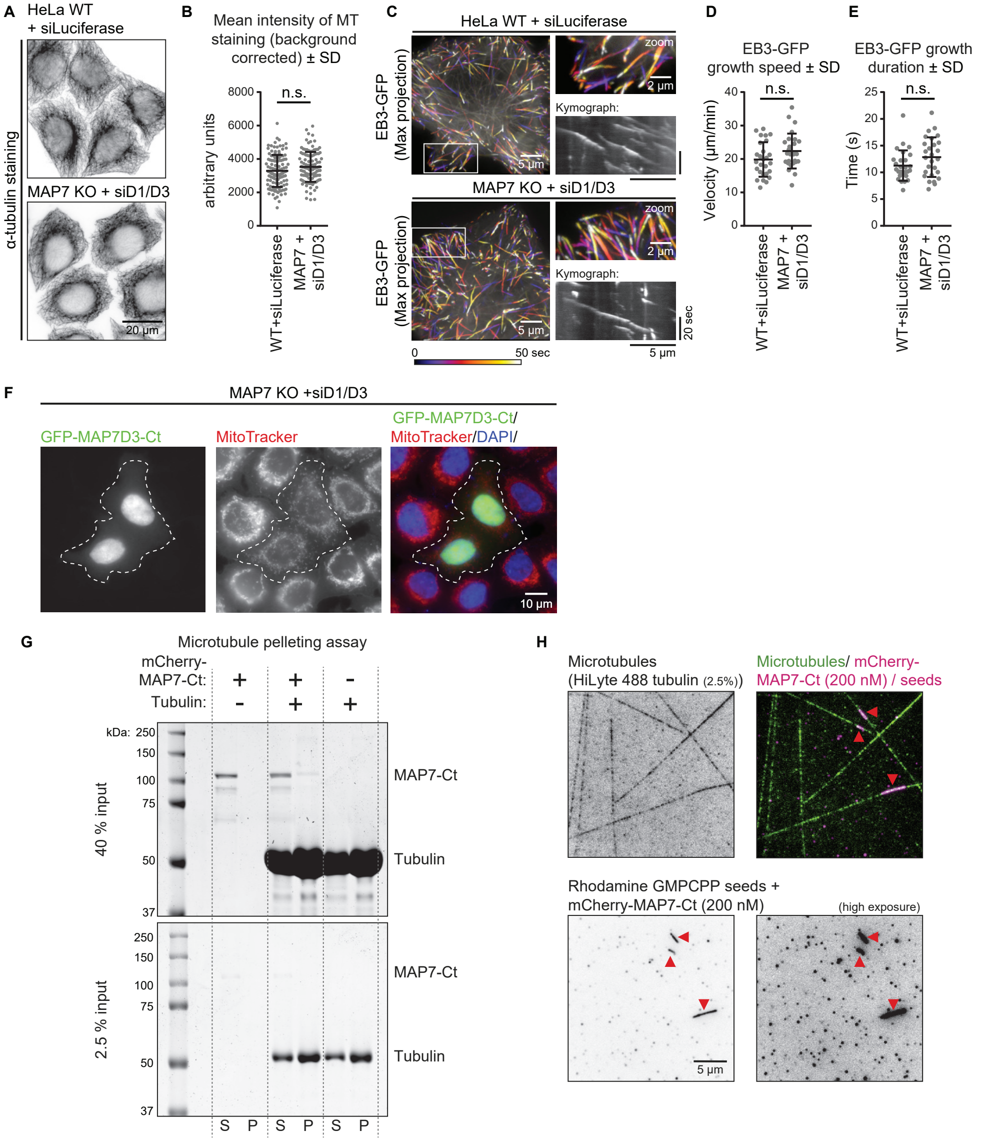
A
HeLa WT + siLuciferase
MAP7 KO + siD1/D3
α-tubulin staining
20 μm
B
Mean intensity of MT staining (background corrected) ± SD
arbitrary units
8000
6000
4000
2000
0
n.s.
WT+siLuciferase
MAP7 + siD1/D3
C
HeLa WT + siLuciferase
MAP7 KO + siD1/D3
EB3-GFP (Max projection)
zoom
2 μm
5 μm
Kymograph:
20 sec
0
50 sec
5 μm
D
EB3-GFP growth speed ± SD
Velocity (μm/min)
40
30
20
10
0
n.s.
WT+siLuciferase
MAP7 + siD1/D3
E
EB3-GFP growth duration ± SD
Time (s)
25
20
15
10
5
0
n.s.
WT+siLuciferase
MAP7 + siD1/D3
F
MAP7 KO +siD1/D3
GFP-MAP7D3-Ct
MitoTracker
GFP-MAP7D3-Ct/ MitoTracker/DAPI/
10 μm
G
Microtubule pelleting assay
mCherry-MAP7-Ct: + + -
Tubulin: - + +
kDa: 250
150
100
75
50
37
40 % input
2.5 % input
MAP7-Ct
Tubulin
S P S P S P
H
Microtubules (HiLyte 488 tubulin (2.5%))
Microtubules/ mCherry-MAP7-Ct (200 nM) / seeds
Rhodamine GMPCPP seeds + mCherry-MAP7-Ct (200 nM)
(high exposure)
5 μm

Figure S1 - Effects of the depletion MAP7 family proteins on the MT network and characterization of their MT binding domains **(A-B)** Control or MAP7 KO + siMAP7D1/D3 HeLa cells were stained for α-tubulin and imaged on a wide field microscope (A) to quantify MT intensity per cell (B); n = 123 cells (WT + siLuciferase) and n = 115 cells (MAP7 KO + siMAP7D1/D3) from three independent experiments, Student's t- test: P = 0.054. **(C)** Live cell imaging of EB3-GFP in control or MAP7 KO + siMAP7D1/D3 Hela cells on a TIRF microscope. Color-coded maximum intensity projections, zooms of the white boxed area and illustrative kymographs of growing EB3-GFP comets are shown per condition. **(D, E)** Quantification of EB3-GFP dynamics: growth rate (D) and growth duration (E). n = 358 comets from 27 cells (WT + siLuciferase) and n = 289 comets from 27 cells (MAP7 KO + siMAP7D1/D3) from three independent experiments, Mann-Whitney *U* test: (D) p = 0.078 and (E) p = 0.138. **(F)** Wide field images of overexpressed GFP-MAP7D3-Ct in MAP7 KO + siMAP7D1/D3 HeLa cells stained with MitoTracker and DAPI to visualize mitochondria and nuclei. **(G)** Unprocessed Coomassie blue-stained SDS-PAGE gel of the MT pelleting assay shown in Fig. 2B. Two gels were loaded with different input quantities: 40 and 2.5% of total samples. The positions of tubulin and

Figure S1 (continued) mCherry-MAP7-Ct truncation on the gel are indicated on the right. **(H)** Images showing *in vitro* polymerized MTs, with HiLyte 488-labeled tubulin, Rhodamine-labeled MT seeds and mCherry-MAP7-Ct. Images were obtained on a TIRF microscope. Rhodamine labeled GMPCPP-stabilized MT seeds are indicated (red arrow). The mCherry-MAP7-Ct image (also showing MT seeds) is shown on the right with linearly increased brightness/contrast (ImageJ software).

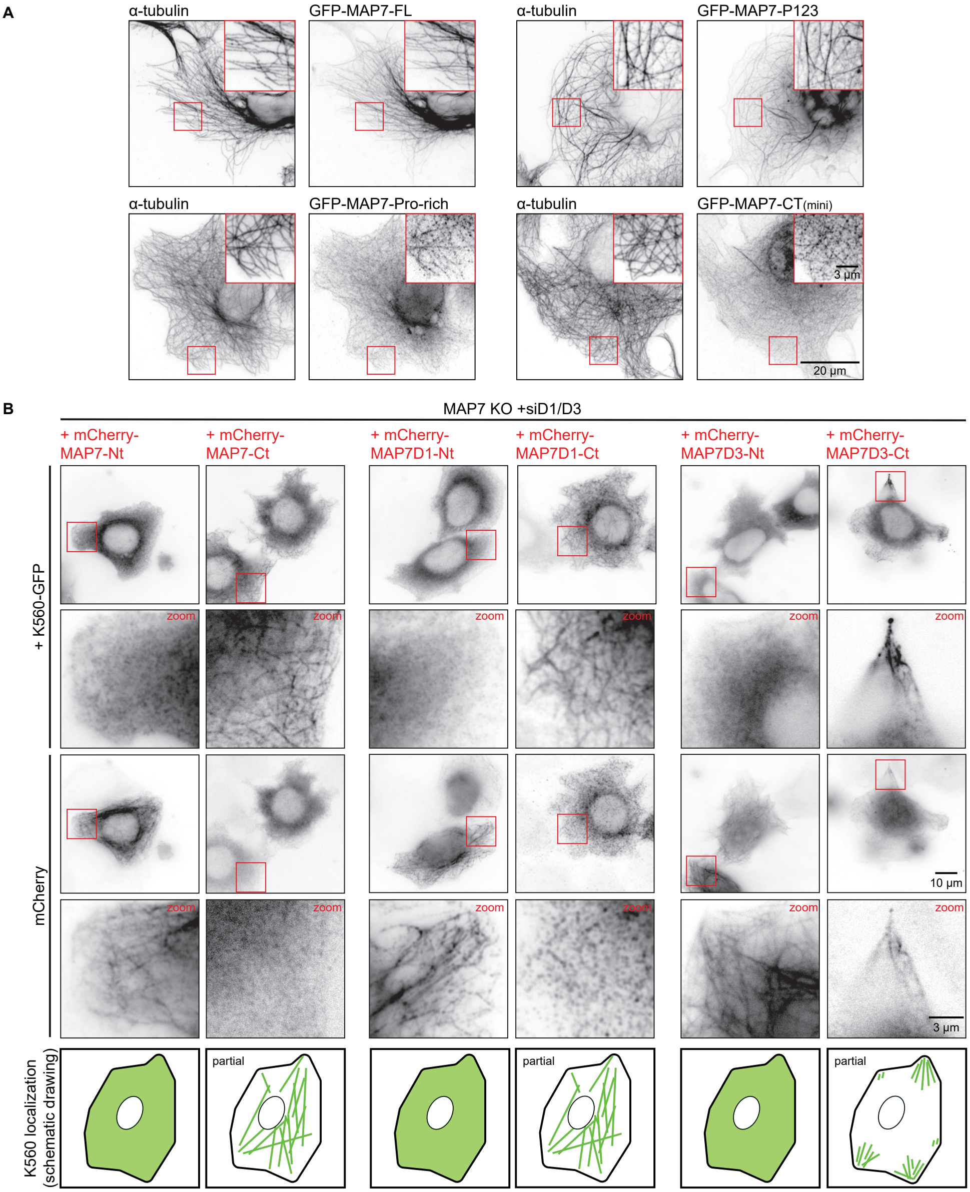
A
α-tubulin
GFP-MAP7-FL
α-tubulin
GFP-MAP7-P123
α-tubulin
GFP-MAP7-Pro-rich
α-tubulin
GFP-MAP7-CT(mini)
3 µm
20 µm
B
MAP7 KO +siD1/D3
+ mCherry-MAP7-Nt
+ mCherry-MAP7-Ct
+ mCherry-MAP7D1-Nt
+ mCherry-MAP7D1-Ct
+ mCherry-MAP7D3-Nt
+ mCherry-MAP7D3-Ct
+ K560-GFP
mCherry
zoom
10 µm
3 µm
K560 localization (schematic drawing)
partial

Figure S2 - Kinesin-1 recruitment to MTs by the C-termini of MAP7 family proteins (A) COS7 cells overexpressing indicated GFP-tagged MAP7 constructs co-stained for α-tubulin. Zooms are indicated with red boxes. **(B)** Wide field images of MAP7 KO + siMAP7D1/D3 HeLa cells overexpressing K560-GFP with mCherry-tagged MAP7-Nt and -Ct constructs. Enlargements of images indicated with a red squared box are shown in the panel row below. A schematic and representative drawing of K560-GFP localization for each condition is shown at the bottom.

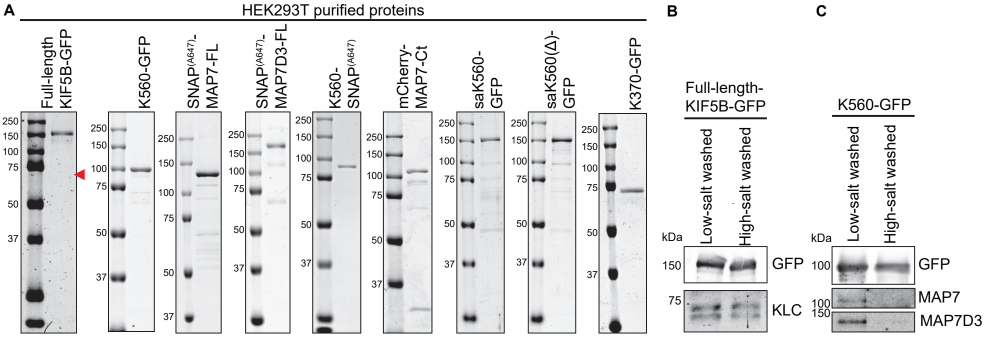
A
HEK293T purified proteins
Full-length KIF5B-GFP
K560-GFP
SNAP(A647)-MAP7-FL
SNAP(A647)-MAP7D3-FL
K560-SNAP(A647)
mCherry-MAP7-Ct
saK560-GFP
saK560(Δ)-GFP
K370-GFP
250
150
100
75
50
37
B
Full-length-KIF5B-GFP
Low-salt washed
High-salt washed
kDa
150
75
GFP
KLC
C
K560-GFP
Low-salt washed
High-salt washed
kDa
100
100
150
GFP
MAP7
MAP7D3

D

Low-Salt (0.3M) washed Full-length-KIF5B-GFP

Name	Score	Coverage (%)	Total Peptides
Kinesin-1 heavy chain (KIF5B)	48608.80	90.13	159
MAP7			-
MAP7D1	172.78	7.73	6
MAP7D3	35.66	1.60	2

High-Salt (1.5M) washed Full-length-KIF5B-GFP

Name	Score	Coverage (%)	Total Peptides
Kinesin-1 heavy chain (KIF5B)	49745.98	92.63	165
MAP7			-
MAP7D1	87.70	4.99	2
MAP7D3	42.41	0.80	1

E

Low-Salt (0.3M) washed K560-GFP

Name	Score	Coverage (%)	Total Peptides
Kinesin-1 heavy chain (KIF5B)	59099.21	63.03	105
MAP7	174.13	10.12	5
MAP7D1	130.75	8.11	5
MAP7D3	162.35	3.12	2

High-Salt (1.5M) washed K560-GFP

Name	Score	Coverage (%)	Total Peptides
Kinesin-1 heavy chain (KIF5B)	54398.88	59.40	98
MAP7			-
MAP7D1	0	1.03	1
MAP7D3			-

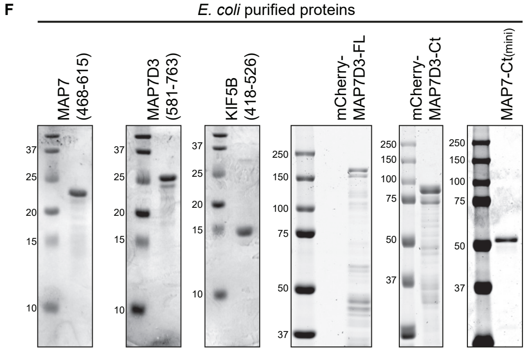
F
E. coli purified proteins
MAP7 (468-615)
MAP7D3 (581-763)
KIF5B (418-526)
mCherry-MAP7D3-FL
mCherry-MAP7D3-Ct
MAP7-Ct(mini)
250
150
100
75
50
37
25
20
15
10

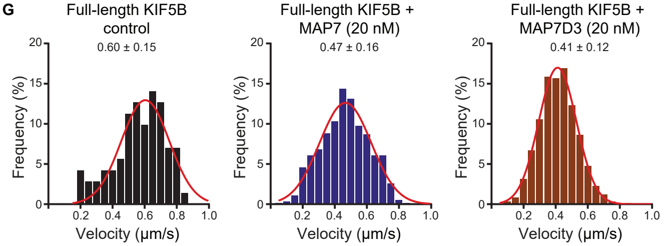

Figure S3 - Overview and analysis of purified proteins
(A) Proteins purified from HEK293T cells used in this study analyzed by SDS-PAGE. **(B, C)** Western blot analysis of purified kinesins washed with low (0.3 M) or high-salt (1.5 M NaCl). Antibodies against GFP, KLC, MAP7 and MAP7D3 were used, GFP serves as a loading control for both experiments. **(D, E)** Mass-Spectrometry analysis of purified kinesins washed with low (0.3 M) or high-salt (1.5 M NaCl) buffer. **(F)** Proteins purified from E. coli used in this study analyzed by SDS-PAGE. **(G)** Histograms of full-length kinesin-1 velocities in control conditions or in the presence of 20 nM MAP7 or MAP7D3. Red lines show fitting with Gaussian distributions, mean values ±SD are indicated in the plot; n = 71 (control), n = 542 (MAP7), n = 568 (MAP7D3), from two or three independent experiments.

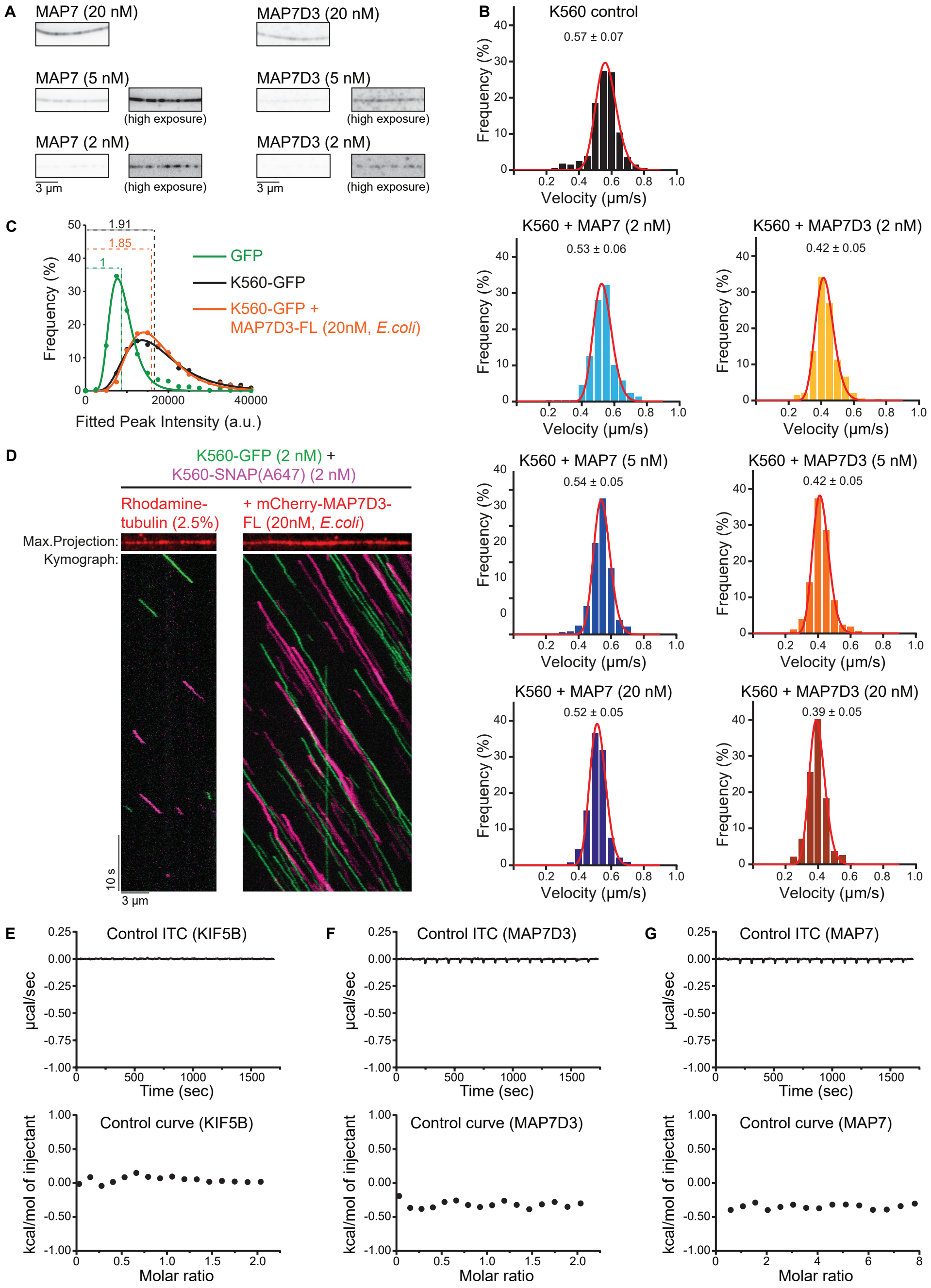

Figure S4 - Velocities and oligomerization state of kinesin constructs in different conditions
(A) Images showing increasing concentrations of SNAP(Alexa647)-tagged MAP7 or MAP7D3 on dynamic MTs *in vitro*. Images were obtained with identical laser power and exposure time on a TIRF microscope. Panels on the right show replicate images from the left with linearly increased brightness/contrast (ImageJ software).**(B)** Histograms of K560-GFP velocities in control conditions or in the presence of indicated proteins. Red lines show fitting with Gaussian distributions, mean values with standard deviation are indicated in the

Figure S4 (continued) plot, n = 241 (control), n = 351 (MAP7, 2 nM), n = 614 (MAP7, 5 nM), n = 361 (MAP7, 20 nM), n =257 (MAP7D3, 2nM), n = 436 (MAP7D3, 5 nM) and n = 303 (MAP7D3, 20 nM) from two independent experiments. **(C)** Histograms of fluorescence intensities of single GFP molecules (immobilized on coverslips) and K560-GFP moving on MTs with or without mCherry-MAP7D3-FL (purified from E. coli) in two separate chambers on the same coverslip (dots) and the corresponding fits with lognormal distributions (lines). n = 858 (GFP), n = 1640 (K560-GFP) and n = 4137 molecules (K560-GFP + mCherry-MAP7D3-FL); fluorophore density was approximately 0.01 μm–2 for GFP and K560-GFP proteins were analyzed from 2-10 MTs per movie. Dashed lines show corresponding relative median values. **(D)** Representative kymographs of 1:1 mixed K560-GFP (green) and K560-SNAP(Alexa647) (magenta) moving on dynamic MTs with or without mCherry-MAP7D3-FL (purified from E.coli). Maximum intensity projections show rhodamine-labeled MTs (control) or mCherry-MAP7D3-FL labeled MTs in red. **(E-G)** Control ITC experiments of KIF5B, MAP7D3 and MAP7. Top panels: Enthalpograms of the respective titrations. Lower panel: Black dots represent the integrated heat change.

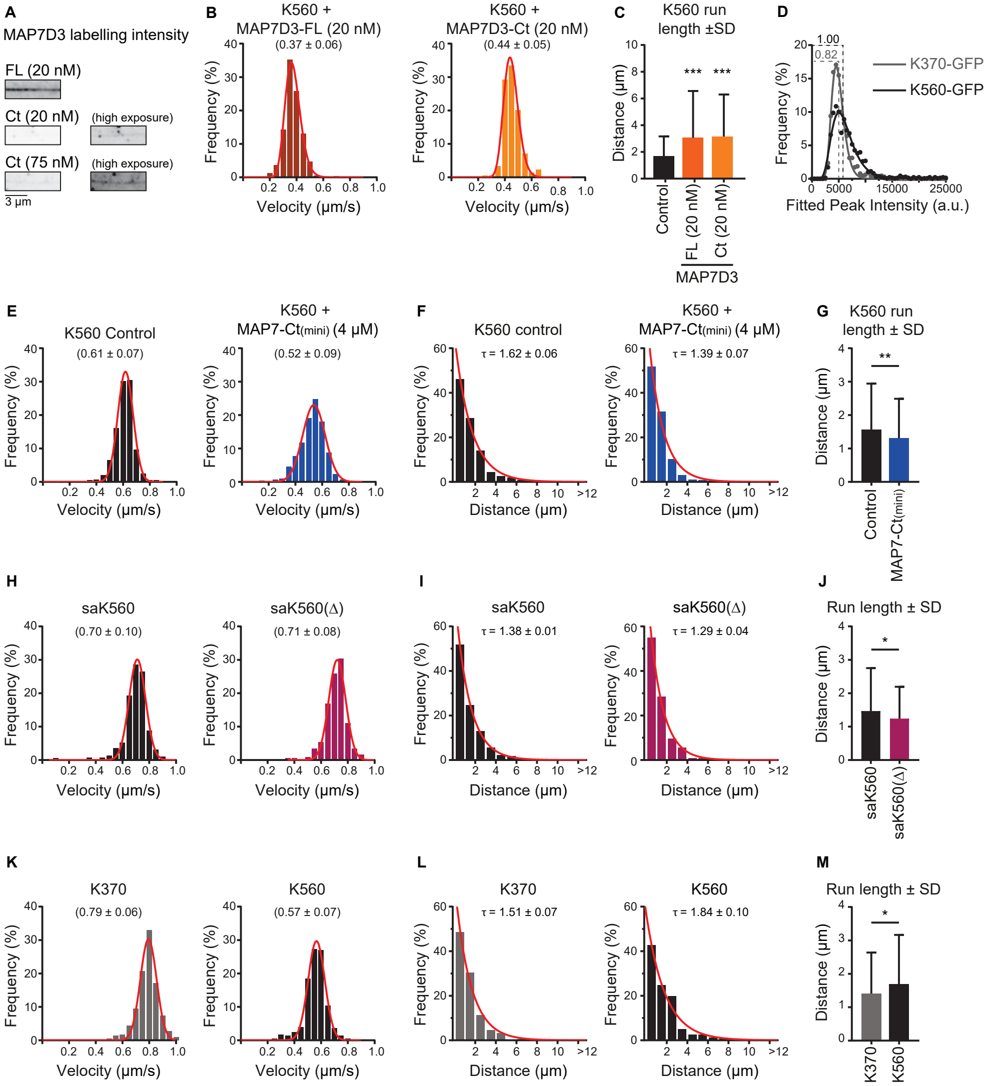

Figure S5 - Kinesin motility parameters

Figure S5 (continued)
(A) Images showing increasing concentration of mCherry-tagged MAP7D3 full-length or Ct (purified from E.coli) on dynamic MTs *in vitro*. Images were obtained with identical laser power and exposure time on a TIRF microscope. Panels on the right show replicate images from the left with linearly increased brightness/ contrast (ImageJ software).**(B)** Histograms of K560-GFP velocities in the presence of indicated MAP7D3 proteins (purified from E. coli). Red lines show fitting with Gaussian distributions; mean values with standard deviation are indicated in the plot, n = 271 (MAP7D3-FL) and n = 209 (MAP7D3-Ct).**(C)** Quantification of K560-GFP run length in control condition or in the presence of the indicated MAP7D3 proteins (purified from E.coli). *** p<0.001, Mann-Whitney *U* test. n = 241 (control), n = 271 (MAP7D3-FL, 20 nM), n = 209 (MAP7D3-Ct, 20 nM). **(D)** Histograms of fluorescence intensities of K370-GFP and K560-GFP motors moving on MTs in two separate chambers on the same coverslip (dots) and the corresponding fits with lognormal distributions (lines). n = 639 (K370-GFP) and n = 1337 molecules (K560-GFP); motor proteins were analyzed from 2-10 MTs per movie. Dashed lines show corresponding relative median values. **(E, H, K)** Histograms of kinesin velocities. Red lines show fitting with Gaussian distributions; mean values with standard deviation are indicated in the plot, (E) n = 404 (control) and n = 648 (MAP7-Ct(mini)), (H) n = 804 (saK560) and n = 380 (saK560(Δ)), (K) n = 723 (K370) and n = 241 (K560). **(F, G, I, J, L, M)** Kinesin run lengths were quantified and are shown as a histogram distribution with a fitted exponential decay curve (red), with indicated rate constants (tau) as a measure of mean run length (F, I, L) or with a bar graph (G, J, M) ** p <0.01, * p <0.05, Mann-Whitney *U* test. n numbers correspond to those of the preceding panels showing kinesin velocities.

3

Concerted action of kinesin-1 KIF5B and kinesin-3 KIF13B promotes efficient transport of exocytotic vesicles to microtubule plus ends

Andrea Serra-Marques[1,4*], Maud Martin[1,5*], Eugene A. Katrukha[1],
Ilya Grigoriev[1], Cathelijn A.E. Peeters[1], Qingyang Liu[1],
Peter Jan Hooikaas[1], Yao Yao[2,] Ihor Smal[2], Lotte B. Pedersen[3],
Erik Meijering[2,6], Lukas C. Kapitein[1] and Anna Akhmanova[1]

Available on: **bioRxiv (2020): 2020.04.06.027862**

*These authors contributed equally

---

[1] Cell Biology, Neurobiology and Biophysics, Department of Biology, Faculty of Science, Utrecht University, Utrecht, Netherlands

[2] Departments of Medical Informatics and Radiology, Biomedical Imaging Group Rotterdam, Erasmus University Medical Center, 2040, 3000 CA, Rotterdam, the Netherlands

[3] Department of Biology, Section of Cell Biology and Physiology, the August Krogh Building, University of Copenhagen, Universitetsparken 13, Copenhagen OE DK-2100, Denmark

[4] Current address: Departments of Cell and Tissue Biology and Bioengineering and Therapeutic Sciences, University of California, San Francisco, San Francisco, USA.

[5] Current address: Laboratory of Neurovascular Signaling, Department of Molecular Biology, Université libre de Bruxelles (ULB), B-6041 Gosselies, Belgium.

[6] Current address: Faculty of Engineering, the University of New South Wales, Sydney, NSW 2052, Australia

Abstract

Intracellular transport relies on different types of kinesins, but it is poorly understood which kinesins are present on a particular cargo, what their specific roles are and whether they can act simultaneously on the same cargo. Here, we show that Rab6-positive secretory vesicles are transported from the Golgi apparatus to the cell periphery by kinesin-1 KIF5B and kinesin-3 KIF13B, which determine the location of secretion events. KIF5B plays a dominant role, whereas KIF13B helps Rab6 vesicles to reach freshly polymerized microtubule ends, to which KIF5B binds poorly, likely because its cofactors, MAP7-family proteins, are slow in populating these ends. Sub-pixel localization demonstrated that during microtubule plus-end directed transport, both kinesins localize to the vesicle front and can be engaged on the same vesicle. When vesicles reverse direction, KIF13B relocates to the middle of the vesicle, while KIF5B shifts to the back, suggesting that KIF5B but not KIF13B undergoes a tug-of-war with a minus-end directed motor.

Introduction

Intracellular transport is driven by the collective activity of multiple motors. Transport towards microtubule (MT) plus ends depends on several kinesin families, whereas minus-end directed movement in animal cells is mostly driven by cytoplasmic dynein (Akhmanova and Hammer, 2010; Hirokawa and Tanaka, 2015). Different types of kinesins can participate in transporting the same cargo, but for many cellular organelles it is currently unclear which motors contribute to motility, what their specific roles are and whether different types of motors can be engaged in transport simultaneously. Furthermore, a common feature of many cellular cargoes is their bidirectional transport along MTs, and it is well established that both kinesins and dynein can operate on the same cargo. Motors of opposite polarity can engage in a tug-of-war, be switched on and off in a coordinated fashion or even depend on each other for motility (Gross, 2004; Hancock, 2014; Welte, 2004). Distinguishing these mechanisms requires the detection of motor activity on cellular cargo, which in many situations proved to be highly challenging.

Carriers of constitutive secretion represent a convenient and functionally important cellular model to study intracellular transport. Members of the plus-end directed kinesin-1 family (KIF5A/B/C) and kinesin-3 (KIF13A, KIF13B) have been implicated in the transport of Golgi-derived carriers to the cell surface in different cell types (Astanina and Jacob, 2010; Burgo et al., 2012; Jaulin et al., 2007; Nakagawa et al., 2000; Yamada et al., 2014). In both constitutive and inducible secretion assays in mammalian cells, exocytotic carriers positive for different exocytotic cargoes, such as NPY or temperature sensitive VSV-G, can be readily labeled with the small GTPases Rab6 and Rab8 (Grigoriev et al., 2007; Grigoriev et al., 2011; Jasmin et al., 1992; Miserey-Lenkei et al., 2010; Wakana et al., 2012). Recent work conclusively demonstrated that the majority of post-Golgi carriers, irrespective of the marker used, are positive for Rab6, which appears to be a general regulator of post-Golgi secretion and thus represents an excellent marker for secretory vesicles (Fourriere et al., 2019). It was further shown that cytoplasmic dynein drives transport of Rab6-positive membranes to MT minus ends, whereas kinesin-1 KIF5B and the kinesin-3 family members KIF1B and KIF1C have been implicated in the plus-end directed motility (Grigoriev et al., 2007; Lee et al., 2015; Matanis et al., 2002; Schlager et al., 2010; Schlager et al., 2014; Short et al., 2002; Wanschers et al., 2008). Moreover, KIF1C was shown to interact with Rab6 directly (Lee et al., 2015). However, siRNA-mediated co-depletion of KIF5B, KIF1B and KIF1C was not sufficient to block MT plus-end directed movement of Rab6 vesicles in HeLa cells (Schlager et al., 2014), and it is thus possible that additional kinesins are involved. For example, it has been proposed that the Golgi derived carriers named CARTS (carriers of the TGN to the cell surface), which are labeled with Rab6, Rab8 and a protein cargo pancreatic adenocarcinoma up-regulated factor (PAUF) are driven by the mitotic kinesin-5 family member KIF11/Eg5 (Ferenz et al., 2010; Wakana et al., 2012; Wakana et al., 2013), but the exact contribution of this motor requires further clarification.

Another important question concerns the specific roles of different kinesins on the same cargo. An increasing body of evidence suggests that different kinesins can preferentially bind to specific MT tracks, and the presence of different kinesins on the same cargo might thus help these cargos to navigate heterogeneous MT networks. For example, kinesin-1 shows a strong preference for more stable MT populations enriched in acetylated and detyrosinated tubulin, whereas kinesin-3 prefers dynamic, tyrosinated MTs (Cai et al., 2009; Guardia et al., 2016; Konishi and Setou, 2009; Liao and Gundersen, 1998; Lipka et al., 2016; Tas et al., 2017). These kinesins also require different MT-associated proteins (MAPs) for their activity: kinesin-1 critically depends on MAP7 family proteins whereas the activity of kinesin-3 is stimulated by doublecortin and doublecortin-like kinase (Chaudhary et al., 2019; Hooikaas et al., 2019; Lipka et al., 2016; Liu et al., 2012; Metivier et al., 2019; Metzger et al., 2012; Monroy et al., 2018; Pan et al., 2019). Whether and how the MAP-kinesin cross-talk contributes to motor selectivity is currently unknown.

In addition to kinesin preferences for specific tracks, other differences in the properties of the motors can affect their collective behaviors. *In vitro* and cellular studies have shown that kinesin-3 motors are faster than kinesin-1, but detach more easily from MTs, and therefore, when the two motors are combined *in vitro*, kinesin-1 predominates (Arpag et al., 2019; Arpag et al., 2014; Norris et al., 2014). In cells, the situation is more complex, because the presence of MAPs and post-translational tubulin modifications can affect MT-motor interaction and thus determine which motor will dominate (Gumy et al., 2017; Norris et al., 2014). It was also proposed that in situations where kinesin-1 is dominant, kinesin-3 can enhance overall transport efficiency by preventing cargo detachment from MTs and helping to navigate around obstacles (Arpag et al., 2019; Norris et al., 2014). Importantly, much of what is known about motor preferences for specific tracks and the details of their individual and collective properties is based on the observation of kinesin rigor mutants or kinesin fragments, either unloaded or recruited to artificial cargo (Arpag et al., 2019; Arpag et al., 2014; Guardia et al., 2016; Kapitein et al., 2010a; Norris et al., 2014; Tas et al., 2017), whereas much less is known about the behavior of motors attached to endogenous cargo by their natural adaptors.

Here, by using gene knockout and rescue experiments, we dissected the composition and behavior of the motor machinery responsible for the transport of secretory vesicles from the Golgi complex to the cell surface. We showed that the transport of Rab6/PAUF vesicles to the cell periphery relies on kinesin-1 KIF5B and the kinesin-3 KIF13B. In the absence of both kinesins, the efficiency of secretion was not perturbed, but exocytotic vesicles fused with the plasma membrane close to the Golgi and not at the cell periphery. KIF5B plays a dominant role in the secretory vesicle transport, and this transport is also strongly affected by the depletion of its co-factors, MAP7 family members. MAP7 proteins are more abundant on perinuclear MTs, likely because freshly polymerized MT ends, which are enriched at the cell periphery, are populated by these MAPs with some delay. Accordingly, KIF5B shows less activity on newly grown MT segments compared to the older MT lattices. In contrast, KIF13B can reach newly grown MT ends efficiently and contributes to the transport of

Rab6 vesicles to these ends.

Rab6 vesicle transport in kinesin knockout cells could be rescued by fluorescently tagged versions of KIF5B and KIF13B. High-resolution imaging of these kinesins on moving vesicles showed that when only one type of kinesin was present, it was enriched at the front of a vesicle moving to the cell periphery. When the two kinesins were present on a vesicle simultaneously, the faster KIF13B was located in front of the slower KIF5B. When vesicles reversed direction, KIF13B re-located to the vesicle center, whereas KIF5B was positioned at the back, suggesting that KIF5B but not KIF13B undergoes some mechanical competition with dynein. Our work thus provides insight into the spatial regulation and function of multimotor assemblies during bidirectional cargo transport.

Results

The Kinesin-3 KIF13B associates with Rab6-positive secretory vesicles

To image secretory carriers, we used the small GTPase Rab6, which was shown to be a highly robust and ubiquitous marker of exocytotic vesicles (Fourriere et al., 2019; Grigoriev et al., 2007). In non-neuronal cells, Rab6 is represented by the Rab6A and Rab6A' isoforms that will be collectively called Rab6; in this study, the Rab6A isoform was used in all live imaging experiments. While testing colocalization of Rab6 vesicles with different kinesins, we found that KIF13B, as well as its motorless tail region, were abundantly present on Rab6-positive vesicles in both fixed and live HeLa cells (Figure 1A-D). In contrast, its closest homologue KIF13A displayed little binding to Rab6 vesicles (Figure 1C, Figure 1 – figure supplement 1A), in line with previous work showing that KIF13A specifically binds to recycling endosomes by associating with the Rab11 family members Rab11A, Rab11B and Rab25 (Delevoye et al., 2014). The kinesin-5 Eg5/KIF11 has been previously implicated in the transport of the Golgi-derived carriers named CARTS, which are also positive for Rab6 and Rab8 (Wakana et al., 2012; Wakana et al., 2013). We analyzed the colocalization between the CARTS cargo protein, PAUF-mRFP and Rab6 and found that they indeed colocalized both in fixed cells stained for endogenous Rab6 (Figure 1 – figure supplement 1B), and also in live cells (Figure 1E). Only a sub-population of Rab6-positive vesicles contained PAUF (~60% and 50% in fixed and live cells, respectively) (Figure 1 – figure supplement 1B). This suggests that Rab6 vesicles may serve multiple exocytotic routes, with PAUF utilizing one of these routes. In line with this view, in secretion assays, less than 20% of PAUF vesicles contained the classic secretion marker, the temperature-sensitive VSV-G (Wakana et al., 2012), while a high degree of colocalization of VSV-G and Rab6 has been observed (Grigoriev et al., 2007). Even though we were able to confirm that PAUF-positive carriers are labeled with Rab6, we could not detect any colocalization between Rab6 and GFP-Eg5, both in fixed and in live cells (Figure 1 – figure supplement 1C,D), in contrast with a previous report (Wakana et al., 2013). However, PAUF colocalized with KIF13B, as 50.7 ± 22.3 % of PAUF-mRFP-positive vesicles were labeled with GFP-KIF13B (determined from 10 cells), and kymograph analysis of PAUF/Rab6-positive vesicles clearly showed that they move together (Figure 1F). These results support our observation on KIF13B/Rab6-vesicle colocalization and show that KIF13B is involved in the transport of secretory vesicles containing both PAUF and Rab6.

Analysis of vesicle fusion with the plasma membrane by total internal reflection fluorescence microscopy (TIRFM) revealed that KIF13B persists on the vesicles until the actual fusion event takes place and then disappears together with the Rab6 signal (Figure 1G). By performing fluorescence recovery after photobleaching (FRAP) experiments, we

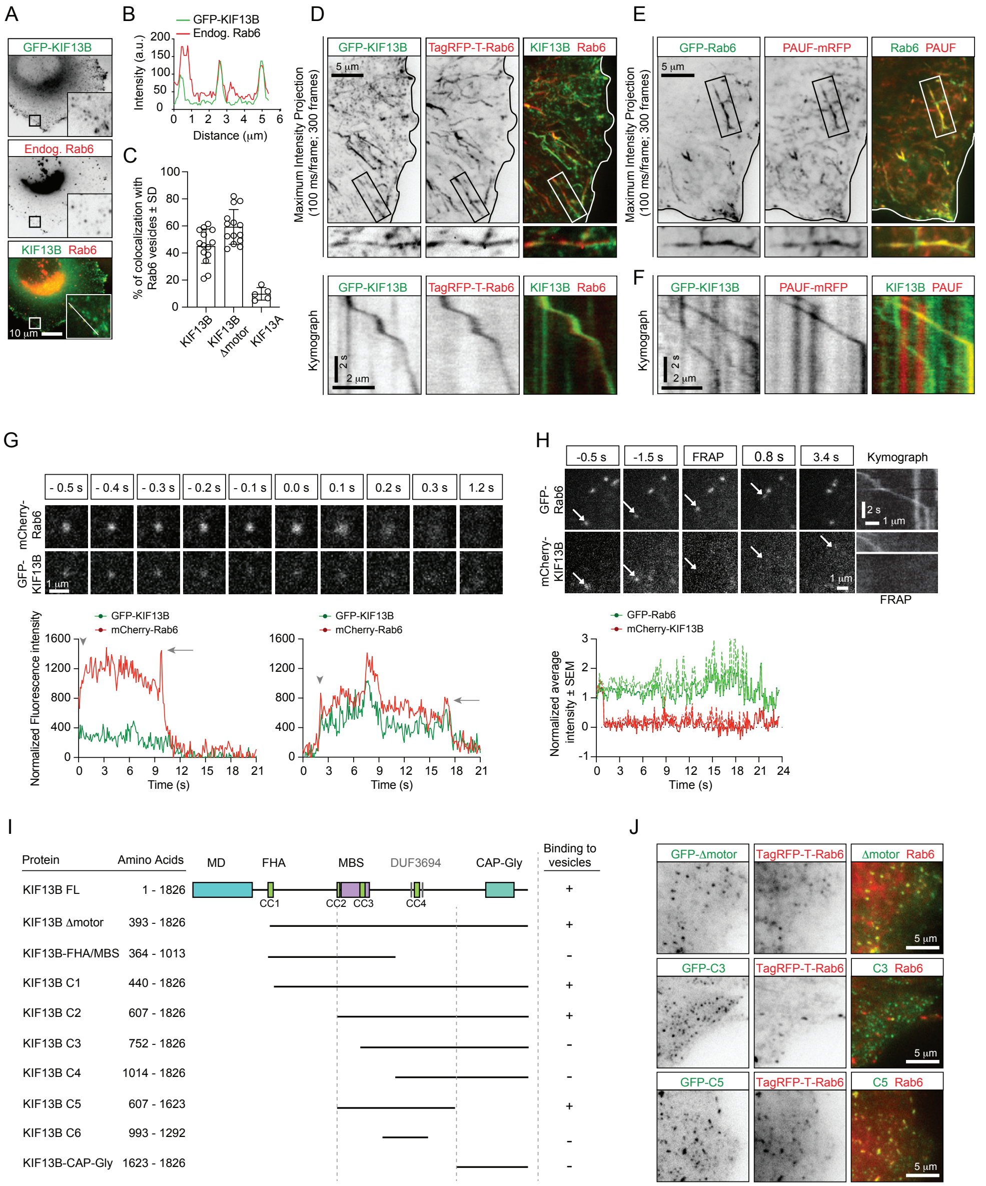
A
GFP-KIF13B
Endog. Rab6
KIF13B Rab6
10 µm
B
GFP-KIF13B
Endog. Rab6
Intensity (a.u.)
200
150
100
50
0
0 1 2 3 4 5 6
Distance (µm)
C
% of colocalization with Rab6 vesicles ± SD
100
80
60
40
20
0
KIF13B
KIF13B Δmotor
KIF13A
D
Maximum Intensity Projection (100 ms/frame; 300 frames)
GFP-KIF13B
TagRFP-T-Rab6
KIF13B Rab6
5 µm
Kymograph
2 s
2 µm
E
GFP-Rab6
PAUF-mRFP
Rab6 PAUF
5 µm
F
GFP-KIF13B
PAUF-mRFP
KIF13B PAUF
2 s
2 µm
G
- 0.5 s
- 0.4 s
- 0.3 s
- 0.2 s
- 0.1 s
0.0 s
0.1 s
0.2 s
0.3 s
1.2 s
mCherry-Rab6
GFP-KIF13B
1 µm
Normalized Fluorescence intensity
GFP-KIF13B
mCherry-Rab6
1600
1200
800
400
0
0 3 6 9 12 15 18 21
Time (s)
H
-0.5 s
-1.5 s
FRAP
0.8 s
3.4 s
Kymograph
GFP-Rab6
mCherry-KIF13B
2 s
1 µm
1 µm
FRAP
GFP-Rab6
mCherry-KIF13B
Normalized average intensity ± SEM
3
2
1
0
-1
0 3 6 9 12 15 18 21 24
Time (s)
I
Protein
Amino Acids
MD
FHA
MBS
DUF3694
CAP-Gly
Binding to vesicles
CC1
CC2
CC3
CC4
KIF13B FL 1 - 1826 +
KIF13B Δmotor 393 - 1826 +
KIF13B-FHA/MBS 364 - 1013 -
KIF13B C1 440 - 1826 +
KIF13B C2 607 - 1826 +
KIF13B C3 752 - 1826 -
KIF13B C4 1014 - 1826 -
KIF13B C5 607 - 1623 +
KIF13B C6 993 - 1292 -
KIF13B-CAP-Gly 1623 - 1826 -
J
GFP-Δmotor
TagRFP-T-Rab6
Δmotor Rab6
GFP-C3
C3 Rab6
GFP-C5
C5 Rab6
5 µm

Figure 1 - KIF13B localizes to Rab6-positive secretory carriers
(A) Imaging of a GFP-KIF13B expressing HeLa cell stained for Rab6. The insets correspond to magnified views of the boxed areas. **(B)** Signal intensity profile of GFP-KIF13B (green) and endogenous Rab6 (red) along the white line in panel A. **(C)** Quantification of the percentage of TagRFP-T labelled Rab6A vesicles colocalizing with GFP-KIF13B, GFP-KIF13B Δmotor and GFP-KIF13A. n=14 (GFP-KIF13B, GFP-KIF13B Δmotor) and n=5 cells (GFP-KIF13A). **(D)** Maximum intensity projections (300 consecutive frames, 100 ms interval) illustrating imaging of HeLa cells expressing GFP-KIF13B and TagRFP-T-Rab6A using TIRFM. Magnifications of the boxed area and kymographs illustrating the movement of co-labeled vesicle are shown below. **(E)** Maximum intensity projections with magnified views of the boxed areas illustrating TIRFM imaging of HeLa cells transfected with GFP-Rab6A and PAUF-mRFP. **(F)** Kymographs illustrating the movement of vesicles labeled with GFP-KIF13B and PAUF-mRFP. **(G)** (Top) Frames from TIRFM imaging showing the behavior of GFP-KIF13B

Figure 1 (continued) and mcherry-Rab6A vesicles before and during fusion. 0.0 s corresponds to the sharp increase of fluorescent signal associated with vesicle docking at the plasma membrane. (Bottom) Two examples showing the average fluorescence intensity of a single vesicle labelled with GFP-KIF13B and mCherry-Rab6A plotted versus time. Vesicle appearance in the focal plane is indicated by an arrowhead. Arrow points to the peaks of fluorescence intensity prior to vesicle fusion with the plasma membrane. An additional example is shown. **(H)** (Top) TIRFM imaging combined with FRAP was performed in HeLa cells containing exocytotic vesicles labeled for GFP-Rab6A and mCherry-KIF13B. The mCherry signal was photobleached (frames labeled FRAP) on moving vesicles labelled with GFP-Rab6A. Arrows indicate the same vesicle over time. Kymographs are shown to illustrate the absence of fluorescence recovery of mCherry-KIF13B on the vesicle. (Bottom) Quantification of the signal intensity of mCherry-KIF13B (red) on moving GFP-Rab6A vesicle (green) over time after FRAP. n=6 vesicles in 4 cells. **(I)** Scheme of the GFP-KIF13B deletion constructs used in this study. The constructs were transfected in HeLa cells and colocalization with TagRFP-T-Rab6A-positive vesicles was determined by live cell imaging. The amino acid positions in KIF13B are indicated. MD, motor domain; FHA, forkhead-associated domain, MBS, MAGUK binding stalk; DUF, domain of unknown function; CC, coiled coil. **(J)** Live images of HeLa cells expressing TagRFP-T-Rab6A and the indicated GFP-KIF13B deletion construct using TIRF microscopy.

observed that GFP-KIF13B does not exchange on exocytotic vesicles (Figure 1H), similar to what we have previously observed for Rab6 and Rab8 (Grigoriev et al., 2007; Grigoriev et al., 2011). Our data indicate that the motor is stably bound to the vesicles, and its detachment is not required prior for vesicle fusion with the plasma membrane.

Next, we mapped the region of KIF13B responsible for the binding to Rab6 vesicles by testing the ability of KIF13B deletion mutants to associate with Rab6 vesicles in live cells. KIF13B contains an N-terminal motor domain (MD), a forkhead-associated (FHA) domain, several predicted coiled-coil regions (CC), a MAGUK binding stalk (MBS), two predicted domains of unknown function (DUF3694) and a C-terminal cytoskeleton-associated protein-glycine-rich (CAP-Gly) domain. The MBS and a region containing a coiled-coil and the DUF3694 domains were necessary and sufficient for the binding to Rab6 vesicles, whereas the CAP-Gly domain and the motor domain were dispensable for the binding (Figure 1I,J). Together, our results show that kinesin-3 KIF13B robustly and specifically interacts with PAUF/Rab6-positive exocytotic vesicles.

KIF5B and KIF13B are the main drivers of Rab6 vesicle transport in HeLa cells

To critically test the role of different kinesins in the transport of secretory vesicles, we used CRISPR/Cas9 technology to knock out kinesin-encoding genes in HeLa cells. We generated gene knockout cell lines lacking KIF5B, KIF13B, KIF5B and KIF13B together (KIF5B/KIF13B-KO), or KIF5B, KIF13B, KIF1B and KIF1C (4X-KO), and observed that the silencing of these kinesin genes led to the loss of the respective proteins (Figure 2A). All obtained cell lines were viable and showed no proliferation defects. For kinesin-1 KIF5B knockout, these data are in line with previous genetic inactivation work in mice, which showed that although the mouse is embryonically lethal, extraembryonic cells are viable (Tanaka et al., 1998). Different kinesin knockout cells could spread normally as formation of focal adhesions was not perturbed, though the total cell area showed some variability between different cell lines, possibly due to clonal effects (Figure 2 – figure supplement 1A,B). The microtubule cytoskeleton was somewhat less focused around the microtubule-organizing center in all cells lacking KIF5B, whereas the staining for EB1 comets appeared normal (Figure 2 – figure supplement 1A). Endosomes showed increased perinuclear clustering, particularly in the 4X-KO cells, and their number appeared reduced in this cell line, although we cannot exclude that this effect was due to the fact that strongly clustered endosomes are more difficult to count (Figure 2 – figure supplement 1A,C). Furthermore, mitochondria were shifted towards the perinuclear region in all cell lines lacking KIF5B (Figure 2 – figure supplement 1 A,D), as described previously (Hooikaas et al., 2019; Tanaka et al., 1998). Altogether, we generated a robust cellular system to study the individual contribution of several kinesin motors to intracellular transport.

To quantify the effects of kinesin knockouts on Rab6 vesicle motility, we performed automated vesicle tracking using an improved version of a particle tracking algorithm described previously (Yao et al., 2017) (Figure 2B). Trajectories of individual Rab6 vesicles consisted of alternating periods of diffusive “jiggling” movement and persistent direction-

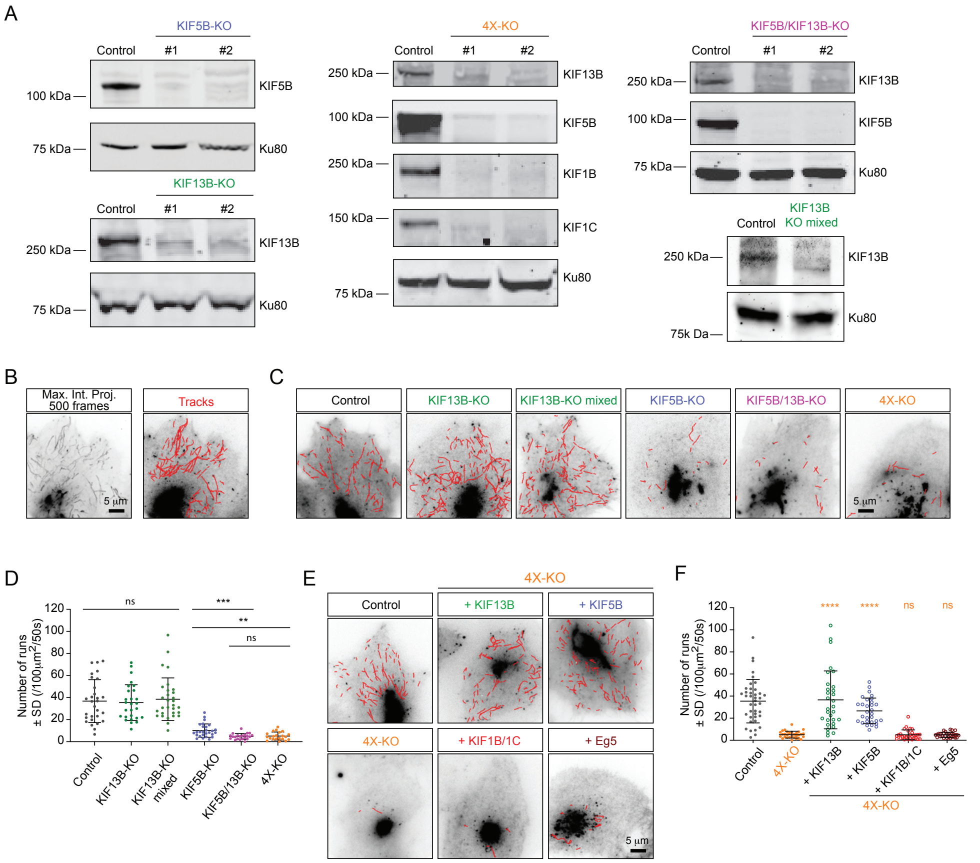

Figure 2 - Transport of Rab6 vesicles in HeLa cells is driven by KIF5B and KIF13B
(A) Western blots of HeLa cell extracts showing the knockout of the different kinesins, using the indicated antibodies. Ku80 antibody was used as loading control. KIF13B-KO clone #1, KIF5B-KO clone #1, KIF5B/KIF13B-KO clone #1 and 4X-KO clone #2 have been used in latter experiments. **(B)** A maximum intensity projection over 500 frames (100 ms exposure with no delays) illustrating mCherry-Rab6A vesicle movement imaged by TIRFM and automated tracking using the SOS/MTrackJ plugin of mCherry-Rab6A labeled vesicles in the same HeLa cells. **(C,E)** Examples of automatic tracking of mCherry-Rab6A labeled vesicles using the SOS/MTrackJ plugin in the indicated knockout HeLa cells (C), or in 4X-KO cells expressing the indicated kinesins. **(D)** Analysis of the number of vesicle runs in the conditions depicted in (C). n=29, 27, 30, 27, 22 and 21 cells, respectively, in 3 independent experiments. Mann-Whitney *U* test: ***p=0.0001; **p=0.0015; ns, no significant difference. **(F)** Analysis of the number of vesicle runs in the conditions depicted in (E). n=40, 30, 30, 30, 30 and 30 cells in 3 independent experiments for each condition except for Eg5 (2 independent experiments). Mann-Whitney *U* test: ****p<0.0001; ns, no significant difference.

al motion, which we attributed to the active transport along MTs. From complete vesicle tracks we extracted the segments of directional movement (here termed “runs”) using the velocity vector as a directional correlation measure as described previously (Katrukha et al., 2017). We compared the average numbers of vesicle runs, which report on active displacement along MTs, in control and in the different knockout cell lines (Figure 2C,D; Figure 2 – figure supplement 2A). In KIF13B-KO cells, the number of vesicle runs was very similar to control. Since some compensatory changes could have occurred during cell line selection of the clonal line, we also included in the analysis the population of cells that were used for KIF13B-KO clone selection (KIF13B-KO mixed population). These cells were transfected with a vector co-expressing a puromycin resistance gene, the single guide RNA sequence specific for KIF13B and Cas9, subjected to puromycin selection for 2 days and left to recover for 5 days before analysis (Figure 2A; “KIF13B KO mixed”). Also these cells did not show a major reduction in the number of runs, similar to KIF13B knockout clones (Figure 2C,D). In contrast, a very strong reduction in the number of runs was observed in the KIF5B-KO cells. Interestingly, the double knockout of KIF5B and KIF13B (KIF5B/KIF13B-KO) had a synergistic effect, as the number of Rab6 vesicle runs was reduced compared to the single KIF5B-KO (Figure 2C,D). These results indicate that both kinesins cooperate in the transport of Rab6 vesicles, with KIF5B being the major player. This is also in line with our previous observations showing that siRNA-mediated depletion of KIF5B had a strong impact on the post-Golgi transport of Rab6 vesicles (Grigoriev et al., 2007). The 4X-KO cells did not show a stronger reduction in the number of runs compared to the double KIF5B/KIF13B-KO (Figure 2C,D, Figure 2 – figure supplement 2A), suggesting that KIF1B and KIF1C are not sufficient for Rab6 vesicle transport.

Next, we performed rescue experiments using the 4X-KO cells. We re-expressed in these cells KIF5B, KIF13B, a combination of KIF1B and KIF1C, or Eg5/KIF11, and analyzed Rab6 vesicle motility. Expression of KIF5B restored the number of vesicle runs to values similar to control, and the same was observed when KIF13B was re-expressed (Figure 2E, F). It has been previously shown that the knockdown of kinesin-1 heavy chain reduces the levels of kinesin light chains (KLC) (Zhou et al., 2018). Using immunofluorescence cell staining and Western blotting, we confirmed this observation (Figure 2 – figure supplement 2B). KLC levels were restored by transiently re-expressing GFP-KIF5B in the KIF5B-KO line (Figure 2 – figure supplement 2C).

Interestingly, simultaneous re-expression of KIF1B and KIF1C did not rescue Rab6 vesicle motility in 4X-KO cells (Figure 2E,F). Importantly, these kinesins were functional, as their expression could rescue the localization of Rab11-positive endosomes: compared to control cells, the distribution of Rab11 carriers was strongly shifted towards the Golgi area in the 4X-KO cells, and this phenotype was reversed upon simultaneous re-expression of KIF1B and KIF1C (Figure 2 – figure supplement 2D). Furthermore, expression of Eg5 in the 4X-KO did not restore vesicle movement (Figure 2E,F), consistent with our observations that Eg5 does not localize to Rab6-positive vesicles (Figure 1 – figure supplement 1C,D). In agreement with these data, the number of vesicle runs was not affected by siRNA-mediated depletion of Eg5 (Figure 2 – figure supplement 2E,F). Together, these data indicate that Eg5 and KIF1B/1C make no major contribution to the motility of Rab6 vesicles, whereas KIF5B and KIF13B are the main drivers of this process in HeLa cells.

KIF5B and KIF13B have different velocities and set the speed range of Rab6 vesicles

Next, we used automated vesicle tracking to examine how the presence of KIF5B and KIF13B affects different parameters of vesicle movement. Vesicle speeds obtained from the automated analysis were very similar to those determined manually from the analysis of kymographs drawn along Rab6-positive tracks, as we described previously (Grigoriev et al., 2007; Schlager et al., 2014) (Figure 3 – figure supplement 1A). Taking this approach, we examined the speed of the residual vesicle movements in different knockout cell lines. While the average Rab6 vesicle speed in KIF13B-KO cell clones and the mixed KIF13B-KO population was mildly but significantly reduced compared to control, the few Rab6 vesicles that still moved in the KIF5B-KO, KIF5B/KIF13B-KO and 4X-KO cells displayed speeds much higher than those in control cells, an effect that was particularly obvious when speeds of all individual tracks rather than average velocities per cell were plotted (Figure 3A,B; Figure 2 – figure supplement 2A). Interestingly, we observed the appearance of vesicles moving with speeds exceeding 3 μm/s, which were very rare in control cells but could be readily detected in KIF5B-KO, KIF5B/KIF13B-KO and 4X-KO cells (Figure 3B, Figure 3 – figure supplement 1B). The residual, faster movements of Rab6 vesicles in cells lacking KIF5B and KIF13B could be driven by another kinesin or by dynein, as our previous work has shown that dynein-dependent Rab6 vesicle movements can occur with velocities of 2-4 μm/s (Schlager et al., 2014; Splinter et al., 2012). We also analyzed other parameters of Rab6 vesicle motility, namely the duration and length of individual vesicle runs. We found that run duration was relatively constant in all conditions (Figure 3 – figure supplement 1B). Loss of KIF13B had no significant impact on run length, indicating that this motor does not significantly contribute to the processivity of vesicle movement driven by KIF5B. Interestingly, the residual runs observed in the absence of KIF5B were significantly longer than those in control cells (Figure 3 – figure supplement 1B), possibly reflecting the strong sensitivity of this motor to obstacles (Telley et al., 2009).

We next analyzed the distribution of Rab6 vesicle speeds in more detail, focusing on the conditions where the number of vesicle movements was reasonably high (4X-KO cells and their rescues with KIF1B/C and Eg5 were not included in this analysis because the overall number of Rab6 vesicle movements in these cells was too low to fit speed distributions in a reliable manner). If only one motor were involved in vesicle movement, one Gaussian curve would be expected to fit the data. However, in most cases, the distributions of vesicle speeds matched much better the sum of two Gaussians (Figure 3 – figure supplement 1C, Figure 3C, D), indicating that there are at least two populations of vesicles with different average speeds per run. In control, there is a slower vesicle population with speed 1.20 ± 0.26 μm/sec (average ± SD), and a faster one with a value of 1.71 ± 0.49 μm/s (average ± SD) (Figure 3 – figure supplement 1C, Figure 3C,D). The fraction of higher speed runs was reduced in the clonal and mixed KIF13B-KO cells, while it was increased in the KIF5B-KO and KIF13B rescue of 4X-KO (Figure 3C,D, Figure 3 – figure supplement 1C). The speed distributions were quite similar in KIF13B-KO cells and in 4X-KO cells rescued with KIF5B (Figure 3C, second plot), in line with idea that KIF5B is the major motor on both cases.

In contrast, Rab6 vesicles in 4X-KO cells rescued by expressing KIF13B moved significantly faster than those in cells rescued with KIF5B (Figure 3C,D, Figure 3 – figure supplement 1C). It is important to emphasize that in cells rescued by expressing either KIF5B or KIF13B, vesicle tracks were distributed throughout the whole cytoplasm (Figure 2E). Thus, the observed speed difference could not be explained by differences in cell regions where the movement took place, such as cell thickness or interference with other organelles. However, the observed difference in vesicle speeds can be explained by previous observations showing that KIF13B is a faster motor compared to KIF5B (Arpag et al., 2014; Norris et al., 2014). Indeed, single-molecule imaging of dimeric motor-containing fragments lacking the cargo binding tails, KIF13B-380-LZ and KIF5B-560, in 4X-KO cells confirmed that KIF13B moves significantly faster than KIF5B (Figure 3E). To show that this difference is also observed when these kinesins are linked to cargo, we next used the FRB-FKBP chemical dimeriza-

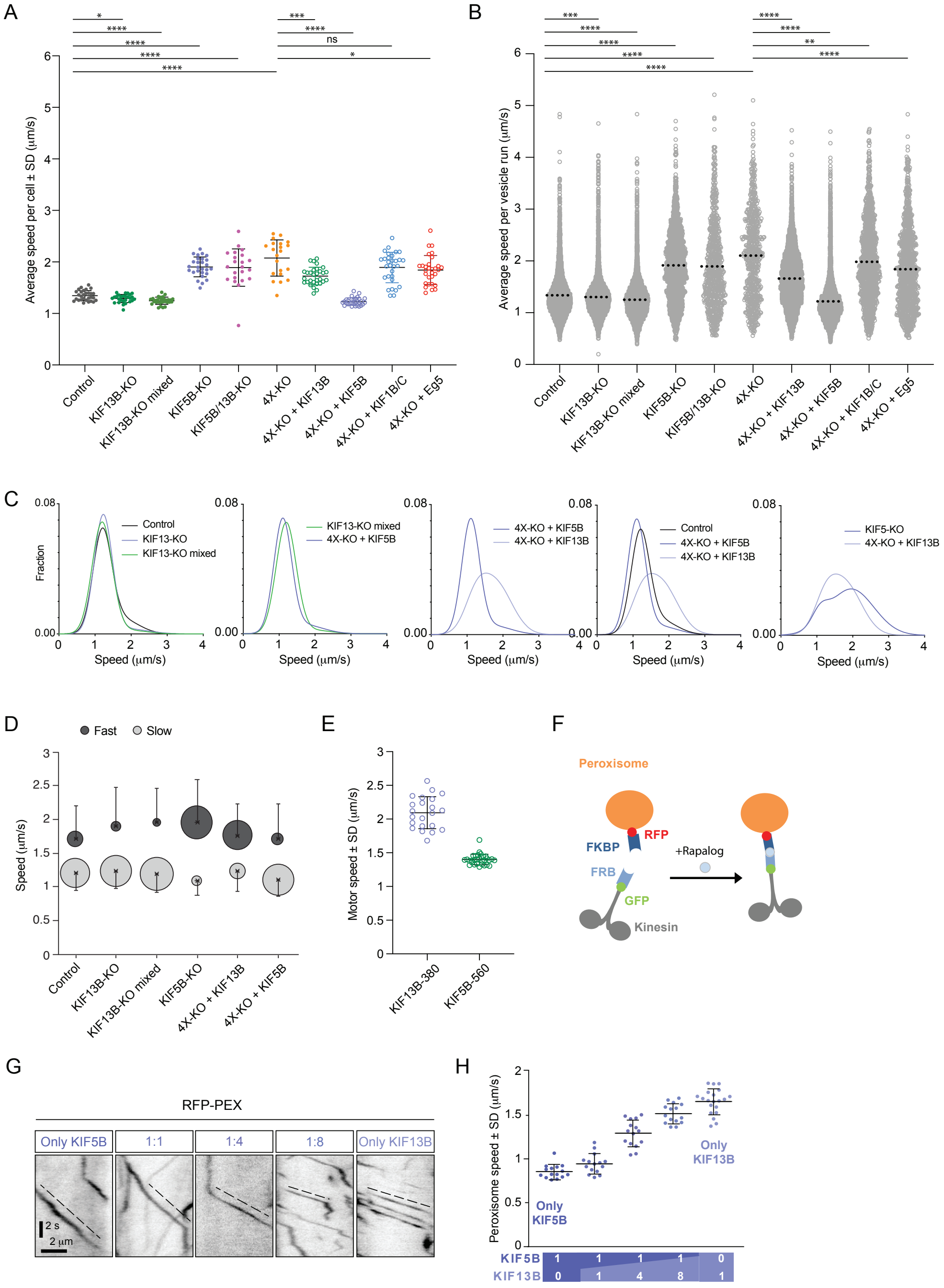

Figure 3 - KIF5B and KIF13B have distinct speeds

(A) Analysis of the mean speed of automatically tracked mCherry-Rab6A-positive vesicles per cell in the indicated conditions. n=29, 27, 30, 27, 22, 21, 30, 30, 30 and 30 cells, respectively, in 2 independent experiments for Eg5 and 3 independent experiments in all other conditions. Unpaired t-test: ****p<0.0001; ***p=0.0002; *p<0.025, ns, no significant difference. **(B)** Violin plots showing the speed of individual automatically

Figure 3 (continued) tracked mCherry-Rab6A-positive vesicles in the indicated conditions. Doted lines represent the mean. n=29, 27, 30, 27, 22, 21, 30, 30, 30 and 30 cells, respectively, in 2 independent experiments for Eg5 and 3 independent experiments in all other conditions. Same data as shown in Figure 3A, but displayed here for individual vesicle runs rather than averaged per cell. Mann-Whitney *U* test: ****p<0.0001; ***p=0.0002; **p=0.0064. (C) Combinations of sums of two Gaussian fits to the distribution of Rab6 vesicles run speeds for the indicated conditions (see Figure 3 – figure supplement 1C). **(D)** Parameters of "slow" (light grey) and "fast" (dark grey) Gaussians components from fits in Figure 3 – figure supplement 1C. Crosses correspond to the mean value and error bars to the standard deviation of fitted Gaussians. The area of the circles corresponds to the fraction of runs associated with "slow" and "fast" components, i.e. represents the area under the curve of each Gaussian (total sum of areas for each condition is the same). n=7099 runs in 29 cells, 6682 runs in 27 cells, 8192 runs in 30 cells, 1772 runs in 27 cells, 7616 runs in 30 cells and 5651 runs in 30 cells, respectively. **(E)** Speed of kinesin-positive particles imaged with TIRF microscopy in 4X-KO HeLa cells expressing KIF5B-560-GFP (n=30 cells, 3 experiments) or KIF13B-380-LZ-GFP (n=22 cells, 2 experiments). **(F)** A scheme of inducible peroxisome trafficking assay performed by the rapalog-dependent recruitment of FRB-tagged KIF5B(1-807) or KIF13B(1-444) to FKBP-tagged PEX3, a peroxisome protein. **(G)** Kymographs illustrating peroxisome movements in cells transfected with the indicated FRB-tagged KIF5B(1-807):KIF13B(1-444) plasmid ratios. **(H)** MRC5 cells were co-transfected with PEX3-mRFP-FKBP and the indicated ratios of FRB-tagged KIF5B and KIF13B plasmids mentioned in (F) simultaneously, while the total amount of DNA was kept constant. Peroxisomes were imaged by TIRF or SD microscopy and their speeds were measured at 10-40 min after rapalog addition. n=15, 15, 15, 15 and 20 cells, respectively in 3 experiments (Kif13B alone - in 4 experiments).

tion system in combination with rapalog (an analog of rapamycin) to trigger the binding of KIF5B(1-807)-GFP-FRB and/or KIF13B(1-444)-GFP-FRB motor-containing fragments to peroxisomes, which are relatively immobile organelles (Kapitein et al., 2010b; Splinter et al., 2012)(Figure 3F-H). We used different ratios of KIF5B and KIF13B-expressing plasmids as a way to manipulate the relative motor abundance on peroxisomes and observed that peroxisome speed increased when the KIF5B:KIF13B plasmid ratio decreased (Figure 3G,H), similar to what we described previously for KIF5B and KIF1A (Gumy et al., 2017). Kymographs of peroxisome movements showed that when the two kinesins were co-expressed, intermediate velocities were observed, suggesting simultaneous engagement or very rapid switching between the two types of motors (Figure 3G). This behavior is different from that previously described for the kinesin-1/kinesin-3 motor pairs connected by a stiff linker, where typically only one of the two kinesins was engaged at a given moment (Norris et al., 2014). Interestingly, a significant excess of KIF13B-encoding plasmid was needed to shift peroxisome speeds to higher values (Figure 3G,H), in agreement with *in vitro* gliding assays, which indicated that the slower kinesin-1 predominated when combined with kinesin-3 at a 1:1 molar ratio (Arpag et al., 2014).

Next, we imaged fluorescent fusions of the full length KIF5B and KIF13B in 4X-KO cells. The expression of GFP-tagged kinesins in combination with mCherry-Rab6A in 4X-KO allowed us to directly determine the speeds of vesicles driven by a particular motor and also to estimate the number of kinesins present on the vesicles in our rescue experiments (Figure 4A-D). By manually measuring the speeds of mCherry-Rab6A labeled vesicles decorated with either GFP-KIF13B or KIF5B-GFP in 4X-KO cells, we again confirmed that KIF13B is the faster motor (Figure 4C,D). To determine the number of motors present on a vesicle, we used KIF5B-560-GFP, a dimeric KIF5B fragment that lacks the tail and therefore does not bind to cargo, as a fluorescence intensity standard (Figure 4A). We observed that approximately 1-2 dimers of KIF5B-GFP and 3-5 dimers of KIF13B-GFP could be detected on the vesicles (Figure 4A,B). Since these experiments were performed with overexpressed full-length kinesins, these data suggest that the maximum number of KIF5B binding sites

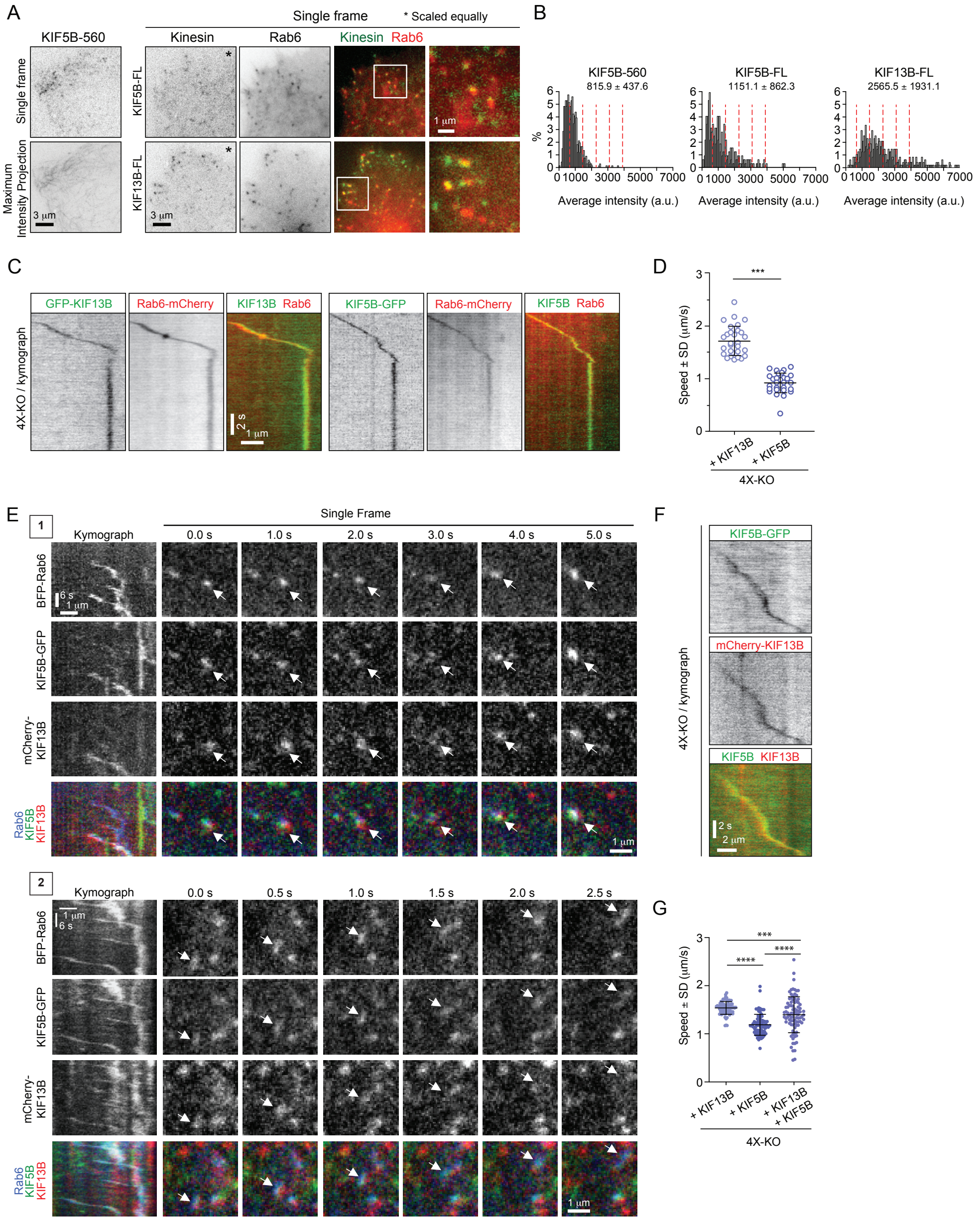
A
Single frame
* Scaled equally
KIF5B-560
Kinesin
Rab6
Kinesin Rab6
Single frame
Maximum Intensity Projection
KIF5B-FL
KIF13B-FL
*
*
1 µm
3 µm
3 µm
B
KIF5B-560
815.9 ± 437.6
KIF5B-FL
1151.1 ± 862.3
KIF13B-FL
2565.5 ± 1931.1
%
0 1000 3000 5000 7000
Average intensity (a.u.)
C
GFP-KIF13B
Rab6-mCherry
KIF13B Rab6
KIF5B-GFP
Rab6-mCherry
KIF5B Rab6
4X-KO / kymograph
2 s
1 µm
D
***
Speed ± SD (µm/s)
+ KIF13B
+ KIF5B
4X-KO
E
1
Kymograph
Single Frame
0.0 s
1.0 s
2.0 s
3.0 s
4.0 s
5.0 s
BFP-Rab6
KIF5B-GFP
mCherry-KIF13B
Rab6 KIF5B KIF13B
6 s
1 µm
1 µm
2
Kymograph
0.0 s
0.5 s
1.0 s
1.5 s
2.0 s
2.5 s
1 µm
6 s
1 µm
F
KIF5B-GFP
mCherry-KIF13B
KIF5B KIF13B
4X-KO / kymograph
2 s
2 µm
G
***
****
****
Speed ± SD (µm/s)
+ KIF13B
+ KIF5B
+ KIF13B + KIF5B
4X-KO

Figure 4 - KIF5B and KIF13B colocalize on moving vesicles
(A) Live TIRFM imaging of 4X-KO cells expressing either KIF5B-560-GFP alone or mCherry-Rab6A together with the full-length (FL) KIF5B-GFP or GFP-KIF13B. A single frame and a maximum intensity projection of a KIF5B-560-GFP movie is shown on the left, and single frames illustrating the localization of KIF5B-FL-GFP and GFP-KIF13B-FL on mCherry-Rab6A-labeled vesicles is shown on the right. Insets show enlargement of boxed areas. **(B)** Histograms showing the frequency distributions of the average intensity of the indicated kinesin constructs in 4X-KO cells; for KIF5B-FL-GFP and GFP-KIF13B-FL, only the signal colocalizing with Rab6 vesicles were quantified. n=660 in 17 cells, 320 in 24 cells and 495 in 19 cells in 2 independent experiments (KIF5B-560) and 3 independent experiments (KIF5B-FL and KIF13B-FL). Dashed lines mark intensity

Figure 4 (continued) of 1, 2, 3, 4 and 5 kinesin molecules estimated from the average value of KIF5B-560 distribution. **(C-D)** 4X-KO HeLa cells expressing mCherry-Rab6A together with GFP-KIF13B-FL or KIF5B-FL-GFP were imaged using TIRFM. Kymographs illustrating the movement of Rab6 vesicles positive for KIF13B or KIF5B were drawn and used to manually measure the velocity of each motor. n=30 and 28 cells in three independent experiments. Mann-Whitney *U* test: ***p<0.001. **(E)** Live confocal imaging of 4X-KO cells co-expressing TagBFP-Rab6, full-length KIF5B-GFP and full-length mCherry-KIF13B. Kymographs of two different moving vesicles and corresponding consecutive single frames (1 and 2) are shown to illustrate the simultaneous localization of KIF5B-GFP and mCherry-KIF13B on moving TagBFP-Rab6-positive vesicles. **(F)** A kymograph illustrating the movement of a particle co-labeled with KIF5B-GFP and mCherry-KIF13B and expressed in a 4X-KO HeLa cell. **(G)** Automated analysis of speeds of Rab6 vesicles colocalized with indicated full length kinesins in 4X-KO HeLa cells expressing either KIF5B-GFP and mCherry-KIF13B alone, or the condition where two kinesins colocalize together. Same data and analysis as in Figure 5G,H. Dots show average speed per cell, bars represent mean and SD. n=82, 79 and 89 cells, same as in Figure 5G,H. Mann-Whitney *U* test: ****p<0.0001; ***p=0.0006.

on Rab6 vesicle is lower than that of KIF13B. However, it is likely that in the endogenous situation the KIF13B abundance is low and the KIF13B binding sites are not saturated. This would explain why overexpressed but not endogenous KIF13B can rescue Rab6 vesicle motility in the absence of KIF5B. This would also explain why Rab6 vesicle speed distributions in KIF5B-KO cells and 4X-KO cells rescued with KIF13B differ: in 4X-KO cells rescued with KIF13B this motor predominates, while in KIF5B-KO cells, the population of vesicles moving with the speed characteristic of KIF13B is relatively small, whereas the other residual movements in these cells are driven by even faster motors such as dynein (Figure 3C,D, Figure 3 – figure supplement 1C).

Finally, we co-expressed KIF5B-GFP and mCherry-KIF13B together and found that they could be present simultaneously on the same Rab6-positive vesicle (Figure 4E,F). We developed an algorithm to automatically detect movements of two colocalized markers (see next section and Materials and Methods) and used it to measure vesicle speeds. In cells where the two kinesins were expressed separately, this analysis showed that KIF5B-GFP and mCherry-Rab6A-positive vesicles moved slower than the GFP-KIF13B-positive ones, whereas in co-expressing cells, the particles that contained both motors had speeds that were intermediate between those of KIF5B and KIF13B (Figure. 4F,G), in agreement with the data on the recruitment of these two motors to peroxisomes (Figure 3H).

KIF5B and KIF13B are differently distributed on moving Rab6 vesicles

We next set out to test whether the distribution of the motors on moving cargo correlates with the movement direction and therefore can be used to infer motor activity. We reasoned that the motors linked to the lipid bilayer will redistribute to the front of the vesicle if they are pulling it, will localize at the rear of the vesicle if they generate a hindering force or will display no shift if they are not engaged. We co-expressed GFP-KIF13B or KIF5B-GFP together with mCherry-Rab6A in 4X-KO HeLa cells and imaged vesicle motility using TIRFM (Figure 5A,B). PAUF-mRFP, in combination with GFP-Rab6A, was used as a control of localization of a vesicle marker lacking motor activity. The positions of the centers of two fluorescent signals on each vesicle were determined with sub-pixel localization precision using 2D Gaussian fitting. The alignment of the two fluorescent channels and the sub-pixel correction of chromatic aberrations were performed using a calibration photomask (Figure 5 – figure supplement 1A). Vesicle and motor trajectories (Figure 5C) were separated into phases of directed and random movement (Figure 5D,E), and only the periods of colocalized directional runs were used for further analysis. To describe the relative positions of the fluorescent markers during movement, we determined the projection of the vector l be-

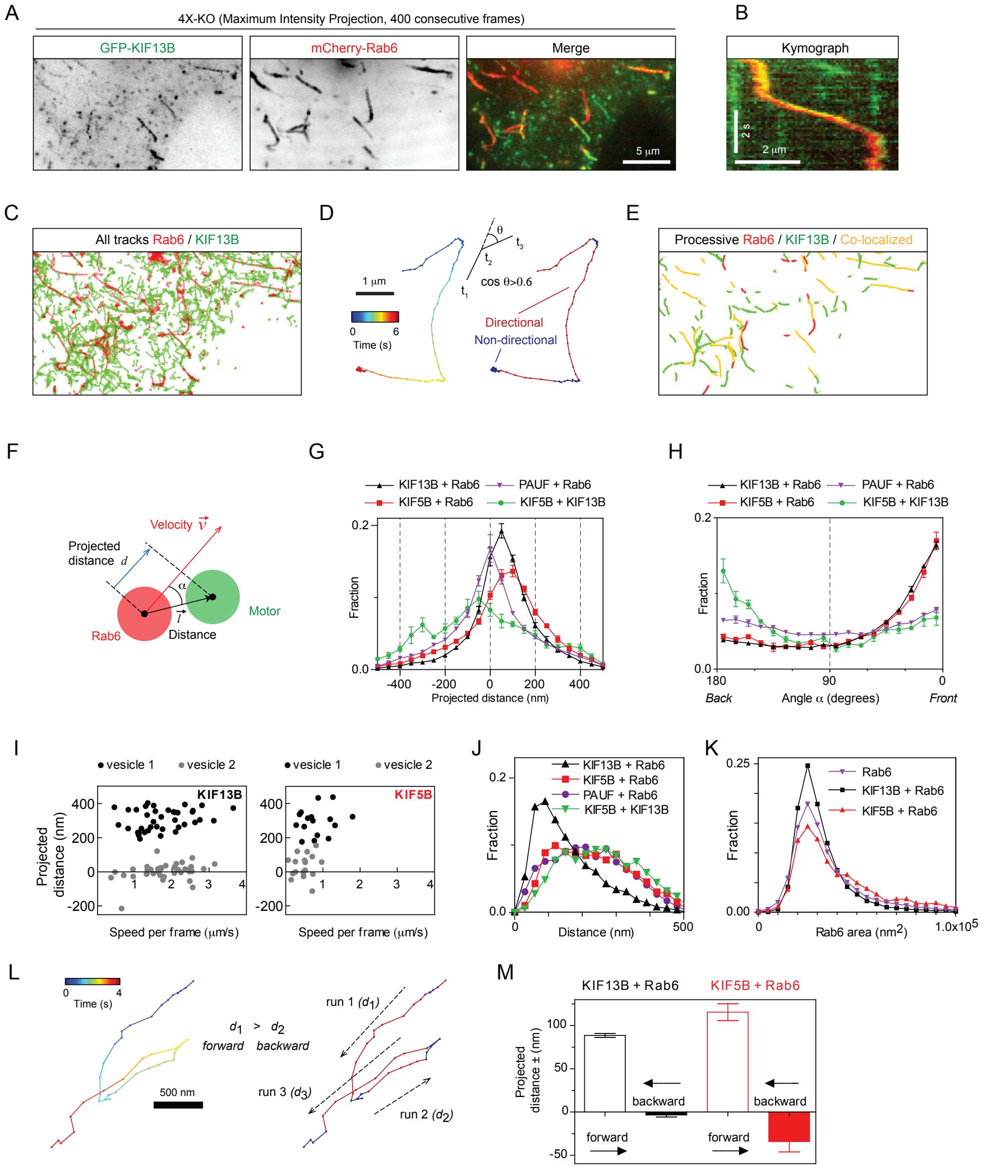

Figure 5 - Kinesins exhibit distinct distributions on Rab6 vesicles
(A) A representative example of maximum intensity projection (400 consecutive frames, 100 ms interval) of 4X-KO HeLa cells expressing mCherry-Rab6A and GFP-KIF13B to visualize events of Rab6-vesicle movement. Chromatic aberration of the red channel (mCherry-Rab6A) was corrected based on calibration, as illustrated in Figure 5 – figure supplement 1A. **(B)** A kymograph from the movie shown in (A) illustrating the movement of a mCherry-Rab6A-labeled vesicle positive for GFP-KIF13B. **(C)** Automatically extracted trajectories of mCherry-Rab6A- and GFP-KIF13B-positive particles (detected independently) from the movie shown in (A). **(D)** Segmentation of trajectories into periods of random and directed motion. (Left) An example of Rab6 vesicle trajectory with color-coded time. (Middle) Definition of directional movements: Movement was classified as directional when a cosine of the angle θ between two consecutive velocity vectors (t3-t2 and t2-t1) was larger than 0.6. (Right) Final segmentation result with directional (red) and random (blue) periods of

Figure 5 (continued) movement. **(E)** Directional segments of the tracks shown in (C), with colocalizing tracks labeled in yellow. **(F)** Schematics of the parameters used to characterize the distribution of two markers on the same vesicle. The projected distance d is calculated as a projection of distance between the centers of motor and cargo fluorescent signals (l) onto the axis defined by the instant velocity vector (v) of the cargo. The angle α is defined as the angle between the distance and velocity vectors. **(G,H)** The averaged histograms of the instantaneous projected distance (G) and the angle α (H) for GFP-KIF13B (black), KIF5B-GFP (red) with respect to FKBP-mCherry-Rab6A, PAUF-mRFP with respect to GFP-Rab6A (purple) and for KIF5B-GFP with respect to mCherry-KIF13B (green). Each dot and bar represent the average and SEM over several independent experiments, each including 8-20 cells. KIF13B (N=6 independent experiments, 82 cells, 11333 runs, 55129 time points), KIF5B (N=6, 79 cells, 2826 runs, 10023 time points), KIF5B and KIF13B (N=7, 89 cells, 1558 runs, 4371 time points) and PAUF (N=2, 20 cells, 5807 runs, 21359 time points). **(I)** Plots of projected distance between Rab6A and KIF13B (left) or KIF5B (right) signals against speed for four different vesicles/runs (two different vesicles with distinct maximum projected distances, likely reflecting different vesicle sizes, are shown for each kinesin). **(J,K)** Histograms of the distance between the indicated markers (J) and Rab6A area (K) averaged per run and pooled together for all experiments. Same statistics as in (G,H). **(L)** Extraction of opposite polarity runs from Rab6 vesicle trajectories. On the left, an example of a trajectory with color coded time; on the right, the same trajectory where the color denotes movement characteristics, directed (red) or random (blue). For each processive segment (run) the average direction of the velocity vector (dashed arrows) and average projected distance value (di) are calculated. Within one trajectory, the algorithm searches for all possible pair combination and keeps only those where the average movement direction is opposite. Within each pair a run with the higher average projected displacement is assigned to be the "forward" run and the other one the "backward" run. **(M)** Instantaneous (per frame) projected displacements for pairs of opposite runs, average ± SEM for the denoted conditions. The data are the same as in (G-K); for KIF13B, 664 opposite run pairs found, 3262 forward and 3122 backward time points; for KIF5B, 83 run pairs, 289 forward and 274 backward time points.

tween the two signals on the axis defined by vesicle's velocity vector and termed it projected distance d (Figure 5F). This value is positive if a marker is at the front of a moving vesicle and negative if it is at the back. As expected, the projected distances between Rab6 and PAUF were symmetrically distributed around zero (Figure 5G). In contrast, the projected distances between KIF5B or KIF13B and Rab6 were strongly skewed towards positive values, with a median value of 76 and 56 nm, respectively (Figure 5G). The angles between the line connecting the centers of the two fluorescent signals (the distance vector) and the velocity vector (angle α, Figure 5F) were distributed randomly when the positions of Rab6 and PAUF were analyzed. In contrast, in the case of Rab6 and the two kinesins, the angles close to zero predominated, as can be expected if the kinesins were accumulating at the front of the moving vesicles (Figure 5H).

Analysis of individual vesicles showed that the maximal projected distance between Rab6 and KIF5B or KIF13B signals observed for a given vesicle varied from a few tens of nanometers to ~500 nm (Figure 5I), as expected given that vesicles can have different sizes. Since the average projected distances between KIF13B and Rab6 signals were smaller than those between KIF5B and Rab6 signals (Figure 5G), it appears that smaller vesicles are generated when the 4X-KO cells are rescued with KIF13B compared to KIF5B. This observation was confirmed when we measured absolute distances between Rab6 and other markers without projecting them on the velocity direction (Figure 5J).Importantly, vesicles detected by imaging PAUF and Rab6 , without overexpressing any motors, were in the same size range as those found in 4X-KO cells rescued with KIF5B, whereas vesicles in 4X-KO cells rescued with KIF13B were smaller (Figure 5J). In addition, more vesicles with larger areas were observed when 4X-KO cells were rescued with KIF5B compared to KIF13B (Figure 5K). These data suggest that KIF5B, which is normally the main motor transporting Rab6 vesicles, is important for controlling vesicle size, a function that cannot be compensated by KIF13B, possibly because it performs less well under hindering load (Arpag et al., 2019; Arpag et al., 2014). We could not detect any dependence of the distance between Rab6 and the kinesins on vesicle speed (Figure 5I; Figure 5 – figure supplement 1B).

Next, we compared the distribution of KIF5B-GFP and mCherry-KIF13B when they were colocalized on the same moving particle (Figure 5G,H, green line). Interestingly, in this situation, KIF5B was shifted to the rear compared to KIF13B, which would be consistent with the idea that KIF5B, which is slower and has a lower detachment probability under load (Arpag et al., 2019; Arpag et al., 2014), exerts a drag force, whereas the faster KIF13B accumulates at the front of the vesicle. This is consistent with the fact that the average speeds of particles bearing both motors are slower than those transported by kinesin KIF13B alone, but faster than those moved by KIF5B (Figure 4G).

As the large majority of Rab6 vesicles are transported towards cell periphery and thus MT plus ends, we assumed that most of the displacements we analyzed represent kinesin-driven runs. However, there is a small fraction of Rab6 vesicles that are transported to the MT minus-ends by dynein (Grigoriev et al., 2007; Matanis et al., 2002) and, therefore, we next analyzed in more detail the behavior of kinesins on vesicles moving in the minus-end direction. To identify such runs, we automatically selected trajectories where a vesicle underwent a clear and acute switch of direction, and split such tracks into pairs of runs (for example, run1 and run2 or run2 and run3) where average movement direction was opposite (Figure 5L and Methods). We then calculated the projected distance d between the kinesin and Rab6 signals for each directional run within the run pair. The run with the higher projected distance d was assigned as the forward run, and the other run as the backward run (Figure 5L,M). The projected distance between kinesins and Rab6 in the forward runs was positive, as expected, and similar to that observed in the full dataset shown in Figure 5G, where the tracks were not selected for the presence of opposite polarity runs. Interestingly, for the backward runs, the average displacement was close to zero for KIF13B (~ 3.5 nm) and was slightly negative (~ - 34.1 nm) for KIF5B (Figure 5M). These data suggest that when a vesicle switches to dynein-driven motility, KIF13B does not undergo any tug-of-war with dynein, whereas KIF5B might be exerting some hindering force. These data would be consistent with the observations that a kinesin-3 is readily detached under force while kinesin-1 is more resistant to force (Arpag et al., 2019; Arpag et al., 2014). Overall, our sub-pixel localization analysis suggests that both kinesins can actively engage on the vesicle when it moves towards MT plus end, but only KIF5B can oppose dynein.

Kinesin-driven Rab6 vesicle transport spatially regulates secretion in mammalian cells

We next analyzed the functional importance of kinesin-mediated transport for secretion in HeLa cells. Previous work showed that partial depletion of KIF5B did not have a major effect on the overall secretion of neuropeptide Y (NPY), a soluble cargo present in Rab6 vesicles (Grigoriev et al., 2007). Now that we have established a system (the 4X-KO line) where Rab6 vesicle motility was dramatically suppressed, we reassessed the impact of kinesin-based transport of post-Golgi vesicles on the secretion levels. We took advantage of the retention using selective hooks (RUSH) system (Boncompain et al., 2012) to synchronize secretion. The interaction of SBP-GFP-E-Cadherin with streptavidin-KDEL (Hook) allows for the retention of E-Cadherin-GFP at the ER and its subsequent release for transport towards to the Golgi apparatus and the plasma membrane upon biotin addition (Figure 6A). We performed the RUSH assay by overexpressing SBP-GFP-E-Cadherin and streptavidin-KDEL in control or 4X-KO HeLa cells, and induced secretion by adding biotin. We performed live imaging and observed similar E-Cadherin accumulation at the plasma membrane in both conditions (Figure 6B). To quantify this, we specifically labelled surface-exposed E-Cadherin using a primary GFP/secondary Alexa641-conjugated antibody pair and used flow cytometry to analyze the intensity of the surface staining of E-Cadherin (Alexa641) against its total expression (GFP) (Figure 6 – figure supplement 1). One hour after the addition of biotin, the surface staining of GFP in 4X-KO cells was similar to that in control cells (Figure 6C, Figure 6 – figure supplement 1). To confirm these results, we used a different version of the RUSH system and analyzed the synchronized secretion of soluble-GFP upon biotin addition (Figure 6A). Similarly, control or 4X-KO HeLa cells expressing soluble GFP-SBP and streptavidin-KDEL were treated with biotin and analyzed by flow cytometry. We did not observe any difference in the secretion of soluble GFP two hours after biotin addition (Figure 6D).

We also used TIRFM to investigate the spatial distribution of exocytosis sites using NPY-GFP, a soluble Rab6 vesicle cargo. Events of NPY-GFP exocytosis are characterized by a burst of fluorescence followed by rapid signal disappearance (Grigoriev et al., 2007) (Figure 6E). We did not observe significant differences in the number of exocytotic events in the 4X-KO compared to control cells (Figure 6F). However, whereas in control cells these events

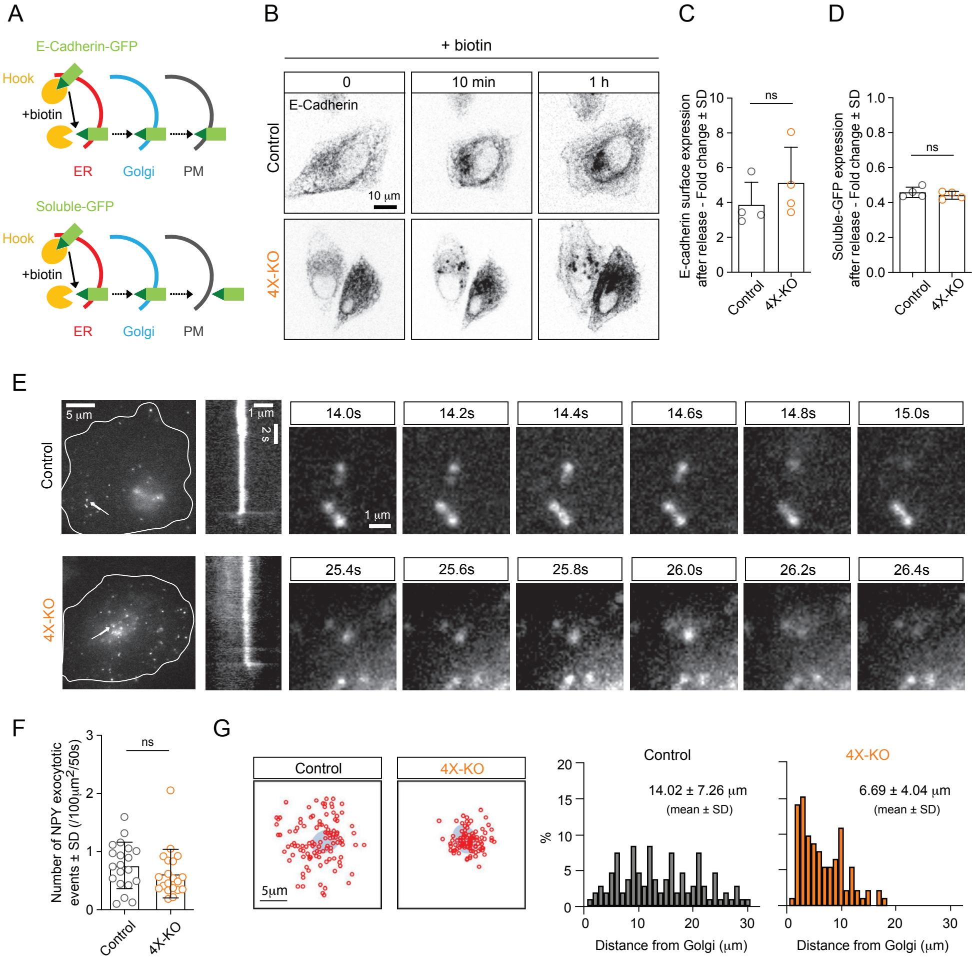

Figure 6 - Kinesins control the spatial distribution but not the efficiency of exocytosis

Figure 6 (continued) (A) A scheme depicting the RUSH assay used in this study. The interaction of SBP-GFP-E-Cadherin or soluble-GFP-SBP with streptavidin-KDEL (Hook) allows for the retention of E-Cadherin-GFP or soluble-GFP in the ER and their release for transport to the Golgi and the plasma membrane (PM) upon the addition of biotin, which competes with SBP for streptavidin binding. **(B,C)** RUSH assay was performed by expressing SBP-GFP-E-Cadherin and streptavidin-KDEL from the same bicistronic expression plasmid in control or 4X-KO HeLa cells. Cells were treated with biotin and imaged using time-lapse spinning-disk confocal microscopy (B, GFP-E-Cadherin signal) or subjected to surface staining with anti-GFP antibody to specifically label plasma membrane-exposed E-Cadherin followed by flow cytometry analysis (C). Plot shows the fold change of Alexa641 mean intensity (surface staining) in E-Cadherin expressing cells before and after biotin addition (1 h). n=4 independent experiments. Mann-Whitney *U* test: ns, no significant difference. **(D)** Control or 4X-KO HeLa cells expressing soluble-GFP-SBP and streptavidin-KDEL were treated with biotin and analyzed by flow cytometry to quantify the fold change of GFP mean intensity after biotin addition. n=4 independent experiments. Mann-Whitney *U* test: ns, no significant difference. **(E,F)** TIRF microscopy was used to visualize and analyze exocytosis events in control or 4X-KO HeLa cells expressing NPY-GFP. Exocytotic events, defined by a fast burst of fluorescence followed by the disappearance of the signal were visually identified, confirmed by kymograph analysis and counted per cell and per surface area and per duration of movie (50s) (F) n=20 cells in 2 independent experiments. Mann-Whitney *U* test: ns, no significant difference. Individual time frames in (E) illustrate representative exocytotic events; their localization is indicated by white arrows, and the corresponding kymographs are shown. **(G)** Analysis of the spatial distribution of the NPY exocytotic events shown in (E). Schematized positions of NPY exocytosis events (red circles) compared to the position of the Golgi (blue) are shown on the left (sum of 20 cells) and frequency distributions of the distance between the center of the Golgi and the sites of exocytosis in control and 4X-KO HeLa cells are shown on the right. n=109 and 93 tracks from 20 cells in 2 independent experiments.

were distributed along the entire radius of the cell, with many events at the cell periphery, in 4X-KO cells exocytotic events were restricted to the vicinity of the Golgi (Figure 6G). Kinesin-driven Rab6-vesicle transport is thus not essential for secretion efficiency, but it is required for the correct spatial distribution of exocytotic events.

Combination of KIF5B and KIF13B allows Rab6 vesicles to reach growing MT plus ends

Next, we set out to investigate the spatial regulation of the activity of the kinesins associated with Rab6 vesicles. Previous work has shown that KIF5B depends on the members of MAP7 family for its activation (Hooikaas et al., 2019; Metzger et al., 2012; Monroy et al., 2018; Pan et al., 2019), while kinesin-3 is inhibited by MAP7 (Monroy et al., 2018; Monroy et al., 2020). We used a previously described MAP7-KO HeLa cell line either alone or in combination with siRNAs against MAP7D1 and MAP7D3 to inhibit the expression of all three MAP7 homologues expressed in HeLa cells (Hooikaas et al., 2019) (Figure 7A). The number of Rab6 vesicle runs was not significantly affected in MAP7-KO cells, but it was significantly reduced in cells lacking all MAP7 proteins (Figure 7B,C). These results are similar to those observed in KIF5B-KO cells (Figure 2C,D). The speed of Rab6 vesicle movement was similar in control and MAP7-KO cells, but increased in cells lacking all MAP7 proteins (Figure 7D), consistent with the results obtained in KIF5B-KO cells (Figure 3A-D; Figure 3 – figure supplement 1B,C).

Simultaneous labeling of MTs with antibodies against α-tubulin and MAP7, MAP7D1 or MAP7D3 showed that the MAP7/tubulin intensity ratio decreases along the cell radius (Figure 8A). We reasoned that MAP7 enrichment may contribute to the activation of KIF5B in the central part of the cell, and, given the fact that KIF5B is a slower motor compared to KIF13B, this would result in slower velocity of Rab6 vesicle transport close to the Golgi compared to the cell periphery. Indeed, the increase of Rab6 vesicle velocity observed

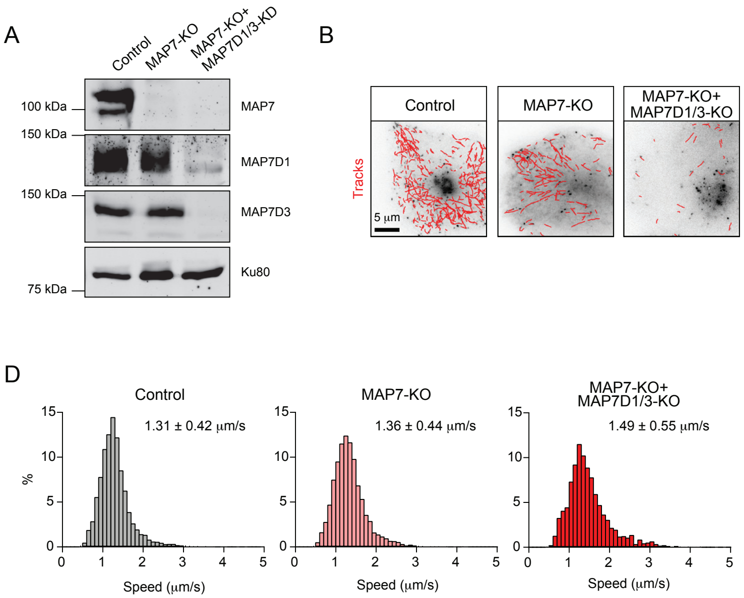

Figure 7 - MAP7 family proteins are required for the transport of Rab6 vesicles
(A) Western blot analysis of the extracts of control or MAP7 knockout (MAP7-KO) HeLa cells or MAP7-KO cells transfected with siRNAs against MAPD1 and MAP7D3 (MAP7-KO+MAP7D1/3-KO) with the indicated antibodies. **(B-D)** GFP-Rab6A was expressed and imaged using TIRFM in Hela cells described in (A). Automatic tracking using the SOS/MTrackJ plugin (500 consecutive frames, 100 ms interval) of the Rab6A signal (B), number of Rab6 vesicle runs per cell, n=20 cells in 2 experiment in each condition (C) and the frequency distributions of Rab6 vesicle speeds after automatic tracking annotated with the mean ± SD (D) are shown. n=5038, 4056 and 2366 tracks from 20 cells in 2 independent experiments. Mann-Whitney *U* test: ***p=0.0002, ns, no significant difference.

in cells lacking MAP7 proteins was more pronounced in the center of the cell compared to the cell periphery (Figure 8B). Furthermore, the absence of KIF13B, the faster motor, led to a decrease in Rab6 vesicle speed at the cell margin (Figure 8B), where the contribution of this motor would be expected to be more substantial.

The gradient of MAP7 protein distribution along the cell radius could be caused by MT dynamics: freshly polymerized MT segments are enriched at the cell periphery, and they can be expected to be less populated by MAP7 proteins if MAP7 binding to MTs is relatively slow. Indeed, live cell imaging showed that MAP7 displays a delay in binding to freshly grown, EB3-positive MT ends (Figure 8C,D). Also KIF5B followed this localization pattern: the dimeric motor fragment KIF5B-560 was significantly less abundant on EB3-positive MT ends compared to older, EB3-negative MT lattices (Figure 8E,F). In contrast, the motor-domain containing fragment of KIF13B, KIF13B-380, was enriched at the growing MT ends (Figure 8G,H). Based on these results, we hypothesized that in the absence of KIF13B, Rab6 vesicles will be less efficient in reaching the newly grown, EB3 positive MT ends and found that this was indeed the case (Figure 8I,J). This effect was obvious in KIF13B mixed KO but was less apparent in the clonal KIF13B cell lines, possibly because some compensatory changes have occurred during clone selection. Altogether, our results suggest that the combined action of KIF5B and KIF13B allows Rab6 vesicles to efficiently navigate different MT populations. MAP7 proteins contribute to the spatial regulation of exocytotic vesicle transport by promoting the activation of KIF5B and possibly by inhibiting KIF13B on older MTs.

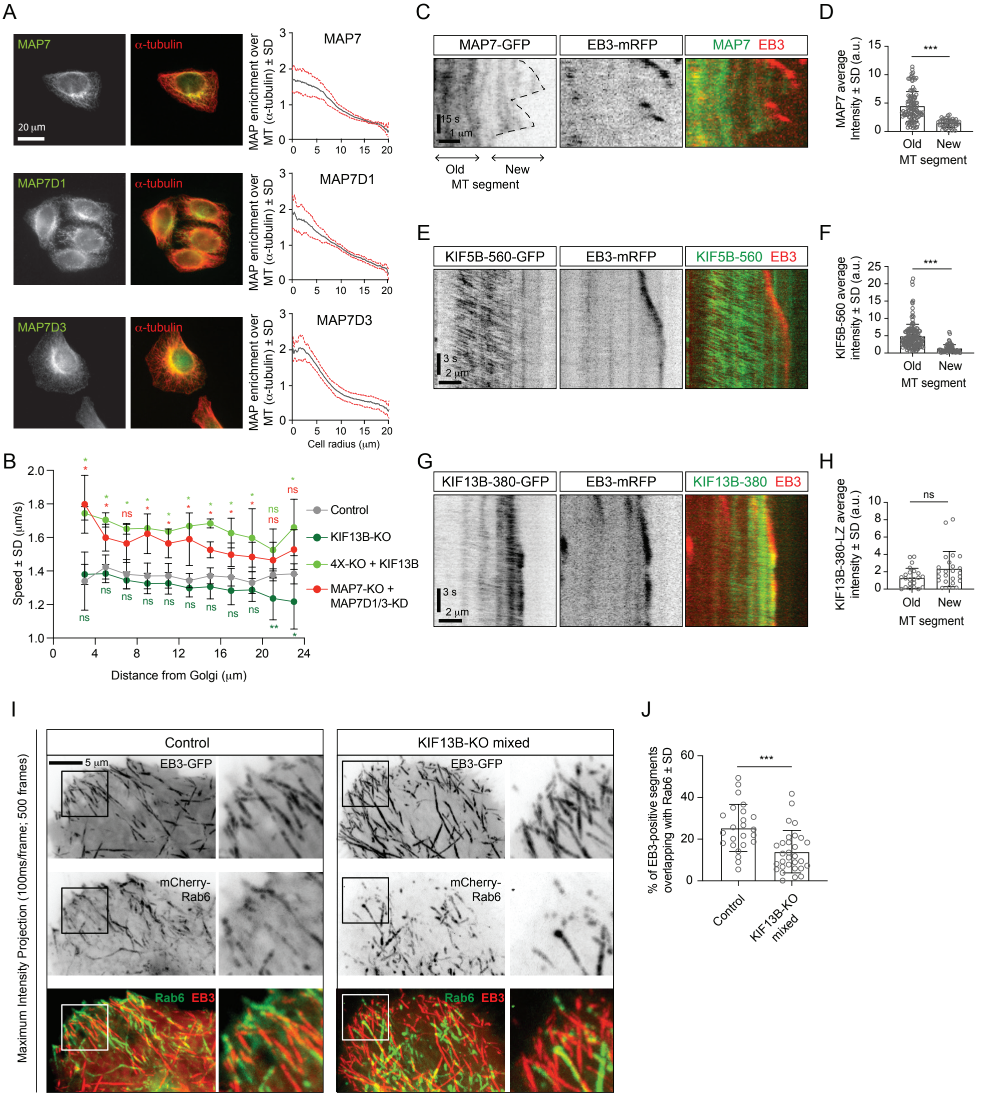

Figure 8 - KIF13B promotes Rab6 vesicle transport to freshly polymerized MT ends
(A) Staining of HeLa cells for endogenous MAP7, MAP7D1 or MAP7D3 together with α-tubulin and quantification of the relative enrichment of MAP7 signal intensity over the tubulin signal calculated and plotted against the distance from the cell center. n= 50, 48 and 42 cells, respectively, from 4 independent experiments. **(B)** Automatic tracking of GFP-Rab6A or mCherry-Rab6A labeled vesicles was performed on data obtained by TIRFM imaging in control, KIF13B-KO or MAP7-KO+MAP7D1/3-KD HeLa cells. Tracking results were analyzed using the SAID plugin of MTrackJ as described in the Methods to extract the velocity of the Rab6 runs in relation to their distance from the Golgi. n= 49, 47, 30 and 40 cells, respectively, in 5, 5, 3 and 4 independent experiments. Mann-Whitney *U* test: **p=0.0079, *p<0.032, ns, no significant difference. **(C,**

E, G) Kymographs illustrating the dynamics of a MT labeled with EB3-mRFP together with MAP7-GFP (C), KIF5B-560-GFP (E) or KIF13B-380-LZ-GFP (G) imaged using TIRFM. **(D, F, H)** Quantification of the average intensity of MAP7-GFP (D), KIF5B-560-GFP (F) and KIF13B-380-LZ-GFP (H) on old (further than 3 μm from plus end) and new (within 2 μm from plus end) MT segments visualized with EB3-mRFP (mean ± SD). D: n=109 (14 cells in 2 independent experiments) and n=47 (14 cells in 2 experiments). F: n=115 (19 cells in 2 independent experiments) and n=71 (19 cells in 2 experiments). H: n=24 (15 cells in 3 experiment) and n=24 (15 cells in 3 experiment). Mann-Whitney *U* test: ***p<0.0001, ns, no significant difference. **(I)** Maximum intensity projections (500 consecutive frames, 100 ms interval) of control or KIF13B-KO mixed HeLa cells expressing mCherry-Rab6A and EB3-GFP. Magnified views of the boxed areas are shown on the right. Colors in the merged images were inverted for display purposes. **(J)** Quantification of the percentage of EB3-GFP-positive MT segments colocalizing with mCherry-Rab6A vesicles. Measuring has been performed in MetaMorph software using Measure Co-localization option on Threshold images. n=24 and 30 cells, respectively, in 3 independent experiments. Mann-Whitney *U* test: ***p<0.0003.

Discussion

In this study, we have dissected kinesin-driven transport of Rab6-positive secretory carriers and the behavior of kinesins on these carriers. We showed that in HeLa cells, kinesin-1 KIF5B and kinesin-3 KIF13B are the main motors driving secretory vesicle motility. Rab6 vesicle transport was profoundly perturbed in a knockout cell line (4X-KO) lacking KIF5B, KIF13B, KIF1B and KIF1C and could be restored by re-expression of KIF5B and KIF13B but not KIF1B or KIF1C. KIF5B is the predominant motor driving Rab6 vesicle motility in HeLa cells: its knockout impairs vesicle movement much stronger than that of KIF13B, and the average speed of Rab6 vesicle movement in control cells is more similar to that of KIF5B than of KIF13B. This is likely due to the relatively low abundance of KIF13B in HeLa cells, because when overexpressed, KIF13B alone can restore Rab6 vesicle motility, in line with the previous studies showing that KIF13B and its *Drosophila* counterpart, Kinesin-73, are super-processive kinesins that can drive long-distance cargo transport (Huckaba et al., 2011; Siddiqui and Straube, 2017; Soppina et al., 2014). Efficient rescue of Rab6 vesicle movement with KIF13B in 4X-KO cells suggests that defective motility of Rab6 vesicles is due to the lack of motors attached to these vesicles rather than indirect effects caused the lack of KIF5B and its impact on MTs or other organelles.

Rab6 represents a robust marker of a broad variety of post-Golgi carriers (Fourriere et al., 2019; Grigoriev et al., 2007). Such vesicles are likely to be heterogeneous, and the composition of motors controlling their motility is expected to be cell type-specific. Indeed, our previous work established the involvement of KIF1A/B/C family in the transport of Rab6-positive carriers in neurons and Vero cells (Gumy et al., 2017; Schlager et al., 2010). Kinesin recruitment to the vesicles depends on the expression of specific adaptor proteins. KIF5B was recently shown to be bound to different membranes including Rab6 vesicles by the Dopey1-Mon2 complex, which functions as a lipid-regulated cargo-adaptor (Mahajan et al., 2019). KIF1C was shown to interact with Rab6-positive membranes directly (Lee et al., 2015) and also by associating with a cell-specific adaptor protein BICDR-1, which is absent from HeLa cells (Schlager et al., 2010). How KIF13B is recruited to Rab6 vesicles is currently unclear. Interestingly, our experiments with overexpression of fluorescently tagged kinesins in 4X-KO cells indicate that the number of KIF5B binding sites on a Rab6 vesicle is more limited than that for KIF13B, suggesting that the two kinesins use different adaptors. It is possible that the adaptor complexes for KIF5B and KIF13B on Rab6 vesicles have some overlapping components, similar to lysosomes, where the BORC/Arl8 complex recruits KIF5B through the interaction with SKIP and KLC and binds to kinesin-3 KIF1A/B directly, through the interaction with the coiled-coil domains of the motors (Guardia et al., 2016). However, spatial segregation of KIF5B and KIF13B present on the same vesicles (see below) suggests that they are not part of the same molecular complex.

Performing rescue experiments in kinesin knockout cells allowed us to generate cells where all kinesins driving Rab6 vesicle transport were fluorescently labeled, thus enabling us to study their distribution on cargo. We found that when expressed separately in 4X-KO cells, both KIF5B and KIF13B localized at the front of moving vesicles; however, when the two motors were co-expressed, KIF5B tended to be positioned behind KIF13B on moving particles. This can be explained by the distinct speeds of kinesin-1 and kinesin-3, described in previous studies (Arpag et al., 2014; Guedes-Dias et al., 2019; Soppina et al., 2014) and confirmed here: KIF13B, being a faster motor, relocates to the front of the vesicle, while KIF5B, being slower, stays behind. The higher resistance of KIF5B to detachment under load, which is thought to be the main determinant of motor behavior in a mixture of motors (Arpag et al., 2014), also likely contributes to this distribution. The reported interaction between KIF5B and the dynein adaptor BICD2 (Grigoriev et al., 2007) or some additional interactions between KIF5B and the dynein-dynactin complex could in principle control the localization of this kinesin on the vesicle. Importantly, we find that KIF5B tends to move to the rear of the vesicle when it switches directions and is presumably driven to MT minus ends by cytoplasmic dynein. These data are incompatible with the idea that KIF5B and dynein are part of the same protein complexes on secretory vesicles. Our data further suggest that KIF5B, which is attached to the vesicles independently of dynein, is engaged when dynein is driving transport towards the minus ends, and this could also be explained by KIF5B's resistance to hindering load. Thus, unlike KIF13B, which detaches under hindering load, KIF5B can engage in a tug-of-war with the dynein motor.

The generation of 4X-KO cells also allowed us to critically test the functional importance of kinesin-mediated transport for constitutive secretion. In line with previous work showing that drug-mediated MT disassembly does not block post-Golgi trafficking (Fourriere et al., 2016; Hirschberg et al., 1998; Rindler et al., 1987; Rogalski et al., 1984; Van De Moortele et al., 1993), we found that the efficiency of secretion was normal is cells lacking four kinesins. Previous work suggested that kinesin-1 contributes to the generation of Rab6 vesicles by pulling membrane tubules before their fission from the Golgi apparatus (Miserey-Lenkei et al., 2010). While our data indicate that such contribution is not essential for the formation of secretory carriers, we did find that Rab6 vesicles generated in the presence of KIF13B alone were smaller than those formed when KIF5B was also expressed. As indicated above, KIF5B detaches less readily under load than KIF13B (Arpag et al., 2019; Arpag et al., 2014), and could be more efficient in pulling out a longer membrane tube before its fission.

An obvious function of kinesins in secretory vesicle transport, confirmed by our work, is the control of the spatial distribution of exocytosis events. In HeLa cells, Rab6 vesicles preferentially fuse with the plasma membrane at the cell periphery in the vicinity of focal adhesions (Fourriere et al., 2019; Grigoriev et al., 2007; Stehbens et al., 2014). Exocytosis preferentially occurs at the sites where dynamic MT plus ends are attached to the cell cortex by the complex of CLASPs, LL5β, KANK1 and ELKS, which together with MICAL3 regulates vesicle fusion (Grigoriev et al., 2011; Lansbergen et al., 2006). Such spatial organization can contribute to cell migration by directing secretion of new membrane and extracellular matrix proteins to the leading edge of the cell and also by controlling focal adhesion turnover (Schmoranzer et al., 2000; Stehbens et al., 2014).

Our data suggest that KIF13B, being a minor player in Rab6 vesicle transport in HeLa cells, likely due to its low abundance, nevertheless makes some contribution to the spatial organization of exocytosis by bringing the vesicles to the tips of dynamic MTs. Cargo unloading at dynamic MT ends could be a general property of kinesin-3 family members, as it was also recently proposed for KIF1A (Guedes-Dias et al., 2019). KIF5B, which strongly dominates Rab6 vesicle transport, is in contrast restricted to the older, more stable MT population (Cai et al., 2009; Guardia et al., 2016; Tas et al., 2017). The underlying mechanisms of kinesin-1 selectivity are complex, and might involve the ability of the motor to regulate the properties of the tracks on which it walks (Shima et al., 2018). Importantly, KIF5B shows a very strong dependence on MAP7 family members, which control both kinesin recruitment to the MT and its activation (Hooikaas et al., 2019; Metzger et al., 2012; Monroy et al., 2018; Pan et al., 2019). MAP7 and its homologues are more abundant on older MTs, apparently because of their slow association with growing MTs. In COS7 cells, where MTs are more dynamic than in HeLa cells studied here, overexpressed GFP-MAP7 was reported to form a sharp boundary along the MT shaft, associated with the end of the stable MT segment (Tymanskyj and Ma, 2019). It can be expected that in cells with highly dynamic MTs, Rab6 transport to MT plus ends will be more dependent on kinesin-3 family members.

To summarize, our work demonstrated how the cooperation of two different kinesins promotes efficient cargo transport along complex MT networks. Furthermore, our study shows that direct visualization of motors on moving cargo, which in future work could be extended to cargo adaptors, provides insight into the motor activity and can be used to study the relationships between different players during bi-directional multimotor MT-dependent transport.

Methods

Constructs, antibodies and reagents

GFP-Rab6A construct (Matanis et al., 2002), GFP-Eg5 (Jiang et al., 2012), pßactin-PEX3-mRFP and KIF5B(1-807)-GFP-FRB (Kapitein et al., 2010b), GFP-Rab11 (Hoogenraad et al., 2010), NPY-GFP (Schlager et al., 2010), KIF13B(1-444)-GFP-FRB (Lipka et al., 2016), KIF13A-GFP (Schou et al., 2017) and FKBP-mCherry-Rab6A (Schlager et al., 2014) were described previously. The addition of FKBP to the N-terminus of mCherry in the mCherry-Rab6 fusion had no detectable effect on the behavior of this marker (Schlager et al., 2014), and it is termed mCherry-Rab6A throughout the paper. GFP-KIF13B was a gift from Dr. Athar Chishti (University of Illinois College of Medicine, Chicago, USA) and used as a template for GFP-KIF13B deletion constructs prepared by PCR-based strategy. PCR products were subcloned in pEGFP expression vectors (Clontech). KIF13B was amplified by PCR from GFP-KIF13B and inserted into a Bio-mCherry-C1 vector to make mCherry-KIF13B. Expression constructs for KIF5B, KIF1B and KIF1C were obtained by inserting the corresponding human cDNA (image clone 8991997 and KIAA1448 and KIAA0706 cDNAs, a gift from Kazusa DNA Research Institute Foundation (Kikuno et al., 2004)) into pβactin-GFP vector (KIF5B) or pEGFP vector (Clontech) with excised GFP (KIF1B and KIF1C) by PCR-based strategies.

PAUF-mRFP (Wakana et al., 2012) was a gift from Dr. Vivek Malhotra (Centre for Genomic Regulation, Barcelona, Spain), TagRFP-T-Rab6A a gift from Dr. Yuko Mimori-Kiyosue (RIKEN Center for Developmental Biology, Japan) and streptavidin-KDEL-SBP-GFP-E-Cadherin and streptavidin-KDEL-solubleGFP-SBP (Boncompain et al., 2012) were a gift from Dr. Franck Perez (Institut Curie, Paris, France).

The following antibodies were used in this study: mouse monoclonal antibodies against Rab6 (Schiedel et al., 1995) and Ku80 (BD Biosciences, Cat#611360, RRID:AB_398882), mouse polyclonal antibody against MAP7 (Abnova, Cat#H00009053-B01P, RRID:AB_10714227), rabbit polyclonal antibodies against KIF1B (Bethyl, Cat#A301-055A, RRID:AB_2131416), KIF1C (Cytoskeleton, Cat# AKIN11-A, RRID:AB_10708792), KIF5B/UKHC (Santa Cruz Biothnology, Cat# SC28538, clone H50, RRID:AB_2280915), Eg5 (Abcam, Cat#ab61199, RRID:AB_941397), KLC-1 (Santa Cruz Biotechnology, Cat# sc25735, clone H75, RRID:AB_2280879), MAP7D1, (Atlas Antibodies, Cat# HPA028075, RRID:AB_10603778), MAP7D3 (Atlas Antibodies, Cat# HPA035598, RRID:AB_10671108) and GFP (Abcam, Cat# ab290, RRID:AB_303395), and rat monoclonal antibody against α-tubulin YL1/2 (Abcam, Cat#ab6160, RRID:AB_305328). The anti-KIF13B polyclonal antibody was produced by immunizing rabbits with a purified GST-KIF13B protein (amino acids 1096–1143) expressed in BL21 E. coli using the pGEX-5X-3 vector (GE Healthcare). The antiserum was affinity purified using the antigen coupled to Dyna M-280 Streptavidin beads (Life Technologies).

For immunofluorescence and flow cytometry experiments we used Alexa488-, Alexa568- and Alexa-641 conjugated goat secondary antibodies (Invitrogen/Molecular probes). For Western blotting we used IRDye 680LT and 800CW goat anti-mouse and anti-rabbit antibodies (Li-Cor Biosciences).

Thymidine and biotin were from Sigma-Aldrich and rapalog was from Clontech.

Cell culture and treatment

HeLa (Kyoto) and MRC5 cell lines were cultured in DMEM/Ham's F10 medium (50/50%) supplemented with 10% fetal calf serum, penicillin and streptomycin and were routinely checked for mycoplasma contamination (LT07-518 Mycoalert assay, Lonza).

Plasmid transfection was performed using FuGENE 6 (Promega) according to the manufacturers' protocol 24 hours before experiments whereas HiPerfect (Qiagen) reagent was used for transfecting 10 nM siRNA per target 72 hours before experiments. The siRNAs used in this study were synthesized by Sigma and were directed against the following sequences:

Control/Luciferase: 5'-CGTACGCGGAATACTTCGA-3'
Eg5: 5'-GAGCCCAGATCAACCTTTA-3'
MAP7D1: 5'-TCATGAAGAGGACTCGGAA-3'
MAP7D3: 5'-AACCTACATTCGTCTACTGAT-3'

For Eg5-related experiments, HeLa cells were treated with 2mM thymidine 12 hours after transfection (with control and Eg5 siRNA) until the end of the experiment.

HeLa knockout lines were generated using the CRISPR/Cas9 method (Ran et al., 2013) by transfecting pSpCas9-2A-Puro (Addgene) vectors containing the following targeting sequences for gRNAs:

KIF13B: 5'-TGCGGATACGACCCATGAAC-3'
KIF5B: 5'-CCGATCAAATGCATAAGGCT-3'
KIF1B: 5'-GCTGGTCTCTCGAGAATTGA-3'
KIF1C: 5'-GCTGGTCTCACGGGCGTTAA-3'
MAP7: 5'-CGCCCTGCCTCTGCAATTTC-3'

One day after transfection, cells were treated with 2 μg/ml puromycin for 2 days and allowed to recover for 5 days. Selected cells were then diluted in 96-wells plates for growing single cell colonies that were tested by Western blotting. Alternatively, the polyclonal population obtained right after puromycin selection and recovery was tested by Western blotting, aliquots were frozen and used within 2 months after thawing (KO mixed population).

For RUSH assays (Boncompain et al., 2012), 24 hours after transfection with Streptavidin-KDEL-SBP-GFP-E-Cadherin and Streptavidin-KDEL-solubleGFP-SBP, HeLa cells were treated with 40 μM biotin for synchronization of secretion before live imaging or flow cytometry analysis.

For inducible peroxisome trafficking assay (Kapitein et al., 2010b), MRC5 cells were treated with 100 nM rapalog for kinesin recruitment before live imaging, which was performed ~10-40 min later .

Western blotting

Extracts of HeLa cells were prepared in RIPA buffer (10 mM Tris-HCl pH 8, 140 mM NaCl, 1 mM EDTA, 1 mM EGTA, 1% Triton X-100, 0.1% SDS, protease inhibitor cocktail (Complete - Sigma)). SDS-PAGE and Western blot analysis were performed according to standard procedures and developed with the Odyssey Infrared Imaging system (Li-Cor Biosciences).

Immunofluorescence cell staining

HeLa cells were fixed in 4% paraformaldehyde for 10 min at room temperature or with 100% methanol for 10 min at -20°C for tubulin staining, permeabilized with 0.15% Triton X-100 in phosphate buffered saline (PBS) for 5 min, blocked in 2% bovine serum albumin/0.07% Tween 20 in PBS and sequentially incubated with primary and secondary antibodies in blocking buffer for 1 hour at room temperature. Cells were washed three times with 0.07% Tween 20 in PBS after each labeling step. Slides were then air-dried and mounted in Vectashield mounting medium, which in some cases was supplemented with DAPI (Vector laboratories).

Flow cytometry

After biotin treatment for the indicated time, HeLa cells were harvested and surface immunostaining was performed on ice. Cells were labeled with anti-GFP antibody for 45 min, fixed with 2% paraformaldehyde for 10 min, washed with PBS, incubated with Alexa641-conjugated secondary antibody, washed with PBS again and analyzed using a FACS Canto Flow Cytometry System (BD Biosciences). Viable cells were selected using FSC and SSC parameters, and signals for "cellular" GFP (intrinsic GFP signal) and "surface-expressed" GFP (from staining with the Alexa641-conjugated secondary antibodies) were collected per cell. Cells positive for E-cadherin expression were gated using the GFP channel and the geometric mean of the Alexa641 signal intensity was calculated for this population. This value was quantified before and 1 hour after biotin treatment and the fold change was calculated. The same procedure was applied to quantify the decrease in soluble GFP cellular content using the GFP signal without immunostaining.

Image acquisition

Images of fixed cells were collected with a wide-field fluorescence microscope Nikon Eclipse 80i equipped with C-HGFI Fiber Illuminator "Intensilight" (Nikon), Plan Apo VC 100x N.A. 1.40 oil objective (Nikon) and ET-DAPI (49000, Chroma), ET-GFP (49002, Chroma), ET-mCherry (49008, Chroma) and ET-GFP/mCherry (59022, Chroma) filters and a CoolSNAP HQ2 CCD camera (Photometrics) or with a confocal fluorescence microscope LSM 700 (Zeiss) equipped with a Plan-Apochromat 63x/1.40 (oil) objective (Zeiss).

For live cell imaging Total Internal Reflection Fluorescence microscopy (TIRFM) and Spinning Disc confocal fluorescent microscopy were used.

TIRFM was performed on an inverted research microscope Nikon Eclipse Ti-E (Nikon), equipped with the perfect focus system (Nikon), Nikon Apo TIRF 100x N.A. 1.49 oil objective (Nikon) and Nikon TIRF-E motorized TIRF illuminator modified by Roper Scientific France/PICT-IBiSA, Institut Curie (currently Gataca Systems). The system was also equipped with ASI motorized stage MS-2000-XY (ASI), Photometrics Evolve 512 EMCCD camera (Photometrics) and controlled by the MetaMorph 7.8 software (Molecular Devices). 491nm 100mW Calypso (Cobolt) and 561nm 100mW Jive (Cobolt) lasers were used as the light sources. We used ET-GFP filter set (49002, Chroma) for imaging of proteins tagged with GFP; ET-mCherry filter set (49008, Chroma) for imaging of proteins tagged with mCherry; for simultaneous imaging of green and red fluorescence we used ET-GFP/mCherry filter set (59022, Chroma) together with Optosplit III beamsplitter (Cairn Research Ltd, UK) equipped with double emission filter cube configured with ET525/50m, ET630/75m and T585LPXR (Chroma). 16-bit images were projected onto the EMCCD chip with intermediate lens 2.5X (Nikon C mount adapter 2.5X) at a magnification of 0.063 μm/pixel. To keep cells at 37°C we used stage top incubator (model INUBG2E-ZILCS, Tokai Hit).

Azimuthal spinning TIRFM was performed on an inverted research microscope Nikon Eclipse Ti-E (Nikon), equipped with the perfect focus system (Nikon), Nikon Apo TIRF 100x N.A. 1.49 oil objective (Nikon) and iLas2 system (Dual Laser illuminator for azimuthal spinning TIRF (or Hilo) illumination and Simultaneous Targeted Laser Action) from Roper Scientific (Evry, France; now Gataca Systems) with a custom modification for targeted Photoablation using a 532 nm pulsed laser. The system was also equipped with ASI motorized stage MS-2000-XY (ASI), Photometrics Evolve Delta 512 EMCCD camera (Photometrics) and controlled by the MetaMorph 7.8 software (Molecular Devices). Stradus 405 nm (100mW, Vortran), Stradus 488 nm (150 mW, Vortran) and OBIS 561 nm (100 mW, Coherent) lasers were used as the light sources. We used ET-GFP filter set (49002, Chroma) for imaging of proteins tagged with GFP; ET-mCherry filter set (49008, Chroma) for imaging of proteins tagged with mCherry; for simultaneous imaging of green and red fluorescence we used ET-GFP/mCherry filter set (59022, Chroma) together with Optosplit III beamsplitter (Cairn Research Ltd, UK) equipped with double emission filter cube configured with ET525/50m, ET630/75m and T585LPXR (Chroma). For simultaneous imaging of blue, green and red fluorescence we used ZT405/488/561/640rpc ZET405/488/561/635m filter set (TRF89901, Chroma) together with Optosplit III beamsplitter (Cairn Research Ltd, UK) equipped with triple emission filter cube configured with ET460/50m, ET525/50m, ET630/75m, T495LPXR and T585LPXR (Chroma). 16-bit images were projected onto the EMCCD chip with intermediate lens 2.5X (Nikon C mount adapter 2.5X) at a magnification of 0.065 μm/pixel. To keep cells at 37°C we used stage top incubator (model INUBG2E-ZILCS, Tokai Hit).

For time-lapse fluorescence imaging of GFP-E-Cadherin, images were collected with spinning disk confocal microscopy on inverted research microscope Nikon Eclipse Ti-E (Nikon), equipped with the perfect focus system (Nikon) Nikon Plan Apo 60x N.A. 1.40 oil objective (Nikon) and a spinning disk-based confocal scanner unit (CSU-X1-A1, Yokogawa). The system was also equipped with ASI motorized stage with the piezo plate MS-2000-XYZ (ASI), Photometrics Evolve Delta 512 EMCCD camera (Photometrics) and controlled by the MetaMorph 7.8 software (Molecular Devices). 491nm 100mW Calypso (Cobolt) laser was used as the light sources. We used ET-GFP filter set (49002, Chroma) for imaging of proteins tagged with GFP; 16-bit images were projected onto the EMCCD chip with intermediate lens 2.0X (Edmund Optics) at a magnification of 111 μm/pixel. To keep cells at 37°C we used stage top incubator (model INUBG2E-ZILCS, Tokai Hit).

Fluorescence Recovery After Photobleaching (FRAP) experiments have been performed on either TIRF or Spinning Disc microscopes, equipped with iLas or iLas2 platforms and using Targeted Laser Action options of iLas or iLas2 and controlled with iLas / iLas2 softwares (Roper Scientific, now Gataca Systems).

Image analysis

To prepare images for publication, we used ImageJ to perform adjustments of levels and contrast and generate maximum intensity projections. Two color-intensity profiles along a line were made using the 'plot profile' option in ImageJ for each channel.

For manual analysis, kymographs of Rab6 and kinesin tracks were made using MetaMorph 7.8 software (Kymograph option). Kymographs have been analyzed in MetaMorph software. Two parameters have been measured for the segments of kymograph representing particle displacements, the angle and the length, and these parameters were used to calculate the speed of movement in SigmaPlot software.

The distribution of MAP7 and α-tubulin signals along the cell radius was determined using the 'Radial Profile Angle' plugin of ImageJ with an integration angle of 45°. Each intensity profile was then normalized according to: (x-x_min)/(x_max-x_min) and the profile of the ratio between the normalized values for MAP7 and α-tubulin was calculated per cell.

For analyzing the distribution Rab11-positive endosomes, the ratio between the mean signal intensity in the perinuclear region (obtained by scaling-down the cell outline by 25%) and in the whole cell was calculated using maximum intensity projections over time of GFP-Rab11 signal and expressed in percent.

Kinesin-GFP fluorescence intensities were analyzed by measuring the mean GFP intensity in circles of 7 pixels in diameter centered on the GFP dots and correcting it for the mean intensity in circles of the same size positioned just next to the fluorescent spot. For full-length kinesins, only GFP spots colocalizing with Rab6 vesicles were selected.

The NPY exocytosis events were analyzed by visually inspecting TIRF imaging of NPY-GFP and looking for a fast burst of fluorescence followed by the disappearance of the signal and confirming it by kymograph analysis. The position of NPY exocytosis was determined by measuring the distance between the exocytosis spot and the center of the Golgi region (determined based on the morphology of NPY signal).

Automatic tracking of Rab6 vesicles

TIRFM images of Rab6 vesicles were analyzed using ImageJ software with the recently developed SOS plugin (Yao et al., 2017), where we combined 'SOS detector 3D module' as particle detector and 'SOS linker (NGMA) module' for particle linking. MTJ (MTrackJ) Simple Track Segment module was applied to the resulting tracks to find segments of directional movement (runs) inside each trajectory. For this analysis, only tracks of 20 or more frames were considered. A segment was assigned to be a directional run if the cosine of angle between all two consecutive velocity vectors was above 0.6 and it lasted more than 6 frames. If inside such a segment there were more than 3 consecutive displacements of one pixel or less per frame, at this point the segment was further split into two. Duration and length of each directional run was extracted and its speed was calculated using the complementary SAID plugin (Yao et al., 2017).

The resulting speeds were expressed in two ways: either the mean of the speed was calculated per cell or a frequency distribution of the speed of all individual runs was built.

The fitting of the distribution of Rab6 velocity with either one Gaussian or the sum of two Gaussian curves, as well as their comparison using extra sum-of-squares F test method were performed using GraphPad Prism5.

Analysis of kinesin distribution on moving vesicles

Detection. For simultaneous two-color imaging of vesicles labeled with Rab6, motor proteins and PAUF, we used OptoSplit III beamsplitter (Cairn Research Ltd, UK) equipped with double emission filter cube projecting two channels on the camera chip simultaneously. To account for chromatic aberrations of the objective, images of a calibration photomask with round 500 nm features positioned equidistantly at 2 μm distance (Compugraphics, UK) were acquired simultaneously in GFP and mCherry channels using transmitted bright-field illumination using the procedures described in (Aher et al., 2018; Maurer et al., 2014). Based on feature detections we made sub-pixel channel alignment and non-linear registration using B-spline transform implemented in our Detection of Molecules ImageJ plugin and described earlier (version 1.1.6, https://github.com/ekatrukha/DoM_Utrecht, (Chazeau et al., 2016)). The plugin provided sub-pixel localized coordinates of spots in the "green" channel and corrected for chromatic aberration coordinates of spots in the "red" channel.

Colocalization and tracking. To determine colocalization, for each time frame we imported "green" coordinates as frame 1 and "red" coordinates as frame 2 to Matlab (MathWorks, 2011b, Natick, 2011). We used SimpleTracker routine by Jean-Yves Tinevez (https://www.github.com/tinevez/simpletracker), implementing nearest neighbor search with a distance threshold of 8 pixels (0.52 μm) to assemble "short" two frame tracks. Linked detections were considered colocalized, and for each detection average x and y coordinates between two channels were calculated and stored. For each colocalization detection, we kept records of the original coordinates in each channel. On the next step, we used those averaged coordinates to assemble tracks of colocalized particles over the duration of the whole movie using the same SimpleTracker routine with a distance threshold of 10 pixels (0.65 μm) and the maximum number of gap closing frames equal to 5. From those tracks we extracted segments of persistent directional movement (runs) as described earlier (Katrukha et al., 2017). In short, for each track, an array of instant velocity vectors was generated as a difference between two positions of a vesicle in two consecutive frames divided by the time between frames. A cosine of the angle between two consecutive velocity vectors was used as a directional correlation measure. For every trajectory we filtered segments where the value of cosine was above defined threshold. To find runs we used the lower threshold value of 0.6, corresponding to an approximately 100° cone facing in the direction of movement. Only runs longer than 0.3 s and with displacement above 0.5 µm were considered. For the directional filtering of GFP-KIF13B/KIF5B-GFP and mCherry-Rab6A pairs, we used coordinates of mCherry-Rab6A. For PAUF-mRFP and GFP-Rab6A pair we used GFP-Rab6A, and for KIF5B-GFP and mCherry-KIF13B pair we used averaged coordinates. The projected distance was calculated as a dot product between the velocity vector and the vector from the cargo to the motor, divided by the length of the velocity vector.

Analysis of opposite polarity runs. For each directional movement segment with colocalizing signals of the two markers, we first calculated the average velocity vector vi, coordinates of the center of mass and the average value of the projected distance. For trajectories with more than one run we listed all possible different run pairs. For each pair we calculated the cosine between average velocity vectors. If the cosine value was below -0.6 (i.e. angle between the velocity vectors was larger than 125 degrees), we considered these runs to have opposite polarity. As an additional constraint, we only considered pairs where the distance between the centers of mass was smaller than 1 µm. The run with the larger average projected distance was considered the “forward” run, while the other one was assigned to be the “backward” run.

FRAP analysis

To measure the KIF13B turnover on moving Rab6 vesicles, GFP-Rab6A stably expressing cells were transfected with mCherry-KIF13B. We used Targeted Laser Action option of iLas platform (Roper Scientific, now Gataca Systems) installed on Nikon-based TIRF microscope. Using FRAP-on-Fly option of iLas software we photobleached mCherry-KIF13B with a 561 laser (100%) in a ~ 0.5 µm circle area surrounding a moving vesicle. Keeping unaffected green signal of GFP-Rab6A as a reference, we measured the intensities of both GFP-Rab6A and mCherry-KIF13B in ~ 0.5 µm circle area of a vesicle over time after bleaching. We subtracted the background (measured in the ~ 0.5 µm circle area next to the vesicle). Next, we normalized the measured intensities to the average of intensities at 10 time points before photobleaching. We then averaged all measured vesicles.

Statistics

Statistical analyses were performed using GraphPad Prism 5 and significance was assessed using Mann-Whitney *U* test. The sample size is indicated in the figure legends. All graphs show mean ±SD, except in Figure 1H that depicts mean ± SEM. No explicit power analysis was used to determine sample size and no masking was used for the analysis.

Data and software availability

All data that support the conclusions are available from the authors on request, and/or available in the manuscript itself. The custom software used for data analysis in this manuscript can be found at http://smal.ws/wp/software/sosplugin/ (Yao et al., 2017).

Acknowledgements

We thank V. Malhotra, F. Perez, Y. Mimori-Kiyosue, A. Chishti, F. Perez and Kazusa DNA Research Institute Foundation for the gift of materials, and the members of the Dumont, Chang and Wittman labs (Department of Cell and Tissue Biology, UCSF, USA) for helpful discussions.

This work was supported by the European Research Council (ERC) Synergy grant 609822 and Netherlands Organization for Scientific Research ALW Open Program grant 824.15.017 to A.A., the Marie Curie IEF fellowships to M.M., a Netherlands Organization for Scientific Research STW grant OTP13391 to E.M. and A.A., and a Fundação para a Ciência e a Tecnologia fellowship to A.S.-M., and the ERC Consolidator grant 819219 to L.C.K..

Author contributions

A.S.-M. and M.M. designed, conducted and analyzed the experiments. E.A.K. designed, conducted and analyzed Rab6-kinesin colocalization experiments and contributed to overall data analysis. I.G. designed and contributed to cellular experiments, TIRFM imaging, automated tracking and data analysis. C.A.E.P. and P.J.H. contributed to MAP7 experiment design and analysis. Y. Y., I.S. and E.M. contributed to the development of automated tracking and data analysis. Q. L. and L.B.P. contributed reagents. L.C.K. contributed to experiment planning and data analysis. A.A. supervised the study. A.A. and A.S.-M. wrote the manuscript with input from all authors.

Competing financial interests

The authors declare no competing financial interests.

References

Aher, A., M. Kok, A. Sharma, A. Rai, N. Olieric, R. Rodriguez-Garcia, E.A. Katrukha, T. Weinert, V. Olieric, L.C. Kapitein, M.O. Steinmetz, M. Dogterom, and A. Akhmanova. 2018. CLASP Suppresses Microtubule Catastrophes through a Single TOG Domain. Developmental cell. 46:40-58.

Akhmanova, A., and J.A. Hammer, 3rd. 2010. Linking molecular motors to membrane cargo. Current opinion in cell biology. 22:479-487.

Arpag, G., S.R. Norris, S.I. Mousavi, V. Soppina, K.J. Verhey, W.O. Hancock, and E. Tuzel. 2019. Motor Dynamics Underlying Cargo Transport by Pairs of Kinesin-1 and Kinesin-3 Motors. Biophys J. 116:1115-1126.

Arpag, G., S. Shastry, W.O. Hancock, and E. Tuzel. 2014. Transport by populations of fast and slow kinesins uncovers novel family-dependent motor characteristics important for in vivo function. Biophys J. 107:1896-1904.

Astanina, K., and R. Jacob. 2010. KIF5C, a kinesin motor involved in apical trafficking of MDCK cells. Cell Mol Life Sci. 67:1331-1342.

Boncompain, G., S. Divoux, N. Gareil, H. de Forges, A. Lescure, L. Latreche, V. Mercanti, F. Jollivet, G. Raposo, and F. Perez. 2012. Synchronization of secretory protein traffic in populations of cells. Nature methods. 9:493-498.

Burgo, A., V. Proux-Gillardeaux, E. Sotirakis, P. Bun, A. Casano, A. Verraes, R.K. Liem, E. Formstecher, M. Coppey-Moisan, and T. Galli. 2012. A molecular network for the transport of the TI-VAMP/VAMP7 vesicles from cell center to periphery. Developmental cell. 23:166-180.

Cai, D., D.P. McEwen, J.R. Martens, E. Meyhofer, and K.J. Verhey. 2009. Single molecule imaging reveals differences in microtubule track selection between Kinesin motors. PLoS Biol. 7:e1000216.

Chaudhary, A.R., H. Lu, E.B. Krementsova, C.S. Bookwalter, K.M. Trybus, and A.G. Hendricks. 2019. MAP7 regulates organelle transport by recruiting kinesin-1 to microtubules. J Biol Chem. 294:10160-10171.

Chazeau, A., E.A. Katrukha, C.C. Hoogenraad, and L.C. Kapitein. 2016. Studying neuronal microtubule organization and microtubule-associated proteins using single molecule localization microscopy. Methods in cell biology. 131:127-149.

Delevoye, C., S. Miserey-Lenkei, G. Montagnac, F. Gilles-Marsens, P. Paul-Gilloteaux, F. Giordano, F. Waharte, M.S. Marks, B. Goud, and G. Raposo. 2014. Recycling endosome tubule morphogenesis from sorting endosomes requires the kinesin motor KIF13A. Cell Rep. 6:445-454.

Ferenz, N.P., A. Gable, and P. Wadsworth. 2010. Mitotic functions of kinesin-5. Semin Cell Dev Biol. 21:255-259.

Fourriere, L., S. Divoux, M. Roceri, F. Perez, and G. Boncompain. 2016. Microtubule-independent secretion requires functional maturation of Golgi elements. Journal of cell science. 129:3238-3250.

Fourriere, L., A. Kasri, N. Gareil, S. Bardin, H. Bousquet, D. Pereira, F. Perez, B. Goud, G. Boncompain, and S. Miserey-Lenkei. 2019. RAB6 and microtubules restrict protein secretion to focal adhesions. J Cell Biol. 218:2215-2231.

Grigoriev, I., D. Splinter, N. Keijzer, P.S. Wulf, J. Demmers, T. Ohtsuka, M. Modesti, I.V. Maly, F. Grosveld, C.C. Hoogenraad, and A. Akhmanova. 2007. Rab6 regulates transport and targeting of exocytotic carriers. Developmental cell. 13:305-314.

Grigoriev, I., K.L. Yu, E. Martinez-Sanchez, A. Serra-Marques, I. Smal, E. Meijering, J. Demmers, J. Peranen, R.J. Pasterkamp, P. van der Sluijs, C.C. Hoogenraad, and A. Akhmanova. 2011. Rab6, Rab8, and MICAL3 Cooperate in Controlling Docking and Fusion of Exocytotic Carriers. Curr Biol. 21:967-974.

Gross, S.P. 2004. Hither and yon: a review of bi-directional microtubule-based transport. Phys Biol. 1:R1-11.

Guardia, C.M., G.G. Farias, R. Jia, J. Pu, and J.S. Bonifacino. 2016. BORC Functions Upstream of Kinesins 1 and 3 to Coordinate Regional Movement of Lysosomes along Different Microtubule Tracks. Cell Rep. 17:1950-1961.

Guedes-Dias, P., J.J. Nirschl, N. Abreu, M.K. Tokito, C. Janke, M.M. Magiera, and E.L.F. Holzbaur. 2019. Kinesin-3 Responds to Local Microtubule Dynamics to Target Synaptic Cargo Delivery to the Presynapse. Curr Biol. 29:268-282.

Gumy, L.F., E.A. Katrukha, I. Grigoriev, D. Jaarsma, L.C. Kapitein, A. Akhmanova, and C.C. Hoogenraad. 2017. MAP2 Defines a Pre-axonal Filtering Zone to Regulate KIF1- versus KIF5-Dependent Cargo Transport in Sensory Neurons. Neuron. 94:347-362.

Hancock, W.O. 2014. Bidirectional cargo transport: moving beyond tug of war. Nat Rev Mol Cell Biol. 15:615-628.

Hirokawa, N., and Y. Tanaka. 2015. Kinesin superfamily proteins (KIFs): Various functions and their relevance for important phenomena in life and diseases. Experimental cell research. 334:16-25.

Hirschberg, K., C.M. Miller, J. Ellenberg, J.F. Presley, E.D. Siggia, R.D. Phair, and J. Lippincott-Schwartz. 1998. Kinetic analysis of secretory protein traffic and characterization of golgi to plasma membrane transport intermediates in living cells. J Cell Biol. 143:1485-1503.

Hoogenraad, C.C., I. Popa, K. Futai, E. Sanchez-Martinez, P.S. Wulf, T. van Vlijmen, B.R. Dortland, V. Oorschot, R. Govers, M. Monti, A.J. Heck, M. Sheng, J. Klumperman, H. Rehmann, D. Jaarsma, L.C. Kapitein, and P. van der Sluijs. 2010. Neuron specific Rab4 effector GRASP-1 coordinates membrane specialization and maturation of recycling endosomes. PLoS Biol. 8:e1000283.

Hooikaas, P.J., M. Martin, T. Muhlethaler, G.J. Kuijntjes, C.A.E. Peeters, E.A. Katrukha, L. Ferrari, R. Stucchi, D.G.F. Verhagen, W.E. van Riel, I. Grigoriev, A.F.M. Altelaar, C.C. Hoogenraad, S.G.D. Rudiger, M.O. Steinmetz, L.C. Kapitein, and A. Akhmanova. 2019. MAP7 family proteins regulate kinesin-1 recruitment and activation. J Cell Biol. 218:1298-1318.

Huckaba, T.M., A. Gennerich, J.E. Wilhelm, A.H. Chishti, and R.D. Vale. 2011. Kinesin-73 is a processive motor that localizes to Rab5-containing organelles. J Biol Chem. 286:7457-7467.

Jasmin, B.J., B. Goud, G. Camus, and J. Cartaud. 1992. The low molecular weight guanosine triphosphate-binding protein Rab6p associates with distinct post-Golgi vesicles in Torpedo marmorata electrocytes. Neuroscience. 49:849-855.

Jaulin, F., X. Xue, E. Rodriguez-Boulan, and G. Kreitzer. 2007. Polarization-dependent selective transport to the apical membrane by KIF5B in MDCK cells. Developmental cell. 13:511-522.

Jiang, K., G. Toedt, S. Montenegro Gouveia, N.E. Davey, S. Hua, B. van der Vaart, I. Grigoriev, J. Larsen, L.B. Pedersen, K. Bezstarosti, M. Lince-Faria, J. Demmers, M.O. Steinmetz, T.J. Gibson, and A. Akhmanova. 2012. A Proteome-wide screen for mammalian SxIP motif-containing microtubule plus-end tracking proteins. Curr Biol. 22:1800-1807.

Kapitein, L.C., M.A. Schlager, M. Kuijpers, P.S. Wulf, M. van Spronsen, F.C. Mackintosh, and C.C. Hoogenraad. 2010a. Mixed Microtubules Steer Dynein-Driven Cargo Transport into Dendrites. Curr Biol. 20:290-299.

Kapitein, L.C., M.A. Schlager, W.A. van der Zwan, P.S. Wulf, N. Keijzer, and C.C. Hoogenraad. 2010b. Probing intracellular motor protein activity using an inducible cargo trafficking assay. Biophys J. 99:2143-2152.

Katrukha, E.A., M. Mikhaylova, H.X. van Brakel, P.M. van Bergen En Henegouwen, A. Akhmanova, C.C. Hoogenraad, and L.C. Kapitein. 2017. Probing cytoskeletal modulation of passive and active intracellular dynamics using nanobody-functionalized quantum dots. Nat Commun. 8:14772.

Kikuno, R., T. Nagase, M. Nakayama, H. Koga, N. Okazaki, D. Nakajima, and O. Ohara. 2004. HUGE: a database for human KIAA proteins, a 2004 update integrating HUGEppi and ROUGE. Nucleic Acids Res. 32:D502-504.

Konishi, Y., and M. Setou. 2009. Tubulin tyrosination navigates the kinesin-1 motor domain to axons. Nat Neurosci. 12:559-567.

Lansbergen, G., I. Grigoriev, Y. Mimori-Kiyosue, T. Ohtsuka, S. Higa, I. Kitajima, J. Demmers, N. Galjart, A.B. Houtsmuller, F. Grosveld, and A. Akhmanova. 2006. CLASPs attach microtubule plus ends to the cell cortex through a complex with LL5beta. Developmental cell. 11:21-32.

Lee, P.L., M.B. Ohlson, and S.R. Pfeffer. 2015. Rab6 regulation of the kinesin family KIF1C motor domain contributes to Golgi tethering. Elife. 4:eLife.06029.

Liao, G., and G.G. Gundersen. 1998. Kinesin is a candidate for cross-bridging microtubules and intermediate filaments. Selective binding of kinesin to detyrosinated tubulin and vimentin. J Biol Chem. 273:9797-9803.

Lipka, J., L.C. Kapitein, J. Jaworski, and C.C. Hoogenraad. 2016. Microtubule-binding protein doublecortin-like kinase 1 (DCLK1) guides kinesin-3-mediated cargo transport to dendrites. EMBO J. 35:302-318.

Liu, J.S., C.R. Schubert, X. Fu, F.J. Fourniol, J.K. Jaiswal, A. Houdusse, C.M. Stultz, C.A. Moores, and C.A. Walsh. 2012. Molecular basis for specific regulation of neuronal kinesin-3 motors by doublecortin family proteins. Molecular cell. 47:707-721.

Mahajan, D., H.C. Tie, B. Chen, and L. Lu. 2019. Dopey1-Mon2 complex binds to dual-lipids and recruits kinesin-1 for membrane trafficking. Nat Commun. 10:3218.

Matanis, T., A. Akhmanova, P. Wulf, E. Del Nery, T. Weide, T. Stepanova, N. Galjart, F. Grosveld, B. Goud, C.I. De Zeeuw, A. Barnekow, and C.C. Hoogenraad. 2002. Bicaudal-D regulates COPI-independent Golgi-ER transport by recruiting the dynein-dynactin motor complex. Nat Cell Biol. 4:986-992.

Maurer, S.P., N.I. Cade, G. Bohner, N. Gustafsson, E. Boutant, and T. Surrey. 2014. EB1 accelerates two conformational transitions important for microtubule maturation and dynamics. Curr Biol. 24:372-384.

Metivier, M., B.Y. Monroy, E. Gallaud, R. Caous, A. Pascal, L. Richard-Parpaillon, A. Guichet, K.M. Ori-McKenney, and R. Giet. 2019. Dual control of Kinesin-1 recruitment to microtubules by Ensconsin in Drosophila neuroblasts and oocytes. Development. 146:dev171579.

Metzger, T., V. Gache, M. Xu, B. Cadot, E.S. Folker, B.E. Richardson, E.R. Gomes, and M.K. Baylies. 2012. MAP and kinesin-dependent nuclear positioning is required for skeletal muscle function. Nature. 484:120-124.

Miserey-Lenkei, S., G. Chalancon, S. Bardin, E. Formstecher, B. Goud, and A. Echard. 2010. Rab and actomyosin-dependent fission of transport vesicles at the Golgi complex. Nat Cell Biol. 12:645-654.

Monroy, B.Y., D.L. Sawyer, B.E. Ackermann, M.M. Borden, T.C. Tan, and K.M. Ori-McKenney. 2018. Competition between microtubule-associated proteins directs motor transport. Nat Commun. 9:1487.

Monroy, B.Y., T.C. Tan, J.M. Oclaman, J.S. Han, S. Simo, S. Niwa, D.W. Nowakowski, R.J. McKenney, and K.M. Ori-McKenney. 2020. A Combinatorial MAP Code Dictates Polarized Microtubule Transport. Developmental cell:S1534-5807(1520)30061-30067.

Nakagawa, T., M. Setou, D. Seog, K. Ogasawara, N. Dohmae, K. Takio, and N. Hirokawa. 2000. A novel motor, KIF13A, transports mannose-6-phosphate receptor to plasma membrane through direct interaction with AP-1 complex. Cell. 103:569-581.

Norris, S.R., V. Soppina, A.S. Dizaji, K.I. Schimert, D. Sept, D. Cai, S. Sivaramakrishnan, and K.J. Verhey. 2014. A method for multiprotein assembly in cells reveals independent action of kinesins in complex. J Cell Biol. 207:393-406.

Pan, X., Y. Cao, R. Stucchi, P.J. Hooikaas, S. Portegies, L. Will, M. Martin, A. Akhmanova, M. Harterink, and C.C. Hoogenraad. 2019. MAP7D2 Localizes to the Proximal Axon and Locally Promotes Kinesin-1-Mediated Cargo Transport into the Axon. Cell Rep. 26:1988-1999.

Ran, F.A., P.D. Hsu, J. Wright, V. Agarwala, D.A. Scott, and F. Zhang. 2013. Genome engineering using the CRISPR-Cas9 system. Nat Protoc. 8:2281-2308.

Rindler, M.J., I.E. Ivanov, and D.D. Sabatini. 1987. Microtubule-acting drugs lead to the nonpolarized delivery of the influenza hemagglutinin to the cell surface of polarized Madin-Darby canine kidney cells. J Cell Biol. 104:231-241.

Rogalski, A.A., J.E. Bergmann, and S.J. Singer. 1984. Effect of microtubule assembly status on the intracellular processing and surface expression of an integral protein of the plasma membrane. J Cell Biol. 99:1101-1109.

Schiedel, A.C., A. Barnekow, and T. Mayer. 1995. Nucleotide induced conformation determines posttranslational isoprenylation of the ras related rab6 protein in insect cells. FEBS letters. 376:113-119.

Schlager, M.A., L.C. Kapitein, I. Grigoriev, G.M. Burzynski, P.S. Wulf, N. Keijzer, E. de Graaff, M. Fukuda, I.T. Shepherd, A. Akhmanova, and C.C. Hoogenraad. 2010. Pericentrosomal targeting of Rab6 secretory vesicles by Bicaudal-D-related protein 1 (BICDR-1) regulates neuritogenesis. EMBO J. 29:1637-1651.

Schlager, M.A., A. Serra-Marques, I. Grigoriev, L.F. Gumy, M. Esteves da Silva, P.S. Wulf, A. Akhmanova, and C.C. Hoogenraad. 2014. Bicaudal d family adaptor proteins control the velocity of Dynein-based movements. Cell Rep. 8:1248-1256.

Schmoranzer, J., M. Goulian, D. Axelrod, and S.M. Simon. 2000. Imaging constitutive exocytosis with total internal reflection fluorescence microscopy. J Cell Biol. 149:23-32.

Schou, K.B., J.B. Mogensen, S.K. Morthorst, B.S. Nielsen, A. Aleliunaite, A. Serra-Marques, N. Furstenberg, S. Saunier, A.A. Bizet, I.R. Veland, A. Akhmanova, S.T. Christensen, and L.B. Pedersen. 2017. KIF13B establishes a CAV1-enriched microdomain at the ciliary transition zone to promote Sonic hedgehog signalling. Nat Commun. 8:14177.

Shima, T., M. Morikawa, J. Kaneshiro, T. Kambara, S. Kamimura, T. Yagi, H. Iwamoto, S. Uemura, H. Shigematsu, M. Shirouzu, T. Ichimura, T.M. Watanabe, R. Nitta, Y. Okada, and N. Hirokawa. 2018. Kinesin-binding-triggered conformation switching of microtubules contributes to polarized transport. J Cell Biol. 217:4164-4183.

Short, B., C. Preisinger, J. Schaletzky, R. Kopajtich, and F.A. Barr. 2002. The Rab6 GTPase regulates recruitment of the dynactin complex to Golgi membranes. Curr Biol. 12:1792-1795.

Siddiqui, N., and A. Straube. 2017. Intracellular Cargo Transport by Kinesin-3 Motors. Biochemistry. Biokhimiia. 82:803-815.

Soppina, V., S.R. Norris, A.S. Dizaji, M. Kortus, S. Veatch, M. Peckham, and K.J. Verhey. 2014. Dimerization of mammalian kinesin-3 motors results in superprocessive motion. Proc Natl Acad Sci U S A. 111:5562-5567.

Splinter, D., D.S. Razafsky, M.A. Schlager, A. Serra-Marques, I. Grigoriev, J. Demmers, N. Keijzer, K. Jiang, I. Poser, A.A. Hyman, C.C. Hoogenraad, S.J. King, and A. Akhmanova. 2012. BICD2, dynactin, and LIS1 cooperate in regulating dynein recruitment to cellular structures. Molecular biology of the cell. 23:4226-4241.

Stehbens, S.J., M. Paszek, H. Pemble, A. Ettinger, S. Gierke, and T. Wittmann. 2014. CLASPs link focal-adhesion-associated microtubule capture to localized exocytosis and adhesion site turnover. Nat Cell Biol. 16:561-573.

Tanaka, Y., Y. Kanai, Y. Okada, S. Nonaka, S. Takeda, A. Harada, and N. Hirokawa. 1998. Targeted disruption of mouse conventional kinesin heavy chain, kif5B, results in abnormal perinuclear clustering of mitochondria. Cell. 93:1147-1158.

Tas, R.P., A. Chazeau, B.M.C. Cloin, M.L.A. Lambers, C.C. Hoogenraad, and L.C. Kapitein. 2017. Differentiation between Oppositely Oriented Microtubules Controls Polarized Neuronal Transport. Neuron. 96:1264-1271.

Telley, I.A., P. Bieling, and T. Surrey. 2009. Obstacles on the microtubule reduce the processivity of Kinesin-1 in a minimal in vitro system and in cell extract. Biophys J. 96:3341-3353.

Tymanskyj, S.R., and L. Ma. 2019. MAP7 Prevents Axonal Branch Retraction by Creating a Stable Microtubule Boundary to Rescue Polymerization. The Journal of neuroscience : the official journal of the Society for Neuroscience. 39:7118-7131.

Van De Moortele, S., R. Picart, A. Tixier-Vidal, and C. Tougard. 1993. Nocodazole and taxol affect subcellular compartments but not secretory activity of GH3B6 prolactin cells. Eur J Cell Biol. 60:217-227.

Wakana, Y., J. van Galen, F. Meissner, M. Scarpa, R.S. Polishchuk, M. Mann, and V. Malhotra. 2012. A new class of carriers that transport selective cargo from the trans Golgi network to the cell surface. EMBO J. 31:3976-3990.

Wakana, Y., J. Villeneuve, J. van Galen, D. Cruz-Garcia, M. Tagaya, and V. Malhotra. 2013. Kinesin-5/Eg5 is important for transport of CARTS from the trans-Golgi network to the cell surface. J Cell Biol. 202:241-250.

Wanschers, B., R. van de Vorstenbosch, M. Wijers, B. Wieringa, S.M. King, and J. Fransen. 2008. Rab6 family proteins interact with the dynein light chain protein DYNLRB1. Cell Motil Cytoskeleton. 65:183-196.

Welte, M.A. 2004. Bidirectional transport along microtubules. Curr Biol. 14:R525-537.

Yamada, K.H., Y. Nakajima, M. Geyer, K.K. Wary, M. Ushio-Fukai, Y. Komarova, and A.B. Malik. 2014. KIF13B regulates angiogenesis through Golgi to plasma membrane trafficking of VEGFR2. Journal of cell science. 127:4518-4530.

Yao, Y., I. Smal, I. Grigoriev, M. Martin, A. Akhmanova, and E. Meijering. 2017. Automated Analysis of Intracellular Dynamic Processes. Methods Mol Biol. 1563:209-228.

Zhou, J., J. Scherer, J. Yi, and R.B. Vallee. 2018. Role of kinesins in directed adenovirus transport and cytoplasmic exploration. PLoS Pathog. 14:e1007055.

Supplemental Figures

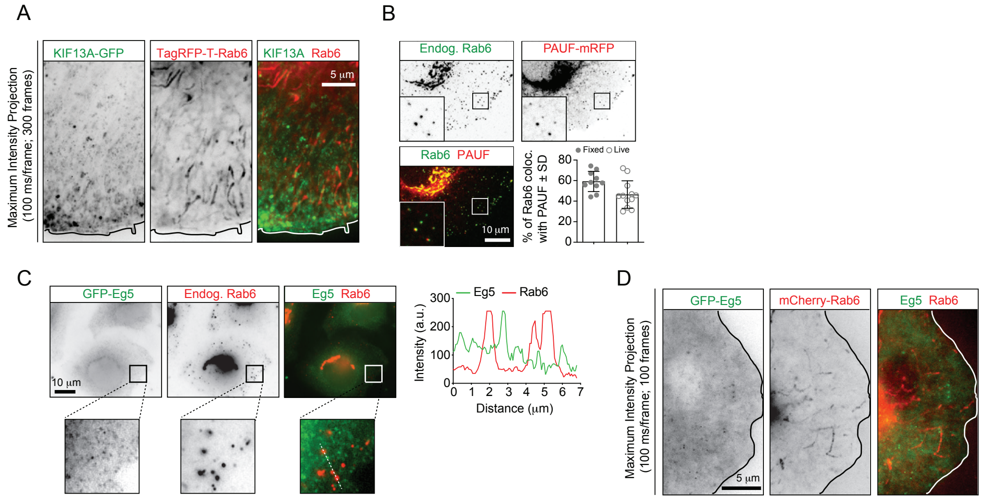
A
Maximum Intensity Projection (100 ms/frame; 300 frames)
KIF13A-GFP
TagRFP-T-Rab6
KIF13A Rab6
5 μm
B
Endog. Rab6
PAUF-mRFP
Rab6 PAUF
10 μm
% of Rab6 coloc. with PAUF ± SD
● Fixed ○ Live
0
20
40
60
80
C
GFP-Eg5
Endog. Rab6
Eg5 Rab6
10 μm
— Eg5 — Rab6
Intensity (a.u.)
0
100
200
300
0 1 2 3 4 5 6 7
Distance (μm)
D
Maximum Intensity Projection (100 ms/frame; 100 frames)
GFP-Eg5
mCherry-Rab6
Eg5 Rab6
5 μm

Figure 1 – figure supplement 1. Analysis of localization of different markers to Rab6 vesicles
(A) Maximum intensity projections (300 consecutive frames, 100 ms interval) of a HeLa cell expressing KIF13A-GFP and TagRFP-T-Rab6A imaged using TIRFM. **(B)** Imaging of HeLa cells expressing PAUF-mRFP and stained for endogenous Rab6. The insets correspond to magnified views of the boxed areas. The plot shows quantification of the percentage of PAUF-mRFP positive vesicles colocalizing with endogenous Rab6 or with GFP-Rab6A. n= 10 and 12 cells, respectively, in 2 independent experiments. **(C)** Imaging of a GFP-Eg5-expressing HeLa cell stained for Rab6. Panels at the bottom correspond to magnified views of the boxed areas. The graph displays the signal intensity profile of GFP-Eg5 (green) and Rab6 (red) along the white dashed line. **(D)** Maximum intensity projections (100 consecutive frames, 100 ms interval) of a HeLa cell expressing GFP-Eg5 and mCherry-Rab6A imaged using TIRFM.

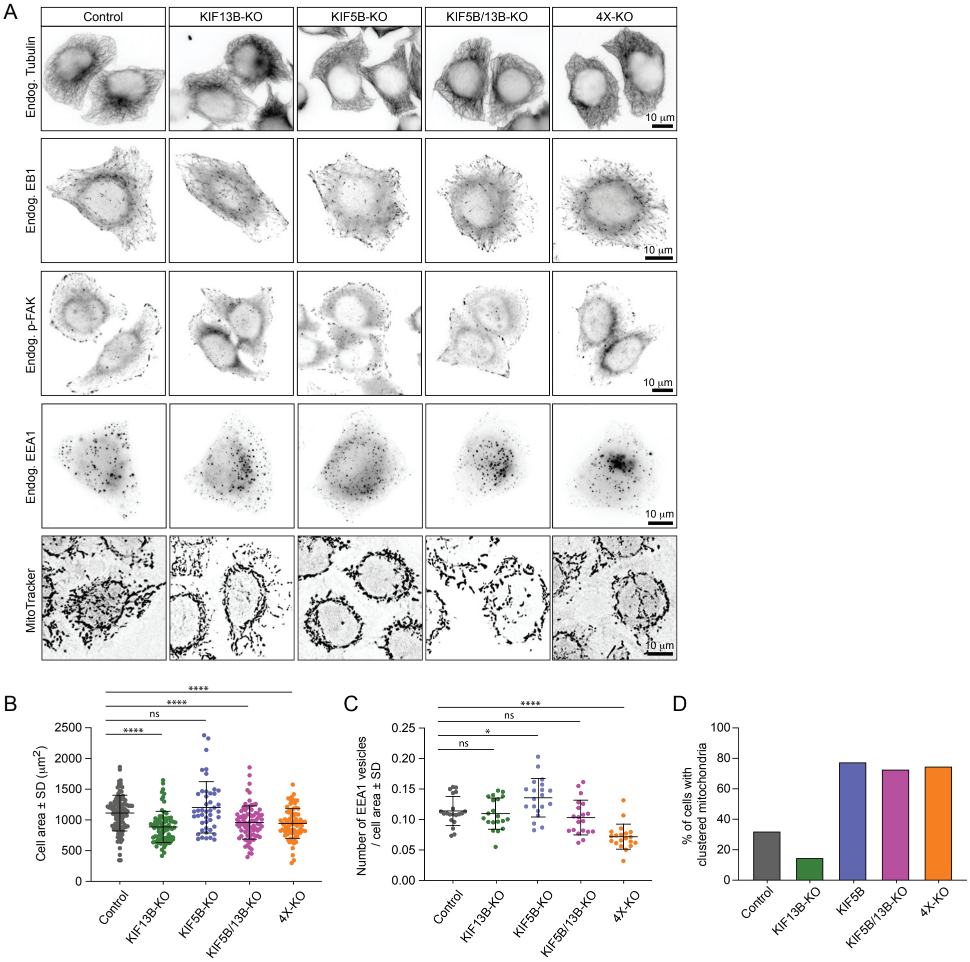
A
Control
KIF13B-KO
KIF5B-KO
KIF5B/13B-KO
4X-KO
Endog. Tubulin
Endog. EB1
Endog. p-FAK
Endog. EEA1
MitoTracker
10 µm
B
Cell area ± SD (µm^2)
2500
2000
1500
1000
500
0
****
****
ns
****
Control
KIF13B-KO
KIF5B-KO
KIF5B/13B-KO
4X-KO
C
Number of EEA1 vesicles / cell area ± SD
0.25
0.20
0.15
0.10
0.05
0.00
****
ns
*
ns
Control
KIF13B-KO
KIF5B-KO
KIF5B/13B-KO
4X-KO
D
% of cells with clustered mitochondria
100
80
60
40
20
0
Control
KIF13B-KO
KIF5B
KIF5B/13B-KO
4X-KO

Figure 2 – figure supplement 1: Validation of kinesin knockout cell lines
(A) Representative immunofluorescence images showing the effect of the knockout of different kinesins on the microtubule cytoskeleton, EB1-positive microtubule plus ends and distribution of focal adhesions, early endosomes and mitochondria. **(B-D)** Quantification of cell area (B), number of EEA1-positive vesicles (C) and percentage of cells of with clustered mitochondria (D) in the different knockout lines. B: n=104, 81, 45, 81 and 81 cells, respectively. C and D: n=20 in all conditions. Mann-Whitney *U* test: ****p<0.0001, ***p=0.0009, *p=0.02, ns, no significant difference.

A

	Control	KIF13B-KO		KIF13B-KO mixed	KIF5B-KO		KIF5B/KIF13B-KO		4X-KO	
	Mean ± SD	Clone	Mean ± SD	Mean ± SD	Clone	Mean ± SD	Clone	Mean ± SD	Clone	Mean ± SD
Number of Runs (100μ*m*^{2}/*50s*)	36.8 ± 19.5	1	35.4 ± 16.3	35.8 ± 19.4	1	10.1 ± 6.1	1	4.7 ± 2.6	1	3.5 ± 2.0
		2	25.5 ± 19.1		2	9.2 ± 4.2	2	8.2 ± 5.0	2	5.1 ± 3.6
Speed (μ*m/s*)	1.3 ± 0.4	1	1.3 ± 0.4	1.3 ± 0.4	1	1.9 ± 0.7	1	1.9 ± 0.8	1	2.0 ± 0.9
		2	1.3 ± 0.4		2	2.0 ± 0.7	2	1.9 ± 0.7	2	2.1 ± 0.9

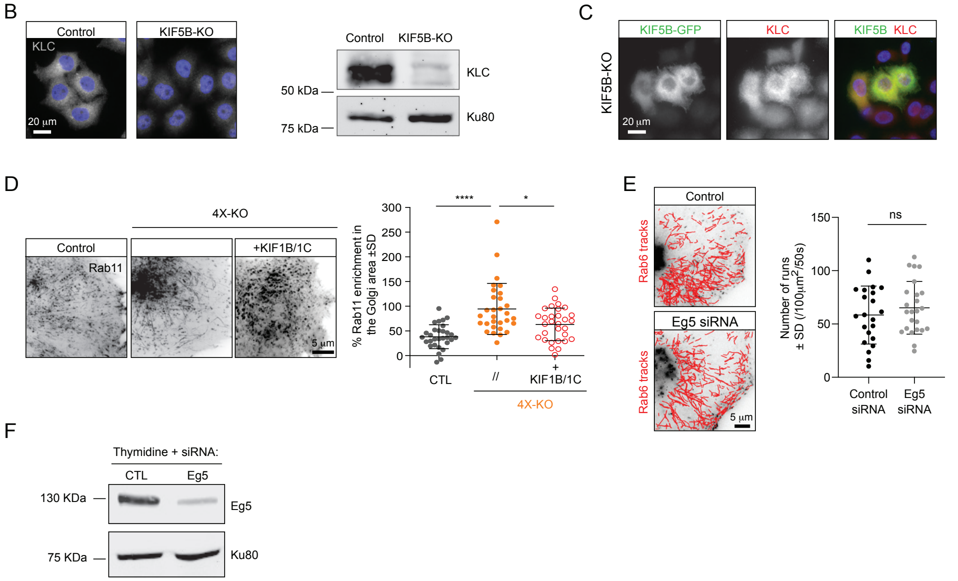

Figure 2 – figure supplement 2. Characterization of kinesin knockout cell lines
(A) Table summarizing parameters of Rab6 runs (number and speed) in 2 independent HeLa cell clones for each kinesin knockout. Data for the mixed population of KIF13B-KO cells is included for comparison. KIF13B-KO clone #1, KIF5B-KO clone #1, KIF5B/KIF13B-KO clone #1 and 4X-KO clone #2 have been used in latter experiments. **(B)** Impact of KIF5B-KO on the expression of kinesin light chain (KLC) assessed by immunostaining with KLC antibody and Western blotting. **(C)** Representative images of KIF5B-KO HeLa cells expressing a KIF5B-GFP construct and stained for KLC. **(D)** Analysis of Rab11 tracks in control and 4X-KO HeLa cells or 4X-KO cells expressing KIF1B and KIF1C. Maximum intensity projections (500 consecutive frames, 100 ms interval) of GFP-Rab11 were used to calculate the enrichment of Rab11 signal in the perinuclear region as described in Methods. n=30 cells for each condition in three independent experiments. Mann-Whitney *U* test: ****p<0.0001, *p=0.0225. **(E)** Automatic tracking with SOS/MTrackJ plugin of GFP-Rab6A labeled vesicles imaged by TIRFM and quantification of the number of Rab6 vesicle runs in HeLa cells transfected with control or Eg5 siRNA and treated with thymidine to prevent mitotic entry. Number of runs in control is a bit high compared to controls in Figure 2D, F. We attribute this difference to the transfection of control Luciferase siRNA and slightly different acquisition settings. n=22 and 24 cells in two independent experiments. Unpaired t-test: ns, no significant difference. **(F)** Western blot demonstrating Eg5 knockdown efficiency in HeLa cells using an antibody against Eg5.

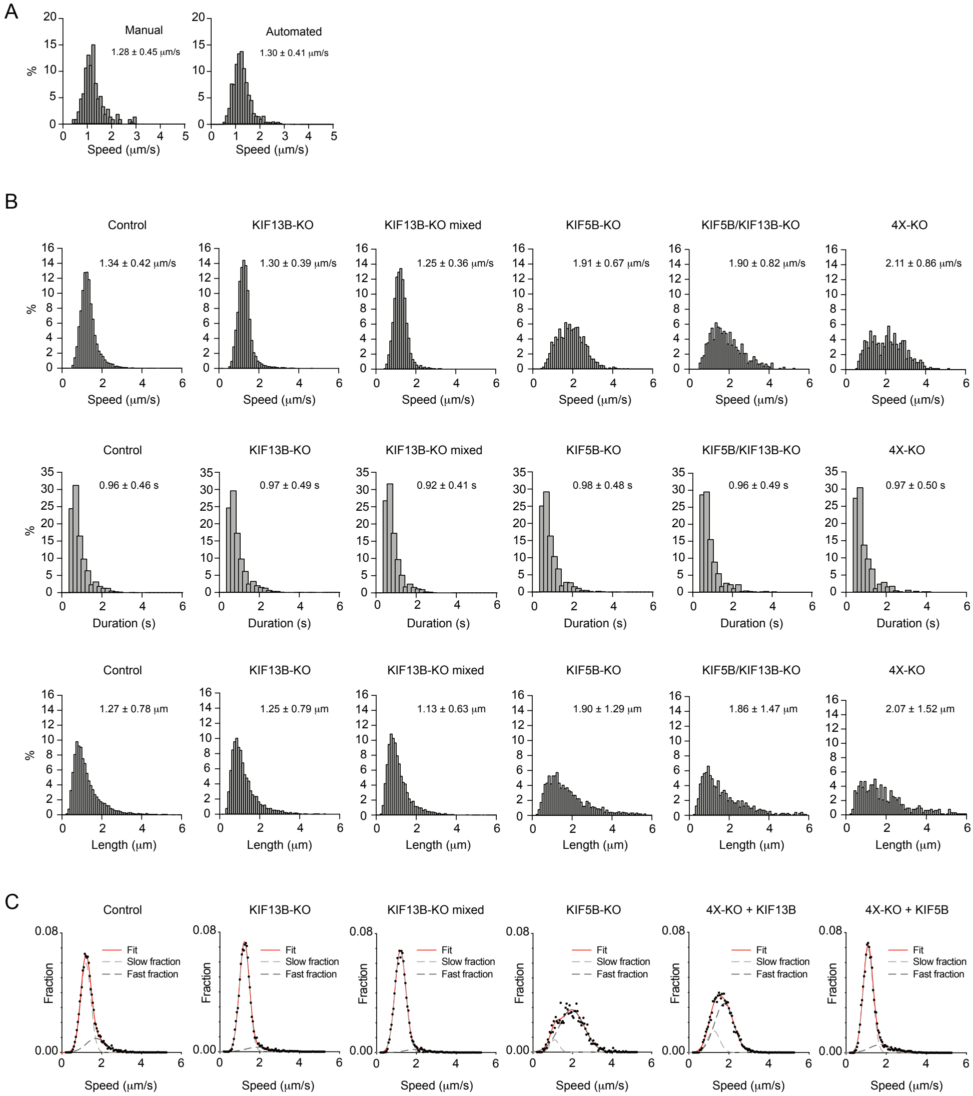

Figure 3 – figure supplement 1. Characterization of Rab6 vesicle motility in kinesin knockout lines **(A)** Analysis of Rab6 vesicle speeds per run using manual and automatic tracking in HeLa cells expressing mCherry-Rab6A and imaged using TIRF microscopy. The speed of Rab6 vesicles was calculated either manually based on kymograph analysis or automatically using the SOS/MTrackJ plugin, as shown in Figure 2B. Plots show frequency distribution histograms annotated with the mean ±SD. n=205 and 1213 tracks from the same 5 cells. **(B)** Histograms of the run speed, run duration and run length distributions of Rab6-positive vesicles in the indicated conditions. n=7099 in 29 cells, 6682 in 27 cells, 8192 in 30 cells, 1772 in 27 cells, 707 in 22 cells and 617 in 21 cells in 3 independent experiments each condition. **(C)** Distribution of Rab6 run speeds (dots) and their fit to sum of two Gaussians model (red solid line). Light and dark grey dashed lines represent "slow" and "fast" Gaussian components of fits. For all condition data represents 3 independent experiments. n=7099 runs in 29 cells, 6682 runs in 27 cells, 8192 runs in 30 cells, 1772 runs in 27 cells, 7616 runs in 30 cells and 5651 runs in 30 cells, respectively. For all conditions the sum of two Gaussian functions describes distributions better than one, according to extra sum-of-squares F test (all conditions p<0.0001). Same data as shown in Figure 3C,D.

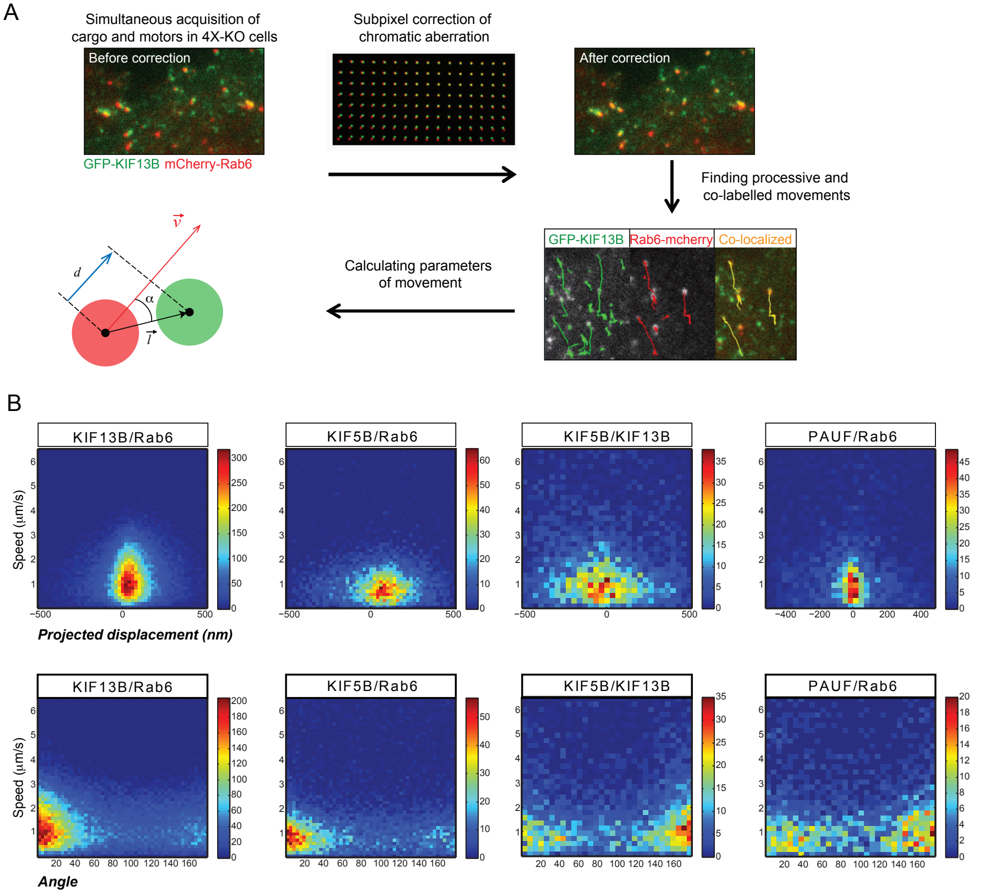

Figure 5 – figure supplement 1. Analysis of kinesin distribution on Rab6 vesicles
(A) Scheme depicting the workflow for subpixel localization of kinesins. Pairs of fluorescent markers were expressed in 4X-KO cells (for all kinesin constructs) or control HeLa cells (PAUF) and imaged using TIRFM. The acquired signals were corrected for chromatic aberrations using a grid of fluorescent beads as described in Methods, and vesicle runs were automatically tracked and processed. Processive runs with both markers present were used to calculate the parameters of movement: the distance vector between the center of the two fluorescent signals (mCherry and GFP spots) was projected onto the Rab6 instant velocity vector to determine the projected displacement (d) (blue segment). α is the angle between the distance and velocity vector. **(B)** The projected displacement and the angle as described in Figure 5 – figure supplement 1A plotted as heat maps against speed. Same data as shown in Figure 5G,H.

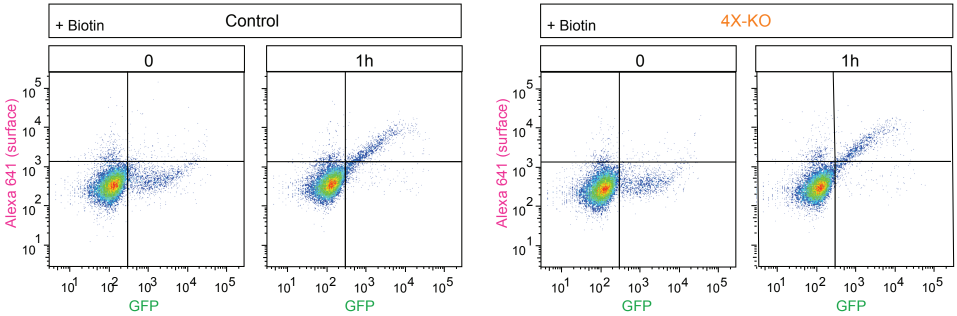

Figure 6 – figure supplement 1. Quantification of secretion using flow cytometry
RUSH assay was performed in control or 4X-KO HeLa cells expressing SBP-GFP-E-Cadherin and streptavidin-KDEL and analyzed by flow cytometry as shown in Figure 6C. The dot plots show the intensity of the signal of GFP-E-Cadherin (GFP) plotted against the signal of the surface staining (Alexa 641) per cell. Scale is logarithmic.

4

MAP7D2 contains a conserved motif that can tether clathrin to microtubules

Peter Jan Hooikaas[1], Lisa A.E. Catsburg[1], Stanley W. J. H. F. Fronik[1], Xingxiu Pan[1], Qingyang Liu[1,2], Babet van der Vaart[1], A.F. Maarten Altelaar[2], Casper. C. Hoogenraad[1], Martin Harterink[1], Stephen J. Royle[3], Harold D. MacGillavry[1] and Anna Akhmanova[1]

---

[1] Cell Biology, Neurobiology and Biophysics, Department of Biology, Faculty of Science, Utrecht University, Utrecht, Netherlands
[2] Biomolecular Mass Spectrometry and Proteomics, Bijvoet Center for Biomolecular Research, Utrecht Institute for Pharmaceutical Sciences and The Netherlands Proteomics Centre, Utrecht University, Utrecht, Netherlands
[3] Centre for Mechanochemical Cell Biology, Warwick Medical School, University of Warwick, Coventry, UK

Abstract

MAP7 proteins are essential co-factors of kinesin-1 that recruit and activate this motor to drive transport of various cargoes. Among the four mammalian MAP7 family members, MAP7D2 was shown to be specifically involved in promoting kinesin-1 activity in axons. Here, we identified novel binding partners of all MAP7 proteins and found that MAP7D2 can directly bind clathrin through a conserved clathrin-box motif. Overexpressed MAP7D2 can tether clathrin to microtubules and increase clathrin accumulation in the proximal axon of hippocampal neurons. Clathrin shows punctuated distribution in the proximal axon, and this localization is severely reduced by MAP7D2 depletion. We confirmed that there is a direct interaction between clathrin and the tail of kinesin-1, which might suggest that clathrin triskelia can be directly transported by this motor. We propose that future experiments should investigate a model where axonal MAP7D2 serves as a microtubule-bound loading factor for clathrin assemblies to promote their entry and transport in a kinesin-1-dependent manner.

Introduction

Neurons are highly polarized cells where the axon and the somatodendritic compartment have strikingly distinct organization and function. The axon initial segment (AIS) plays an essential role in keeping these two cellular compartments separated. Diffusion of membrane-bound receptors and lipids is limited by transmembrane proteins according to the "pickets and fences" model (Nakada et al., 2003). Here, the fences are formed by a dense actin- and protein-network inside of the AIS; the pickets are the AIS-transmembrane proteins that are part of, or linked to the inner-axon fences forming highly dense structures at the AIS membrane thereby impairing membrane diffusion (Leterrier, 2018). What happens to large soluble proteins and protein complexes that need to pass through the dense AIS fences is less well understood.

Past studies have used variously sized molecules such as bovine serum albumin (BSA), green fluorescent protein (GFP) and dextrans to study diffusional transport in axons. The use of non-specific proteins limited the possibility that their localization was determined by selective transport. Overexpressed GFP (~27 kDa), or a related derivative, is often used as a "fill" to label both axons and dendrites, where labelling is observed within a day after transfection. Macromolecules such as dextrans can be fluorescently labeled and micro-injected into the soma after which their diffusion into neurites can be traced over time. Small dextrans (~10 kDa) rapidly entered the axon within 30 min, whereas larger dextran assemblies (~70 kDa) and fluorescently labeled BSA (~90 kDa) were mostly excluded from the axon, but only when it contained an AIS structure (Song et al., 2009; Sun et al., 2014). These experiments suggest that axonal entry of larger proteins and protein assemblies is either slow or selective. Indeed, a growing body of evidence suggests that the axon contains multiple complementary mechanisms that determine the entry of molecules, vesicles and organelles (Gumy and Hoogenraad, 2018; Leterrier, 2018). After entry, soluble proteins often still have a long journey ahead of them since presynaptic structures can up to a meter away from the cell body in some type of neurons (Guedes-Dias and Holzbaur, 2019). Early studies that used pulse-chase radiolabeling have established that axonal transport includes two populations of cargoes, fast transport generally represented by membranous vesicles and slow transport responsible for axonal distribution of cytoplasmic proteins and protein assemblies (Black, 2016; Roy, 2020). More recent studies involving neurofilaments and clathrin have revealed that slow axonal transport comprises stationary phases alternated with phases of fast movement (Ganguly et al., 2020; Roy et al., 2000; Wang et al., 2000). These phases of fast movement were dependent on the presence of microtubules (MTs), which would suggest that these movements are motor dependent. This view is supported by velocity measurements of synapsin, CamKIIα and clathrin as these were observed to be in the range of kinesin- and/or dynein-dependent motility parameters (Ganguly et al., 2020; Scott et al., 2011; Tang et al., 2013). Normally, cytosolic clathrin consists of triskelia containing three copies of both clathrin heavy chain (CHC) and light chain (LC), with a total molecular weight of ~650 kDa. However, in axons clathrin forms larger protein assemblies named "clathrin-packets", which are associated with the plasma membrane but are rather found in close proximity to MTs and are presumably important for axonal transport of clathrin to synapses (Ganguly et al., 2020). This would suggest the presence of cytoskeletal linkers that may directly recruit clathrin to the MT network.

Apart from clathrin's well-described role in clathrin-mediated endocytosis, clathrin has a non-endocytic function during mitosis to stabilize kinetochore MTs. As a result, clathrin depletion leads to defects in spindle integrity and chromosome alignment during metaphase (Royle et al., 2005). MT binding of clathrin is mediated by a complex of Transforming Acidic Coiled-Coil-containing protein 3 (TACC3) and the MT polymerase ch-TOG that bind to each foot of the clathrin triskelion. Via this complex, clathrin can bind MTs and organize them into bundles (Royle, 2012). In addition, clathrin binds to GTSE1, an intrinsically disordered protein which in turn sequesters the MT depolymerizing kinesin MCAK to promote stability of spindle MTs (Rondelet et al., 2020). Despite, the direct role of clathrin to structurally support the mitotic spindle via specific adaptor proteins, no such MT-binding partners have been described in interphase cells.

Members of the MAP7 protein family are well-known activators of kinesin-1. In flies, MAP7 is represented by a single homologue (ensconsin) and it is firmly established that this MAP is essential for all kinesin-1 activity (Barlan et al., 2013; Metivier et al., 2019; Sung et al., 2008). Recent studies have shown that this is also true for mammalian MAP7 (Chaudhary et al., 2019; Metzger et al., 2012; Monroy et al., 2018; Tymanskyj et al., 2018); however, the protein family is more diverse in mammals and contains four homologues that display redundancy: MAP7, MAP7D1, MAP7D2 and MAP7D3 (Hooikaas et al., 2019; Pan et al., 2019; Serra-Marques et al., 2020). MAP7 family proteins have a similar structural organization with two conserved domains that are predicted to be helical (Luo et al., 2020; Sun et al., 2011). The N-terminal helical domain strongly binds to MTs, while the C-terminal domain, also referred to as the MAP7-homology domain, binds kinesin-1. In addition, it has been demonstrated that the binding affinities of these domains for both MTs and kinesin-1 can differ between MAP7 homologues (Hooikaas et al., 2019). In non-neuronal cells, MAP7 family proteins are represented by MAP7, MAP7D1 and MAP7D3 that act redundantly to activate kinesin-1. MAP7D2 is brain specific (Niida and Yachie, 2011) and is localized to the proximal part of the axon in hippocampal neurons where it is the sole MAP7 required for entry of kinesin-1-dependent cargoes (Pan et al., 2019). MAP7 and MAP7D1 are also expressed in neurons, but their localization seems to be more dominant in the somatodendritic compartment of hippocampal neurons (Pan et al., 2019), although it has also been reported that MAP7 and MAP7D1 are involved in axon development of other neuronal cell types (Koizumi et al., 2017; Tymanskyj and Ma, 2019; Tymanskyj et al., 2017; Tymanskyj et al., 2018). So far, there has been increasing understanding of how MAP7 family proteins regulate kinesin-1 activity, but the biochemical and functional differences between the four mammalian MAP7 family members are poorly understood. It is possible that such differences may offer opportunities for fine-tuning of kinesin-1 activity or enable the recruitment of specific protein partners for transport and other processes.

In this study, we screened for novel binding partners of all MAP7 family members and found clathrin as a unique interaction candidate for the neuron-specific MAP7D2. Overexpression of MAP7D2 induces strong recruitment of clathrin to MTs in both COS-7 cells and the proximal axon of hippocampal neurons. Binding to clathrin is dependent on the C-terminal tail of MAP7D2 which contains a conserved clathrin binding motif that has been well characterized for many other clathrin adaptors. Clathrin can also interact with kinesin-1, either directly or in a triple protein complex together with MAP7D2. Depletion of MAP7D2 reduces the number of clathrin assemblies in the proximal axon and this could be rescued by re-expression of full-length MAP7D2. Future experiments in neurons and the use of *in vitro* reconstitution assays with purified clathrin, kinesin-1 and MAP7D2 should clarify how the interplay between these proteins may be important for the entry and transport of clathrin into the axon.

Results

MAP7D2, but not the other mammalian MAP7 family members, can associate with clathrin
To identify novel binding partners of all mammalian MAP7 family members (Figure 1A), we performed pull down assays from HEK293T cells followed by mass spectrometry analysis and made a list of the Top 10 interactors after filtering (Figure 1B and S1A). As expected based on previous work (Hooikaas et al., 2019; Pan et al., 2019), we found kinesin-1 heavy and light chain proteins to interact with all MAP7 family proteins. In addition, several novel interaction candidates were found that bound to several MAP7 homologues such as Kinase D-interacting substrate of 220 kDa (KIDINS220), CEP55, Pericentrin and A-kinase anchor protein 9 (AKAP9) which are all involved MT-based processes. However, MAP7D2 showed unique interaction candidates such as clathrin heavy chain (CHC) and the associated light chains α and β. Surprisingly, also several neurofilament polypeptides were found (Figure 1B). We followed up on clathrin by performing pull down assays and immunofluorescence (IF) experiments and validated that MAP7D2, but not the other MAP7 proteins, binds CHC (Figure 1C, D). In agreement with these data, MAP7D2 efficiently recruited endogenous CHC to MTs when overexpressed at both low (decoration of single MTs) as well as high (dense MT bundling) levels (Figure 1D, S1B). In addition, we confirmed that this MT-associated CHC was still able to bind to LCα, required for triskelia formation, which suggests that MT-bound CHC is represented by triskelia (Figure S1C). Next, we investigated whether MAP7D2 could form a triple complex between CHC and kinesin-1 by performing a pull down assay with a truncated KIF5B mutant "K560" (aa 1-560) that is still able to move on MTs and bind MAP7 proteins. We found that K560 did not bind endogenous CHC by itself but could efficiently pull down CHC when full-length MAP7D2 was overexpressed, indicating that forming a triple complex is sterically possible (Figure 1E). Furthermore, we found that CHC could also directly bind, albeit weakly, to kinesin-1 via its tail domain (KIF5B aa 808-963) (Figure 1F). This interaction was also reported in a recent study describing a role of direct binding by the kinesin-1 KIF5B in the uncoating of clathrin-coated vesicles (Ni et al., 2018). Altogether, we have identified clathrin as a novel MAP7D2-specific interaction partner and showed that these proteins can form a triple complex together with kinesin-1.

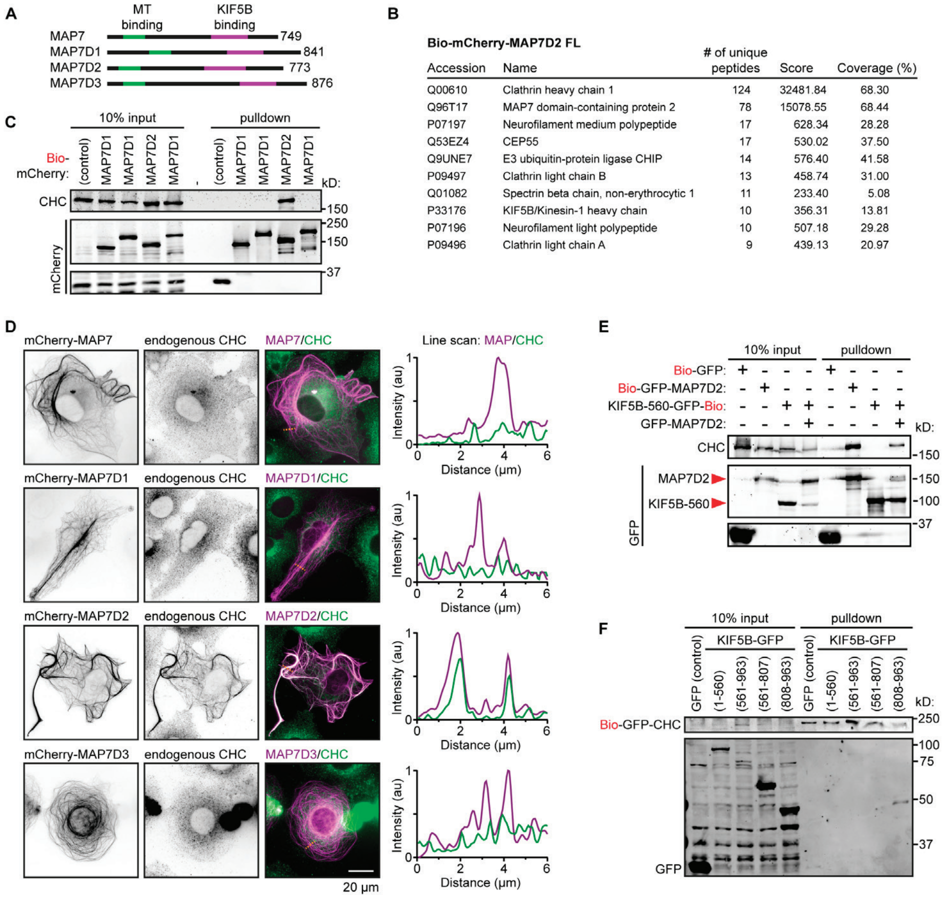
A
MT binding
KIF5B binding
MAP7
749
MAP7D1
841
MAP7D2
773
MAP7D3
876
B
C
10% input
pulldown
Bio-mCherry:
(control)
MAP7D1
MAP7D1
MAP7D2
MAP7D1
kD:
CHC
150
250
150
mCherry
37
D
mCherry-MAP7
endogenous CHC
MAP7/CHC
Line scan: MAP/CHC
mCherry-MAP7D1
MAP7D1/CHC
mCherry-MAP7D2
MAP7D2/CHC
mCherry-MAP7D3
MAP7D3/CHC
Intensity (au)
Distance (µm)
20 µm
E
10% input
pulldown
Bio-GFP:
Bio-GFP-MAP7D2:
KIF5B-560-GFP-Bio:
GFP-MAP7D2:
CHC
MAP7D2
KIF5B-560
GFP
kD:
150
150
100
37
F
10% input
pulldown
KIF5B-GFP
GFP (control)
(1-560)
(561-963)
(561-807)
(808-963)
Bio-GFP-CHC
GFP
kD:
250
100
75
50
37

Bio-mCherry-MAP7D2 FL

Accession	Name	# of unique peptides	Score	Coverage (%)
Q00610	Clathrin heavy chain 1	124	32481.84	68.30
Q96T17	MAP7 domain-containing protein 2	78	15078.55	68.44
P07197	Neurofilament medium polypeptide	17	628.34	28.28
Q53EZ4	CEP55	17	530.02	37.50
Q9UNE7	E3 ubiquitin-protein ligase CHIP	14	576.40	41.58
P09497	Clathrin light chain B	13	458.74	31.00
Q01082	Spectrin beta chain, non-erythrocytic 1	11	233.40	5.08
P33176	KIF5B/Kinesin-1 heavy chain	10	356.31	13.81
P07196	Neurofilament light polypeptide	10	507.18	29.28
P09496	Clathrin light chain A	9	439.13	20.97

Figure 1 - MAP7D2 binds and recruits clathrin to MTs
(A) Schematic representation of full length MAP7 family proteins used in this chapter. The MT-binding domain is indicated in green, the kinesin-1 (KIF5B) binding domain is indicated in magenta. **(B)** Identification of binding partners of Bio-mCherry full length MAP7D2 by streptavidin pull-down assay from HEK293T cells co-expressing BirA followed by mass spectrometry. Results table shows the top 10 interactors after contaminants were filtered out. **(C)** Streptavidin pull-down assay with extracts of HEK293T cells expressing BirA and the indicated Bio-mCherry–labeled full length MAP7 family proteins (bait) analyzed by Western blotting using antibodies against mCherry and endogenous CHC. **(D)** Widefield images of COS-7 cells overexpressing mCherry-labeled full length MAP7 family proteins stained for endogenous CHC. Dotted line (orange) indicates the position of the line scan for Cherry and CHC shown on the right. **(E)** Streptavidin pull-down assay with extracts of HEK293T cells expressing BirA and the indicated (Bio-)GFP–labeled proteins (bait) analyzed by Western blotting using antibodies against GFP and endogenous CHC. **(F) S**treptavidin pull-down assay with extracts of HEK293T cells expressing BirA, Bio-GFP-CHC full length (bait) and the indicated GFP–labeled KIF5B fragments (prey) analyzed by Western blotting using an antibody against GFP.

The MAP7D2 C-terminus binds the N-terminal domain of clathrin

Next, we mapped the minimal binding regions for the MAP7D2-clathrin interaction. The MAP7D2 N-terminus, containing the MT-binding domain, was not able to recruit endogenous CHC to MTs in cells as seen with full length MAP7D2 (Figure 1D, S1B, S2A). There-

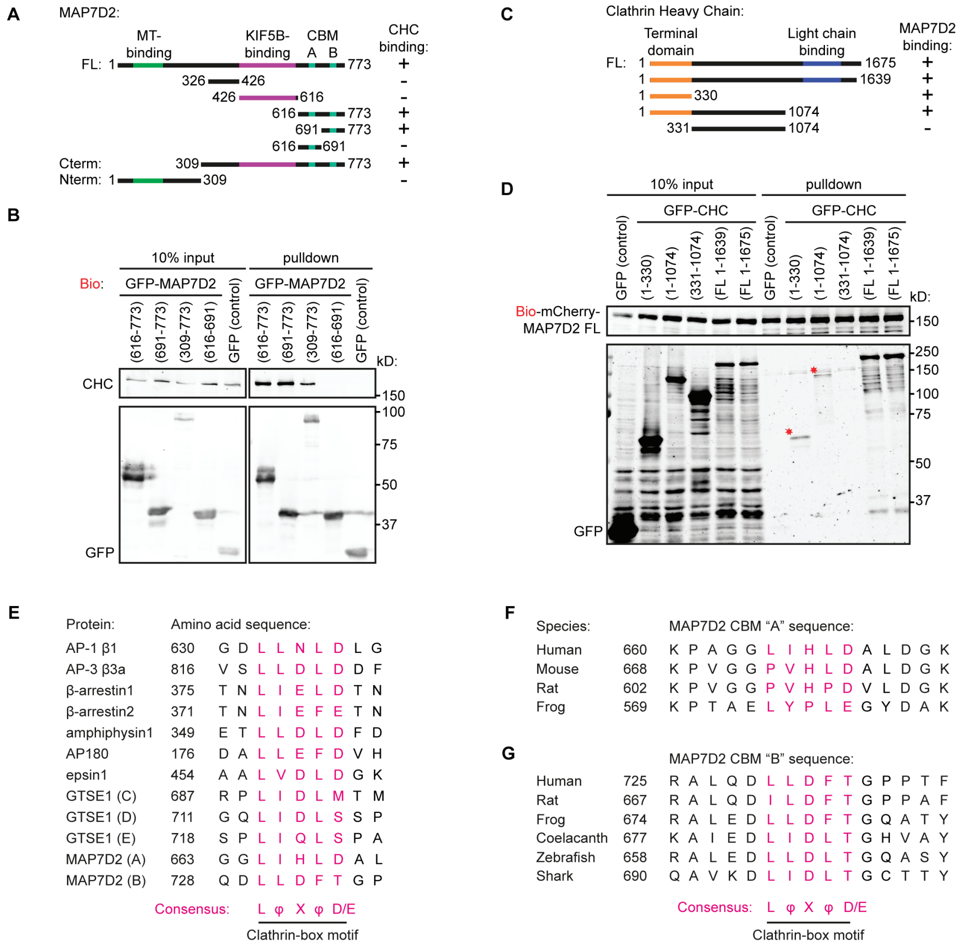
A
MAP7D2:
MT-binding
KIF5B-binding
CBM A B
CHC binding:
FL: 1 773 +
326 426 -
426 616 -
616 773 +
691 773 +
616 691 -
Cterm: 309 773 +
Nterm: 1 309 -
B
Bio:
10% input
pulldown
GFP-MAP7D2
(616-773)
(691-773)
(309-773)
(616-691)
GFP (control)
kD:
CHC
GFP
150
100
75
50
37
C
Clathrin Heavy Chain:
Terminal domain
Light chain binding
MAP7D2 binding:
FL: 1 1675 +
1 1639 +
1 330 +
1 1074 +
331 1074 -
D
10% input
pulldown
GFP-CHC
GFP (control)
(1-330)
(1-1074)
(331-1074)
(FL 1-1639)
(FL 1-1675)
kD:
Bio-mCherry-MAP7D2 FL
GFP
150
250
150
100
75
50
37
*
E
F
G

Protein:		Amino acid sequence:
AP-1 β1	630	G D L L N L D L G
AP-3 β3a	816	V S L L D L D D F
β-arrestin1	375	T N L I E L D T N
β-arrestin2	371	T N L I E F E T N
amphiphysin1	349	E T L L D L D F D
AP180	176	D A L L E F D V H
epsin1	454	A A L V D L D G K
GTSE1 (C)	687	R P L I D L M T M
GTSE1 (D)	711	G Q L I D L S S P
GTSE1 (E)	718	S P L I Q L S P A
MAP7D2 (A)	663	G G L I H L D A L
MAP7D2 (B)	728	Q D L L D F T G P
Consensus:		L φ X φ D/E

Clathrin-box motif

Species:		MAP7D2 CBM “A” sequence:
Human	660	K P A G G L I H L D A L D G K
Mouse	668	K P V G G P V H L D A L D G K
Rat	602	K P V G G P V H P D V L D G K
Frog	569	K P T A E L Y P L E G Y D A K

		MAP7D2 CBM “B” sequence:
Human	725	R A L Q D L L D F T G P P T F
Rat	667	R A L Q D I L D F T G P P A F
Frog	674	R A L E D L L D F T G Q A T Y
Coelacanth	677	K A I E D L I D L T G H V A Y
Zebrafish	658	R A L E D L L D L T G Q A S Y
Shark	690	Q A V K D L I D L T G C T T Y
Consensus:		L φ X φ D/E

Clathrin-box motif

Figure 2 - MAP7D2 interacts with the clathrin N-terminus through a conserved motif
(A) **S**chematic representation of full length MAP7D2 and MAP7D2 fragments used in this figure. The MT-binding domain is indicated in green, the kinesin-1 (KIF5B) binding domain is indicated in magenta. The ability of MAP7D2 fragments to bind to CHC is indicated on the right. **(B)** Streptavidin pull-down assay with extracts of HEK293T cells expressing BirA and the indicated Bio-GFP–labeled MAP7D2 fragments (bait) analyzed by Western blotting using antibodies against GFP and endogenous CHC. **(C)** Schematic representation of full length CHC and CHC fragments used in this figure. The N-terminal domain is indicated in orange, the LC-binding domain is indicated in blue. The ability of CHC fragments to bind to MAP7D2 is indicated on the right. **(D)** Streptavidin pull-down assay with extracts of HEK293T cells expressing BirA, Bio-mCherry-labeled full length MAP7D2 (bait) and GFP-labeled CHC fragments (prey) analyzed by Western blotting using antibodies against mCherry and GFP. **(E)** Amino acid sequence alignment of the clathrin-box motifs of various clathrin-binding proteins. Amino acids that are part of the consensus sequence are indicated in pink. The consensus sequence of the CBM is indicated below the sequence alignment where ϕ indicates hydrophobic residues and X any residue. **(F-G)** Amino acid sequence alignment of the MAP7D2 CBM #1 (A) and #2 (B) motifs of various vertebrate species. Amino acids that are part of the consensus sequence are indicated in pink. The consensus sequence of the CBM is indicated below the sequence alignment where ϕ indicates hydrophobic residues and X any possible residue.

fore, we made deletion constructs of the MAP7D2 C-terminus and found that a C-terminal 82 amino acid construct (aa 691-773) was sufficient to pull down endogenous CHC from HEK293T cell lysates (Figure 2A, B and S2B). Using full length MAP7D2 bait constructs, we performed pull down assays to find the minimal binding domain of CHC. We found that both full length CHC isoforms bound efficiently to MAP7D2, while the N-terminal domain (NTD) fragment (aa 1-330) and an extended fragment (aa 1-1074) showed weaker binding (Figure 2C, D). This is likely due to the oligomerization state of the CHC deletion constructs. Because full length CHC self-organizes into triskelia, a single MAP7D2 protein, assuming that it is monomeric, can pull down three heavy chains by binding just one foot of a triskelion. The NTD cannot form trimers and can thus only bind MAP7D2 in a 1:1 ratio.

MAP7D2 contains an atypical, but conserved clathrin-box motif

The clathrin NTD has a 3D-structure of a β-propeller and forms the binding hub for clathrin adaptor proteins, which are important for clathrin's binding to membranes and the formation of clathrin-coated vesicles. The NTD contains four specific interaction sites: the clathrin box, W-box, arrestin box and Royle box. These sites are located in between the blades of the β-propeller and recruit binding partners containing the appropriate short linear sequence motif. However, there is some flexibility observed in this binding as some adaptor protein motifs that are predicted to bind the arrestin box, are also capable of binding the clathrin box (Muenzner et al., 2017). We screened all four MAP7 family proteins for clathrin-binding short linear motifs and found that both MAP7 and MAP7D3 contained a single and MAP7D2 contained two (sequence A and B) putative Clathrin-Box Motif (CBM) sequences (Figure S2C) (Gouw et al., 2018); which showed resemblance to the LΦXΦ[DE] (Φ = a hydrophobic residue and X = any amino acid) CBM consensus sequence (Dell'Angelica et al., 1998; ter Haar et al., 2000). Since we validated that only the most C-terminal part of MAP7D2 can bind CHC (Figure 2A, B, S2B), we concluded that the MAP7, MAP7D3 and MAP7D2 "A" putative CBM motifs are not capable of binding CHC efficiently. We next compared the MAP7D2 "B" CBM motif with that of well-known clathrin adaptor proteins and found that it has an unusual threonine at the fifth position that usually consists of negatively charged aspartic or glutamic acid (Figure 2E). Whether this threonine can gain a negative charge by phosphorylation and how this might modulate clathrin binding has not been investigated. However, this specific threonine site has not been identified as a phosphorylation target in PhosphoSitePlus (Hornbeck et al., 2015). The MAP7D2 CBM "B" sequence including its threonine shows strong sequence conservation among many vertebrate species, contrary to sequence "A" which is less conserved and more variable among species, supporting the observation that it does not contribute to clathrin binding (Figure 2F, G). Altogether, we found a conserved amino acid sequence, a CBM, in the C-terminal tail of MAP7D2 that mediates binding to one of the adaptor protein interaction sites within the clathrin NTD.

Localization of clathrin in the proximal axon depends on MAP7D2

To investigate the functional relationship between MAP7D2 and clathrin in a relevant cellular context we chose to look at axons of hippocampal neurons as was done before to study the role of MAP7D2 in kinesin-1 activity (Pan et al., 2019). To analyze clathrin localization at endogenous levels we used ORANGE, a CRISPR/Cas9-based knock-in strategy (Willems et al., 2020) to label endogenous clathrin light chain α (LCα) with GFP and found that in control conditions, clathrin localizes in the axon shaft in a punctuated manner (Figure 3A). Overexpression of a full length MAP7D2 construct showed enrichment of clathrin at the proximal axon where MAP7D2 is localized, perhaps similar to the MT recruitment observed in COS-7 cells (Figure 1D, S1B, 3A). Next, we performed a depletion experiment with

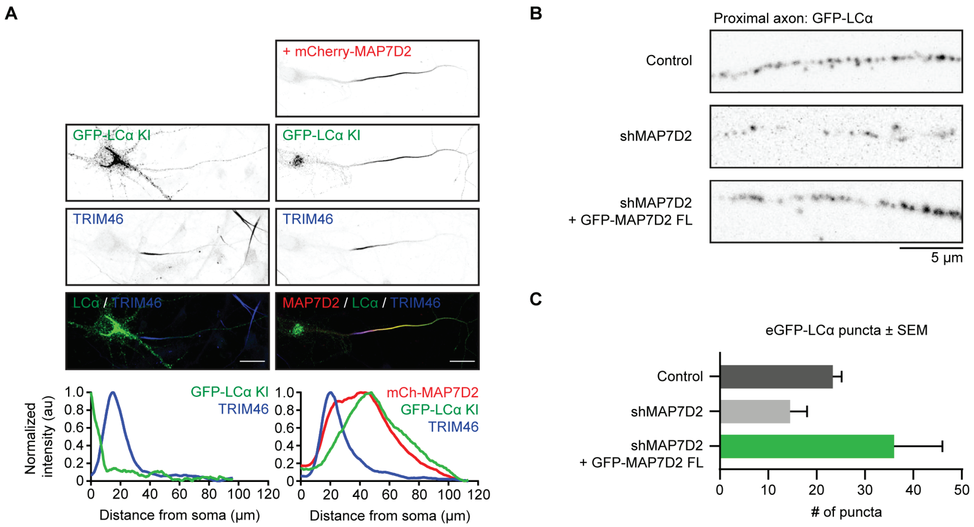

Figure 3 -MAP7D2 is required for the axonal localization of clathrin
(A) Widefield images of control (left) and mCherry-MAP7D2 overexpressing (right) hippocampal neurons at DIV 14 expressing endogenously tagged GFP- LCα stained for the axonal marker TRIM46. Line scans show normalized intensities for indicated proteins. **(B-C)** Confocal images of GFP- LCα-overexpressing hippocampal neurons at DIV 11 at indicated conditions. The number of GFP- LCα puncta per condition are quantified in C, for a 20 µm distance, starting 5 µm away from the soma.

MAP7D2 shRNA that had been validated before (Pan et al., 2019), and counted the number of clathrin puncta in the proximal axon. MAP7D2-depleted neurons showed a reduction in axonal clathrin puncta and this could be rescued by re-expression of full-length MAP7D2 (Figure 3B, C).

Generation of tools to study MAP7D2 and clathrin in neurons and *in vitro*

To further dissect the role of MAP7D2 in neurons using depletions and rescue constructs, we designed CHC- and kinesin-binding mutants of full-length MAP7D2 (Figure 4A). A kinesin-1-binding mutant (KIF-mut) was designed by replacing five conserved amino acids of the kinesin-binding domain with alanines (Hooikaas et al., 2019; Monroy et al., 2018). Similarly, a clathrin-binding mutant was designed by replacing the novel identified CBM sequence “B” by five alanines as well. We also generated a double mutant (C+K-mut). The mutants were validated by IF and pull down assays and all constructs displayed binding or loss of binding according to their design (Figure 4B, C). These constructs can be used in future to rescue MAP7D2 depletion to dissect the relative importance of kinesin-1 and clathrin-binding sites for MAP&D2 function and clathrin localization in neurons.

In addition, we designed a strategy to perform *in vitro* reconstitution assays with purified MAP7D2, kinesin-1 and clathrin. While MAP7 proteins and kinesin-1 are easy to purify from HEK293T cells (Hooikaas et al., 2019; Hua and Jiang, 2020), such an approach is unlikely to succeed for the purification of clathrin triskelia, which is normally performed by differential centrifugation steps using sucrose gradients (Giovedi, 2018). Since we would wish to use for our reconstitution assays fluorescently tagged clathrin, we generated a Strep-tag-eGFP-containing CRISPR/Cas9 donor plasmid to endogenously tag the *LCα* gene with a purification and fluorescent tag (Figure S2D, E). Purification of endogenous clathrin light chains under mild buffer conditions should yield intact triskelia containing GFP-tagged light chains. This approach can be optimized by using low kDa cut-off filters to remove non-triskelia bound Streptag-GFP-LCα and by selection of a homozygous Streptag-GFP-LCα HeLa cell clone to enhance GFP-labelling of all clathrin triskelia.

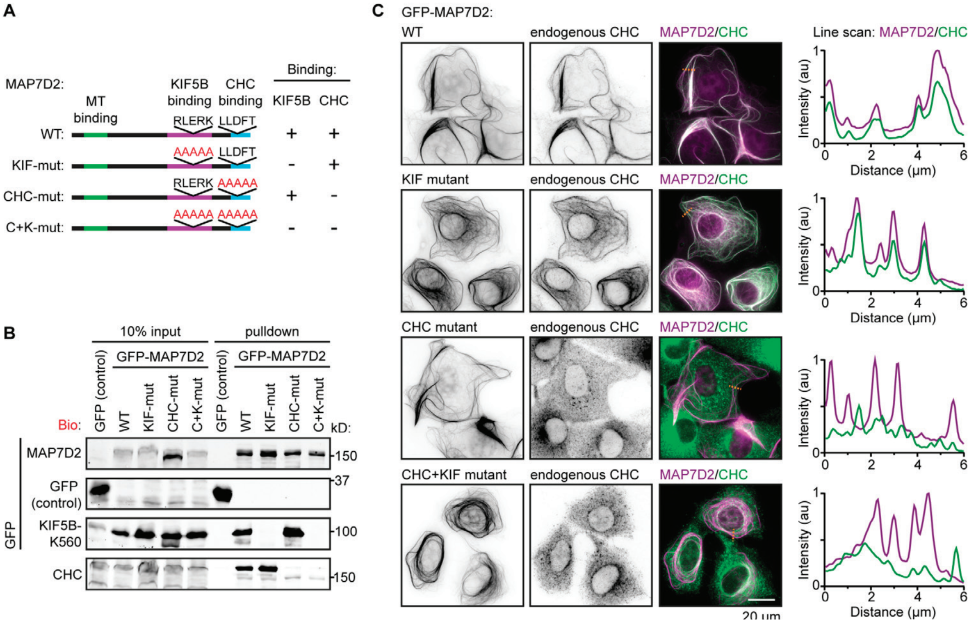
A
MAP7D2:
MT binding
KIF5B binding
CHC binding
Binding:
KIF5B
CHC
WT:
RLERK
LLDFT
+
+
KIF-mut:
AAAAA
LLDFT
-
+
CHC-mut:
RLERK
AAAAA
+
-
C+K-mut:
AAAAA
AAAAA
-
-
B
10% input
pulldown
Bio:
GFP (control)
GFP-MAP7D2
WT
KIF-mut
CHC-mut
C+K-mut
kD:
GFP
MAP7D2
GFP (control)
KIF5B-K560
CHC
150
37
100
150
C
GFP-MAP7D2:
WT
KIF mutant
CHC mutant
CHC+KIF mutant
endogenous CHC
MAP7D2/CHC
Line scan: MAP7D2/CHC
Intensity (au)
Distance (µm)
0
1
0
2
4
6
20 µm

Figure 4 - Generation of MAP7D2 binding mutants
(A) Schematic representation of full length MAP7D2 proteins used in this figure. MAP7D2 mutants were made by substituting the core binding motifs for KIF5B and/or CHC by 5 alanines. The MT-binding domain is indicated in green, the kinesin-1 (KIF5B) binding domain is indicated in magenta and the minimal CHC-binding domain is indicated in cyan. The ability of these MAP7D2 proteins to bind to KIF5B or CHC is indicated on the right. **(B)** Streptavidin pull-down assay with extracts of HEK293T cells expressing BirA, Bio-GFP-labeled full length MAP7D2 mutants (bait) and GFP-labeled KIF5B-560 (prey) analyzed by Western blotting using antibodies against GFP and endogenous CHC. **(C)** Widefield images of COS-7 cells overexpressing GFP-labeled full length MAP7D2 mutants stained for endogenous CHC. Dotted line (orange) indicates the position of the line scan for GFP and CHC shown on the right.

Discussion

In this study, we have systematically screened for new interaction candidates of all MAP7 family members in order to explore additional roles of this protein family. We found clathrin as a unique hit in the mass spectrometry analysis of MAP7D2 interactome. The C-terminus of MAP7D2 contains a CBM that can potently recruit CHC to MTs and to the proximal axon of neurons. To our knowledge, MAP7D2 is the first example of a protein that recruits clathrin to MTs in interphase cells.

MAP7D2 is exclusively expressed in brain tissue (Niida and Yachie, 2011) and specifically localizes to the proximal part of the axon where it is required for kinesin-1-dependent entry of cargo (Pan et al., 2019). Whether clathrin is part of kinesin-1-dependent cargo transport in neurons has not been investigated. Axonal clathrin is assembled in "packets" that are not associated to the plasma membrane, but localized in close vicinity to MTs (Ganguly et al., 2020). These assemblies are mostly static; but when motile, they move at velocities of ~0.6 – 0.7 µm/s with an anterograde bias (Ganguly et al., 2020). Such velocities are typical for kinesin-1 motor-driven cargo. Therefore, it is possible that a direct association of kinesin-1 with clathrin is used for directed transport of clathrin assemblies, although the involvement of other MT motors cannot be ruled out. With the current data and available literature, we hypothesize that MAP7D2 and kinesin-1 may be required for proper transport of clathrin into axons (Figure 5). Apart from its role in activating kinesin-1, MAP7D2 may tether clathrin to MTs either by binding single triskelia or by binding to (non-)membranous clathrin assemblies (Figure 5B). We propose a multi-step mechanism for this axonal clathrin transport. First, MAP7D2 has an active role in promoting kinesin-1 activity at the proximal axon. Second, MAP7D2 is responsible for tethering clathrin to axonal MTs where clathrin can subsequently be loaded onto moving kinesin-1 motors. This transfer might involve formation of a triple complex; kinesin-1 motor activity would subsequently release clathrin from MAP7D2 to facilitate anterograde transport of clathrin (Figure 5C).

Future experiments should unravel whether the hypothetic model is correct. We developed MAP7D2 binding mutants which can be used for rescue experiments in MAP7D2-depleted neurons. Such mutants can be used to dissect whether MAP7D2 is required for clathrin recruitment and/or motility and whether this is dependent on the presence of kinesin-1. Other cellular experiments may involve measuring endocytosis efficiencies in MAP7D2-depleted neurons or the use of kinesin-1 depletions and rescue experiments with kinesin-1 motors that lack the clathrin binding region at the tail. We identified a CBM sequence in the MAP7D2 C-terminus, but unlike all other clathrin adaptor proteins, it contains a threonine instead of an aspartic or glutamic acid at the fifth position of the CBM. Phosphorylation of this threonine may enhance its affinity for clathrin and can add a regulatory layer to the binding. Pulldown assays combined with a phosphatase treatment or the use of phosphomimetic and phosphomutant MAP7D2 variants can be used to investigate this notion.

To gain mechanistic insight in clathrin recruitment by MAP7D2 and its potential transport by kinesin-1, we propose to set up *in vitro* reconstitution experiments involving purified clathrin, MAP7D2 and kinesin-1. We need to experimentally address whether clathrin is still recruited to MTs by MAP7D2 in a minimal system, establish whether kinesin-1 is a clathrin-transporting motor and, if so, how MAP7D2 may play a role in promoting this process. So far, all kinesin-1-related experiments involved the ubiquitously expressed KIF5B motor; yet, neurons mainly express KIF5A and KIF5C. Therefore, it is important to assess whether clathrin is also capable of binding these closely related kinesin paralogues. Clathrin was described to be assembled into "packets" at the axon (Ganguly et al., 2020); such assemblies

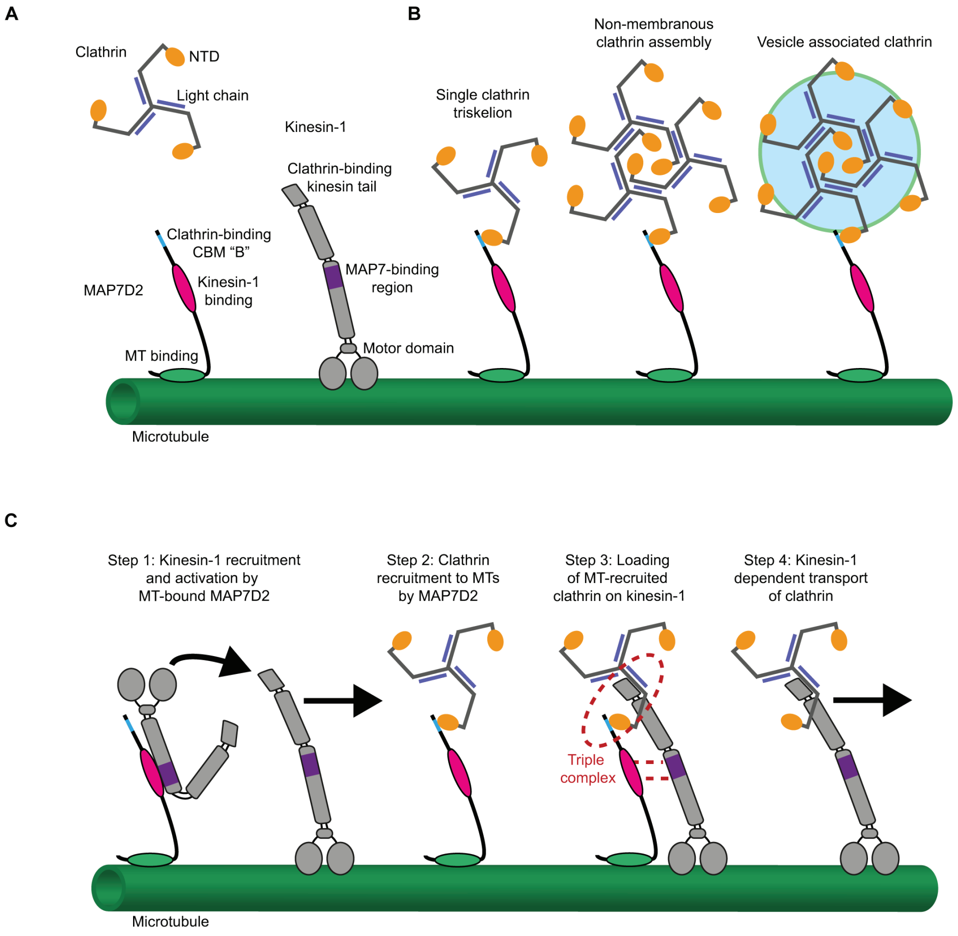
A
Clathrin
NTD
Light chain
Kinesin-1
Clathrin-binding kinesin tail
Clathrin-binding CBM “B”
MAP7D2
Kinesin-1 binding
MAP7-binding region
MT binding
Motor domain
Microtubule
B
Single clathrin triskelion
Non-membranous clathrin assembly
Vesicle associated clathrin
C
Step 1: Kinesin-1 recruitment and activation by MT-bound MAP7D2
Step 2: Clathrin recruitment to MTs by MAP7D2
Step 3: Loading of MT-recruited clathrin on kinesin-1
Step 4: Kinesin-1 dependent transport of clathrin
Triple complex
Microtubule

Figure 5. Proposed model of motor-driven clathrin transport facilitated by MAP7D2
(A) Cartoons depicting clathrin, MAP7D2 and kinesin-1 and indicated protein domains relevant for this study. **(B)** Model of how MAP7D2 may recruit clathrin to the MT. Recruitment may involve direct association of a clathrin triskelion to the MAP7D2 C-terminus (left). Clathrin may also be recruited to the MT in an assembly of multiple clathrin triskelia, either in a non-membranous fashion (middle) or associated with a vesicle (right). Additional adaptors or linking proteins may be involved in the assembly of such “clathrin packets” (not depicted here). **(C)** Model of how kinesin-1-dependent transport of clathrin might be steered by MAP7D2. MAP7D2 has a prominent role in kinesin-1 activation and the recruitment of clathrin or clathrin assemblies to MTs. MAP7D2 may be a loading platform where a triple complex is formed between MAP7D2, kinesin-1 and clathrin. Such a complex would enable the transfer of MT-tethered clathrin onto a moving kinesin-1 motor to initiate anterograde transport into axons. Note that a triple complex can be formed in two ways, indicated in red.

may promote motor-driven transport and explain why soluble triskelia are perhaps poorly transported in non-neuronal cells. How “clathrin packets” are formed in unclear, but for *in vitro* reconstitution experiments, such assemblies may be artificially made with antibodies against clathrin or GFP to form larger clathrin complexes.

It has been proposed that selective decoration of MT subsets by specific MAPs (a "MAP code") has the capacity to bias directed motor transport and thus help in the sorting of motors and cargo in neurons (Monroy et al., 2020). Distinct roles of individual MAP7 family members may contribute to this code, as we have shown that these MAPs differ significantly in their properties to bind MTs, kinesin-1 and additional binding partners (Hooikaas et al., 2019). MAP7D2 is the only family member that is found in the axon and is essential for all kinesin-1-dependent movement in this neuronal compartment (Pan et al., 2019). Here, we show that MAP7D2 has the unique property of binding and recruiting clathrin to MTs and that this MAP is important for the localization of clathrin in the axon. Kinesin-1 can also bind clathrin directly (Ni et al., 2018); we therefore hypothesize that MAP7D2 has a dual role in steering kinesin-1 transport and loading cargo onto the motor. Future experiments may resolve how large cytosolic protein complexes such as clathrin and neurofilaments are sorted and transported, and how specific MAPs can contribute to this process in a spatially regulated manner.

Materials & Methods

Cell culture

Human embryonic kidney (HEK293T) and African Green Monkey SV40-transformed kidney fibroblast (COS-7) cell lines were cultured in medium that consisted of 45% Ham's F10, 45% DMEM and 10% fetal calf serum (FCS) supplemented with streptomycin and penicillin. The cell lines were checked for mycoplasma contamination using LT07-518 Mycoalert assay (Lonza). HEK293T cells were transfected with plasmids using polyethylenimine (Polysciences), for streptavidin pull-down assays and immunoprecipitation. COS-7 cells were transfected with plasmids using FuGENE 6 (Promega) for immunofluorescence staining experiments.

Dissociated hippocampal cultures were prepared from embryonic day 18 (E18) rat brains of both genders. Dissociated neurons were plated on Ø18-mm coverslips coated with poly-L-lysine (37.5 μg/ml, Sigma-Aldrich) and laminin (1.25 μg/ml, Roche Diagnostics) at a density of 100,000 neurons per well. Neurons were grown in Neurobasal medium (NB) supplemented with 1% penicillin and streptomycin (pen/strep), 2% B27, 0.5 mM L-glutamine (all from Gibco) , and 15.6 mM glutamate (Sigma-Aldrich) (NB-complete medium) at 37°C in 5% CO_2.

Neurons were transfected at DIV 4–7 using Lipofectamine 2000 reagent (Invitrogen). Briefly, for one Ø18-mm coverslip covered with 100,000 neurons, 1–2 μg DNA was mixed with 3.3 μl Lipofectamine in 200 μl NB medium and incubated for 30 minutes at room temperature (RT). Next, 500 μl conditioned medium was transferred to a new culture plate. The DNA mix was added to the neurons and incubated at 37°C and 5% CO_2. After 90–120 minutes, neurons were transferred to the new culture plate with conditioned medium and 500 μl new NB medium supplemented with L-glutamine, B27, and pen/strep and kept at 37°C and 5% CO_2 for at least 5 days.

DNA constructs

All MAP7D2 and CHC constructs were cloned by a PCR-based strategy into a pBio-mCherry-C1, mCherry-C1, or pBio-EGFP-C1 vector. The Bio-tag consisted of the coding sequence MASGLNDIFEAQKIEWHEGGG, the substrate of biotin ligase (BirA). MAP7D2 (cDNA) was derived from the IMAGE clone 3063898 (SourceBioscience). MAP7D2 truncations and binding mutants were generated by a PCR-based strategy. Biotin ligase BirA expression construct (Driegen et al., 2005) was a kind gift from D. Meijer (University of Edinburgh, Edinburgh, UK). Bio-mCherry MAP7 family protein constructs were described before (Hooikaas et al., 2019); human GFP-tagged CHC and LCα constructs were described before (Royle et al., 2005). A rat specific Halo- LCα construct was used for overexpression; a rat specific GFP-Clathrin LCα pOrange plasmids was used for endogenous tagging, as described before (Willems et al., 2020). A twin-Streptag (SII) containing human specific SII-GFP-Clathrin LCα pORANGE construct was cloned using the novel ORANGE strategy for CRISPR/Cas9-based knock-in. In short, a 20 basepair PAM-containing target sequence was identified and oligonucleotides containing this sequence were annealed and ligated into the BbsI restriction sites of a pORANGE plasmid. Primers for the SII-eGFP-containing donor sequence were flanked by two Cas9 target sites matching the genomic target site. The GFP sequence is flanked on both sides by a linker region: GSLPVAT (N-terminal) and SGRNGSSS (C-terminal). The donor sequence was amplified using PCR and ligated into the multiple cloning site of the target sequence-containing pORANGE plasmids using HindIII and XhoI restriction sites.

Target sequences for ORANGE knock-ins:

Gene	Species	Protein	Target sequence (PAM is underlined)
Clta	rat	Clathrin light chain α	GGATCCAACTCAGCCATGACGG
Clta	human	Clathrin light chain α	CCATGGCTGAGCTGGATCCGTTC

Donor PCR primers (5' - 3'):
Knock-in GFP-Clathrin LCα (rat)
Forward: ATAAAGCTTGGATCCAACTCAGCCATGAGGGCAGGTAGCGGAGTGAGCAAGGGCGAGGA
Reverse: ATACTCGAGCCCTCATGGCTGAGTTGGATCCTCCGCTACCCTTGTACAGCTCGTCCATGC

Knock-in SII-GFP-Clathrin LCα (human)
Forward: ATAAAGCTTGAACGGATCCAGCTCAGCCAGGGGTTCTTGGAGTCATCCACAATTT
Reverse: ATACTCGAGCCCTGGCTGAGCTGGATCCGTTCCTGCCTGACTTGTACAGCTCGTCCATGC

For depletion experiments, a RAT MAP7D2 shRNA (#1) was used:
Sequence: 5'-GGAACCTCCTATGAGTAAA-3'

Antibodies, Western blotting and immunofluorescence cell staining

For Western blotting and immunofluorescence cell staining rabbit polyclonal antibodies were used against GFP (ab290; Abcam), mouse monoclonal antibodies against mCherry (632543; Clontech) and against clathrin heavy chain (610499; BD Transduction Laboratories). The following secondary antibodies were used: IRDye 800CW/680LT goat anti–rabbit, and anti–mouse for Western blotting and Alexa Fluor 488– and 594––conjugated goat antibodies against mouse or rabbit IgG (Molecular Probes). F-actin was stained using AlexaFluor 594-conjugated phalloidin (Life Technologies).

Total HeLa cell extracts were prepared in a buffer containing 20 mM Tris, pH 7.5, 150 mM NaCl, 1 mM $MgCl_2$, 1% Triton X-100, and cOmplete protease inhibitor cocktail (Roche).

For immunofluorescence cell staining of COS-7 and HeLa cells, cells were fixed in –20°C methanol for 10 min and stained for CHC. In the case of phalloidin staining, cells were fixed with 4% PFA in PBS for 10 min and not washed with ethanol at the final steps. Cells were then permeabilized with 0.15% Triton X-100 in PBS for 2 min; subsequent wash steps were performed in PBS supplemented with 0.05% Tween-20. Epitope blocking and antibody labelling steps were performed in PBS supplemented with 0.05% Tween-20 and 1% BSA. Before mounting in Vectashield mounting medium (Vector Laboratories), slides were washed with 70% and 100% ethanol and air-dried.

For immunofluorescence cell staining of dissociated hippocampal neurons, cells were fixed with 4% PFA (paraformaldehyde) for 10-15 minutes, washed 3 times with PBS (phosphate buffer saline), and incubated with primary antibodies in GDB buffer (0.2% BSA, 0.8 M NaCl, 0.5% Triton X-100, 30 mM phosphate buffer) overnight at 4°C. Cells were then washed with PBS for 3 times, incubated with secondary antibodies in GDB buffer for 45 minutes at room temperature, followed by washing 3 times with PBS and mounting with Vectashield mounting medium (Vector Laboratories).

Image acquisition

Imaging of fixed neurons was performed using an LSM700 confocal laser-scanning microscope (Zeiss) equipped with a Plan-Apochromat 63×N.A.1.40 oil DIC objective, using 405 nm, 488 nm, 555 nm, and 633 nm laser lines.

Imaging of fixed COS-7 and HeLa cells was performed using a Nikon Eclipse 80i upright fluorescence microscope equipped with Plan Apo VC NA 1.40 oil 100× and 60× or Plan Fluor 40x NA 1.30 oil objective, or a Nikon Eclipse Ni-E upright fluorescence microscope equipped with Plan Apo Lambda 100× NA 1.45 oil and 60× NA 1.40 oil objectives microscopes, Chroma ET-BFP2, -GFP, -mCherry, or -Cy5 filters, and a Photometrics CoolSNAP HQ2 charge-coupled device (CCD) camera (Roper Scientific). The microscopes were controlled by Nikon NIS Br software.

Live imaging of neurons was performed on a Nikon Eclipse TE2000E inverted microscope equipped with Evolve 512 EMCCD camera (Roper Scientific), spinning disk confocal (Roper Scientific), with Plan Apo VC 100x 1.40 NA oil objective (Nikon), incubation chamber (Tokai Hit) and MetaMorph 7.7.5 software (Molecular Device). Neurons were maintained in 37°C /5% CO_2.

Streptavidin pull down assays

Streptavidin pull down assays were performed from HEK293T cell lysates by coexpressing biotin ligase BirA with mCherry- or GFP-tagged constructs containing a biotinylation site. For some pull downs the prey protein was co-expressed, other pull downs would target endogenous expressed proteins as indicated per experiment. Constructs were transfected together into HEK293 cells using polyethylenimine with a 24-h incubation time for protein expression. M-280 Streptavidin Dynabeads (Invitrogen) were blocked in a buffer containing 20 mM Tris, pH 7.5, 20% glycerol, 150 mM NaCl, and 10 μg chicken egg albumin followed by three washes with wash buffer containing 20 mM Tris, pH 7.5, 150 mM NaCl, and 0.1% Triton X-100. HEK293T cells were scraped and collected in ice-cold PBS followed by lysis on ice in a buffer containing 20 mM Tris, pH 7.5, 150 mM NaCl, 1 mM $MgCl_2$, 1% Triton X-100, and cOmplete protease inhibitor cocktail (Roche). To separate cell debris, the lysates were cleared by centrifugation at 4°C for 15 min at 16,000 g, and 10% of each lysate was saved as input control. Cell lysates were incubated with pre-blocked streptavidin beads for 60 min at 4°C followed by five washes with the buffer containing 20 mM Tris, pH 7.5, 150 mM NaCl, and 0.1% Triton X-100. Streptavidin beads were pelleted and boiled in Laemmli sample buffer. Protein lysates and pull down of both bait and prey proteins were analyzed by Western blotting.

Mass spectrometry

Samples of streptavidin-purified proteins were ran on a SDS-PAGE gel. Gel pieces were reduced, alkylated and digested overnight with trypsin. Peptides were extracted with acetonitrile and dried down in a vacuum centrifuge. The resuspended peptides were subjected to LC-LC MS/MS using an Agilent 1290 Infinity coupled to an Orbitrap Q Exactive HF mass spectrometer (Thermo Scientific, Bremen, Germany). Peptides were first trapped (Dr Maisch Reprosil C18, 3 μm, 2 cm × 100 μm) before being separated on an analytical column (Agilent Poroshell EC-C18, 2.7 μm, 50 cm × 75 μm). Trapping was performed for 10 min in solvent A (0.1 M acetic acid in water), and the gradient was as follows: 13–44% solvent B (0.1 M acetic acid in 80% ACN) in 35 min, 44–100% in 3 min and 100% for 1 min. Flow was passively split to 300 nL min^{-1} . The mass spectrometer was operated in data-dependent mode. Full-scan MS spectra from m/z 375–1600 were acquired at a resolution of 30 000 at m/z 400 after accumulation to a target value of 3 × 106 . Up to 15 most intense precursor ions were selected for fragmentation. HCD fragmentation was performed at a normalized collision energy of 27.

Raw files were processed using Proteome Discoverer (version 1.4.0.288, Thermo Scientific, Bremen, Germany). Database searching was performed using Mascot (version 2.5.1, Matrix Science, UK) against a Swiss-Prot human database (downloaded 29th of January 2016). Carbamidomethylation of cysteines was set as a fixed modification and oxidation of methionine as a variable modification. Trypsin was specified as enzyme and up to two miss cleavages were allowed. Data filtering was performed using percolator, resulting in 1% false discovery rate (FDR). Additional filters were; search engine rank 1 peptides and ion score>20.

Proteomics analysis

Proteomics analysis of MAP7D2 amino acid sequence conservation across species was performed with Clustal Omega sequence alignment tool (https://www.ebi.ac.uk/Tools/msa/clustalo/). The amino acid sequences were obtained from UniProt, except for Callorhinchus milii (elephant shark), obtained from NCBI.

References

Barlan, K., W. Lu, and V.I. Gelfand. 2013. The microtubule-binding protein ensconsin is an essential cofactor of kinesin-1. Curr Biol. 23:317-322.

Black, M.M. 2016. Axonal transport: The orderly motion of axonal structures. Methods Cell Biol. 131:1-19.

Chaudhary, A.R., H. Lu, E.B. Krementsova, C.S. Bookwalter, K.M. Trybus, and A.G. Hendricks. 2019. MAP7 regulates organelle transport by recruiting kinesin-1 to microtubules. J Biol Chem. 294:10160-10171.

Dell'Angelica, E.C., J. Klumperman, W. Stoorvogel, and J.S. Bonifacino. 1998. Association of the AP-3 adaptor complex with clathrin. Science. 280:431-434.

Ganguly, A., F. Wernert, S. Phan, D. Boassa, U. Das, R. Sharma, G. Caillol, X. Han, J.R. Yates, M.H. Ellisman, C. Leterrier, and S. Roy. 2020. Mechanistic Determinants of Slow Axonal Transport and Presynaptic Targeting of Clathrin Packets. bioRxiv:2020.2002.2020.958140.

Giovedi, S. 2018. Purification of Clathrin-Coated Vesicles from Adult Rat Brain. Methods Mol Biol. 1847:1-11.

Gouw, M., S. Michael, H. Samano-Sanchez, M. Kumar, A. Zeke, B. Lang, B. Bely, L.B. Chemes, N.E. Davey, Z. Deng, F. Diella, C.M. Gurth, A.K. Huber, S. Kleinsorg, L.S. Schlegel, N. Palopoli, K.V. Roey, B. Altenberg, A. Remenyi, H. Dinkel, and T.J. Gibson. 2018. The eukaryotic linear motif resource - 2018 update. Nucleic Acids Res. 46:D428-D434.

Guedes-Dias, P., and E.L.F. Holzbaur. 2019. Axonal transport: Driving synaptic function. Science. 366.

Gumy, L.F., and C.C. Hoogenraad. 2018. Local mechanisms regulating selective cargo entry and long-range trafficking in axons. Curr Opin Neurobiol. 51:23-28.

Hooikaas, P.J., M. Martin, T. Muhlethaler, G.J. Kuijntjes, C.A.E. Peeters, E.A. Katrukha, L. Ferrari, R. Stucchi, D.G.F. Verhagen, W.E. van Riel, I. Grigoriev, A.F.M. Altelaar, C.C. Hoogenraad, S.G.D. Rudiger, M.O. Steinmetz, L.C. Kapitein, and A. Akhmanova. 2019. MAP7 family proteins regulate kinesin-1 recruitment and activation. J Cell Biol. 218:1298-1318.

Hornbeck, P.V., B. Zhang, B. Murray, J.M. Kornhauser, V. Latham, and E. Skrzypek. 2015. PhosphoSitePlus, 2014: mutations, PTMs and recalibrations. Nucleic Acids Res. 43:D512-520.

Hua, S., and K. Jiang. 2020. Expression and Purification of Microtubule-Associated Proteins from HEK293T Cells for In Vitro Reconstitution. Methods Mol Biol. 2101:19-26.

Koizumi, H., H. Fujioka, K. Togashi, J. Thompson, J.R. Yates, 3rd, J.G. Gleeson, and K. Emoto. 2017. DCLK1 phosphorylates the microtubule-associated protein MAP7D1 to promote axon elongation in cortical neurons. Dev Neurobiol. 77:493-510.

Leterrier, C. 2018. The Axon Initial Segment: An Updated Viewpoint. J Neurosci. 38:2135-2145.

Luo, Y., S. Xiang, P.J. Hooikaas, L. van Bezouwen, A.S. Jijumon, C. Janke, F. Forster, A. Akhmanova, and

M. Baldus. 2020. Direct observation of dynamic protein interactions involving human microtubules using solid-state NMR spectroscopy. Nat Commun. 11:18.

Metivier, M., B.Y. Monroy, E. Gallaud, R. Caous, A. Pascal, L. Richard-Parpaillon, A. Guichet, K.M. Ori-McKenney, and R. Giet. 2019. Dual control of Kinesin-1 recruitment to microtubules by Ensconsin in Drosophila neuroblasts and oocytes. Development. 146.

Metzger, T., V. Gache, M. Xu, B. Cadot, E.S. Folker, B.E. Richardson, E.R. Gomes, and M.K. Baylies. 2012. MAP and kinesin-dependent nuclear positioning is required for skeletal muscle function. Nature. 484:120-124.

Monroy, B.Y., D.L. Sawyer, B.E. Ackermann, M.M. Borden, T.C. Tan, and K.M. Ori-McKenney. 2018. Competition between microtubule-associated proteins directs motor transport. Nat Commun. 9:1487.

Monroy, B.Y., T.C. Tan, J.M. Oclaman, J.S. Han, S. Simo, S. Niwa, D.W. Nowakowski, R.J. McKenney, and K.M. Ori-McKenney. 2020. A Combinatorial MAP Code Dictates Polarized Microtubule Transport. Dev Cell. 53:60-72 e64.

Muenzner, J., L.M. Traub, B.T. Kelly, and S.C. Graham. 2017. Cellular and viral peptides bind multiple sites on the N-terminal domain of clathrin. Traffic. 18:44-57.

Nakada, C., K. Ritchie, Y. Oba, M. Nakamura, Y. Hotta, R. Iino, R.S. Kasai, K. Yamaguchi, T. Fujiwara, and A. Kusumi. 2003. Accumulation of anchored proteins forms membrane diffusion barriers during neuronal polarization. Nat Cell Biol. 5:626-632.

Ni, Y.X., N. Zhou, W.Q. Xue, L. Rong, W.H. Yung, R.Z. Lin, R.Y. Kao, Z.G. Duan, H.T. Sun, H.R. Gong, X.M. Tang, M.F. Liu, W. Zhang, S. Qi, S. Chung, Y.Q. Song, and J.D. Huang. 2018. A new role of anterograde motor Kif5b in facilitating large clathrin-coated vesicle mediated endocytosis via regulating clathrin uncoating. Cell Discov. 4:65.

Niida, Y., and A. Yachie. 2011. MAP7D2 is a brain expressing X-linked maternal imprinted gene in humans. Nature Precedings.

Pan, X., Y. Cao, R. Stucchi, P.J. Hooikaas, S. Portegies, L. Will, M. Martin, A. Akhmanova, M. Harterink, and C.C. Hoogenraad. 2019. MAP7D2 Localizes to the Proximal Axon and Locally Promotes Kinesin-1-Mediated Cargo Transport into the Axon. Cell Rep. 26:1988-1999 e1986.

Rondelet, A., Y.C. Lin, D. Singh, A.T. Porfetye, H.C. Thakur, A. Hecker, P. Brinkert, N. Schmidt, S. Bendre, F. Muller, L. Mazul, P.O. Widlund, T. Bange, M. Hiller, I.R. Vetter, and A.W. Bird. 2020. Clathrin's adaptor interaction sites are repurposed to stabilize microtubules during mitosis. J Cell Biol. 219.

Roy, S. 2020. Finding order in slow axonal transport. Curr Opin Neurobiol. 63:87-94.

Roy, S., P. Coffee, G. Smith, R.K. Liem, S.T. Brady, and M.M. Black. 2000. Neurofilaments are transported rapidly but intermittently in axons: implications for slow axonal transport. J Neurosci. 20:6849-6861.

Royle, S.J. 2012. The role of clathrin in mitotic spindle organisation. J Cell Sci. 125:19-28.

Royle, S.J., N.A. Bright, and L. Lagnado. 2005. Clathrin is required for the function of the mitotic spindle. Nature. 434:1152-1157.

Scott, D.A., U. Das, Y. Tang, and S. Roy. 2011. Mechanistic logic underlying the axonal transport of cytosolic proteins. Neuron. 70:441-454.

Serra-Marques, A., M. Martin, E.A. Katrukha, I. Grigoriev, C.A.E. Peeters, Q. Liu, P.J. Hooikaas, Y. Yao, I. Smal, L.B. Pedersen, E. Meijering, L.C. Kapitein, and A. Akhmanova. 2020. Concerted action of kinesin-1 KIF5B and kinesin-3 KIF13B promotes efficient transport of exocytotic vesicles to microtubule plus ends. bioRxiv:2020.2004.2006.027862.

Song, A.H., D. Wang, G. Chen, Y. Li, J. Luo, S. Duan, and M.M. Poo. 2009. A selective filter for cytoplasmic transport at the axon initial segment. Cell. 136:1148-1160.

Sun, X., X. Shi, M. Liu, D. Li, L. Zhang, X. Liu, and J. Zhou. 2011. Mdp3 is a novel microtubule-binding protein that regulates microtubule assembly and stability. Cell Cycle. 10:3929-3937.

Sun, X., Y. Wu, M. Gu, Z. Liu, Y. Ma, J. Li, and Y. Zhang. 2014. Selective filtering defect at the axon initial segment in Alzheimer's disease mouse models. Proc Natl Acad Sci U S A. 111:14271-14276.

Sung, H.H., I.A. Telley, P. Papadaki, A. Ephrussi, T. Surrey, and P. Rorth. 2008. Drosophila ensconsin promotes productive recruitment of Kinesin-1 to microtubules. Dev Cell. 15:866-876.

Tang, Y., D. Scott, U. Das, D. Gitler, A. Ganguly, and S. Roy. 2013. Fast vesicle transport is required for the slow axonal transport of synapsin. J Neurosci. 33:15362-15375.

ter Haar, E., S.C. Harrison, and T. Kirchhausen. 2000. Peptide-in-groove interactions link target proteins to the beta-propeller of clathrin. Proc Natl Acad Sci U S A. 97:1096-1100.

Tymanskyj, S.R., and L. Ma. 2019. MAP7 Prevents Axonal Branch Retraction by Creating a Stable Microtubule Boundary to Rescue Polymerization. J Neurosci. 39:7118-7131.

Tymanskyj, S.R., B. Yang, A. Falnikar, A.C. Lepore, and L. Ma. 2017. MAP7 Regulates Axon Collateral Branch Development in Dorsal Root Ganglion Neurons. J Neurosci. 37:1648-1661.

Tymanskyj, S.R., B.H. Yang, K.J. Verhey, and L. Ma. 2018. MAP7 regulates axon morphogenesis by recruiting kinesin-1 to microtubules and modulating organelle transport. Elife. 7.

Wang, L., C.L. Ho, D. Sun, R.K. Liem, and A. Brown. 2000. Rapid movement of axonal neurofilaments interrupted by prolonged pauses. Nat Cell Biol. 2:137-141.

Willems, J., A.P.H. de Jong, N. Scheefhals, E. Mertens, L.A.E. Catsburg, R.B. Poorthuis, F. de Winter, J. Verhaagen, F.J. Meye, and H.D. MacGillavry. 2020. ORANGE: A CRISPR/Cas9-based genome editing toolbox for epitope tagging of endogenous proteins in neurons. PLoS Biol. 18:e3000665.

Supplemental Figures

A

Bio-mCherry-MAP7 FL

Accession	Name	# of unique peptides	Score	Coverage (%)
Q14244	Ensconsin	63	9036.19	70.09
Q9ULH0	Kinase D-interacting substrate of 220 kDa	19	557.15	11.07
P33176	Kinesin-1 heavy chain	10	243.43	13.29
P81947	Tubulin alpha-1B chain	9	514.33	30.16
P68399	Casein kinase II subunit alpha	8	522.26	26.85
P40227	T-complex protein 1 subunit zeta	8	156.78	14.5
Q9BQ67	Glutamate-rich WD repeat-containing protein 1	7	384.08	14.8
Q9UBH6	Xenotropic and polytropic retrovirus receptor 1	7	269.82	12.64
O95793	Double-stranded RNA-binding protein Staufen homolog 1	7	230.49	14.21
P05455	Lupus La protein	7	173.31	17.65

Bio-mCherry-MAP7D1 FL

Accession	Name	# of unique peptides	Score	Coverage (%)
Q3KQU3	MAP7 domain-containing protein 1	67	8111.44	57.79
O95714	E3 ubiquitin-protein ligase HERC2	20	551.9	5.01
O95613	Pericentrin	14	379.3	5.07
P05455	Lupus La protein	13	526.39	27.7
Q99996	A-kinase anchor protein 9	12	311.06	3.32
Q9ULH0	Kinase D-interacting substrate of 220 kDa	11	266.89	5.36
P62261	14-3-3 protein epsilon	11	768.1	57.65
O94763	Unconventional prefoldin RPB5 interactor 1	10	277.78	22.62
P21333	Filamin-A	10	266.79	4.95
Q96MX6	WD repeat-containing protein 92	9	385.37	25.49

Bio-mCherry-MAP7D3 FL

Accession	Name	# of unique peptides	Score	Coverage (%)
Q8IWC1	MAP7 domain-containing protein 3	78	18302.56	55.71
P33176	Kinesin-1 heavy chain	25	1835.32	31.15
Q99996	A-kinase anchor protein 9	22	561.19	6.57
Q9H0B6	Kinesin light chain 2	10	1138.4	19.77
Q07065	Cytoskeleton-associated protein 4	9	405.94	18.94
Q9ULH0	Kinase D-interacting substrate of 220 kDa	9	320.72	5.99
Q96SN8	CDK5 regulatory subunit-associated protein 2	8	492.14	5.65
O94763	Unconventional prefoldin RPB5 interactor 1	8	357.28	15.7
O95613	Pericentrin	8	315.44	2.91
Q9NSK0	Kinesin light chain 4	7	517.17	16.32

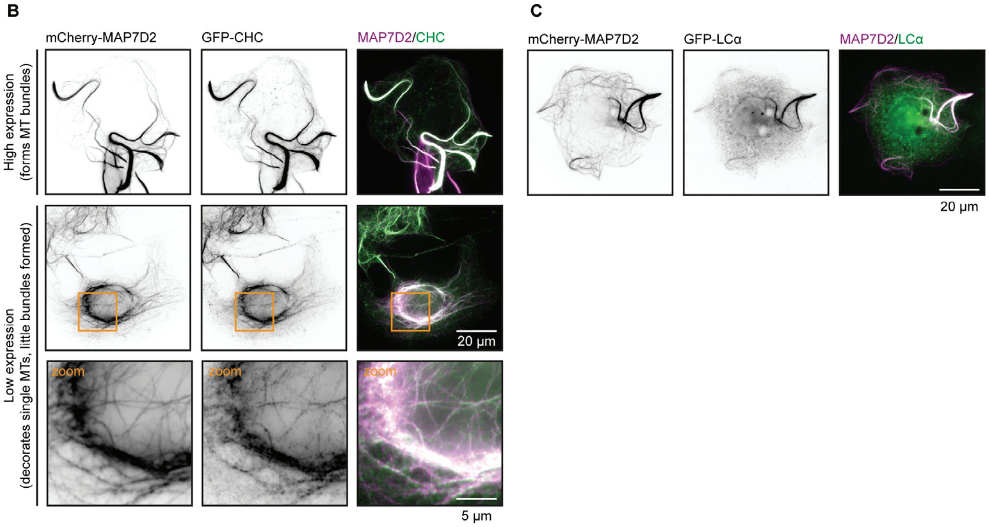
B
mCherry-MAP7D2
GFP-CHC
MAP7D2/CHC
High expression (forms MT bundles)
Low expression (decorates single MTs, little bundles formed)
20 µm
zoom
zoom
zoom
5 µm
C
mCherry-MAP7D2
GFP-LCα
MAP7D2/LCα
20 µm

Supplemental Figure 1 - Mass spectrometry analysis of MAP7 proteins and analysis of clathrin recruitment to MTs by MAP7D2
(A) Identification of binding partners of Bio-mCherry full length MAP7, MAP7D1 and MAP7D3 by streptavidin pull-down assays from HEK293T cells co-expressing BirA followed by mass spectrometry. Results table

Figure S1 (continued) shows the top 10 interactors after contaminants were filtered out. **(B)** Widefield images of COS-7 cells overexpressing mCherry-labeled full length MAP7D2 and GFP-labeled full length CHC. Upper panel shows an example of high MAP7D2 expression levels. Lower panels show an example of low MAP7D2 expression, a zoom (indicated in orange) is shown below. **(C)** Widefield images of COS-7 cells overexpressing mCherry-labeled full length MAP7D2 and GFP-labeled full length LCα.

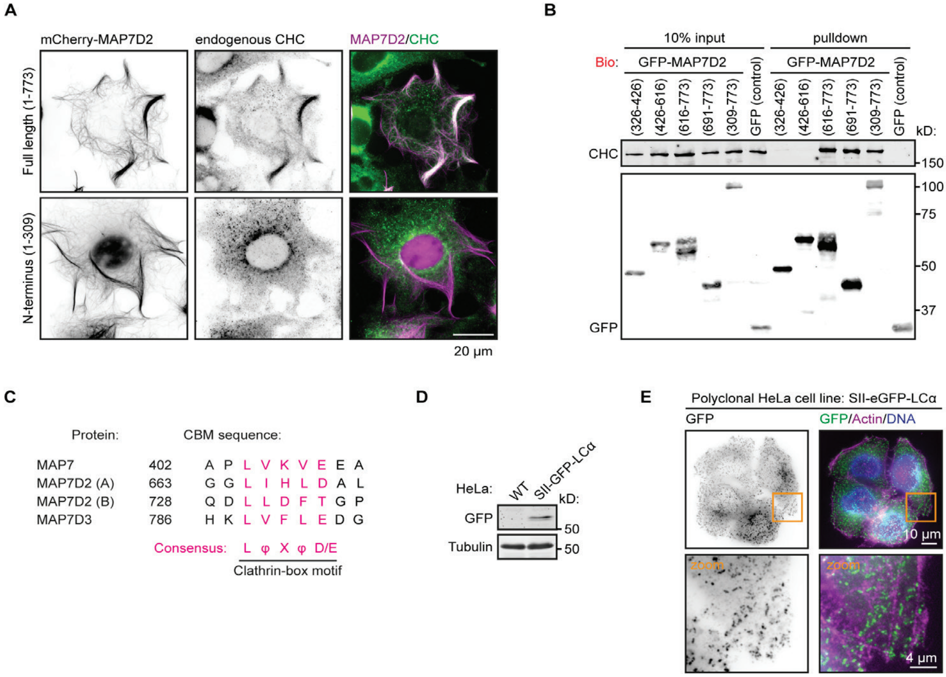
A
mCherry-MAP7D2
endogenous CHC
MAP7D2/CHC
Full length (1-773)
N-terminus (1-309)
20 μm
B
10% input
pulldown
Bio:
GFP-MAP7D2
GFP-MAP7D2
(326-426)
(426-616)
(616-773)
(691-773)
(309-773)
GFP (control)
(326-426)
(426-616)
(616-773)
(691-773)
(309-773)
GFP (control)
kD:
CHC
150
100
75
50
37
GFP
C
Protein:
CBM sequence:
MAP7 402 A P L V K V E E A
MAP7D2 (A) 663 G G L I H L D A L
MAP7D2 (B) 728 Q D L L D F T G P
MAP7D3 786 H K L V F L E D G
Consensus: L φ X φ D/E
Clathrin-box motif
D
HeLa:
WT
SII-GFP-LCα
kD:
GFP
50
Tubulin
50
E
Polyclonal HeLa cell line: SII-eGFP-LCα
GFP
GFP/Actin/DNA
10 μm
zoom
zoom
4 μm

Supplemental Figure 2. Analysis of clathrin-MAP7D2 binding and generation of a stable cell line with endogenously tagged LCα
(A) Widefield images of COS-7 cells overexpressing mCherry-labeled full length MAP7D2 or the MT-binding MAP7D2 N-terminus (1-309) stained for endogenous CHC. **(B)** Streptavidin pull-down assay with extracts of HEK293T cells expressing BirA and the indicated Bio-GFP–labeled MAP7D2 fragments (bait) analyzed by Western blotting using antibodies against GFP and endogenous CHC. **(C)** Amino acid sequence alignment of all CBM motifs present in the MAP7 protein family. Amino acids that rare part of the consensus sequence are indicated in pink. The consensus sequence of the clathrin-box motif is indicated below the sequence alignment where ϕ indicates hydrophobic residues and X any possible residue. **(D)** Western blot analysis of a polyclonal GFP-sorted HeLa cell line expressing endogenously tagged StrepII-tag-GFP-labeled LCα. Protein expression was analyzed using antibodies specific for indicated proteins. WT HeLa cells were used as a negative control. **(E)** Widefield images of polyclonal GFP-sorted HeLa cells with endogenously SII-GFP-tagged LCα stained for GFP and actin (phalloidin). Zooms of the boxed areas (orange squares) are shown in the bottom row panels.

5

Direct observation of dynamic protein interactions involving human microtubules using solid-state NMR spectroscopy

Yanzhang Luo[1*], Shengqi Xiang[1*], Peter Jan Hooikaas[2],
Laura van Bezouwen[3], Jijumon A.S.[4,5], Carsten Janke[4,5],
Friedrich Förster[3], Anna Akhmanova[2] and Marc Baldus[1]

Nature Communications (2020); 11:18

* These authors contributed equally

---

[1] NMR Spectroscopy, Bijvoet Center for Biomolecular Research, Utrecht University, Padualaan 8, 3584 CH Utrecht, The Netherlands.

[2] Cell Biology, Neurobiology and Biophysics, Department of Biology, Faculty of Science, Utrecht University, Padualaan 8, 3584 CH, Utrecht, The Netherlands.

[3] Cryo-Electron Microscopy, Bijvoet Center for Biomolecular Research, Utrecht University, Padualaan 8, 3584 CH, Utrecht, The Netherlands.

[4] Institut Curie, PSL Research University, CNRS UMR3348, F-91405, Orsay, France.

[5] Université Paris Sud, Université Paris-Saclay, CNRS UMR3348, F-91405, Orsay, France

Abstract

Microtubules are important components of the eukaryotic cytoskeleton. Their structural organization is regulated by nucleotide binding and many microtubule-associated proteins (MAPs). While cryo-EM and X-ray crystallography have provided detailed views of interactions between MAPs with the microtubule lattice, little is known about how MAPs and their intrinsically disordered regions interact with the dynamic microtubule surface. NMR carries the potential to directly probe such interactions but so far has been precluded by the low tubulin yield. We present a protocol to produce [13C, 15N]-labeled, functional microtubules (MTs) from human cells for solid-state NMR studies. This approach allowed us to demonstrate that MAPs can differently modulate the fast time-scale dynamics of C-terminal tubulin tails, suggesting distinct interaction modes. Our results pave the way for in-depth NMR studies of protein dynamics involved in MT assembly and their interactions with other cellular components.

Introduction

In eukaryotic cells, microtubules (MTs) are cytoskeletal polymers essential for many biological processes, including cell division, migration, polarization, and intracellular trafficking. MTs are assembled from α/β-tubulin heterodimers and are intrinsically polarized, with the highly dynamic, β-tubulin-exposed plus end, which rapidly switches between growth and shrinkage in a process termed "dynamic instability" (Desai and Mitchison, 1997). The dynamic instability of MTs is caused by GTP binding and hydrolysis on tubulin dimers.

Many MT-associated proteins (MAPs) regulate MT structure and function by interacting with MT lattices and/or MT ends (Akhmanova and Hoogenraad, 2015; Akhmanova and Steinmetz, 2008). Cryo-electron microscopy (EM) has made substantial progress to elucidate the interaction between MAPs and the MT lattice (Alushin et al., 2014; Nogales and Zhang, 2016), including the cryo-EM reconstruction of the MAP tau binding to MTs (Kellogg et al., 2018). However, the direct observation of dynamic regions of tubulin, including the unstructured C-terminal tails that are critical for binding of different MT-associated proteins such as tau (Kellogg et al., 2018) has remained challenging due to their intrinsic flexibility. To model such tubulin regions computational approaches were used, for example in the context of tau binding to MTs (Kellogg et al., 2018) or, more recently, to determine the effect of α-tubulin acetylation on MT structure and stability (Eshun-Wilson et al., 2019). Given the wide-spread relevance of protein dynamics for MT function and, in particular, of tubulin tails for cellular processes and human disorders (Gadadhar et al., 2017), direct experimental insight into the dynamic interaction of MTs with MAPs is hence of significant interest.

Nuclear magnetic resonance (NMR) spectroscopy has been shown to provide unique structural insights into heterogeneous and dynamical systems at atomic resolution and on different time scales (see, e.g., (Peng, 2012; Quinn and Polenova, 2017; Renault et al., 2010; Wright and Dyson, 2015)). Previously, solid- and solution-state NMR have been used to study the interactions between MTs and isotope-labeled MAPs or small drugs (Atherton et al., 2017; Atherton et al., 2019; Kadavath et al., 2018; Kesten et al., 2019; Kubo et al., 2013; Kumar et al., 2010; Yan et al., 2015). However, these studies were restricted to studying ligands that could be isotope labeled using bacterial expression systems. Thus far, the direct study of functional MTs from human cells that carry NMR-active labeling was precluded due to insufficient protein amounts. In addition, solution-state NMR studies on intact MTs are hampered by protein size and insufficient molecular tumbling. In the following, we describe a solid-state NMR (ssNMR) approach to directly study the interaction of labeled MTs with their binding partners. In particular, this method enables us to probe the dynamics of intact MTs. Moreover, we examine the influence of two different MT-associated proteins upon the C-terminal tail dynamics. We investigate the binding of the CKK domain that is important for the minus-end recognition of the calmodulin-regulated spectrin-associated protein (CAMSAP) (Atherton et al., 2017; Atherton et al., 2019). Furthermore, we examine the effect of the microtubule-binding domain (MTBD) of the MAP7 family of proteins, which play an important role in regulating kinesin-based intracellular transport and for which the structural details of MT binding are currently unknown (Chaudhary et al., 2019; Hooikaas et al., 2019; Monroy et al., 2018; Pan et al., 2019). Our results suggest that MAP-tubulin tail interactions can involve both fast-time scale interactions between mobile chains as well as slow-time scale binding/unbinding events within stable MT–MAP complexes.

Results

Functional MTs for ssNMR studies

To obtain milligram quantities of human MTs we used HeLa S3 cells that not only grow as adherent culture but also in suspension, thereby increasing the efficiency of large-scale cultures (Souphron et al., 2019). In addition, HeLa S3 cells express only a few tubulin isotypes (Davis et al., 2010; Newton et al., 2002) resulting in comparatively homogeneous samples. We isolated tubulin from cell lysates by using a polymerization and depolymerization cycle

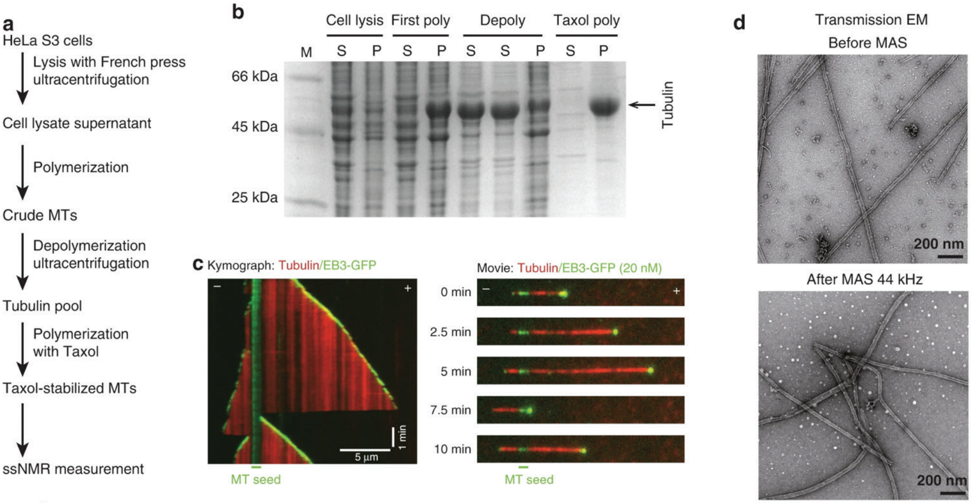
a
HeLa S3 cells
Lysis with French press ultracentrifugation
Cell lysate supernatant
Polymerization
Crude MTs
Depolymerization ultracentrifugation
Tubulin pool
Polymerization with Taxol
Taxol-stabilized MTs
ssNMR measurement
b
Cell lysis
First poly
Depoly
Taxol poly
M
S
P
S
P
S
S
P
S
P
66 kDa
45 kDa
25 kDa
Tubulin
C Kymograph: Tubulin/EB3-GFP
−
+
1 min
5 µm
MT seed
Movie: Tubulin/EB3-GFP (20 nM)
0 min
2.5 min
5 min
7.5 min
10 min
MT seed
d
Transmission EM
Before MAS
200 nm
After MAS 44 kHz
200 nm

Figure 1 - MT preparation from HeLa S3 cells and sample characterization.
(A) Schematic overview of the sample preparation. **(B)** SDS-PAGE analysis from each purification step. M: protein marker; S: supernatant; P: pellet; first poly: first polymerization; depoly: depolymerization; Taxol poly: polymerization with Taxol. The uncropped gel is provided as a Source Data file. **(C)** Functional characterization of purified HeLa S3 tubulin. Kymograph (left) and movie stills (right) of an *in vitro* polymerized MT imaged for 10 min on a TIRF microscope correspond to Fig. S1C. Time points and MT plus (+) and minus (−) ends are indicated. **(D)** Characterization of morphology of HeLa MTs before and after MAS NMR experiments by EM.

to remove contaminations (Fig. 1a, b). Subsequently, we polymerized tubulin into MTs with high concentration of 1,4-piperazinediethanesulfonic acid (PIPES) to remove MAPs binding and stabilized MTs with Taxol (Weaver, 2014). As demonstrated by sodium dodecyl sulfate (SDS) polyacrylamide gel electrophoresis, Taxol-stabilized MTs showed a purity of 90% (Fig. 1b). To check functionality, we incubated our prepared MTs with a fluorescently tagged MTBD of MAP7 domain-containing protein 3 (MAP7D3, in the following abbreviated by MAP7), which served as a MT-binding probe, and found that the purified MTs were decorated by this protein fragment (Supplementary Fig. 1A, B, left). Notably, the binding of MAP7 induced some bundling of MTs (Supplementary Fig. 1A, B). However, the MT bundling does not affect the structure and the dynamics of tubulin C-terminal tails of each individual MT (Walczak and Shaw, 2010), and hence did not interfere with our ssNMR experiments presented below. We also investigated whether HeLa S3-derived tubulin can polymerize without Taxol and shows dynamic instability by preparing an additional sample without Taxol, leading to soluble tubulin after a subsequent depolymerization. The resulting tubulin was used in an *in vitro* reconstitution assay where MTs are polymerized from stable MT seeds with GFP-tagged end binding protein 3 (EB3) as a marker for growing ends. The tubulin we prepared polymerized into MTs and showed phases of growth and shortening (Fig. 1c and Supplementary Fig. 1C, Movie 1), demonstrating that the purified tubulin remains polymerization-competent using our protocol. Taken together, this protocol allowed us to purify functional tubulin from mammalian cells that could form MTs, thus providing the basis for our NMR experiments described below.

To obtain isotope-labeled MTs for ssNMR studies, we grew HeLa S3 cells in 2L [13C, 15N] labeled medium and obtained isotope-labeled, Taxol-MTs (in the following abbreviated by MTs) using the procedure described above. The sample was then packed into a 1.3 mm MAS NMR rotor and subjected to extended measurement periods using fast MAS rates. To ensure sample integrity under such conditions, we used transmission EM and TIRF microscopy that confirmed that our MT samples remained intact (Fig. 1d and Supplementary Fig. 1B).

MT samples as seen by 13C and 31P ssNMR spectroscopy

To evaluate the sample quality, we first recorded a 2D 13C–13C dipolar-based correlation spectrum using radio frequency-driven recoupling (RFDR) (Bennett et al., 1998) recoupling and compared our data to chemical-shift predictions for MTs (PDB ID: 5SYF) using FANDAS 2.0 (Narasimhan et al., 2018). Overall, the spectrum agreed with in silico estimates (Fig. 2a, left). For example, in Cα–Cβ regions of serine, threonine and alanine residues, signals were observed in qualitative agreement with predictions for α-helical and β-strand conformations (Fig. 2a, right). Interestingly, alanine signals that were not observed (Fig. 2a, top right) resided in random-coil conformation and related to residues in tubulin loops. The latter observation would be consistent with the occurrence of loop motion as discussed elsewhere (Eshun-Wilson et al., 2019) at the experimental temperature (~298 K) in our dipolar-based experiments. While residue-specific analysis of such effects will require the extension to 3D ssNMR spectroscopy, possibly in combination with amino acid specific labeling11, the spectral resolution observed in Fig. 2 for such a large complex hence speaks in favor of a homogenous sample of polymerized MTs.

This notion was further confirmed by 31P NMR signals stemming from nucleotides binding to MTs. In general, α/β-tubulin dimers contain two nucleotide-binding sites. The GTP molecule bound to α-tubulin is non-hydrolysable, whereas, the nucleotide bound to β-tubulin is exchangeable, and GTP is hydrolyzed to GDP upon MT polymerization (Menendez et al., 1998) (Fig. 2b, left). Indeed, we observed ssNMR signals from both GTP and

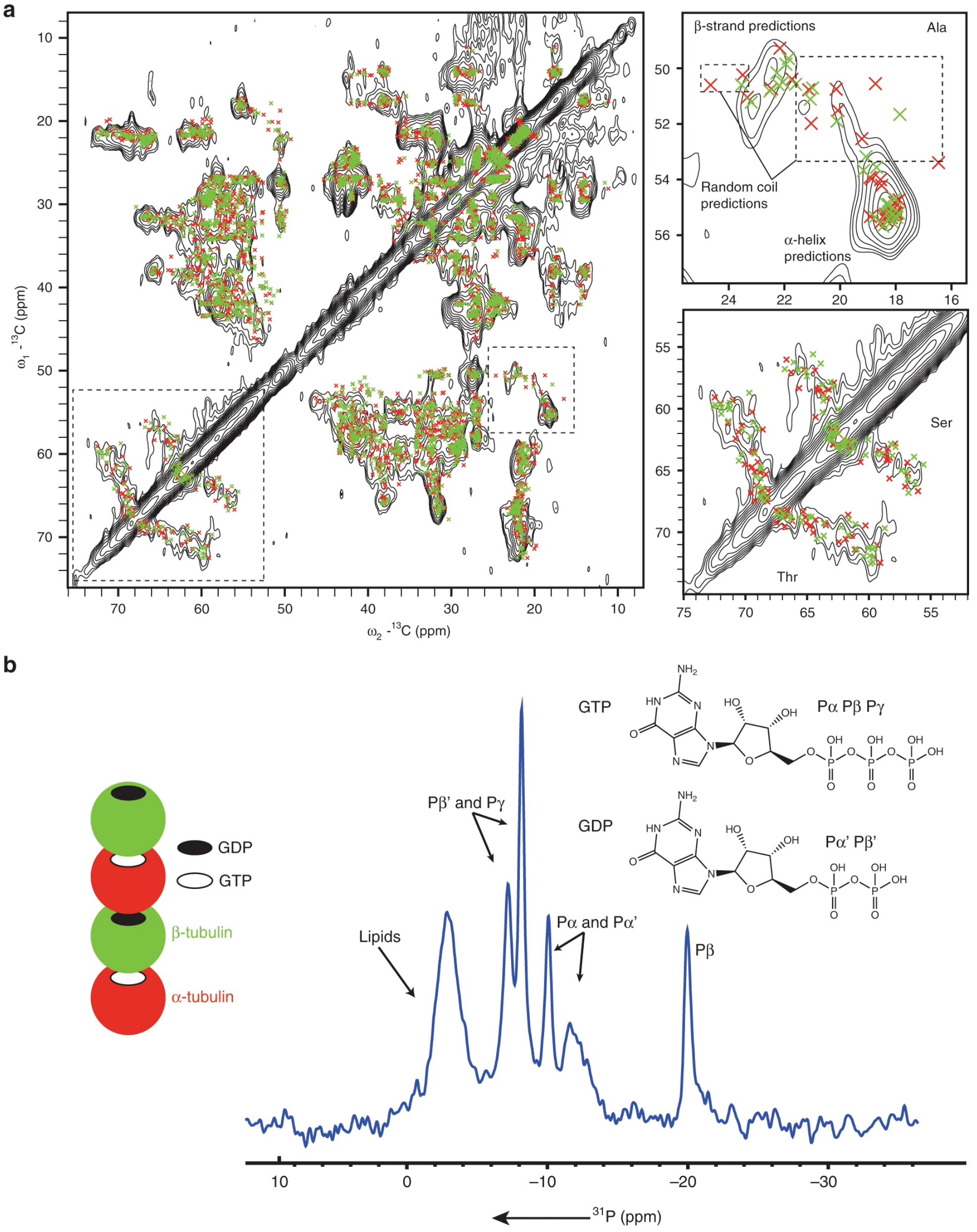

Figure 2 - SsNMR spectra of [13C, 15N]-labeled MTs.
(A) The 2D 13C–13C radio frequency-driven recoupling (RFDR) experiment was performed at 270 K set temperature with a MAS rate of 44 kHz with zoom in's on serine, threonine and alanine Cα–Cβ regions. Crosses indicate the chemical shift predictions for MTs from SHIFTX2 (Han et al., 2011) and FANDAS 2.0 (Narasimhan et al., 2018) based on the EM structure (PDB 5SYF). Red and green crosses represent predictions for α-tubulin and β-tubulin, respectively. **(B)** Schematic representation of the GTP/GDP binding to tubulin in MTs (left), and 1D H–31P CP experiment at ambient temperature with MAS rate of 11 kHz allows to observe GTP and GDP bound to MTs.

GDP in 1D 31P CPMAS spectrum (Fig. 2b, right) that were well resolved compared to previous results on lyophilized MTs (Lee et al., 2015). The observed spectral resolution allowed us to distinguish NMR signals from both molecules (Supplementary Table 1) (Lee et al., 2015; Spoerner et al., 2017). Integrated peak intensities (Supplementary Table 1) correlated well with the notion that the molar ratio of GDP:GTP was 1:1, which is in agreement with previous studies (Alushin et al., 2014; Menendez et al., 1998)further supporting the idea that our ssNMR preparations were well folded and functional. Interestingly, we also observed an additional broad peak at –2.7 ppm, which may result from co-purified lipids (Kaur et al., 2016).

Probing tubulin tails by ssNMR

To probe mobile MT protein segments including the C-terminal tubulin tails (Fig. 3a), we carried out a series of scalar-based (J-based) ssNMR experiments (Alam and Holland, 2006) that previously revealed flexible parts within large biomolecules (Andronesi et al., 2005; Damman et al., 2019; Ward et al., 2015; Xiang et al., 2018). As discussed elsewhere (Andronesi et al., 2005; Schmidt-Rohr and Spiess, 1994), significant molecular motions with correlation times in the range of 10^{-9} to 10^{-7} s must be present to generate NMR signals in such ssN-

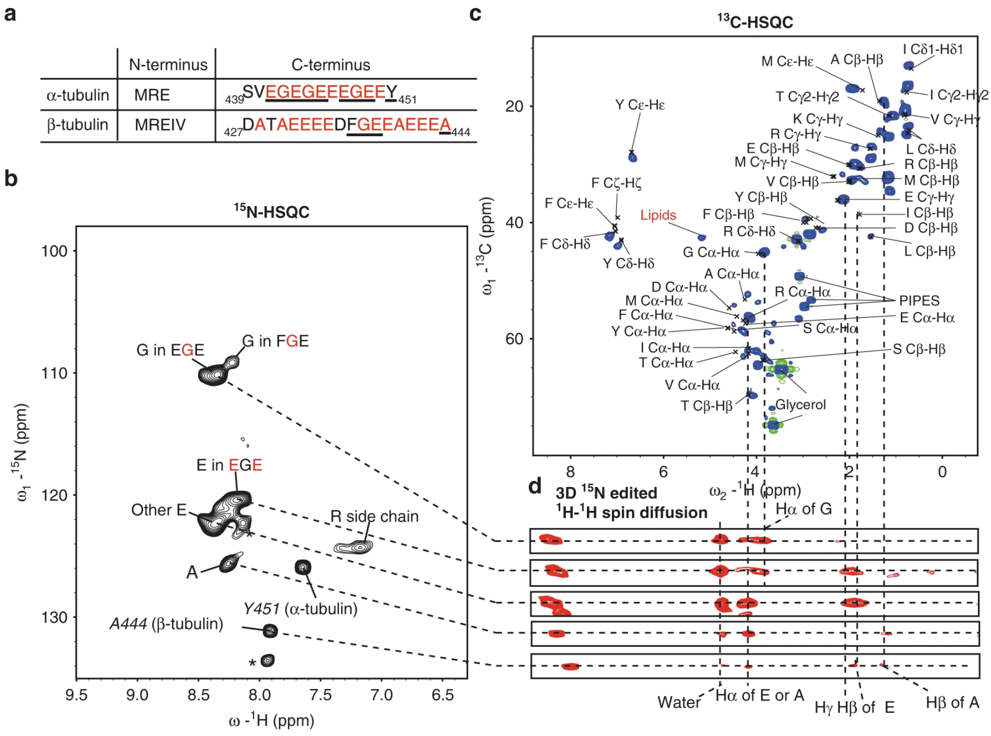

Figure 3 - Flexible tubulin C-terminal investigated by J-based ssNMR.
(A) The sequences of N- and C-termini of tubulin. Underlined residues showed sequential correlations in our ssNMR data sets. The protein sequences of α1 and β1 tubulin isotypes were used for analysis based on previous results (Davis et al., 2010). **(B)** 2D 15N-HSQC of [13C, 15N]-labeled MTs showed the flexible tubulin tails. **(C)** 2D 13C-HSQC of [13C, 15N]-labeled MTs showing the residues present in the tubulin tails. Due to the high flexibility, the signals from side chains of leucine, lysine as well as buffer compounds and lipids were also observed. **(D)** Strips of a 3D 15N-edited 1H–1H spin diffusion experiment showing the connections between 13C-HSQC and 15N-HSQC.

MR correlation experiments. Slower motions (in the range of milliseconds or slower) will, on the other hand, lead to signal loss (vide infra). In the current context, a 2D 15N-HSQC spectrum contained several signals with a limited spectral dispersion (Fig. 3b), in line with the presence of a mobile unstructured protein region. Using additional 2D 13C-HSQC (Fig. 3c, d) 15N-edited 1H–1H spin diffusion spectra (Fig. 3d), we could confirm that correlations observed in the 15N-HSQC spectrum are mainly due to glycine, glutamate, and alanine, which are the most abundant residues in the tubulin tails (Fig. 3a). Moreover, the corresponding resonance frequencies seen in the 2D 13C-HSQC reflected random-coil chemical shifts of these amino acids. Note that the latter spectrum contained additional signals from mobile side chains as well as correlations stemming from residual lipids (Fig. 2b) and buffer.

We could further identify correlations stemming from glutamate and alanine residues by tracing HN to Hβ or Hγ correlations. Interestingly, one glutamate NH signal showed correlations to the Hα of glycine, indicating that the corresponding glutamate residues are next to glycine residues (Fig. 3d, second strip). Such correlations are only expected for the α-tubulin C-terminal tails (Fig. 3a). On the other hand, the other glutamate peak showed no contacts to glycine Hα (Fig. 3d, third strip), suggesting that these correlations most likely reflect glutamate residues of the β-tubulin C-terminal tail (Fig. 3a). In addition, we detected two glycine signals with an approximately 3:1 intensity ratio in line with three glycine residues in EGE motifs of the α-tubulin tail and one glycine representing the FGE motif of the β-tubulin. These tentative assignments were in good agreement with previous solution-state NMR studies(Lefevre et al., 2011) of a peptide that contained C-terminal residues of human α-tubulin and enabled us to tentatively assign the most C-terminal residue of α-tubulin, i.e., Tyr451 (Fig. 3a). Moreover, we could identify one alanine correlation which most likely reflects the last residue of the β-tubulin based on its high 15N chemical-shift value, and the correlations from its amide proton to the Hβ of Ala and Glu. Lastly, two correlations which may at least in part stem from the N-terminal residues (Fig. 3a) remained unassigned due to lack of cross peaks in the 3D spectrum (Fig. 3b, peaks indicated by asterisks). The corresponding resonance frequencies would speak against posttranslational modifications (PTMs) seen in previous solution-state NMR on *Tetrahymena thermophila* tubulin (Wall et al., 2016). Indeed, earlier work showed that HeLa tubulin mostly lacks PTMs on tubulin tails (Barisic et al., 2015). Taken together, our results suggested that both α- and β-tubulin tails are disordered and highly mobile on a nanosecond time scale.

Tubulin tail dynamics are modulated by the CKK domain

In our previous work we could decipher molecular properties that enable CKK domains of the CAMSAP protein family to preferentially associate with the transition zone between curved protofilaments and the regular MT lattice at MT minus ends (Atherton et al., 2017; Atherton et al., 2019). We found that the CKK domain that consists of folded protein core and disordered termini associates with the groove between two laterally attached tubulin dimers and discovered that CKKs can subtly differentiate specific tubulin conformations to enable MT minus-end recognition (Atherton et al., 2019). However, these studies did not reveal how tubulin tails, which are important for CKK binding (Atherton et al., 2017) are involved in these events. Using our ssNMR protocol, we in the following investigated the influence of CKK binding upon the C-terminal tubulin tails. For this purpose, we purified the unlabeled CAMSAP1 CKK N1492A mutant that exhibits reduced minus-end selectivity and binds with higher affinity to MTs compared to wild-type CKK (Atherton et al., 2017; Atherton et al., 2019)We then added unlabeled CKK to [13C, 15N]-labeled MTs and repeated our 15N-HSQC experiments. Compared to free [13C, 15N]-labeled MTs, we observed strong changes in the 2D correlation spectrum (Fig. 4a) that relate to arginine residues of MTs as

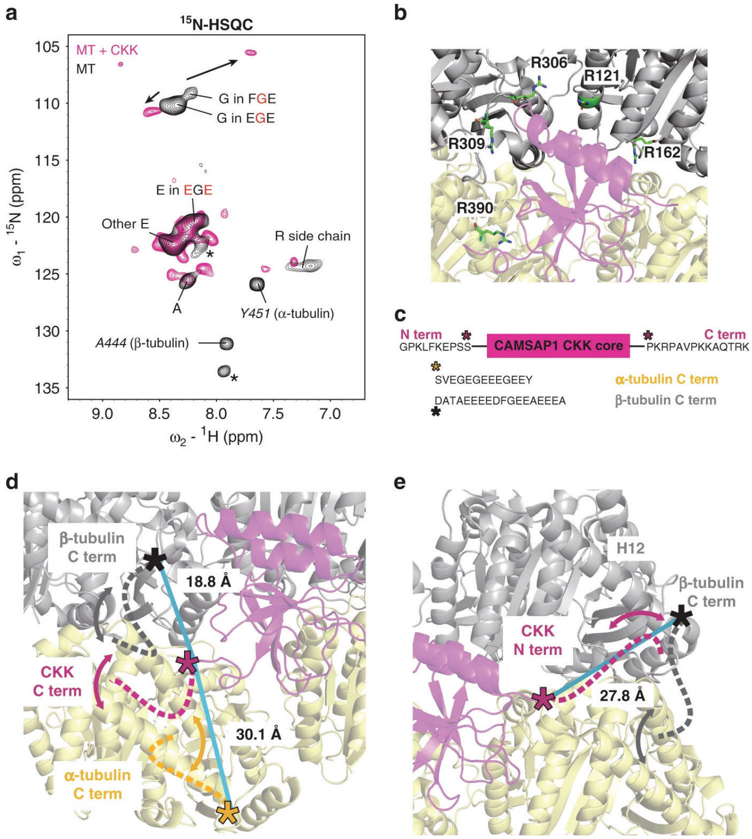

Figure 4 -Tubulin C-terminal tail dynamics are modulated by the CKK domain.
(A) Comparison of 2D 15N-HSQC spectra obtained from [13C, 15N]-labeled MTs (black) and unlabeled CAMSAP1 CKK N1492A in complex with [13C, 15N]-labeled MTs (magenta). **(B)** Zoom-in on arginine residues found in the CKK-MT cryo-EM structure (PDB 5M5C), ref. 15) that are located on α-tubulin (yellow) and β-tubulin (gray) and within 6 Å to CKK domain (magenta). **(C)** Top: amino-acid sequences of CKK termini with last residues observed in the cryo-EM structure (PDB 5M5C) indicated by stars. Bottom: C-terminal tails of α-tubulin and β-tubulin with last residues detected the cryo-EM structure (PDB 5M5C) are indicated by yellow and black stars, respectively. **(D)** Dynamic (indicated by double-headed arrows) C-terminal tubulin (dashed black and yellow lines) and CKK (magenta) tails. Blue lines measure the distance between the last residues observed in the cryo-EM structure of both tubulin tails (indicated by black and yellow stars) to the last CKK C-terminal residue observed in cryo-EM (magenta star).

well as to the C-terminal residues of α-tubulin and of β-tubulin. In the following, we discuss our ssNMR spectral findings and their relationship to previous results for each of these three aspects.

Firstly, signals for the side chains of arginine residues were strongly reduced compared to free MTs. This observation confirmed our previous findings that arginine residues of both α- and β-tubulin tubulin are located in the binding region of the CKK domain (Atherton et al., 2017) (Fig. 4b). Furthermore, our recent studies also showed that the binding of CKK induces protofilament skew leading to a reduced lateral space between tubulin dimers (Atherton et al., 2017; Atherton et al., 2019). Arginine residues located in regions distant from the CKK binding epitope but involved in these lateral interactions between tubulin may hence also become less dynamic (Zhang et al., 2015).

Secondly, several correlations including the last C-terminal residue of β-tubulin, A444, disappeared after CKK was bound to MTs and correlations appeared in the alanine, glycine and tyrosine regions (Fig. 4a). These spectral changes would be consistent with conformational exchange on the fast time scale (Peng, 2012) upon CKK binding. Interestingly, glycines in the FGE segment and alanine residues are only found in the C-terminal tail of β-tubulin suggesting that the β-tubulin tail is involved in this dynamic interaction. Notably, the C-termini of both β-tubulin (17 residues, Fig. 4c) and of the CKK domain (13 residues, Fig. 4c) were not observed in the previous cryo-EM structure (Atherton et al., 2017). Most likely, the CKK C-terminus hence retains conformational variability upon binding to MTs. Assuming fully extended backbone conformations, both CKK and tubulin C-terminal tails could sample a distance range of at least 60 and 45Å (Ainavarapu et al., 2007), respectively, which would readily allow for such dynamic interactions between both mobile tails as indicated in Fig. 4d. Notably, previous EM and ssNMR experiments suggested that the N-terminus of CKK (9 residues) could interact with the C-terminal part of β-tubulin (Fig. 4c, e), which would be in line with our NMR data.

Thirdly, we also observed changes in ssNMR signal frequencies and intensities after CKK binding for glycine in EGE segments and residue Y451, respectively, that are both found in the C-terminal tail of α-tubulin (Fig. 4a). As shown in Fig. 4c, d, the C-terminal tail of α-tubulin with its 12 residues could hence also dynamically interact with the C-terminus of CKK.

Taken together, our results strongly suggest that that the C-terminal tubulin tails dynamically interact with CKK domain on the nano- to microsecond time scale. Combination of these results with our previous EM and ssNMR data further refines this notion, suggesting that the CKK C-terminus interacts with both α- and β-tubulin while the CKK N-terminus engages in fast interactions with the C-terminus of β-tubulin. Future ssNMR experiments may allow us to further dissect the details of these dynamic interactions, including the more precise determination of motional time scales in a residue-specific manner.

MAP7-binding reduces MT tail dynamics

The MAP7 family of proteins plays an important role in regulating kinesin-based intracellular transport. However, the structural details of MAP7–MT interaction are currently unknown (Chaudhary et al., 2019; Monroy et al., 2018; Pan et al., 2019). A secondary-structure prediction of MAP7 on the basis of its amino acid sequence as well as preliminary NMR experiments on free MAP7 in solution suggest that the MAP7 domain adopts a highly α-helical structure separated by a short loop comprising R144 to T146 and flanked by unstructured termini (Fig. 5a).

To obtain insight into the interaction of MT tails with bound MAP7, we repeated our J-based experiments on [13C, 15N]-labeled MTs after adding unlabeled MAP7 in a 2:1 ratio ensuring full decoration of MTs (see Methods). Interestingly and unlike in the case of binding of the CKK domain to MTs, we did not detect any frequency changes in the 2D 15N-HSQC ssNMR correlation spectrum (Fig. 5b, cyan) compared to the case of free MTs. Instead, signals from both C-terminal tubulin tails, including the identified EGE and FGE segments as well as other E residues were strongly attenuated (Fig. 5c and Supplementary Fig. 2) compared to the most C-terminal residues of α- and β-tubulin, Y451 and A444, respectively. These observations can be explained by a slow exchange process (millisecond time scale or longer) between freely mobile α- and β-tubulin tail conformations (visible in

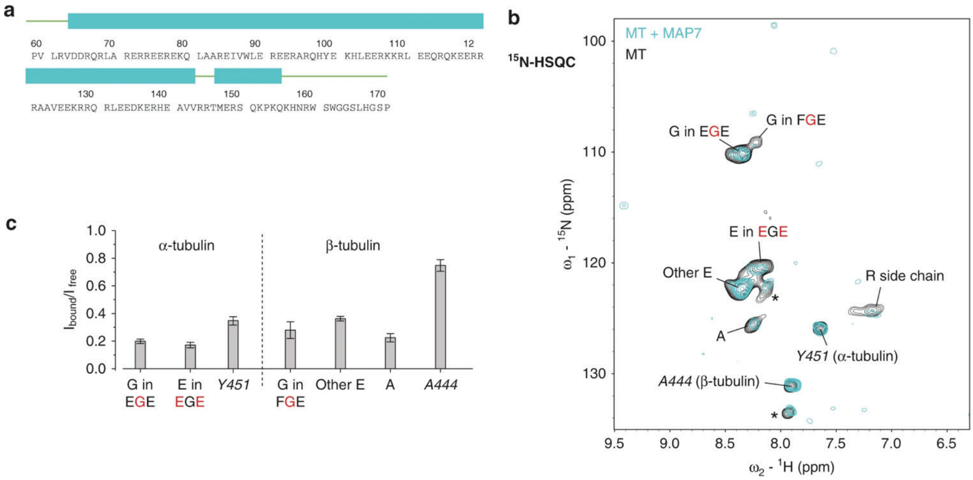

Figure 5 - Tubulin C-terminal tails interact with MAP7.
(A) Secondary structure prediction of MAP7-MTBD by JPred (Drozdetskiy et al., 2015). **(B)** Spectral comparison of 2D 15N-HSQC spectra obtained from [13C, 15N]-labeled MTs (black) and unlabeled MAP7-MTBD in complex with [13C, 15N]-labeled MTs (cyan). **(C) S**ignal intensity ratios of resolved peaks in 15N-HSQC between MAP7-MTBD bound MTs and free MTs. Error bars were calculated based on the NMR signal to noise ratio of each peak in the two spectra. Signal intensity ratios are provided as a Source Data file.

the spectra) and C-terminal tails directly bound to MAP7. Note that the latter states would be invisible in our J-based experiments. In a simple two-state model, the relative amount of bound populations would be given by $P^{bound} = 1 - I^{bound}/I^{free}$ (see, e.g. (Lakomek et al., 2019; Peng, 2012)) seen in Fig. 5c leading to values of up to a 80% bound tail residues around the EGE and FGE terminal segments in α and β tubulin tails, respectively, and decreasing to around to a 65% and 25% bound population for the most C-terminal residues of α-tubulin (Tyr451) and of β-tubulin (Ala444), respectively. Unlike the case of CKK where dynamic tubulin C termini retain fast dynamics, these observations hence suggested that the MT termini directly bind to MAP7 at a time scale of milliseconds or longer. At the same time the formation of the MT–MAP7 complex also leads to the reduction of Arg side-chain dynamics which are apparent from our experimental data (Fig. 4b) and reminiscent of our findings in the case of CKK binding.

Discussion

Protein dynamics are critically involved in MT organization including the stochastic switching between growing and shrinking states as well as in the regulation of MTs by MAPs and other cellular factors. NMR carries the potential to directly probe such processes provided that functional and NMR-active MTs can be obtained. We have shown that high-resolution ssNMR spectra can be recorded on [13C, 15N] labeled MTs obtained from human cells. The MTs were polymerized from tubulin in functional form (Souphron et al., 2019), as confirmed by *in vitro* MT dynamics assays. In addition, our protocol allows obtaining purified, functional tubulin if Taxol is not included in the second polymerization (see Fig. 1c). Such preparations allow for NMR studies of human tubulin in solution (or after depolymerization), e.g., to study MT nucleation and its regulation by different MAPs and potentially related phase transitions (Hernandez-Vega et al., 2017). The narrow 31P NMR lines indicated homogenous binding of nucleotides on tubulin subunits that resulted in correctly polymerized MTs. This notion was further confirmed by 2D dipolar-based correlation experiments that are in qualitative agreement with a MT lattice as seen in cryo-EM structures. The absence of loop signals in our 2D ssNMR dipolar based data possibly points towards enhanced dynamics in protein loop regions as expected for tubulin domains, which are critical for MT dynamic instability or involved in PTMs such as the α-tubulin loop of residues P37–D47 (also known as αK40 loop7). Further ssNMR studies, possibly using three- or higher-dimensional ssNMR experiments may, in combination with tailored labeling, reveal the exact details of these motions.

Complementary to these experiments, proton-detected scalar-based 2D and 3D ssNMR experiments allowed us to directly study the disordered, flexible tubulin tails that are critically involved in MAP binding (Lefevre et al., 2011) and which are invisible in all available high-resolution structures. In the current context, we tracked the effect of binding of the CKK domain of CAMSAP and of MAP7 for the dynamics of α- and β-tubulin C-terminal tails. Our data suggest that MAP-tubulin tail interactions can take place over a remarkably wide time scale. In the case of CKK, the dynamics of both α- and β-tubulin C-terminal tails are rapidly (in the nano to microsecond scale) modulated by the CKK domain, confirming our previous finding that tubulin C-terminal tails are important for CKK binding. Combination of these experiments with results of our earlier cryo-EM and ssNMR studies (Atherton et al., 2017; Atherton et al., 2019) provided further insight regarding the details of these dynamic interactions and suggest that the disordered termini of CKK are involved in these interactions. On the other hand, MAP7 binding to MTs is characterized by tubulin C-terminal tails that exchange between bound (major state) and free (minor state) conformations on a much slower (millisecond or longer) time scale.

The remarkable difference between CKK and MAP7 binding to the tubulin tails may be related in part to the structural and dynamical properties of the MAP itself. For example, the mobile CKK termini comprise several positively charged amino acids (Fig. 4c), whereas, in the case of MAP7, such residues are mostly found in the putatively structured core of MAP7 (Fig. 5a). In addition, the molecular details of the MAP binding epitope on MTs may play a role in defining tail interactions. As we have shown earlier (Atherton et al., 2017; Atherton et al., 2019), CKK binding takes place between protofilaments. On the other hand, MAP7 is known to compete for binding to MTs (Monroy et al., 2018) with the protein tau and hence is likely to be associated with the protofilament crest as seen for tau (Kellogg et al., 2018). Further ssNMR studies may help to dissect these dependencies, including the exact CKK and MAP7 regions interacting with the C-terminal tails. Such studies may involve isotope labeled MAPs or mixed labeled (Etzkorn et al., 2004) MAP-MT preparations.

Moreover, the presented approach could be readily extended to study the interactions of longer variants of MAPs that, in addition to the minimal MT binding region, comprise intrinsically disordered protein domains as well as the Kinesin-1 binding domain (Pan et al., 2019). As we have shown recently for the case of mRNA processing bodies (Damman et al., 2019), such studies not only could target bona fide MTs but they could also reveal dynamic interactions leading to the compartmentalization of the MT lattice by condensation of tau or other MAPs (Hernandez-Vega et al., 2017; Siahaan et al., 2019; Tan et al., 2019). Combination of such NMR experiments with data obtained from cryo-EM and fluorescence microscopy experiments could lead to a comprehensive view on the structural and dynamical aspects that define the interaction between MT and MAPs or other cellular players that regulate MT function.

Methods

Preparation of MTs for ssNMR experiments and *in vitro* assays

The HeLa S3 cell line (ATCC® CCL2.2™) was used for culturing. [13C, 15N] labeled DMEM medium was prepared in the same way as described in a previous study (Kaplan et al., 2016) except that we used 3.5 g/L glucose in order to maintain cell viability in suspension culture. The cells were first cultured in the labeled medium on two 150 mm cell culture dishes, and then transferred into 12 dishes with the same medium. When the culture reached a confluence of ~80% on the plates, cells were trypsinized and transferred into 2 L labeled medium and cultured in 7 1 L Erlenmeyer shaker flasks (Corning) until the cell density reached ~1.2–1.5 × 106/mL. Cells were then harvested by centrifugation at 500 × g for 20 min at 4 °C. The cell pellet was collected and resuspended in phosphate-buffered saline and centrifuged again at 500 × g for 15 min at 4 °C and used for MT preparation.

The purification of Taxol-stabilized MTs was performed based on the published protocols (Guedes-Dias et al., 2019; Nirschl et al., 2016) with minor modifications. Harvested cells were first resuspended with 1g cell/mL lysis buffer (80 mM PIPES pH 6.8, 1 mM EGTA, 1 mM MgCl2, 1 mM β-mercaptoethanol, 1 mM PMSF and protease inhibitors (Roche) and lysed on ice by passing through a French Press homogenizer 3 times at 1000 psi. Subsequently, lysed cells were spun down at 120,000 × g at 4 °C for 30 min and the supernatant was collected. The supernatant was centrifuged again at 5000 × g at 4 °C for 15 min to remove the remaining cell debris and then a half volume of glycerol and 1 mM GTP were added and mixed well. MT polymerization was carried out by incubating the mixture at 30 °C for 30 min. Subsequently, the crude MT pellet was spun down at 150,000 × g (Type 70.1 Ti, Beckman Coulter) at 30 °C for 30 min and placed on ice. The pellet was then resuspended in BRB80 buffer (80 mM PIPES pH 6.8, 1 mM EGTA, 1 mM MgCl2) supplemented with protease inhibitors and kept on ice for 30 min to allow for MT depolymerization. For a more efficient depolymerization, the solution was resuspended frequently and then centrifuged at 150,000 × g (Type 70.1 Ti, Beckman Coulter) at 4 °C for 30 min, and the supernatant was collected. An equal volume of high concentration PIPES buffer (1 M PIPES pH 6.8, 10 mM MgCl2, 20 mM EGTA), together with an equal volume of glycerol and 1 mM GTP were then added to the supernatant and mixed well. MT polymerization was again performed at 30 °C for 30 min. Subsequently, 20 μM Taxol (Paclitaxel, Sigma) was added to the reaction and incubated for 20 min to generate Taxol-stabilized MTs. Taxol-stabilized MTs were then spun down at 150,000 × g (TLA-55, Beckman Coulter) at 30 °C for 30 min washed with BRB80 containing 20 μM Taxol and protease inhibitors.

For all in-vitro assays, Taxol-stabilized MTs were prepared in the same way as described above. Regarding the sample used in the *in vitro* dynamics assay, the preparation of tubulin was similar except that Paclitaxel was not included during the second MT polymerization. After the second MT polymerization, MTs were spun down and resuspended in ice cold BRB80 supplemented with protease inhibitors. The second depolymerization was done on ice for 30 min and then centrifuged at 150,000 × g at 4 °C for 30 min. Purified tubulin was aliquoted and snap-frozen in liquid nitrogen, stored at –80 °C until use.

***In vitro* assays**

MT seeds were prepared by incubating 20 μM porcine tubulin mix containing 70% unlabeled, 18% biotin–tubulin and 12% HiLyte488-tubulin with 1 mM guanylyl-(α,β)-methylenediphosphonate (GMPCPP) at 37 °C for 30 min. Polymerized MTs were separated from the mix by centrifugation in an Airfuge for 5 min. MTs were subjected to one round of depolymerization and polymerization in 1 mM GMPCPP, and the final MT seeds were stored in MRB80 buffer (80 mM K-PIPES pH 6.8, 1 mM EGTA, 4 mM MgCl2) containing 10% glycerol.

In vitro reconstitution assays were performed in flow chambers. Flow chambers were assembled by sticking plasma-cleaned glass coverslips on microscopic slides with double-sided tape. Assays with Taxol-stabilized HeLa MTs were performed in MRB80 prewashed chambers. The *in vitro* reaction mixture consisted of 15 μM HeLa MTs (stabilized by 20 μM Taxol) that were either before or after MAS at 44 kHz for 24 h, 150 nM MAP7D3-MTBD, 50 mM

KCl, 0.1% Methylcellulose, 0.5 mg/ml κ-casein, 1 mM GTP, oxygen scavenging system (20 mM glucose, 200 µg/ml catalase, 400 µg/ml glucose-oxidase, 4 mM DTT). After centrifugation in an Airfuge for 5 min at 119,000 × g, the reaction mixture was added to the flow chamber and sealed with vacuum grease.

Dynamic MT assays were performed in flow chambers that were functionalized by sequential incubation with 0.2 mg/ml PLL-PEG-biotin (Surface Solutions, Switzerland) and 1 mg/ml NeutrAvidin in MRB80 buffer for 5 min. MT seeds were attached to the biotin-NeutrAvidin links and incubated with 1 mg/ml κ-casein. The *in vitro* reaction mixture consisted of 15 µM HeLa tubulin (quantified using bovine serum albumin standard), 20 nM GFP-EB3 and 0.5 µM rhodamine-labeled porcine brain tubulin, 50 mM KCl, 0.1% methylcellulose, 0.5 mg/ml κ-casein, 1 mM GTP, oxygen scavenging system (20 mM glucose, 200 µg/ml catalase, 400 µg/ml glucose-oxidase, 4 mM DTT). After centrifugation in an Airfuge for 5 min at 119,000 g, the reaction mixture was added to the flow chamber containing the HiLyte-488 MT seeds and sealed with vacuum grease. HiLyte488- and rhodamine-tubulin were purchased from Cytoskeleton Inc.

All *in vitro* experiments were conducted at 30 °C. Data were collected using total internal reflection fluorescence (TIRF) microscopy on an inverted research microscope Nikon Eclipse Ti-E (Nikon) with the perfect focus system (Nikon), equipped with Nikon CFI Apo TIRF 100× 1.49 N.A. oil objective (Nikon, Tokyo, Japan), Photometrics Evolve 512 EMCCD (Roper Scientific) and Photometrics CoolSNAP HQ2 CCD (Roper Scientific) and controlled with MetaMorph 7.7 software (Molecular Devices, CA). The microscope was equipped with TIRF-E motorized TIRF illuminator modified by Roper Scientific France/PICT-IBiSA, Institut Curie. For excitation lasers we used 491 nm 100 mW Stradus (Vortran), 561 nm 100 mW Jive (Cobolt) and 642 nm 110 mW Stradus (Vortran). We used an ET-GFP 49002 filter set (Chroma) for imaging of proteins tagged with GFP and an ET-mCherry 49008 filter set (Chroma) for imaging X-rhodamine labeled tubulin amd mCherry-labeled MTBD of MAP7D3. For simultaneous imaging of green and red fluorescence we used an Evolve512 EMCCD camera (Photometrics), ET-GFP/mCherry filter cube (59022, Chroma) together with an Optosplit III beamsplitter (Cairn Research Ltd.) equipped with double emission filter cube configured with ET525/50m, ET630/75m, and T585lprx (Chroma). To keep *in vitro* samples at 30 °C, we used a stage top incubator (model INUBG2E-ZILCS; Tokai Hit). Images were processed using ImageJ. All images were modified by linear adjustments of brightness and contrast. Kymographs were generated using ImageJ plugin KymoResliceWide v.0.4. https://github.com/ekatrukha/KymoResliceWide; copy archived at https://github.com/elifesciences-publications/KymoResliceWide).

Transmission EM

Taxol-stabilized MTs were prepared with and without MAS spinning as described above. The protein samples were negatively stained with 2% uranyl acetate on glow-discharged carbon coated copper grids. Images were recorded on a Tecnai 20 electron microscope with a LaB6 filament, operating at 200 kV with a BM Eagle 4 K CCD camera (ThermoFisher, Eindhoven, The Netherlands). Images were acquired with a defocus of approximately 5 µm The magnification used at 19,000 × g resulting in an effective pixel size of 1.14 nm on the specimen level.

Preparation of CAMSAP1 CKK N1492A in complex with MTs

[13C, 15N] labeled MTs were prepared as described above. The purification of CKK domain and preparation of CKK–MT complexes were performed based on the method published in (Atherton et al., 2017). CKK was first purified by a ÄKTA pure system with a POROS™ MC column that was saturated with Ni2+. The column was first equilibrated using washing buffer (50 mM phosphate buffer, pH 8, 500 mM NaCl, 1 mM β-mercaptoethanol and 20 mM imidazole). The protein was eluted with the same buffer but containing 400 mM imidazole. Subsequently, the protein was loaded onto a SEC HiLoad Superdex 75 26/60 column (GE Healthcare) equilibrated with 40 mM phosphate buffer, pH 7, supplemented with 150 mM NaCl and 1 mM DTT. The purified protein was then concentrated and used for ssNMR sample preparation. CKK N1492A was then added to a final concentration of 65.3 µM (4:1 CKK/tubulin) and incubated with labeled MTs at 37 °C for 30 min. The pellet was centrifuged down at 180,000 × g (Beckman TLA-55 rotor) at 30 °C for 30 min and washed with BRB80, without disturbing the pellet. The pellet was then transferred and packed into a 1.3 mm rotor.

Preparation of MAP7-MTBD and of MAP7-MTBD- MT complexes

The cDNA of human MAP7-MTBD (residues 59–170) was cloned into the pLICHIS vectors with the gene encoding a N-terminal His tag-Maltose-binding protein (MBP)-thrombin cleavage site by using ligation independent cloning (de Jong et al., 2006).Transformation was done with Escherichia coli Rosetta 2 cells and grown in 1 L unlabeled M9 medium. Induction of the protein was done when OD600 reached 0.6 with 0.3 mM IPTG at 20 °C for 16 h. The cultures were then centrifuged with 4000 × g at 4 °C for 20 min to harvest cells. Cell pellets were washed with 50 mM sodium phosphate buffer, pH 8, 500 mM NaCl, 1 mM β-mercaptoethanol and 20 mM imidazole and store at −80 °C.

For protein purification, cell lysis was done by sonication on ice and the cell lysate was collected by centrifugation of 40,000 × g at 4 °C for 30 min. Subsequently, the proteins were purified by a ÄKTA pure system with a POROS™ MC column that was saturated with Ni2+. The column was first equilibrated with the same buffer as above mentioned. The cell lysate was then loaded onto the column and the column was washed with 20 column volumes with the same buffer. Proteins were eluted with 50 mM sodium phosphate buffer, pH 8, 150 mM NaCl, 1 mM β-mercaptoethanol and 400 mM imidazole supplemented with protease inhibitors. The protein was concentrated and then diluted with 40 mM sodium phosphate buffer, pH 6.5 to reach a final concentration of imidazole of 20–30 mM. Subsequently, a cation exchange purification was performed with the Hitrap HP SP chromatography column (GE Healthcare Life Sciences). The column was first equilibrated with buffer A (40 mM sodium phosphate buffer, pH 6.5). The sample was then loaded onto the column and washed 5 column volumes with buffer A. A gradient elution was used by combining buffer A and buffer B (40 mM sodium phosphate buffer, 1 M NaCl, pH 6.5) to elute the protein. The protein was then concentrated and stored at 4 °C. Finally, thrombin was used to cleave the MBP fusion and then supplemented with protease inhibitors.

A 10 mg/ml porcine brain tubulin was diluted in BRB80 buffer (80 mM K-PIPES, pH 6.8, 1 mM EGTA, 1 mM MgCl2) to 2 mg/ml. After the addition of 1 mM GTP, the sample was incubated on ice for 5 min. MT polymerization was performed at 30 °C for 20 min. Subsequently, 20 µM taxol was added and incubated for 15 min at 30 °C. MT pelleting assays in the presence of MAP7-MTBD were performed by mixing with different molar ratios of MAP7-MTBD:MTs. As control treatments, taxol-stabilized MTs or MAP7-MTBD was applied alone. All the samples were then centrifuged at 180,000 × g for 30 min at 30 °C, an aliquot was taken from the supernatant. After removal of the supernatant, the pellet was resuspended in SDS sample buffer. Samples of supernatant and pellet fractions were loaded and analyzed on Coomassie-stained 12.5% SDS gels.

Before sample preparation for ssNMR, the purified unlabeled MBP-MAP7-MTBD was first incubated with 5 U thrombin at 4 °C for 16 h to cleave the fused MBP protein. Protease inhibitors were then added to the proteins. To prepare MAP7-MTBD-MT complexes, 2 mg of purified [13C, 15N] labeled MTs were prepared and resuspended in warm BRB80 buffer with 20 µM taxol. MAP7-MTBD was then added to molar ratio of 2:1 for MAP7-MTBD:MT and incubated at 30 °C for 30 min. The pellet was centrifuged down at 180,000 × g (Beckman TLA-55 rotor) at 30 °C for 30 min and washed with warm BRB80 buffer with 20 µM taxol and protease inhibitors, without disturbing the pellet. The pellet was then transferred and packed into a 1.3 mm rotor.

ssNMR experiments

NMR experiments of [13C, 15N] labeled MTs (free MTs, CKK-bound MTs and MAP7-bound MTs) were performed on a standard-bore 700 MHz, a wide-bore 500 MHz (Bruker Biospin). SsNMR experiments on 700 MHz included 2D 13C–13C RFDR29, 1H–13C/15N HSQC and 3D 15N-edited 1H–1H spin diffusion experiments35 (set temperature 270 K, MAS rate 44 kHz). The actual temperature during the ssNMR experiments for both apo as well as MAP-bound microtubular samples was 293 K. The 13C–13C mixing was 3 ms in the RFDR experiment. The PISSARRO decoupling (Weingarth et al., 2011) scheme of 120 kHz was employed on the 1H channel during the RFDR mixing and the detection of 13C. The proton spin diffusion time was 200 ms. In all proton-detected experiments, the PISSARRO decoupling scheme was applied at 11 kHz on 1H, 13C and 15N channels. 31P NMR experiment was conducted on the 500 MHz spectrometer (set temperature 290 K, MAS rate 11 kHz). The CP MAS experiment was recorded using a 100–50% ramp on 1H-channel of 95.4 kHz, and 71.7 kHz on the 31P-channel, with 1.2 ms CP contact time. A SPINAL decoupling (Fung et al., 2000) of 1H during the acquisition of 31P was applied at 90 kHz. 31P chemical shifts were referenced externally using phosphate buffer, pH 7 and set the signal at 0 ppm.

Supplementary Movie 1 - Dual-color video of a polymerizing MT using HeLa S3 purified tubulin

A low percentage of rhodamine-labeled porcine tubulin (3%) and 20 nM GFP-EB3 was used to visualize the MT lattice and ends respectively. MTs were grown from stable HiLyte-488- labeled GMPCPP MT seeds. Images were collected using a TIRF microscope at a 2^{-s} interval. Video is sped up 90 times and time is shown in the format of minutes.

Acknowledgements

We thank Gert Folkers for helpful discussions and Johan van der Zwan for technical support. This work was supported by the Dutch Science Foundation NWO: VENI grant 722.016.002 to S.X., ALW Open program grant 824.15.017 to A.A., NWO-Groot (no. 175.010.2009.002) and TOP-PUNT (no. 718.015.001) grant to M.B. and by uNMR-NL, the National Roadmap Large-Scale NMR Facility of the Netherlands (grant 184.032.207). C.J. is supported by the grants ANR-10-IDEX-0001-02 PSL, ANR-11-LBX-0038, FRM DEQ20170336756. S.B. was supported by the FRM grant FDT201805005465, and CEFIPRA 5703-1, and J.A.S. by the European Union's Horizon 2020 Marie Skłodowska-Curie grant agreement No. 675737, and the FRM grant FDT201904008210.

Author contributions

Y.L., S.X., A.A., and M.B. designed the experiments, analyzed the data and wrote the paper. Y.L. and P.J.H. produced labeled microtubules with advise from J.A.S. and C.J. Y.L. and S.X. performed and analyzed the NMR experiments; P.J.H. performed the *in vitro* assays. L.v.B. and F.F. performed the transmission EM experiments. All authors critically reviewed the paper.

Data availability

Data supporting the findings of this manuscript are available from the corresponding authors upon reasonable request. A reporting summary for this Article is available as a Supplementary Information file. The source data underlying Figs. 1b and 5c and Supplementary Figs. 2 and 3 are provided in a Source Data file.

References

Ainavarapu, S.R., J. Brujic, H.H. Huang, A.P. Wiita, H. Lu, L. Li, K.A. Walther, M. Carrion-Vazquez, H. Li, and J.M. Fernandez. 2007. Contour length and refolding rate of a small protein controlled by engineered disulfide bonds. Biophys J. 92:225-233.

Akhmanova, A., and C.C. Hoogenraad. 2015. Microtubule minus-end-targeting proteins. Curr Biol. 25:R162-171.

Akhmanova, A., and M.O. Steinmetz. 2008. Tracking the ends: a dynamic protein network controls the fate of microtubule tips. Nat Rev Mol Cell Biol. 9:309-322.

Alam, T.M., and G.P. Holland. 2006. (1)H-(13)C INEPT MAS NMR correlation experiments with (1)H-(1)H mediated magnetization exchange to probe organization in lipid biomembranes. J Magn Reson. 180:210-221.

Alushin, G.M., G.C. Lander, E.H. Kellogg, R. Zhang, D. Baker, and E. Nogales. 2014. High-resolution microtubule structures reveal the structural transitions in alphabeta-tubulin upon GTP hydrolysis. Cell. 157:1117-1129.

Andronesi, O.C., S. Becker, K. Seidel, H. Heise, H.S. Young, and M. Baldus. 2005. Determination of membrane protein structure and dynamics by magic-angle-spinning solid-state NMR spectroscopy. J Am Chem Soc. 127:12965-12974.

Atherton, J., K. Jiang, M.M. Stangier, Y. Luo, S. Hua, K. Houben, J.J.E. van Hooff, A.P. Joseph, G. Scarabelli, B.J. Grant, A.J. Roberts, M. Topf, M.O. Steinmetz, M. Baldus, C.A. Moores, and A. Akhmanova. 2017. A structural model for microtubule minus-end recognition and protection by CAMSAP proteins. Nat Struct Mol Biol. 24:931-943.

Atherton, J., Y. Luo, S. Xiang, C. Yang, A. Rai, K. Jiang, M. Stangier, A. Vemu, A.D. Cook, S. Wang, A. Roll-Mecak, M.O. Steinmetz, A. Akhmanova, M. Baldus, and C.A. Moores. 2019. Structural determinants of microtubule minus end preference in CAMSAP CKK domains. Nat Commun. 10:5236.

Barisic, M., R. Silva e Sousa, S.K. Tripathy, M.M. Magiera, A.V. Zaytsev, A.L. Pereira, C. Janke, E.L. Grishchuk, and H. Maiato. 2015. Mitosis. Microtubule detyrosination guides chromosomes during mitosis. Science. 348:799-803.

Bennett, A.E., C.M. Rienstra, J.M. Griffiths, W. Zhen, P.T. Lansbury, and R.G. Griffin. 1998. Homonuclear radio frequency-driven recoupling in rotating solids. The Journal of Chemical Physics. 108:9463-9479.

Chaudhary, A.R., H. Lu, E.B. Krementsova, C.S. Bookwalter, K.M. Trybus, and A.G. Hendricks. 2019. MAP7 regulates organelle transport by recruiting kinesin-1 to microtubules. J Biol Chem. 294:10160-10171.

Damman, R., S. Schutz, Y. Luo, M. Weingarth, R. Sprangers, and M. Baldus. 2019. Atomic-level insight into mRNA processing bodies by combining solid and solution-state NMR spectroscopy. Nat Commun. 10:4536.

Davis, A., S. Martinez, D. Nelson, and K. Middleton. 2010. A tubulin polymerization microassay used to compare ligand efficacy. Methods Cell Biol. 95.

de Jong, R.N., M.A. Daniels, R. Kaptein, and G.E. Folkers. 2006. Enzyme free cloning for high throughput gene cloning and expression. J Struct Funct Genomics. 7:109-118.

Desai, A., and T.J. Mitchison. 1997. Microtubule polymerization dynamics. Annu Rev Cell Dev Biol. 13:83-117.

Drozdetskiy, A., C. Cole, J. Procter, and G.J. Barton. 2015. JPred4: a protein secondary structure prediction server. Nucleic Acids Res. 43:W389-394.

Eshun-Wilson, L., R. Zhang, D. Portran, M.V. Nachury, D.B. Toso, T. Lohr, M. Vendruscolo, M. Bonomi, J.S. Fraser, and E. Nogales. 2019. Effects of alpha-tubulin acetylation on microtubule structure and stability. Proc Natl Acad Sci U S A. 116:10366-10371.

Etzkorn, M., A. Bockmann, A. Lange, and M. Baldus. 2004. Probing molecular interfaces using 2D magic-angle-spinning NMR on protein mixtures with different uniform labeling. J Am Chem Soc. 126:14746-14751.

Fung, B.M., A.K. Khitrin, and K. Ermolaev. 2000. An improved broadband decoupling sequence for liquid crystals and solids. J Magn Reson. 142:97-101.

Gadadhar, S., S. Bodakuntla, K. Natarajan, and C. Janke. 2017. The tubulin code at a glance. J Cell Sci. 130:1347-1353.

Guedes-Dias, P., J.J. Nirschl, N. Abreu, M.K. Tokito, C. Janke, M.M. Magiera, and E.L.F. Holzbaur. 2019. Kinesin-3 Responds to Local Microtubule Dynamics to Target Synaptic Cargo Delivery to the Presynapse. Curr Biol. 29:268-282 e268.

Han, B., Y. Liu, S.W. Ginzinger, and D.S. Wishart. 2011. SHIFTX2: significantly improved protein chemical shift prediction. J Biomol NMR. 50:43-57.

Hernandez-Vega, A., M. Braun, L. Scharrel, M. Jahnel, S. Wegmann, B.T. Hyman, S. Alberti, S. Diez, and A.A. Hyman. 2017. Local Nucleation of Microtubule Bundles through Tubulin Concentration into a Condensed Tau Phase. Cell Rep. 20:2304-2312.

Hooikaas, P.J., M. Martin, T. Muhlethaler, G.J. Kuijntjes, C.A.E. Peeters, E.A. Katrukha, L. Ferrari, R. Stucchi, D.G.F. Verhagen, W.E. van Riel, I. Grigoriev, A.F.M. Altelaar, C.C. Hoogenraad, S.G.D. Rudiger, M.O. Steinmetz, L.C. Kapitein, and A. Akhmanova. 2019. MAP7 family proteins regulate kinesin-1 recruitment and activation. J Cell Biol. 218:1298-1318.

Kadavath, H., Y. Cabrales Fontela, M. Jaremko, L. Jaremko, K. Overkamp, J. Biernat, E. Mandelkow, and M. Zweckstetter. 2018. The Binding Mode of a Tau Peptide with Tubulin. Angew Chem Int Ed Engl. 57:3246-3250.

Kaplan, M., S. Narasimhan, C. de Heus, D. Mance, S. van Doorn, K. Houben, D. Popov-Celeketic, R. Damman, E.A. Katrukha, P. Jain, W.J.C. Geerts, A.J.R. Heck, G.E. Folkers, L.C. Kapitein, S. Lemeer, P.M.P. van Bergen En Henegouwen, and M. Baldus. 2016. EGFR Dynamics Change during Activation in Native Membranes as Revealed by NMR. Cell. 167:1241-1251 e1211.

Kaur, H., A. Lakatos-Karoly, R. Vogel, A. Noll, R. Tampe, and C. Glaubitz. 2016. Coupled ATPase-adenylate kinase activity in ABC transporters. Nat Commun. 7:13864.

Kellogg, E.H., N.M.A. Hejab, S. Poepsel, K.H. Downing, F. DiMaio, and E. Nogales. 2018. Near-atomic model of microtubule-tau interactions. Science. 360:1242-1246.

Kesten, C., A. Wallmann, R. Schneider, H.E. McFarlane, A. Diehl, G.A. Khan, B.J. van Rossum, E.R. Lampugnani, W.G. Szymanski, N. Cremer, P. Schmieder, K.L. Ford, F. Seiter, J.L. Heazlewood, C. Sanchez-Rodriguez, H. Oschkinat, and S. Persson. 2019. The companion of cellulose synthase 1 confers salt tolerance through a Tau-like mechanism in plants. Nat Commun. 10:857.

Kubo, S., N. Nishida, Y. Udagawa, O. Takarada, S. Ogino, and I. Shimada. 2013. A gel-encapsulated bioreactor system for NMR studies of protein-protein interactions in living mammalian cells. Angew Chem Int Ed Engl. 52:1208-1211.

Kumar, A., H. Heise, M.J. Blommers, P. Krastel, E. Schmitt, F. Petersen, S. Jeganathan, E.M. Mandelkow, T. Carlomagno, C. Griesinger, and M. Baldus. 2010. Interaction of epothilone B (patupilone) with microtubules as detected by two-dimensional solid-state NMR spectroscopy. Angew Chem Int Ed Engl. 49:7504-7507.

Lakomek, N.A., H. Yavuz, R. Jahn, and A. Perez-Lara. 2019. Structural dynamics and transient lipid binding of synaptobrevin-2 tune SNARE assembly and membrane fusion. Proc Natl Acad Sci U S A. 116:8699-8708.

Lee, G.H., S.Y. Oh, K.J. Yeo, T. Ferdous, M. Cho, and Y. Paik. 2015. Solid-state 31P NMR investigation on the status of guanine nucleotides in paclitaxel-stabilized microtubules. Magn Reson Chem. 53:330-336.

Lefevre, J., K.G. Chernov, V. Joshi, S. Delga, F. Toma, D. Pastre, P.A. Curmi, and P. Savarin. 2011. The C terminus of tubulin, a versatile partner for cationic molecules: binding of Tau, polyamines, and calcium. J Biol Chem. 286:3065-3078.

Menendez, M., G. Rivas, J.F. Diaz, and J.M. Andreu. 1998. Control of the structural stability of the tubulin dimer by one high affinity bound magnesium ion at nucleotide N-site. J Biol Chem. 273:167-176.

Monroy, B.Y., D.L. Sawyer, B.E. Ackermann, M.M. Borden, T.C. Tan, and K.M. Ori-McKenney. 2018. Competition between microtubule-associated proteins directs motor transport. Nat Commun. 9:1487.

Narasimhan, S., D. Mance, C. Pinto, M. Weingarth, A. Bonvin, and M. Baldus. 2018. Rapid prediction of multi-dimensional NMR data sets using FANDAS. Methods Mol Biol. 1688:111-132.

Newton, C.N., J.G. DeLuca, R.H. Himes, H.P. Miller, M.A. Jordan, and L. Wilson. 2002. Intrinsically slow dynamic instability of HeLa cell microtubules in vitro. J Biol Chem. 277:42456-42462.

Nirschl, J.J., M.M. Magiera, J.E. Lazarus, C. Janke, and E.L. Holzbaur. 2016. alpha-Tubulin Tyrosination and CLIP-170 Phosphorylation Regulate the Initiation of Dynein-Driven Transport in Neurons. Cell Rep. 14:2637-2652.

Nogales, E., and R. Zhang. 2016. Visualizing microtubule structural transitions and interactions with associated proteins. Curr Opin Struct Biol. 37:90-96.

Pan, X., Y. Cao, R. Stucchi, P.J. Hooikaas, S. Portegies, L. Will, M. Martin, A. Akhmanova, M. Harterink, and C.C. Hoogenraad. 2019. MAP7D2 Localizes to the Proximal Axon and Locally Promotes Kinesin-1-Mediated Cargo Transport into the Axon. Cell Rep. 26:1988-1999 e1986.

Peng, J.W. 2012. Exposing the Moving Parts of Proteins with NMR Spectroscopy. J Phys Chem Lett. 3:1039-1051.

Quinn, C.M., and T. Polenova. 2017. Structural biology of supramolecular assemblies by magic-angle spinning NMR spectroscopy. Q Rev Biophys. 50:e1.

Renault, M., A. Cukkemane, and M. Baldus. 2010. Solid-state NMR spectroscopy on complex biomolecules. Angew Chem Int Ed Engl. 49:8346-8357.

Schmidt-Rohr, K., and H.W. Spiess. 1994. Multidimensional Solid-State NMR and Polymers. . Academic Press, 1994.

Siahaan, V., J. Krattenmacher, A.A. Hyman, S. Diez, A. Hernandez-Vega, Z. Lansky, and M. Braun. 2019. Kinetically distinct phases of tau on microtubules regulate kinesin motors and severing enzymes. Nat Cell Biol. 21:1086-1092.

Souphron, J., S. Bodakuntla, A.S. Jijumon, G. Lakisic, A.M. Gautreau, C. Janke, and M.M. Magiera. 2019. Purification of tubulin with controlled post-translational modifications by polymerization-depolymerization cycles. Nat Protoc. 14:1634-1660.

Spoerner, M., M. Karl, P. Lopes, M. Hoering, K. Loeffel, A. Nuehs, J. Adelsberger, W. Kremer, and H.R. Kalbitzer. 2017. High pressure (31)P NMR spectroscopy on guanine nucleotides. J Biomol NMR. 67:1-13.

Tan, R., A.J. Lam, T. Tan, J. Han, D.W. Nowakowski, M. Vershinin, S. Simo, K.M. Ori-McKenney, and R.J. McKenney. 2019. Microtubules gate tau condensation to spatially regulate microtubule functions. Nat Cell Biol. 21:1078-1085.

Walczak, C.E., and S.L. Shaw. 2010. A MAP for bundling microtubules. Cell. 142:364-367.

Wall, K.P., M. Pagratis, G. Armstrong, J.L. Balsbaugh, E. Verbeke, C.G. Pearson, and L.E. Hough. 2016. Molecular Determinants of Tubulin's C-Terminal Tail Conformational Ensemble. ACS Chem Biol. 11:2981-2990.

Ward, M.E., E. Ritz, M.A.M. Ahmed, V.V. Bamm, G. Harauz, L.S. Brown, and V. Ladizhansky. 2015. Proton detection for signal enhancement in solid-state NMR experiments on mobile species in membrane proteins. J Biomol NMR. 63:375-388.

Weaver, B.A. 2014. How Taxol/paclitaxel kills cancer cells. Mol Biol Cell. 25:2677-2681.

Weingarth, M., J. Trebosc, J.P. Amoureux, G. Bodenhausen, and P. Tekely. 2011. Efficiency at high spinning frequencies of heteronuclear decoupling methods designed to quench rotary resonance. Solid State Nucl Magn Reson. 40:21-26.

Wright, P.E., and H.J. Dyson. 2015. Intrinsically disordered proteins in cellular signalling and regulation. Nat Rev Mol Cell Biol. 16:18-29.

Xiang, S., U.B. le Paige, V. Horn, K. Houben, M. Baldus, and H. van Ingen. 2018. Site-Specific Studies of Nucleosome Interactions by Solid-State NMR Spectroscopy. Angew Chem Int Ed Engl. 57:4571-4575.

Yan, S., C. Guo, G. Hou, H. Zhang, X. Lu, J.C. Williams, and T. Polenova. 2015. Atomic-resolution structure of the CAP-Gly domain of dynactin on polymeric microtubules determined by magic angle spinning NMR spectroscopy. Proc Natl Acad Sci U S A. 112:14611-14616.

Zhang, R., G.M. Alushin, A. Brown, and E. Nogales. 2015. Mechanistic Origin of Microtubule Dynamic Instability and Its Modulation by EB Proteins. Cell. 162:849-859.

Supplemental Figures

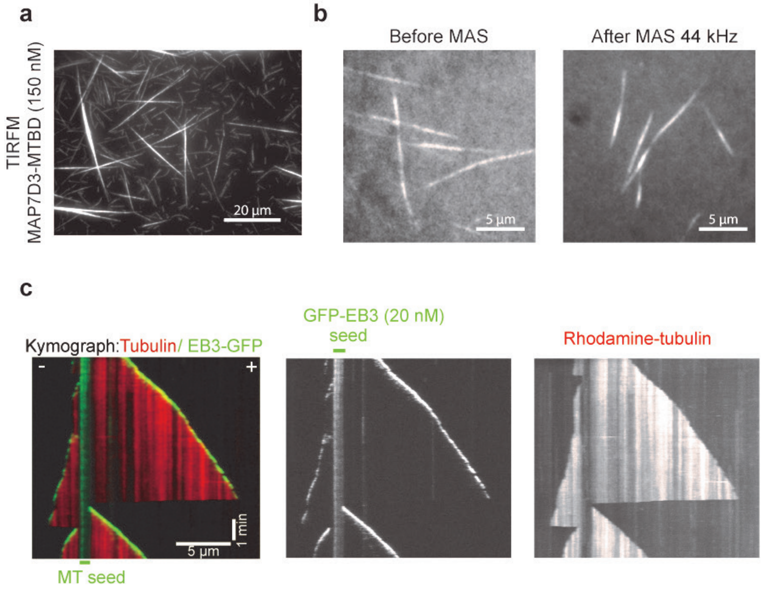
a
TIRFM
MAP7D3-MTBD (150 nM)
20 µm
b
Before MAS
After MAS 44 kHz
5 µm
5 µm
c
Kymograph:Tubulin/ EB3-GFP
-
+
1 min
5 µm
MT seed
GFP-EB3 (20 nM)
seed
Rhodamine-tubulin

Supplementary Figure 1 - Functional characterization of purified tubulin
(A) MTs were observed by TIRF microscopy using purified mCherry-labeled MAP7D3-MT binding domain (150 nM) as labeling agent. The MT sample was stabilized by 20 µM Taxol. **(B)** Characterization of functionality of HeLa MTs after MAS NMR experiments. Taxol-stabilized MTs were incubated with purified mCherry-labeled MAP7D3-MTBD (150 nM) before or after MAS spinning and observed by TIRF microscopy. **(C)** Kymographs of MT growth at the plus (+) and minus (–) end from a HiLyte-488 seed with 20 nM GFP-EB3 and 3% rhodamine-labeled tubulin together with purified HeLa S3 tubulin. The panel corresponds to the merged kymograph image shown in Figure 1C of the main text.

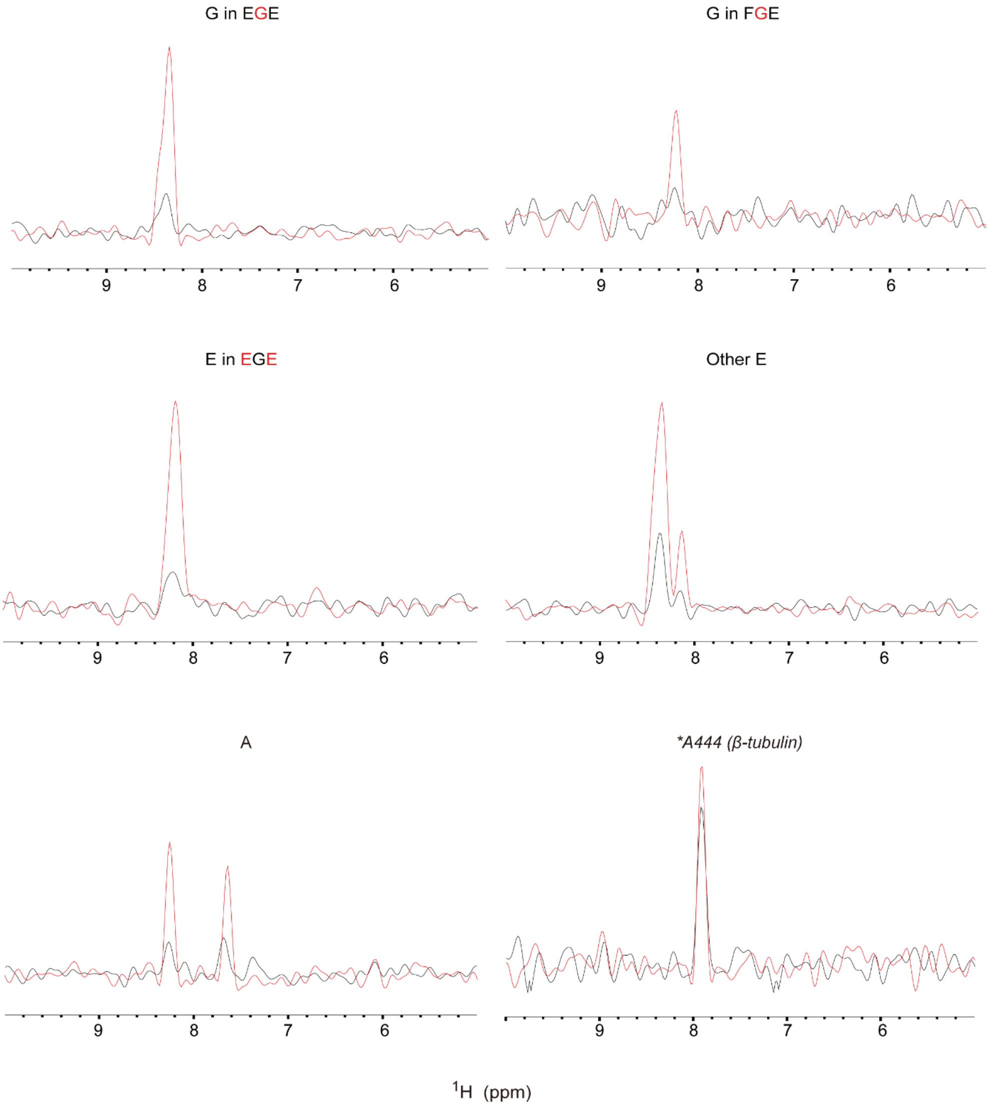

Supplementary Figure 2 – The effect of MAP7 binding on 15N-HSQC data on labeled MTs state. 1D slices taken from the 15N-HSQC experiments of MTs (red) and MAP7-MTBD in complex with MTs (black). The labels of the peaks are indicated as shown in Figure 5A.NMR intensities are provided as a Source Data file.

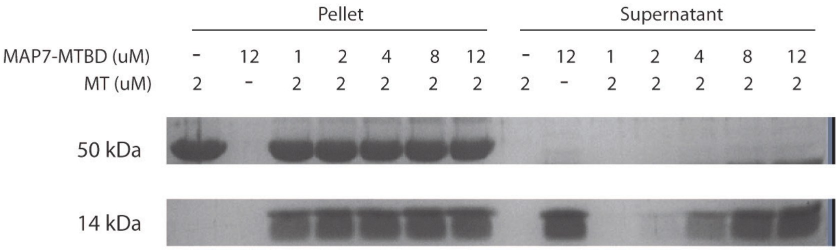
Pellet
Supernatant
MAP7-MTBD (uM) - 12 1 2 4 8 12 - 12 1 2 4 8 12
MT (uM) 2 - 2 2 2 2 2 2 - 2 2 2 2 2
50 kDa
14 kDa

Supplementary Figure 3 - Microtubule pelleting assay with MAP7 analyzed by SDS-PAGE.
The MT pelleting assay was performed with different molar ratios of MAP7-MTBD:tubulin as indicated above the SDS-PAGE gel. As a result, a molar ratio of MAP7-MTBD:MTs=2:1 was used for sample preparation for ssNMR studies to allow maximum decoration of MAP7-MTBD on MTs. Uncropped protein gel is provided as a Source Data file.

Supplementary Table 1 - Spectral analysis and results of 31P ssNMR

	δ (ppm)	Integrations
Pα and Pα'	-10.08 and -11.6	0.6589 and 0.639
Pγ and Pβ'	-7.18 and -8.15	1.0000 and 1.1272
Pβ	-19.9	0.5762
Co-purified lipids	-2.7	2.1469

Supplementary Table 2 - Primer sequences used for MAP7-MTBD and CKK constructs

Primer name	Primer sequence (5' - 3')
MAP7_59fw	TGCCTGTGTTACGTGTTGATGAC
MAP7_59fwl	GCCGCGCGGCAGCCTGCCTGTGTTACGTGTTGATGAC
MAP7_170rv	TCAAGGGCTCCCATGGAGAGAGC
MAP7_170rvl	CAAGAAGAACCCCTCAAGGGCTCCCATGGAGAGAGC
CKK:CAM1-1474F_BamHI	CGGGGATCCGGTCCCAAGCTCTTTAAG
CKK:CAM1-1613R_SalI	ACGCGTCGACTCATTTACGAGTCTGGGCC

6

MKLP2 is a motile kinesin that transports the Chromosomal Passenger Complex during anaphase

Ingrid E. Adriaans[1,2*], Peter Jan Hooikaas[3*], Amol Aher[3],
Martijn J. M. Vromans[1,2], Robert M. van Es[1,2], Ilya Grigoriev[3],
Anna Akhmanova[3] and Susanne M. A. Lens[1,2]

Current Biology (2020); 30:2628-2637

* These authors contributed equally

---

[1] Oncode Institute and [2] Center for Molecular Medicine, University Medical Center Utrecht, Utrecht University, 3584 CG Utrecht, The Netherlands.
[3] Cell Biology, Neurobiology and Biophysics, Department of Biology, Faculty of Science, Utrecht University, 3584 CH Utrecht, The Netherlands.

Summary

During cytokinesis, signals from the anaphase spindle direct the formation and position of a contractile ring at the cell cortex (Green et al., 2012). The chromosomal passenger complex (CPC) participates in cytokinesis initiation by signaling from the spindle midzone and equatorial cortex (Adriaans et al., 2019), but the mechanisms underlying the anaphase-specific CPC localization are currently unresolved. Accumulation of the CPC at these sites requires the presence of microtubules and the mitotic kinesin-like protein 2, MKLP2 (KIF20A), a member of the kinesin-6 family (Cesario et al., 2006; Gruneberg et al., 2004; Hummer and Mayer, 2009; Kitagawa et al., 2013; Murata-Hori and Wang, 2002), and this has led to the hypothesis that the CPC is transported along microtubules by MKLP2 (Gruneberg et al., 2004; Hummer and Mayer, 2009; Kitagawa et al., 2013; Murata-Hori and Wang, 2002). However, the structure of the MKLP2 motor domain with its extended neck-linker region suggests that this kinesin might not be able to drive processive transport (Atherton et al., 2017; Landino et al., 2017). Furthermore, experiments in *Xenopus* egg extracts indicated that the CPC might be transported by kinesin-4, KIF4A (Nguyen et al., 2014). Finally, CPC-MKLP2 complexes might be directly recruited to the equatorial cortex via association with actin and myosin II, independent of kinesin activity (Kitagawa et al., 2013; Landino et al., 2017). Using microscopy-based assays with purified proteins, we demonstrate that MKLP2 is a processive plus-end directed motor that can transport the CPC along microtubules *in vitro*. In cells, strong suppression of MKLP2-dependent CPC motility by expression of an MKLP2 P-loop mutant perturbs CPC accumulation at both the spindle midzone and equatorial cortex, whereas a weaker inhibition of MKLP2 motor using Paprotrain mainly affects CPC localization to the equatorial cortex. Our data indicate that control of cytokinesis initiation by the CPC requires its directional MKLP2-dependent transport.

Results and Discussion

The Extended Neck and Coiled Coil Domain of MKLP2 Binds to the CPC via the N Termini of INCENP and Borealin

To test the hypothesis that mitotic kinesin-like protein 2 (MKLP2) is a chromosomal passenger complex (CPC)-transporting motor, we first mapped the interaction between them. The CPC consists of INCENP, Survivin, Borealin, and Aurora B (van der Horst and Lens, 2014), and previous work suggested that the C-terminal half of MKLP2 binds the N terminus of INCENP (Hummer and Mayer, 2009; Kitagawa et al., 2014). We generated several GFP-tagged fragments of MKLP2 and INCENP, expressed these in mitotic HEK293T cells, and assessed their ability to immunoprecipitate endogenous CPC or MKLP2, respectively (Figures 1A, 1B, and S1A–S1C). Although cyclin B-Cdk1-dependent phosphorylation of either INCENP or MKLP2 is thought to interfere with CPC-MKLP2 binding (Hummer and Mayer, 2009; Kitagawa et al., 2014), we consistently co-immunoprecipitated endogenous CPC with MKLP2::GFP, as well as endogenous MKLP2 with INCENP::GFP from these mitotic extracts (Figures S1A–S1C). In mitotic cells, a fraction of (overexpressed) INCENP and MKLP2 might not be phosphorylated, and this could be the fraction we pulled down.

Interaction with the CPC depended on a small MKLP2 region (amino acids [aas] 513–765), composed of the extended kinesin neck and coiled coil domain (Figures 1A and S1A). A recombinant N-terminal fragment of INCENP (aas 1–58; referred to as CEN-box; essential for centromere targeting of the CPC via Borealin and Survivin) (Ainsztein et al., 1998;

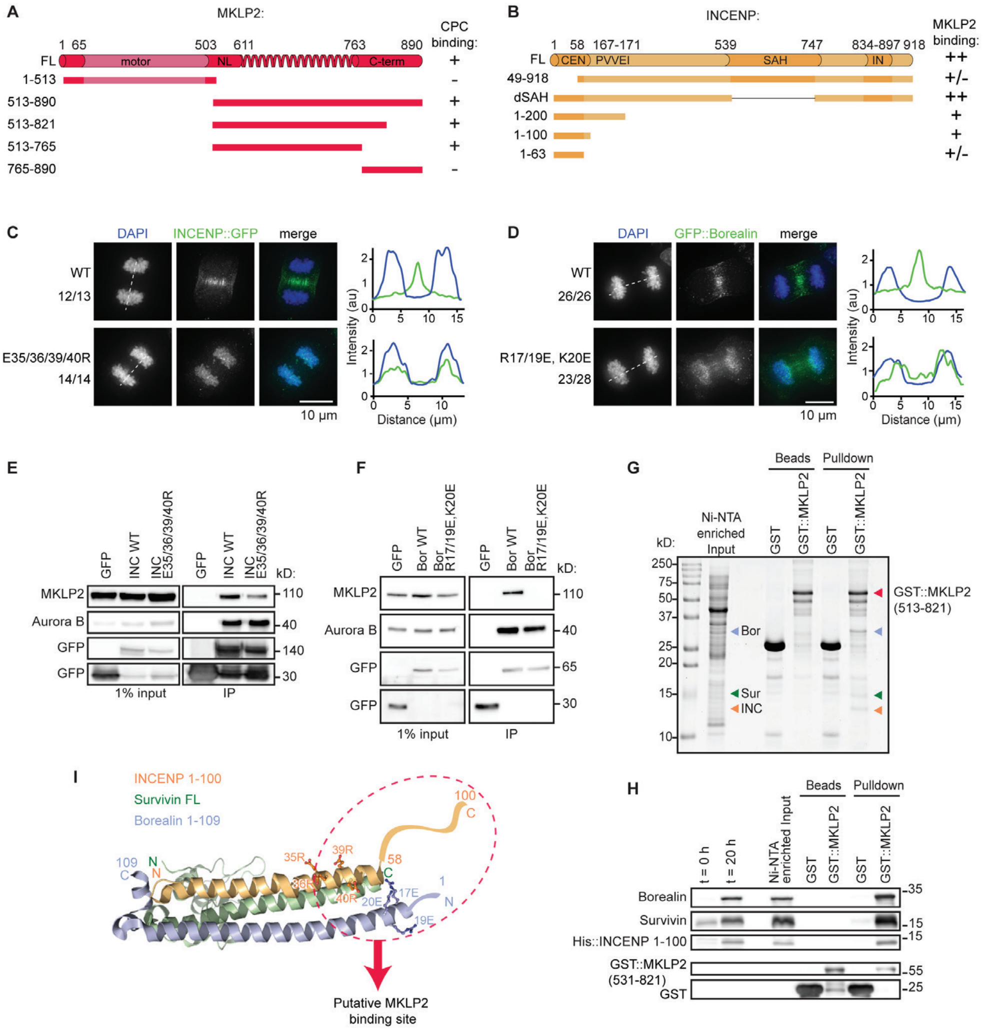

Figure 1 - The Extended Neck and Coiled Coil Domain of MKLP2 Binds to the CPC via the N Termini of INCENP and Borealin

(A) Cartoon of full-length (FL) human MKLP2 protein and used MKLP2 fragments. C-term, C-terminal domain; motor, motor domain; NL, neck linker region. Their ability to pull down detectable amounts of endogenous CPC (Figure S1A) is indicated. **(B)** Cartoon of human INCENP and used INCENP deletion mutants. CEN, centromere-targeting domain interacting with Borealin and Survivin; IN, IN box interacting with Aurora B; PVVEI, HP1 binding motif; SAH, single α helix. Their ability to pull down detectable amounts of endogenous MKLP2 (Figures S1B and S1C) is indicated. **(C and D)** IF for GFP of HeLa cells expressing INCENP::GFP or INCENP E35/36/39/40R::GFP (C) or expressing GFP::Borealin or GFP::Borealin R17/19E, K20E (D). DNA is visualized by DAPI. Dotted line indicates line scan position for GFP and DAPI shown on the right. The number of times the depicted localization was observed/total number of imaged cells is indicated. **(E and F)** HEK293T cells were transfected with plasmids encoding: GFP, INCENP WT::GFP or E35/36/39/40R::GFP (E) and GFP, GFP::Borealin WT or R17/19E, K20E (F). Immunoprecipitations were performed with GFP-Trap beads. Samples were analyzed by western blotting. **(G)** Coomassie-stained SDS-PAGE gel of a pull-down assay with GST and GST::MKLP2 513-821 (red arrowhead). The CPC components expressed from a tricistronic vector containing 6xHis::INCENP 1–100 (orange), Survivin (green), and Borealin (blue) were enriched from

Figure 1 (continued) the input lysate using Ni-NTA beads. **(H)** Western blots of a pull-down with GST and GST-tagged MKLP2 513-821 probed with the indicated antibodies. Time points indicate inputs of bacterial lysates before and after IPTG induction. **(I)** Ribbon representation of the 3-helix-bundle structure of the CPC core complex, consisting of INCENP (aas 1–58), Borealin (aas 10–109), and Survivin (aas 1–140) (Jeyaprakash et al., 2007) with amino acid side chains E35/36/39/40 in INCENP and R17/19, K20 in Borealin indicated (PDB: 2QFA). The hypothetical location of the C-terminal aas 59–100 of INCENP and N-terminal aas 1–9 of Borealin is added to the crystal structure.

Jeyaprakash et al., 2007; Klein et al., 2006; Mackay et al., 1993) has been shown to interact with recombinant MKLP2 (Kitagawa et al., 2014). However, we found that INCENP 1–63 did not efficiently bind endogenous MKLP2, although a somewhat longer N-terminal fragment of INCENP (aas 1–100) bound MKLP2 more efficiently (Figures 1B and S1B). We therefore conclude that there are additional interactions between MKLP2 and INCENP outside the CEN-box. Deletion of the first 48 aas of INCENP (INCENP 49–918), which severely impaired INCENP interaction with Borealin and Survivin (Figures 1B and S1C) (Jeyaprakash et al., 2007; Klein et al., 2006; Vader et al., 2006), reduced the binding to endogenous MKLP2 as compared to full-length INCENP (Figure S1C), suggesting a potential contribution of Borealin and/or Survivin to the interaction with MKLP2. To further define CPC-MKLP2 interaction sites, we mutated a conserved set of exposed glutamic acids in the N terminus of INCENP to positively charged residues (E35/36/39/40R) or mutated several positively charged residues in the N terminus of Borealin to negatively charged residues (R17/19 and K20E). These mutations do not interfere with the interactions between CPC members (Jeyaprakash et al., 2007) but do perturb the translocation of the CPC from chromosomes in (pro)metaphase to the spindle midzone in anaphase, very similar to what is seen after knockdown of MKLP2 (Gruneberg et al., 2004; Hummer and Mayer, 2009; Jeyaprakash et al., 2007; Kitagawa et al., 2013) (Figures 1C, 1D, and S1D). The INCENP E35/36/39/40R mutant was less efficient, and the Borealin R17/19, K20E mutant was deficient in precipitating MKLP2 compared to their wild-type counterparts (Figures 1E and 1F). Finally, glutathione S-transferase (GST)::MKLP2 513–821 purified from bacteria, precipitated 6xHis::INCENP 1–100, Borealin, and Survivin expressed in bacteria (Figures 1G and 1H). This strongly suggests that the interaction between the non-enzymatic CPC core members and MKLP2 is direct.

INCENP 1–58, Borealin 10–109, and Survivin form a three-helix bundle structure *in vitro* (Jeyaprakash et al., 2007). Based on this structure, the residues of INCENP and Borealin involved in MKLP2 binding are clustered on one side of the three-helix bundle (Figure 1I). Moreover, aas 63–100 of INCENP would be oriented toward the N terminus of Borealin, and together, they could form the interface for binding MKLP2. Whether Survivin also makes direct contacts with MKLP2 is currently unclear; it may contribute to MKLP2 binding by participating in the formation of the three-helix bundle with INCENP and Borealin.

MKLP2 Is a Motile Kinesin that Becomes More Processive in the Presence of the CPC

Next, we investigated whether MKLP2 can transport the CPC by using *in vitro* reconstitution assays in combination with total internal reflection fluorescence (TIRF) microscopy. In these assays, dynamic microtubules were grown from GMPCPP-stabilized microtubule seeds that are attached to a glass coverslip (Bieling et al., 2007; Mohan et al., 2013). Imaging was performed using fluorescently labeled proteins and (un)labeled tubulin (Hooikaas et al., 2019). Full-length GFP-tagged human MKLP2 (MKLP2::GFP) was purified from

HEK293T cells using StrepII-tag affinity purification (Figure S2A). Fluorescence intensity measurements of single MKLP2::GFP molecules showed they were homodimers (Figure S2B). Mass spectrometry analysis revealed MKLP2 as the main protein in the elution, although some contaminants were present. Notably, a few KIF4A peptides were detected, but intensity-based quantification estimated the KIF4A abundance to be at least 9,000 times less than that of MKLP2 (Figure S2C). We used a similar approach to purify GFP::StrepII- or mCherry::StrepII-tagged human CPC, but the complex containing full-length INCENP was highly unstable. We therefore generated a recombinant "coreCPC" consisting of full-length Survivin and Borealin with INCENP(1–100)::GFP/mCherry (Figures 2A and S2D). In addition, we also generated a complex that contained full-length Survivin, Borealin, and INCENP(1–100)-linker-INCENP(834–918)::GFP/mCherry. Because INCENP(834–918) interacts with Aurora B (Honda et al., 2003; Sessa et al., 2005), it could be loaded with a wild-type (WT) or kinase-dead (KD) variant of Aurora B (Figures 2A, S2E, and S2F). We refer to this complex as "miniCPC." Aurora B kinase activity in miniCPC containing WT Aurora B, but not the KD mutant, was confirmed by an *in vitro* kinase assay (Figure S2G).

Single MKLP2::GFP molecules exhibited plus-end directed movement on microtubules with an average run length of 1.1 ± 1.2 µm and a velocity of 0.15 ± 0.05 µm/s (Figures 2B–2D and S2H–S2J). Importantly, this velocity differs from that of the mouse (0.92 ± 0.15 µm/s) and *X. laevis* (0.8 µm/s) KIF4A homologs (Bieling et al., 2010; Yue et al., 2018), making it highly unlikely that the observed motility was caused by co-purified KIF4A. In fact, similar to C. elegans MKLP1 (KIF23; ~ 0.2 µm/s), MKLP2 is relatively slow compared to other processive kinesins (e.g., KIF1A, KIF5B, and KIF21A/B), which all move at velocities higher than 0.5 µm/s (Hooikaas et al., 2019; Monroy et al., 2018; van der Vaart et al., 2013; van Riel et al., 2017). In the presence of mCherry-tagged coreCPC, MKLP2::GFP became more processive with an increased run length of 1.5 ± 1.6 µm (Figures 2B, 2C, and S2I). This value might be an underestimation because it is based on the analysis of "complete" motor tracks, where both landing and dissociation of the motor were observed, and does not include "incomplete" tracks. In addition, coreCPC negatively affected the landing frequency of MKLP2::GFP although velocities remained unchanged (Figures 2B, 2D, and S2K).

Next, we assayed the influence of Aurora B on MKLP2::GFP motility using mCherry-tagged miniCPC complexes, with either WT or KD Aurora B. Although coreCPC caused a modest increase of MKLP2::GFP processivity by 48.3%, the presence of miniCPC made MKLP2::GFP motors hyperprocessive. For most tracks, no start and/or end point could be detected, and run length could thus not be determined (Figures 2E and 2F). Furthermore, MKLP2::GFP velocity was decreased to 0.08 ± 0.03 µm/s by miniCPC(WT) and 0.10 ± 0.04 µm/s by miniCPC(KD), respectively (Figures 2E, 2G, and S2L). Importantly, Aurora B kinase activity had no clear effect on any measured motility parameter, as miniCPC(KD) showed similar effects as miniCPC(WT) (Figures 2E–2G, S2L, and S2M). Thus, MKLP2 is a motile kinesin that displays increased processivity in the presence of CPC, irrespective of Aurora B kinase activity.

MKLP2 Transports the CPC along Microtubules *In Vitro*

In the absence of MKLP2, both core- and miniCPC showed some binding and diffusive behavior on microtubules *in vitro*. Because the microtubule binding SAH (single α helix) domain of INCENP is not present in our recombinant complexes (Ainsztein et al., 1998; Mackay et al., 1993; Samejima et al., 2015; Tseng et al., 2010; van der Horst et al., 2015), their ability to interact with microtubules most likely involves Borealin and the N terminus of INCENP, in line with the fact that both co-pellet with microtubules *in vitro* (Trivedi et al., 2019; Wheatley et al., 2001). Interestingly, the miniCPC bound microtubules significantly

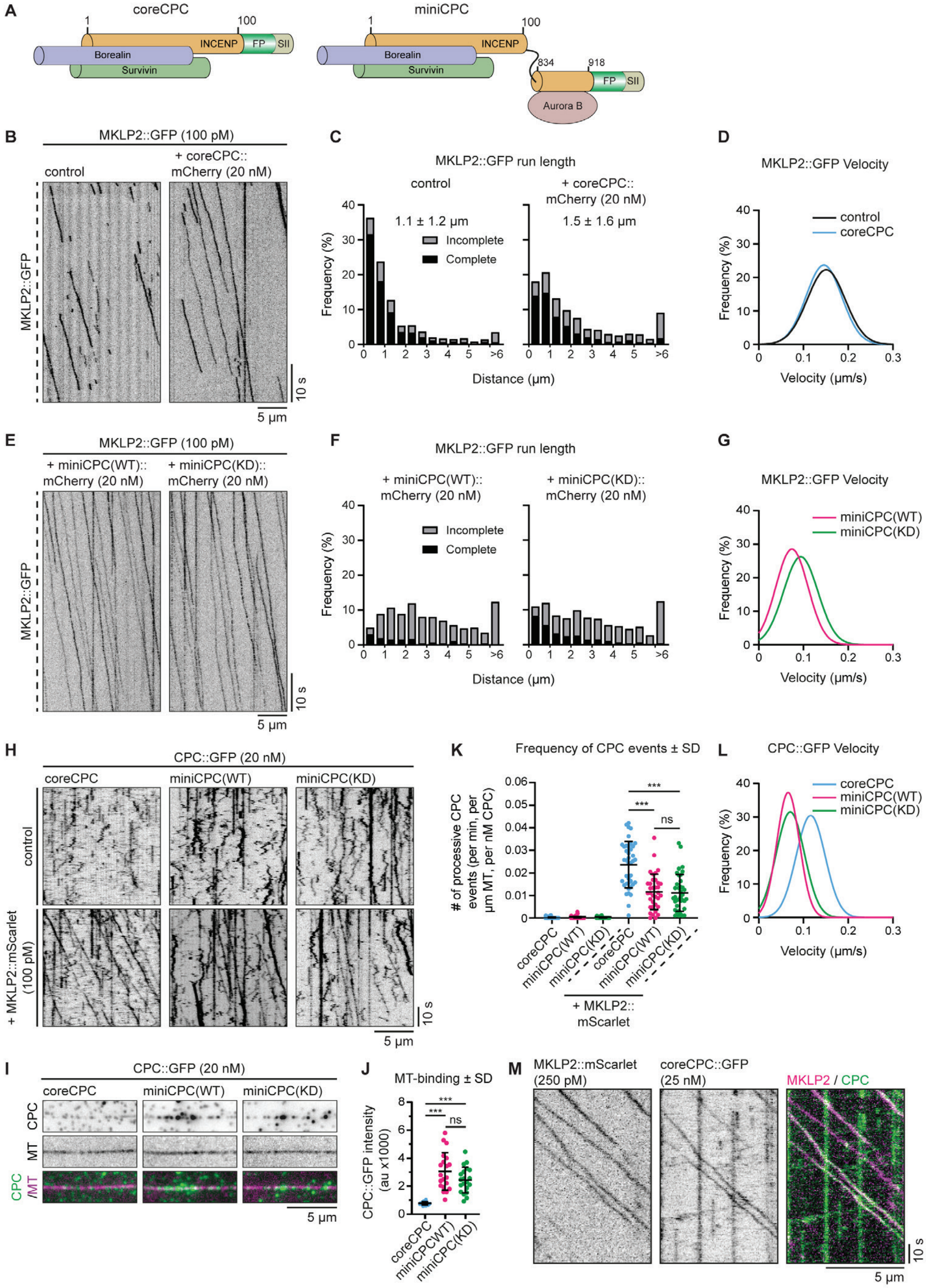

Figure 2 - MKLP2 Is a Motile Motor that Transports CPC Complexes*In Vitro*
(A) Cartoons of purified coreCPC and miniCPC complexes. FP, fluorescent protein (GFP or mCherry); SII, StrepII-tag. **(B)** Representative kymographs of MKLP2::GFP on dynamic microtubules. Image acquisition: 10 frames per second (fps). **(C)** Histograms of MKLP2::GFP run length. Complete tracks: both landing and dissociation of the motor were observed. Incomplete tracks: tracks exceed the 90-s acquisition time or partially

Figure 2 (continued) took place outside the acquisition area. Average run length ± standard deviation (SD) of complete tracks is indicated (Figure S2I); n = 1,145 and 1,137 kinesins from three experiments. **(D)** Gaussian fits of MKLP2::GFP velocities. Histograms are in Figure S2J. **(E)** Representative kymographs of MKLP2::GFP on dynamic microtubules in the presence of miniCPC::mCherry with active (WT) or inactive (kinase-dead [KD]) Aurora B. Image acquisition: 10 fps. **(F)** Histograms of MKLP2::GFP run length in the presence of miniCPC::mCherry. n = 459 and 657 kinesins from two experiments. **(G)** Gaussian fits of MKLP2::GFP velocities in the presence of miniCPC. Histograms are in Figure S2L. **(H)** Kymographs of core- and miniCPC::GFP on dynamic microtubules ± MKLP2::mScarlet. Image acquisition: 4 fps. **(I)** Representative images showing core- or miniCPC on dynamic rhodamine-labeled microtubules. **(J)** Quantification of core- and CPC::GFP intensities on dynamic microtubules. n = 20 microtubules/condition. *** $p < 0.001$ (t test). Error bars denote SD. **(K)** Quantification of processive CPC events per microtubule normalized for microtubule length, time of acquisition, and CPC concentration. n = 44, 48, 47, 40, 35, and 37 microtubules from three experiments. *** $p < 0.001$ (Mann-Whitney *U* test). Error bars denote SD. **(L)** Gaussian fits of core- and miniCPC::GFP velocities. Histograms are in Figure S2N. **(M)** Kymographs of dual-color *in vitro* reconstitution experiments with MKLP2::mScarlet and coreCPC::GFP. Image acquisition: 2 fps.

better than coreCPC (Figures 2H–2J), suggesting that the INCENP C terminus together with Aurora B increases microtubule binding affinity of the complex. Addition of MKLP2::mScarlet to both core- and miniCPC induced processive plus-end directed movement of CPC on microtubules (Figures 2H, 2K, and S2A). CoreCPC movement was seen more frequently than that of miniCPC, although Aurora B activity again did not seem to affect motility (Figures 2H and 2K). In agreement with the observation that miniCPC, but not coreCPC, slowed down MKLP2::GFP (Figures 2D and 2G), miniCPC::GFP moved at a lower velocity (WT: 0.07 ± 0.03 μm/s; KD: 0.08 ± 0.03 μm/s) compared to coreCPC::GFP (0.11 ± 0.03 μm/s) in the presence of MKLP2::mScarlet (Figures 2L and S2N). These data suggest that the interaction of miniCPC with microtubules promotes processivity of an MKLP2-CPC complex at the expense of velocity. Finally, using dual-color TIRF imaging, we confirmed that MKLP2 tracks correspond to those of moving coreCPC on a single microtubule (Figure 2M). In summary, we show that MKLP2 is a motile kinesin capable of transporting a CPC complex along microtubules *in vitro*.

MKLP2 and INCENP Display Directional Motility toward the Midzone and Equatorial Cortex in Anaphase Cells

To investigate whether MKLP2 and CPC also show directional motility in cells, we analyzed HeLa cells stably expressing either MKLP2::GFP or INCENP::GFP (Figures S3A–S3E) (van der Horst et al., 2015). Live-cell imaging during anaphase revealed the presence of discrete particles labeled with MKLP2::GFP or INCENP::GFP (Figures 3A and 3B ; Videos S1 and S2). In line with previous work (Landino et al., 2017), we found that the majority of particles showed diffusive behavior or remained static. However, motile events displaying clear directionality were also observed (Figures 3A and 3B; Videos S1 and S2). Quantification of unidirectional events with a duration >2.5 s and a velocity >0.05 μm/s revealed that the majority of these events (59% for MKLP2::GFP; 54% for INCENP::GFP) were oriented toward the equatorial cortex (magenta tracks). Co-expression of β-tubulin::Halo showed that MKLP2::GFP punctae were present on microtubules directed toward the equatorial cortex (Figure 3C). Some of these punctae could correspond to protein localization to growing microtubule ends as described for D. melanogaster Aurora B (Verma and Maresca, 2019). Motile events directed toward the spindle midzone (orange tracks) constituted 28% (MKLP2) and 33% (INCENP) of all directional tracks. This may be an underestimation because molecular crowding in the midzone area made it more difficult to discern motile events. The remaining tracks showed no preferred direction (Figures 3A, 3B, 3D, and 3E; Videos S1 and

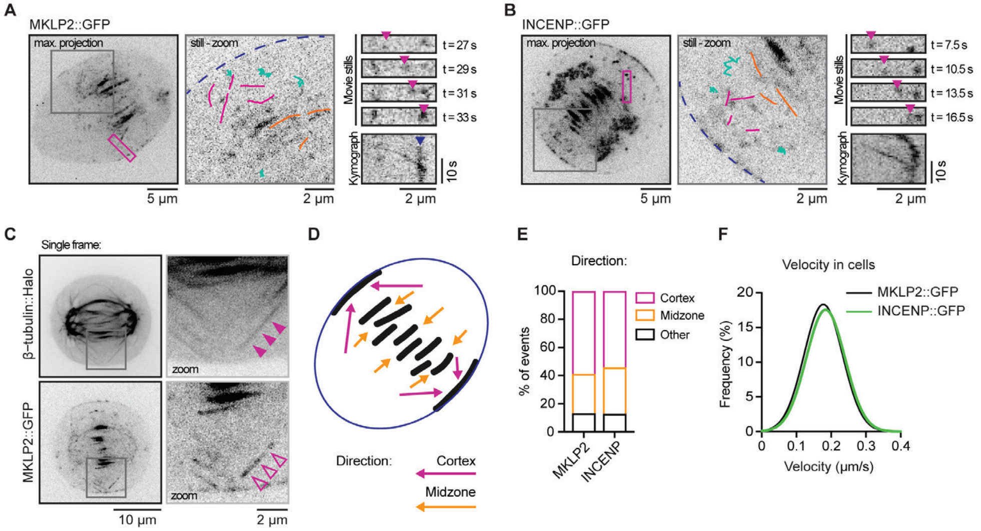
A
MKLP2::GFP
max. projection
still - zoom
Movie stills
t = 27 s
t = 29 s
t = 31 s
t = 33 s
Kymograph
10 s
5 µm
2 µm
2 µm
B
INCENP::GFP
max. projection
still - zoom
Movie stills
t = 7.5 s
t = 10.5 s
t = 13.5 s
t = 16.5 s
Kymograph
10 s
5 µm
2 µm
2 µm
C
Single frame:
β-tubulin::Halo
MKLP2::GFP
zoom
zoom
10 µm
2 µm
D
Direction:
Cortex
Midzone
E
Direction:
% of events
100
80
60
40
20
0
Cortex
Midzone
Other
MKLP2
INCENP
F
Velocity in cells
MKLP2::GFP
INCENP::GFP
Frequency (%)
20
15
10
5
0
0
0.1
0.2
0.3
0.4
Velocity (µm/s)

Figure 3 - MKLP2 and INCENP Display Directional Motility in Cells
(A and B) Maximum intensity projections and corresponding zooms of HeLa cells in anaphase expressing MKLP2::GFP (A; Video S1; Figures S3A and S3C) or INCENP::GFP (B; Video S2; Figure S3B). A number of representative particles were traced and categorized as non-directional (diffusive or static, turquoise) or directional toward the equatorial cortex (magenta) or the spindle midzone (orange). Blue dotted line in zoom indicates the cell cortex. Panels on the right (magenta box in max. projection) are stills of different time points and corresponding kymograph of a directional event (magenta arrowheads) going toward the equatorial cortex (blue arrowhead). Note that ectopically expressed INCENP::GFP was frequently detected on chromatin in anaphases of otherwise untreated cells. See also (Landino et al., 2017). **(C) R**epresentative stills and corresponding zooms of a HeLa cell in anaphase expressing MKLP2::GFP and co-transfected with β-tubulin::Halo. Microtubules were visualized by fluorescent TMR ligand. Zooms show a microtubule close to the cell cortex (solid arrowheads) positive for MKLP2::GFP (open arrowheads). **(D)** Cartoon of an anaphase cell with spindle midzone and equatorial cortex in black and arrows displaying the two main orientations of directional MKLP2::GFP and INCENP::GFP motility events: toward the equatorial cortex (magenta) and midzone (orange). **(E)** Quantification of MKLP2::GFP and INCENP::GFP particle directionality. n = 107 events from 32 cells (MKLP2) and n = 94 events from 19 cells (INCENP). **(F)** Gaussian fits of MKLP2::GFP (black) and INCENP::GFP (green) velocities. Histograms are shown in Figures S3F and S3G.

S2). Strikingly, the directional MKLP2 and INCENP events had similar velocities of 0.19 ± 0.05 µm/s and 0.19 ± 0.06 µm/s, respectively (Figures 3F, S3F, and S3G). The MKLP2 and INCENP velocities in cells were slightly higher compared to those measured *in vitro* (Figures 2D, 2G, 2L, S2J, S2L, and S2N), possibly because our *in vitro* assays were performed at 30°C, whereas cell culture experiments were carried out at 37° C. Furthermore, the influence of additional cellular factors on velocity cannot be ruled out. In short, we show that MKLP2 and INCENP show not only diffusive (Landino et al., 2017) but also directional motility in cells during anaphase.

MKLP2 Motor Activity Specifies CPC Localization in Anaphase

To test whether MKLP2-mediated transport is involved in CPC localization in anaphase, we used two approaches to perturb MKLP2 motor activity. First, we generated a P-loop mutation (T167N), conserved among all kinesin families and described to lock kinesin-1 in a strong microtubule-binding (“rigor”) state (Nakata and Hirokawa, 1995) (Figures S4A and S4B). Second, we made use of Paprotrain, an MKLP2-specific non-competitive ATPase inhibitor, which does not affect KIF4A and the two MKLP2-related kinesin-6 motors, MKLP1 and MPP1 (KIF20B) (Tcherniuk et al., 2010). MKLP2 *in vitro* motility on dynamic microtubules was blocked by the T167N mutation and severely reduced by 50 µM Paprotrain (Figure 4A). Although WT and T167N motors showed similar microtubule-binding efficiencies, the addition of Paprotrain reduced the number of motors landing on microtubules by 50% (Figure 4B). Moreover, MKLP2 dwell time was reduced from 8.5 ± 9.3 s (WT) to 3.7 ± 4.1 s (T167N) and 3.1 ± 4.2 s (Pap; Figures 4C and S4C). Thus, MKLP2 T167N does not exhibit “rigor”-like, microtubule binding but is impaired in movement with an increased off rate. Paprotrain showed a dose-dependent effect on MKLP2 motility parameters; run length, landing frequency, and velocity were reduced at increasing Paprotrain concentrations (Figures S4D–S4H). Furthermore, 47% of motors were static in the presence of 50 µM Paprotrain (Figures 4A, S4D, and S4I). The capacity of T167N and Paprotrain-treated MKLP2::mScarlet motors to recruit coreCPC::GFP complexes to microtubules *in vitro* was reduced by 50% and 56%, respectively, compared to WT MKLP2 (Figures 4D and 4E). Furthermore, most coreCPC complexes were stalled in the presence of the T167N mutant (Figures 4F and 4G), whereas the addition of 50 µM Paprotrain reduced the number of transport events as well as the velocity of moving coreCPC complexes (Figures 4F, 4G, S4J, and S4K).

We subsequently knocked down endogenous MKLP2 by small interfering RNA (siRNA) in HeLa cell lines expressing MKLP2(T167N)::GFP or WT MKLP2::GFP (Figures 4H, S3A, and S3C). Similar to WT MKLP2::GFP, MKLP2(T167N)::GFP was cytosolic in metaphase (Figure S3H). However, in anaphase, MKLP2(T167N)::GFP decorated the entire anaphase spindle instead of localizing to the spindle midzone and equatorial cortex (Figure 4H). Endogenous CPC (detected by immunofluorescence [IF] for Aurora B) followed the alternative localization of MKLP2(T167N)::GFP in anaphase (Figure 4H). MKLP2(T167N)::GFP thus allows the relocation of the CPC from chromosomes to anaphase spindle microtubules, but in the absence of motor activity, the CPC fails to concentrate at the spindle midzone and equatorial cortex.

Addition of 50 µM Paprotrain 50 min after release from a Cdk1 inhibitor block also allowed the relocation of either MKLP2 and CPC from the chromosomes to the anaphase spindle (Figures 4I, upper panel, and 4J). However, MKLP2 and CPC were absent from the equatorial cortex, visualized by staining for Anillin (Figures 4I, middle panel, and 4J), and their localization on the spindle midzone, visualized by staining for PRC1, was reduced and more dispersed (Figures 4I and 4J). Similarly, live-cell imaging of INCENP::GFP revealed that, in the majority of the Paprotrain-treated cells, the midzone pool of INCENP::GFP was detectable but somewhat more dispersed (Figures 4K and S3I; Videos S3 and S4), whereas the cortical pool of INCENP::GFP was hardly detectable (Figures 4K, 4L, and S3I). Importantly, localization of the microtubule crosslinker PRC1, which concentrates on the antiparallel microtubule overlaps in the anaphase spindle midzone (Bieling et al., 2010; Mollinari et al., 2002; Pamula et al., 2019; Zhu et al., 2006), was unchanged (Figure 4I, lower panel). This most likely explains why Paprotrain addition at this time point did not impair cleavage furrow ingression (Figures S3I and S3J; Videos S3 and S4) and hardly affected the completion of cytokinesis (Figure S3K), as spindle midzone-derived signals can induce cytokinesis even when MKLP2 is absent or Aurora B inhibited (Adriaans et al., 2019; Ahonen et al., 2009; Guse et al., 2005). Taken together, strong suppression of MKLP2-dependent CPC motility with the T167N mutant perturbs CPC accumulation at both the spindle midzone and equatorial cortex, whereas a weaker inhibition of MKLP2 motor using Paprotrain mainly affects CPC localization to the equatorial cortex.

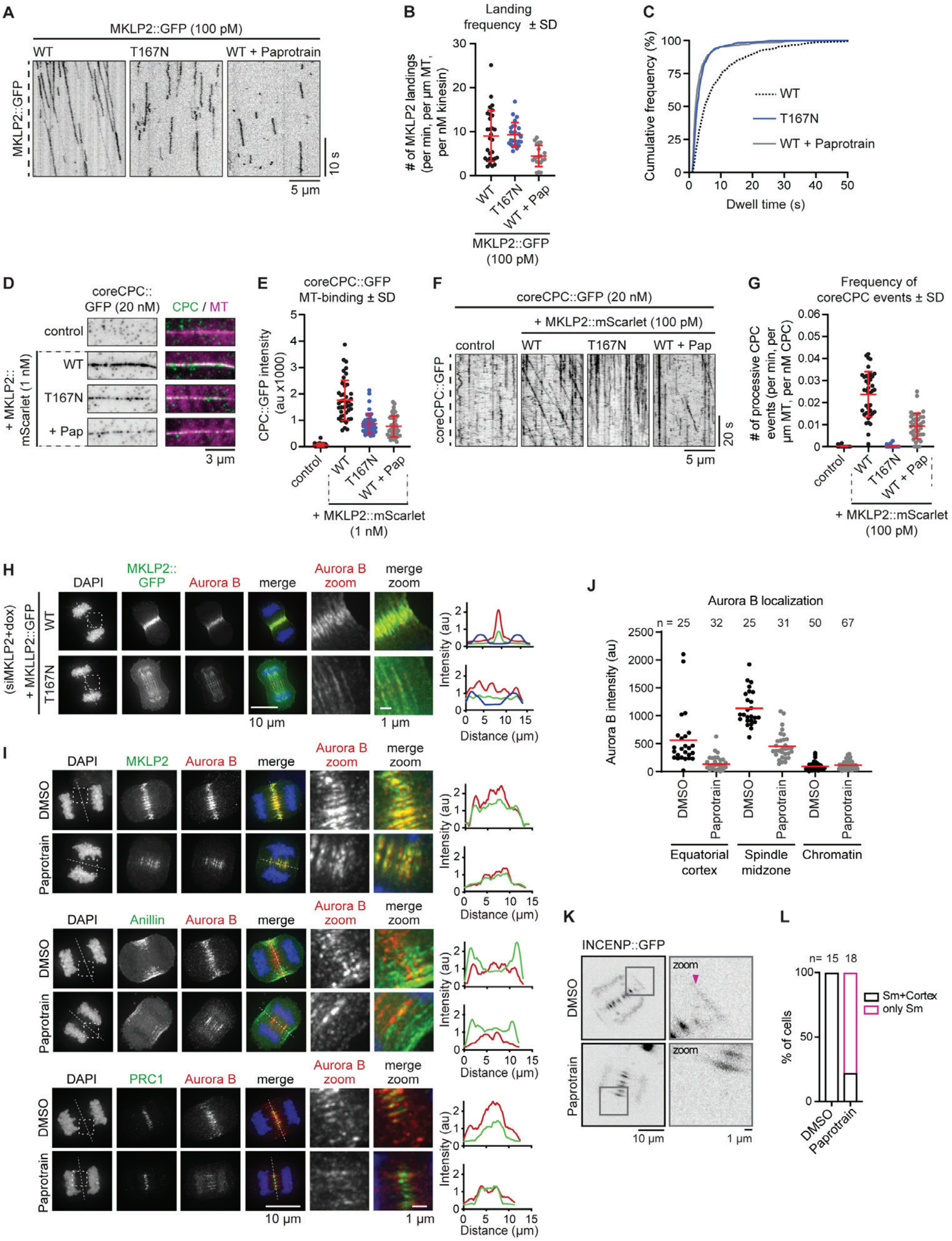

Figure 4 - Inhibition of MKLP2 Activity Perturbs CPC Localization in Anaphase
(A) Representative kymographs of WT, T167N, and 50 µM Paprotrain-treated MKLP2::GFP on dynamic microtubules. Image acquisition: 10 fps. Quantifications of different motor properties are in Figures S4D–S4I. **(B)** Quantification of MKLP2::GFP landing frequency normalized for microtubule length, time of acquisition, and kinesin concentration. n = 29, 26, and 20 microtubules from two or three experiments. Error bars denote SD. **(C)** Cumulative frequency plot of dwell times. n = 845 (WT), 929 (T167N), and 336 (WT+Paprotrain) kinesins from two or three experiments. **(D)** Representative images showing coreCPC::GFP on dynamic rhodamine-labeled microtubules *in vitro*. **(E)** Quantification of coreCPC::GFP intensities on dynamic

Figure 4 (continued) microtubules. n = 42, 42, 47, and 45 microtubules from two experiments. Error bars denote SD. **(F)** Representative kymographs of coreCPC::GFP on dynamic microtubules. Image acquisition: 4 fps. **(G)** Quantification of processive coreCPC events per microtubule normalized for microtubule length, time of acquisition, and coreCPC concentration. n = 58, 40, 58, and 38 microtubules from two or three experiments. Error bars denote SD. Data points for MKLP2 WT correspond to Figure 2K. **(H)** Representative IF images of HeLa cells expressing MKLP2::GFP or MKLP2 (T167N)::GFP (Figures S3A and S3C). Endogenous MKLP2 was depleted by siRNA (Figures S3D and S3E). Anaphase cells were stained for GFP and Aurora B, DNA by DAPI. Dotted box and line in DAPI indicates respectively zoom area and position of the line scan shown on the right. MKLP2::GFP (green), Aurora B (red), and DAPI (blue) are shown. **(I)** Representative IF images of anaphase HeLa cells minus (DMSO) or plus 50 μM Paprotrain (10 min treatment; fixation 60 min after Cdk1 inhibitor release). Dotted box and line in DAPI indicates, respectively, zoom area and position of the line scan shown on the right for, respectively, MKLP2, Anillin, and PRC1 (green) with Aurora B (red). **(J)** Quantification of Aurora B intensity levels on the equatorial cortex, the spindle midzone, and on chromatin in anaphase cells treated with either DMSO or 50 μM Paprotrain. n, number of cells analyzed. Red bars represent mean values. **(K)** Representative stills (corresponds to 02:30 [DMSO] and 03:00 [Paprotrain] of Figure S3I and Videos S3 and S4) with zooms of HeLa cells expressing INCENP::GFP. Paprotrain (50 μM) or DMSO was added after Cdk1 inhibitor release. Arrowhead indicates cortical localization. (L) Percentage of living cells showing spindle midzone (Sm) or Sm plus cortical localization of INCENP::GFP.

Conclusions

Our combined *in vitro* and cell-based experiments indicate that MKLP2 functions as a processive motor that focuses the CPC at the antiparallel microtubule overlaps of the anaphase spindle midzone and transports the CPC along microtubules toward the equatorial cortex. The MKLP2-CPC complex might subsequently dock at the cell cortex through interactions with myosin II and actin (Kitagawa et al., 2013; Landino et al., 2017). Despite the fact that the motor domain of MKLP2 has an atypical structure and mechanochemistry (Atherton et al., 2017), full-length MKLP2 can move processively along microtubules. Furthermore, our *in vitro* reconstitution experiments suggest that the interaction with the CPC promotes processivity of MKLP2 at the expense of its velocity and independently of Aurora B kinase activity. This property is likely caused by direct interactions of different CPC components with microtubules (Ainsztein et al., 1998; Mackay et al., 1993; Trivedi et al., 2019; Tseng et al., 2010; van der Horst et al., 2015; Wheatley et al., 2001), although some effects on the conformation of the MKLP2 molecule may also be involved. Because miniCPC, used in our experiments, lacks the microtubule binding SAH domain of INCENP, we cannot exclude that, in the presence of full-length INCENP, motor velocity is further reduced. However, we deem it unlikely that MKLP2 is stalled by binding to full-length CPC in cells, as both MKLP2 and INCENP exhibit directional motility with similar velocities in cells. Because of the differences in ionic strength, temperature, and molecular crowding in cells versus the *in vitro* conditions, it is possible that MKLP2 by itself would move in cells faster than in our *in vitro* assays and that the CPC slows it down in cells, similar to what we observed *in vitro*. Why only a subset of MKLP2-CPC complexes moves directionally in cells is currently unclear. Post-translational modification of MKLP2, the CPC, or microtubules or the presence of specific microtubule-associated proteins may control the motility of MKLP2-CPC complexes or their preference for specific microtubule tracks. Overall, our data provide a mechanistic basis for the anaphase-specific CPC accumulation at the spindle midzone and equatorial cortex.

Materials & Methods

Cell lines and cell culture
HeLa Flp-In T-Rex (female) and human embryonic kidney 239T (HEK293T, female) cells were cultured in Dulbecco's modified Eagle's Medium (DMEM, Sigma-Aldrich) supplemented with 6% Fetal Calf Serum (FCS, Sigma-Aldrich), 2 mM UltraGlutamine (Lonza), 100 units/ml penicillin and 100 μg/ml Streptomycin (Sigma-Aldrich). HeLa Flp-In T-Rex cells were additionally supplemented with 4 μg/ml Blasticidin (PAA Laboratories). Cell lines were cultured at 37°C with 5% CO_2. Polyclonal HeLa Flp-In T-Rex cells with stable integration of GFP-tagged INCENP, GFP-tagged Borealin and GFP-tagged MKLP2 were cultured in the presence of 800 μg/ml Hygromycin B (Sigma-Aldrich) and 6% Tet-approved HyClone Fetal Bovine Serum (GE Healthcare). Protein expression was induced with 1 μg/ml of doxycycline (Sigma-Aldrich) for minimal 12 hr.

Plasmids
Full length MKLP2 (aa 1-890) was obtained by PCR from a human thymus cDNA library and was subsequently cloned into a pEGFP-N1 vector to generate MKLP2::GFP. This plasmid was used to generate the T167N MKLP2 mutant by site-directed mutagenesis, and to create the deletion mutants aa 1-513, aa 513-890, aa 513-821, aa 513-765 and aa 765-890 by PCR and restriction cloning into pEGFP-N1. MKLP2 deletion mutant aa 513-821, used for protein purification from E. coli, was inserted into a pGEX-6P-1 vector by PCR and restriction cloning. MKLP2 WT/T167N::GFP was cloned into a cDNA5/FRT/TO-hygromycin B vector (Invitrogen) for stable cell line production. Full length MKLP2 cDNA was also cloned into a pTT5 vector (Novopro labs) containing a C-terminal GFP::StrepII- or mScarlet::StrepII-tag used for protein purification. β-tubulin::Halo (TUBB5-Halo) was a gift from Yasushi Okada (Addgene plasmid # 64691; http://n2t.net/addgene:64691; RRID:Addgene_64691) (Uno et al., 2014). Full length VSV-tagged INCENP, INCENP 49-918 (delta CEN-box) and INCENP d539-747 (deletion of single alpha helix, SAH) constructs were made as previously described (Vader et al., 2007; Vader et al., 2006; van der Horst et al., 2015). Full length INCENP cDNA was used to generate the following INCENP fragments: aa 1-63, 1-100, 1-200 by PCR and restriction enzyme-based cloning into pEGFP-N1. Site directed mutagenesis was used to generate the INCENP mutant R35/36/39/40E. INCENP WT and INCENP R35/36/39/40E were subsequently cloned into a pcDNA5/FRT/TO-hygromycin B vector (Invitrogen) for stable cell line generation. INCENP (aa 1-100) and INCENP (aa 1-100) linker (GGGGS) INCENP (aa 834-918) were also cloned into a pTT5 vector (Novoprolabs) with a C-terminal GFP::StrepII- or mCherry::StrepII-tag for protein purification. A plasmid encoding full length Borealin (pCR3; Invitrogen), and previously described (Vader et al., 2006), was used as a template for site directed mutagenesis to generate the GFP::Borealin mutant R17/19E, K20E. The N-terminally GFP-tagged Borealin WT and Borealin R17/19E, K20E were subsequently cloned into a pcDNA5/FRT/TO-hygromycin B vector (Invitrogen) for stable cell line production. Full length Borealin, Survivin and Aurora B were amplified by PCR from previously described plasmids (Hengeveld et al., 2012; Vader et al., 2007; Vader et al., 2006) and cloned into a pTT5 vector lacking GFP and StrepII coding DNA (Novoprolabs) and these were used for protein purification together with INCENP. The Aurora B (K106R), kinase dead, mutant was generated by site directed mutagenesis of pTT5-Aurora B. All newly generated plasmids were checked by DNA sequencing. Due to a point mutation in the stop codon of Aurora B K106R the protein has a short extension of 15 amino acids which is visible by western blot in Figure S2F. Finally, a tri-cistronic pET28a vector expressing 6xHis::INCENP1-58-Survivin-Borealin (gift from PT Stukenberg) was used for bacterial expression of the coreCPC after replacement of INCENP 1-58 for INCENP 1-100.

siRNA and plasmid transfection
HeLa Flp-In T-Rex cells were transfected with siRNAs for either INCENP (Dharmacon/3'UTR; GGCUUGGCCAGGUGUAUAUdTdT), MKLP2 (Dharmacon/3'UTR; CCACCUAUGUAAUCUCAUGdTdT) or Borealin (Dharmacon/3'-UTR; AGGUAGAGCUGUCUUCAdTdT) using HiPerfect Transfection Reagent (#301705; QIAGEN) and a standard HiPerfect transfection protocol with a 1:3 ratio for siRNA:HiPerfect (37°C for 20 min) in Opti-MEM culture medium. The final concentration of siRNAs was 20 nM for siINCENP and siBorealin, and 40 nM for siMKLP2. Cells were analyzed 48 hr after siRNA transfection. Transient transfection of plasmids was performed with X-tremeGENE 9 DNA Transfection Reagent (Roche) according the manufacturer's protocol. To generate stable cell lines with doxycyclin-inducible expression of wild-type (WT) or E35/36/39/40R INCENP::GFP; WT or R17/19E, K20E GFP::Borealin; or WT or T167N MKLP2::GFP, HeLa Flp-In T-Rex cells were co-transfected with pOG44 (Invitrogen) and pcDNA5/FRT/TO-hygromycin B plasmids encoding the indicated proteins. After transfection, cells were selected in medium supplemented with 800 μg/ml hygromycin B and 4 μg/ml blasticidin (Invitrogen). Polyclonal cell lines expressing the indicated GFP-tagged proteins were used for analysis. HEK293T cells were transfected with pTT5 plasmids using Polyethylenimine (PEI, Polysciences) with a 1:3 ratio for plasmid:PEI. Alternatively, HEK293T were transfected with pEGFP-N1 plasmids using a standard Calcium Phosphate transfection protocol.

Immunoprecipitation (IP)
HeLa Flp-In T-Rex cells were plated in 2.5 mM thymidine (Sigma-Aldrich) for 24 hr and released into 20 μM of the Eg5 inhibitor S-Trityl-L-Cysteine (STLC, Tocris Bioscience) (DeBonis et al., 2004) for 16 hr. Where indicated, doxycycline (1 μg/ml, Sigma-Aldrich) was added together with STLC to induce protein expression. HeLa Flp-In T-Rex

cells or HEK293T cells transfected with plasmids encoding GFP-tagged MKLP2, INCENP and Borealin constructs were collected and washed twice in ice-cold PBS. Since endogenous CPC proteins and MKLP2 are poorly expressed in interphase (Chang et al., 2006; Hill et al., 2000; Kimura et al., 2004; Li et al., 1998), we enriched for mitotic cells by the addition of STLC. Cell pellets were lysed in lysis buffer (50 mM Tris-HCl, 150 mM NaCl, 0.5% NP-40, 0.1% sodium deoxycholate, 40 mM glycerol phosphate, 10mM NaF, 0.3 mM NaVO3, 100 µM ATP, 100 µM MgCl2, 100 nM okaidic acid and supplemented with protease inhibitors (Roche)) with 4 U/ml MNase (New England Biolabs) and 30 µg/ml RNase (Sigma-Aldrich). After clearing debris by centrifugation, a standard Bradford assay was performed to measure protein concentration, and cell lysates were incubated with 15 µl of GFP-Trap beads (Chromotek) for 2 hr at 4°C while rotating. Beads were washed three times with washing buffer (50 mM Tris-HCl, 400 mM NaCl, 0.5% NP-40, 0.1% sodium deoxycholate, 40 mM glycerol phosphate, 10 mM NaF, 0.3 mM NaVO3, 100 µM ATP, 100 µM MgCl2, 100 nM okaidic acid and supplemented with protease inhibitors (Roche)). Proteins were eluted by adding 20 µl of standard SDS sample buffer and by boiling the samples for 5 min. Samples were stored at –20°C until SDS-PAGE and western blotting.

Protein expression and pulldown from E. coli

For protein expression and purification from E. coli, BL21(DE3) cells were transformed with the respective GST-tagged constructs: GST control and GST::MKLP2(513-821). Bacteria were grown to an OD600 of 0.6-0.8 at 37°C, after which protein expression was induced with 0.1 mM Isopropyl β-d-1-thiogalactopyranoside (IPTG) for 20 hr at 25°C. Bacteria were spun down and subjected to one freeze-thaw cycle using liquid nitrogen to stimulate proper lysis. Bacteria were resuspended and sonicated on ice in cold lysis buffer containing 50 mM Tris pH 7.5, 300 mM NaCl, 5% glycerol, 0.5 mM DTT, 0.5 mM PMSF and Complete protease inhibitor cocktail (Roche). Lysates were centrifuged at ~ 18.000 g for 60 min, and the supernatants were incubated with Glutathione Sepharose beads (GE Healthcare) for 4 hr at 4°C, followed by extensive washes on column with a wash buffer containing 50 mM Tris pH 7.5, 300 mM NaCl, 5% glycerol and 0.5 mM DTT. The glutathione beads containing GST (control) or GST::MKLP2(513-821) bound proteins were stored at 4°C and used for pulldown assay the same day.

For protein expression of CPC components from E. coli, Rosetta2(DE3) (Novagen) cells were transformed with a tricistronic pET28a vector containing 6 × His::INCENP 1–100 Survivin and Borealin. Bacteria were grown to an OD600 of ~0.8 at at 37°C in LB supplemented with 60 mg l^{-1} $ZnCl^2$ and 0.2% glucose, after which protein expression was induced with 0.45 mM IPTG for 20 hr at 18°C. Bacteria were spun down and subjected to one freeze-thaw cycle using liquid nitrogen to stimulate proper lysis. Bacteria were resuspended and sonicated on ice in cold lysis buffer containing 50 mM Tris pH 7.5, 500 mM NaCl, 5% glycerol, 5 mM imidazole, 0.5 mM DTT, 0.5 mM PMSF and Complete protease inhibitor cocktail (Roche). Lysates were centrifuged at ~ 18.000 g for 60 min and the supernatant was kept for the subsequent pulldown assay. The stored glutathione beads containing the GST-tagged proteins were incubated with the bacterial lysates containing the CPC components overnight at 4°C. The beads were washed with a wash buffer containing 50 mM Tris pH 7.5, 300 mM NaCl, 5% glycerol and 0.5 mM DTT. To visualize CPC components on Coomassie-stained SDS-PAGE gels, part of the CPC-containing supernatant was incubated with Ni-NTa beads (QIAGEN) for 2 hr at 4°C, followed by extensive washes on column with a wash buffer containing 50 mM Tris pH 7.5, 500 mM NaCl, 5% glycerol, 25 mM imidazole and 0.5 mM DTT. All pulldown beads and samples were supplemented with Laemmli sample buffer, boiled, and analyzed by SDS-PAGE and western blotting.

Protein purification and Aurora B kinase assay

HEK293T cells transfected with single (WT or T167N MKLP2::GFP::StrepII or WT or T167N MKLP2::mScarlet-t::StrepII) or multiple (coreCPC or miniCPC::GFP::StrepII or mCherry::StrepII, see Figure 2A) pTT5 plasmids were collected and washed twice in ice-cold PBS. Cells were lysed in ice-cold lysis buffer (50 mM HEPES, 300 mM NaCl, 0.5% Triton X-100, pH 7.4) supplemented with protease inhibitors (Roche). After clearing debris by centrifugation at 4°C, cell lysates were incubated with StrepTactin beads (StrepTactin Sepharose High Performance, GE Healthcare) for one hour at 4°C. Beads were washed three times with ice cold washing buffer (50 mM HEPES, 150 mM NaCl, 0.01% Triton X-100). For MKLP2 proteins, beads were washed an additional time with a high salt wash buffer (1M NaCl). The proteins were subsequently eluted in elution buffer (50 mM HEPES, 150 mM NaCl, 0.01% Triton X-100 and 2.5 mM desthiobiotin) for 10 min. Protein concentration was determined by SDS-PAGE and Coomassie Blue staining using InstantBlue (Expedeon), using purified BSA titration as a reference. Purified proteins were snap-frozen and stored at –80°C. A kinase assay was performed by adding 5 µg of purified miniCPC with either Aurora B WT or KD, into a reaction mixture containing kinase buffer (10 mM MgCl2, 25 mM HEPES pH 7.5, 25 mM β-glycerophosphate, 0.5 mM DTT, 0.5 mM vanadate, 100 µM ATP), and 0.2 mg/ml Histone H3 as substrate (Roche Diagnostics). Either DMSO or 2 µM Aurora B inhibitor (ZM447439, Tocris) was added to the reaction as well. After 30 min incubation at 30°C, the reaction was stopped by the addition of sample buffer. Samples were analyzed by western blot using a primary antibody specific for phosphorylated Serine 10 in Histone H3 (H3S10ph).

Western blotting

Mitotic HeLa or transfected HEK293T cells were collected and lysed in standard Laemmli buffer. Protein concentration was determined using a Lowry assay. Protein samples of either whole cell extracts, bacterial lysates or IP's were separated by SDS-PAGE and transferred to nitrocellulose membranes. Membranes were blocked in 4% milk in Tris-buffered saline containing 0.5% Tween-20 (TBST) and subsequently incubated with a primary antibody for 2 hr.

Primary antibodies used were rabbit anti-MKLP2 (Bethyl (ITK) A300-879A), rabbit anti-Aurora B (Abcam 2254-100), rabbit anti-Borealin (gift from Dr. S. Wheatley), rabbit anti-Survivin (R&D Systems AF886), mouse anti-INCENP (Invitrogen 39-2800), rabbit anti-H3S10ph (Upstate 06-570), mouse anti-α-tubulin (Sigma, T5168), mouse anti-GFP (Roche 11814460001), mouse anti-GST B14 (Tebu SC-138), and mouse anti-penta-His (QIAGEN 34660). Membranes were washed three times with TBST, and subsequently incubated with goat anti-mouse or anti-rabbit horseradish peroxidase (HRP)-conjugated secondary antibodies (Bio-Rad). An ECL chemiluminescence detection kit (GE Healthcare) was used to visualize the protein-antibody complex.

Mass spectrometry

Eluted MKLP2::GFP::StrepII or GFP::StrepII samples (three technical replicates of each) were first denatured and alkylated by adding alkylation buffer (10 mM tris(2-carboxyethyl)phosphine (TCEP), 40 mM 2-chloroacetamide (CAA), 8 M urea, 1 M ammonium bicarbonate. After 30 min of incubation the samples were diluted fourfold with 1 M ammonium bicarbonate and 250 ng Trypsin/Lys-C protease (Promega) was added and followed by overnight digestion at 37°C on a shaker. The samples were then cleaned up using homemade C18 stagetips (Rappsilber et al., 2007), and a quarter was used for the analysis with LC-MS (Thermo Easy-nLC 1000, Thermo Orbitrap Fusion Tribrid) running a 140 min gradient (300 nl/min, 30 cm, 1.9 μm C18 column) with 240k (at 200 m/z) full MS resolution and a 1 s MS2 duty cycle (top speed, highest to low intensity, HCD fragmentation). Raw files were analyzed with Maxquant software, version 1.6.3.4. For identification, the Human Uniprot database was searched with oxidation of and carbamidomethylation of cysteine set as fixed modification, while peptide and protein false discovery rates were set to 1%. The median intensity of the iBAQ values was then plotted as Log2 transformed values with a red line (x = 0) and a green line (x+5) added as visual aid.

Immunofluorescence microscopy

For immunofluorescence (IF) of anaphase cells, HeLa Flp-In T-Rex cells were plated in 2.5 mM thymidine (Sigma-Aldrich) for 24 hr in 24 well plates containing 12 mm High Precision coverslips (Superior-Marienfeld GmbH & Co) and subsequently released into medium containing 5 μM Cdk1 inhibitor RO3306 (Calbiochem) for another 16 hr to synchronize cells in G2. Where indicated, doxycycline (1 μg/ml, Sigma-Aldrich) was added together with RO3306 to induce protein expression. Cells were released from the RO3306-induced G2 block by washing three times with warm medium. Where indicated, 50 μM Paprotrain (Millipore) was added 50 min after the release from the Cdk1 inhibitor. After 10 min, cells were processed for IF. To identify binucleates, cells were released from Cdk1 inhibitor, Paprotrain was added 50 min after the release and cells were fixed 24 hr after release. Cells were fixed with 4% PFA in PBS for 7 min and permeabilized in 0.25% Triton X-100 in PBS for 5 min. Cells were blocked in PBS containing 3% BSA and 0.1% Tween-20. Primary antibodies used were: rabbit anti-MKLP2 (Bethyl (ITK) A300-878A), rabbit anti-PRC1 (Santa Cruz sc-8356), mouse anti-Aurora B (BD Transduction labs 611083), rabbit anti-Anillin (a kind gift from Michael Glotzer) and mouse anti-GFP (Roche 11-814-460-001) or GFP booster ATTO-488 (Chromotec GBA488). Secondary antibodies used were: goat anti-mouse or goat anti-rabbit IgG-Alexa 488, goat anti-mouse or goat anti-rabbit IgG-Alexa 568 (Invitrogen). 4',6-Diamidino-2-Phenylindole (DAPI, Sigma-Aldrich) was used for DNA staining. Phalloidin-Alexa 568 (Invitrogen, A12380) was used to visualize F-actin to facilitate scoring of binucleates. Coverslips were mounted in ProLong Antifade (Molecular Probes). Images were taken with a Personal DeltaVision system (Applied Precision) equipped with a 100x / NA 1.40 UPLS Apo-UIS2 objective (Olympus) and a CoolSNAP HQ CCD camera (Photometrics). Images were deconvolved in Softworx. For each experiment, all images were acquired with identical illumination settings. Images are projections of deconvolved Z stacks, unless stated otherwise.

***In vitro* microtubule dynamics assays**

Doubly cycled GMPCPP microtubule seeds were prepared as described before (Mohan et al., 2013), by incubating a tubulin mix containing 70% unlabeled porcine brain tubulin (Cytoskeleton), 18% biotin-tubulin (Cytoskeleton) and 12% rhodamine-tubulin (Cytoskeleton) at a total final tubulin concentration of 20 μM with 1 mM GMPCPP (Jena Biosciences) at 37°C for 30 min. Microtubules were pelleted by centrifugation in an Airfuge for 5 min at 119,000 × g and then depolymerized on ice for 20 min. This was followed by a second round of polymerization at 37°C with 1 mM GMPCPP. microtubule seeds were then pelleted as above and diluted in MRB80 buffer containing 10% glycerol, snap frozen in liquid nitrogen and stored at −80°C.

Flow chambers, assembled from sticking plasma-cleaned glass coverslips onto microscopic slides with a double sided tape were functionalized by sequential incubation with 0.2 mg/ml PLL-PEG-biotin (Susos AG, Switzerland) and 1 mg/ml NeutrAvidin (Invitrogen) in MRB80 buffer (80 mM piperazine-N,N[prime]-bis(2-ethanesulfonic acid), pH 6.8, supplemented with 4 mM MgCl2, and 1 mM EGTA. microtubule seeds were attached to the coverslip through biotin-NeutrAvidin interactions. Flow chambers were further blocked with 1 mg/ml κ-casein (Sigma-Aldrich). The *in vitro* reaction mixture consisted of 18 μM tubulin, 50 mM KCl, 0.1% methylcellulose, 0.5 mg/ml κ-casein, 1 mM GTP, an oxygen scavenging system (20 mM glucose, 200 μg/ml catalase, 400 μg/ml glucose-oxidase, and 4 mM DTT), 2 mM ATP, MKLP2 motors at indicated concentrations (concentrations were calculated for monomeric proteins), and CPC protein complexes at indicated concentrations. After centrifugation in an Airfuge for 5 min at 119,000 x g, the reaction mixture was added to the flow chamber containing the microtubule seeds and sealed with vacuum grease. The experiments were conducted at 30°C, and data were collected using total internal reflection fluorescence (TIRF) microscopy. For most experiments, the reaction mixture was composed of 17.5 μM tubulin supplemented with 0.5 μM rhodamine-labeled tubulin to properly visualize microtubules in the assay. For assays where we labeled growing microtubule ends, bacterial purified mCherry::EB3 (Montenegro Gouveia et al., 2010) was added to the assay at a concentration of 20 nM. All tubulin products were purchased from Cytoskeleton Inc.

TIRF Microscopy

In vitro reconstitution assays were imaged on a TIRF microscope setup as described previously (Mohan et al., 2013) or on an ILAS-2 TIRF setup. The former system consisted of an inverted research microscope Nikon Eclipse Ti-E (Nikon) with the perfect focus system (Nikon), equipped with Nikon CFI Apo TIRF 100x 1.49 N.A. oil objective (Nikon) and controlled with MetaMorph 7.7.5 software (Molecular Devices). The microscope was equipped with TIRF-E motorized TIRF illuminator modified by Roper Scientific France/PICT-IBiSA, Institut Curie. To keep the *in vitro* samples at 30°C, a stage top incubator model INUBG2E-ZILCS (Tokai Hit) was used. For excitation, 491 nm 100 mW Calypso (Cobolt) and 561 nm 100 mW Jive (Cobolt) lasers were used. We used ET-GFP 49002 filter set (Chroma) for imaging of proteins tagged with GFP or ET-mCherry 49008 filter set (Chroma) for imaging of rhodamine-labeled tubulin or proteins tagged with mScarlet or mCherry. For simultaneous imaging of green and red fluorescence, we used an Evolve512 EMCCD camera (Photometrics) and ET-GFP/mCherry filter cube (59022; Chroma) together with an Optosplit III beamsplitter (Cairn Research Ltd) equipped with double-emission filter cube configured with ET525/50 m, ET9630/75 m and T585lprx (Chroma). Fluorescence was detected using an EMCCD Evolve 512 camera (Roper Scientific) with the intermediate lens 2.5X (Nikon C mount adaptor 2.5X). The final magnification using EMCCD camera was 0.063 μm/pixel.

ILAS-2 system (Roper Scientific, Evry, France) is a dual laser illuminator for azimuthal spinning TIRF (or Hilo) illumination and with a custom modification for targeted photomanipulation. This system was installed on Nikon Ti microscope (with the perfect focus system, Nikon), equipped with 150 mW 488 nm laser and 100 mW 561 nm laser, 49002 and 49008 Chroma filter sets. For simultaneous imaging of green and red fluorescence, we used an Evolve512 EMCCD camera (Photometrics) and ET-GFP/mCherry filter cube (59022; Chroma) together with an Optosplit III beamsplitter (Cairn Research Ltd) equipped with double-emission filter cube configured with ET525/50 m, ET9630/75 m and T585lprx (Chroma). Fluorescence was detected using an EMCCD Evolve mono FW DELTA 512x512 camera (Roper Scientific) with the intermediate lens 2.5X (Nikon C mount adaptor 2.5X). The setup was controlled with MetaMorph 7.8.8 software (Molecular Device). To keep the *in vitro* samples at 30°C, a stage top incubator model INUBG2E-ZILCS (Tokai Hit) was used. The final resolution using EMCCD camera was 0.065 μm/pixel.

Single-molecule intensity analysis

Sample preparation for the fluorescence intensity analysis was performed by immobilizing diluted GFP or MKLP2::GFP full length proteins non-specifically to the plasma cleaned glass coverslips in flow chambers. After protein addition, the flow chambers were washed with MRB80 buffer, sealed with vacuum grease and immediately imaged with a TIRF microscope. Approximately 10 images of previously unexposed coverslip areas were acquired. GFP and MKLP2::GFP full length proteins were located in different chambers of the same coverslip, so identical imaging conditions could be preserved. All acquisitions were obtained under identical laser power, exposure time and TIRF angle.

Live cell microscopy

Imaging of MKLP2::GFP and INCENP::GFP in HeLa Flp-In T-Rex cells was done in Lab-tek (8 well, Chambered Coverglass W/Cover #1.5 Borosilicate Sterile, Thermo Fisher Scientific). Cells were blocked in late G2 by overnight Cdk1 inhibition (RO-3306) and released prior to imaging by 3x washing with Leibovitz's medium (Sigma-Aldrich). DMSO or Paprotrain was added 20 min after release from the Cdk1 inhibition. To visualize microtubules, MKLP2::GFP expressing HeLa cells were transfected with a β-tubulin::Halo construct. To label the expressed β-tubulin::Halo, the imaging medium was supplemented with cell-permeable HaloTag TMR Ligand (Promega) 30 min prior to imaging. Medium was changed to Leibovitz's medium (Sigma-Aldrich) supplemented with 10% FCS (FBS, Sigma-Aldrich), 2 mM UltraGlutamine (Lonza) and 100 units/ml penicillin and 100 μg/ml streptomycin (Sigma-Aldrich).

Spinning disk microscopy was performed on inverted research microscope Nikon Eclipse Ti-E (Nikon), equipped with the perfect focus system (Nikon), Plan Apo VC 100x N.A. 1.40 oil objective (Nikon), spinning disk Yokogawa CSU-X1-A1 with 405-491-561-642 quad-band mirror (Yokogawa). The system was also equipped with ASI motorized stage with the piezo plate MS-2000-XYZ (ASI), Back-Illuminated Evolve 512 EMCCD camera (Photometrics) or Back-Illuminated Prime BSI sCMOS camera (Photometrics) and controlled by the MetaMorph 7.10 software (Molecular Devices). 491nm 100mW Calypso (Cobolt), 561nm 100mW Jive (Cobolt) and 642 nm 110 mW Stradus (Vortran) lasers were used as the light sources. ET-GFP filter set (49002, Chroma) was used for imaging of proteins tagged with green fluorescent marker; ET-mCherry filter set (49008, Chroma) was used for imaging of proteins tagged with red fluorescent marker, ET-Cy5 filter set (49006, Chroma) was used for imaging of proteins tagged with far-red fluorescent marker. For simultaneous imaging of green and red fluorescence we used ET-GFP/mCherry filter set (59022, Chroma) together with DualView DV2 beam splitter (Photometrics). 16-bit images were projected onto the Evolve 512 EMCCD camera with intermediate lens 2.0X (Edmund Optics) at a magnification of 0.066 μm/pixel or onto Prime BSI sCMOS camera with no intermediate lens at a magnification of 0.063 μm/pixel. To keep cells at 37°C we used stage top incubator (model INUBG2E-ZILCS, Tokai Hit). Imaging of INCENP::GFP in HeLa Flp-In T-Rex cells with or without Paprotrain (50 μM) was performed on a Spinning Disk Microscope consisting of an inverted research microscope Eclipse Ti2-E (Nikon), equipped with the Perfect Focus System (Nikon), CFI Plan Apo TIRF 60X oil objective (Nikon), spinning disk Yokogawa CSU-W1-T2. The system was also equipped with a Ti2-S-SE-E motorized stage (Nikon) and the piezo insert NANO Z200-N2 (Mad City Labs), environmental chamber for temperature (37°C) and CO2 control (OkoLab) and fully controlled with NIS-Elements-AR_v5.20 software (Nikon). Using the 405-488-568-647quad-band Ex mirror (Yokogawa) in combination with the 561nm 100mW (Oxxius) laser as the light source, the Em-filter 525/50 nm BrightLine (FF03-525/50-25, Semrock) and the Zyla 4.2 Plus sCMOS camera (Andor) we were able to detect INCENP::GFP.

Quantification and Statistical Analysis

Single molecule GFP counting assays

ImageJ plugin Comdet v.0.3.61 and DoM_Utrecht v1.1.1.5 (https://github.com/ekatrukha/DoM_Utrecht) were used for detection and fitting of single molecule fluorescent spots as described previously (Yau et al., 2014). With this method, individual spots were fitted with 2D Gaussian, and the amplitude of the fitted Gaussian function was used as a measure of the fluorescence intensity value of an individual spot. These fitted peak intensity values were used to build fluorescence intensity histograms which could be fitted to a Gaussian curve using GraphPad Prism 7.

Analysis of *in vitro* reconstitution data

Images and videos were processed and analyzed with Fiji image processing software (ImageJ). Maximum intensity projections were made using z projection. Kinesin velocities, run lengths and landing frequencies were obtained from kymograph analysis using ImageJ plugin KymoReslideWide v.0.4 (https://github.com/ekatrukha/KymoResliceWide). Kinesin parameters were quantified for processive events that last > 1 s. Static events were not included in velocity and run length quantifications. Quantification of landing frequencies was corrected for microtubule length, time of acquisition and kinesin concentration. Processive events were quantified and subdivided into "complete" and "incomplete" tracks. Tracks where both kinesin landing and detachment were observed were defined as complete, whereas incomplete tracks were tracks that exceeded the 90 s acquisition time or partially took place outside of the acquisition area. In cases of hyperprocessive events (imaging of miniCPC::GFP, or MKLP2::GFP in the presence of miniCPC) with many incomplete tracks, the observed event frequency per microtubule was quantified instead of landing frequency. Again, these data were corrected for microtubule length, time of acquisition and kinesin or CPC concentration. To distinguish directional and processive CPC events from diffusively behaving particles, only unidirectional events with a duration > 2.5 s were quantified. CPC::GFP labeling intensities on *in vitro* polymerized dynamic microtubules were measured from 2 pixel wide line scans along microtubules. An adjacent line scan 10 pixels away from the same microtubule was used as a background intensity measurement. microtubule labeling intensity was corrected by subtraction of this background intensity measurement. Imaging conditions were kept identical for all samples in the same experiment.

For *in vitro* experiments with Paprotrain or the T167N mutant motor, kinesin dwell time and landing frequency were quantified for all events that last > 1 s. For the *in vitro* experiments with Paprotrain, runs with a velocity < 0.025 μm/s were classified as static events. The percentage of static events per microtubule was quantified as a percentage of all kinesin events per microtubule. In the experiments with Paprotrain, non-motile (static) events were included in velocity and run length quantifications. Kinesins running on GMPCPP microtubule seeds were excluded as much as possible from the analysis.

Analysis of live cell imaging data

Image analysis was performed with Fiji image processing software (ImageJ). MKLP2 and INCENP velocities were obtained from kymograph analysis using ImageJ plugin KymoReslideWide v.0.4 (https://github.com/ekatrukha/KymoResliceWide). To distinguish directional MKLP2::GFP and INCENP::GFP events in cells from diffusive or statically behaving particles, only unidirectional events with a relatively constant velocity > 0.05 μm/s and a duration > 2.5 s were quantified. In addition, only events that could be measured using a kymograph were quantified in these experiments.

Quantification of immunofluorescence

Images were deconvolved in Softworx (Applied Precision). For each experiment, all images were acquired with identical illumination settings. Images are projections of deconvolved z stacks. Image analysis was performed with Fiji image processing software (ImageJ). To quantify and compare the mean fluorescence intensities (MFIs) of Aurora B on the equatorial cortex (marked by Anillin), the spindle midzone (marked by PRC1), and on chromatin (DAPI), a regions of interest (ROIs) were made on the basis of Anillin, PRC1 or DAPI localization. A random region of the cytoplasm was used as background measurement, and background intensity per cell was subtracted from the fluorescence intensity measured in the indicated ROIs. Line plots were performed with Fiji image processing software (ImageJ) and visualized in Graphpad Prism 7 software.

Protein sequence alignment

Protein sequences from several kinesin families were retrieved from Uniprot: kinesin-1, KIF5B (UniProt: P33176);

kinesin-2, KIF17 (UniProt: Q9P2E2); kinesin-3, KIF1A (UniProt: Q12756); kinesin-4, KIF4A (UniProt: O95239); kinesin-5, KIF11 (Eg5) (UniProt: P52732); kinesin-6, KIF20A (MKLP2) (UniProt: O95235); kinesin-6, KIF20B (MPP-1) (UniProt: Q96Q89); kinesin-6, KIF23 (MKLP1) (UniProt: Q02241). These sequences were aligned and analyzed online using ClustalOmega software.

Statistical analysis

Statistical significance was analyzed either using the Mann-Whitney *U* test, or *t* test, as indicated in the figure legends. For the *t* tests, data distribution was checked for normal distribution of the data. Kinesin and CPC velocities are represented using frequency distributions and Gaussian curve fits. For this fitting, data distributions were assumed to be normal, but this was not formally tested. Statistical analysis was performed with Graphpad Prism 7 or Prism 8 software.

Description for Supllemental Videos

Video S1. Representative Movie and Corresponding Zoom of HeLa Cells in Anaphase with Stable Inducible Expression of MKLP2::GFP, Related to Figure 3A

Video S2. Representative Movie and Corresponding Zoom of HeLa Cells in Anaphase with Stable Inducible Expression of INCENP::GFP, Related to Figure 3B

Video S3. Representative Movie of HeLa Cells in Anaphase with Stable Inducible Expression of INCENP::GFP (DMSO Control), Related to Figures 4K and S3I

Video S4. Representative Movie of HeLa Cells in Anaphase with Stable Inducible Expression of INCENP::GFP and Treated with 50 µM Paprotrain, Related to Figures 4K and S3

Author Contributions

I.E.A and S.M.A.L conceived the project. I.E.A, P.J.H, A.A. and S.M.A.L, designed the experiments. I.E.A., P.J.H., A. Aher, M.J.M.V, R.M. van E, and I.G. performed the experiments. I.E.A and P.J.H analyzed the experiments. I.E.A, P.J.H, A.A. and S.M.A.L wrote, reviewed and edited the manuscript. S.M.A.L. and A.A. supervised the project.

Acknowledgments

We thank Drs M. Glotzer, S. Wheatley and T. Stukenberg for their generous gift of reagents, Dr. M. Hadders for his help with Figure 1I, and Dr. H.R. Vos for proteomics support. This work is financially supported by The Netherlands Organization for Scientific Research (NWO-Vici 91812610 to S.M.A.L and NWO ALW Open Program grant 824.15.017 to A.A.). Proteomics was supported by the Proteins at Work Initiative (NWO 184.032.201). The group of S.M.A.L is part of Oncode Institute which is partly financed by the Dutch Cancer Society.

References

Adriaans, I.E., A. Basant, B. Ponsioen, M. Glotzer, and S.M.A. Lens. 2019. PLK1 plays dual roles in centralspindlin regulation during cytokinesis. J Cell Biol. 218:1250-1264.

Ahonen, L.J., A.M. Kukkonen, J. Pouwels, M.A. Bolton, C.D. Jingle, P.T. Stukenberg, and M.J. Kallio. 2009. Perturbation of Incenp function impedes anaphase chromatid movements and chromosomal passenger protein flux at centromeres. Chromosoma. 118:71-84.

Ainsztein, A.M., S.E. Kandels-Lewis, A.M. Mackay, and W.C. Earnshaw. 1998. INCENP centromere and spindle targeting: identification of essential conserved motifs and involvement of heterochromatin protein HP1. J Cell Biol. 143:1763-1774.

Atherton, J., I.M. Yu, A. Cook, J.M. Muretta, A. Joseph, J. Major, Y. Sourigues, J. Clause, M. Topf, S.S. Rosenfeld, A. Houdusse, and C.A. Moores. 2017. The divergent mitotic kinesin MKLP2 exhibits atypical structure and mechanochemistry. Elife. 6.

Bieling, P., L. Laan, H. Schek, E.L. Munteanu, L. Sandblad, M. Dogterom, D. Brunner, and T. Surrey. 2007. Reconstitution of a microtubule plus-end tracking system in vitro. Nature. 450:1100-1105.

Bieling, P., I.A. Telley, and T. Surrey. 2010. A minimal midzone protein module controls formation and length of antiparallel microtubule overlaps. Cell. 142:420-432.

Cesario, J.M., J.K. Jang, B. Redding, N. Shah, T. Rahman, and K.S. McKim. 2006. Kinesin 6 family member Subito participates in mitotic spindle assembly and interacts with mitotic regulators. J Cell Sci. 119:4770-4780.

Chang, J.L., T.H. Chen, C.F. Wang, Y.H. Chiang, Y.L. Huang, F.H. Wong, C.K. Chou, and C.M. Chen. 2006. Borealin/Dasra B is a cell cycle-regulated chromosomal passenger protein and its nuclear accumulation is linked to poor prognosis for human gastric cancer. Exp Cell Res. 312:962-973.

DeBonis, S., D.A. Skoufias, L. Lebeau, R. Lopez, G. Robin, R.L. Margolis, R.H. Wade, and F. Kozielski. 2004. In vitro screening for inhibitors of the human mitotic kinesin Eg5 with antimitotic and antitumor activities. Mol Cancer Ther. 3:1079-1090.

Green, R.A., E. Paluch, and K. Oegema. 2012. Cytokinesis in animal cells. Annu Rev Cell Dev Biol. 28:29-58.

Gruneberg, U., R. Neef, R. Honda, E.A. Nigg, and F.A. Barr. 2004. Relocation of Aurora B from centromeres to the central spindle at the metaphase to anaphase transition requires MKlp2. J Cell Biol. 166:167-172.

Guse, A., M. Mishima, and M. Glotzer. 2005. Phosphorylation of ZEN-4/MKLP1 by aurora B regulates completion of cytokinesis. Curr Biol. 15:778-786.

Hengeveld, R.C., N.T. Hertz, M.J. Vromans, C. Zhang, A.L. Burlingame, K.M. Shokat, and S.M. Lens. 2012. Development of a chemical genetic approach for human aurora B kinase identifies novel substrates of the chromosomal passenger complex. Mol Cell Proteomics. 11:47-59.

Hill, E., M. Clarke, and F.A. Barr. 2000. The Rab6-binding kinesin, Rab6-KIFL, is required for cytokinesis. EMBO J. 19:5711-5719.

Honda, R., R. Korner, and E.A. Nigg. 2003. Exploring the functional interactions between Aurora B, INCENP, and survivin in mitosis. Mol Biol Cell. 14:3325-3341.

Hooikaas, P.J., M. Martin, T. Muhlethaler, G.J. Kuijntjes, C.A.E. Peeters, E.A. Katrukha, L. Ferrari, R. Stucchi, D.G.F. Verhagen, W.E. van Riel, I. Grigoriev, A.F.M. Altelaar, C.C. Hoogenraad, S.G.D. Rudiger, M.O. Steinmetz, L.C. Kapitein, and A. Akhmanova. 2019. MAP7 family proteins regulate kinesin-1 recruitment and activation. J Cell Biol. 218:1298-1318.

Hummer, S., and T.U. Mayer. 2009. Cdk1 negatively regulates midzone localization of the mitotic kinesin Mklp2 and the chromosomal passenger complex. Curr Biol. 19:607-612.

Jeyaprakash, A.A., U.R. Klein, D. Lindner, J. Ebert, E.A. Nigg, and E. Conti. 2007. Structure of a Survivin-Borealin-INCENP core complex reveals how chromosomal passengers travel together. Cell. 131:271-285.

Kimura, M., C. Uchida, Y. Takano, M. Kitagawa, and Y. Okano. 2004. Cell cycle-dependent regulation of the human aurora B promoter. Biochem Biophys Res Commun. 316:930-936.

Kitagawa, M., S.Y. Fung, U.F. Hameed, H. Goto, M. Inagaki, and S.H. Lee. 2014. Cdk1 coordinates timely activation of MKlp2 kinesin with relocation of the chromosome passenger complex for cytokinesis. Cell Rep. 7:166-179.

Kitagawa, M., S.Y. Fung, N. Onishi, H. Saya, and S.H. Lee. 2013. Targeting Aurora B to the equatorial cortex by MKlp2 is required for cytokinesis. PLoS One. 8:e64826.

Klein, U.R., E.A. Nigg, and U. Gruneberg. 2006. Centromere targeting of the chromosomal passenger complex requires a ternary subcomplex of Borealin, Survivin, and the N-terminal domain of INCENP. Mol Biol Cell. 17:2547-2558.

Landino, J., S.R. Norris, M. Li, E.R. Ballister, M.A. Lampson, and R. Ohi. 2017. Two mechanisms coordinate the recruitment of the chromosomal passenger complex to the plane of cell division. Mol Biol Cell. 28:3634-3646.

Li, F., G. Ambrosini, E.Y. Chu, J. Plescia, S. Tognin, P.C. Marchisio, and D.C. Altieri. 1998. Control of apoptosis and mitotic spindle checkpoint by survivin. Nature. 396:580-584.

Mackay, A.M., D.M. Eckley, C. Chue, and W.C. Earnshaw. 1993. Molecular analysis of the INCENPs (inner centromere proteins): separate domains are required for association with microtubules during interphase and with the central spindle during anaphase. J Cell Biol. 123:373-385.

Mohan, R., E.A. Katrukha, H. Doodhi, I. Smal, E. Meijering, L.C. Kapitein, M.O. Steinmetz, and A. Akhmanova. 2013. End-binding proteins sensitize microtubules to the action of microtubule-targeting agents. Proc Natl Acad Sci U S A. 110:8900-8905.

Mollinari, C., J.P. Kleman, W. Jiang, G. Schoehn, T. Hunter, and R.L. Margolis. 2002. PRC1 is a microtubule binding and bundling protein essential to maintain the mitotic spindle midzone. J Cell Biol. 157:1175-1186.

Monroy, B.Y., D.L. Sawyer, B.E. Ackermann, M.M. Borden, T.C. Tan, and K.M. Ori-McKenney. 2018. Competition between microtubule-associated proteins directs motor transport. Nat Commun. 9:1487.

Montenegro Gouveia, S., K. Leslie, L.C. Kapitein, R.M. Buey, I. Grigoriev, M. Wagenbach, I. Smal, E. Meijering, C.C. Hoogenraad, L. Wordeman, M.O. Steinmetz, and A. Akhmanova. 2010. In vitro reconstitution of the functional interplay between MCAK and EB3 at microtubule plus ends. Curr Biol. 20:1717-1722.

Murata-Hori, M., and Y.L. Wang. 2002. Both midzone and astral microtubules are involved in the delivery of cytokinesis signals: insights from the mobility of aurora B. J Cell Biol. 159:45-53.

Nakata, T., and N. Hirokawa. 1995. Point mutation of adenosine triphosphate-binding motif generated rigor kinesin that selectively blocks anterograde lysosome membrane transport. J Cell Biol. 131:1039-1053.

Nguyen, P.A., A.C. Groen, M. Loose, K. Ishihara, M. Wuhr, C.M. Field, and T.J. Mitchison. 2014. Spatial organization of cytokinesis signaling reconstituted in a cell-free system. Science. 346:244-247.

Pamula, M.C., L. Carlini, S. Forth, P. Verma, S. Suresh, W.R. Legant, A. Khodjakov, E. Betzig, and T.M. Kapoor. 2019. High-resolution imaging reveals how the spindle midzone impacts chromosome movement. J Cell Biol. 218:2529-2544.

Rappsilber, J., M. Mann, and Y. Ishihama. 2007. Protocol for micro-purification, enrichment, pre-fractionation and storage of peptides for proteomics using StageTips. Nat Protoc. 2:1896-1906.

Samejima, K., M. Platani, M. Wolny, H. Ogawa, G. Vargiu, P.J. Knight, M. Peckham, and W.C. Earnshaw. 2015. The Inner Centromere Protein (INCENP) Coil Is a Single alpha-Helix (SAH) Domain That Binds Directly to Microtubules and Is Important for Chromosome Passenger Complex (CPC) Localization and Function in Mitosis. J Biol Chem. 290:21460-21472.

Sessa, F., M. Mapelli, C. Ciferri, C. Tarricone, L.B. Areces, T.R. Schneider, P.T. Stukenberg, and A. Musacchio. 2005. Mechanism of Aurora B activation by INCENP and inhibition by hesperadin. Mol Cell. 18:379-391.

Tcherniuk, S., D.A. Skoufias, C. Labriere, O. Rath, F. Gueritte, C. Guillou, and F. Kozielski. 2010. Relocation of Aurora B and survivin from centromeres to the central spindle impaired by a kinesin-specific MKLP-2 inhibitor. Angew Chem Int Ed Engl. 49:8228-8231.

Trivedi, P., A.V. Zaytsev, M. Godzi, F.I. Ataullakhanov, E.L. Grishchuk, and P.T. Stukenberg. 2019. The binding of Borealin to microtubules underlies a tension independent kinetochore-microtubule error correction pathway. Nat Commun. 10:682.

Tseng, B.S., L. Tan, T.M. Kapoor, and H. Funabiki. 2010. Dual detection of chromosomes and microtubules by the chromosomal passenger complex drives spindle assembly. Dev Cell. 18:903-912.

Uno, S.N., M. Kamiya, T. Yoshihara, K. Sugawara, K. Okabe, M.C. Tarhan, H. Fujita, T. Funatsu, Y. Okada, S. Tobita, and Y. Urano. 2014. A spontaneously blinking fluorophore based on intramolecular spirocyclization for live-cell super-resolution imaging. Nat Chem. 6:681-689.

Vader, G., C.W. Cruijsen, T. van Harn, M.J. Vromans, R.H. Medema, and S.M. Lens. 2007. The chromosomal passenger complex controls spindle checkpoint function independent from its role in correcting microtubule kinetochore interactions. Mol Biol Cell. 18:4553-4564.

Vader, G., J.J. Kauw, R.H. Medema, and S.M. Lens. 2006. Survivin mediates targeting of the chromosomal passenger complex to the centromere and midbody. EMBO Rep. 7:85-92.

van der Horst, A., and S.M. Lens. 2014. Cell division: control of the chromosomal passenger complex in time and space. Chromosoma. 123:25-42.

van der Horst, A., M.J. Vromans, K. Bouwman, M.S. van der Waal, M.A. Hadders, and S.M. Lens. 2015. Inter-domain Cooperation in INCENP Promotes Aurora B Relocation from Centromeres to Microtubules. Cell Rep. 12:380-387.

van der Vaart, B., W.E. van Riel, H. Doodhi, J.T. Kevenaar, E.A. Katrukha, L. Gumy, B.P. Bouchet, I. Grigoriev, S.A. Spangler, K.L. Yu, P.S. Wulf, J. Wu, G. Lansbergen, E.Y. van Battum, R.J. Pasterkamp, Y. Mimori-Kiyosue, J. Demmers, N. Olieric, I.V. Maly, C.C. Hoogenraad, and A. Akhmanova. 2013. CFEOM1-associated kinesin KIF21A is a cortical microtubule growth inhibitor. Dev Cell. 27:145-160.

van Riel, W.E., A. Rai, S. Bianchi, E.A. Katrukha, Q. Liu, A.J. Heck, C.C. Hoogenraad, M.O. Steinmetz, L.C. Kapitein, and A. Akhmanova. 2017. Kinesin-4 KIF21B is a potent microtubule pausing factor. Elife. 6.

Verma, V., and T.J. Maresca. 2019. Microtubule plus-ends act as physical signaling hubs to activate RhoA during cytokinesis. Elife. 8.

Wheatley, S.P., S.E. Kandels-Lewis, R.R. Adams, A.M. Ainsztein, and W.C. Earnshaw. 2001. INCENP binds directly to tubulin and requires dynamic microtubules to target to the cleavage furrow. Exp Cell Res. 262:122-127.

Yau, K.W., S.F. van Beuningen, I. Cunha-Ferreira, B.M. Cloin, E.Y. van Battum, L. Will, P. Schatzle, R.P. Tas, J. van Krugten, E.A. Katrukha, K. Jiang, P.S. Wulf, M. Mikhaylova, M. Harterink, R.J. Pasterkamp, A. Akhmanova, L.C. Kapitein, and C.C. Hoogenraad. 2014. Microtubule minus-end binding protein CAMSAP2 controls axon specification and dendrite development. Neuron. 82:1058-1073.

Yue, Y., T.L. Blasius, S. Zhang, S. Jariwala, B. Walker, B.J. Grant, J.C. Cochran, and K.J. Verhey. 2018. Altered chemomechanical coupling causes impaired motility of the kinesin-4 motors KIF27 and KIF7. J Cell Biol. 217:1319-1334.

Zhu, C., E. Lau, R. Schwarzenbacher, E. Bossy-Wetzel, and W. Jiang. 2006. Spatiotemporal control of spindle midzone formation by PRC1 in human cells. Proc Natl Acad Sci U S A. 103:6196-6201.

Supplemental Figures

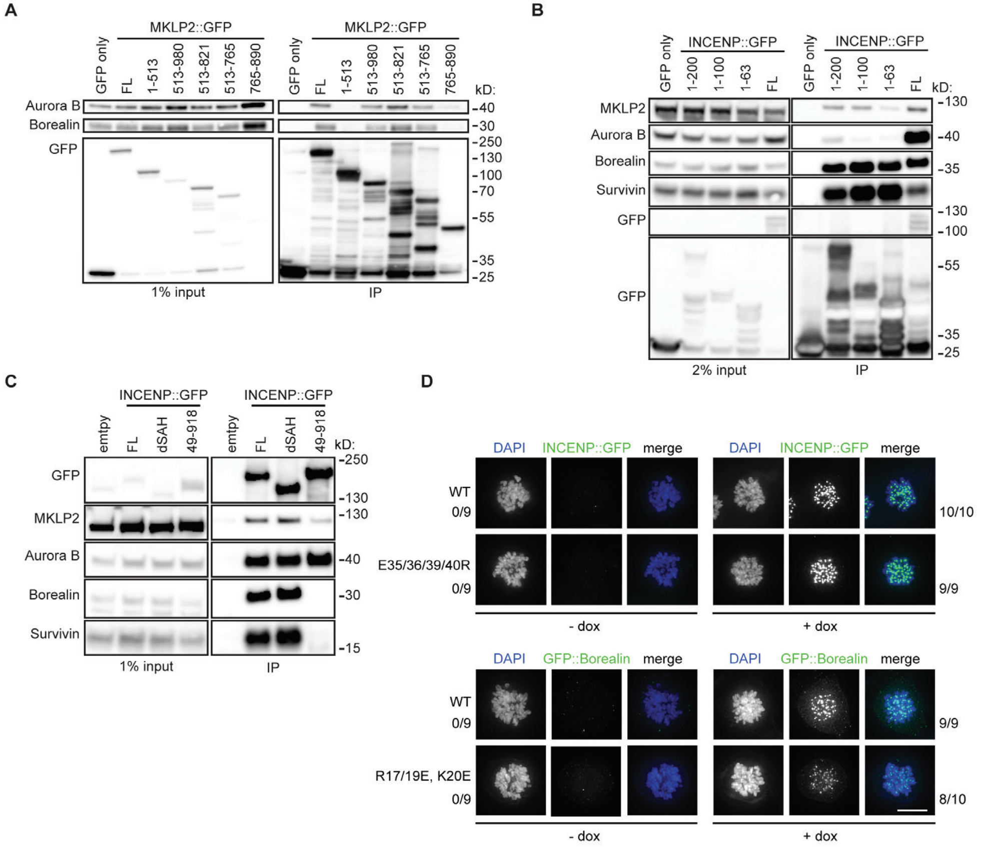
A
MKLP2::GFP
MKLP2::GFP
GFP only
FL
1-513
513-980
513-821
513-765
765-890
GFP only
FL
1-513
513-980
513-821
513-765
765-890
kD:
Aurora B
Borealin
GFP
-40
-30
-250
-130
-100
-70
-55
-35
-25
1% input
IP
B
INCENP::GFP
INCENP::GFP
GFP only
1-200
1-100
1-63
FL
GFP only
1-200
1-100
1-63
FL
kD:
MKLP2
Aurora B
Borealin
Survivin
GFP
GFP
-130
-40
-35
-130
-100
-55
-35
-25
2% input
IP
C
INCENP::GFP
INCENP::GFP
emtpy
FL
dSAH
49-918
emtpy
FL
dSAH
49-918
kD:
GFP
MKLP2
Aurora B
Borealin
Survivin
-250
-130
-130
-40
-30
-15
1% input
IP
D
DAPI
INCENP::GFP
merge
DAPI
INCENP::GFP
merge
WT
0/9
10/10
E35/36/39/40R
0/9
9/9
- dox
+ dox
DAPI
GFP::Borealin
merge
DAPI
GFP::Borealin
merge
WT
0/9
9/9
R17/19E, K20E
0/9
8/10
- dox
+ dox

Figure S1 - Mapping of the MKLP2-CPC interaction, Related to Figure 1
(A, B) HEK293T cells were transfected with the indicated MKLP2 (A) or INCENP (B) plasmids. Immunoprecipitations were performed with GFP-Trap beads, and samples were analyzed by Western blotting using antibodies specific for the indicated proteins. **(C)** IPs of GFP-tagged INCENP full length (FL), INCENP-dSAH (d539-747) and INCENP 49-918 from mitotic HeLa cells stably expressing the indicated doxycyclin-inducible protein. Blots were stained for MKLP2, Aurora B, Borealin, Survivin and GFP. The anti-GFP antibody gave a background band in the 'empty' HeLa cell line, which did not show up in the IP. **(D)** IF for GFP of HeLa cells expressing INCENP::GFP or INCENP E35/36/39/40R::GFP (upper panel), and expressing GFP::Borealin or GFP::Borealin R17/19E, K20E (lower panel) from a doxycyclin-inducible promotor. Cells were synchronized in mitosis by addition of STLC. DNA was visualized using DAPI. Scale bar = 10 μm. Numbers on the left indicate the number of times the depicted localization was observed/total number of cells that were imaged. Scale bar = 10 μm.

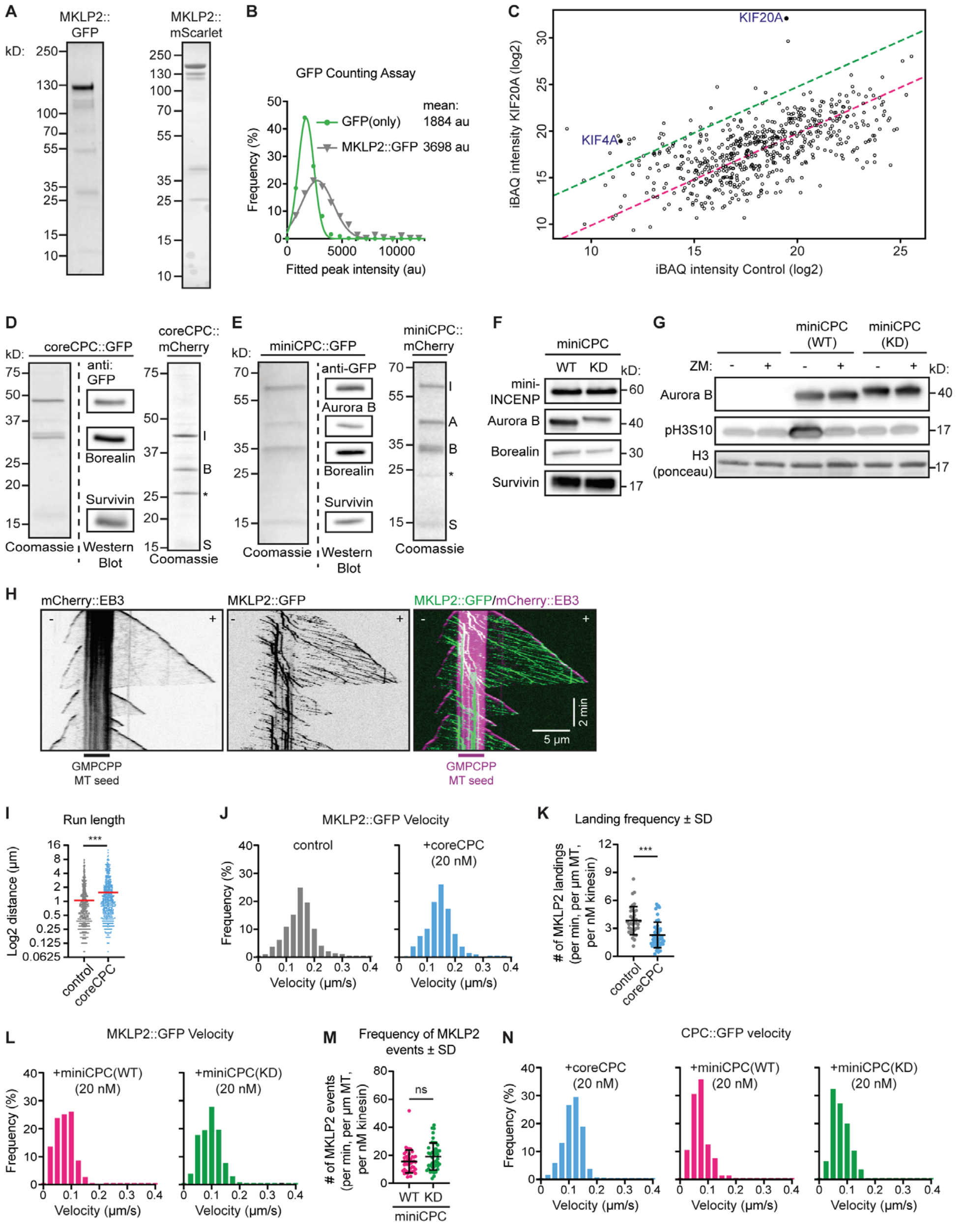

Figure S2 - Analysis of purified MKLP2 and CPC, Related to Figure 2
(A) SDS-PAGE of full length MKLP2::GFP and MKLP2::mScarlet purified from HEK293T cells. Gels were stained with Coomassie Brilliant Blue. **(B)** Histograms of peak-fitted fluorescence intensities of single GFP (green dots) and MKLP2::GFP molecules (grey triangles) immobilized on coverslips in two separate chambers on the same coverslip and the corresponding Gaussian fits (green and grey lines). Imaging conditions were identical for both conditions. n = 1909 (GFP) and n = 324 (MKLP2::GFP) molecules. Fluorophore density was approximately 0.04-0.10 µm−2. Mean values for each condition are indicated in the plot. **(C)** Scatter plot of protein abundance comparison between MKLP2::GFP and GFP purified from HEK293T cells using LC MS/MS. Enrichment of proteins is estimated using a linear model through all median iBAQ intensities of

Figure S2 (continued) identified proteins (N = 3) (Red line). Green line indicates 25 times enrichment based on the linear model. KIF20A(MKLP2) and KIF4A are indicated. Raw data/spectra can be found on ProteomeXchange Consortium via the PRIDE partner repository with the dataset identifier PXD014665.
(D) SDS-PAGE of purified coreCPC::GFP (left panel) and coreCPC::mCherry (right panel). Gels were stained with Coomassie Brilliant Blue. In the middle panel, individual proteins of coreCPC::GFP were visualized by Western blot probed with the indicated antibodies. INCENP 1-100 is visualized with anti-GFP. *An additional band around 25 kD appeared in the coreCPC::mCherry preparation, which corresponds to mCherry. **(E)** SDS-PAGE of purified miniCPC::GFP (left panel) and miniCPC::mCherry (right panel) loaded with Aurora B WT. Gels were stained with Coomassie Brilliant Blue. In the middle, individual proteins of miniCPC::GFP were visualized by Western blot probed with the indicated antibodies. INCENP (1-100)-linker-INCENP (834-918) is visualized with anti-GFP. *An additional band around 25 kD appeared in the coreCPC::mCherry preparation, which corresponded to mCherry. **(F)** Western blot of purified miniCPC loaded with either wild-type Aurora B (WT) or kinase dead Aurora B (KD). Blots were probed with antibodies specific for GFP, Aurora B, Borealin and Survivin. **(G)** *In vitro* kinase assay for purified miniCPC loaded with either WT or KD Aurora B. The kinase reaction was separated by SDS-PAGE and Western blots were probed with antibodies specific for Aurora B and phosphorylated serine 10 in Histone H3. Bottom panel is a Ponceau staining of Histone H3. **(H)** Kymographs showing a dynamic microtubule growing from a stable rhodamine-labeled GMPCPP microtubule seed. Addition of mCherry::EB3 marks growing microtubule-ends, MKLP2::GFP shows motility towards the microtubule plus-end. Microtubule plus (+) and (-) ends could be identified by their characteristic growth rates and are indicated in all images. Experiment was performed in the presence of 15 μM tubulin. **(I)** Quantification of MKLP2::GFP run length in control condition or in the presence coreCPC::mCherry. *** $p < 0.001$ (Mann-Whitney *U* test). n = 832 (control), n = 618 kinesins (coreCPC) from three independent experiments. Mean values are indicated with red bars. **(J)** Histograms of MKLP2::GFP velocities. n = 1145 and 1137 kinesin runs from three independent experiments. Histograms correspond to the velocity fits shown in Figure 2D. **(K)** Quantification of MKLP2::GFP landing frequency in control condition or in the presence coreCPC::mCherry normalized for microtubule length, time of acquisition and kinesin concentration. *** $p < 0.001$ (Mann-Whitney *U* test). n = 37 microtubules (control), n = 49 microtubules (coreCPC) from three independent experiments. **(L)** Histograms of MKLP2::GFP velocities. n = 459 and 657 kinesin runs from two independent experiments. Histograms correspond to the velocity fits shown in Figure 2G. **(M)** Quantification of MKLP2 event frequency corrected for microtubule length, time of acquisition and kinesin concentration. n = 43 (WT) and n = 42 (KD) microtubules from three independent experiments. **(N)** Histograms of CPC::GFP velocities. n = 708, 305 and 372 kinesin runs from three independent experiments. Histograms correspond to the velocity fits shown in Figure 2L.

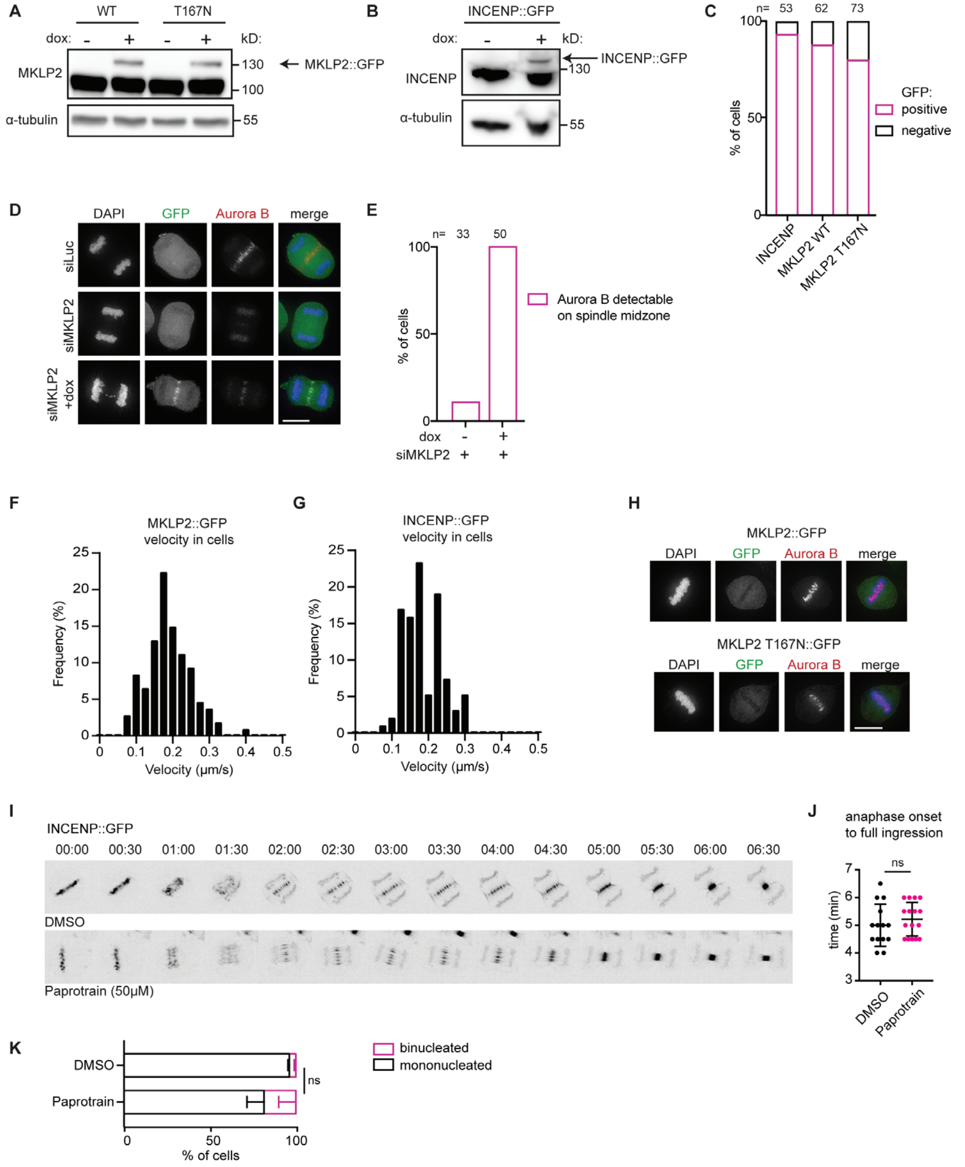

Figure S3 - Characterization of MKLP2::GFP, MKLP2(T167N)::GFP and INCENP::GFP expressing cell lines, their dynamics in HeLa cells in anaphase, and the effect of Paprotrain addition, Related to Figure 3 and Figure 4
(A, B) Western blot of the MKLP2::GFP, MKLP2 (T167N)::GFP (A) and INCENP::GFP (B) expressing cell lines probed with antibodies specific for MKLP2 (A) or INCENP (B) and α-tubulin (A,B). Expression of the exogenous GFP-tagged proteins was induced by addition of doxycycline (dox). **(C)** The MKLP2::GFP and INCENP::GFP expressing cell lines were released from a Cdk1 inhibitor-induced G2 block for 60 min and fixed anaphases were scored for the presence of spindle midzone-localized GFP-tagged protein after IF using anti-GFP. n = number of cells analyzed. **(D)** IF for GFP and Aurora B of HeLa cells in anaphase with or without expression of MKLP2::GFP from a dox-inducible promotor. Cells were transfected with siRNAs targeting either Luciferase (control) or MKLP2 (siMKLP2), and DNA was visualized using DAPI. Scale bar = 10 µm.

Figure S3 (continued) (E) Cells shown in D) were scored for the presence of Aurora B at the spindle midzone. n = number of cells analyzed.**(F,G)** Histograms showing the velocities of directional motility events of MKLP2::GFP (F) and INCENP::GFP (G) measured in HeLa cells. n = 107 (F) and 94 kinesin (G) runs from two or three independent experiments. Histograms correspond to the velocity fits shown in Figure 3F. **(H)** IF for GFP and Aurora B of HeLa cells in metaphase with expression of MKLP2::GFP or MKLP2(T167N)::GFP from a dox-inducible promotor. Endogenous MKLP2 was knocked down by siRNA. DNA was visualized using DAPI. Scale bar = 10 µm.

(I) Still images of a HeLa cell going through anaphase with stable inducible expression of INCENP::GFP. Paprotrain (50 µM) or DMSO was added 20 min after Cdk1 release. Still images correspond to Videos 3 and 4 and Figure 4K. **(J)** Timing of anaphase onset to full cleavage furrow ingression in presence or absence of Paprotrain (added 20 min after a Cdk1 inhibitor release). Corresponds to Figure 4K,L and S3I. ns = not significant (t test). **(K)** Quantification of mono- and binucleated HeLa cells 24 hrs after release from a Cdk1 inhibitor-induced G2 block. DMSO or Paprotrain was added 50 min after Cdk1 inhibitor release. Fixed cells were stained with Phalloidin-Alexa 568 to visualize F-actin and to facilitate scoring of binucleated cells. The mean percentage of cells of two independent experiments are shown. Error bars indicate SEM. n = 77, 84 (DMSO), 48, 107 (Paprotrain) cells analyzed in two independent experiments. ns = not significant (t test).

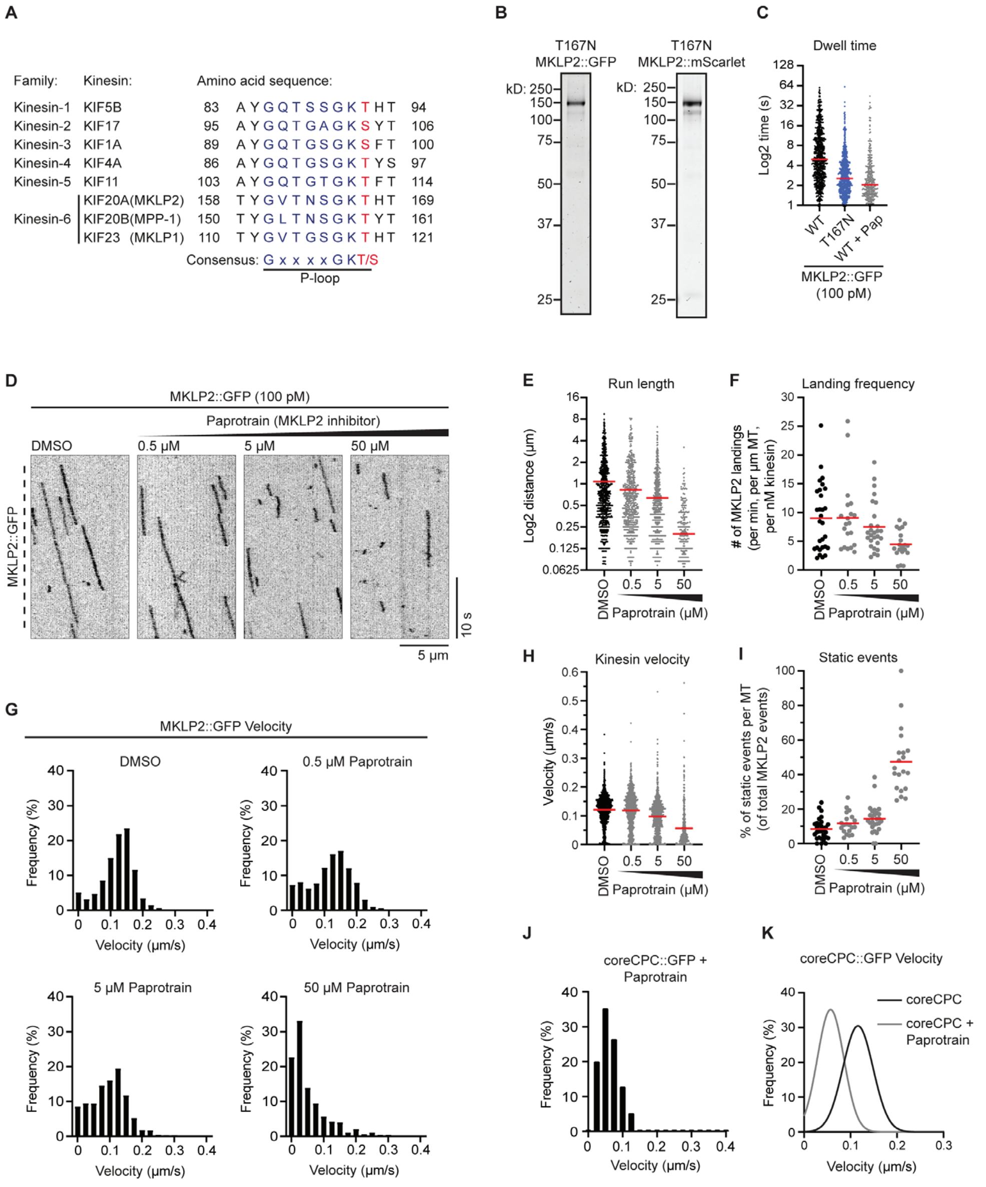

Figure S4 - Analysis of MKLP2 T167N motor, MKLP2 WT motor and CPCcore parameters in the presence of Paprotrain, Related to Figure 4
(A) Amino acid sequence alignment of the P-loops of various kinesins. Amino acids that are part of the P-loop consensus sequence, are indicated in blue. The position of the putative "rigor" kinesin mutation is indicated in red. **(B)** SDS-PAGE of full length MKLP2::GFP and MKLP2::mScarlet containing a T167N point mutation purified from HEK293T cells. Gels were stained with Coomassie Brilliant Blue. **(C)** Quantification of MKLP2::GFP dwell time. n = 845, 929 and 336 kinesins from two or three independent experiments. Mean values are indicated with red bars. Datapoints correspond with the cumulative frequency plot shown in Figure 4C. **(D)** Representative kymographs of MKLP2::GFP on dynamic microtubules in DMSO (control) conditions or in the presence of increasing concentrations MKLP2 inhibitor Paprotrain. Image acquisition was performed at 10 fps. **(E)** Quantification of MKLP2::GFP run length. n = 845, 626, 778 and 336 kinesins

Figure S4 (continued) from two or three independent experiments. Mean values are indicated with red bars. **(F)** Quantification of MKLP2::GFP landing frequencies per microtubule corrected for microtubule length, time of acquisition and kinesin concentration. n = 29, 20, 27, 20 microtubules from two or three independent experiments. Mean values are indicated with red bars. **(G, H)** Histograms (G) and quantification (H) of MKLP2::GFP velocities in DMSO or in the presence of increasing Paprotrain concentrations. n = 1262, 899, 1014 and 423 kinesins from two or three independent experiments. Mean values are indicated with red bars (H). **(I)** Quantification of static MKLP2::GFP events per microtubule as a percentage of the total number of MKLP2::GFP events observed per microtubule. Events were categorized as static when the velocity was < 0.025 µm/s. n = 29, 20, 27, 20 microtubules from two or three independent experiments. Mean values are indicated with red bars.**(J)** Histogram of coreCPC::GFP velocities in the presence of 100 pM MKLP2::mScarlet treated with 50 µM Paprotrain, n = 250 events from two independent experiments. **(K)** Gaussian fits of coreCPC::GFP velocities. Histograms are shown in Figures S2N and S4J.

Table S1

siRNA:

siINCENP	Dharmacon/3'UTR; GGCUUGGCCAGGUGUAUAUdTdT
siBorealin	Dharmacon/3'-UTR; AGGUAGAGCUGUCUUCAdTdT
siMKLP2	Dharmacon/3'UTR; CCACCUAUGUAAUCUCAUGdTdT

Primers:

Description	Primers ('5-'3)
F BsmBI-BglII-kozak-atg-Mklp2 N-term	agagaCGTCTCagatctcACCatgtcgcaagggatcctttctcc
R Mklp2-no stop-SalI-BsmBI-890	AGAGAcgtctcGTCGACttgtactttttgccaaaaggcccaga
F Muta BsmBI and Sequencing primer	ctctgtcgtatctacctccctagaggaca
R Muta BsmBI and Sequencing primer	gaggtagatacgacagagcagtctgatagcagg
R Mklp2-no stop-SalI-BsmBI-513	AGAGAcgtctcGTCGACttcataggtggggcatgcacaagc
F BsmBI-BglII-kozak-atg-Mklp2 513-	agagaCGTCTCagatctcACCatgcaactgggattcccatcc
F BsmBI-BglII-kozak-atg-Mklp2 765-	agagaCGTCTCagatctcACCatgagcactggggcaggaaaacttc
F MKLP2 -> pTT5 N1-GFP HindIII	agagaAAGCTTcaccATGTCGCAAGGGATCC
R MKLP2 fl -> pTT5 N1-GFP EcoRI	tctctGAATTCcGTACTTTTTGCCAAAAGGCCCAG
R MKLP2 513R -> pTT5 N1-GFP EcoRI	tctctGAATTCgCATAGGTGGGGCATGCACAAGC
R MKLP2 821 no stop	AGAGAcgtctcGTCGACttttggagtttcaacacagtatgatactgctc
F Muta INCENP E35/36/39/40R	tgtggcttcggcggatccaacggcgggccgagcgcatgttcacc
R Muta INCENP E35/36/39/40R	tcggcccgccgttggatccgccgaagccacaccaagtccttattatccatg
F Muta Borealin R17/19E K20E	tccttagagagggaggagctcgcctcctttctgaaagacttc
R Muta Borealin R17/19E K20E	aggcgagctcctccctctctaaggagttggtcttggccac
R 100	agagaGTCGACgggcgtcgggagctcagctggc
R 200	agagaGTCGACggtggagtcggggacagagtgcg
F NHeI --> pTT5 StrepII	agagaGCTAGCccaccatggggacgacggccccaggg
F HinDIII --> pTT5	agagaAAGCTTccaccatggctcctaggaagggcagtagtcg
R XbaI --> pTT5	agagaTCTAGAtcatttgtgggtccgtatgctgctgc
F HinDIII --> pTT5	agagaAAGCTTccaccatgggtgccccgacgttgc
R XbaI --> pTT5	agagaTCTAGAtcaatccatggcagccagctgc
R HinDIII --> pTT5 1-100 GFP StrepII	agagaAAGCTTgcgtcgggagctcagctgg
F INCENP linker 834 HinDIII --> pTT5	agagaAAGCTTggtggcggagggtctgatgaggcccatccccg
R INCENP no stop BamHI --> Ptt5	agagaGGATCCcagtgcttcttcaggctgtaggc
Fw513_MKLP2_pGEX_BamHI	TCCAGGGGCCCCTGGGATCCggcagtGGATCCatgcaactgggattcccatccc
Rv821_MKLP2_pGEX_XhoI	CGCGAGGCAGATCGCTCGAGTCAttggagtttcaacacagtatgatac
Fw1.mScarlet.MKLP2	ACGGTACCGCGGGCCCGGGATCCACCGGTCGCCACCatggtgagcaagggcgaggcag
Rv.mScarlet-mRuby3	AGCGCTGCCACTAGTcttgtacagctcgtccatgccg
F muta T167N	AGGGAAAAaCCACACGATTCAAGGTACC
R muta T167N	AATCGTGTGGtTTTTCCCTGAGTTAGTGACTCC
5' primer for mutagenesis (K106Rmutant)	CATCGTGGCGCTCAGGGTCCTCTTCAAGTC
3' primer for mutagenesis (K106Rmutant)	GACTTGAAGAGGACCCTGAGCGCCACGATG
F AurB NheI pTT5 C1	agagaGCTAGCgccaccatggcccagaagg
R AurB SalI --> pTT5 C1	agagaGTCGACtcaggcgacagattgaagggc

7

Kinesin-4 KIF21B limits microtubule growth to allow rapid centrosome polarization in T cells

Peter Jan Hooikaas[1*], Hugo G.J. Damstra[1*], Oane J. Gros[1],
Wilhelmina E. van Riel[1], Maud Martin[1,2], Yesper T.H. Smits[3],
Jorg van Loosdregt[3], Lukas C. Kapitein[1], Florian Berger[1]
and Anna Akhmanova[1]

Available on: **bioRxiv (2020): 2020.08.28.271643**

* These authors contributed equally

---

[1] Cell Biology, Neurobiology and Biophysics, Department of Biology, Faculty of Science, Utrecht University, Utrecht, Netherlands

[2] Current address: Laboratory of Neurovascular Signaling, Department of Molecular Biology, Université libre de Bruxelles (ULB), B-6041 Gosselies, Belgium.

[3] Laboratory of Translational Immunology, Department of Pediatric Immunology & Rheumatology, University Medical Center Utrecht, University of Utrecht, Utrecht, Netherlands

Abstract

When a T cell and an antigen-presenting cell form an immunological synapse, rapid dynein-driven translocation of the centrosome towards the contact site leads to reorganization of microtubules and associated organelles. Currently, little is known about how the regulation of microtubule dynamics contributes to this process. Here, we show that the knockout of KIF21B, a kinesin-4 linked to autoimmune disorders, causes microtubule overgrowth and perturbs centrosome translocation. KIF21B restricts microtubule length by inducing microtubule pausing typically followed by catastrophe. Catastrophe induction with vinblastine prevented microtubule overgrowth and was sufficient to rescue centrosome polarization in KIF21B-knockout cells. Biophysical simulations showed that a relatively small number of KIF21B molecules can restrict microtubule length and promote an imbalance of dynein-mediated pulling forces that allows the centrosome to translocate past the nucleus. We conclude that proper control of microtubule length is important for allowing rapid remodeling of the cytoskeleton and efficient T cell polarization.

Introduction

Large-scale reorganization of the microtubule (MT) cytoskeleton is essential for a variety of processes, such as cell division, differentiation and polarization. In dividing cells, a balance of dynein-dependent pulling forces and MT pushing forces determines the positioning of the MT-based mitotic spindle (Howard and Garzon-Coral, 2017; Kotak and Gonczy, 2013). In interphase cells with dense, non-centrosomal MT arrays, such as epithelial or neuronal cells, polarization is a slow process that requires hours, if not days (reviewed in (Kapitein and Hoogenraad, 2015; Meiring et al., 2020)). In contrast, interphase cells with sparse centrosome-based networks can rapidly switch polarity and reposition their MTs. For example, when a T cell encounters an antigen-presenting cell (APC), it translocates its centrosome and associated MTs towards the APC-contact side (Geiger et al., 1982; Kupfer et al., 1983; Stinchcombe et al., 2006; Yi et al., 2013) and forms an immunological synapse (reviewed in (Dustin et al., 2010)), a highly specialized compartment encircled by an actin-rich ring. The immunological synapse facilitates T-cell signaling and polarized secretion of cytokines or lytic molecules towards the APC (Figure 1A). The process of centrosome repositioning takes only a few minutes and is driven by membrane-associated dynein that pulls MTs with the attached centrosome towards the synapse (Combs et al., 2006; Liu et al., 2013a; Martin-Cofreces et al., 2008; Nath et al., 2016).

Whereas the role of dynein as force generator in centrosome translocation in T cells is firmly established, little is known about the properties of the MT network and MT dynamics that facilitate this rapid cytoskeletal reorganization, and only a few MT regulators participating in this process have been identified. Among them, MT-associated protein MAP4 was shown to be required for centrosome translocation (Bustos-Moran et al., 2017), potentially due its ability to regulate dynein (Samora et al., 2011; Semenova et al., 2014; Seo et al., 2016). In addition, both acetylation and detyrosination of MTs and a complex of casein kinase Iδ with EB1 were suggested to be important for efficient centrosome polarization (Andres-Delgado et al., 2012; Serrador et al., 2004; Zyss et al., 2011). Finally, a study describing the knockout of stathmin/OP18, a MT-destabilizing protein, in mouse cytotoxic T cells showed decreased centrosome polarization efficiency (Filbert et al., 2012). Yet, how these cytoskeletal perturbations affect the MT network of T cells as a whole and how this would consequently hinder centrosome translocation is poorly understood.

An interesting candidate to regulate MT dynamics in immune cells is kinesin-4 KIF21B. Kinesin-4 family members are well known for their ability to limit MT growth in a variety of cellular processes (Bieling et al., 2010; Bringmann et al., 2004; He et al., 2014; Yue et al., 2018). Among them are two closely related motors KIF21A and KIF21B, which consist of an N-terminal motor domain, several coiled-coil regions and a C-terminal WD40 domain (Marszalek et al., 1999). KIF21A is expressed in many tissues; it is well studied because point mutations impairing its auto-inhibition lead to congenital fibrosis of the extraocular muscles type 1 (CFEOM1), a neurodevelopmental disorder that affects eye movement (Bianchi et al., 2016; Cheng et al., 2014; Traboulsi and Engle, 2004; van der Vaart et al., 2013; Yamada et al., 2003). *In vitro*, KIF21A slows down MT growth and suppresses catastrophes, whereas in cells it prevents overgrowth of MTs at the cell cortex (van der Vaart et al., 2013).

KIF21B is expressed in brain, eyes and spleen (Marszalek et al., 1999). Several studies have linked the *KIF21B* gene to neurodevelopmental and immune-related disorders, including multiple sclerosis and inflammatory conditions such as Crohn's disease and ankylosing spondylitis (Anderson et al., 2009; Asselin et al., 2020; Barrett et al., 2008; Garcia-Etxebarria et al., 2016; Goris et al., 2010; International Multiple Sclerosis Genetics, 2010; Kannan et al., 2017; Kreft et al., 2014; Li et al., 2017; Liu et al., 2013b; Robinson et al., 2015; Yang et al., 2015). Kif21b knock out mice are viable but show behavioral deficits and defects in synaptic transmission (Ghiretti et al., 2016; Gromova et al., 2018; Morikawa et al., 2018; Muhia et al., 2016). At the cellular level, KIF21B has been reported to be a processive kinesin involved in neuronal transport (Ghiretti et al., 2016; Gromova et al., 2018; Labonte et al., 2014) and Rac1 inactivation (Morikawa et al., 2018). Furthermore, similar to all other kinesin-4 family members, KIF21B acts as a MT growth regulator both *in vitro* and in cells (Ghiretti et al., 2016; Muhia et al., 2016; van Riel et al., 2017). However, the activity of this kinesin is a matter of controversy, because one study reported that it acts as a positive regulator of MT dynamicity by increasing MT growth rate and catastrophe frequency; in these assays, KIF21B was present at relatively high concentrations (50-300 nM) and was mainly observed to bind to depolymerizing MT ends and lattices (Ghiretti et al., 2016). In contrast, our own work showed that KIF21B walks to MT plus ends where it slows down MT growth and potently induces MT pausing already at low nanomolar concentrations, with only one or two KIF21B molecules being sufficient to block elongation of a MT plus end (van Riel et al., 2017). Somewhat conflicting results have also been reported on the effects of the loss of KIF21B on MT plus end growth in neurons: two different studies found opposite effects on MT growth rates, although they agreed that KIF21B reduces MT growth processivity (Ghiretti et al., 2016; Muhia et al., 2016). Therefore, further analyses of KIF21B behavior and function are required to elucidate its role in regulating MT dynamics.

Here, we have investigated the role of KIF21B in regulating MT organization and dynamics in T cells. We generated KIF21B knockout (KIF21B-KO) Jurkat T cell lines, which displayed defects during immunological synapse formation, particularly in translocating their centrosome towards the synapse. These defects were rescued by KIF21B-GFP re-expression, and live-cell imaging of single KIF21B-GFP motors showed that they walked to MT plus ends and often induced MT pausing followed by depolymerization, very similar to our previous *in vitro* observations (van Riel et al., 2017). Using expansion microscopy, we visualized three-dimensional MT organization in Jurkat T cells and found that MTs were longer in KIF21B-KO cells. Interestingly, we could rescue centrosome polarization defects in KIF21B-KO cells by mildly increasing MT catastrophe frequency with a low dose of vinblastine, a MT-depolymerizing drug. These results were recapitulated in a two-dimensional computational model demonstrating that long MTs impaired centrosome polarization by altering the balance of dynein-drive pulling forcing in a way that prevents symmetry breaking, which could be restored by introducing more frequent catastrophes that limit MT length. We conclude that proper control of MT growth plays a critical role in T cell polarization.

Results

KIF21B knockout T cells are defective in centrosome polarization after activation

To study MT reorganization during immune synapse formation, we used Jurkat T lymphocyte cells. We mimicked *in vivo* T-cell activation by exposing these cells to anti-CD3 coated surfaces, as described previously (Bunnell et al., 2001; Parsey and Lewis, 1993)(Figure 1A,B). We confirmed KIF21B protein expression in these cells by Western blotting (Figure 1C). Using CRISPR/Cas9 technology we generated KIF21B knockout cells and selected two clones (#1 and #2) that were analyzed further. To perform rescue experiments, these two knockout cell lines were infected with a lentivirus expressing full-length KIF21B-GFP and the obtained polyclonal cell lines were sorted for GFP-positive cells and analyzed by Western blotting (Figure 1C). KIF21B expression was lost in both knockout lines, whereas KIF21B-GFP expression mildly exceeded endogenous KIF21B. In addition, we established that these Jurkat T cell lines were responsive to stimulus by first confirming the presence of CD3ε, a subunit of the T cell receptor (TCR) (Figure 1C). Next, we stimulated control and KIF21B-KO cells with phorbol 12-myristate 13-acetate (PMA) and ionomycin, which increase the downstream intermediates of TCR signaling, protein kinase C activity and intracellular calcium levels, respectively. This stimulation regime upregulates Interleukin-2 (IL-2) mRNA expression, a hallmark of T cell activation, and we found that our knockout cell lines responded similarly to control cells (Figure S1A, B).

To monitor immunological synapse formation, we added Jurkat cells to anti-CD3 coated coverslips, fixed the cells 10 min later and stained them with phalloidin to visualize the peripheral actin ring (Figure 1B, D). We measured synapse size and noticed that KIF21B-KO cell lines formed 28.4 % (KO #1) and 27.3 % (KO #2) smaller synapses compared to control cells and that this phenotype could be partially rescued by re-expression of KIF21B-GFP (Figure 1E). The reduction in the size of immunological synapses in KIF21B-KO cells was not due to smaller overall size of these cells, as their volume was the same as that of control cells (Figure S1C, D). Live-cell imaging using Differential Interference Contrast (DIC) microscopy showed that synapse formation was slower in KIF21B-KO cells (Figure S1E-G).

Next, we analyzed the overall MT organization in these cells by Total Internal Reflection Fluorescence (TIRF) microscopy, which visualizes a thin optical section located above the coverslip. In fully polarized cells, the centrosome-centered MT aster was visible in the TIRF focal plane, whereas in cells that failed to polarize properly, the centrosome was not visible by TIRF, and MTs located in the vicinity of the coverslip appeared disorganized (Figure 1F). In this experiment, the centrosome was located in the plane of the synapse in the majority of control (76 %) and KIF21B-GFP expressing cells (74.3 and 63.3 %), whereas this was the case only in 45.5 % (KO #1) and 43.6 % (KO #2) of KIF21B-KO cells (Figure 1G).

During T cell activation, lysosomes cluster around the centrosome and relocate together with it towards the synapse (Figure 1A, B). Immunostaining of non-activated Jurkat cells indeed showed that lysosomes were scattered throughout the cytoplasm, while after activation, both control and knockout cells showed lysosome clustering, indicating that KIF21B knockout does not affect the minus-end directed transport of lysosomes (Figure 1H, I). We then analyzed the position of the lysosome cluster relative to the coverslip using

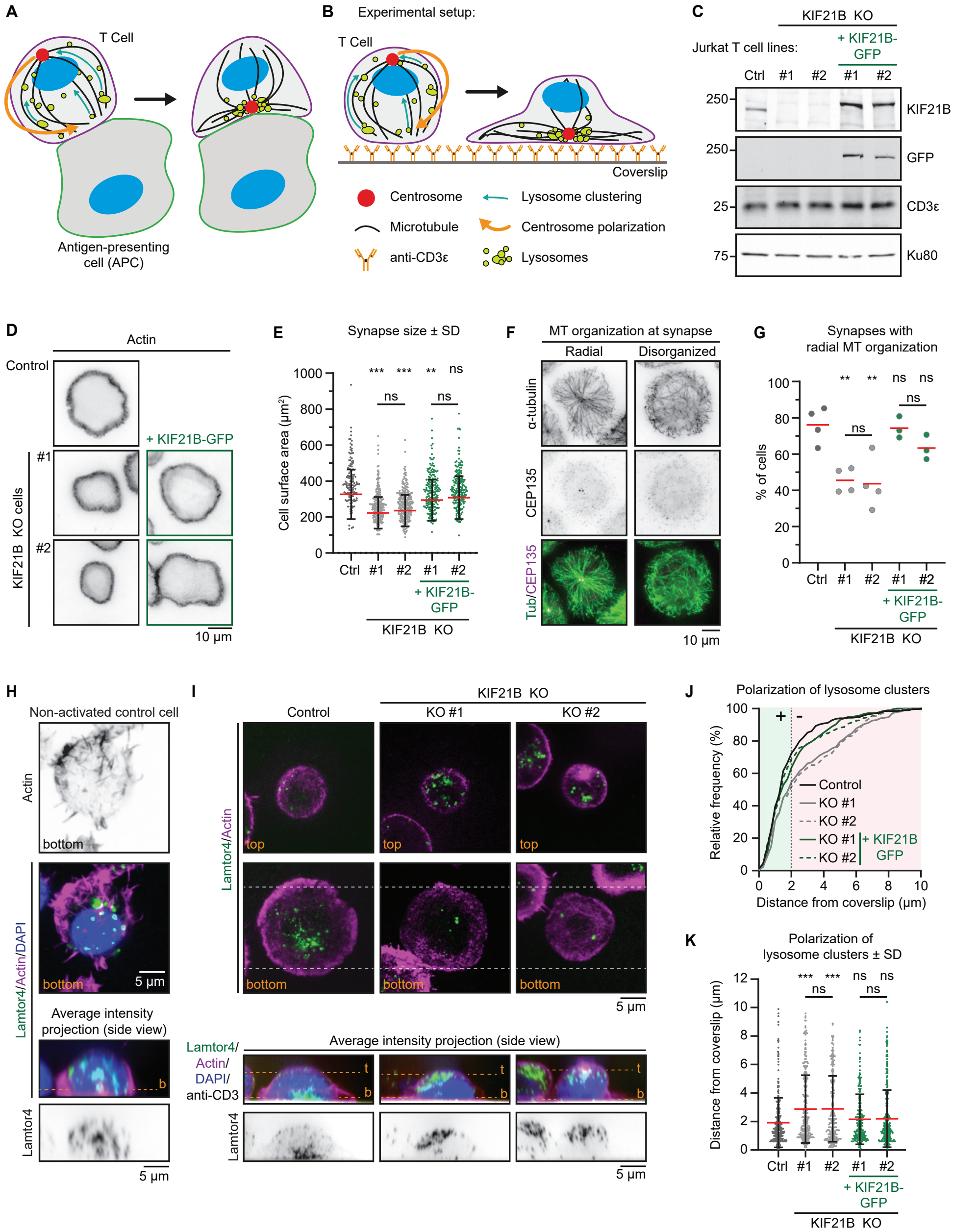

Figure 1 - Immunological synapse formation is impaired in KIF21B-KO Jurkat T cells
(A-B) Schematic representation of T cells forming an immunological synapse upon target recognition. *In vivo*, T cells recognize an antigen-presenting cell (APC) via the T cell receptor (CD3)-complex which triggers T cell activation. Upon activation, several organelles including lysosomes are transported to the centrosome by dynein. Simultaneously, the centrosome and its associated organelle cluster polarize to the synapse through MT pulling by membrane-anchored dynein at the synapse. B) To achieve spatiotemporal control on T cell activation we used anti-CD3 coated glass surfaces to mimic the APC and induce T cell activation and centrosome polarization. **(C)** Western blot analysis of the indicated Jurkat knockout (KO) cell lines with indicated antibodies. KIF21B-KO clone #1 and #2 were transduced with a KIF21B-GFP construct to generate two

Figure 1 (continued)
polyclonal cell lines re-expressing full-length KIF21B. **(D)** Phalloidin staining to show F-actin structures in indicated Jurkat T cell lines imaged on a widefield microscope. **(E)** Quantification of synapse size expressed as surface area based on a F-actin staining of indicated Jurkat T cells. n = 134, 218, 241, 185 and 194 cells from three independent experiments. ** $p < 0.01$, *** $p < 0.001$, ns = not significant (Mann-Whitney *U* test). **(F)** Immunostaining of Jurkat T cells showing two examples of MT organization at the immunological synapse. Cells were stained for α-tubulin and CEP135 and were imaged on a TIRF microscope. **(G)** Quantification of MT organization at immunological synapses. Cells were scored per condition either as "radial" or "disorganized" depending their MT organization as shown in Fig 1E. n = 4, 4, 4, 3 and 3 experiments. In total, 373, 389, 306, 367 and 354 cells were quantified per condition. ** $p < 0.01$, ns = not significant (t test). **(H)** Confocal images of a non-activated Jurkat T cell on a poly-D-lysine coated coverslip stained for Lamtor4, F-actin and DAPI. Single Z-plane images (upper panels) show the bottom part of the cell. The position of the single Z-plane images is indicated in the average intensity z-projection (bottom panels) with a dashed line (orange) labeled with "b" (bottom z-plane). **(I)** Confocal images of indicated Jurkat T cells stained for Lamtor4, F-actin and DAPI. In addition, the anti-CD3 antibody with which the coverslip was coated was also stained with a Alexa-dye-conjugated secondary antibody. Single Z-plane images (upper panels) show the top part of the cell and the bottom synapse part (indicated in orange). Dashed lines (white) indicated the area of the average intensity Z-projections shown in the bottom panels. The position of the single Z-plane images shown in the upper panels is indicated with dashed lines (orange) labeled with "t" (top z-plane) and "b" (bottom z-plane, synapse). **(J-K)** Quantification of lysosome positioning relative to the synapse-coverslip interface in indicated conditions. The z-positions of lysosome clusters were analyzed by identifying the peak Lamtor4 fluorescence intensity per cell analyzed from an average intensity side-projection of the cell. Cumulative frequency distribution (J) shows the percentage of cells with fully polarized Lamtor4 clusters. A 2 µm threshold was used to distinguish successful (green area) from failed (red area) Lamtor4 cluster polarization events. Dot plot (K) shows all individual cells quantified in (J). n = 318, 284, 244, 216 and 281 cells from four independent experiments. *** $p < 0.001$, ns = not significant (Mann-Whitney *U* test).

z-projections of these cells and found that only 52.4 % KIF21B-KO #1 and 50.4 % KIF21B-KO #2 cells contained a polarized lysosome cluster compared to 71% in control cells (Figure 1I, J). Again, we could rescue this phenotype by re-expressing KIF21B-GFP (Figure 1J, K). These data suggest that KIF21B-KO Jurkat cells exhibit defects in immunological synapse formation: they are less efficient in polarizing their centrosome and the associated lysosomes.

MT organization is altered in KIF21B knockout T cells

We next examined the organization of the MT network of control and KIF21B-KO T cells in more detail using Stimulated Emission Depletion (STED) microscopy. For optimal labelling of MTs, cells were added to anti-CD3 coated coverslips for 7 min followed by pre-permeabilization, cytoplasm extraction and fixation as described before (Tas et al., 2018). To compare MT organization in the presence or absence of KIF21B we focused on fully polarized cells, despite centrosome polarization often being impaired in KIF21B-KO cells (Figure 1F, G). We found that while in control cells most MTs were organized in an aster-like pattern, the knockout cells often contained circular MT bundles at the cell periphery. To analyze this phenotype, we made use of a custom-developed ImageJ plugin (Martin et al., 2018) to separate our images into radial and non-radial components based on MT orientation in relation to the centrosome (Figure 2B). This analysis showed that KIF21B-KO cells have an increased proportion of non-radially oriented MTs, which are organized into peripheral MT bundles at the immunological synapse (Figure 2A-C).

To analyze whether the MT network as a whole is affected by KIF21B depletion, we used Expansion Microscopy (ExM) to visualize the complete MT network and distinguish single MT polymers in 3D. With ExM, samples are physically magnified by embedding fixed cells in a isotropically swellable polymer, giving an approximate 4.5x-fold increase in reso-

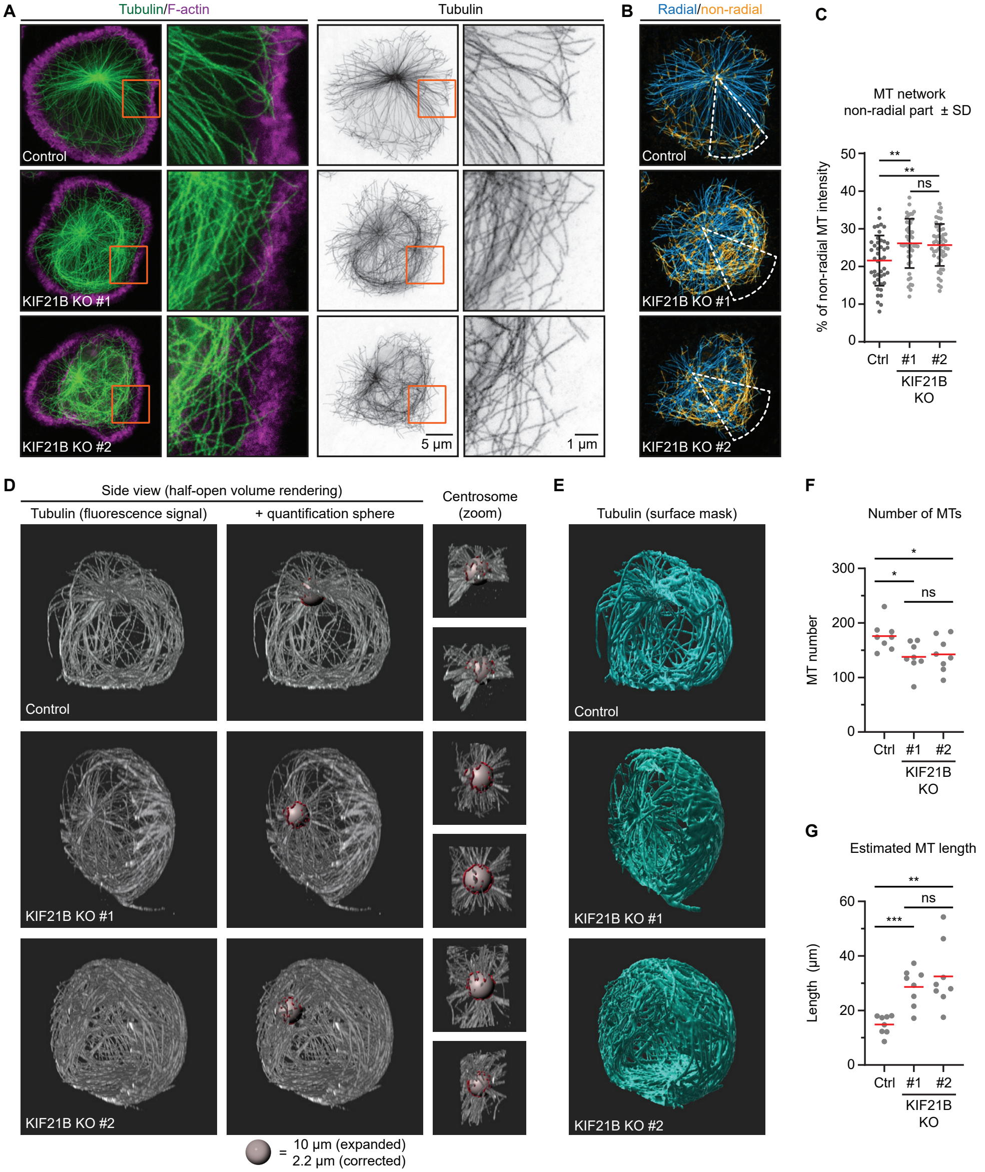
A
Tubulin/F-actin
Tubulin
Control
KIF21B KO #1
KIF21B KO #2
5 µm
1 µm
B
Radial/non-radial
Control
KIF21B KO #1
KIF21B KO #2
C
MT network
non-radial part ± SD
% of non-radial MT intensity
0
10
20
30
40
50
**
**
ns
Ctrl
#1
#2
KIF21B
KO
D
Side view (half-open volume rendering)
Tubulin (fluorescence signal)
+ quantification sphere
Centrosome
(zoom)
Control
KIF21B KO #1
KIF21B KO #2
= 10 µm (expanded)
2.2 µm (corrected)
E
Tubulin (surface mask)
Control
KIF21B KO #1
KIF21B KO #2
F
Number of MTs
MT number
0
100
200
300
*
*
ns
Ctrl
#1
#2
KIF21B
KO
G
Estimated MT length
Length (µm)
0
20
40
60
**
ns
***
Ctrl
#1
#2
KIF21B
KO

Figure 2. Knockout of KIF21B causes MT overgrowth in Jurkat cells
(A-B) STED images of indicated Jurkat T cell lines stained for α-tubulin and F-actin. Orange boxes indicate zoomed areas shown on the right. (B) Images were background subtracted and split into radial and non-radial components based on the MT orientation in relation to the centrosome. Radial intensity profiles were made from a 45 degree sector starting from the centrosome and directed towards the farthest removed portion of the cell periphery (white). The resulting heat maps were used to quantify the proportion of non-radially oriented MTs as described in Methods. **(C)** Quantification of the proportion of non-radially oriented MTs analyzed per cell. n = 44, 45 and 52 cells from three independent experiments. ** $p < 0.01$, ns = not significant (t test). **(D-E)** Volume renderings of indicated T cell lines stained for α-tubulin. T cells were fixed 2 min after activation on anti-CD3 coated coverslips. Samples were expanded ~ 4.5 times following an ExM protocol and MTs were imaged using on a confocal microscope. Imaris software was used to create volume

Figure 2 (continued) renders and analysis. MTs emanating from the centrosome were analyzed using a spherical shell with a 10 μm inner diameter and a thickness of 1 μm (grey); filaments crossing the sphere are highlighted (red). Zooms of the centrosome are shown from two different angles. (E) Fluorescence signal was converted to a surface mask using Imaris software to analyze total tubulin intensity. Additional examples are shown in Figure S2B. **(F)** Quantification of the total number of MTs per cell emanating from the centrosome quantified at 5 μm distance from the centrosome of indicated Jurkat T cell lines. n = 8 cells for all conditions. * $p < 0.05$, ns = not significant (t test). **(G)** Quantification of estimated MT length per cell in indicated Jurkat T cell lines. Fluorescence intensity of 1 μm filament length was measured for all MTs crossing a spherical shell of 1 um width with a 5 μm inner radius located around the centrosome, as shown in Figure 2D. The average MT length per cell was calculated by correcting the total fluorescence intensity per cell by the number of MTs at the centrosome. n = 8 cells for all conditions. *** $p < 0.001$, ** $p < 0.01$, ns = not significant (t test).

lution in x, y, and z (Chen et al., 2015; Jurriens et al., 2020). To understand how the state of the MT network before T cell activation may affect centrosome translocation, we looked at the very early stage of immunological synapse formation. T cells were fixed after 2 min of activation, when the majority of control cells did not yet fully polarize. We noticed that the MT network appeared to be denser in KIF21B-KO cells compared to control cells (Figure 2D, E, Video S1-3). To exclude that this was caused by increased levels of MT nucleation, we counted the number of MTs originating from the centrosome by analyzing the number of filaments passing through a 1 μm thick spherical shell with an inner radius of 5 μm generated around the centrosome (Figure 2D, Video S1-3). We found that MT number was slightly reduced in KIF21B-KO cells, by 21.7 % in KO #1 and 19 % in KO #2 (Figure 2F). Since T cells have highly centrosome-focused MT arrays, we assumed that all MTs are anchored to the centrosome and that these numbers thus represent the total number of MTs per cell. Next, we estimated an average MT length per cell. We generated surface masks based on the colocalization of the MTs and the 1 μm-thick spherical shell around the centrosome (Fig 2D, red surfaces). Since MTs cross through the shell orthogonally to its surface, the mean intensity corresponding to 1 μm MT was determined by averaging the fluorescence intensity per surface adjusted for the number of MTs in each surface. We then used a surface mask to determine the total fluorescence intensity corresponding to the complete MT network and divided it by the MT intensity per micron and by the number of MTs. We found that KIF21B-KO cells contain fewer MTs but they are on average longer than those in control cells (Figure 2E-G). Since the overall MT mass is higher in KIF21B-KO cells (Figure S2A, B), the concentration of free tubulin in these cells might be lower; this would diminish MT nucleation at the centrosome, causing a reduction in MT number.

We furthermore examined the geometry of MTs in polarizing control and KIF21B-KO cells (Figure S2B). Considering the immunological synapse as the basal side of the cell, with nucleus located above it, the centrosome could be positioned on top or on the side of the nucleus, or between the nucleus and the synapse. In agreement with the previously described observations (Yi et al., 2013), a MT bundle directed from the centrosome to the synapse (“stalk”) could be found in some cells (Figure S2C). We note that it was not obvious from our images that all MTs in such a stalk terminated at synapse; rather it appeared that many of them made side contacts with the membrane. In other cases, a single basally directed MT bundle could not be distinguished (Figure S2B), possibly because these cells were at an earlier stage of centrosome polarization. In cells with apically located centrosomes, MTs appeared to embrace the nucleus from all sides and then make lateral contacts with the synapse surface. In KIF21B-KO cells, such MTs formed a dense network in the basal half of the cell (Figure S2B).

To summarize, T cells that lack KIF21B show MT overgrowth at the immunological synapse. Using 3D ExM, we confirmed this observation and showed that KIF21B-KO cells have overly long MTs that form dense arrays at the immunological synapse.

KIF21B is a processive motor that induces MT pausing and catastrophes

Next, we investigated the localization and dynamics of KIF21B by live-cell imaging of the KIF21B-KO cell line rescued by re-expressing KIF21B-GFP. In HeLa cells, the closely related paralogue KIF21A displays strong peripheral localization at cortical MT stabilizing complexes (CMSC), to which it binds through KANK proteins (Noordstra and Akhmanova, 2017; van der Vaart et al., 2013). Structural studies have elucidated the binding interface of this interaction, and it is clear that KIF21B does not possess the KANK-binding region required for association with the CMSC (Guo et al., 2018; Pan et al., 2018; Weng et al., 2018). Likewise, KIF21B-GFP did not show any obvious cortical accumulation in T cells but was rather diffusely distributed in the cytoplasm or associated to MTs on which it moved processively (Figure 3A, Video S4). The average velocity of KIF21B-GFP puncta was 0.77 ± 0.14 µm/s (mean ± SD) (Figure 3A, B), which is 1.2 and almost 4 times faster compared to velocities measured for the full-length motor in COS-7 cells and hippocampal neurons, respectively (Ghiretti et al., 2016; van Riel et al., 2017).

To investigate whether the observed KIF21B-GFP signals correspond to single kinesin dimers, we compared their fluorescence intensity to that of single GFP molecules, as described previously for *in vitro* reconstitution assays (Aher et al., 2018; Hooikaas et al., 2019; van Riel et al., 2017). We imaged dual chamber slides that contained purified monomeric GFP in one chamber and activated KIF21B-GFP-expressing T cells in the other chamber. Intracellular KIF21B-GFP motors were detected using DoM software (see Methods for details) and the detected signals were filtered for molecules belonging to tracks ≥ 1s (Figure S3A). We found that their signal was ~ 1.5 times brighter than that of monomeric GFP (Figure 3C, S3B). Given that the evanescent field used for excitation decays exponentially and the KIF21B-GFP motors observed were localized intracellularly, one should take into account the distance between the coverslip and fluorescent molecules. Although we could not measure this distance precisely, we assumed that the thickness of the plasma membrane, cortical actin, cytoplasm and the 25 nm width of a MT would result, on average, in at least 50 nm spacing. Given the penetration depth d in these imaged cells was calibrated at 180 nm, we estimated that the corrected the KIF21B-GFP fluorescence signal intensity was ~ 2 times brighter than that of monomeric GFP (~ 1.8 times assuming 50 nm distance from the coverslip or ~ 2.1 times assuming 75 nm distance) (Figure 3C, S3B). Most of the motile KIF21B-GFP puncta in Jurkat cells thus likely corresponded to single kinesin dimers, which did not form any clear accumulations.

Our previous *in vitro* work showed that single KIF21B molecules walked towards a growing plus end and induced transient pauses ultimately followed by a catastrophe, whereas multiple KIF21B molecules accumulated at a MT plus end induced prolonged pauses (van Riel et al., 2017). Consequently, we asked whether KIF21B behaves similarly in T cells to regulate MT dynamics. To observe the interactions of KIF21B-GFP with MT plus ends in Jurkat cells, we transfected them with EB3-mCherry, which labels growing MT ends and shows some MT lattice decoration, and imaged these cells on a TIRF microscope. We traced processive KIF21B-GFP motors and quantified events where the motor reached the tip of an EB3-mCherry comet. Most of KIF21B-GFP molecules (56.7 %) transitioned to a paused state upon reaching the plus end; some motors (29.5 %) dissociated from the MT and in a few cases KIF21B tracked the MT tip and then either transitioned to a paused state (9.8 %) or dissociated from the MT (4 %) (Figure 3D-G). It should be noted that even in cases where KIF21B motor rapidly dissociated from the MT tip, we sometimes could observe a reduc-

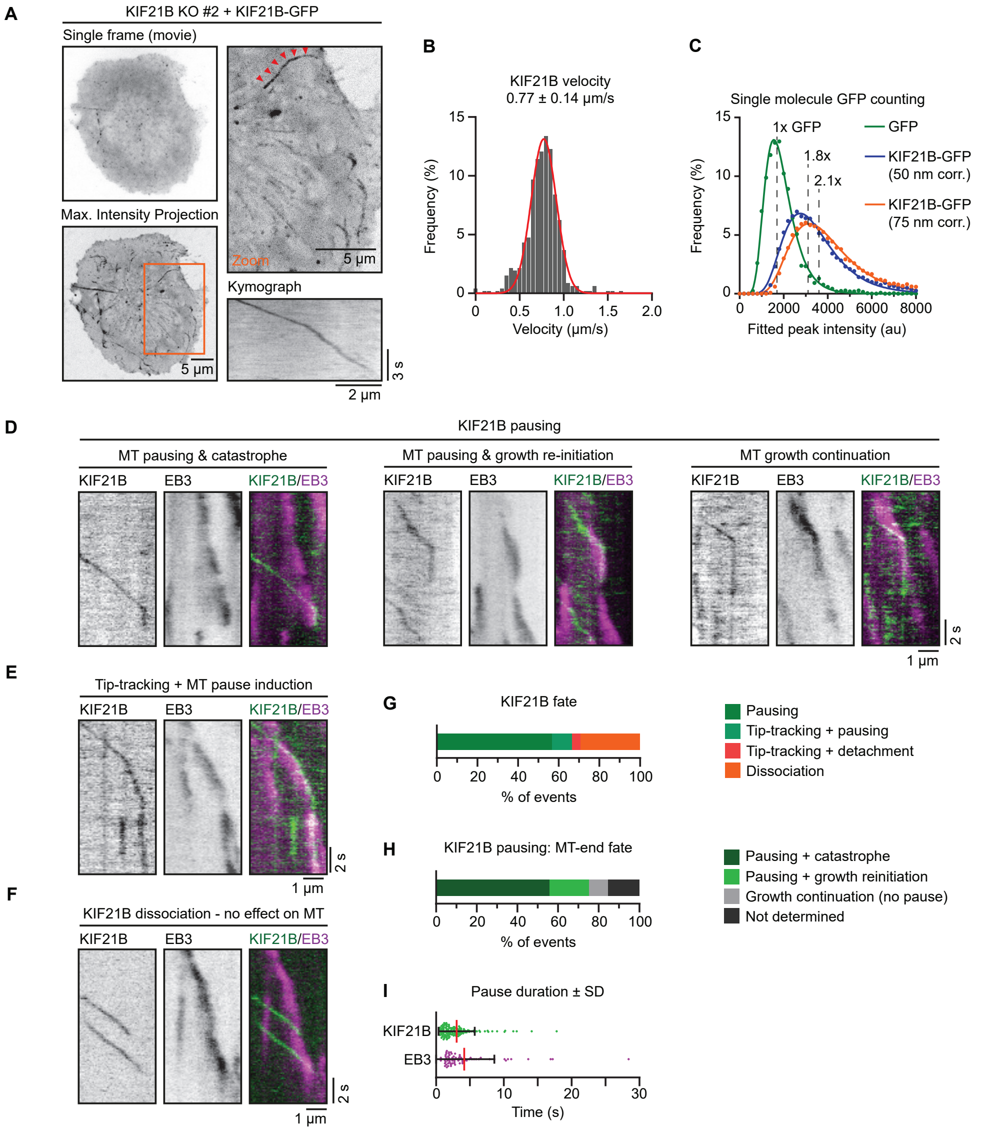

Figure 3 - KIF21B induces MT pausing and catastrophes in T cells
(A) Live imaging of Jurkat KIF21B-KO T cells stably overexpressing KIF21B-GFP. Images show a single movie frame and a maximum intensity projection of a background-subtracted movie. Zoomed areas are indicated (orange), and the kinesin track corresponding to the kymograph shown is indicated with red arrowheads. **(B)** Frequency distribution of KIF21B-GFP velocity in cells measured from data obtained imaging of KIF21B-KO #2 Jurkat T cell line stably overexpressing KIF21B-GFP on a TIRF microscope at 10 fps. Velocities were measured by kymograph analysis and the numbers were fitted to a Gaussian (red curve). n = 464 events from 102 cells from four independent experiments. **(C)** Histograms (dots) of peak-fitted fluorescence intensities of monomeric GFP immobilized on glass (green dots) and KIF21B-GFP motors imaged in Jurkat T cells (blue/orange) in two separate chambers on the same coverslip and the corresponding lognormal fits (solid lines). Imaging conditions were identical for both samples. KIF21B-GFP intensity values were corrected for a 50 and 75 nm distance from the coverslip, as illustrated in Figure S3B. n = 2601 (GFP) and n = 16523 (6 cells) (KIF21B-GFP) molecules. Mean values relative to monomeric GFP are indicated in the plot. **(D-I)** Live-cell

Figure 3 (continued) imaging of KIF21B-KO #2 Jurkat T cell line stably overexpressing KIF21B-GFP and transiently overexpressing EB3-mCherry to label growing MT plus ends, imaged on a TIRF microscope at 10 fps. **(D)** Kymographs illustrating KIF21B-GFP motors switching from walking to a pausing state. Growing MTs are visualized by EB3-mCherry overexpression. Examples show a growing plus end that undergoes pausing after KIF21B-GFP arrival followed by a catastrophe event (left), or growth re-initiation when the pausing KIF21B-GFP dissociates (middle). Some plus ends are not affected by the KIF21B-GFP motor pause event (right). **(E)** Kymograph illustrating a KIF21B-GFP tip-tracking on a growing EB3-mCherry plus end followed by a pausing event of both KIF21B-GFP and the MT plus end. **(F)** Kymograph illustrating two KIF21B-GFP motors reaching a growing EB3-mCherry plus-end causing the motors to dissociate from the MT plus-end, which continues growing, though EB3-mCherry signal is reduced. **(G)** Quantification of KIF21B-GFP fates observed when a moving KIF21B motor reaches an EB3-mCherry-labeled MT plus end, as illustrated in Figure 3D-F. n = 224 events from two independent experiments. **(H)** Quantification of MT plus-end fates when a KIF21B-GFP motor reaches a growing EB3-mCherry-labeled MT plus end and transitions to a paused state, as illustrated in Figure 3D, E and S3C. n = 149 events from two independent experiments. **(I)** Quantification of pause duration of KIF21B-GFP and EB3-mCherry-labeled MT plus ends, illustrated in Figure 3G and H. n = 144 and 75 events from two independent experiments.

tion in EB3 comet intensity (Figure 3F), suggesting a transient MT growth perturbation. A pausing KIF21B-GFP motor typically did affect MT plus end growth, and the events where a MT first paused and ultimately switched to depolymerization were most frequent (55.7 %). In other cases, a MT first paused but then switched back to growth after the paused KIF21B-GFP motor dissociated from the plus end (19.5 %). In a few cases (9.4 %), a growing plus end kept growing after a KIF21B-GFP motor transitioned to pausing; often, such events coincided with a reduced EB3 comet intensity (Figure 3D, G, H). On average, KIF21B-GFP motors were paused for 3.0 ± 2.7 s (mean ± SD) (Figure 3I), whereas MT plus end pause durations measured with EB3-mCherry were somewhat longer, 4.2 ± 4.4 s (mean ± SD) (Figure 3I). This can be explained either by photobleaching of the GFP or by participation of additional cellular factors that could stabilize paused MT ends after KIF21B dissociates. In some cases, growing MT plus end appeared to be static; these events likely corresponded to MTs growing against an obstacle, where MT tip remained stationary while the growing MT shaft buckled and formed a loop (Figure S3C, D). Events where KIF21B-GFP dissociated from a MT end affected the growing MT plus end much less compared to KIF21B-GFP pausing events; only a few of such events coincided with the initiation of a MT pause or a direct catastrophe event (Figure S3E, F). All these data represent events where KIF21B-GFP was observed to arrive to the MT tip by walking along the MT shaft. We also occasionally observed events where KIF21B-GFP directly bound to the MT plus end and affected MT growth, but such events were infrequent and were therefore were not quantified (Figure S3G). We conclude that KIF21B is a fast and processive kinesin in T cells and that its activity at the plus ends limits growth by inducing MT pausing and catastrophes.

MTs grow faster and more processively in cells lacking KIF21B

Since we directly observed MT growth perturbation by KIF21B-GFP, we next set out to perform a more global analysis of MT plus-end dynamics in Jurkat cells either expressing or lacking this motor. To this end, we used lentiviral transduction to introduce EB3-GFP as a MT plus-end marker into control and KIF21B-KO cell lines. We used these cells for live imaging of growing MT plus ends in cells that were polarized after activation (Figure 4A). We found that the MT growth rate was on average increased by 18 % (KO #1) and 15 % (KO #2) compared to control Jurkat cells (Figure 4A, B). These observations were in line with previous work showing that overexpression of KIF21B-GFP in COS-7 cells, which do not have endogenous KIF21B, reduced MT growth rates by ~ 1.5 fold (van Riel et al., 2017). These data are also consistent with the observation of increased MT growth rate after transient KIF21B depletion in neurons (Ghiretti et al., 2016), but contradict the analysis of MT growth speed in Kif21b knockout neurons (Muhia et al., 2016). Furthermore, we observed a decrease in MT catastrophe rate in KIF21B knockout cells (Figure 4C), which fits well with previous studies in neurons (Ghiretti et al., 2016; Muhia et al., 2016).

To further evaluate MT plus-end fate in cells lacking KIF21B, we infected control and KIF21B-KO cell lines with a GFP-β-tubulin construct as a MT marker. These cells were imaged on a TIRF microscope and we quantified events where the plus end of a radially growing MT reached the cell periphery. In control cells, a small minority (9.8 %) of MTs underwent a catastrophe or continued to grow by sliding along the cell cortex (Figure 4D, E). However, most MTs paused in this region (44.2 %) or continued their growth and this led to MT buckling, because MT plus end remained stationary whereas the increasingly long MT shaft was pushed backwards and formed a loop (40.9 %) (Figure 4D, E). In KIF21B-KO cells, MTs displayed less pausing at the cell periphery, whereas buckling became more frequent (Figure 4E). A closer examination of MT pauses revealed that these events in control cells were significantly more long-lived: 8.3 ± 5.6 s (mean ± SD) compared to those in KIF21B-KO cells: 4.1 ± 2.2 s (KO #1, mean ± SD) and 4.3 ± 2.4 s (KO #2, mean ± SD) (Figure 4F, S4A). We note that these pause durations are longer than those observed with EB3-mCherry (Fig. 3I), because the latter labels growing MTs, and its signal is gradually lost when MT plus ends switch to pausing and lose the GTP cap that EB3 labels (Roostalu et al., 2020). Overall, these data indicate that in T cells, KIF21B acts as a factor that inhibits MT growth and induces pausing and catastrophes.

MT growth inhibition with vinblastine rescues the defects in KIF21B knockout cells

To establish a causal connection between MT overgrowth and defects in immune synapse formation, we sought for a way to mildly inhibit MT growth in KIF21B-KO cells. Our previous work has shown that a low dose of vinblastine mildly perturbs growth and promotes catastrophes but does not induce MT depolymerization (Bouchet et al., 2016; Mohan et al., 2013). Indeed, at a low (0.5 nM) vinblastine concentration, MT network was preserved and was similar to that in control cells but different from KIF21B-KO cells, as no circular MT bundles were present at the cell periphery (compare Figure S4B to Figure 2A). MT organization in KIF21B-KO cells treated with 0.5 nM vinblastine was similar to that of KIF21B-KO cells rescued with KIF21B-GFP (Figure S4B). In vinblastine-treated KIF21B-KO cells, MT growth events visualized with EB3-GFP were less continuous, and the growth rates were reduced approximately to the level seen in control Jurkat cells (Figure 4A-C). We also examined the effect of 0.5 nM vinblastine on the dynamics of MTs labeled with GFP-β-tubulin and found that vinblastine application resulted in an increased catastrophe frequency, while long-lived MT pauses were not restored (Figure 4E, F, S4A).

We next tested whether such a mild vinblastine-induced MT growth inhibition would rescue the ability of the KIF21B-KO cells to polarize their centrosome. Jurkat cells were added to anti-CD3 coated coverslips and stained for CEP135, a centriole marker, to analyze polarization using z-projections (Figure 4G). We scored polarization events as successful when the centrosome was located within 2 μm from the coverslip and found that most control cells (87.2 %) were polarized contrary to knockout cells (36.7 and 42.9 %) (Figure 4H). This phenotype could be partially rescued by re-expressing KIF21B-GFP in these cells (58.9 and 51.7 %), and an even slightly better rescue was observed after applying 0.5 nM vinblastine to both KIF21B-KO cell lines (65.4 and 66.9 %) (Figure 4H, I). Altogether, we found that KIF21B depletion alters MT growth dynamics and that centrosome polarization defects in KIF21B-depleted cells can be rescued by the application of a drug, vinblastine, that inhibits MT growth. This indicates that cell polarization defects caused by the absence of KIF21B are due to its effect on MT dynamics rather than potential perturbation of transport or signaling processes.

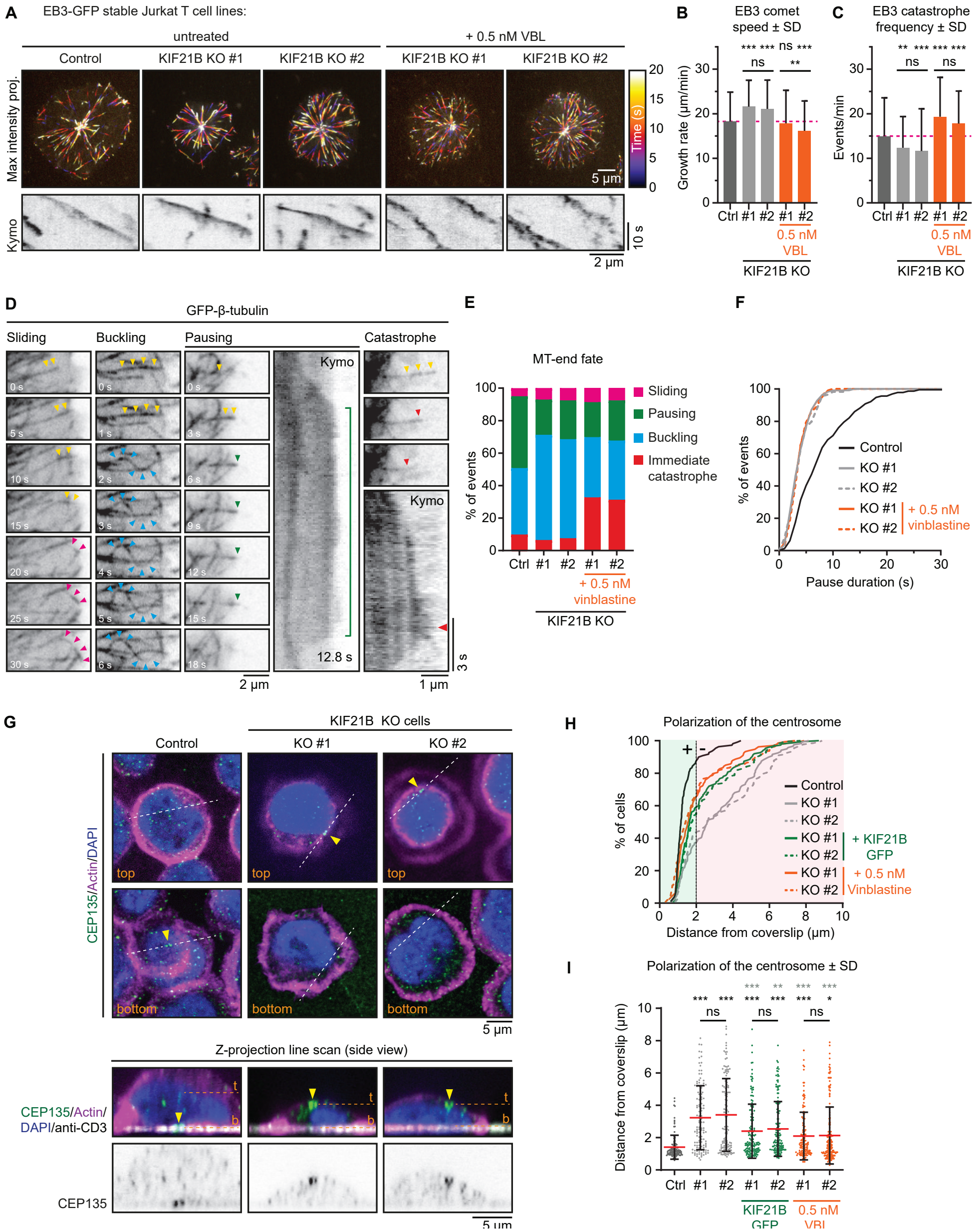

Figure 4 - Mild inhibition of MT growth with vinblastine rescues centrosome repositioning in KIF21B-KO cells

(A) Live-cell imaging of indicated EB3-GFP overexpressing Jurkat T cell lines, imaged on a TIRF microscope

Figure 4 (continued) at 2.5 fps. Color-coded maximum intensity projections and illustrative kymographs of growing EB3-GFP comets are shown per condition. KIF21B-KO cells were untreated or treated with 0.5 nM vinblastine 30 min prior to imaging as indicated. A scale for the time-dependent color-coding is indicated on the right. **(B)** Quantification of MT growth rates determined from imaging EB3-GFP in indicated Jurkat T cell lines. Dashed line (magenta) indicates the average growth rate for control cells. n = 470, 478, 250, 255 and 267 events from three independent experiments. *** $p < 0.001$, ns = not significant (Mann-Whitney *U* test). **(C)** Quantification of MT catastrophe frequencies determined from imaging EB3-GFP in indicated Jurkat T cell lines. Dashed line (magenta) indicates the average catastrophe frequency for control cells. n = 178, 178, 170, 205 and 173 events from two independent experiments *** $p < 0.001$, ** $p < 0.01$, ns = not significant (Mann-Whitney *U* test). **(D)** Live-cell imaging of β-tubulin-GFP overexpressing Jurkat T cell lines, imaged on a TIRF microscope at 10 fps. Movie stills and kymographs show examples of MTs that undergo sliding (pink arrowheads), buckling (cyan arrowheads), pausing (green arrowheads) or catastrophe (red arrowheads) after reaching the cell periphery. Yellow arrowheads indicate growing MTs before the highlighted events take place. Kymographs show the corresponding MT pausing and catastrophe events; the catastrophe initiation (red arrowhead) and total pause time (green line) are indicated. **(E)** Quantification of MT plus-end fates after reaching the cell periphery based on live-cell imaging of indicated β-tubulin-GFP overexpressing Jurkat T cell lines. n = 518, 508, 477, 544 and 409 events from 46, 49, 38, 37 and 32 cells obtained from three independent experiments. **(F)** Cumulative frequency distribution shows pause duration of events quantified in Figure 4E based on live-cell imaging of indicated β-tubulin-GFP overexpressing Jurkat T cell lines. A quantification of these data is shown in Figure S4A. n = 229, 110, 114, 117 and 101 events from 46, 49, 38, 37 and 32 cells obtained from three independent experiments. **(G)** Confocal images of indicated Jurkat T cells stained for CEP135, F-actin and DAPI. In addition, the anti-CD3 antibody with which the coverslip was coated was also stained with a Alexa-dye-conjugated secondary antibody. Single Z-plane images (upper panels) show the top part of the cell and the bottom synapse part. White dashed lines indicate the position of the average intensity Z-projections shown in the bottom panels. Yellow arrowheads indicate the position of the CEP135-positive centriole staining. The positions of the single Z-plane images shown in the upper panels are indicated with dashed lines (orange) labeled with “t” (top z-plane) and “b” (bottom z-plane, synapse). **(H-I)** Quantification of CEP135 distance from the synapse-coverslip interface for indicated conditions. Cumulative frequency distribution (H) shows the percentage of cells with fully polarized centrosomes. A 2 μm threshold was used to distinguish successful (green area) from failed (red area) centrosome polarization events. Dot plot (I) shows the distance values for individual cells quantified in (H). n = 109, 119, 132, 150, 150, 133 and 175 cells from three independent experiments. *** $p < 0.001$, ** $p < 0.01$, * $p < 0.05$, ns = not significant (Mann-Whitney *U* test).

Biophysical simulation of MT dynamics suggests that a small number of KIF21B molecules can limit MT overgrowth

To gain more insight into the regulatory effects of KIF21B and to explore possible mechanisms explaining how overly long MTs hinder centrosome polarization, we constructed a biophysical model based on Cytosim (Nedelec and Foethke, 2007). In contrast to previous more coarse-grained computational studies (Kim and Maly, 2009) and less modular models (Hornak and Rieger, 2020), we chose Cytosim to explicitly investigate the effects of KIF21B on MT dynamics. Cytosim uses overdamped Langevin equations to simulate the cytoskeleton with associated proteins and organelles restricted in a defined space. To model a T cell, we assumed a rotationally invariant space and simplified it to a two-dimensional object. Our model cell contains a nucleus and a centrosome, which is confined to one side of the cell and has 90 MTs attached. The cell boundary and the nucleus acted as elastic objects: when deflected, they exert a restoring force. The centrosome was modeled as a rigid sphere with uniformly spread MT anchoring points with a rotational elasticity (Figure 5A).

In our model, MTs are flexible polymers and their growth dynamics are described by two states. In the growth state, fibers elongate with a force-dependent growth speed. In the shrinkage state, fibers shorten with a constant shrinkage speed. The growth speed decreases exponentially with the force exerted on the fiber’s tip, termed antagonistic force

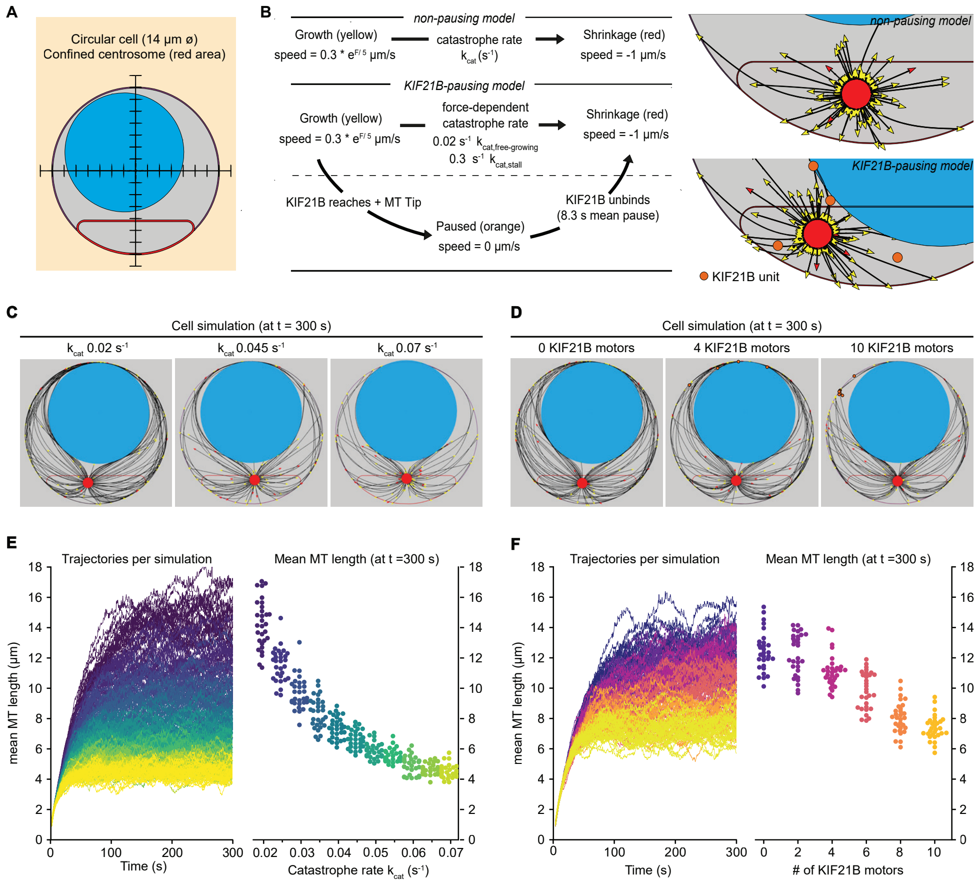

Figure 5 - Biophysical simulation shows how KIF21B affects MT network length
(A) A T cell is modeled as a circular cell with a nucleus (light blue) and centrosome confinement space (red). The cell is 14 µm in diameter, the nucleus is 10 µm in diameter. **(B)** Description of modelled microtubule dynamics using two models: a non-pausing model with MTs undergoing force-dependent growth and transitioning to depolymerization stochastically with a constant catastrophe rate, and a KIF21B-pausing model, in which MT growth and catastrophe are dependent on the antagonistic force exerted on the fiber's tip. Cropped snapshots of the initial state of the non-pausing model (left, catastrophe rate = 0.045 s^{-1}) and KIF21B-pausing model (right, 10 KIF21B motors) are shown. Growing MT plus ends are indicated by yellow arrowheads, depolymerizing MT plus ends are indicated by red arrowheads, and KIF21B units by orange circles. **(C)** Snapshots of the non-pausing model after 300 s for different values of catastrophe rate: 0.02 s^{-1} (left), 0.045 s^{-1} (middle) and 0.07 s^{-1} (right). **(D)** Trajectories (left) showing mean MT length per simulated cell over a 300 s time period. Traces are colored according to the catastrophe rate (from k_{cat} = 0.02 to 0.07 s^{-1}). Quantification (right) displaying mean MT length per simulated cell at steady state (t = 300 s) for indicated values of the catastrophe rate (k_{cat}). n = 30 simulated cells per condition. **(E)** Snapshots of the KIF21B-pausing model after 300 s for different numbers of KIF21B motors: 0 (left), 4 (middle), and 10 (right). **(F)** Trajectories (left) showing mean MT length per simulated cell over a 300 s time period. Traces are colored according to the number of KIF21B motors present (ranging from 0 to 10 motors). Quantification (right) displaying mean MT length per simulated cell at steady state (t = 300 s) for indicated number of KIF21B motors. n = 30 simulated cells per condition.

(Dogterom and Yurke, 1997). To describe the transition from growth to shrinkage, we distinguished two models: a basic 'non-pausing' model with a force-independent catastrophe rate, and a 'KIF21B-pausing' model with a force-dependent catastrophe rate (Janson et al., 2003) and KIF21B molecules that induce a paused state before the MT shrinks. To model control or KIF21B-KO cells, the number of KIF21B molecules can be changed. In our simulations, KIF21B motors freely diffuse in the cytosol, can bind to MTs and walk along them towards the plus end. When the motor arrives at a growing plus end, it pauses the MT dynamics until it unbinds. After a KIF21B motor has detached from the tip of a MT, the MT switches to the shrinkage state (Figure 5B).

To estimate numerical values for the parameters describing MT dynamics in our system, we used the experimental data for the KIF21B-KO cells (Figure 4A-F, Table S1). In this condition it is reasonable to assume that every catastrophe and pause is triggered by force exerted on the MT tip, and not by KIF21B because it is absent (Figure S5A-D). Additionally, the KIF21B-induced mean pause time of a MT tip was set to 8.3 s, as experimentally determined (Figure S4A). For the remaining parameters of our simulation that were unrelated to MT growth dynamics, we used numerical values found in the literature (see Table S1).

Simulations of the non-pausing model with the force-independent catastrophe rate implied that increasing the catastrophe rate decreased the mean length of the MTs (Figure 5C). The mean MT length is a measure for MT density in the simulations, as we kept the cell volume and number of MTs constant. The mean MT length reached a steady state within 300 s and decreased more than 3-fold in the range of values for the catastrophe rate we chose (Figure 5D). In the KIF21B-pausing model the fibers grew to a dense MT network in the absence of KIF21B with the force-dependent catastrophe rate matched to the KIF21B-KO (Figure 5E). When we added KIF21B motors to mimic the control condition, MT length decreased with an increasing number of KIF21B motors (Figure 5F). This decrease was approximately 2-fold between the KIF21B-KO-like and the control-like simulations between 0 and 10 KIF21B motors.

These simulations confirmed that by changing the catastrophe rate either directly or by explicitly modeling the behavior of the pause-inducing KIF21B motor, the average length of the MTs can be regulated. Interestingly, in our simulations, a small number of KIF21B motors was sufficient to prevent the overgrowth of the MT network.

Restriction of MT length helps to avoid a force balance that inhibits polarization

To investigate how an overgrown MT network impairs centrosome polarization and whether KIF21B can rescue this defect, we extended our simulations to describe polarization. We converted our steady-state MT dynamics models to a polarizing system by releasing the centrosome confinement and initializing a 'synapse'. The synapse consists of a line with curved ends to which 50 dynein motors are attached (Figure 6A). Dynein motors are uniformly distributed over the synapse. They can bind to a MT in their vicinity and walk along them towards the centrosome. Their walking and unbinding dynamics were calculated in a force-dependent manner. Because dynein motors are anchored, walking along a MT generates a pulling force. Consequently, the centrosome is able to polarize (Figure 6B, Video S5, 6).

In both the non-pausing as well as in the KIF21B-pausing model, the cells with longer MTs needed more time on average to polarize (Figure 5D, F, 6C, D). Some KIF21B-KO-like cells without KIF21B and some cells with a fixed catastrophe rate smaller than 0.03 s^{-1} did not polarize at the end of the simulation (800 s modeled time that we simulated after the MT network reached steady state).

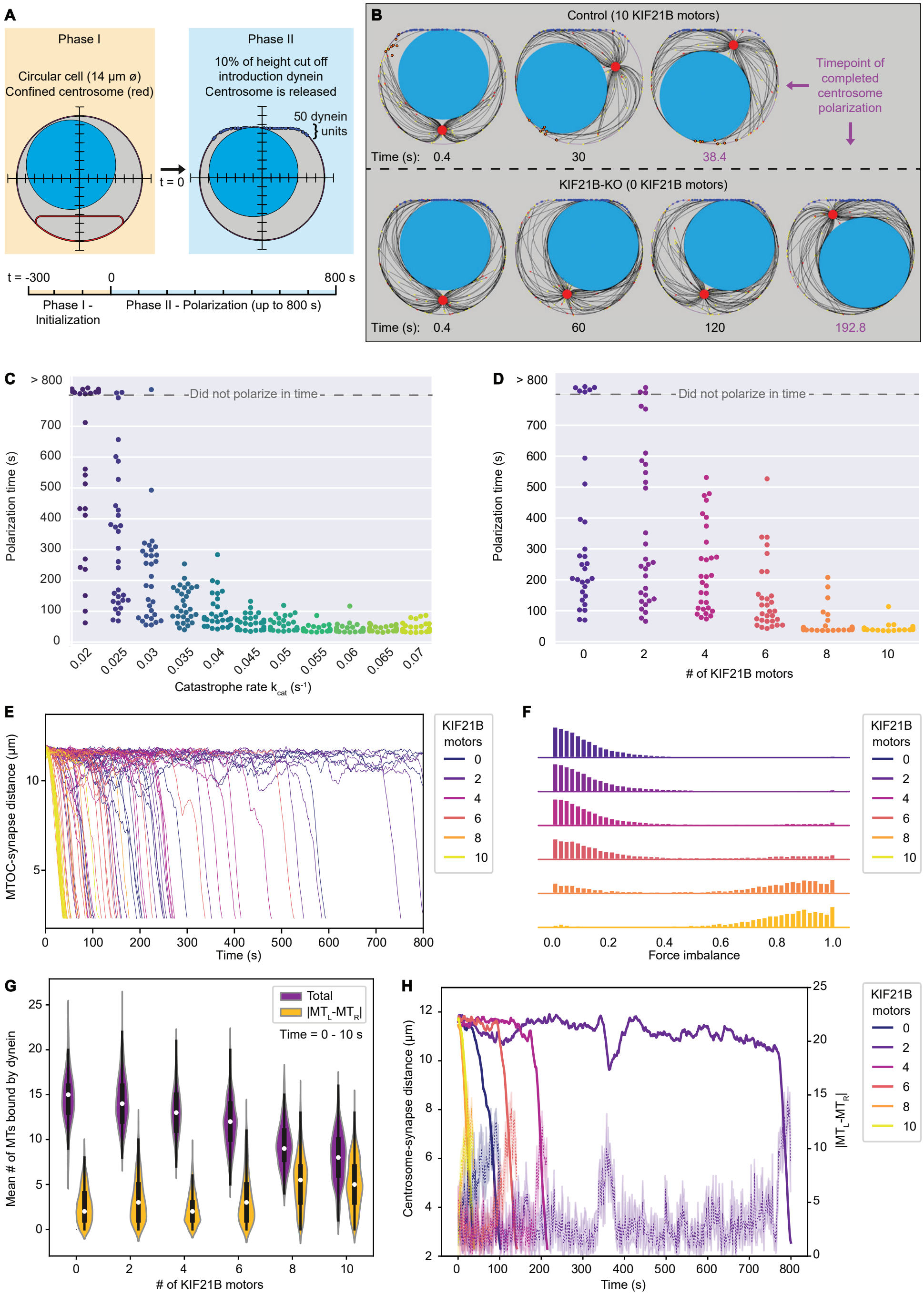

Figure 6 - KIF21B prevents centrosome stalling induced by force balance during polarization by limiting MT length

(A) The T cell model is initialized to a steady state MT network in 300 s (Phase I) and is then extended to a polarizing model (Phase II). In this transition, the cell shape is changed to include a flat side with curved corners with 50 dynein units attached, and the centrosome confinement (red) is released to allow centrosome movement and translocation. **(B) S**napshots of modelled T cells during centrosome polarization in the KIF21B-pausing model with the presence of 10 (top row) or 0 (bottom row) KIF21B motors. The simulations were stopped after the centrosomes reached a polarized position < 2.5 μm away from the synapse. The final snapshot in each row indicates the frame of the simulation when the centrosome was fully polarized. Timepoints are indicated below each snapshot. **(C)** Quantification of polarization time (the time the centrosome needs in Phase II to reach a polarization position) per simulated cell for the non-pausing model at indicated catastrophe rates. Some cells did not polarize within the maximum simulation time (800 s) as indicated in the upper part of the graph. n = 30 simulated cells per condition. **(D)** Quantification of polarization time (the time the centrosome needs in Phase II to reach a polarization position) per simulated cell for the KIF21B-pausing model with indicated numbers of KIF21B motors present. Some cells did not polarize within the maximum simulation time (800 s) as indicated in the upper part of the graph. n = 30 simulated cells per condition. **(E)** Trajectories showing the centrosome-synapse distance during Phase II over time along the vertical axis of the simulated T cell. Trajectories are color coded for the number of KIF21B motors present (see legend). Shown are 15 runs per condition. **(F)** Quantification of force imbalance within the KIF21B-pausing model. Force imbalance is calculated from the forces experienced by dynein at a given time point, projected on the horizontal axis. Force imbalance was characterized as the absolute difference of projected forces pointing to the left and forces pointing to the right, normalized by the sum of all forces. This quantity is determined for each timestep between 0 and the polarization time for every repeat and binned to create the according histogram. Histograms are color coded for the number of KIF21B motors present in the simulation (see legend). n = 30 simulated cells per condition. **(G)** Quantification of the mean number of MTs that are bound by dynein to the synapse within the KIF21B-pausing model. Violin plot distributions show the total number of MTs bound (purple), and the absolute difference ($|MT_L-MT_R|$, yellow) between the number of MTs bound on the right versus left side of the cell's vertical axis. Within each violin, a boxplot indicates the quartiles (black) with the inner quartile range (25 – 75%) indicated with the thickened region. Median values are indicated for each violin (white dot). Values were obtained in the first 10 s of Phase II of each simulation. n = 30 simulated cells per condition. **(H)** Trajectories of centrosome-synapse distance over time (solid lines) plotted together with trajectories of the absolute difference |MTL-MTR| between the number of MT bound to dynein and passing the nucleus on the left or on the right (dashed lines). in the same color for the corresponding runs. To make the |MTL-MTR| more legible, the mean and 95% confidence interval is plotted averaged over 3 frames (1.2 s). Trajectories are color coded for the number of KIF21B motors present in the simulation (see legend).

We next analyzed the relation between MT length and polarization dynamics in the KIF21B-pausing model, as this model describes our experimental data. Tracking the time evolution of the centrosome-synapse distance for multiple runs provided insight into the dynamics of centrosome translocation (Figure 6E). The centrosomes of late polarizing cells did not travel more slowly, but rather were localized at the far opposite side of the synapse for most of the time. Once these centrosomes left this position, they quickly moved towards the synapse. This rapid polarization movement seemed independent of the number of KIF21B molecules. However, the trapped localization before the rapid repositioning indicated that the system can be relatively stable in an unpolarized state. This state can apparently be destabilized by decreasing MT length through an increasing number of KIF21B molecules.

For our simulated cells to successfully polarize, the centrosome must travel past the nucleus on either the left or the right side. A possible explanation for the stable unpolarized state may be that the forces that dynein exerts to the left and the right are equal, thus causing a mechanical equilibrium by force balance. To trigger polarization, this equilibrium needs to be broken. We quantified force imbalance by determining all forces exerted by dynein projected on the horizontal axis and sorting them according to their direction. We calculated the sum of forces pointing to the right and the sum of forces pointing to the left.

For any timestep, the absolute difference of these two sums, normalized by the total sum of these forces indicates the force imbalance (Figure 6F, the non-normalized sum of force per timestep is shown in S6). The resulting data revealed that dynein forces were more balanced in the simulations with low KIF21B numbers and impaired polarization than in the simulations where the number of KIF21B molecules was high and polarization occurred rapidly.
To understand the underlying mechanism, we counted the number of MTs that pass the nucleus on either the right (MTR) or the left side (MTL) and are bound by dynein (Figure 6G). We only assessed the first 10 s after initiation of polarization to limit the situation to a period when none of the runs are already actively polarizing. This analysis indicated that with increasing number of KIF21B molecules, the mean number of MTs bound on the left or on right decreases, while the difference between the two fractions averaged over time increases. Tracking this difference as a function of time indicated that it changed together with the centrosome position, and an increased fluctuation in this number seemed necessary to trigger polarization (Figure 6H). Note that the dynamics of KIF21B together with the MTs and the spatial restriction by the nucleus can lead to enrichment of KIF21B on one side of the nucleus (Figure 6B). This specific localization could increase the difference between the number of MTs on the left and right side of the nucleus that reach the synapse and enhance the force imbalance.

We conclude that by effectively increasing catastrophe frequency and restricting MT length, KIF21B reduces the overall number of MTs reaching the synapse from different sides of the nucleus. A smaller number of long MTs leads to larger fluctuations in the number of MTs coming from opposing sides, which enables the force asymmetry that is necessary to trigger polarization when the centrosome is positioned behind the nucleus.

Discussion

In this paper, we set out to investigate which aspects of the regulation of MT organization and dynamics are important during the formation of the immunological synapse and elucidate the role of kinesin-4 KIF21B in this process. MTs are typically quite short and sparse in immune cells, and we found that this property is functionally important, as MT overgrowth inhibited efficient centrosome translocation to the synapse (Figure 7). Furthermore, our data strongly support the notion that KIF21B acts as a factor that prevents excessive MT elongation.

Previous *in vitro* studies reported contradictory results regarding the activity of KIF21B on MT ends. One study found that KIF21B promotes MT growth and catastrophe at relatively high levels (Ghiretti et al., 2016). In contrast, our own work indicated that KIF21B transiently blocks MT elongation and induces subsequent catastrophes at low levels, when only one or two KIF21B molecules are present at the MT tip, and causes prolonged MT pausing when present at a higher concentration, when multiple KIF21B motors accumulate at the plus end (van Riel et al., 2017). In the current study, we showed that the function of KIF21B in knockout cells can be rescued by KIF21B-GFP expressed at levels that were mildly exceeding endogenous. Importantly, imaging of KIF21B-GFP in these cells did not reveal any clear accumulations of the motor at MT plus ends. KIF21B behavior in Jurkat T cells was very similar to that observed at low nanomolar concentrations *in vitro* (van Riel et al., 2017): single KIF21B-GFP kinesin dimers walked processively along MTs, reached their ends and perturbed MT plus end growth by triggering transient pauses followed by catastrophes. Therefore, we conclude that whereas biochemically KIF21B can be described as a MT pausing factor, in T cells, it acts at concentrations that are insufficient to induce prolonged pausing and effectively functions as a catastrophe inducer. This is likely explained by our previous observation that a single KIF21B-GFP molecule can arrest dynamics of a few protofilaments (van Riel et al., 2017). Blocking of even one MT protofilament can already perturb growth of the remaining ones, and this can lead to the loss of the GTP cap and trigger catastrophe (Doodhi et al., 2016). To induce a pause, blocking MT elongation must be accompanied by inhibition of depolymerization of protofilaments lacking a GTP cap. Since a single KIF21B dimer is unlikely to be able to stably block depolymerization of all MT protofilaments, a catastrophe eventually ensues.

While KIF21B is a potent MT regulator, it has also been implicated in other functions, such as MT-based transport and regulation of signaling (Ghiretti et al., 2016; Gromova et al., 2018; Labonte et al., 2014; Morikawa et al., 2018). While our study certainly does not exclude that KIF21B engages in such functions in T cells, we show that centrosome polarization defects observed in KIF21B knockout cells can be rescued by mildly perturbing MT growth with a MT-destabilizing drug. These data strongly suggest that the primary defect induced by the lack of KIF21B is excessive MT elongation. These data also argue against direct participation of KIF21B in dynein-driven capture and shrinkage of MT ends that was proposed to drive centrosome movement in T cells (Yi et al., 2013), although they do not exclude indirect effects of overly long MTs on this process. Furthermore, since KIF21B is a highly processive motor, it can be expected that it would target longer MTs more effectively, like it has been previously shown for kinesin-8 (Gupta et al., 2006; Varga et al., 2006). This would make KIF21B even more efficient in preventing excessive MT growth in T cells. The finding that KIF21B acts as an inhibitor of MT growth is in agreement with the studies in neurons, which showed that KIF21B reduces MT growth processivity (Ghiretti et al., 2016; Muhia et al., 2016).

To further substantiate the idea that KIF21B affects centrosome repositioning in T cells by controlling MT length, we turned to modelling. Our simulations indicated that

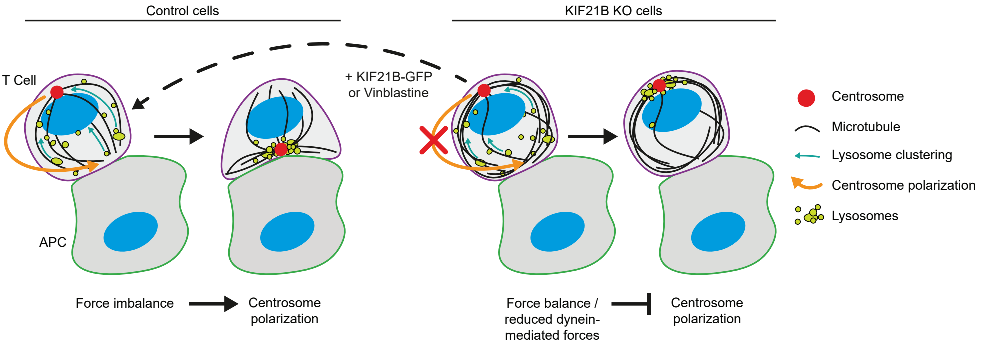

Figure 7 - Overview of the experimental results and a model of centrosome polarization in T cells
Centrosome polarization in T cells is driven by dynein attached to the immunological synapse. KIF21B is a pausing and catastrophe-promoting factor that limits MT growth in T cells; its depletion results in MT overgrowth. Cells with overly long MTs experience difficulties in centrosome polarization. Re-expression of KIF21B-GFP or the application of a low-dose of MT-targeting agent vinblastine restores the centrosome polarization. Computational modelling suggests that an imbalance in MT pulling forces drives the centrosome movement along the nucleus. Overly long MTs create additional connections to the synapse, resulting in a balance of pulling forces on the two sides of the nucleus, thereby hindering centrosome translocation. Overly long MTs may also directly inhibit force generation by dynein at the synapse.

the ability of a relatively small number of KIF21B molecules to restrict MT length can be readily recapitulated in silico. In the model, we assumed that all KIF21B molecules induce a catastrophe, which differs from our experimental findings (Figure 3H). However, even if only half of the KIF21B molecules induce catastrophe, as in our experimental data, the total number of KIF21B molecules needed to significantly inhibit MT overelongation would still be relatively small, and this would also likely be true even in a three-dimensional system, where the diffusional space for the KIF21B molecules would be larger and the probability to bind to a MT lower.

Furthermore, the simulations provided a possible mechanistic explanation for the impairment of centrosome polarization by MT overgrowth. In cells where the nucleus is located between the centrosome and the synapse, as would often be the case in T cells migrating towards a chemoattractant (Roig-Martinez et al., 2019), the centrosome needs to pass it along one side to move to the synapse. This movement would require a force only on one side and thus an asymmetric organization of MTs reaching the synapse from the different sides of the nucleus. Such asymmetries likely originate from fluctuations in the number of MTs contacting the synapse from different sides that occur more readily when the number of MTs is low. The fluctuation-based mechanism of asymmetry generation could explain why some KIF21B knockout cells do polarize and some fail to do so within the observation period.

Although this mechanism for the impaired centrosome polarization in the absence of KIF21B appears plausible, its generalization could be limited by our model assumptions. To reduce complexity, we based our simulations on the force generation by dynein through MT sliding rather than through a MT end-on capture-shrinkage mechanism (Yi et al., 2013). Our model suggests that movement of the centrosome during polarization is a direct effect of a non-zero force along the MT network on one side of the nucleus. The mechanism of how this force is generated does not change the reliance on the force imbalance along the nucleus. It is possible that the precise trajectory of the centrosome depends on the molecular mechanism of how dynein generates the force (Hornak and Rieger, 2020). A comparison between experimentally determined centrosome trajectories and simulation results is beyond the scope of this study, and thus we cannot resolve the precise force generation mechanism of dynein.

A necessary assumption to set up a computable Cytosim simulation was the description of a T cell as a two-dimensional system. It is possible that in a three-dimensional system, the locked centrosome state is more unstable than we conclude from our two-dimensional simulations, because the third dimension provides an additional degree of freedom to break the force balance. However, a previous computational model in three dimensions suggested that in a T cell with a static overgrown MT network the centrosome can be trapped behind the nucleus (Kim and Maly, 2009), and in our ExM data we do observe KIF21B-KO cells with an apically located centrosome and symmetric MT bundles extending to the synapse from different sides (Figure S2B). It is important to note that in other cells in our ExM samples the centrosome is located on the side of the nucleus, a situation that would lead to rapid polarization in our simulations. Since a significant proportion of cells shows a polarization delay in our experiments, it is unlikely that trapping of the centrosome behind the nucleus is the sole explanation of the polarization defect. It is possible that also in situations where the centrosome is positioned on the side of the nucleus, MT overgrowth leads to force balance and prevents efficient centrosome translocation. Furthermore, other mechanisms that are not included in the simulations likely contribute to the inhibition of centrosome repositioning by overgrown MTs. Excessively long MTs could slow down centrosome translocation by directly affecting dynein-mediated force generation, for example, by reducing the number of MT ends contacting the synapse and perturbing MT end capture by dynein. Long MTs could also make MT depolymerization-driven “reeling in” of the centrosome less efficient or create pushing forces and friction that would inhibit repositioning of the MT network. We further note that even in cells that did relocate their centrosome, the immunological synapses formed slower and were smaller, suggesting that the presence of circular MT bundles might perturb synapse formation in some additional ways, for example, by affecting signaling-based cross-talk between MTs and actin (Dogterom and Koenderink, 2019).

Taken together, our data show that the typical features of MT network organization in T cells, with relatively short and sparse MTs, is functionally important and that its maintenance depends on a dedicated regulatory factor, KIF21B, which restricts MT growth.

Materials & Methods

Cell culture, spreading assays and drug treatment

Jurkat T cells (clone E6.1) were grown in RPMI 1640 medium w/ L-Glutamine (Lonza) supplemented with 10% Fetal Bovine Serum and 1% penicillin/streptomycin. Cells were a kind gift of Piero Giansanti. For all spreading assays, coverslips were coated with Poly-D-Lysine (Thermo Fisher Scientific, A3890401), washed with phosphate buffered saline (PBS) and incubated overnight at 4° C with a mouse monoclonal anti-CD3 (clone UCHT1, StemCell Technologies, #60011) 10 µg/mL in PBS, except for the not-activated conditions, here cells were incubated on Poly-D-Lysine coated coverslips for 30 min prior to fixation. For live-cell imaging, Lab-Tek chambers (Thermo Fisher Scientific) were incubated overnight at 4° C with anti-CD3 (Clone UCHT1, StemCell Technologies, #60011) 10 µg/mL in PBS. Prior to spreading, cells were spun down for 4 min at 1000 rpm and resuspended in fresh pre-warmed RPMI 1640 medium.

Vinblastine (Sigma-Aldrich) treatment was performed by spinning down the cells for 4 min at 1000 rpm and resuspending the cells in pre-warmed medium containing 0.5 nM vinblastine 30 min prior to fixation. For live-cell imaging experiments, cells were resuspended in medium and 30 min prior to imaging, an equal amount of medium with 1 nM vinblastine was added to the cells to achieve a final concentration of 0.5 nM vinblastine.

CRIPSR/Cas9 knockouts, lentivirus transduction and DNA constructs

KIF21B knock-out cell lines were generated in Jurkat cells (clone E6.1) using CRISPR/Cas9 technology. Jurkat T cells were transfected using an Amaxa Cell Line Nucleofector® kit V (Lonza), program X-005 with the pSpCas9(B-B)-2A-Puro (PX459) vector (Addgene, #62988) bearing the appropriate targeting sequence (KIF21B: 5’-caccgTGTGTGAGCAAGCTCATCGA-3’). Cells were selected using 2 µg/mL puromycin (InvivoGen).

cDNA for lentivirus constructs were derived from the following sources: human cDNA clone KIAA 0449 for KIF21B (Kazusa DNA Research Institute), the EB3-GFP coding sequence as described in (Stepanova et al., 2003), and the β-tubulin coding sequence was provided by Prof. Dr. Kai Jiang. KIF21B-GFP and β-tubulin-GFP sequences were cloned in pLVX-IRES-Puro vectors (Clontech), EB3-GFP was cloned in pLVX-IRES-Hygro vector (Clontech). EB3-mCherry construct (Stepanova et al., 2003) was transiently transfected using Amaxa Cell Line Nucleofector kit V (Lonza), program X-001.

Lentiviruses were produced by MaxPEI-based transfection of HEK293T cells with the construct of interest and the packaging vectors psPAX2 and pMD2.G (Addgene). Cell supernatant was harvested 48 and 72 hrs after transfection, filtered through a 0.45 µm filter and incubated overnight at 4° C in a polyethylene glycol (PEG) 6000-based precipitation buffer containing 80 g/L PEG 6000 and 82 mM NaCl at pH 7.2. The precipitation mix was centrifuged to concentrate the virus. The pellet containing the lentivirus was resuspended in PBS and Jurkat T cells were transduced in complete medium supplemented with 8 µg/mL polybrene (Merck-Millipore) using a spinoculation protocol: centrifugation of the transduction mix for 30 min at 2400 rpm at 32° C. Cells were selected using 2 µg/mL puromycin or with 100 µg/mL hygromycin, five days after transduction.

Western blotting and antibodies

Jurkat T cells were lysed in a lysis buffer containing 20 mM Tris (pH 7.5), 150 mM NaCl, 1% Triton X-100 and cOmplete protease inhibitor cocktail (Roche). For Western blotting, we used the following polyclonal rabbit antibodies: anti-KIF21B (Sigma-Aldrich, HPA027249), anti-GFP (Abcam, ab290); and the following mouse monoclonal antibodies: anti-CD3 (Clone UCHT1, StemCell Technologies, #60011) and anti-Ku80 (BD Bioscience, 611360). The following secondary antibodies were used for Western blotting: IRDye-800CW-conjugated goat antibody against mouse IgG (#P/N 925-32210) and IRDye-680LT-conjugated goat antibody against rabbit IgG (#P/N 925-68021), both purchased from Li-Cor Biosciences.

For immunofluorescence staining, we used a rabbit polyclonal antibody against CEP135 (Sigma-Aldrich, SAB4503685). A rabbit monoclonal antibody against Lamtor4 (clone D6A4V, Cell Signaling Technology, #12284) and α-tubulin (clone EP1332Y, Abcam, ab52866). A mouse monoclonal antibody against α-tubulin (Sigma-Aldrich, T6199), and a rat monoclonal antibody against α-tubulin (clone γL1/2, Abcam, ab6160). The following secondary antibodies were used for immunofluorescence: Alexa-Fluor-488-conjugated goat antibodies against mouse and rabbit (#A27023 and #A-11034), Alexa-Fluor-594-conjugated goat antibodies against mouse, rabbit and rat (#A-11032, #R37117 and #A-11007) and an Alexa-Fluor-647-conjugated antibody against mouse (#A-21240); all these antibodies were purchased from Life Technologies. F-actin was stained using Alexa-Fluor-488 or 594-conjugated phalloidin (Life Technologies, #12379, #12381).

T cell stimulation, RNA isolation and qRT-PCR analysis

T cells were stimulated with a combination of Phorbol 12-myristate 13-acetate (PMA) (Sigma-Aldrich, P8139) and ionomycin (Sigma-Aldrich, I0634) at indicated time points and concentrations. Cells were collected on ice and total RNA was extracted using TRIzol reagent (Thermo Fisher Scientific, 15596026) and cDNA synthesis was performed using the iScript cDNA synthesis kit (Bio-Rad, 1708891). cDNA samples were amplified with SYBR Select mastermix (Life Technologies, 44-729-19) using a QuantStudio 12K Flex Real-Time PCR System (Applied Biosystems) and the following RT-PCR primer pairs: IL-2 forward 5'-AACTCACCAGGATGCTCACATTTA-3', IL-2 reverse 5'-TCCCTGGGTCTTAAGTGAAAGTTT-3' and GAPDH forward 5'-CAACGGATTTGGTCGTATT-3' and GAPDH reverse 5'- GATGGCAACAATATCCACTT-3'. The LIVAK method was used to calculate relative mRNA expression in respect to the housekeeping gene *GAPDH*.

Immunofluorescence staining and image acquisition

For immunofluorescence staining of tubulin and CEP135 for TIRF microscopy, cells were fixed in −20°C methanol for 10 min, followed by washes with PBS and permeabilization with PBS supplemented with 0.15% Triton X-100 for 2 min. All subsequent wash steps were performed using PBS supplemented with 0.05% Tween-20. Epitope blocking and antibody labeling steps were performed in PBS supplemented with 0.05% Tween-20 and 1% Bovine Serum Albumin (BSA). Before mounting in DAPI-containing Vectashield mounting medium (Vector Laboratories, H-1200-10), slides were washed with 70% and 100% ethanol and air-dried.

For immunofluorescence staining of lysosomes (Lamtor4) and centrosomes (CEP135) for 3D analysis, or labelling with Phalloidin, cells were fixed with 4% paraformaldehyde (PFA) in PBS at room temperature (RT) for 10 min, followed by washes with PBS and permeabilization with PBS supplemented with 0.15% Triton X-100 for 2 min. All subsequent wash steps were performed using PBS supplemented with 0.05% Tween-20. Epitope blocking and antibody labeling steps were performed in PBS supplemented with 0.05% Tween-20 and 1% BSA. Samples were mounted using DAPI-containing Vectashield mounting medium (Vector Laboratories, H1200-10).

Widefield imaging on fixed cells was performed on a Nikon Eclipse Ni-E upright fluorescence microscope equipped with Plan Apo Lambda 100x N.A. 1.45 oil and 60x N.A. 1.40 oil objectives microscopes, ET-BFP2 (49021, Chroma), ET-GFP (49002, Chroma), ET-mCherry (49008, Chroma), ET-Cy5 (49006, Chroma) filter sets and a Photometrics CoolSNAP HQ2 CCD (Roper Scientific, Trenton, NJ) camera. The microscope was controlled by Nikon NIS Br software.

TIRF imaging on fixed cells was performed on an ILAS-2 system (Roper Scientific, Evry, France) with a dual laser illuminator for azimuthal spinning TIRF (or Hilo) illumination and with a custom modification for targeted photomanipulation. This system was installed on Nikon Ti microscope (with the perfect focus system, Nikon), equipped with 405 nm 100 mW Stradus (Voltran), 488 nm 150 mW Stradus (Voltran), 561 nm 100 mW Coherent (OBIS 561-100LS) and 642 nm 110 mW Stradus (Vortran) lasers; and ET-BFP (49021, Chroma), ET-GFP (49002, Chroma) and ET-mCherry (49008, Chroma) filter sets. Fluorescence signal was detected using an EMCCD Evolve mono FW DELTA 512x512 camera (Roper Scientific) with the intermediate lens 2.5X (Nikon C mount adapter 2.5X) or a CCD CoolSNAP MYO M-USB-14-AC camera (Roper Scientific). The final resolution using EMCCD camera was 0.065 µm/pixel, using CCD camera it was 0.045 µm/pixel. The setup was controlled with MetaMorph 7.8.8 software (Molecular Device).

Spinning disk microscopy was performed on inverted research microscope Nikon Eclipse Ti-E (Nikon), equipped with the perfect focus system (Nikon), Plan Apo VC 100x N.A. 1.40 oil objective (Nikon), spinning disk Yokogawa CSU-X1-A1 with 405-491-561-642 quad-band mirror (Yokogawa). The system was also equipped with ASI motorized stage with the piezo plate MS-2000-XYZ (ASI), Back-Illuminated Evolve 512 EMCCD camera (Photometrics) or Back-Illuminated Prime BSI sCMOS camera (Photometrics) and controlled by the MetaMorph 7.10 software (Molecular Devices). 405 nm 100 mW Stradus (Voltran), 491 nm 100 mW Calypso (Cobolt), 561 nm 100 mW Jive (Cobolt) and 642 nm 110 mW Stradus (Vortran) lasers were used as the light sources. The setting was equipped with ET-BFP2 (49021, Chroma), ET-GFP (49002, Chroma), ET-mCherry (49008, Chroma) and ET-Cy5 (49006, Chroma) filter sets to image blue, green, red and far-red fluorescence signals, respectively. 16-bit images were projected onto the Evolve 512 EMCCD camera with intermediate lens 2.0X (Edmund Optics) at a magnification of 0.066 µm/pixel or onto Prime BSI sCMOS camera with no intermediate lens at a magnification of 0.063 µm/pixel. Z-stacks of cells were acquired with a step size of 0.1 µm.

Immunofluorescence staining and image acquisition for STED microscopy and ExM

For all STED and ExM samples, 1.5 mm thick coverslips (Marienfeld, 107032) were used. Jurkat cells were added to anti-CD3 coated coverslips for indicated time points. Cells were pre-extracted for 1 min with pre-warmed (37°C) extraction buffer composed of MRB80 (80 mM K-PIPES pH 6.8, 4 mM $MgCl_2$, 1mM EGTA) supplemented with 0.35% Triton X-100 and 0.2% glutaraldehyde. After extraction, cells were fixed for 15 min with pre-warmed (37°C) 4% PFA in PBS. All subsequent wash steps were performed using PBS supplemented with 0.2% Triton X-100. Epitope blocking and antibody labeling steps were performed in PBS supplemented with 3% BSA. Labelling with primary antibodies was performed overnight at 4°C. After washing with PBS, labelling with secondary antibodies was performed for 3 hrs at RT. For STED microscopy samples, cells were washed with PBS and MiliQ and air dried. Cells were mounted in Prolong Gold (Thermo Fisher).

For ExM, we followed the procedures described by (Jurriens et al., 2020). Samples were post-fixed with 0.1 mg/mL acryloyl X-SE (AcX) (Thermo Fisher, A20770) in PBS overnight at RT. For gelation, monomer solution was prepared containing 2M NaCl, 8.625% sodium acrylate (Sigma-Aldrich, 408220), 2.5% acrylamide (AA), 0.15% N,N'-methylenebisacrylamide (BIS) in PBS. As a source of AA we used 37.5:1 AA/BIS solution (Sigma-Aldrich, A3699) and supplemented it with BIS (Sigma-Aldrich, M1533) to reach final concentrations. Gelation of the monomer solution was initiated with 0.2% ammonium persulfate (APS) and 0.2% tetramethylethylenediamine (TEMED) and 170 uL was transferred to a silicone mold with inner diameter of 13 mm (Sigma-Aldrich, GBL664107) attached to a parafilm-covered glass slide, with the sample put cell-down on top to close off the gelation chamber. After incubation at RT for 1-3 min, the sample was transferred to a humidified 37°C incubator for at least 30 min to fully polymerize the gel. After gelation, the gel was transferred to a 12-well plate and digested in TAE buffer (containing 40 mM Tris, 20 mM acetic acid and 1 mM EDTA) supplemented with 0.5% Triton X-100, 0.8 M guanidine-HCl and 7.5 U/mL Proteinase-K (Thermo Fisher, EO0491) for 4 hrs at 37°C. The gel was transferred to a Petri dish, water was exchanged twice after 30 min and sample was left in water to expand overnight in 50 mL MiliQ. Prior to imaging the cells were trimmed and mounted.

All STED and ExM images have been acquired using a Leica TCS SP8 STED 3X microscope equipped with a HC PL Apo 100x/1.40 Oil STED WHITE objective for STED acquisition and a HC PL APO 86x/1.20W motCORR STED (Leica 15506333) water objective for ExM. A pulsed white laser (80 MHz) was used for excitation, and when using STED a 775 nm pulsed depletion laser was used. The internal Leica GaAsP HyD hybrid detectors were used with a time gate of 1 ≤ tg ≤ 6 ns. The set-up was controlled using LAS X.

Live-cell imaging

Live-cell DIC imaging was performed on an inverted Nikon Ti microscope equipped a perfect focus system (Nikon), a Plan Fluor 40x/1.30 Oil DIC objective, a CoolSNAP HQ2 CCD camera (Photometrics), a motorized stage MS-2000-XYZ with Piezo Top Plate (ASI), and a stage top incubator (TokaiHit) set to 37° C. The microscope was controlled by MicroManager software.

Jurkat cells were live imaged on an ILAS-2 system (Roper Scientific, Evry, France) is a dual laser illuminator for azimuthal spinning TIRF (or Hilo) illumination and with a custom modification for targeted photomanipulation. This system was installed on Nikon Ti microscope (with the perfect focus system, Nikon), equipped with a Nikon Apo TIRF 100x N.A. 1.49 oil objective (Nikon); 488 nm 150 mW Stradus (Voltran) and 561 nm 100 mW Coherent (OBIS 561-100LS) lasers; and ET-GFP (49002, Chroma) and ET-mCherry (49008, Chroma) filter sets. For simultaneous imaging of green and red fluorescence, we used an ET-GFP/mCherry filter cube (59022, Chroma) together with an Optosplit III beamsplitter (Cairn Research Ltd) equipped with double-emission filter cube configured with ET525/50m, ET9630/75m and T585lprx (Chroma). Fluorescence signal was detected using an EMCCD Evolve mono FW DELTA 512x512 camera (Roper Scientific) with the intermediate lens 2.5X (Nikon C mount adapter 2.5X) or a CCD CoolSNAP MYO M-USB-14-AC camera (Roper Scientific) The setup was controlled with MetaMorph 7.8.8 software (Molecular Device). To keep cells at 37° C, a stage top incubator model INUBG2E-ZILCS (Tokai Hit) was used. Or on an inverted research microscope Nikon Eclipse Ti-E (Nikon) with the perfect focus system (PFS) (Nikon), equipped with Nikon CFI Apo TIRF 100 × 1.49 N.A. oil objective (Nikon). For excitation lasers we used 491 nm 100 mW Stradus (Vortran). We used an ET-GFP 49002 filter set (Chroma) for imaging of proteins tagged with GFP. Fluorescence signal was detected using an an Evolve512 EMCCD camera (Photometrics) or a CoolSNAP HQ2 CCD camera(Photometrics). The setup was controlled with MetaMorph 7.8.8 software (Molecular Device). To keep cells at 37° C, a stage top incubator model INUBG2E-ZILCS (Tokai Hit) was used.

Image processing and analysis

Images and movies were processed using ImageJ. All images were modified by linear adjustments of brightness and contrast. Average intensity projections and z-projections were made using the z projection tool. Kymographs were made using the ImageJ plugin KymoResliceWide v.0.4 (https://github.com/ekatrukha/KymoResliceWide; copy archived at https://github.com/elifesciences-publications/KymoResliceWide).

Cell surface area

Cell surface area was measured manually by drawing the cell circumference using the freehand tool in ImageJ. For KIF21B-GFP overexpressing rescue cell lines, very low expressing or GFP-negative cells were not measured.

Cell volumes

Cell volumes were measured based on Phalloidin staining of 3D-imaged Jurkat cells imaged on a Spinning disk confocal microscope. Imaris software (Bitplane/Oxford instruments, version 9.5.1) was used to manually create a cell surface mask using the Isosurface Drawing mode set at 10% density. The cell outline was determined for > 10 positions in z-dimension to create a 3D volume rendering of the Jurkat cell from which the volume was determined using the Statistics feature of the Imaris software.

MT organizing (TIRF microscopy)
For quantifying MT organization in T cells in different KIF21B-KO and rescue conditions, we classified MT networks as "radial" when a clear aster-like MT pattern was observed with an obvious presence of a microtubule organizing center or CEP135-positive fluorescent signal in the TIRF field. Other MT networks were classified as "disorganized" when an aster-like organization indicative of a polarized centrosome was lacking.

3D analysis of lysosomes and centrosomes
To quantify polarization of lysosome clusters in T cells, the distance of these Lamtor4-positive clusters and the anti-CD3-positive coverslip was measured in z. A reslice was made of the entire cell to have a z-projection from which an average intensity projection was made to create a landscape of fluorescence intensities in z. The distance between coverslip and lysosome cluster was determined by taking the distance between the coverslip and the pixel row in z that contained the peak intensity value of all rows. A Lamtor4-stained lysosome cluster was quantified as "polarized" when its peak intensity value was localized within 2 μm distance from the anti-CD3-stained coverslip.

For centrosome polarization quantifications, the distance between the CEP135-stained centrosome and the anti-CD3-positive coverslip was measured in z. A line scan was drawn over the centrosome and a reslice was made to make a z-projection of the cell at the location of the centrosome. The distance between coverslip and centrosome was determined by drawing a line from the center to center of both fluorescence signals. A CEP135-stained centrosome was quantified as "polarized" when it was localized within 2 μm distance from the anti-CD3-stained coverslip.

STED microscopy
STED images of fluorescently labeled MTs were analyzed using ImageJ. Images were background subtracted using the Background Subtraction tool with a rolling ball radius of 50 pixels and were separated into radial and non-radial components using a customized ImageJ macro (https://github.com/ekatrukha/radialitymap)(Martin et al., 2018). In short, we used the 'Cubic Spline Gradient' method and Tensor Sigma parameter of 8 pixels to calculate a radial and a non-radial map image that illustrate the separated radial and non-radial components of the original picture. For both the original image and images showing the separated components, radial intensity profiles were made from the centrosome to the farthest removed portion of the cell periphery using the Radial Profile Angle plugin at a 45 degree integration angle. The output of the Radial Profile Angle plugin was normalized to (xi-MIN(xi))/(MAX(xi)-MIN(xi))*100. Because not all original images had the same size, the normalized output of the Radial Profile Angle plugin was imported in MatLab (MathWorks) and resampled using a custom script to build mean radial intensity profiles per condition using GraphPad PRISM. To quantify the non-radiality of the MT organisation per cell, the areas under the curve (AUC) of the radial intensity profiles of the original image (total intensity) and of the non-radial map images were calculated using GraphPad PRISM. The non-radial intensity as percentage of the total intensity was calculated using: (AUCnon-radial/AUCTotal intensity)*100.

ExM microscopy
For the ExM analyses and all 3D renders Imaris (Bitplane/Oxford instruments, version 9.5.1) was used. Using the Automatic Spot Detection algorithm (set to 10 μm), the centrosome was localized in the 3D renderings as the brightest spot present; and a sphere was generated around the centrosome with a radius of 5 μm. A second sphere was generated with a radius of 6 μm using the Automatic Spot Detection (set to 11 μm). From these two spheres, a spherical shell was generated with an inner spacing thickness of 1 μm using the following steps: all voxels outside the surface of the smaller sphere and all voxels inside the surface of the bigger sphere were set to the maximum intensity value (255). Using the Colocalization function a colocalization channel of both masks was made which generated the spherical shell used for all further quantifications.

To analyze MTs within this spherical shell, a colocalization channel was generated for the tubulin channel using the Colocalization function. Thresholds were adjusted to include all MTs. Based on this colocalization channel, surface masks were generated for the tubulin signal using the Surfaces tool with Split Touching Objects enabled (seed points diameter set at 0.45μm). Seed points and generated surfaces were visually filtered so that all MTs were included. To count the number of MTs, all generated surfaces were checked and the number of MTs were counted manually per spherical shell. The mean intensity corresponding to 1 μm MT was determined from the fluorescence intensity per surface (using the Statistics feature of the Imaris software) corrected for the manually counted number of MTs in each surface. To determine the total fluorescence intensity corresponding to the complete MT network the Surfaces tool was used to generate a surface mask covering the entire MT network (Split Touching Objects setting disabled) and used an automatic threshold to discard very small nonspecific surfaces. To estimate the average MT length, the total intensity as found (using the Statistics feature of the Imaris software) was divided by the MT intensity per micron and by the number of MTs.

Quantification of live-cell imaging
The duration of synapse formation imaged using DIC microscopy was quantified using kymographs. Kymographs were generated using the ImageJ plugin KymoResliceWide v.0.4. along a line from the center of the cell to the cell periphery showing least irregular cell spreading. Cells that exhibited drift on the coverslip during spreading were not used for quantification. The initiation of synapse formation was determined as the moment where the cell started to spread sideways. The synapse was at maximum size when sideway spreading became static (velocity < 0.5 µm/min). The duration of synapse formation was determined as the duration at which the Jurkat cell exhibited sideward spreading at a minimum mean velocity of 1 µm/min.

EB3-GFP growth rates were quantified using kymographs that were generated using the ImageJ plugin KymoResliceWide v.0.4. The slope of EB3-GFP growth events in these kymographs were used to calculate growth rates corrected for acquisition settings. Catastrophe rates were quantified by determining the inverse value of growth time of EB3-GFP growth events.

Single molecule KIF21B velocities were quantified from TIRF-imaged KIF21B-GFP expressing T cells using kymographs that were generated using the ImageJ plugin KymoResliceWide v.0.4. The slope of motile KIF21B-GFP events in these kymographs were used to calculate kinesin velocities corrected for acquisition settings. These values were fitted to a Gaussian curve to determine mean KIF21B velocity.

Single kinesin events at MT plus ends were quantified using TIRF-imaged KIF21B-GFP expressing T cells that were transfected with EB3-mCherry as a marker of growing MT plus ends. Events were quantified when a motile KIF21B-GFP molecule (> 0.1 µm/s velocity) reached the end of a growing EB3-mCherry-positive MT. KIF21B-GFP behavior after a MT plus-end encounter was categorized as “pausing”, “tip-tracking” or “dissociation”. The “tip-tracking” events, where KIF21B tracked a growing plus end at the same velocity as EB3 signal, were subsequently sub-categorized into “tip-tracking + pausing” and “tip-tracking + dissociation” events. The state of the EB3-mCherry-positive plus end was defined as “growing” (> 0.05 µm/s growth velocity) or “static” (< 0.05 µm/s growth velocity) for KIF21B-GFP events that went into a paused state, regardless whether there was tip-tracking or not. The fate of EB3-mCherry plus ends after encountering a pausing KIF21B-GFP molecule was divided into four categories: “pausing + catastrophe”, “pausing + growth re-initiation”, “growth continuation without pausing” or “not determined” for the events that were unclear or took place beyond acquisition time. The fate of EB3-mCherry plus ends after encountering a KIF21B-GFP molecule that directly dissociated upon reaching the plus end was divided into three categories: “no effect”, “coincided with MT pausing” or “coincided with MT catastrophe”. Pause times were quantified for KIF21B-GFP molecules that that appeared static (< 0.1 µm/s velocity and ≥ 0.5 s duration) and underwent pausing at an EB3-mCherry-positive MT plus end. Pause times were quantified for growing EB3-mCherry MT plus ends that appeared static (< 0.05 µm/s growth velocity and ≥ 0.5 s duration) and transitioned into a paused state after an encounter with a KIF21B-GFP molecule. The end time of a pause coincided with either a catastrophe or a growth re-initiation event.

For analysis of β-tubulin-GFP imaging, we scored the fate of growing MTs reaching the plasma membrane into four categories: catastrophe, sliding along the cortex, MT buckling and pausing. Quantified events had to meet the following criteria: 1) events at the MT plus end had to be preceded by a phase of growth before reaching the plasma membrane; 2) the acquisition time had to include a complete pausing event or, in the case of a catastrophe, sliding or buckling event, the initiation of the event. Pause events and pause times were quantified for MT plus ends that appeared static (< 0.05 µm/s growth velocity and ≥ 0.5 s duration). For determining pause duration of a MT reaching the plasma membrane, a kymograph was generated for the growing MT using the ImageJ plugin KymoResliceWide v.0.4 and the length of the pause was determined by the number of vertical pixels in the kymograph multiplied by the exposure time.

Single molecule intensity analysis
Single-molecule fluorescence histograms of monomeric GFP (control) or kinesins moving on MTs intracellularly were built from acquisitions made on a TIRF microscope. To ensure identical imaging conditions, a single imaging slide (with a plasma cleaned coverslip) was used containing two flow chambers to image GFP (control) and KIF21B-GFP expressing T cells. For purified GFP, we used cell lysates from HEK293T cells overexpressing monomeric GFP. The GFP protein was diluted in PBS and added to an imaging flow chamber; chambers were subsequently washed with PBS, leaving a fraction of the GFP proteins immobilized on the coverslip. Protein dilution was optimized to provide images of ~ 0.05 fluorophores/µm^2 for GFP control conditions. For T cells expressing KIF21B-GFP, the imaging chamber was incubated overnight at 4° C with 10 µg/mL of a mouse monoclonal anti-CD3 (clone UCHT1, StemCell Technologies, #60011) in PBS. The chamber was washed three times with PBS and one time with RPMI 1640 medium. T cells expressing KIF21B-GFP were concentrated in RPMI 1640 medium and added to the chamber 2 min before imaging. After sealing the chambers with vacuum grease to prevent evaporation, samples were imaged on a TIRF microscope at 37° C. For monomeric GFP, ~ 40 images were acquired at 100 ms exposure time at different positions on the coverslip to avoid pre-bleaching. For moving kinesins, ~ 5–10 cells were imaged using stream acquisition at a 100 ms exposure time per frame. All acquisitions were obtained under identical laser power and a TIRF angle with a calibrated penetration depth d of 180 nm.

ImageJ plugin DoM_Utrecht v.1.1.6 was used to for detection and fitting of single molecule fluorescent spots as described previously (Yau et al., 2014). In short, individual spots were fitted with 2D Gaussian and the amplitude of the fitted Gaussian function was used as a measure of the fluorescence intensity value of an individual spot. For moving KIF21B-GFP molecules in T cells, ImageJ plugin DoM_Utrecht v.1.1.9 was used for detection and fitting of single molecule fluorescent spots. Using this plugin, these particles were linked to tracks with a maximum distance to search over one frame of 3 pixels and a maximum linking gap of 2 pixels. Tracks were filtered for a duration of ≥ 1 s. The histograms were fitted to lognormal distributions using GraphPad Prism 8. A correction factor (c) was calculated for KIF21B-GFP fitted peak intensities (i) for a series (0-100 nm) of hypothetical distances (h) between the coverslip and KIF21B molecule using the formula:

c=i/e^(-(h/180))

Cytosim modeling

The T cell model was made in the agent-based modeling structure Cytosim (Nedelec and Foethke, 2007), which solves overdamped Langevin equations to calculate the movement of the cytoskeleton and associated proteins. We choose Cytosim to be able to explicitly model the dynamics of KIF21B and dynein and to ensure an easy reproducibility of our results. Cytosim is open-source and together with our configuration file easy to run.

To set up a simulation of the MT network and the associated proteins of a T cell we used the following features and elements.

Shape

The shape of the T cell is encoded as SpaceHemisphere. This space definition makes a circular (2D) or spherical (3D) space, where a plane intersects the space at arbitrary height. In the T cell, this is at 0.9 of the full height. In the space we use to confine the centrosome during initialization this is at 0.2 of the full height of the cell. The corners of the plane are curved, to avoid infinitesimal corners. The curved corners are calculated by finding a smaller circle that interpolates continuously between the synapse and the (circular) cell shape. Any interaction with the shape is calculated by finding the closest point on the space surface and applying a linear force in this direction. If objects are outside of the space, they are pushed inwards.

Steric Interactions

Because we simplified our T cell to a two-dimensional object, we needed to adjust the steric interactions. Fibers in the simulations cannot enter the nucleus, but can cross one another to effectively mimic the third dimension. This behavior is achieved by the'ad-hoc' steric interactions within Cytosim, in which we compare the position of each fiber segment with the nucleus, and if the fiber segment is within the nucleus, a linear force is applied to push the fiber out, similar to cell shape confinement.

Dynein

Dynein motors are uniformly distributed and anchored at the synapse. They bind to MT in their vicinity and walk along them. The walking speed is characterized by a linear force-velocity relation as typically modeled in Cytosim. This definition describes a cortically anchored dynein that slides MTs, which is different from the end-on capture mechanism proposed by (Yi et al. 2013).

KIF21B

The KIF21B units are modeled as a new form of binding Hand in Cytosim: the Capper hand. They are able to bind and walk on the fiber. When they reach a fiber's tip, the fiber is set to a paused state, neither growing or shrinking. The waiting time for the motor at a fiber's tip is redrawn from a distribution to ensure that the pause length is correctly implemented, regardless of how long the Capper has already walked on the fiber. If a Capper unbinds, it sets the MT to the shrinkage state. Subsequently, any other bound Cappers unbind.

As KIF21B is localized in the cytosol, we extended the ad-hoc steric interactions to Singles. Because Singles are modeled as molecules with a negligible inertia displaying a random walk, we cannot easily apply elastic forces to these objects. Thus, we model the KIF21B units to bounce off the nucleus, similar to its interaction with the shape. If a good bounce location cannot be found after 1000 attempts (i.e. the molecule is in a tight corner between nucleus and cell shape), the molecule is set to the edge of the nucleus.

Fitting KIF21B-KO MT dynamics

To match the parameterization of our model to the MT dynamics in the KIF21B-KO system we used a separate Cytosim simulation to mimic the experimental data from the TIRF imaging of the MT dynamics at the synapse. Ultimately this approach suggested a linear relation between the free growing catastrophe rate and the growing force, which is the characteristic force of the MT polymerization. This relation fulfills the constraint that 81% of the MT in the TIRF data did not initiate catastrophe within 3.3 s, while satisfying the 0.3 s^{-1} stalled catastrophe rate. More details are included in Figure S5A-D.

In all simulations outside of fitting the KIF21B-KO MT dynamics, MTs are initialized with slightly different lengths, pulled from an exponential distribution with the mean of 1 µm. This was done so that even with very small catastrophe rates, MT lengths would not be equal. Simulations were run in a slightly altered version of Cytosim to be able to immobilize the centrosome in the center of the synapse (https://gitlab.com/oanegros/cytosim/-/tree/

fix-aster-in-center).

Data and software availability
All data that support the conclusions are available from the authors on request, and/or available in the manuscript itself. The code of our simulations is hosted on https://gitlab.com/oanegros/cytosim/-/tree/full-kif21b-model.

Supplemental videos

Video S1 - 3D volume render of an ExM imaged Jurkat control cell 2 min after activation.
Volume rendering of a control Jurkat cell fixed 2 min after activation on anti-CD3 coated coverslips stained for α-tubulin. Samples were isotropically expanded using an ExM protocol and imaged on a confocal microscope. Images were processed and analyzed using Imaris software. Microtubules emanating from the centrosome were analyzed using a spherical shell with a 5 µm inner radius, filaments crossing the sphere are highlighted (red). Every square in the grid corresponds to 5 x5 µm post expansion. Example corresponds to Figure 2D-E.

Video S2 - 3D volume render of an ExM imaged Jurkat KIF21B-KO cell (KO #1) 2 min after activation.
Volume rendering of a KIF21B-KO Jurkat cell (KO #1) fixed 2 min after activation on anti-CD3 coated coverslips stained for α-tubulin. Samples were isotropically expanded using an ExM protocol and imaged on a confocal microscope. Images were processed and analyzed using Imaris software. Microtubules emanating from the centrosome were analyzed using a spherical shell with a 5 µm inner radius, filaments crossing the sphere are highlighted (red). Every square in the grid corresponds to 5 x5 µm post expansion. Example corresponds to Figure 2D-E.

Video S3 - 3D volume render of an ExM imaged Jurkat KIF21B-KO cell (KO #2) 2 min after activation
Volume rendering of a control KIF21B-KO Jurkat cell (KO #2) fixed 2 min after activation on anti-CD3 coated coverslips stained for α-tubulin. Samples were isotropically expanded using an ExM protocol and imaged on a confocal microscope. Images were processed and analyzed using Imaris software. Microtubules emanating from the centrosome were analyzed using a spherical shell with a 5 µm inner radius, filaments crossing the sphere are highlighted (red). Every square in the grid corresponds to 5 x5 µm post expansion. Example corresponds to Figure 2D-E.

Video S4 - KIF21B-GFP motors imaged at the immunological synapse of an activated Jurkat T cell.
Live imaging of a Jurkat KIF21B-KO T cell (KO #2) stably overexpressing KIF21B-GFP. Video corresponds to Figure 3A. Images were collected using a TIRF microscope at 10 frames per second. Video is sped up 2 times to 20 frames per sec. Time is shown in seconds.

Video S5. -Recording of a simulated T cell in the 'non-pausing' model with 10 KIF21B motors added.
The T cell simulation consists of two phases. At first, the model is initialized to a steady state MT network in the first 300 s, during which the centrosome is confined to the red box at one side of the T cell. Next, the cell shape is changed to include 50 membrane-anchored dynein motors (blue) at a flat immunological synapse surface, and centrosome confinement is released to allow centrosome translocation. KIF21B motors are included throughout the entire simulation (orange). Snapshots of this run are shown in Figure 6B (upper row). Growing MT plus ends are indicated by yellow arrowheads, depolymerizing MT plus ends are indicated by red arrowheads, and KIF21B units by orange circles.

Video S6 - Recording of a simulated T cell in the 'non-pausing' model with 0 KIF21B motors added.
The T cell simulation consists of two phases. At first, the model is initialized to a steady state MT network in the first 300 s, during which the centrosome is confined to the red box at one side of the T cell. Next, the cell shape is changed to include 50 membrane-anchored dynein motors (blue) at a flat immunological synapse surface, and centrosome confinement is released to allow centrosome translocation. Snapshots of this run are shown in Figure 6B (bottom row). Growing MT plus ends are indicated by yellow arrowheads and depolymerizing MT plus ends are indicated by red arrowheads.

Acknowledgements
This work was supported by the European Research Council Synergy grant 609822 and Netherlands Organization for Scientific Research ALW Open Program grant 824.15.017 to A.A, as well as the European Research Council Consolidator Grant 819219 to L.C.K.

Author contributions
P.J. H. and H.G.J. D. designed, conducted and analyzed the cellular experiments. W.E. v R. initiated the project and contributed to the generation of cell lines and conducted cellular experiments. P.J. H. and M. M. contributed to the generation of cell lines. P.J. H., Y.T.H. S. and J. v L. contributed to gene expression experiments. O.J. G. designed, conducted and analyzed computational modelling experiments. F.B. contributed to computational modelling experiments. P.J. H., H.G.J. D., O.J. G., L.C. K., F.B. and A.A. wrote, reviewed and edited the manuscript. A.A., L.C. K. and F.B. supervised the project.

Competing financial interests
The authors declare no competing financial interests.

References

Aher, A., M. Kok, A. Sharma, A. Rai, N. Olieric, R. Rodriguez-Garcia, E.A. Katrukha, T. Weinert, V. Olieric, L.C. Kapitein, M.O. Steinmetz, M. Dogterom, and A. Akhmanova. 2018. CLASP Suppresses Microtubule Catastrophes through a Single TOG Domain. Dev Cell. 46:40-58.

Anderson, C.A., D.C. Massey, J.C. Barrett, N.J. Prescott, M. Tremelling, S.A. Fisher, R. Gwilliam, J. Jacob, E.R. Nimmo, H. Drummond, C.W. Lees, C.M. Onnie, C. Hanson, K. Blaszczyk, R. Ravindrarajah, S. Hunt, D. Varma, N. Hammond, G. Lewis, H. Attlesey, N. Watkins, W. Ouwehand, D. Strachan, W. McArdle, C.M. Lewis, C. Wellcome Trust Case Control, A. Lobo, J. Sanderson, D.P. Jewell, P. Deloukas, J.C. Mansfield, C.G. Mathew, J. Satsangi, and M. Parkes. 2009. Investigation of Crohn's disease risk loci in ulcerative colitis further defines their molecular relationship. Gastroenterology. 136:523-529 e523.

Andres-Delgado, L., O.M. Anton, F. Bartolini, A. Ruiz-Saenz, I. Correas, G.G. Gundersen, and M.A. Alonso. 2012. INF2 promotes the formation of detyrosinated microtubules necessary for centrosome reorientation in T cells. J Cell Biol. 198:1025-1037.

Asselin, L., J. Rivera Alvarez, S. Heide, C.S. Bonnet, P. Tilly, H. Vitet, C. Weber, C.A. Bacino, K. Baranano, A. Chassevent, A. Dameron, L. Faivre, N.A. Hanchard, S. Mahida, K. McWalter, C. Mignot, C. Nava, A. Rastetter, H. Streff, C. Thauvin-Robinet, M.M. Weiss, G. Zapata, P.J.G. Zwijnenburg, F. Saudou, C. Depienne, C. Golzio, D. Heron, and J.D. Godin. 2020. Mutations in the KIF21B kinesin gene cause neurodevelopmental disorders through imbalanced canonical motor activity. Nat Commun. 11:2441.

Barrett, J.C., S. Hansoul, D.L. Nicolae, J.H. Cho, R.H. Duerr, J.D. Rioux, S.R. Brant, M.S. Silverberg, K.D. Taylor, M.M. Barmada, A. Bitton, T. Dassopoulos, L.W. Datta, T. Green, A.M. Griffiths, E.O. Kistner, M.T. Murtha, M.D. Regueiro, J.I. Rotter, L.P. Schumm, A.H. Steinhart, S.R. Targan, R.J. Xavier, N.I.G. Consortium, C. Libioulle, C. Sandor, M. Lathrop, J. Belaiche, O. Dewit, I. Gut, S. Heath, D. Laukens, M. Mni, P. Rutgeerts, A. Van Gossum, D. Zelenika, D. Franchimont, J.P. Hugot, M. de Vos, S. Vermeire, E. Louis, I.B.D.C. Belgian-French, C. Wellcome Trust Case Control, L.R. Cardon, C.A. Anderson, H. Drummond, E. Nimmo, T. Ahmad, N.J. Prescott, C.M. Onnie, S.A. Fisher, J. Marchini, J. Ghori, S. Bumpstead, R. Gwilliam, M. Tremelling, P. Deloukas, J. Mansfield, D. Jewell, J. Satsangi, C.G. Mathew, M. Parkes, M. Georges, and M.J. Daly. 2008. Genome-wide association defines more than 30 distinct susceptibility loci for Crohn's disease. Nat Genet. 40:955-962.

Belyy, V., M.A. Schlager, H. Foster, A.E. Reimer, A.P. Carter, and A. Yildiz. 2016. The mammalian dynein-dynactin complex is a strong opponent to kinesin in a tug-of-war competition. Nat Cell Biol. 18:1018-1024.

Bianchi, S., W.E. van Riel, S.H. Kraatz, N. Olieric, D. Frey, E.A. Katrukha, R. Jaussi, J. Missimer, I. Grigoriev, V. Olieric, R.M. Benoit, M.O. Steinmetz, A. Akhmanova, and R.A. Kammerer. 2016. Structural basis for misregulation of kinesin KIF21A autoinhibition by CFEOM1 disease mutations. Sci Rep. 6:30668.

Bieling, P., I.A. Telley, and T. Surrey. 2010. A minimal midzone protein module controls formation and length of antiparallel microtubule overlaps. Cell. 142:420-432.

Bouchet, B.P., I. Noordstra, M. van Amersfoort, E.A. Katrukha, Y.C. Ammon, N.D. Ter Hoeve, L. Hodgson, M. Dogterom, P.W.B. Derksen, and A. Akhmanova. 2016. Mesenchymal Cell Invasion Requires Cooperative Regulation of Persistent Microtubule Growth by SLAIN2 and CLASP1. Dev Cell. 39:708-723.

Bringmann, H., G. Skiniotis, A. Spilker, S. Kandels-Lewis, I. Vernos, and T. Surrey. 2004. A kinesin-like motor inhibits microtubule dynamic instability. Science. 303:1519-1522.

Bunnell, S.C., V. Kapoor, R.P. Trible, W. Zhang, and L.E. Samelson. 2001. Dynamic actin polymerization drives T cell receptor-induced spreading: a role for the signal transduction adaptor LAT. Immunity. 14:315-329.

Bustos-Moran, E., N. Blas-Rus, N.B. Martin-Cofreces, and F. Sanchez-Madrid. 2017. Microtubule-associated protein-4 controls nanovesicle dynamics and T cell activation. J Cell Sci. 130:1217-1223.

Chen, F., P.W. Tillberg, and E.S. Boyden. 2015. Optical imaging. Expansion microscopy. Science. 347:543-548.

Cheng, L., J. Desai, C.J. Miranda, J.S. Duncan, W. Qiu, A.A. Nugent, A.L. Kolpak, C.C. Wu, E. Drokhlyansky, M.M. Delisle, W.M. Chan, Y. Wei, F. Propst, S.L. Reck-Peterson, B. Fritzsch, and E.C. Engle. 2014. Human CFEOM1 mutations attenuate KIF21A autoinhibition and cause oculomotor axon stalling. Neuron. 82:334-349.

Combs, J., S.J. Kim, S. Tan, L.A. Ligon, E.L. Holzbaur, J. Kuhn, and M. Poenie. 2006. Recruitment of dynein to the Jurkat immunological synapse. Proc Natl Acad Sci U S A. 103:14883-14888.

Daza, R., B. Gonzalez-Bermudez, J. Cruces, M. De la Fuente, G.R. Plaza, M. Arroyo-Hernandez, M. Elices, J. Perez-Rigueiro, and G.V. Guinea. 2019. Comparison of cell mechanical measurements provided by Atomic Force Microscopy (AFM) and Micropipette Aspiration (MPA). J Mech Behav Biomed Mater. 95:103-115.

Dogterom, M., and G.H. Koenderink. 2019. Actin-microtubule crosstalk in cell biology. Nat Rev Mol Cell Biol. 20:38-54.

Dogterom, M., and B. Yurke. 1997. Measurement of the force-velocity relation for growing microtubules. Science. 278:856-860.

Doodhi, H., A.E. Prota, R. Rodriguez-Garcia, H. Xiao, D.W. Custar, K. Bargsten, E.A. Katrukha, M. Hilbert, S. Hua, K. Jiang, I. Grigoriev, C.H. Yang, D. Cox, S.B. Horwitz, L.C. Kapitein, A. Akhmanova, and M.O. Steinmetz. 2016. Termination of Protofilament Elongation by Eribulin Induces Lattice Defects that Promote Microtubule Catastrophes. Curr

Biol. 26:1713-1721.

Dustin, M.L., A.K. Chakraborty, and A.S. Shaw. 2010. Understanding the structure and function of the immunological synapse. Cold Spring Harb Perspect Biol. 2:a002311.

Filbert, E.L., M. Le Borgne, J. Lin, J.E. Heuser, and A.S. Shaw. 2012. Stathmin regulates microtubule dynamics and microtubule organizing center polarization in activated T cells. J Immunol. 188:5421-5427.

Garcia-Etxebarria, K., A. Jauregi-Miguel, I. Romero-Garmendia, L. Plaza-Izurieta, M. Legarda, I. Irastorza, and J.R. Bilbao. 2016. Ancestry-based stratified analysis of Immunochip data identifies novel associations with celiac disease. Eur J Hum Genet. 24:1831-1834.

Geiger, B., D. Rosen, and G. Berke. 1982. Spatial relationships of microtubule-organizing centers and the contact area of cytotoxic T lymphocytes and target cells. J Cell Biol. 95:137-143.

Ghiretti, A.E., E. Thies, M.K. Tokito, T. Lin, E.M. Ostap, M. Kneussel, and E.L.F. Holzbaur. 2016. Activity-Dependent Regulation of Distinct Transport and Cytoskeletal Remodeling Functions of the Dendritic Kinesin KIF21B. Neuron. 92:857-872.

Gittes, F., B. Mickey, J. Nettleton, and J. Howard. 1993. Flexural rigidity of microtubules and actin filaments measured from thermal fluctuations in shape. J Cell Biol. 120:923-934.

Goris, A., S. Boonen, B. D'Hooghe M, and B. Dubois. 2010. Replication of KIF21B as a susceptibility locus for multiple sclerosis. J Med Genet. 47:775-776.

Gromova, K.V., M. Muhia, N. Rothammer, C.E. Gee, E. Thies, I. Schaefer, S. Kress, M.W. Kilimann, O. Shevchuk, T.G. Oertner, and M. Kneussel. 2018. Neurobeachin and the Kinesin KIF21B Are Critical for Endocytic Recycling of NMDA Receptors and Regulate Social Behavior. Cell Rep. 23:2705-2717.

Guo, Q., S. Liao, Z. Zhu, Y. Li, F. Li, and C. Xu. 2018. Structural basis for the recognition of kinesin family member 21A (KIF21A) by the ankyrin domains of KANK1 and KANK2 proteins. J Biol Chem. 293:557-566.

Gupta, M.L., Jr., P. Carvalho, D.M. Roof, and D. Pellman. 2006. Plus end-specific depolymerase activity of Kip3, a kinesin-8 protein, explains its role in positioning the yeast mitotic spindle. Nat Cell Biol. 8:913-923.

He, M., R. Subramanian, F. Bangs, T. Omelchenko, K.F. Liem, Jr., T.M. Kapoor, and K.V. Anderson. 2014. The kinesin-4 protein Kif7 regulates mammalian Hedgehog signalling by organizing the cilium tip compartment. Nat Cell Biol. 16:663-672.

Hooikaas, P.J., M. Martin, T. Muhlethaler, G.J. Kuijntjes, C.A.E. Peeters, E.A. Katrukha, L. Ferrari, R. Stucchi, D.G.F. Verhagen, W.E. van Riel, I. Grigoriev, A.F.M. Altelaar, C.C. Hoogenraad, S.G.D. Rudiger, M.O. Steinmetz, L.C. Kapitein, and A. Akhmanova. 2019. MAP7 family proteins regulate kinesin-1 recruitment and activation. J Cell Biol. 218:1298-1318.

Hornak, I., and H. Rieger. 2020. Stochastic Model of T Cell Repolarization during Target Elimination I. Biophys J. 118:1733-1748.

Howard, J., and C. Garzon-Coral. 2017. Physical Limits on the Precision of Mitotic Spindle Positioning by Microtubule Pushing forces: Mechanics of mitotic spindle positioning. Bioessays. 39.

International Multiple Sclerosis Genetics, C. 2010. Comprehensive follow-up of the first genome-wide association study of multiple sclerosis identifies KIF21B and TMEM39A as susceptibility loci. Hum Mol Genet. 19:953-962.

Janson, M.E., M.E. de Dood, and M. Dogterom. 2003. Dynamic instability of microtubules is regulated by force. J Cell Biol. 161:1029-1034.

Jurriens, D., V. van Batenburg, E.A. Katrukha, and L.C. Kapitein. 2020. Mapping the neuronal cytoskeleton using expansion microscopy. In Methods in Cell Biology. Academic Press.

Kannan, M., E. Bayam, C. Wagner, B. Rinaldi, P.F. Kretz, P. Tilly, M. Roos, L. McGillewie, S. Bar, S. Minocha, C. Chevalier, C. Po, P. Sanger Mouse Genetics, J. Chelly, J.L. Mandel, R. Borgatti, A. Piton, C. Kinnear, B. Loos, D.J. Adams, Y. Herault, S.C. Collins, S. Friant, J.D. Godin, and B. Yalcin. 2017. WD40-repeat 47, a microtubule-associated protein, is essential for brain development and autophagy. Proc Natl Acad Sci U S A. 114:E9308-E9317.

Kapitein, L.C., and C.C. Hoogenraad. 2015. Building the Neuronal Microtubule Cytoskeleton. Neuron. 87:492-506.

Khakshour, S., T.V. Beischlag, C. Sparrey, and E.J. Park. 2015. Probing mechanical properties of Jurkat cells under the effect of ART using oscillating optical tweezers. PLoS One. 10:e0126548.

Kim, M.J., and I.V. Maly. 2009. Deterministic mechanical model of T-killer cell polarization reproduces the wandering of aim between simultaneously engaged targets. PLoS Comput Biol. 5:e1000260.

Kotak, S., and P. Gonczy. 2013. Mechanisms of spindle positioning: cortical force generators in the limelight. Curr Opin Cell Biol. 25:741-748.

Kreft, K.L., M. van Meurs, A.F. Wierenga-Wolf, M.J. Melief, M.E. van Strien, E.M. Hol, B.A. Oostra, J.D. Laman, and R.Q. Hintzen. 2014. Abundant kif21b is associated with accelerated progression in neurodegenerative diseases. Acta Neuropathol Commun. 2:144.

Kupfer, A., G. Dennert, and S.J. Singer. 1983. Polarization of the Golgi apparatus and the microtubule-organizing center within cloned natural killer cells bound to their targets. Proc Natl Acad Sci U S A. 80:7224-7228.

Laan, L., N. Pavin, J. Husson, G. Romet-Lemonne, M. van Duijn, M.P. Lopez, R.D. Vale, F. Julicher, S.L. Reck-Peterson, and M. Dogterom. 2012. Cortical dynein controls microtubule dynamics to generate pulling forces that position microtubule asters. Cell. 148:502-514.

Labonte, D., E. Thies, and M. Kneussel. 2014. The kinesin KIF21B participates in the cell surface delivery of gamma2 subunit-containing GABAA receptors. Eur J Cell Biol. 93:338-346.

Letort, G., F. Nedelec, L. Blanchoin, and M. Thery. 2016. Centrosome centering and decentering by microtubule network rearrangement. Mol Biol Cell. 27:2833-2843.

Li, N., J. Ma, K. Li, C. Guo, and L. Ming. 2017. Different Contributions of CDKAL1, KIF21B, and LRRK2/MUC19 Polymorphisms to SAPHO Syndrome, Rheumatoid Arthritis, Ankylosing Spondylitis, and Seronegative Spondyloarthropathy. Genet Test Mol Biomarkers. 21:122-126.

Liu, X., T.M. Kapoor, J.K. Chen, and M. Huse. 2013a. Diacylglycerol promotes centrosome polarization in T cells via reciprocal localization of dynein and myosin II. Proc Natl Acad Sci U S A. 110:11976-11981.

Liu, Y., H. Zhang, J. Li, H. Zhao, Q. Xin, S. Shan, J. Dang, X. Bian, and Q. Liu. 2013b. Association of common variants in KIF21B and ankylosing spondylitis in a Chinese Han population: a replication study. Immunogenetics. 65:835-839.

Marszalek, J.R., J.A. Weiner, S.J. Farlow, J. Chun, and L.S. Goldstein. 1999. Novel dendritic kinesin sorting identified by different process targeting of two related kinesins: KIF21A and KIF21B. J Cell Biol. 145:469-479.

Martin-Cofreces, N.B., J. Robles-Valero, J.R. Cabrero, M. Mittelbrunn, M. Gordon-Alonso, C.H. Sung, B. Alarcon, J. Vazquez, and F. Sanchez-Madrid. 2008. MTOC translocation modulates IS formation and controls sustained T cell signaling. J Cell Biol. 182:951-962.

Martin, M., A. Veloso, J. Wu, E.A. Katrukha, and A. Akhmanova. 2018. Control of endothelial cell polarity and sprouting angiogenesis by non-centrosomal microtubules. Elife. 7.

Meiring, J.C.M., B.I. Shneyer, and A. Akhmanova. 2020. Generation and regulation of microtubule network asymmetry to drive cell polarity. Curr Opin Cell Biol. 62:86-95.

Mohan, R., E.A. Katrukha, H. Doodhi, I. Smal, E. Meijering, L.C. Kapitein, M.O. Steinmetz, and A. Akhmanova. 2013. End-binding proteins sensitize microtubules to the action of microtubule-targeting agents. Proc Natl Acad Sci U S A. 110:8900-8905.

Morikawa, M., Y. Tanaka, H.S. Cho, M. Yoshihara, and N. Hirokawa. 2018. The Molecular Motor KIF21B Mediates Synaptic Plasticity and Fear Extinction by Terminating Rac1 Activation. Cell Rep. 23:3864-3877.

Muhia, M., E. Thies, D. Labonte, A.E. Ghiretti, K.V. Gromova, F. Xompero, C. Lappe-Siefke, I. Hermans-Borgmeyer, D. Kuhl, M. Schweizer, O. Ohana, J.R. Schwarz, E.L.F. Holzbaur, and M. Kneussel. 2016. The Kinesin KIF21B Regulates Microtubule Dynamics and Is Essential for Neuronal Morphology, Synapse Function, and Learning and Memory. Cell Rep. 15:968-977.

Nath, S., L. Christian, S.Y. Tan, S. Ki, L.I. Ehrlich, and M. Poenie. 2016. Dynein Separately Partners with NDE1 and Dynactin To Orchestrate T Cell Focused Secretion. J Immunol. 197:2090-2101.

Nedelec, F., and D. Foethke. 2007. Collective Langevin dynamics of flexible cytoskeletal fibers. New Journal of Physics. 9:427-427.

Noordstra, I., and A. Akhmanova. 2017. Linking cortical microtubule attachment and exocytosis. F1000Res. 6:469.

Ohashi, K.G., L. Han, B. Mentley, J. Wang, J. Fricks, and W.O. Hancock. 2019. Load-dependent detachment kinetics plays a key role in bidirectional cargo transport by kinesin and dynein. Traffic. 20:284-294.

Pan, W., K. Sun, K. Tang, Q. Xiao, C. Ma, C. Yu, and Z. Wei. 2018. Structural insights into ankyrin repeat-mediated recognition of the kinesin motor protein KIF21A by KANK1, a scaffold protein in focal adhesion. J Biol Chem. 293:1944-1956.

Parsey, M.V., and G.K. Lewis. 1993. Actin polymerization and pseudopod reorganization accompany anti-CD3-induced growth arrest in Jurkat T cells. J Immunol. 151:1881-1893.

Robinson, P.C., T.A. Claushuis, A. Cortes, T.M. Martin, D.M. Evans, P. Leo, P. Mukhopadhyay, L.A. Bradbury, K. Cremin, J. Harris, W.P. Maksymowych, R.D. Inman, P. Rahman, N. Haroon, L. Gensler, J.E. Powell, I.E. van der Horst-Bruinsma, A.W. Hewitt, J.E. Craig, L.L. Lim, D. Wakefield, P. McCluskey, V. Voigt, P. Fleming, A.-A.-A.S.C.I.G.o.A.S.C.W.T.C.C.S.M.D.-E. Spondyloarthritis Research Consortium of Canada, M. Degli-Esposti, J.J. Pointon, M.H. Weisman, B.P. Wordsworth, J.D. Reveille, J.T. Rosenbaum, and M.A. Brown. 2015. Genetic dissection of acute anterior uveitis reveals similarities and differences in associations observed with ankylosing spondylitis. Arthritis Rheumatol. 67:140-151.

Roig-Martinez, M., E. Saavedra-Lopez, P.V. Casanova, G.P. Cribaro, and C. Barcia. 2019. The MTOC/Golgi Complex at the T-Cell Immunological Synapse. Results Probl Cell Differ. 67:223-231.

Roostalu, J., C. Thomas, N.I. Cade, S. Kunzelmann, I.A. Taylor, and T. Surrey. 2020. The speed of GTP hydrolysis determines GTP cap size and controls microtubule stability. Elife. 9.

Samora, C.P., B. Mogessie, L. Conway, J.L. Ross, A. Straube, and A.D. McAinsh. 2011. MAP4 and CLASP1 operate as a safety mechanism to maintain a stable spindle position in mitosis. Nat Cell Biol. 13:1040-1050.

Semenova, I., K. Ikeda, K. Resaul, P. Kraikivski, M. Aguiar, S. Gygi, I. Zaliapin, A. Cowan, and V. Rodionov. 2014. Regulation of microtubule-based transport by MAP4. Mol Biol Cell. 25:3119-3132.

Seo, M., S.O. Lee, J.H. Kim, Y. Hong, S. Kim, Y. Kim, D.H. Min, Y.Y. Kong, J. Shin, and K. Ahn. 2016. MAP4-regulated dynein-dependent trafficking of BTN3A1 controls the TBK1-IRF3 signaling axis. Proc Natl Acad Sci U S A. 113:14390-14395.

Serrador, J.M., J.R. Cabrero, D. Sancho, M. Mittelbrunn, A. Urzainqui, and F. Sanchez-Madrid. 2004. HDAC6 deacetylase activity links the tubulin cytoskeleton with immune synapse organization. Immunity. 20:417-428.

Stepanova, T., J. Slemmer, C.C. Hoogenraad, G. Lansbergen, B. Dortland, C.I. De Zeeuw, F. Grosveld, G. van Cappellen, A. Akhmanova, and N. Galjart. 2003. Visualization of microtubule growth in cultured neurons via the use of EB3-GFP (end-binding protein 3-green fluorescent protein). J Neurosci. 23:2655-2664.

Stinchcombe, J.C., E. Majorovits, G. Bossi, S. Fuller, and G.M. Griffiths. 2006. Centrosome polarization delivers secretory granules to the immunological synapse. Nature. 443:462-465.

Tas, R.P., C.Y. Chen, E.A. Katrukha, M. Vleugel, M. Kok, M. Dogterom, A. Akhmanova, and L.C. Kapitein. 2018. Guided by Light: Optical Control of Microtubule Gliding Assays. Nano Lett. 18:7524-7528.

Traboulsi, E.I., and E.C. Engle. 2004. Mutations in KIF21A are responsible for CFEOM1 worldwide. Ophthalmic Genet. 25:237-239.

van der Vaart, B., W.E. van Riel, H. Doodhi, J.T. Kevenaar, E.A. Katrukha, L. Gumy, B.P. Bouchet, I. Grigoriev, S.A. Spangler, K.L. Yu, P.S. Wulf, J. Wu, G. Lansbergen, E.Y. van Battum, R.J. Pasterkamp, Y. Mimori-Kiyosue, J. Demmers, N. Olieric, I.V. Maly, C.C. Hoogenraad, and A. Akhmanova. 2013. CFEOM1-associated kinesin KIF21A is a cortical microtubule growth inhibitor. Dev Cell. 27:145-160.

van Riel, W.E., A. Rai, S. Bianchi, E.A. Katrukha, Q. Liu, A.J. Heck, C.C. Hoogenraad, M.O. Steinmetz, L.C. Kapitein, and A. Akhmanova. 2017. Kinesin-4 KIF21B is a potent microtubule pausing factor. Elife. 6.

Varga, V., J. Helenius, K. Tanaka, A.A. Hyman, T.U. Tanaka, and J. Howard. 2006. Yeast kinesin-8 depolymerizes microtubules in a length-dependent manner. Nat Cell Biol. 8:957-962.

Weng, Z., Y. Shang, D. Yao, J. Zhu, and R. Zhang. 2018. Structural analyses of key features in the KANK1. KIF21A complex yield mechanistic insights into the cross-talk between microtubules and the cell cortex. J Biol Chem. 293:215-225.

Yamada, K., C. Andrews, W.M. Chan, C.A. McKeown, A. Magli, T. de Berardinis, A. Loewenstein, M. Lazar, M. O'Keefe, R. Letson, A. London, M. Ruttum, N. Matsumoto, N. Saito, L. Morris, M. Del Monte, R.H. Johnson, E. Uyama, W.A. Houtman, B. de Vries, T.J. Carlow, B.L. Hart, N. Krawiecki, J. Shoffner, M.C. Vogel, J. Katowitz, S.M. Goldstein, A.V. Levin, E.C. Sener, B.T. Ozturk, A.N. Akarsu, M.C. Brodsky, F. Hanisch, R.P. Cruse, A.A. Zubcov, R.M. Robb, P. Roggenkaemper, I. Gottlob, L. Kowal, R. Battu, E.I. Traboulsi, P. Franceschini, A. Newlin, J.L. Demer, and E.C. Engle. 2003. Heterozygous mutations of the kinesin KIF21A in congenital fibrosis of the extraocular muscles type 1 (CFEOM1). Nat Genet. 35:318-321.

Yang, X., M. Li, L. Wang, Z. Hu, Y. Zhang, and Q. Yang. 2015. Association of KIF21B genetic polymorphisms with ankylosing spondylitis in a Chinese Han population of Shandong Province. Clin Rheumatol. 34:1729-1736.

Yau, K.W., S.F. van Beuningen, I. Cunha-Ferreira, B.M. Cloin, E.Y. van Battum, L. Will, P. Schatzle, R.P. Tas, J. van Krugten, E.A. Katrukha, K. Jiang, P.S. Wulf, M. Mikhaylova, M. Harterink, R.J. Pasterkamp, A. Akhmanova, L.C. Kapitein, and C.C. Hoogenraad. 2014. Microtubule minus-end binding protein CAMSAP2 controls axon specification and dendrite development. Neuron. 82:1058-1073.

Yi, J., X. Wu, A.H. Chung, J.K. Chen, T.M. Kapoor, and J.A. Hammer. 2013. Centrosome repositioning in T cells is biphasic and driven by microtubule end-on capture-shrinkage. J Cell Biol. 202:779-792.

Yue, Y., T.L. Blasius, S. Zhang, S. Jariwala, B. Walker, B.J. Grant, J.C. Cochran, and K.J. Verhey. 2018. Altered chemomechanical coupling causes impaired motility of the kinesin-4 motors KIF27 and KIF7. J Cell Biol. 217:1319-1334.

Zyss, D., H. Ebrahimi, and F. Gergely. 2011. Casein kinase I delta controls centrosome positioning during T cell activation. J Cell Biol. 195:781-797.

Supplemental Figures

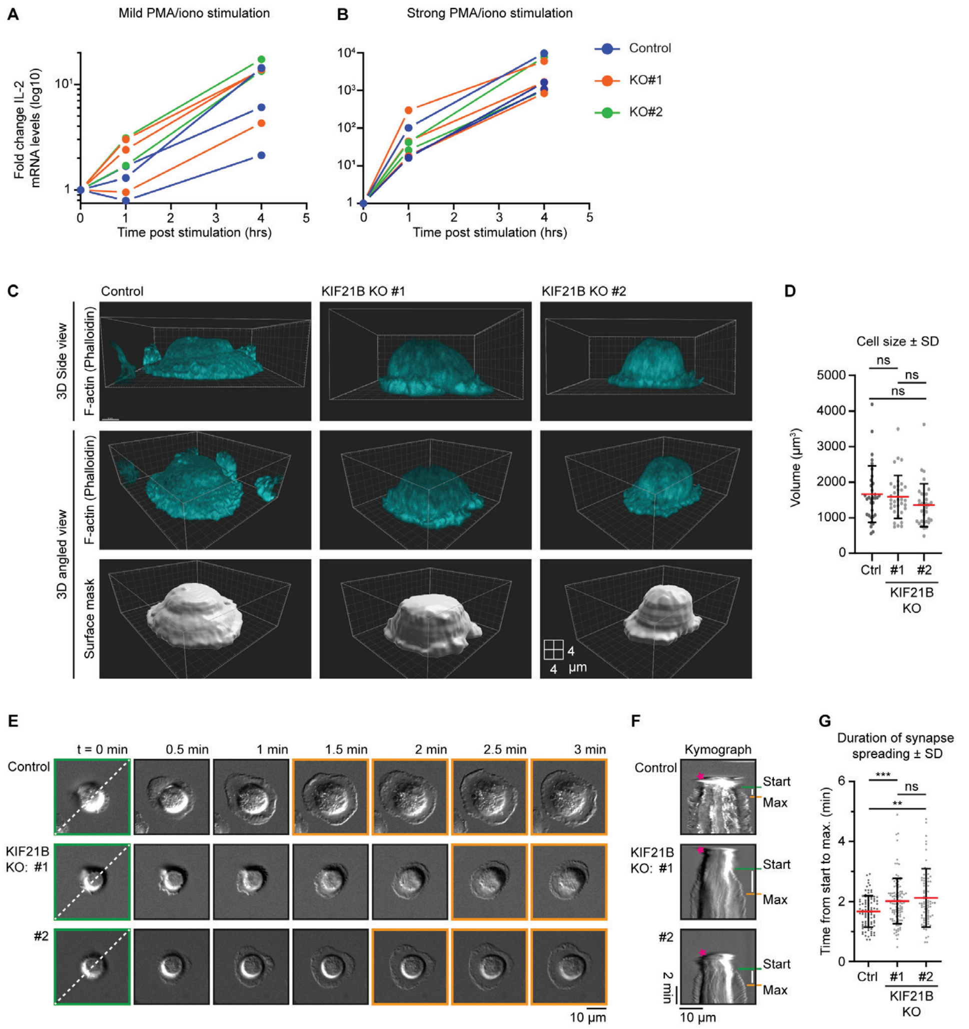

Supplemental Figure S1 - Characterization of KIF21B knockout cell lines.
(A-B) qRT-PCR measurements of IL-2 expression levels after stimulation at indicated timepoints. Indicated Jurkat T cell lines were treated with 2 ng/ml PMA and 100 ng/ml ionomycin (A, mild stimulation) or 20 ng/ml PMA and 1 µg/ml ionomycin (B, strong stimulation), after which RNA was isolated and cDNA was generated. IL-2 expression was measured by qRT-PCR, and values were normalized to GAPDH levels. IL-2 expression is shown in a log10 scale. **(C)** Volume rendering of indicated T cells stained for F-actin (using phalloidin). Side views (top panel row) and angled views (middle and bottom row) are indicated. Cell volume was measured by converting F-actin fluorescence signal to a surface mask using Imaris software (isoline tool). xyz dimensions correspond to 2 µm per block on the displayed grid. **(D)** Quantification of T cell volumes based on F-actin staining. n = 33, 34 and 34 cells from three independent experiments, ns = not significant (Mann-Whitney *U* test). **(E)** Live-cell imaging of Jurkat T cells forming immunological synapses on anti-CD3 coated glass surface, imaged on a widefield microscope using DIC microscopy at 2.5 s per frame interval. Green boxed stills indicate start of synapse formation, orange boxed stills show fully formed synapses at their maximum size. Dotted line in the first movie still indicates the position of the kymograph in Figure S1F. **(F)** Kymographs of immunological synapse formation corresponding to the movie stills shown in Figure S1E.

Supplemental Figure S1 (continued) Landing of the Jurkat T cell on the anti-CD3 coated glass surface is marked by the pink asterisk. The start of synapse formation (Start) is indicated in green, the moment a synapse reaches its maximum size is indicated in orange (Max) and the white bar indicates time between Start and Max. **(G)** Quantification of spreading time. n = 87, 107 and 91 cells from two independent experiments. *** $p < 0.001$, ** $p < 0.01$, ns = not significant (Mann-Whitney *U* test).

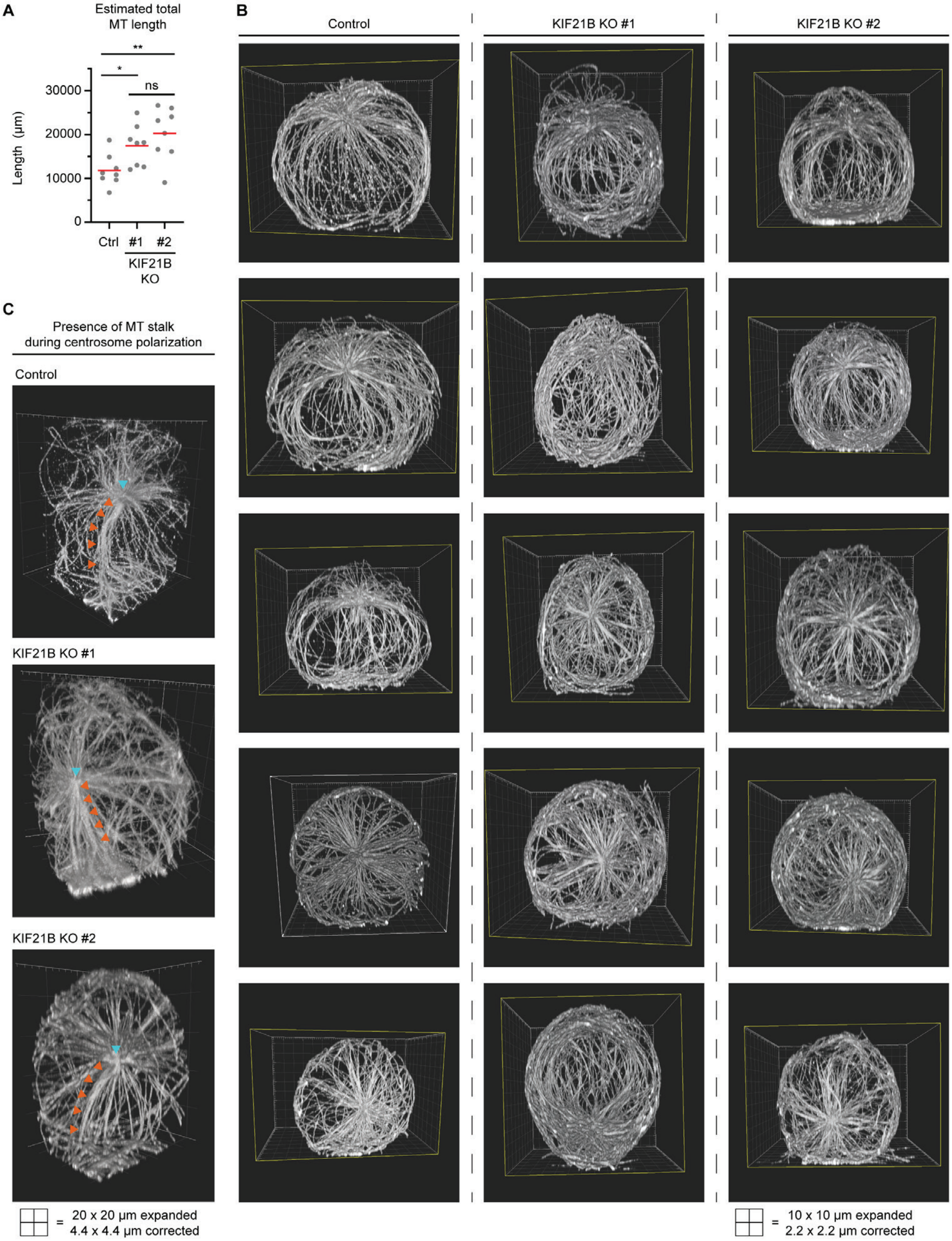
A
Estimated total MT length
**
*
ns
30000
20000
10000
0
Length (μm)
Ctrl
#1
#2
KIF21B KO
B
Control
KIF21B KO #1
KIF21B KO #2
C
Presence of MT stalk during centrosome polarization
Control
KIF21B KO #1
KIF21B KO #2
= 20 x 20 μm expanded 4.4 x 4.4 μm corrected
= 10 x 10 μm expanded 2.2 x 2.2 μm corrected

Supplemental Figure S2 - Characterization of MT network in polarizing T cells by ExM.

Supplemental Figure S2 (continued) (A) Quantification of total estimated MT length per cell indicated in indicated Jurkat T cell lines. Values were obtained by multiplication of total MT numbers by the estimated average MT length per cell. n = 8 cells for all conditions. * $p < 0.05$, ** $p < 0.01$, ns = not significant (t test). **(B)** Series of 5 exemplary volume renderings per indicated T cell lines stained for α-tubulin (related to Figure 2D, E). T cells were fixed 2 min after activation on anti-CD3 coated coverslips. Samples were expanded ~ 4.5 times following an ExM protocol and MTs were imaged using on a confocal microscope. Imaris software was used to create volume renders. **(C)** Volume renderings of indicated T cell lines stained for α-tubulin to highlight examples suggesting that a MT stalk is formed during the process of centrosome polarization. Centrosome (cyan arrowheads) and MT stalks emanating from the centrosome towards the synapse are indicated (orange arrowheads).

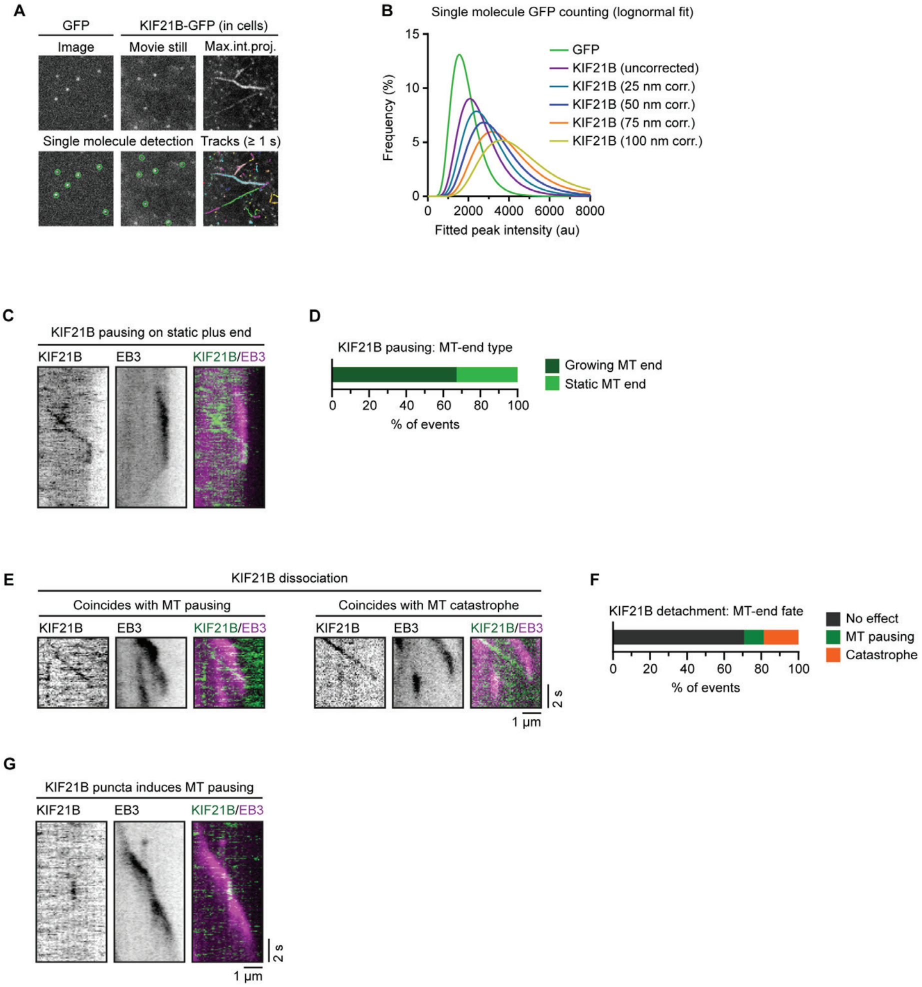

Supplemental Figure S3 - Characterization of KIF21B motility in cells.

Supplemental Figure S3 (continued) **(A)** Workflow for GFP (monomer reference) and KIF21B-GFP single molecule counting. Imaging was performed in a dual-chamber microscope slide in a single imaging session with identical microscope settings. Monomeric GFP was expressed in HEK293T cells and lysates were diluted in PBS to single molecule densities in the first chamber. KIF21B-KO #2 Jurkat T cell line with stable overexpression of KIF21B-GFP were added to the second chamber, which was coated with anti-CD3 antibodies. Single molecules were detected using DoM ImageJ plugin and for KIF21B-GFP motors in cells, single molecules were only analyzed from kinesin tracks with a duration of > 1 s. **(B)** Lognormal fits of peak-fitted fluorescence intensities of monomeric GFP immobilized on glass (green dots) and KIF21B-GFP motors imaged in Jurkat T cells corrected for a hypothetical range of distances between molecule and coverslip. The evanescent field decays exponentially and KIF21B-GFP fluorescence is corrected for that given the TIRF laser angle was fixed at a penetration depth d of 180 nm. **(C)** Kymograph illustrating KIF21B-GFP motors switching from walking to a pausing state. Growing MT end is visualized with EB3-mCherry. A static plus end undergoes a catastrophe after a KIF21B-GFP pausing event (right). **(D)** Quantification of MT plus-end state when a KIF21B-GFP motor reaches the EB3-mCherry-labeled MT plus end and transitions to a paused state, as illustrated in Figure 3D and S3C. Numbers relate to the "Pausing" and "Tip-tracking + pausing" category of Figure 3G. n = 149 events from two independent experiments. **(E)** Kymographs illustrating a KIF21B-GFP motor reaching a growing EB3-mCherry MT plus end where motor dissociation from the MT coincides with MT pausing (left) or a catastrophe event (right).**(F)** Quantification of MT plus-end fate when a KIF21B-GFP motor reaches a growing EB3-mCherry labeled plus-end and dissociates, as illustrated in Figure 3F and S3E. n = 75 events from two independent experiments. **(G)** Kymograph illustrating a KIF21B-GFP motor directly associating to an EB3-mCherry labeled growing MT plus end and affecting MT growth until KIF21B-GFP dissociates.

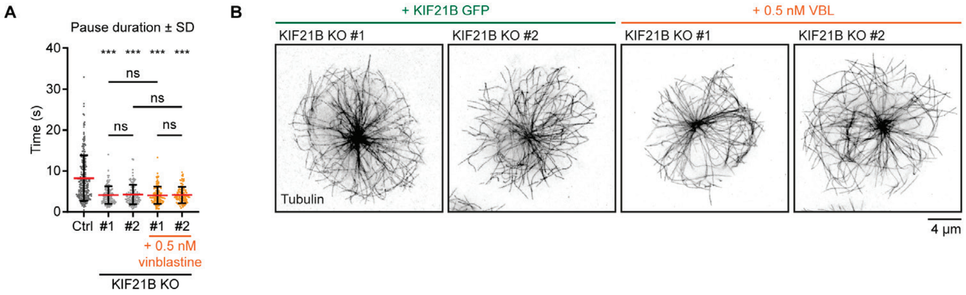

Supplemental Figure S4 - KIF21B-depleted cells lack long MT pause events.
(A) Quantification of MT pause duration as shown in Figure 4F based on live-cell imaging of indicated β-tubulin-GFP overexpressing Jurkat T cell lines. Pause durations are derived from MT pausing events described in Figure 4D and E. n = 229, 110, 114, 117 and 101 events from 46, 49, 38, 37 and 32 cells obtained from three independent experiments. *** $p < 0.001$, ns = not significant (Mann-Whitney *U* test).
(B) STED images of indicated Jurkat T cell lines stained for tubulin.

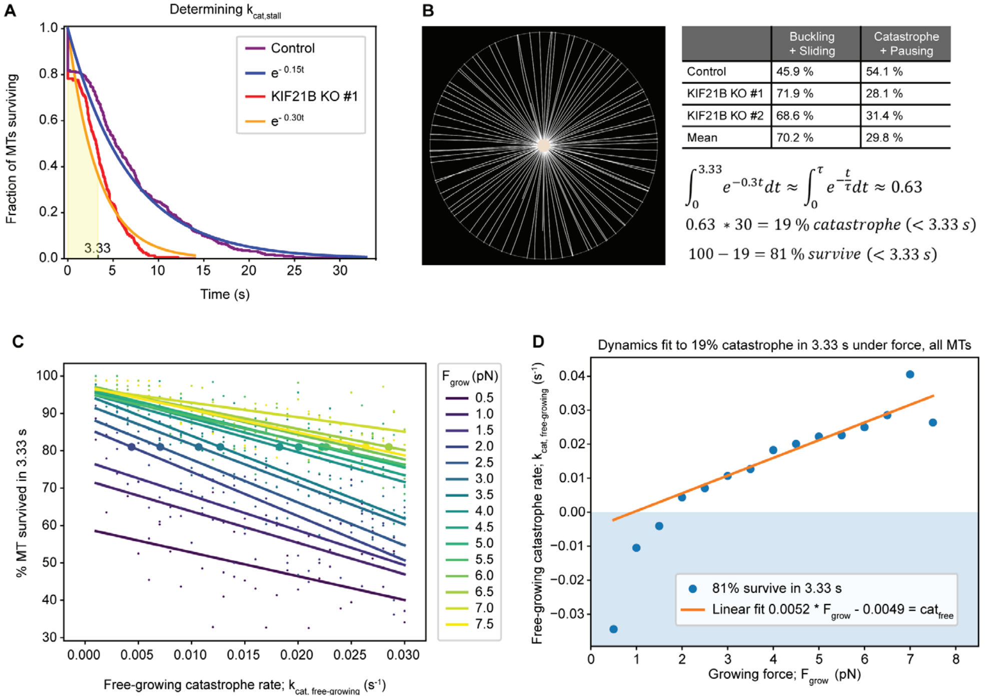

	Buckling + Sliding	Catastrophe + Pausing
Control	45.9 %	54.1 %
KIF21B KO #1	71.9 %	28.1 %
KIF21B KO #2	68.6 %	31.4 %
Mean	70.2 %	29.8 %

$$\int_0^{3.33} e^{-0.3t}dt \approx \int_0^{\tau} e^{-\frac{t}{\tau}}dt \approx 0.63$$

$$0.63 * 30 = 19\ \%\ catastrophe\ (< 3.33\ s)$$

$$100 - 19 = 81\ \%\ survive\ (< 3.33\ s)$$

Supplemental Figure S5 - Characterization of T cell force-dependent catastrophe
(A) Reverse cumulative distribution plot showing MT pause times for KIF21B-KO and control with the immediate catastrophes at t = 0 s. The exponential fit (rate = mean pause time^{-1}) corresponds to a catastrophe rate of 0.3 s^{-1} in the KIF21B-KO and 0.15 s^{-1} in the control. From the assumption that all pausing in the KIF21B-KO cells is from antagonistic force, the stalled catastrophe rate $k_{cat,stall}$ can be set to 0.3 s^{-1}. From this rate follows a characteristic time of 3.33 s (shaded area). **(B)** To match the parametrization of the MT dynamics to the experimental data, a Cytosim model is introduced that describes the fully spread synapse for the KO condition. The space is meant to model the TIRF data of KIF21B-KO synapses after they have spread, thus the cell has a radius of 9.57 µm and no nucleus. For ease of measurement, the centrosome is fixed in the center of the cell. From the stalled catastrophe rate of 0.3 s^{-1} follows that 63% of all catastrophe events happen in the first 3.33 s. From the experimental data, it is known that only approximately 30% of the counted paused KIF21B-KO MTs (under force) do not buckle or slide, but they are counted into the fraction of catastrophe events. Taking 30% of the 63% gives us 19%: the percentage of catastrophe in 3.33 s. Therefore, we can use the constraint that 81% of MTs survive under force for 3.33 s in our synapse model to match the two-state model to our KIF21B-KO pause times. **(C)** Graph showing the number of surviving MTs in 3.33 s under force at indicated free-growing catastrophe rates ($k_{cat,free\text{-}growing}$) and characteristic force exerted by the MT polymerization growth (F_{grow}). Measurements (small dots) and linear fits (lines) are color coded for the value of Fgrow (see legend). The large dots on the lines indicate the level at which 81% of the MTs survive, taken from the linear fit. **(D)** Graph showing points (blue) from Figure S5C at which 81% MT survive in the synapse plotted as a function of the free catastrophe rate ($k_{cat,free\text{-}growing}$) and of the growing force (F_{grow}). A catastrophe rate is obtained from a linear fit (orange line) to the realistic, non-negative points, which gives a linear relationship between F_{grow} and $k_{cat,free\text{-}growing}$, where MT dynamics match that the KIF21B-KO cells.

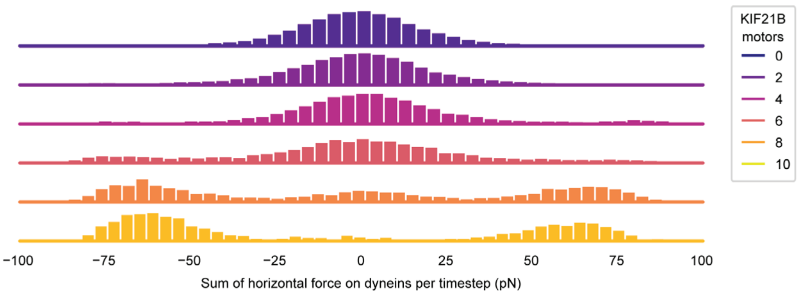

Supplemental Figure S6 - KIF21B affects the balance of force in T cell polarization
Histogram showing the force on dynein at every timestep. The forces on dynein along the x-axis are summed, where left-pointing forces are taken as negative. This sum is taken for every recorded time between 0 and the polarization time of the simulation and binned to create histograms. Histograms are color coded for the number of KIF21B motors present in the simulation (see legend).

Supplemental Table S1 - Parameters used for simulations

Parameter	**Value**	**Description / Reference**
MTs		
Polymerization speed	0.3 µm/s	This study.
Depolymerization speed	1 µm/s	This study.
Rigidity	20 pN/µm	(Gittes et al., 1993)
Stall force	5 pN	Describes the modulation of growth speed and catastrophe rate by antagonistic force (Dogetrom and Yurke, 1997)
Catastrophe rate	0.02 s^{-1}, 0.3 s^{-1}	Matched to TIRF GFP-β-tubulin data (Figure 4D-E)
Cell		
Viscosity	0.1 pN.s/µm^{2}	Internal viscosity of T cells, like most blood cells, is usually estimated to be lower than that of somatic cells. Jurkat cell internal viscosity has been reported at different values (Daza et al., 2019; Khakshour et al., 2015). Because there is no consensus on the value, we used a viscosity such that the KIF21B-mediated polarization happens within the timescale measured for polarization.
Elasticity	100 pN/µm	The spring stiffness of the cell for all objects with inertia. This same stiffness is used for interaction of MTs with the nucleus.
Radius	7 µm	This study, calculated from Figure S1C-D. T
Synapse fraction	0.9	his corresponds to a synapse cutting off 10% of the height of the cell (1.4 µm).
Interpolation distance	1 µm	The curvature starts 1 µm under the synapse (at 2.4 µm from the top of the unpolarized cell).
Centrosome		
First anchoring stiffness	500 pN/µm	Rotational stiffness on the MTs at the center of the centrosome, as proposed previously (Letort et al., 2016).
Second anchoring stiffness	500 pN/µm	Rotational stiffness on the MTs exerted at the periphery of the centrosome, as proposed previously (Letort et al., 2016).
Number of MTs	90	

Supplemental Table S1 (continued)

Dynein

Walking speed	1 µm/s	Average value from MT gliding over dynein (Laan et al., 2012).
Number	50	
Stall force	4 pN	(Belyy et al., 2016)
Unbinding rate	1 s^{-1}	(Ohasi et al., 2019)
Initialization	unifrom on synapse	Dynein is initialized on the synapse and part of the interpolated curve connecting the synapse to the rest of the cell. The region is defined as being within 1.6 µm of the synapse along the vertical axis.
Link stiffness	100 pN/µm	Describes the elastic stiffness of the link between MT-binding site and anchoring point (Letort et al., 2016).

KIF21B

Walking speed	0.71 µm/s	This study.
MT state after a KIF21B-induced pause	shrinkage	We inflate the effect of KIF21B to always cause catastrophe in order to more clearly display the effect of KIF21B as a delayed catastrophe inducer.
Capable of pausing a shrinking MT	no	This means that the KIF21B motors do not cooperatively pause: if one of them unbinds, the fiber is set to shrinkage and another bound KIF21B cannot pause this shrinking fiber.

System

Dimensionality	2D	The overgrown KIF21B-KO MT system requires much computation per timestep, and thus we were not able to expand to 3D and keep our fit of the system.
Number of repeats	30 per condition	In some figures, fewer repeats are shown for readability. If so, the ones were chosen that were run first chronologically, to avoid bias in run selection.

8

General discussion and future perspectives

Peter Jan Hooikaas[1]

---

[1] Cell Biology, Neurobiology and Biophysics, Department of Biology, Faculty of Science, Utrecht University, Utrecht, Netherlands

Microtubules in our cells resemble highways along which molecules, vesicles and even entire organelles are being transported by two classes of motor proteins: kinesins and dyneins. In this thesis, we tried to shed some light on how binding of microtubule associated proteins (MAPs) and cargo regulates and stimulates kinesin activity. In **Chapter 1**, we reviewed what kind of motors are responsible for microtubule-based transport and focused on how kinesin motors may be regulated by cellular factors. We then took a closer look at a specific family of MAPs, MAP7, and investigated how the members of this family regulate kinesin-1 activity (**Chapter 2**) and investigated their contribution to the multimotor transport of exocytotic vesicles (**Chapter 3**). Novel interaction candidates were identified for all MAP7 proteins, and we have studied the MAP7D2-specific interaction with clathrin and its potential role in axonal transport (**Chapter 4**). We have set up a novel tubulin purification protocol that enabled us to study isotype-labeled microtubules with NMR. This approach allows to study the dynamics of MAPs binding to microtubules and vice versa (**Chapter 5**). Using *in vitro* reconstitutions and cellular experiments, we looked at the mitotic kinesin MKLP2 and unraveled that it is a motile motor. Furthermore, we showed that this kinesin is involved in the translocation of Chromosomal Passenger Complexes (CPC) during the transition from metaphase to anaphase (**Chapter 6**). The final experimental chapter is focused on another kinesin, KIF21B, which acts as a regulator of microtubule dynamics. In T cells, this motor is involved in restricting microtubule growth, which is important for the cell to rapidly polarize the centrosome and the whole microtubule network during immunological synapse formation (**Chapter 7**). In this final chapter, we will discuss our findings, put them in a broader context and give direction for future experimental work.

Mechanistic aspects of kinesin-1 activation by MAP7 proteins

Kinesin-1 is the best studied plus-end directed motor protein, and many properties and functions of this kinesin have been subject of intensive research. Activation of kinesin-1 is regulated by autoinhibition and cargo binding (Verhey and Hammond, 2009). In recent years, it became widely accepted that the microtubule-bound MAP7/ensconsin is a positive regulator of kinesin-1 (Barlan et al., 2013; Metivier et al., 2019; Monroy et al., 2018; Sung et al., 2008; Tymanskyj et al., 2018), although the mechanistic details were not extensively investigated. In **Chapter 2**, we sought to find molecular understanding of this mechanism and discovered that kinesin-1 motility relies on a combination of microtubule recruitment and allosteric activation by MAP7 proteins. Although activation by MAP7 can be mediated without microtubule-binding, its tethering to microtubules makes the process much more efficient. These *in vitro* data were also supported by *in vivo* experiments in *Drosophila* where the kinesin-binding domain of ensconsin was sufficient to rescue the effect of ensconsin depletion in several kinesin-1-dependent processes (Metivier et al., 2019). Combined with our data, we therefore proposed that MAP7 proteins are microtubule-bound activation modules of kinesin-1, with which the kinesin transiently interacts as it walks over a microtubule.

Most studies involving kinesin-1 activation by MAP7 did not take into account the role and alternative function of the other mammalian MAP7 family members: MAP7D1, MAP7D2 and MAP7D3. In **Chapter 2**, we investigated all four family members and found redundancy among these MAPs in activating kinesin-1 in cells. In other words, removal of all expressed MAP7 family members (MAP7, MAP7D1 and MAP7D3) was needed to affect kinesin-1 activity. Despite the functional similarity between MAP7 proteins, we also found differences between these MAPs when we studied MAP7 and MAP7D3 using cellular, biochemical and *in vitro* reconstitution assays. MAP7 binds tightly to microtubules and remains immobile on the microtubule lattice for several minutes (Monroy et al., 2018); yet, MAP7 only displays a low affinity for kinesin-1. In contrast, MAP7D3 readily diffuses along microtubules, but shows a stronger binding to kinesin-1. Because of this combination of affinities, MAP7D3 can be co-transported together with the kinesin. MAP7D3-bound kinesin-1 motors also have a reduced velocity because the MAP exerts some drag on the microtubule. Although we were able to show this phenomenon using an optogenetic technique to rapidly release a bulk of kinesin-1 motors, we deem it unlikely that MAP co-transport with the kinesin plays a major role in cells: in control conditions we did not observe MAP7D3 accumulation in the vicinity of microtubule plus ends. However, these results imply that MAP7 family proteins consists of microtubule- and kinesin-binding modules with different affinities. Combining these modules affects the dynamic process of kinesin-1 activation and determines whether the MAP binds MTs rigidly or is able to move together with the kinesin over short distances. The affinity of MAP7D1 and MAP7D2 for microtubules and kinesin-1 was not analyzed in detail, but such analysis may aid in understanding the possible diversification between these MAPs in their kinesin-activating role. Knowing the microtubule- and kinesin-binding affinities of all these MAPs would offer the opportunity to perform modelling studies on the dynamics of kinesin-1 activation by the different members of the MAP7 protein family. This is of interest because different MAP combinations and expression levels can be employed by the cell to finetune kinesin-1 activity. In addition, analyzing tissue-specific expression levels of MAP7 proteins might be predictive of how kinesin-1 is regulated and distributed in a cell-type specific manner.

We found that the kinesin-binding domain of MAP7 proteins is sufficient to activate kinesin-1 in an allosteric manner. This discovery raises the question of how such binding to the kinesin stalk domain promotes activity of the motor. The most intuitive answer would be that it involves the release of kinesin-1 auto-inhibition. Although this mechanism may be involved when we look at activation of the full-length motor (Blasius et al., 2007; Cai et al., 2007; Verhey and Hammond, 2009), the allosteric effect is still strongly observed when the kinesin is truncated and lacks its auto-inhibitory tail domain. Although experimental evidence is lacking, it might be possible that the kinesin stalk, to which MAP7 binds, possesses a binding site for the kinesin motor domain. If so, the kinesin would have to adopt a folded structure that enables the kinesin stalk to interact with the motor domains. It is questionable whether such interaction precludes the known auto-inhibitory fold between the kinesin tail and motor domain. Pull down assays with kinesin motor domain, stalk and tail deletion constructs could be used to test this idea. In addition, it would be interesting to perform single particle electron microscopy experiments to reveal the different 3D conformations that kinesin-1 may adopt natively and in the presence of the light chains and/or MAP7. A second and more likely explanation for the allosteric MAP7 effect is that binding to kinesin-1 induces a conformational change in the stalk itself or in the positioning of the stalk in relation to the motor domains that would positively affect the engagement of the kinesin with microtubules. Such a conformational change could be initiated in the stalk region and could encompass rotation and/or separation of the two stalk coils upon MAP7 binding. This rearrangement would then need to be transferred to a conformational change of the motor domain, neck linkers and/or coils to promote more efficient landing and increased processivity of the kinesin. It is therefore be interesting to test whether substituting these downstream kinesin structural elements with alternative coiled-coil domains, neck linkers or a motor domain from a different kinesin family would abolish allosteric activation by MAP7. Ultimately, such experiments would need to be supported by structural data to determine the structural changes that MAP7 proteins induce when they bind to the kinesin stalk.

Kinesin-1 motors are dimers, and it is therefore important to consider the stoichiometry of an allosteric activation module at the stalk. Our data in **Chapter 2** suggested that

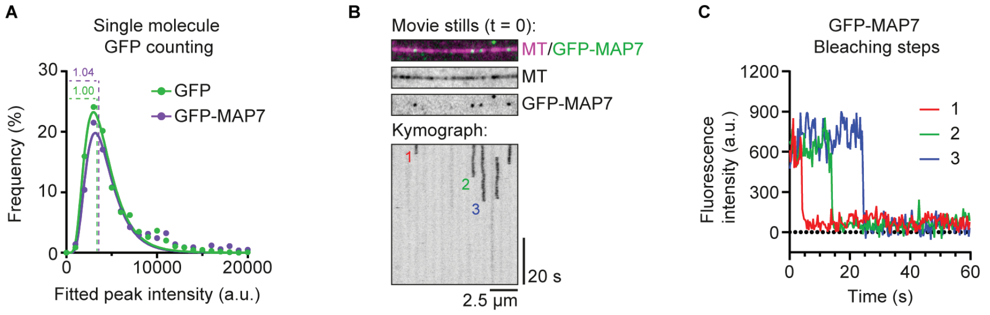

Figure 1 – MAP7 proteins are monomers at low concentration
(A) Histograms of peak-fitted fluorescence intensities of single GFP (green dots) and GFP-MAP7 molecules (purple dots) immobilized on coverslips in two separate chambers on the same coverslip and the corresponding lognormal fits (green and purple lines). Imaging conditions were identical for both conditions. n = 1042 (GFP) and n = 1002 (GFP-MAP7) molecules. Fold change of mean fluorescence intensity relative to monomeric GFP is indicated on top of the fits. **(B)** Movie stills and kymograph of single molecules of GFP-MAP7 on dynamic rhodamine-labeled microtubules *in vitro*. Acquisition was performed at high laser power to induce photobleaching of GFP. Single molecules of MAP7 used for quantification in Figure 1C are indicated with numbers. **(C)** Photobleaching time traces of individual GFP-MAP7 molecules. Bleaching molecules correspond to those indicated in Figure 1B.

the kinesin stalk can bind two MAP7 molecules at the same time. The logical consequence of this observation is to assume that MAP7 proteins are dimers as well. We tested this hypothesis by comparing fluorescence intensity of single GFP-MAP7 molecules to that of single GFP molecules. This technique was also used in **Chapter 2, 6 and 7**. Surprisingly, we found that GFP-MAP7 signals were as bright as that of monomeric GFP (Figure 1A). We next tested whether microtubule binding would force GFP-MAP7 to form dimers. We counted the number of bleaching steps of microtubule-bound GFP-MAP7 at high laser power and found that these molecules displayed one-step photobleaching, showing that these were behaving as monomers (Figure 1B, C). These experiments were performed at single molecule protein concentrations and it is therefore still possible that MAP7 can form weak dimers when they populate the microtubule lattice more densely. Nevertheless, these experimental data currently suggest that MAP7 monomers allosterically activate kinesin-1 dimers by binding to a single alpha helix of the kinesin stalk. It is therefore an interesting question how asymmetric binding of MAP7 would induce a downstream conformational change in the kinesin. Is one MAP7 molecule sufficient to alter the structure of the kinesin dimer or do two MAP7 monomers need to bind? Or is asymmetric binding of MAP7 actually involved in the first kinesin step by only changing the conformation of the leading motor domain? Such questions could be addressed in the future with structural biology techniques. The biochemical and *in vitro* reconstitution techniques described in this thesis could be employed to study domain swaps of kinesin-1 to understand the allosteric activation mechanism.

MAP7 behavior on the microtubule lattice

Until now, there is no comprehensive structural data available regarding any MAP7 proteins and their binding site on microtubules. It has been established that MAP7 binds microtubules tightly (Monroy et al., 2018)(**Chapter2**) and that MAP7 is capable of displacing tau from microtubules through competitive binding (Monroy et al., 2018). Interestingly, tau is a potent inhibitor of kinesin-1 because it competes with its motor domain's binding site (Ebneth et al., 1998; Hagiwara et al., 1994; Shigematsu et al., 2018). These data suggest that the MAP7 binding interface must overlap with that of tau. Furthermore, kinesin-3 motors are inhibited by tau and MAP7 (Monroy et al., 2018; Monroy et al., 2020). A mutated kinesin-1 motor domain containing the kinesin-3-specific K-loop also made this motor sensitive to MAP7 inhibition, showing that positioning of the kinesin-3 motor domain is blocked by MAP7 through this specific K-loop. Tau binds longitudinally along the crest of a microtubule protofilament (Kellogg et al., 2018), partially overlapping with the kinesin-1 binding site at the crest. To displace tau, MAP7 may bind at a similar longitudinal interface, but presumably deeper in the protofilament valley to not compete with the kinesin-1 motor domain. How the positively charged K-loop of kinesin-3 is blocked by MAP7 is not clear. The microtubule binding domain of MAP7 contains many charged amino acid residues which may repel the positive lysine charges of the kinesin-3 K-loop. Future efforts using Cryo-electron microscopy (Cryo-EM) combined with solid-state NMR and other structural and biophysical approaches will be needed to map out the binding of MAP7 proteins and understand their (non-)competitive behavior with motors and other MAPs.

Some first steps in getting structural understanding of MAP7 binding to microtubules was provided in **Chapter 5**. Here, we developed an efficient protocol to produce isotope-labeled tubulin from HeLa cells that can be polymerized for solid-state NMR studies on intact microtubules. The microtubule binding domain of MAP7 was used since it would strongly decorate the microtubule lattice. In these experiments, we observed that MAP7 rigidifies the C-terminal tails of both α- and β-tubulin. In addition, NMR experiments on free MAP7 indicated that its microtubule binding domain likely adopts an α-helical conformation, which fits with structure predictions (Masson and Kreis, 1993). Although tubulin tails exhibited less dynamic behavior in the presence of MAP7, it was not clear whether these tails are essential for binding of MAP7 to the microtubule lattice. To test this, we generated GMPCPP-stabilized microtubule seeds that were either untreated (control) or treated with subtilisin to remove all tubulin tails. The efficiency of this treatment was analyzed using Western blotting and SDS PAGE (Figure 2A). In addition, we visualized subtilisin-treated seeds by adding a low percentage of Alexa488-labeled tubulin; control seeds were visualized by immunofluorescence staining with an antibody specific for the EEY-motif present on the α-tubulin tail (Figure 2B, C). To assess binding preference to seeds with or without tubulin tails, we added full-length mCherry-MAP7D3, purified from E. coli, to a mix of both seed types (Figure 2D, E). Comparing mCherry fluorescence intensities on these seed types showed that MAP7D3 exhibited no preference for binding to microtubules with or without tubulin tails (Figure 2E, F). One can argue that this is because we used MAP7D3 instead of MAP7; this may be true since MAP7 binds microtubules more tightly than MAP7D3 **(Chapter 2)**. Another issue could be that we used GMPCPP (Figure 2) instead of Taxol **(Chapter 5)** to stabilize microtubules and that this caused a different effect on MAP7 binding and/or tubulin tails. Nevertheless, these data suggest that tubulin tails are not essential for MAP7 binding to microtubules. Instead, MAP7 affects the dynamics of the tubulin tails which exchange between bound and free states at a millisecond time scale **(Chapter 5)**. In contrast, the CKK domain of CAMSAP2 interacts at much faster time scales (nano to microsecond scale)**(Chapter 5)** and it was shown that removing tubulin tails affects CKK's affinity for microtubules (Atherton et al., 2017a). Therefore, measuring tubulin tail dynamics upon MAP binding is an interesting approach to study how MAPs interact with microtubules as many structural biology techniques, such as Cryo-EM, do not provide the ability to look at flexible protein regions such as tubulin tails.

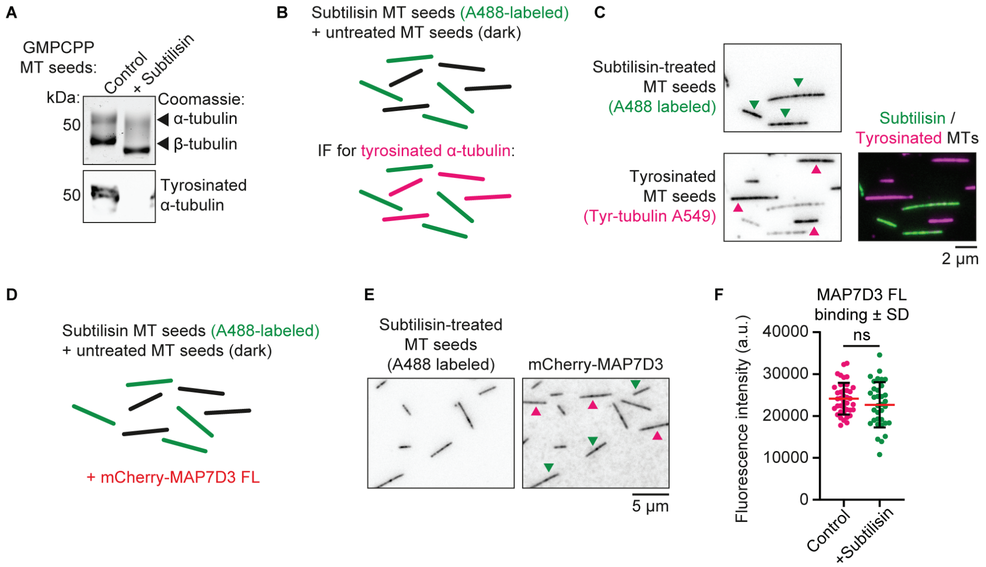

Figure 2 – MAP7 does not require tubulin tails for microtubule binding
(A) Analysis of control and subtilisin-treated GMPCPP-stabilized microtubule seeds. Molecular weight shifts of α- and β-tubulin were visualized on a Coomassie-stained gel (top). To separate the similar sized α- from β-tubulin a modified resolving gel was prepared at pH 9.8 using low-grade Sodium dodecyl sulfate (SDS). Western blot (bottom) shows the presence of α-tubulin tails using a monoclonal antibody specific for the C-terminal EEY motif of the α-tubulin tail. **(B)** Cartoon showing experimental setup of Figure 2C for a dual microtubule seed assays. Subtilisin-treated microtubule seeds are marked with a low percentage of A488-labeled tubulin (green). Regular microtubule seeds are kept unlabeled (black) but can be stained with an antibody specific for the C-terminal EEY motif of the α-tubulin C-terminus which recognizes tubulin tails (magenta). **(C)** Images of GMPCPP microtubule seeds imaged on a TIRF microscope. Subtilisin-treated microtubule seeds are visualized with a low percentage of A488-labeled tubulin. Untreated and unlabeled microtubule seeds are visualized using an on-stage immunofluorescence assay. Using flushing of the imaging chamber, the anchored seeds were treated with a primary antibody specific for the C-terminal EEY motif of α-tubulin for 2 min, followed by a wash step and incubation with an A594-conjugated secondary antibody for 2 min. **(D)** Cartoon showing experimental setup of Figure 2E for a dual microtubule seed assay. A488-labeled subtilisin-treated microtubule seeds (green) and unlabeled microtubule seeds (black) were incubated with bacterial purified mCherry-MAP7D3 and imaged on a TIRF microscope. **(E)** Images of GMPCPP microtubule seeds and mCherry-MAP7D3 imaged on a TIRF microscope. Left image shows A488-labeled subtilisin-treated microtubule seeds. Right image shows mCherry-MAP7D3 on untreated (magenta arrows) and subtilisin-treated microtubule seeds (green arrows). **(F)** Quantification of mCherry-MAP7D3 fluorescence intensity on two types of microtubule seeds corresponding to Figure 2E. n = 39 and 34 microtubule seeds. ns = not significant, (*t test*).

Altogether, the solid-state NMR approach described in this thesis has increased the toolbox for structural biologists to study the relationship and dynamics between microtubules and MAPs. Further NMR studies may involve isotope labeling of MAPs and kinesins, or even combined labelling of both the microtubule and cytoskeletal factor of interest. Such experiments may be especially interesting for MAP domains that exhibit unstructured regions or linkers that are impossible to crystallize or to be studied by electron microscopy. Here, MAP7 is an interesting candidate since we have shown that its unstructured regions possess microtubule affinity as well (**Chapter 2**). Mapping their interactions to the microtubule lattice and investigating whether and how phosphorylation might reduce binding may be an exciting new line of research to follow.

How MAP7 proteins may contribute to kinesin-1 selectivity

It has been well established that kinesin-1 has a preference for a subset of stable, long-lived microtubules. These tracks are often associated with post-translational modifications (PTMs) of microtubules, such as acetylation and detyrosination (Dunn et al., 2008; Reed et al., 2006). However, *in vitro* studies have shown that these PTMs alone do not solely explain kinesin-1 lattice preference (Kaul et al., 2014; Walter et al., 2012). In **Chapter 3**, we showed that the kinesin-1 KIF5B and the kinesin-3 KIF13B cooperate to transport exocytotic vesicles to the cell periphery. Their tasks are well separated because KIF5B is most active on perinuclear, long-lived microtubules and KIF13B takes the last steps towards the plus end along freshly polymerized microtubule lattices. MAP7 has a slow on-rate (Tymanskyj et al., 2018)(**Chapter 2)** and mainly populates perinuclear microtubules where KIF5B is most active. Removal of MAP7 and its homologs diminished KIF5B activity, and this suggests that crosstalk between this kinesin and MAPs might contribute to kinesin-1 selectivity. A novel view is that kinesin-1 stepping modifies the microtubule via longitudinal lattice expansion to create memory and promote binding of subsequent motors (Peet et al., 2018; Shima et al., 2018). Such a mechanism may generate a positive feedback loop that, in the absence of additional factors, can determine which microtubule will be favored by kinesin-1. The addition of a kinesin-1-activating factor, such as a MAP7 protein, can promote the generation of these preferred tracks if MAP7s show selectivity as well. Whether MAP7 proteins show selective binding to subsets of microtubules was not extensively studied in this thesis **(Chapter 2 and 3**). This was mainly due to the moderate quality of the antibodies used to detect endogenous proteins and the well-described effect that overexpression of a MAP results in whole-lattice decoration and microtubule bundling artefacts. Ultimately, endogenous tagging of each individual MAP7 family member may be an effective approach to determine their binding dynamics and preference for specific microtubule subsets.

One interesting hypothesis that has not been addressed before is whether the microtubule binding domain of MAP7 by itself, independent of kinesin-1 recruitment, can modify the microtubule lattice to promote kinesin-1 landing. In **Chapter 2**, we performed rescue experiments with the microtubule binding domain of all MAP7 proteins, but found that this was insufficient to rescue kinesin-1 activity in MAP7-depleted cells. These results suggest, that microtubule binding of MAP7 proteins does not play a major role in promoting kinesin-1 activity. Yet, it is not an improbable idea that an abundant MAP like MAP7 and its homologues could alter the physical properties of a microtubule, for example, via lattice expansion, that would favor kinesin-1 binding to some extent. This idea could be best tested with a minimal set of components using *in vitro* reconstitution assays. Such experiments should involve measuring microtubule lattice expansion when MAP7 is added to the system and measuring the additive effect on kinesin-1 motility in the presence of the microtubule-binding component of MAP7. For the latter, it is important to realize that the unstructured regions of MAP7 possess additional microtubule binding properties, which likely contribute to the tight association of these MAPs to microtubules (Tymanskyj et al., 2018)(**Chapter 2**). Whether the initial binding of MAP7 would also show selectivity or undergo a positive feedback process of promoting its own binding would need to be addressed experimentally.

Role of MAP7 proteins in microtubule organization

In **Chapter 2**, we briefly examined the effect of MAP7 depletion on microtubule density and growth rates in HeLa cells and found that these parameters were not affected. However, we did notice that the overall microtubule network appeared to be altered (**Chapter 2**, figure S1A). Whereas in control cells microtubules were strongly enriched in the perinuclear region, cells depleted of all MAP7 proteins lost this density and microtubules seemed to be more evenly distributed throughout the cell. It is important to note that the centrosome in HeLa cells is not a dominant factor in organizing microtubules (Jeffery et al., 2013; Lansbergen et al., 2006), but that this role is mainly fulfilled by the Golgi apparatus (Yang et al., 2017). At this organelle, CAMSAP2 decorates and stabilizes microtubule minus ends and these "caps" can be anchored at the Golgi through a protein complex of AKAP450 and myomegalin (Wu et al., 2016). We thus hypothesized that in the absence of MAP7 proteins this organization of non-centrosomal microtubules may be perturbed. To test this, we stained control and MAP7/MAP7D1/MAP7D3-depleted HeLa cells for CAMSAP2 and the Golgi marker GM130 and found that the Golgi-associated pool of CAMSAP2-decorated minus ends was diminished in cells lacking MAP7 proteins (Figure 3). CAMSAP2-stabilized microtubule minus ends did not disappear, but rather detached from the Golgi and were more randomly distributed in the cytoplasm. Interestingly, this phenotype was also observed when HeLa cells depleted of KIF5B, the only kinesin-1 isoform expressed in these cells (Figure 3).

On the one hand, this suggests that minus-end attachment to the Golgi is dependent on kinesin-1 activity. On the other hand, these data do not rule out that a stable complex of MAP7 with kinesin-1 is required to anchor these minus ends. One could think of several models on how this could work. First, kinesin-1 may be important for delivering Golgi-attached factors that are important for anchoring CAMSAP2-decorated minus ends. However, to our knowledge, none of these proteins have been shown to be a cargo of kinesin-1 and the microtubules are not in the correct orientation for kinesin-1 to reach the Golgi. Second,

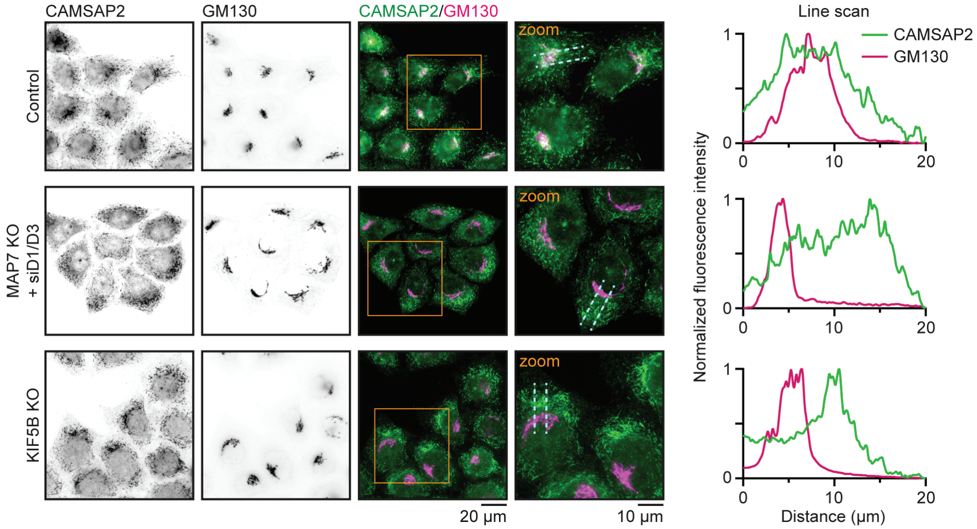

Figure 3 – CAMSAP2-decorated minus-ends detach from the Golgi in cells depleted of kinesin-1 or MAP7 proteins.
Immunofluorescence images of indicated HeLa cells stained for GM130 (cis-Golgi marker) and CAMSAP2. Areas used for zooms are indicated in the merged images (orange). The location of an 8 µm wide line scan (white dashed lines) is indicated in the zoom image. Lines scans on the right show normalized fluorescence intensity of GM130 and CAMSAP2 per condition.

kinesin-1 may be involved in microtubule sliding to deliver microtubule minus-ends to the Golgi. This sliding phenomenon may depend on the kinesin's microtubule-binding tail domain or on binding to MAP7 proteins bound to cargo microtubules. Third, MAP7 proteins may be required at the Golgi to anchor microtubules in a similar way as lattice-bound EB1/EB3 and CLASPs (Yang et al., 2017). Yet, this model does not explain the requirement of kinesin-1. Fourth, the latter mechanism might also involve kinesin-1 bound in a stable complex with MAP7 protein at the Golgi to support the anchorage of minus-ends.

To some extent, our data may provide some preliminary support for the fourth model. In **Chapter 4**, we sought to find additional binding partners of the MAP7 protein family and found some interaction candidates involved in microtubule anchoring and nucleation. MAP7D1 and MAP7D3, but not MAP7, showed binding to AKAP450. In addition, pull-downs of MAP7D1 and MAP7D3 contained some peptides that corresponded to CDK5RAP2, a protein shown to be involved in microtubule nucleation at both centrosomes and Golgi. Also, the pericentriolar material protein pericentrin was found to bind to these two MAPs, suggesting a role at the centrosome. Thus, perhaps in HeLa cells, a population of MAP7D1 and MAP7D3 might be involved in the organization of microtubules through an association with microtubule-nucleating scaffolds.

To check the involvement of kinesin-1, we designed deletion constructs containing the MAP7-binding stalk, C-terminal microtubule binding tail or a combination of both domains and overexpressed these in KIF5B-KO HeLa cells to analyze their localization (Fig-

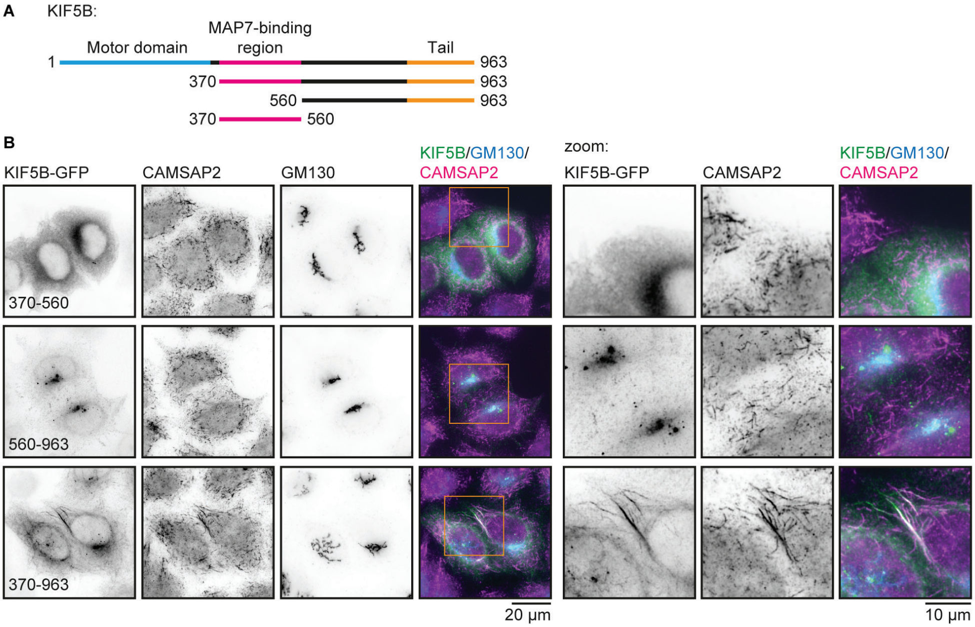

Figure 4 - A motorless kinesin-1 truncation is a MAP associating with CAMSAP2-decorated microtubule regions.
(A) KIF5B deletion constructs used in this figure. Indicated are the motor domain (blue), MAP7-binding region at the kinesin stalk (magenta) and tail domain (orange), which is involved in cargo binding but also contains a microtubule-binding region. **(B)** Immunofluorescence images of KIF5B KO HeLa cells overexpressing the indicated KIF5B deletion constructs. Cells were stained using antibodies against GM130 (cis-Golgi marker) and CAMSAP2. Zoomed areas (orange) are indicated in the merged image.

ure 4A). Instead of association with microtubules via MAP7 proteins, the MAP7-binding domain of KIF5B was present diffusely in the cytoplasm. The kinesin-1 tail did not show microtubule labelling either, but formed punctuated clusters displaying some overlap with the Golgi apparatus. We only observed microtubule binding when the MAP7-binding domain was combined with the kinesin tail (Figure 4B). Surprisingly, this construct showed a preference for CAMSAP2-decorated minus ends, although CAMSAP2-bound microtubule stretches seemed to be increased in length by binding of this construct. Nevertheless, none of these KIF5B deletion constructs was capable of rescuing the minus end detachment phenotype caused by kinesin-1 depletion. These data might suggest that MAP7 family proteins cooperate with kinesin-1 to anchor CAMSAP2-stabilized minus ends at the Golgi. Future experiments should further involve the use of KIF5B rescue constructs which allow dissecting the minimal components and molecular activities involved in this process. Recent advances in optogenetic and drug-inducible kinesin tools greatly improved our toolbox to study transport and microtubule organization in cells. It would be interesting to assess the involvement of MAP7 binding domain and the microtubule binding kinesin tail by mutating these domains of kinesin-1. To elucidate whether a Golgi-associated pool of MAP7 proteins or kinesin-1 exists and contributes to microtubule organization, it would be beneficial to perform endogenous tagging of these proteins with fluorescent markers.

Alternative roles of MAP7 family proteins

So far, most work on MAP7 family proteins has been focused on their common and conserved properties: microtubule association and activation of kinesin-1. However, the domains involved in these two functions comprise less than half of the amino acid sequence of each MAP. The remaining regions are predicted to be unstructured and there is little homology between family members. Consequently, different family members may have distinct binding partners and have various alternative roles in the cell that are kinesin independent.

In **Chapter 4**, we performed a pull down assay combined with mass spectrometry analysis to identify novel binding partners of each MAP7 family member. Next to the kinesin-1 binding shared by all MAP7 family members, this mass spectrometry screen also revealed KIDINS220 (Kinase D-interacting substrate of 220 kDa, also known as ARMS) and CKAP4 (Cytoskeleton-associated protein 4, also known as CLIMP-63) to interact with all four MAP7 proteins. KIDINS220 is a transmembrane scaffold protein found in various tissue types, but predominantly in neurons (Iglesias et al., 2000). Its function is not well understood, but connections to the microtubule cytoskeleton have been described through binding to kinesin-1 and several MAPs, like MAP1b and 1b, MAP2 and two stathmin family members (Bracale et al., 2007; Higuero et al., 2010). MAP7 proteins may provide additional attachments for KIDINS220 to the microtubule network. A similar mechanism may also apply for CKAP4. This transmembrane protein is mostly found in the endoplasmic reticulum and can directly bind microtubules depending on its phosphorylation status (Klopfenstein et al., 1998; Sandoz and van der Goot, 2015; Vedrenne et al., 2005).

Furthermore, CEP55, a mitotic protein that is essential for successful completion of cytokinesis (Fabbro et al., 2005; Martinez-Garay et al., 2006; Zhao et al., 2006), was found as one of the top hits for both MAP7D1 and MAP7D2. Although a role for MAP7 proteins during cytokinesis has not been described, it cannot be ruled out that a cytokinetic function of one or more MAP7 proteins contributes to our failure to generate triple MAP7 knockout cell lines, as discussed **Chapter 2**. In general, what the mitotic contribution of MAP7 family proteins is and whether these MAPs act redundantly is an interesting direction for future work.

The most prominent protein identified in the mass spectrometry experiment was clathrin, which was only found in the pull down with the brain expressed MAP7D2. We validated this interaction and found that MAP7D2 contains a conserved clathrin box motif that is able to recruit clathrin to microtubules. We hypothesized that this recruitment is required for the entry and transport of clathrin into axons and that this process might depend on kinesin-1. More experiments involving neuronal cell cultures are required to prove this idea. To mechanistically dissect the process, future work may include *in vitro* reconstitution experiments with dynamic microtubules, purified MAP7D2, clathrin and kinesin. Such an approach could enable us, by using minimal components, to determine what is normally happening in the dense and crowded environment of the axon. Since tagging the clathrin heavy chain is likely affecting its functionality, this is not common practice in the field. Therefore, we initiated the development of an alternative purification strategy to obtain fluorescently tagged clathrin triskelia. In **Chapter 4**, we generated a polyclonal cell line where the clathrin light chain subunit was endogenously tagged with a GFP-coupled Streptag, and these cells could be used in future to efficiently purify GFP-tagged clathrin. With these *in vitro* experiments, we might be able to address the question whether MAP7D2 can indeed recruit clathrin to microtubules *in vitro*. Next, it would be interesting to investigate whether the direct interaction between kinesin-1 and clathrin is sufficient for kinesin-based transport of triskelia. MAP7D2 could act as a loading factor for clathrin-kinesin-1 complexes as it can concentrate clathrin on microtubules. From here, MAP7D2 could transfer clathrin onto moving kinesin-1 motors to drive its directed transport further down the axon. Interestingly, apart from clathrin, our mass spectrometry experiments also identified several neurofilament polypeptides as interaction candidates of MAP7D2. It is known that neurofilaments can interact and be transported by kinesin-1 (Uchida et al., 2009; Wang and Brown, 2010; Xia et al., 2003). Therefore, MAP7D2 might also be involved in axonal transport of neurofilaments, perhaps in similar ways as we have mechanistically proposed for clathrin. Alternatively, neurofilaments may also interact with MAP7D2 to form an axonal scaffold that could play a role in organizing stable microtubule arrays.

Dissecting MKLP2 activity and regulation

The *in vitro* reconstitution techniques applied in **Chapter 2** to study the relationship between kinesin-1 and MAP7 proteins were used in this thesis to study the mitotic kinesin-6 MKLP2. It is well established that MKLP2 is required for the translocation of the Chromosomal Passenger Complexes (CPC) from chromatin and centromeres to the spindle midzone and equatorial cortex during the transition from metaphase to anaphase (Kitagawa and Lee, 2015). Yet, the mechanism was debated and it was also unclear whether MKLP2 motors were actually motile (Atherton et al., 2017b). In **Chapter 6**, we demonstrated that purified MKLP2 is a slow, but motile kinesin when added to *in vitro* polymerized microtubules. Interestingly, addition of purified CPC enhances MKLP2 processivity at the expense of its velocity. We reasoned that the latter is due to drag exerted by CPC due to its microtubule affinity. This phenomenon was also observed in **Chapter 2** where we measured reduced kinesin-1 velocities when the motor was bound to the MAP7D3 C-terminus, a domain that also possesses some weak microtubule affinity (Yadav et al., 2014). We assume that these velocity reductions caused by drag may be observed for many other kinesin-related processes when a cargo or co-factor displays some weak affinity for the microtubule track.

In cells, we showed that MKLP2 and CPC display directional motility towards the spindle midzone and equatorial cortex. CPC localization at these sites required MKLP2 motor activity because mutating the motor domain or applying an MLKP2-specific drug reduced CPC translocation towards these sites. Although we demonstrated the transporting role of MKLP2 both *in vitro* as in cells, we do not yet understand how this process is

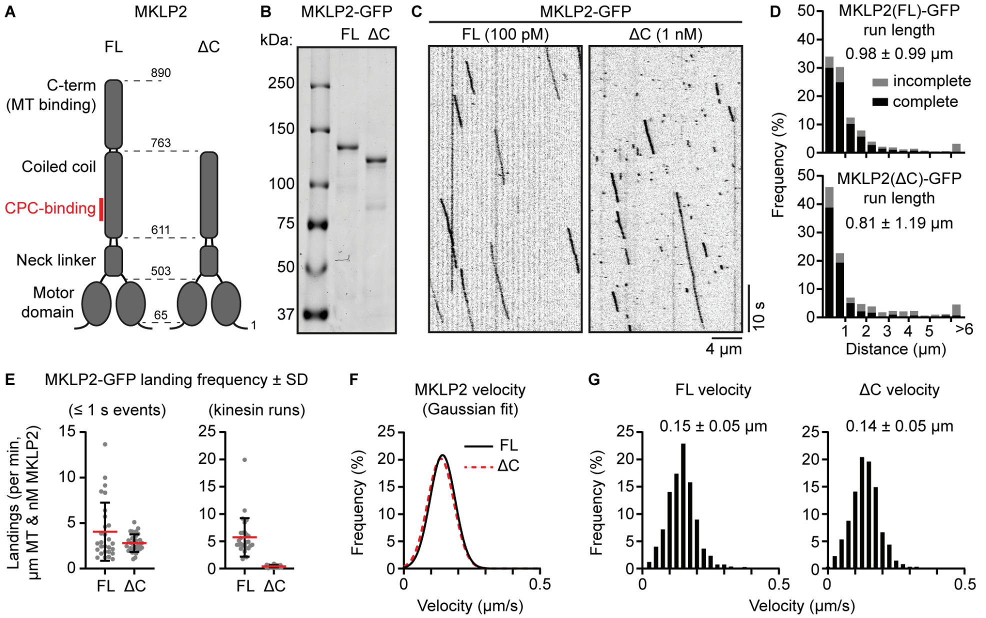

Figure 5 – The MKLP2 C-terminus is important to initiate processive movement
(A) Overview of full-length (FL) MKLP2 and a deletion mutant lacking the C-terminus (ΔC). Protein domains, corresponding amino acid positions and CPC-binding site (red) are indicated. **(B)** Purified MKLP2(-FL)-GFP and MKLP2(ΔC)-GFP proteins analyzed by SDS-PAGE. **(C)** Kymographs of MKLP2(FL)-GFP and MKLP2(ΔC)-GFP proteins on dynamic microtubules. **(D)** Histograms of run lengths of indicated MKLP2-GFP kinesins. Complete tracks: both landing and dissociation of the motor was observed. Incomplete tracks: tracks that exceeded the 90 s acquisition time or partially took place outside the acquisition area. Average run length with corresponding standard deviation of complete tracks is indicated. n = 1070 kinesins (FL) and 617 kinesins (ΔC) from three independent experiments. **(E)** Quantification of MKLP2-GFP landing frequencies per microtubule and corrected for microtubule length, time of acquisition, and kinesin concentration. n = 28 and 32 microtubules from three independent experiments. **(F-G)** Gaussian fits of MKLP2-GFP velocities (G) derived from velocity histograms (F). Average velocity with the corresponding standard deviation is indicated at each histograms. n = 1070 kinesins (FL) and 617 kinesins (ΔC) from three independent experiments

regulated. CPC and MKLP2 both undergo phosphorylation by Cdk1 that promotes histone binding of CPC and prevents MKLP2 from binding to microtubules and targeting to chromosomes before anaphase (Kitagawa and Lee, 2015). Dephosphorylation of CPC promotes the release from chromosomes (van der Horst and Lens, 2014); MKLP2 dephosphorylation promotes CPC- and microtubule binding. A recent study showed that the C-terminal domain of MKLP2 serves as a microtubule binding domain but is also capable of binding the motor domain when it is in an unphosphorylated state (Kitagawa 2014). The latter provides a mechanism where CPC binding to the MKLP2 stalk may release a presumed auto-inhibited state of the kinesin. Such a mechanism, where the kinesin can only move long distances when it is cargo-bound, may explain how the CPC translocation can be timed and orchestrated. Indeed, the presence of CPC increases MKLP2 ATPase activity (Serena et al., 2020) and makes MKLP2 movement on microtubules hyper-processive **(Chapter 6)**. We attempted to understand the role of the MKLP2 C-terminus by comparing the *in vitro* motility of full-length MKLP2-GFP with the ΔC mutant (Figure 5A, B). On the one hand, MKLP2-ΔC may exhibit impaired motility because it lacks an additional microtubule binding domain that might be required for landing on the microtubule lattice. On the other hand, MKLP2-ΔC may also lack auto-inhibition as the C-terminus that can bind and perhaps block the motor domain is absent. In our experiment, MKLP2-FL displayed more frequent landing on microtubules and had a slightly longer run length (Figure 5C-E); yet, the velocities of these motors were identical (Figure 5F, G). The most striking observation was that MKLP2-ΔC exhibited a high degree of short (< 1 s) engagements with microtubules that did not result in processive movement (Figure 5E). We reasoned that the C-terminal microtubule-binding domain of MKLP2 promotes the transitioning of the motor to a motile state after landing on a microtubule. One problem with these experiments is that we lacked proper control of the phosphorylation status of these MKLP2 motors. Therefore, it is not clear whether they still exhibit the described intra-molecular association between motor and tail domains and to what extend phosphorylated residues were inhibiting microtubule binding. It is interesting to further explore MKLP2 auto-inhibition and its potential release by CPC *in vitro* by comparing phosphorylated and unphosphorylated MKLP2 motors. Alternatively, deletion mutants such as MKLP2-ΔC and a phophomimetic or phosphomutant MKLP2 may be used as a complementary strategy to understand the regulatory interplay between cargo binding, phosphorylation and auto-inhibition to temporally regulate MKLP2 activity during mitosis. Our work also raises questions on how the other two kinesin-6 motors (MKLP1/KIF23 and MPP-1/KIF20B) behave on microtubules and how similar they are to MKLP2 in terms of their motility.

Shaping microtubule networks in immune cells by a single kinesin

In **Chapter 7**, we focused on T cells and the microtubule growth regulator KIF21B, a member of the kinesin-4 family. Kinesin-4 motors are well-known regulators of microtubule dynamics in various processes and cell types. KIF4 is involved in the regulation of the spindle midzone and controls the length of PRC1-stabilized anti-parallel microtubule overlaps (Bieling et al., 2010; Hannabuss et al., 2019; Kurasawa et al., 2004). The paralogue pair KIF7 and KIF27 are (near-)static motors (Yue et al., 2018), and KIF7 motors were shown to localize at cilia tips where they are involved in the control of axoneme length (He et al., 2014). KIF21A, which shows high homology with KIF21B, localizes with KANK proteins at cortical microtubule stabilizing complexes (CMSC), where it limits microtubule growth (Noordstra and Akhmanova, 2017; van der Vaart et al., 2013). In neurons, KIF21A controls microtubule dynamics at the axon growth cone, a process important for proper axon guidance (Cheng et al., 2014). KIF21B was described to have various functions in neurons as well, including a role in transporting several neuronal receptors (Ghiretti et al., 2016; Gromova et al., 2018; Labonte et al., 2014). However, there has not been a unified view on how KIF21B may regulate microtubule dynamics (Muhia et al., 2016; van Riel et al., 2017). Previous *in vitro* work has indicated that KIF21B can walk towards the plus end, where it could pause microtubule growth. When the number of KIF21B molecules was high, prolonged pauses ensued, but when only one or two KIF21B motors were present at the tip, microtubule pausing ultimately resulted in a catastrophe event, indicating that a few KIF21B molecules can restrict microtubule growth (van Riel et al., 2017). Since KIF21B is mainly expressed in the brain and the immune system (Marszalek et al., 1999), we decided to investigate its role in Jurkat T cells. We found that KIF21B can indeed induce microtubule plus-end pausing in cells. Yet, since the expression of KIF21B is not high in these cells, the net result of its activity is to induce catastrophes and thus restrict microtubule growth in these cells. This regulation is important in T cells, as overly long microtubules impaired the polarization of the centrosome and the whole microtubule network when T cells were activated.

Centrosome polarization in T cells is rapid, and we only studied the mechanistic aspect of the process in the first few minutes after T-cell activation. Other immune cells such as Natural Killer cells, B cells and Dendritic cells also form immunological synapses, but these structures are less well studied compared to those of T cells. Whether KIF21B also plays a role in regulating microtubule growth in other immune cell types is not clear. In immune cells, microtubules and their organizing centers also play a role during cell migration. For example, dendritic cells use amoeboid migration mode to navigate through complex 3D surroundings (Renkawitz et al., 2019). Several cell protrusions scan the environment for a migratory path. Protrusions leading to a “dead end” need to be retracted by the cell, which was recently shown to involve microtubule depolymerization at these protrusions (Kopf et al., 2020). No microtubule plus-end regulators were identified in this study; whether KIF21B might be involved in controlling microtubule growth in these dendritic cell protrusions in a spatially-regulated manner is an interesting question for future studies.

Although several genetics studies have pointed towards a role of the *KIF21B* gene in autoimmune-related syndromes (Goris et al., 2010; International Multiple Sclerosis Genetics, 2010; Liu et al., 2013; Yang et al., 2015), it is not clear what the long-term consequences are for T cells that have reduced polarization efficiencies. Earlier studies have shown that a *Kif21b* knockout mouse is viable and that these animals only showed impaired learning capabilities and reduced social behavior, which all point towards a role in neurons (Morikawa et al., 2018; Muhia et al., 2016). The simplest explanation for why immune-related KIF21B effects were not found is that these studies simply did not focus on immunological phenotypes. Problems related to the immune system may only surface when these animals are challenged, for example, with an infection, inflammation or during tumor development. However, our data also indicated that a reasonable proportion of KIF21B knockout cells are still capable of polarizing their centrosome, showing that it is highly unlikely that the absence of KIF21B would severely compromise the whole immune system. Experiments where KIF21B-depleted primary T cells, from mice or human, are challenged in their immune response may pave the way to understand why KIF21B is genetically linked to many autoimmune-related conditions. The use of primary T cells is also interesting from a technical perspective: since these cells are much smaller than Jurkat T cells (Lasserre et al., 2010), they are an exciting cell type to map and trace microtubules completely from nucleation sites to plus ends. In addition, since these cells only have a sparse network and only anchor a few microtubules at the centrosome, these cells are very well suited for super-resolution and electron microscopy studies to investigate microtubule anchorage in detail (Bowler et al., 2019; Yang et al., 2018).

Another aspect that was not addressed in **Chapter 7** is whether KIF21B may be involved in intracellular transport or signaling pathways. Although rescue experiments involving a microtubule targeting drug demonstrated that such a secondary function does not play a role in centrosome polarization, we cannot exclude that KIF21B does transport some cargo in T cells. Furthermore, a complementary role of the related kinesin-4 motor KIF21A has not been addressed in these cells. KIF21A is expressed in T cells and Natural Killer cells (Protein Atlas) and may thus contribute to the regulation of microtubule dynamics. If it does, this presumably happens at the cell cortex at the immunological synapse. Therefore, it may be of interest to perform immunofluorescence experiments on KIF21A and its known CMSC linking partners, such as KANK proteins, to analyze their localization in T cells. If their expression would be confirmed, the next step would be to assess whether KIF21A depletion affects centrosome polarization or alters the morphology of the microtubule network. Interestingly, many KIF21B-paused microtubules remained undynamic even after the kinesin detached from the plus end. These events might involve KIF21A, as KIF21B-stabilized microtubule ends may get captured by cortical KIF21A to ensure a prolonged pausing event.

In T cells, KIF21B induces microtubule pausing followed by catastrophe, and such events appear to often be triggered by a single KIF21B molecule (van Riel et al., 2017)**(Chapter 7)**. It was shown that several microtubule binding domains in this kinesin are involved in the regulation of this activity of the motor, including a part of the stalk and the WD40-containing KIF21B tail, which has a binding preference for GTP-type lattices (van Riel et al., 2017). Microtubule pausing is an interesting type of an event as it requires both growth perturbation and stabilization of the plus end. How KIF21B structurally alters the plus end is not clear; it may involve blocking incoming tubulin dimers from binding to the tip of the microtubule polymer. Previous work has shown that blocking of a single protofilament can be sufficient to perturb microtubule polymerization (Doodhi et al., 2016). However, protofilament blocking cannot explain how a single kinesin can stabilize the plus end and keep it in a paused state for several seconds, preventing it from switching to depolymerization. Binding and stabilization of several protofilaments on one side of the tubule may be sufficient to prevent catastrophe initiation (Sharma et al., 2016). It is possible the C-terminus of KIF21B switches into a conformation where the WD40 domains, and perhaps parts of the stalk are spatially separated to embrace multiple protofilaments of the microtubule. The ability of KIF21B to pause microtubule plus ends might be dependent on protofilament number. A 13-protofilament tubule might be easier to stabilize by a single motor than a 14- or 15-protofilament tubule. Therefore, it would be interesting to further study KIF21B on different microtubule substrates *in vitro*. Ultimately, single molecules of KIF21B on paused microtubules ends would need to be studied by electron tomography to fully understand how different microtubule-interacting domains of the kinesin can cap and stabilize a microtubule to maintain a paused state.

Concluding remarks

In this thesis, we have combined *in vitro* reconstitution experiments with biochemical and cellular assays to increase our understanding of several kinesin motors, MAPs and the relationship between these cytoskeletal factors. We showed how MAPs can regulate and activate kinesin motors and what this means for the transport of exocytotic vesicles. In addition, we obtained novel insights in the function of a mitotic and a T-cell specific kinesin and tried to link their behavior in cells to their activity observed in an *in vitro* reconstituted environment. Collectively, these studies provide conceptual frameworks that may be used in future studies of other cytoskeletal factors.

References

Atherton, J., K. Jiang, M.M. Stangier, Y. Luo, S. Hua, K. Houben, J.J.E. van Hooff, A.P. Joseph, G. Scarabelli, B.J. Grant, A.J. Roberts, M. Topf, M.O. Steinmetz, M. Baldus, C.A. Moores, and A. Akhmanova. 2017a. A structural model for microtubule minus-end recognition and protection by CAMSAP proteins. Nat Struct Mol Biol. 24:931-943.

Atherton, J., I.M. Yu, A. Cook, J.M. Muretta, A. Joseph, J. Major, Y. Sourigues, J. Clause, M. Topf, S.S. Rosenfeld, A. Houdusse, and C.A. Moores. 2017b. The divergent mitotic kinesin MKLP2 exhibits atypical structure and mechanochemistry. Elife. 6.

Barlan, K., W. Lu, and V.I. Gelfand. 2013. The microtubule-binding protein ensconsin is an essential cofactor of kinesin-1. Curr Biol. 23:317-322.

Bieling, P., I.A. Telley, and T. Surrey. 2010. A minimal midzone protein module controls formation and length of antiparallel microtubule overlaps. Cell. 142:420-432.

Blasius, T.L., D. Cai, G.T. Jih, C.P. Toret, and K.J. Verhey. 2007. Two binding partners cooperate to activate the molecular motor Kinesin-1. J Cell Biol. 176:11-17.

Bowler, M., D. Kong, S. Sun, R. Nanjundappa, L. Evans, V. Farmer, A. Holland, M.R. Mahjoub, H. Sui, and J. Loncarek. 2019. High-resolution characterization of centriole distal appendage morphology and dynamics by correlative STORM and electron microscopy. Nat Commun. 10:993.

Bracale, A., F. Cesca, V.E. Neubrand, T.P. Newsome, M. Way, and G. Schiavo. 2007. Kidins220/ARMS is transported by a kinesin-1-based mechanism likely to be involved in neuronal differentiation. Mol Biol Cell. 18:142-152.

Cai, D., A.D. Hoppe, J.A. Swanson, and K.J. Verhey. 2007. Kinesin-1 structural organization and conformational changes revealed by FRET stoichiometry in live cells. J Cell Biol. 176:51-63.

Cheng, L., J. Desai, C.J. Miranda, J.S. Duncan, W. Qiu, A.A. Nugent, A.L. Kolpak, C.C. Wu, E. Drokhlyansky, M.M. Delisle, W.M. Chan, Y. Wei, F. Propst, S.L. Reck-Peterson, B. Fritzsch, and E.C. Engle. 2014. Human CFEOM1 mutations attenuate KIF21A autoinhibition and cause oculomotor axon stalling. Neuron. 82:334-349.

Doodhi, H., A.E. Prota, R. Rodriguez-Garcia, H. Xiao, D.W. Custar, K. Bargsten, E.A. Katrukha, M. Hilbert, S. Hua, K. Jiang, I. Grigoriev, C.H. Yang, D. Cox, S.B. Horwitz, L.C. Kapitein, A. Akhmanova, and M.O. Steinmetz. 2016. Termination of Protofilament Elongation by Eribulin Induces Lattice Defects that Promote Microtubule Catastrophes. Curr Biol. 26:1713-1721.

Dunn, S., E.E. Morrison, T.B. Liverpool, C. Molina-Paris, R.A. Cross, M.C. Alonso, and M. Peckham. 2008. Differential trafficking of Kif5c on tyrosinated and detyrosinated microtubules in live cells. J Cell Sci. 121:1085-1095.

Ebneth, A., R. Godemann, K. Stamer, S. Illenberger, B. Trinczek, and E. Mandelkow. 1998. Overexpression of tau protein inhibits kinesin-dependent trafficking of vesicles, mitochondria, and endoplasmic reticulum: implications for Alzheimer's disease. J Cell Biol. 143:777-794.

Fabbro, M., B.B. Zhou, M. Takahashi, B. Sarcevic, P. Lal, M.E. Graham, B.G. Gabrielli, P.J. Robinson, E.A. Nigg, Y. Ono, and K.K. Khanna. 2005. Cdk1/Erk2- and Plk1-dependent phosphorylation of a centrosome protein, Cep55, is required for its recruitment to midbody and cytokinesis. Dev Cell. 9:477-488.

Ghiretti, A.E., E. Thies, M.K. Tokito, T. Lin, E.M. Ostap, M. Kneussel, and E.L.F. Holzbaur. 2016. Activity-Dependent Regulation of Distinct Transport and Cytoskeletal Remodeling Functions of the Dendritic Kinesin KIF21B. Neuron. 92:857-872.

Goris, A., S. Boonen, B. D'Hooghe M, and B. Dubois. 2010. Replication of KIF21B as a susceptibility locus for multiple sclerosis. J Med Genet. 47:775-776.

Gromova, K.V., M. Muhia, N. Rothammer, C.E. Gee, E. Thies, I. Schaefer, S. Kress, M.W. Kilimann, O. Shevchuk, T.G. Oertner, and M. Kneussel. 2018. Neurobeachin and the Kinesin KIF21B Are Critical for Endocytic Recycling of NMDA Receptors and Regulate Social Behavior. Cell Rep. 23:2705-2717.

Hagiwara, H., H. Yorifuji, R. Sato-Yoshitake, and N. Hirokawa. 1994. Competition between motor molecules (kinesin and cytoplasmic dynein) and fibrous microtubule-associated proteins in binding to microtubules. J Biol Chem. 269:3581-3589.

Hannabuss, J., M. Lera-Ramirez, N.I. Cade, F.J. Fourniol, F. Nedelec, and T. Surrey. 2019. Self-Organization of Minimal Anaphase Spindle Midzone Bundles. Curr Biol. 29:2120-2130 e2127.

He, M., R. Subramanian, F. Bangs, T. Omelchenko, K.F. Liem, Jr., T.M. Kapoor, and K.V. Anderson. 2014. The kinesin-4 protein Kif7 regulates mammalian Hedgehog signalling by organizing the cilium tip compartment. Nat Cell Biol. 16:663-672.

Higuero, A.M., L. Sanchez-Ruiloba, L.E. Doglio, F. Portillo, J. Abad-Rodriguez, C.G. Dotti, and T. Iglesias. 2010. Kidins220/ARMS modulates the activity of microtubule-regulating proteins and controls neuronal polarity and development. J Biol Chem. 285:1343-1357.

Iglesias, T., N. Cabrera-Poch, M.P. Mitchell, T.J. Naven, E. Rozengurt, and G. Schiavo. 2000. Identification and cloning of Kidins220, a novel neuronal substrate of protein kinase D. J Biol Chem. 275:40048-40056.

International Multiple Sclerosis Genetics, C. 2010. Comprehensive follow-up of the first genome-wide association study of multiple sclerosis identifies KIF21B and TMEM39A as susceptibility loci. Hum Mol Genet. 19:953-962.

Jeffery, J.M., I. Grigoriev, I. Poser, A. van der Horst, N. Hamilton, N. Waterhouse, J. Bleier, V.N. Subramaniam, I.V. Maly, A. Akhmanova, and K.K. Khanna. 2013. Centrobin regulates centrosome function in interphase cells by limiting pericentriolar matrix recruitment. Cell Cycle. 12:899-906.

Kaul, N., V. Soppina, and K.J. Verhey. 2014. Effects of alpha-tubulin K40 acetylation and detyrosination on kinesin-1 motility in a purified system. Biophys J. 106:2636-2643.

Kellogg, E.H., N.M.A. Hejab, S. Poepsel, K.H. Downing, F. DiMaio, and E. Nogales. 2018. Near-atomic model of microtubule-tau interactions. Science. 360:1242-1246.

Kitagawa, M., and S.H. Lee. 2015. The chromosomal passenger complex (CPC) as a key orchestrator of orderly mitotic exit and cytokinesis. Front Cell Dev Biol. 3:14.

Klopfenstein, D.R., F. Kappeler, and H.P. Hauri. 1998. A novel direct interaction of endoplasmic reticulum with microtubules. EMBO J. 17:6168-6177.

Kopf, A., J. Renkawitz, R. Hauschild, I. Girkontaite, K. Tedford, J. Merrin, O. Thorn-Seshold, D. Trauner, H. Hacker, K.D. Fischer, E. Kiermaier, and M. Sixt. 2020. Microtubules control cellular shape and coherence in amoeboid migrating cells. J Cell Biol. 219.

Kurasawa, Y., W.C. Earnshaw, Y. Mochizuki, N. Dohmae, and K. Todokoro. 2004. Essential roles of KIF4 and its binding partner PRC1 in organized central spindle midzone formation. EMBO J. 23:3237-3248.

Labonte, D., E. Thies, and M. Kneussel. 2014. The kinesin KIF21B participates in the cell surface delivery of gamma2 subunit-containing GABAA receptors. Eur J Cell Biol. 93:338-346.

Lansbergen, G., I. Grigoriev, Y. Mimori-Kiyosue, T. Ohtsuka, S. Higa, I. Kitajima, J. Demmers, N. Galjart, A.B. Houtsmuller, F. Grosveld, and A. Akhmanova. 2006. CLASPs attach microtubule plus ends to the cell cortex through a complex with LL5beta. Dev Cell. 11:21-32.

Lasserre, R., S. Charrin, C. Cuche, A. Danckaert, M.I. Thoulouze, F. de Chaumont, T. Duong, N. Perrault, N. Varin-Blank, J.C. Olivo-Marin, S. Etienne-Manneville, M. Arpin, V. Di Bartolo, and A. Alcover. 2010. Ezrin tunes T-cell activation by controlling Dlg1 and microtubule positioning at the immunological synapse. EMBO J. 29:2301-2314.

Liu, Y., H. Zhang, J. Li, H. Zhao, Q. Xin, S. Shan, J. Dang, X. Bian, and Q. Liu. 2013. Association of common variants in KIF21B and ankylosing spondylitis in a Chinese Han population: a replication study. Immunogenetics. 65:835-839.

Marszalek, J.R., J.A. Weiner, S.J. Farlow, J. Chun, and L.S. Goldstein. 1999. Novel dendritic kinesin sorting identified by different process targeting of two related kinesins: KIF21A and KIF21B. J Cell Biol. 145:469-479.

Martinez-Garay, I., A. Rustom, H.H. Gerdes, and K. Kutsche. 2006. The novel centrosomal associated protein CEP55 is present in the spindle midzone and the midbody. Genomics. 87:243-253.

Masson, D., and T.E. Kreis. 1993. Identification and molecular characterization of E-MAP-115, a novel microtubule-associated protein predominantly expressed in epithelial cells. J Cell Biol. 123:357-371.

Metivier, M., B.Y. Monroy, E. Gallaud, R. Caous, A. Pascal, L. Richard-Parpaillon, A. Guichet, K.M. Ori-McKenney, and R. Giet. 2019. Dual control of Kinesin-1 recruitment to microtubules by Ensconsin in Drosophila neuroblasts and oocytes. Development. 146.

Monroy, B.Y., D.L. Sawyer, B.E. Ackermann, M.M. Borden, T.C. Tan, and K.M. Ori-McKenney. 2018. Competition between microtubule-associated proteins directs motor transport. Nat Commun. 9:1487.

Monroy, B.Y., T.C. Tan, J.M. Oclaman, J.S. Han, S. Simo, S. Niwa, D.W. Nowakowski, R.J. McKenney, and K.M. Ori-McKenney. 2020. A Combinatorial MAP Code Dictates Polarized Microtubule Transport. Dev Cell. 53:60-72 e64.

Morikawa, M., Y. Tanaka, H.S. Cho, M. Yoshihara, and N. Hirokawa. 2018. The Molecular Motor KIF21B Mediates Synaptic Plasticity and Fear Extinction by Terminating Rac1 Activation. Cell Rep. 23:3864-3877.

Muhia, M., E. Thies, D. Labonte, A.E. Ghiretti, K.V. Gromova, F. Xompero, C. Lappe-Siefke, I. Hermans-Borgmeyer, D. Kuhl, M. Schweizer, O. Ohana, J.R. Schwarz, E.L.F. Holzbaur, and M. Kneussel. 2016. The Kinesin KIF21B Regulates Microtubule Dynamics and Is Essential for Neuronal Morphology, Synapse Function, and Learning and Memory. Cell Rep. 15:968-977.

Noordstra, I., and A. Akhmanova. 2017. Linking cortical microtubule attachment and exocytosis. F1000Res. 6:469.

Peet, D.R., N.J. Burroughs, and R.A. Cross. 2018. Kinesin expands and stabilizes the GDP-microtubule lattice. Nat Nanotechnol. 13:386-391.

Reed, N.A., D. Cai, T.L. Blasius, G.T. Jih, E. Meyhofer, J. Gaertig, and K.J. Verhey. 2006. Microtubule acetylation promotes kinesin-1 binding and transport. Curr Biol. 16:2166-2172.

Renkawitz, J., A. Kopf, J. Stopp, I. de Vries, M.K. Driscoll, J. Merrin, R. Hauschild, E.S. Welf, G. Danuser, R. Fiolka, and M. Sixt. 2019. Nuclear positioning facilitates amoeboid migration along the path of least resistance. Nature. 568:546-550.

Sandoz, P.A., and F.G. van der Goot. 2015. How many lives does CLIMP-63 have? Biochem Soc Trans. 43:222-228.

Serena, M., R.N. Bastos, P.R. Elliott, and F.A. Barr. 2020. Molecular basis of MKLP2-dependent Aurora B transport from chromatin to the anaphase central spindle. J Cell Biol. 219.

Sharma, A., A. Aher, N.J. Dynes, D. Frey, E.A. Katrukha, R. Jaussi, I. Grigoriev, M. Croisier, R.A. Kammerer, A. Akhmanova, P. Gonczy, and M.O. Steinmetz. 2016. Centriolar CPAP/SAS-4 Imparts Slow Processive Microtubule Growth. Dev Cell. 37:362-376.

Shigematsu, H., T. Imasaki, C. Doki, T. Sumi, M. Aoki, T. Uchikubo-Kamo, A. Sakamoto, K. Tokuraku, M. Shirouzu, and R. Nitta. 2018. Structural insight into microtubule stabilization and kinesin inhibition by Tau family MAPs. J Cell Biol. 217:4155-4163.

Shima, T., M. Morikawa, J. Kaneshiro, T. Kambara, S. Kamimura, T. Yagi, H. Iwamoto, S. Uemura, H. Shigematsu, M. Shirouzu, T. Ichimura, T.M. Watanabe, R. Nitta, Y. Okada, and N. Hirokawa. 2018. Kinesin-binding-triggered conformation switching of microtubules contributes to polarized transport. J Cell Biol. 217:4164-4183.

Sung, H.H., I.A. Telley, P. Papadaki, A. Ephrussi, T. Surrey, and P. Rorth. 2008. Drosophila ensconsin promotes productive recruitment of Kinesin-1 to microtubules. Dev Cell. 15:866-876.

Tymanskyj, S.R., B.H. Yang, K.J. Verhey, and L. Ma. 2018. MAP7 regulates axon morphogenesis by recruiting kinesin-1 to microtubules and modulating organelle transport. Elife. 7.

Uchida, A., N.H. Alami, and A. Brown. 2009. Tight functional coupling of kinesin-1A and dynein motors in the bidirectional transport of neurofilaments. Mol Biol Cell. 20:4997-5006.

van der Horst, A., and S.M. Lens. 2014. Cell division: control of the chromosomal passenger complex in time and space. Chromosoma. 123:25-42.

van der Vaart, B., W.E. van Riel, H. Doodhi, J.T. Kevenaar, E.A. Katrukha, L. Gumy, B.P. Bouchet, I. Grigoriev, S.A. Spangler, K.L. Yu, P.S. Wulf, J. Wu, G. Lansbergen, E.Y. van Battum, R.J. Pasterkamp, Y. Mimori-Kiyosue, J. Demmers, N. Olieric, I.V. Maly, C.C. Hoogenraad, and A. Akhmanova. 2013. CFEOM1-associated kinesin KIF21A is a cortical microtubule growth inhibitor. Dev Cell. 27:145-160.

van Riel, W.E., A. Rai, S. Bianchi, E.A. Katrukha, Q. Liu, A.J. Heck, C.C. Hoogenraad, M.O. Steinmetz, L.C. Kapitein, and A. Akhmanova. 2017. Kinesin-4 KIF21B is a potent microtubule pausing factor. Elife. 6.

Vedrenne, C., D.R. Klopfenstein, and H.P. Hauri. 2005. Phosphorylation controls CLIMP-63-mediated anchoring of the endoplasmic reticulum to microtubules. Mol Biol Cell. 16:1928-1937.

Verhey, K.J., and J.W. Hammond. 2009. Traffic control: regulation of kinesin motors. Nat Rev Mol Cell Biol. 10:765-777.

Walter, W.J., V. Beranek, E. Fischermeier, and S. Diez. 2012. Tubulin acetylation alone does not affect kinesin-1 velocity and run length in vitro. PLoS One. 7:e42218.

Wang, L., and A. Brown. 2010. A hereditary spastic paraplegia mutation in kinesin-1A/KIF5A disrupts neurofilament transport. Mol Neurodegener. 5:52.

Wu, J., C. de Heus, Q. Liu, B.P. Bouchet, I. Noordstra, K. Jiang, S. Hua, M. Martin, C. Yang, I. Grigoriev, E.A. Katrukha, A.F.M. Altelaar, C.C. Hoogenraad, R.Z. Qi, J. Klumperman, and A. Akhmanova. 2016. Molecular Pathway of Microtubule Organization at the Golgi Apparatus. Dev Cell. 39:44-60.

Xia, C.H., E.A. Roberts, L.S. Her, X. Liu, D.S. Williams, D.W. Cleveland, and L.S. Goldstein. 2003. Abnormal neurofilament transport caused by targeted disruption of neuronal kinesin heavy chain KIF5A. J Cell Biol. 161:55-66.

Yadav, S., P.J. Verma, and D. Panda. 2014. C-terminal region of MAP7 domain containing protein 3 (MAP7D3) promotes microtubule polymerization by binding at the C-terminal tail of tubulin. PLoS One. 9:e99539.

Yang, C., J. Wu, C. de Heus, I. Grigoriev, N. Liv, Y. Yao, I. Smal, E. Meijering, J. Klumperman, R.Z. Qi, and A. Akhmanova. 2017. EB1 and EB3 regulate microtubule minus end organization and Golgi morphology. J Cell Biol. 216:3179-3198.

Yang, T.T., W.M. Chong, W.J. Wang, G. Mazo, B. Tanos, Z. Chen, T.M.N. Tran, Y.D. Chen, R.R. Weng, C.E. Huang, W.N. Jane, M.B. Tsou, and J.C. Liao. 2018. Super-resolution architecture of mammalian centriole distal appendages reveals distinct blade and matrix functional components. Nat Commun. 9:2023.

Yang, X., M. Li, L. Wang, Z. Hu, Y. Zhang, and Q. Yang. 2015. Association of KIF21B genetic polymorphisms with ankylosing spondylitis in a Chinese Han population of Shandong Province. Clin Rheumatol. 34:1729-1736.

Yue, Y., T.L. Blasius, S. Zhang, S. Jariwala, B. Walker, B.J. Grant, J.C. Cochran, and K.J. Verhey. 2018. Altered chemomechanical coupling causes impaired motility of the kinesin-4 motors KIF27 and KIF7. J Cell Biol. 217:1319-1334.

Zhao, W.M., A. Seki, and G. Fang. 2006. Cep55, a microtubule-bundling protein, associates with centralspindlin to control the midbody integrity and cell abscission during cytokinesis. Mol Biol Cell. 17:3881-3896.

&

Addendum

Summary

Nederlandse samenvatting

Curriculum vitae

List of publications

Lekensamenvatting

Dankwoord/Acknowledgements

Summary

A network of microtubule filaments serves as a highway system in our cells. Motor proteins, like kinesin and dynein use these microtubules as tracks to move along or exert dedicated functions. While dynein is the major minus-end-directed motor, the kinesin superfamily is more diverse and contains over 40 members. Although many kinesin families, such as kinesin-1, -2 and -3, are well-known cargo transporters, many other kinesins have alternative roles (**Chapter 1**). Some kinesin motors, such as members of the kinesin-4, -5, -6, -7, -8, -10, -12 and -13 family, are important for proper cell division. Others, such as members of the kinesin-4, -8 and -13 family, are specialized in regulating microtubule dynamics by inducing microtubule depolymerization, inhibiting polymerization or stabilizing the microtubule end. In addition, kinesin motors can be tissue-specific or function at specific cellular sites such as cilia.

Kinesin-1 is one of the best-studied motors of the kinesin superfamily. In **Chapter 2**, we show that members of the MAP7 family of microtubule-associated proteins (MAP7, MAP7D1, MAP7D2 and MAP7D3) act redundantly in activating kinesin-1. In cells, kinesin-1 is dependent on the presence of at least one of these family members. To study the underlying mechanism, we made use of *in vitro* reconstitution assays where we grew microtubules on glass and added purified fluorescently labeled proteins, such as a kinesin or MAP. Subsequently, we used fluorescence microscopy to image these microtubules and molecules. *In vitro*, MAP7 proteins promote kinesin-1 landing on microtubules and increase its processivity. In addition, MAP7 proteins activate the motor through an allosteric effect. We show that kinesin-1 motility is promoted through a continuous flow of weak transient interactions with MAP7 bound along the microtubule.

In **Chapter 3**, we looked at microtubule-based transport of Rab6-marked exocytotic vesicles by the kinesin-1 KIF5B and kinesin-3 KIF13B motor. Although both kinesins could be present on the same vesicle, during vesicle transport their tasks were clearly divided. KIF5B is most active on perinuclear MAP7-decorated microtubules while KIF13B becomes important when a vesicle moves on the freshly polymerized microtubule segment. We showed that KIF5B is less dominant on such microtubule segments because MAP7 binds to them slowly and is less abundant there.

The microtubule binding region and kinesin-1-binding region of MAP7 family proteins show high sequence homology. However, the termini and the long linker region between these domains show little conservation between family members. Therefore, we sought to find new binding partners for all MAP7 family proteins in **Chapter 4**. We found novel potential interaction partners of which some may bind uniquely to a single family member, while others appeared to associate with multiple or even all MAP7 proteins. Specifically, we identified and validated clathrin as a unique binding partner of MAP7D2 and showed that clathrin can be potently recruited to microtubules through a conserved clathrin-binding motif located at the C-terminus of MAP7D2. We propose that MAP7D2 might play a role in transporting clathrin into axons in a microtubule-dependent manner.

To study the dynamic interactions between microtubules and microtubule-binding proteins such as kinesins and MAPs, we developed a protocol to produce isotope-labeled microtubules from mammalian cells to study such interactions using solid-state NMR (**Chapter 5**). As an example, we looked at the dynamic interactions between tubulin tails and MAPs such as MAP7 and the CKK domain of CAMSAP and found that these MAPs differently affect the fast time-scale dynamics of these tubulin termini. NMR studies like these can be employed in the future to study interaction dynamics between microtubules and MAPs.

Although kinesin motors are widely studied, the molecular activity of many motors is still poorly understood. The mitotic kinesin-6 MKLP2 (KIF20A) is known to be required for the relocation of the Chromosomal Passenger Complex from chromatin to the spindle midzone during the transition from metaphase to anaphase. Whether this translocation depends on motor activity of MKLP2 has long been debated. Here, we showed that MKLP2 is a motile kinesin, capable of transporting the Chromosomal Passenger Complex along microtubules *in vitro* (**Chapter 6**). Cellular experiments revealed that MKLP2 motor activity is indeed required for proper translocation of the complex during cell division. Combining cellular experiments with *in vitro* reconstitution assays may be used to understand the other mitotic motors whose molecular function are unclear.

In **Chapter 7**, we investigated the role of kinesin-4 KIF21B during immunological synapse formation in T cells. When a T cell binds an antigen presenting cell, a synapse is formed to which the centrosome and associated organelles are translocated. The *KIF21B* gene has been associated with autoimmune-related conditions and we demonstrated that KIF21B is indeed expressed in T cells. In these cells, KIF21B induces catastrophes and thus limits microtubule length. This activity is crucial to shape the microtubule network to allow centrosome polarization as overly long microtubules impair rapid remodeling of the network.

In this thesis, we shed light on the function and regulation of several kinesin motors. Our insights and methods may support future research in the field of motors and MAPs to understand how the microtubule network is exploited by these proteins to support the molecular processes in our cells.

Nederlandse samenvatting

Een netwerk van lange buisvormige filamenten, microtubuli, vormen een snelwegsysteem in onze cellen. Motoreiwitten, zoals dyneïne en kinesine gebruiken deze microtubuli als paden om langs te bewegen of om een specifieke functie op uit te oefenen. In tegenstelling tot de dyneïne motor, is de kinesine superfamilie van motoreiwitten heel divers en bevat deze meer dan 40 verschillende kinesine eiwitten. Hoewel sommige kinesine families, zoals kinesine-1, -2 en -3 bekend staan als de vrachtvervoerders in onze cellen, hebben veel andere kinesines een alternatieve functie (**Hoofdstuk 1**). Sommige kinesine motoren, van onder meer de kinesine-4, -5, -6, -7, -8, -10, -12 en -13 familie hebben een belangrijke rol tijdens de celdeling. Andere motoreiwitten, waaronder leden van de kinesine-4, -5 en -13 familie, zijn gespecialiseerd in het reguleren van de groeidynamica van microtubuli. Zo kunnen deze motoren de depolymerisatie van microtubuli induceren, polymerisatie remmen of het uiteinde van de microtubulus juist stabiliseren. Daarnaast zijn sommige kinesine motoren weefselspecifiek of functioneren op specifieke celstructuren zoals cilia.

Kinesine-1 is één van de meest bestudeerde motoreiwitten in het de kinesine superfamilie. In **Hoofdstuk 2** laten we zien dat eiwitten van de MAP7 familie van microtubuli geassocieerde eiwitten (MAP7, MAP7D1, MAP7D2 en MAP7D3) een overlappende functie hebben in het activeren van kinesine-1. Voor kinesine-1 activiteit in cellen is de aanwezigheid van minimaal één van deze vier MAP7 eiwitten nodig. Om het onderliggende mechanisme te begrijpen, hebben we gebruik gemaakt van *in vitro* reconstitutie experimenten, waarbij we microtubuli polymeriseren op glas en gepurificeerde fluorescent gelabelde eiwitten, zoals kinesine of MAP7, toevoegen. Vervolgens maken we gebruiken van de fluorescentie microscoop om processen op de microtubulus te bekijken en vast te leggen. In deze proeven werd duidelijk dat MAP7 eiwitten de landing van kinesine-1 motoren op de microtubulus bevorderen en dat de motor meer processief werd. Daarnaast activeren MAP7 eiwitten de motor door een allosterisch effect. We laten zien dat de motiliteit van kinesine-1 bevorderd wordt door een continue flux van korte en zwakke interacties met MAP7.

In **Hoofdstuk 3** hebben we gekeken naar de transport van Rab6-geassocieerde exocytotische vesikels door de kinesine-1 KIF5B en de kinesine-3 KIF13B motor. Hoewel beide kinesines aanwezig kunnen zijn op hetzelfde vesikel, is er een duidelijke taakverdeling tussen de twee motoren. KIF5B is het meest actief op MAP7-gedecoreerde microtubuli dicht bij de nucleus van de cel terwijl KIF13B pas in actie komt op nieuw gepolymeriseerde segmenten van de microtubulus. We laten zien dat KIF5B minder dominant is op deze segmenten, omdat MAP7 hier slechts langzaam op accumuleert en daardoor in mindere mate aanwezig is om KIF5B activiteit te stimuleren.

MAP7 eiwitten vertonen veel homologie in de domeinen die aan microtubuli en kinesine-1 binden. Dit in tegenstelling tot de termini en lange linker tussen deze twee domeinen; hier is de aminozuursequentie namelijk erg variabel tussen de verschillende MAP7 eiwitten. Om die reden zijn we in **Hoofdstuk 4** op zoek gegaan naar nieuwe interactiepartners voor alle MAP7 eiwitten. We hebben nieuwe potentiële interactiepartners geïdentificeerd, waarvan sommigen slechts aan één eiwit van de MAP7 familie binden, terwijl anderen bleken te binden aan meerderen of zelfs alle MAP7 eiwitten. Eén van de MAP7 eiwitten, MAP7D2, leek specifiek aan clathrine te binden. We hebben deze interactie gevalideerd en vonden dat MAP7D2 clathrine specifiek naar microtubuli toe brengt door een geconserveerd aminozuurmotief in de C-terminus van MAP7D2. Onze hypothese is dat MAP7D2 mogelijk een rol speelt in axonaal transport van clathrin op een microtubuli afhankelijke manier.

Om de dynamische interactie tussen microtubuli en microtubuli geassocieerde eiwitten (MAPs) te bestuderen hebben we een protocol ontwikkeld om isotoop-gelabelde microtubuli te produceren in zoogdiercellen. Deze techniek maakt het mogelijk om de binding van MAPs aan microtubuli te kunnen bestuderen met solid-state NMR technieken (**Hoofdstuk 5**). Als casestudy hebben we gekeken naar de dynamische interactie tussen de C-terminale staarten van tubuline en MAPs zoals MAP7 of het CKK domein van het CAMSAP eiwit. NMR metingen aan tubuline termini lieten zien dat deze MAPs een verschillend effect hebben op de dynamiek van deze flexibele staarten. Hier laten we zien dat NMR technieken zeer geschikt zijn om dynamische interacties te bestuderen tussen microtubuli en daaraan gebonden eiwitten.

Hoewel kinesine eiwitten veel bestudeerd worden, is de moleculaire activiteit van veel van deze motoreiwitten nog onduidelijk. Van de mitotische kinesine-6 MKLP2 (KIF20A) is bekend dat deze nodig is voor de verplaatsing van het Chromosomal Passenger Complex van chromatine naar overlappende microtubuli in het midden van het spoelfiguur tijdens de overgang van metafase naar anafase. Of motoractiviteit van MKLP2 nodig is voor de translocatie van dit complex is lang onderwerp van discussie geweest. Hier laten we zien dat MKLP2 motiliteit vertoont en in staat is om het Chromosomal Passenger Complex te vervoeren over microtubuli *in vitro* (**Hoofdstuk 6**). Experimenten in cellen tonen aan dat motoractiviteit van MKLP2 belangrijk is voor de translocatie van het complex tijdens de celdeling. Het combineren van dergelijke cellulaire proeven met *in vitro* reconstitutie proeven kan een krachtige benadering zijn om de moleculaire activiteit van andere mitotische motoreiwitten beter leren te begrijpen.

In **Hoofdstuk 7** staat de kinesine-4 KIF21B centraal en hebben we gekeken naar de rol van dit motoreiwit in de formatie van de immunologische synaps in T-cellen. Als een T-cel bindt aan een antigeen-presenterende cel, vormt de T-cel een synaps waarnaartoe het centrosoom met de daaraan geassocieerde organellen polariseren. Het gen wat codeert voor KIF21B is geassocieerd met auto-immuunaandoeningen zoals Multiple Sclerosis (MS) en de ziekte van Crohn en in onze proeven laten we zien dit KIF21B inderdaad tot expressie komt in T cellen. In deze cellen reguleert KIF21B de lengte van microtubuli door catastrofes te induceren aan de uiteinden van de polymeren. Deze activiteit is cruciaal voor de algehele organisatie van microtubuli, omdat het hebben van te lange microtubuli een remmende werking heeft op centrosoom polarisatie in T cellen.

In dit proefschrift hebben we gekeken naar de functie en regulatie van een aantal motoreiwitten. Onze verkregen inzichten en methodiek kan verder onderzoek in het gebied van motoreiwitten en microtubuli geassocieerde eiwitten vooruit helpen. Zulk onderzoek helpt ons te begrijpen hoe dit soort eiwitten de moleculaire processen in onze cellen ondersteunen.

Lekensamenvatting

Een netwerk van microtubuli vormt een snelwegenkaart in onze cellen. Motoreiwitten zoals kinesine bewegen stapsgewijs over een microtubulus en kunnen onder andere celonderdelen verplaatsen. Er zijn meer dan 40 verschillende typen kinesines die elk een unieke functie hebben in verschillende cellen van ons lichaam. In dit proefschrift is gekeken naar de functie en regulatie van een aantal van deze kinesines.

Eén van de meest bestudeerde kinesines is kinesine-1 en in dit proefschrift is aangetoond dat aan microtubuli gebonden MAP7 eiwitten essentieel zijn voor de motiliteit van dit motoreiwit in cellen. MAP7 eiwitten helpen kinesine-1 te landen op de microtubulus en stimuleren bovendien de activiteit van kinesine-1 door een directe binding.

In het tweede deel van het proefschrift is gekeken naar twee minder bestudeerde motoreiwitten: MKLP2 en KIF21B. De kinesine MKLP2 is betrokken bij de celdeling, maar de moleculaire activiteit was lang onduidelijk. Doormiddel van een karakterisering op moleculair niveau is nu duidelijk dat MKLP2 zich langzaam over microtubuli beweegt en het Chromosomal Passenger Complex, een belangrijke signaleringsmodule voor delende cellen, kan vervoeren. De KIF21B kinesine komt specifiek voor in T cellen, welke een belangrijk onderdeel vormen van ons immuunsysteem. In deze cellen reguleert KIF21B de lengte van microtubuli door aan de uiteinden van de microtubulus afbraak te stimuleren. Deze activiteit is belangrijk voor de mobiliteit van het microtubulus netwerk wat een snelle reorganisatie ondergaat als T cellen communiceren met andere immuuncellen of wanneer ze een ziekmakende cel moeten uitschakelen.

Curriculum Vitae

Peter Jan Hooikaas was born on June 16th 1991 in Hardinxveld-Giessendam, The Netherlands. He obtained his high school degree (Atheneum) at Lyceum Oudehoven in Gorinchem in 2009 and continued studying Biology at Utrecht University in 2010. After obtaining his bachelor's diploma in 2013, Peter Jan followed his interest in molecular biology by entering the Master's program Molecular and Cellular Life Sciences, again at Utrecht University. During a first internship in this program, he joined the lab of Prof. Dr. Anna Akhmanova to study the interaction between the kinesin KIF21A and a set of microtubule associated proteins. For a second internship, he moved to Paris to join the lab of Dr. Marco Vignuzzi. There, he studied insect-borne viruses and the immune response against these pathogens both in mammalian as in insect cells. Upon his return in The Netherlands, he broadened his horizon by following a minor "Fundamentals of Business and Economics", the theoretical component of the Science and Business Management master's program at Utrecht University. His fascination for microtubules and motor proteins and interest in performing fundamental research behind the microscope resulted in a PhD position in 2016 under the supervision of Prof. Dr. Anna Akhmanova. The results Peter Jan obtained during this research projects are described in this dissertation.

List of publications

Adriaans, I.E*., **P.J. Hooikaas***, A. Aher, M.J.M. Vromans, R.M. van Es, I. Grigoriev, A. Akhmanova, and S.M.A. Lens. 2020. MKLP2 Is a Motile Kinesin that Transports the Chromosomal Passenger Complex during Anaphase. Curr Biol. 30:2628-2637 e2629.

Luo, Y., S. Xiang, **P.J. Hooikaas**, L. van Bezouwen, A.S. Jijumon, C. Janke, F. Forster, A. Akhmanova, and M. Baldus. 2020. Direct observation of dynamic protein interactions involving human microtubules using solid-state NMR spectroscopy. Nat Commun. 11:18.

Hooikaas, P.J.*, M. Martin*, T. Muhlethaler, G.J. Kuijntjes, C.A.E. Peeters, E.A. Katrukha, L. Ferrari, R. Stucchi, D.G.F. Verhagen, W.E. van Riel, I. Grigoriev, A.F.M. Altelaar, C.C. Hoogenraad, S.G.D. Rudiger, M.O. Steinmetz, L.C. Kapitein, and A. Akhmanova. 2019. MAP7 family proteins regulate kinesin-1 recruitment and activation. J Cell Biol. 218:1298-1318.

Pan, X., Y. Cao, R. Stucchi, **P.J. Hooikaas**, S. Portegies, L. Will, M. Martin, A. Akhmanova, M. Harterink, and C.C. Hoogenraad. 2019. MAP7D2 Localizes to the Proximal Axon and Locally Promotes Kinesin-1-Mediated Cargo Transport into the Axon. Cell Rep. 26:1988-1999 e1986.

Mounce, B.C., T. Cesaro, G. Moratorio, **P.J. Hooikaas**, A. Yakovleva, S.W. Werneke, E.C. Smith, E.Z. Poirier, E. Simon-Loriere, M. Prot, C. Tamietti, S. Vitry, R. Volle, C. Khou, M.P. Frenkiel, A. Sakuntabhai, F. Delpeyroux, N. Pardigon, M. Flamand, G. Barba-Spaeth, M. Lafon, M.R. Denison, M.L. Albert, and M. Vignuzzi. 2016. Inhibition of Polyamine Biosynthesis Is a Broad-Spectrum Strategy against RNA Viruses. J Virol. 90:9683-9692.

Poirier, E.Z., B.C. Mounce, K. Rozen-Gagnon, **P.J. Hooikaas**, K.A. Stapleford, G. Moratorio, and M. Vignuzzi. 2015. Low-Fidelity Polymerases of Alphaviruses Recombine at Higher Rates To Overproduce Defective Interfering Particles. J Virol. 90:2446-2454.

Preprints:

Serra-Marques, A., M. Martin, E.A. Katrukha, I. Grigoriev, C.A.E. Peeters, Q. Liu, **P.J. Hooikaas**, Y. Yao, I. Smal, L.B. Pedersen, E. Meijering, L.C. Kapitein, and A. Akhmanova. 2020. Concerted action of kinesin-1 KIF5B and kinesin-3 KIF13B promotes efficient transport of exocytotic vesicles to microtubule plus ends. bioRxiv:2020.2004.2006.027862.

Hooikaas, P.J., H.G.J. Damstra, O.J. Gros, W.E. van Riel, M. Martin, Y.T.H. Smits, J. van Loosdregt, L.C. Kapitein, F. Berger, and A. Akhmanova. 2020. Kinesin-4 KIF21B limits microtubule growth to allow rapid centrosome polarization in T cells. bioRxiv:2020.2008.2028.271643.

Dankwoord

Het schrijven van de thesis lijkt op voorhand een eenzaam avontuur. Mijn terugblik aan deze periode lijkt mij echt het tegendeel doen geloven. Ik heb me namelijk continu heel erg gesteund gevoeld in het hele proces wat geëindigd is met dit boekje. Ik ben daarom iedereen in mijn omgeving enorm dankbaar voor alle gegeven succeswensen, oprechte interesse en hulp die ik in de afgelopen maanden van schrijven en jaren van onderzoek doen heb gekregen. Je doet en kunt het echt niet in je eentje. Mijn dank!

Anna, het begon allemaal ruim 7 jaar geleden met een masterstage in jouw lab. Ik ben je nog steeds enorm dankbaar voor de positie die je me in 2016 in je lab gegeven hebt. Wat heb ik in al die jaren enorm veel van je geleerd! Van de moleculaire biologie en bijkomende academische vaardigheden tot aan het managen van projecten en alle bijkomende politiek. Ik bewonder je toewijding, je onstilbare interesse in de moleculaire vraagstukken en je doorzettingsvermogen wat aan dit alles verbonden zit. Je probeert altijd het beste in mensen naar boven te halen en bent enorm behulpzaam en bereikbaar als het nodig is. Dank voor al je supervisie, al je feedback en hele fijne samenwerking; ik weet zeker dat ik het allemaal onwijs ga missen in m'n volgende carrièrestap.

Ik wil ook alle leden van de **lees- en promotiecommissie**, Erwin Peterman, Judith Klumperman, Geert Kops, Sander van den Heuvel en Alexandre Bonvin bedanken voor het lezen, het beoordelen van het proefschrift en het deelnemen aan de ceremonie.

Lukas, dankjewel voor al je hulp en de kritische blik over mijn kinesine data; het heeft veel van de hoofdstukken in mijn proefschrift enorm vooruit geholpen. Je enthousiasme voor de microscoop en het imagen zullen me altijd bijblijven. Ik twijfel er niet aan dat we nog veel mooie papers met gave imaging uit jouw lab gaan zien de komende jaren!

Paul, Corette, Casper, Sabrina, Ginny, Sander, Mike, thanks for all your great questions and the input you gave me during the meetings!

I want to thank the many, many people that were part of all the projects in this thesis. A big thank you to **Michel**, **Tobias**, **Stefan** and **Luca**, I'm very thankful for your help on the MAP7 project and I very much enjoyed our discussions. **Susanne** en **Ingrid**. Dankjewel voor de enorm fijne samenwerking en gezelligheid die we hebben gehad met het MKLP2 project. Wetenschap doe je samen! Ik wens jullie allebei het allerbeste toe. **Marc** and **Jon**. Thank you both for the nice collaboration! Jon, we had such a great scientific trip to Carsten Janke's lab in Paris. It was an amazing and fruitful experience. I hope you are doing well at Wageningen University and wish you the best for the future! **Agnes**, good luck on the continuation of the MAPs & NMR project, I'm pretty sure you'll find some interesting results!

Dankjewel **Helma**! In 2013 maakte ik mijn eerste stappen in het lableven en deze waren zeker niet makkelijk, voordat dingen begonnen te werken. Dank voor al je geduld, hulp en gezelligheid gedurende die tijd! Ik wens je het allerbeste toe, zowel voor je carrière als persoonlijk voor jou, Roel en Rowan.

I'd also like to thank my previous supervisors who helped me tremendously in becoming the scientist I am today! **Enzo**, thank you so much for your great supervision, your wisdom and life lessons on the French life. I will never forget the disturbing look on your face when

I suggested to get a bottle of red wine to accompany a cheese fondue party. **Bryan**, thanks for all the life lessons and insights you gave me on life as a scientist. Thanks for all the fun moments in Paris. I wish you and your lab the best for the future! **Gonzalo**, I will never forget our goodbye: “never change who you are”. It meant a lot to me, thank you for all your life lessons! **Marco**, thanks a lot for having me in your lab! I'm still very grateful for that opportunity. I hope the plants I left behind are still thriving! **Stéphanie**, merci beaucoup for all your great company and fun in the lab and I'm sorry for all the practical jokes that got out of hand. **Jacob, Gabriel, Rasmus** and **Yingdi**, thank you guys so much for your friendship and all the good times we had in Paris. I cherish great memories of those days.

Maud! Thanks a lot for the great time and fun! I'm very grateful that we could talk so much on the struggles of our scientific lifes. I'm so happy we were able to make such a cool MAP7 story together. Also thanks again for having us over in Belgium, it was such a lovely weekend! I wish you the best for you, your family and the lab in Belgium! À bientôt!

Hugo, toen je als Bachelor student een projectje kwam doen was ik al meteen overtuigd: “wat een slimme gast!” Als masterstudent ben je helemaal losgegaan met alle microscopen op het T-cell project, wat een gave dingen heb je toen laten zien. Ik was enorm blij dat je na je master terug wilde komen om als PhD collega verder te gaan. Ik wens je enorm veel succes met je gave projecten. Dank voor alle gezelligheid, discussies en interessante gesprekken in onze tijd op het lab! **Gert-Jan**, lekker nuchter en met een goede portie humor! We konden het echt goed met elkaar vinden op het lab en ik mis die tijd nog zeker. Ik vind het superknap dat je een joint-PhD ben begonnen tussen twee labs, tussen twee verschillende steden. Heel veel succes met het afronden van je PhD binnenkort en ik wens je het beste voor wat de toekomst je gaat brengen. **Stanley**, man, man, man, wat heb jij je enorm weten te ontwikkelen in die tijd op ons lab! Altijd vriendelijk, vrolijk en in voor een grapje. Ik ben enorm trots op hoe je bent afgestudeerd van je HBO Bachelor en je hebt doorgepakt richting de MCLS master. Ik hoop dat je je passie in het lab weet te vinden en wens je het allerbeste toe voor de toekomst!

Thanks for all the amazing and cool people (**Amol**, **Helma**, **Qingyang**, **Chiung-Yi**, **York**, **Dipti** and **Cyntha**) I got to share the Z502 office with! Muchos thanks **Amol** for all the great times, discussions and talks we had! I still miss these days very much and I hope we can hang out for a drink in the future! Thanks for all the fun times **Chiung-Yi**! I'm very happy we could share our love for kinesins in the office; I hope I didn't block your sunlight too much in the office these years. I expect to hear great things from you as a data scientist :). Thank you **Dipti**! I've always been amazed with your dedication and work ethos in the lab. I very much hope you can make your scientific dreams come true, I believe in you! Thanks for all the discussions we had and suggestions you gave me these years. **Cyntha**! Begin 2013 werden we huisgenoten en eigenlijk zijn we dat nog steeds in Z502 (pre-COVID); wie had dat toen kunnen verzinnen! Dankjewel voor alle leuke tijden, gezelligheid en je mentale support in de bekende ups en downs. Ik ben echt superblij je als collega op het lab te hebben meegemaakt. Ik wens je veel succes en plezier met het voortzetten van je toffe experimenten! **York**, soul-mate York! Samen hebben we de PhD overleeft! Ik weet zeker dat onze “donkere humor” daar enorm bij geholpen heeft, haha! Dank voor al je support en het klankbord wat je vaak voor me was tijdens de PhD. Ik twijfel er niet aan dat je volgende carrièrestap een groot succes wordt! Ik wens jou en Elodie het aller, allerbeste toe voor de toekomst! (Oh ja, sorry voor de keren dat ik je heb laten schrikken in het lab).

Ankit, we have spent the past almost 5 years together in the lab and I've learned so much from you in all these days, thank you! I wish you the best in finding an exciting new opportunity in India and I wish you and your family all the best for the future! **Kyle**, thanks for all the nice chats and discussions we had! Great to see that the science on motors is safe in your hands, I'm looking forward to see the results somewhere published in the future! **Funso**, thanks a lot for all the nice lab chats in the early morning. I wish you the best in the remainder of your post-doc! **Joyce**, leuk je ontmoet te hebben in Anna's lab! Dankjewel voor al onze leuke gesprekken over positive vibes, het buitenleven en de natuur! Ik hoop dat je iets ontzettends moois weet te maken van je light-inducible projecten met microtubuli, je bent er zeker geknipt voor! **Boris**, thank you for expanding my horizon in music taste! It is a pleasure having you in the lab, I'm for sure going to miss the daily 2 minunte Dutch vocabulary classses we did. I wish you the best both with the research on muscle cells as well as with your personal life! **Babet**, dankjewel voor alle gezellige kletspraat en dolletjes in de lab en ook zeker dank voor alle serieuzere gesprekken die we op z'n tijd hadden. Ik wens je het allerbeste toe voor je toekomst, zowel carrièrewijs als persoonlijk! **Ruddi**, it was so much fun having you in the lab as a colleague! I enjoyed our conversations and would like to thank you for your hospitality and of course the road trip to Belgium! I wish you and your family the best for the future! **Ruben**, de stiekeme collega die al die jaren de weg naar het Akhmanova lab niet wist te vinden. Dank voor al je vriendelijkheid en gezelligheid op de afdeling! **Milena**, I remember very well the struggles of me walking too fast through the department when I had to show you around, I'm so sorry for the times you almost had to run to keep up with me :'). Thanks for all the talks, fun and good times in the lab and I wish you the best for your PhD projects! **Emma**, de nieuwste toevoeging op het lab! Het zijn echt rare tijden om je PhD in te beginnen, maar volgens mij pak je het echt onwijs goed op! Ik wens je heel veel succes en het allerbeste toe voor de toekomst. **Fangrui**, my neighbour for almost 4 years! I'm so so impressed how you run your complex project in the complex setup of your lab bench. You're always happy, cheerful and helpful! I wish you the best of luck finishing your PhD and wish you and your family the best for the future! **Eugene**, wat jij allemaal doet en bewerkstelligt op onze afdeling is heel indrukwekkend! Ontzettend veel dank voor al je hulp en adviezen over de jaren. Je bent zo'n aardige, toffe gast en ik denk nog vaak terug naar de Belgium road trip die we vorig jaar maakten. Ik wens je veel succes en geluk toe! **Ivar**, ik heb je altijd bewonderd om je time management en hoe soepel alles bij jou lijkt te gaan op het lab. Dank voor al je hulp en gezelligheid op het lab en dat je mee meegesleurd hebt naar het vroege ochtend baantjes trekken in de Kromme Rijn! Man, man, man, wat is dat water toch "dik en stroperig" in de vroege ochtend. Ik wens je heel veel succes en plezier met de voortzetting van je post-doc daar in het verre Brisbane! Also a big thank you to all the other lab members in the past, **Kai, Shasha, Ben, Chao, Andrea,** I'm grateful for meeting you guys and all the things you've helped me with in the lab. Next to all the Akhmanova-pipetters that were there as a colleague, I'd also like to thank all the students (**Chris, Sanne, Martyna, Matthijs, Vika, Gert-Jan, Cédric, Wouter, Tonja, Guus, Cathelijn, Bas, Floranne, Hugo, Gianmarco, Jacob, Ola, Jelle, Arianna, Miquel, Christie, Maxime, Stanley, Imke, Robin, Jannes, Stefanos**) that joined the lab over the past years and contributed to the "Gezelligheid" in the lab; I enjoyed having you guys around!

To the MacGillavry lab, **Harold** en **Lisa**, dank voor jullie hulp met het MAP7D2-clathrine zijspoor! Lisa, dank voor al die neuronen die je hebt getransfecteerd voor ons, je gezelligheid en kletspraat over die gekke Auriollaan. Ik wens je heel veel succes en plezier in het laatste beetje van je PhD! **Nicky**, **Jelmer** en **Manon**, wat een supergave, interessante projecten laten jullie elke keer weer zien! Echt indrukwekkend. Dank voor al jullie gezelligheid op de

verdieping en met alle IB avonden, ik wens jullie een mooie toekomst!

To the neighbours from the Hoogenraad lab, **Martin**, altijd in voor een borrel of feestje! Dank voor je gezelligheid en niet te stuiten enthousiasme over projecten en toffe experimenten! Ik weet zeker dat de toekomst ondanks sommige hobbels een hoop goede dingen voor je in petto heeft! **Xingxiu**, Dr. Pan! Thanks for all our interesting discussions and chats on the MAP7 proteins. You're such a great and enthousiastic scientist and wish you the best of luck for your future career! **Feline**, Dr. Lindhout! Dank voor al je gezelligheid en discussies die we sinds 2013 (!) gehad hebben. Ik wens je echt onwijs veel succes en plezier toe in Cambridge; je bent een hele goede wetenschapper zowel sociaal als op de inhoud en ik twijfel er niet aan dat je het met deze combi ver gaat schoppen! **Jessica**, ik ben echt diep onder de indruk van je wilskracht, al je skills en projecten! Ik wens je heel veel succes met het afronden van je PhD! **Sybren**, wie had in 2013 verwacht dat we anno 2020 nog steeds samen op dezelfde verdieping van het Kruijt zouden rondlopen?! Dank voor al je gezelligheid in die tijd en veel succes ook met de laatste lootjes van de PhD! **Robbelien**, ooit komt er een dag dat we foto's kunnen uitwisselen van de scharrelende kipjes en schaapjes die vrolijk ronddartelen op onze eigen stukjes platteland! Dank voor al je gezelligheid en humor in de afgelopen jaren en wat tof dat ik ook nog een klein dingetje voor je CRMPs heb kunnen doen.

Wilco, "Ik kan het altijd nog aan Wilco vragen, die heeft er sowieso een antwoord of suggestie op" hoort definitief op de uitspraken-bingokaart in mijn PhD. Man, man, wat weet jij veel en wat heb je een enorm goede blik op de zaak. Dank voor alle keren dat je me van hulp en advies hebt voorzien. Ik ga je humor en gezelligheid zeker missen! Ik wens je veel geluk en succes toe in de toekomst! **Klara**, altijd behulpzaam, in voor gezelligheid of een discussie over kinesines, dank daarvoor! Je bent een enorm gedreven en pientere wetenschapper; ik wens je veel succes met al je toffe projecten! **Roderick**, de kinesine-goeroe! Ik heb heel veel van je geleerd over kinesine-1 en hoe je dat gekke ding zou moeten purificeren. Je bent een hele toffe gast en ik vind het leuk dat ik een groot deel van m'n PhD met je heb doorgebracht. Je hebt een dappere switch gemaakt voor je post-doc en ik twijfel er niet aan dat het je heel goed af gaat daar in Eindhoven! **Anne**, dank voor alle gezelligheid aan de lunchtafel en met IB-avonden, onze leuke gesprekken en ook al je morele support! Ik hoop dat je het ontzettend naar je zin hebt in Cambridge en dat het een onwijs succesvol avontuur voor je is.

Dennis, wat een gemis sinds je weg bent bij Cellbio! Altijd wel in voor een leuk kletspraatje en even een portie gemopper waar we daarna hard om kunnen lachen. Ik vind het jammer dat ik je nooit heb weten te overtuigen van de correcte samenstelling van een "frikandel speciaal"; deze is namelijk met curry, geen ketchup. Dank voor alle leuke momenten op de afdeling en ik hoop dat je het ontzettend leuk gaat hebben als docent in Amsterdam! **Lotte** en **Marijn**, de dappere opvolgers van mijn IT-taakje (dank voor de verlossing)! Dank voor alle gezelligheid en heel veel succes met het laatste deel van de PhD. **Florian** and **Oane**, what an awesome project to model those T cells! I'm very impressed with your expertise. Thank you both for the great discussions and chats on the KIF21B project, let's hope it gets out there soon. I wish you both the best for your future careers! **Ilya**, Thank you so much on all your help with the microscopes, it's incredible how you keep the whole facility running with your magic hands. Thanks also for your feedback on my imaging and all the fun talk we had in the lab. **Bart, Phebe, Esther** en **Lena**, jullie zijn voor mij echt de vertrouwde gezichten van Cellbio en ik ga jullie en de kletspraatjes op de gang zeker missen! Bart, hoe moet ik nou de week doorkomen zonder een gezond portie "Bart-grappen"? Misschien moeten we er nog maar snel even een bundel van maken. Phebe, dank voor al je hulp en je enorme werk om de boel draaiende te houden; we zouden niet zonder je kunnen!

Sofia, thanks for all the nice chats and laughs whenever I visited the north wing. I'll never forget you witnessing my hilarious crash I made from the small stool at the Odyssey. I wish you the best of luck at the other end of the Science Park! **Robin, Katerina, Maria Cátia & Reinier**, a.k.a. the West-Side squad! Thank you guys for all the great times and friendship! Our times at Cellbio are ending or have ended, but I'm sure you all have a bright future ahead! Let's keep the West-side spirit alive :). Robin and Katerina, thanks a lot for all the moral support with finishing the PhD, I hope we'll get to see your defenses and writings soon as well! Good luck on those final experiments and writing.

René, Anna, Mithila, Amélie, Yolanda, Arthur, Max, Josiah, Eitan, Ate, Wouter, Derk, Liu, Malina, Daphne, Giel, Thomanai, Jian, Vida, Mai Dan, Nazmiye, Carlijn, Sara, Sebas, Erik, Yujie, Elena, Gabriela, Eliana, Olga, Inês, Desiree, Riccardo, Marvin, Andrea, Carol, Kah Wai, Bas, Marta, Jingchao, Michael, Dieudonnée, Hai Yin, Elske, **Jan Andries**, **Laurens**, **Ron** and **Marjolein**, thanks for all the nice chats and laughs in the corridors, behind the microscopes, at the lunch tables, during lab outings, etc!

Ik wil ook alle lieve familie en vrienden bedanken buiten het lab bedanken! Wat fijn dat jullie er waren als ik wat stoom moest afblazen over dit hele lab avontuur. Het is altijd lastig uit te leggen wat er überhaupt in dit boekje geschreven staat, maar dank dat jullie altijd een luisterend oor waren.

Mijn zwemtalenten hebben er de afgelopen jaren erg onder geleden en onhandig een sneeuwbal gooien heeft het er allemaal niet beter op gemaakt. Desalniettemin dank dat het als vanouds gezellig met jullie is, **Berrie & Eveline (en Sophie!), Arjen, Linda & André, Niels, Richard, Robbert & Manon**!

Hendrik-Jan en **Arjen**, (pand)epische filmavonden en gezellige biertjes in de stad; dank voor jullie gezellige afleiding in dit hele onderzoeksavontuur! Hendrik-Jan, dit keer geen boekenruil, en eerlijk gezegd zou ik dit boekje ook niet aanraden voor je leeslijst. Ik waardeer onze leuke discussies, laten we ook weer een keertje boekje wisselen!

Shout out naar de Coole mensen! **Marlon, Elder & Laura, Nick, Judith & Javi**, wat tof om allemaal gezellige avondjes met jullie te hebben; drankje hier, spelletje daar, avondje Tivoli, etc. Fijn dat ik bij jullie ook altijd kan kletsen over de frustraties van de PhD; ik ben echt heel blij dat ik jullie dan nu eindelijk het boekje kan laten zien!

Eva & Randy, dank voor alle leuke avondjes en onwijze gezelligheid. Dagje Efteling, Oudjaarsavond of gewoon in de regen met de tuin bezig zijn, met jullie is het altijd onwijs leuk! Dank dat ik altijd m'n verhaal ook kwijt kon over alle ups en downs die ik onderweg heb meegemaakt.

Marisa, hoe hadden we onszelf door de crisis moeten slepen zonder alle quarantaine-theetjes! Dank voor alle bemoedigende woorden en gezelligheid in het hele schrijfproces. Wat fijn om zo'n toffe buurvrouw te hebben!

Lima & Sanjay, wat zijn jullie allebei toch een lieverds! Onwijs veel respect voor hoe jullie het samen doen in Nepal, 2020 maak het er allemaal niet makkelijker op. Dank voor alle interessante gesprekken en ook jullie oprechte interesse in wat ik op het lab allemaal probeer te doen; ik hoop dat ik het een beetje heb kunnen uitleggen.

Victor & Miriam, dankjulliewel voor de leuke avondjes en gezelligheid. Als we elkaar zien is het altijd heel fijn en gezellig als vanouds!

Mirjam & Jean-Paul, alweer flink wat jaartjes kom ik bij jullie over de vloer. Dank voor jullie lieve, warme ontvangst, alle gezellige momenten en het meeleven met het hele promotietraject! **Paul & Marjolein**, dank voor al jullie gezelligheid en spelletjesmomenten; het is onwijs fijn om lekker even een maffe bui met jullie te kunnen hebben om al het serieuze gedoe even te kunnen vergeten! Paul, dank voor alle discussies en carrière suggesties. Oma **Floor**, ik geef je dit boekje met veel trots! Per heden een "Doctor of Philosophy (PhD)" in de familie! **Amira & Clive**, dank voor al jullie medeleven, support en gezelligheid!

Ik wil hier een speciaal stukje schrijven voor tante **Paulien**. Zo'n 20 jaar geleden stonden we samen paddenstoelen te plukken en uit te graven in een bos bij Oosterhout, omdat ik daar zo nodig in groep 8 een spreekbeurt over wilde geven. Ik weet zeker dat die ervaring een vlammetje in mij heeft ontstoken wat me naar de natuur en biologie toe trok. Dank voor het onbewust geven van dit juiste zetje in de richting waar ik op ben gegaan en natuurlijk ook dank voor al je bekommeringen, wijsheid én inspiratie door de jaren heen!

Dank ook voor alle lieve familie in Hardinxveld en omstreken (**Dicky & Arie, Ina & Jan, Kees & Cobi, Wilma & Martien en Thom, Angela, Sonja, Ard en Sophie, Jan & Susanna en de kids)** voor jullie meeleven, steun en interesse de afgelopen jaren!

Pap & mam, dank voor jullie onvoorwaardelijke steun in al die jaren. Jullie hebben me al de mogelijkheden gegeven om te komen tot waar ik nu ben. In de afgelopen jaren ben ik jullie steeds meer en meer gaan terugzien in mezelf: het de boel managen en het 'out of the box' creatieve van jou, pap en de enorme betrokkenheid en het doorzettingsvermogen van jou, mam. Ik ben enorm dankbaar dat er een warm thuis is waar ik altijd welkom ben. Het afgelopen jaar was en is nog steeds een taaie, maar ik twijfel er niet aan dat we weer stappen naar voren aan het zetten zijn. Alles komt goed, dit boek draag ik op aan jullie!

En dan **Rosanna**, je hebt de rit van A tot Z met me meegemaakt en ik kan in woorden niet uitdrukken wat je in die tijd allemaal voor me hebt betekend. Je was er als het allemaal even tegen zat en je praatte me van tijd tot tijd uit de spreekwoordelijke put. Samen hebben we ook alle hoogtepunten en overwinninkjes gevierd; de ene keer met een fles champagne, de andere keer met gewoon een heel gek dansje. Je bent mijn rots in de branding. Ik hou van jou en heb onwijs veel zin in alle avonturen (en burgerlijkheid) die de toekomst ons gaat brengen!

Zo dan, c'est tout!